7 of 20

SCIENTIFIC NOTEBOOK

by

Stuart A. Stothoff

No. 163

SCIENTIFIC NOTEBOOK

by

Stuart A. Stothoff

No. 163

Southwest Research Institute
Center for Nuclear Waste Regulatory Analyses
San Antonio, Texas

July 15, 1997

Initial Entries

Scientific NoteBook: # 163

Issued to: S. A. Stothoff

Issue Date: Tuesday, November 16, 1993

By agreement with the CNWRA QA this NoteBook is to be printed at approximate quarterly intervals. This computerized Scientific NoteBook is intended to address the criteria of CNWRA QAP–001.

Table 0-1: Computing Equipment

Machine Name	Type	OS	Location
sierra.cnwra.swri.edu	Sun SPARC 20	SUNOS 4.1.3_U1	desk Rm A-212, Bldg. 189
sisyphus.cnwra.swri.edu	Sun SPARC 20	SUNOS 4.1.3_U1	network
dopey.cnwra.swri.edu	Sun SPARC 10	SUNOS 4.1.3_U1	network
performer.cnwra.swri.edu	SGI Onyx	IRIX 5.3	network
yosemite.cnwra.swri.edu	SGI Onyx	IRIX 5.3	network
bemore.cnwra.swri.edu	SGI Onyx	IRIX 6.2	network
redwood.cnwra.swri.edu	SGI Indy	IRIX 6.2	network
bigbend.cnwra.swri.edu	Sun Ultra-2	SUNOS 5.5.1	network
scratchy1.cnwra.swri.edu	Sun Ultra-2	SUNOS 5.5.1	network
hornet.cnwra.swri.edu	Sun Ultra-2	SUNOS 5.5.1	network

Contents

Initial Entries ii

List of Figures iv

List of Tables v

1 Ambient Hydrology KTI – Infiltration 1

2 Thermal Hydrology KTI 63

3 Iterative Performance KTI 64

4 Iterative Performance KTI - Total Performance Assessment Phase 3 65

5 Breath code development 84

6 Ambient KTI – Vertical ODE Solver 94

7 Boundary Element Methods for Steady-State Unsaturated Fractured Media 95

8 Geomorphology of Mountain Erosion 96

9 Environ - Evaluation of Mass Balance Errors in PTC 97

10 Quick Looks 98

List of Figures

1-1 1/13/97. Regression of borehole alluvium depths with nearest-neighbor DEM slopes. 34

1-2 1/15/97. Least-squares fit of simulation prediction to abstraction prediction for various exponents in Equation 1-20. 35

1-3 2/27/97. Time history of decadal-average moisture flux after each of 6 decades, as a function of AAP and AAT, for (a) hourly meteorologic input and bedrock 1, (b) daily meteorologic input and bedrock 1, (c) hourly meteorologic input and bedrock 2, and (d) daily meteorologic input and bedrock 2. 40

1-4 7/14/97. Areal-average MAI for Yucca Mountain area, using regression formula based on soil/open-fracture system, (a) in dimensional form, and (b) in nondimensional form. 59

List of Tables

0-1 Computing Equipment ii

1-1 Statistical behavior of net infiltration (AAI in mm/yr). 3

1-2 Summary of tight-grid infiltration simulation results 5

1-3 Summary of alluvium ($abcd$) and fracture ($efgh$) parameter codes 6

1-4 Summary of colluvium and matrix properties used in simulations. 26

1-5 Best-fit abstractions to material properties in deep alluvium. 36

1-6 Regression values for deep-alluvium meteorologic abstraction. 37

1-7 Regression coefficients for deep-alluvium meteorologic abstraction. 37

1-8 Hydraulic conductivity measurements in Solitario Canyon on March 27 and 28, 1997. 48

1-9 Summary of alluvium ($abcd$) and fracture ($efgh$) parameter codes 52

1-10 Net infiltration (mm/yr) for various cases with soil- and calcite-filled fractures 53

4-1 Adjustable parameters for creating colluvium distributions. 73

1. Ambient Hydrology KTI – Infiltration

Account Number: **20-5708-861**
Collaborators: **Amvrossios Bagtzoglou, Gordon Wittmeyer**
Directories: **$SubRegBreath and as noted**

Objective: Perform detailed analysis of the spatial and temporal distribution of infiltration at Yucca Mountain. A good deal of previous work is documented in the Scientific Notebook for the Subregional Flow and Transport Processes Research Project (subregional project) and various publications under the subregional project and the umbrella of the Iterative Performance Assessment and Performance Assessment Research projects. The research projects were closed out due to reorganization of the NRC and consequently CNWRA; infiltration work is largely being subsumed under the Ambient Hydrology KTI, with some applications possible under the Thermal Effects on Flow KTI in order to examine heating effects on infiltration. Initial efforts in the new project are to be directed towards documenting the work already completed in journal articles. Future work will depend very much on funding and time availability, but several avenues that may be explored include: (i) the impact of matrix-fracture interactions; (ii) watershed-scale modelling, with vegetation and lateral flow accounted for; (iii) geochemical tracer verification; and (iv) "shallow" diversion of infiltration due to the PTn layer.

1/26/96 Initial entry. SAS

Work on infiltration under the subregional project and IPA is currently being documented in two journal articles. The first article deals with the impacts of hydraulic properties on 1D infiltration; the second looks at meteorology, documents the alluvium flow model, and estimates spatial and temporal distributions of infiltration. All simulations to date have been 1D; the first sets examined semi-infinite alluvium columns, with later sets looking at a shallow alluvium layer over a fracture continuum. It is quite clear that the fracture continuum will allow far more water to infiltrate than the alluvium columns; a relatively thin alluvium coating (less than 50 cm) will shut off fracture flow entirely, but sufficiently deep alluvium (greater than 5 m) will allow the flow to resume; hillslopes and ridgetops are the most important infiltration areas; micrometeorology is not a great factor, nor is the fracture description if there is enough fracture porosity; alluvium hydraulic properties have a significant influence, increasing with depth, but the depth of alluvium is the single most important parameter; detailed hourly description of meteorology is only important near precipitation events; and it is critical to use arithmetic averaging or upstream weighting for conductivities in the fracture

continuum.

In the process of creating traces of infiltration rates, it became apparent that several of the cases with very shallow alluvium covers (2 cm and 5 cm) spuriously created mass for one or more storms. Increasing the resolution in the top layer from roughly 1 cm per element to 1 mm per element fixed the problem for the simulations that were rerun this week (temperature and precipitation perturbations). Unfortunately, even though the new results show excellent self-consistency, there is significant deviation between the coarse and fine cases (roughly 50 percent less infiltration for 2-cm cases). A revised set were set off today for the hydraulic properties, but it takes roughly a day per simulation so it will be several weeks before all are completed.

1/30/96 Data Analysis. SAS

Created matlab files to analyze the lowest flux trace from a set of breath runs. The workhorse file, **stat_infil.m**, is in ***$HOME2/Matlab/BreathUtil***. Copies of the driver routine, **eval_all_stat.m**, must be put in the result directory of interest. Filled out a table for temporal behavior of infiltration in the paper on the spatial/temporal distribution of infiltration, aside from the 10-cm case which must be rerun due to accidental erasure of the trace files. The table is included here as Table 1-1. Also tracked down many of the figures to be included and rearranged the directory structure below ***$HOME2/Subreg*** to have better segregation of figures. New directories containing figures now are listed as ***FigureXxxx***, where ***Xxxx*** is one of ***Paper*** or ***YMElev***.

2/17/96 Error in viscosity units. SAS

A persistent mistake was found in the specification of viscosity, dating from the earliest runs using *breath*. *breath* uses consistent units for all variables; however, the *Matlab* files used to create inputs for *breath* consistently uses viscosities three orders of magnitude too large. There is no net impact on the results when saturated conductivity is provided as data, as *breath* requires intrinsic permeability rather than saturated conductivity and intrinsic permeability is obtained by scaling hydraulic conductivity with the incorrect viscosity, which in turn is scaled back internally to *breath*. Accordingly, test problems based on saturated conductivity have been correctly calculated, since intrinsic permeability and viscosity are incorrect in compensating ways. Many other simulations are perfectly valid. Unfortunately, all sequences of infiltration experiments performed with alluvium and fractures have alluvium permeability specified (fracture saturated conductivity is specified), so that the reported permeabilities are actually off by three orders of magnitude. The *breath* code has

Table 1-1: Statistical behavior of net infiltration (AAI in mm/yr).

Depth (cm)	Multiple of AAP	°C Added to AAT	AAI	Wettest Year AAI	Wettest Year Events	Driest Year AAI	Driest Year Events	Events Max	Events Min
2	1.0	0	58.2	172.5	5	9.5	1	7 (1)	1 (1)
2	0.9	0	48.1	149.5	5	7.9	1	6 (2)	1 (1)
2	1.1	0	67.0	196.5	5	11.16	1	10 (1)	1 (1)
2	1.0	+3	50.6	158.2	5	8.79	1	6 (2)	1 (2)
2	1.0	−3	68.7	191.2	5	10.34	1	10 (1)	1 (1)
5	1.0	0	31.0	124.7	7	0.29	0	7 (1)	0 (1)
5	0.9	0	23.7	101.2	5	> 0.01	0	7 (1)	0 (2)
5	1.1	0	38.6	147.9	5	2.98	1	5 (2)	1 (3)
5	1.0	+3	25.3	108.3	5	0.59	0	5 (1)	0 (1)
5	1.0	−3	38.7	148.3	5	2.18	1	6 (1)	1 (3)
10	1.0	0	12.5	60.1	4	> 0.01	0	4 (1)	0 (3)
10	0.9	0	8.73	42.8	4	> 0.01	0	4 (1)	0 (5)
10	1.1	0	TBD	TBD	TBD	TBD	TBD	TBD	TBD
10	1.0	+3	9.68	49.9	4	> 0.01	0	4 (1)	0 (4)
10	1.0	−3	16.8	81.8	4	> 0.01	0	4 (1)	0 (3)
15	1.0	0	4.61	26.7	2	> 0.01	0	2 (2)	0 (7)
15	0.9	0	2.65	13.9	1	> 0.01	0	2 (1)	0 (8)
15	1.1	0	6.26	33.3	3	> 0.01	0	3 (1)	0 (6)
15	1.0	+3	3.18	17.3	2	> 0.01	0	2 (1)	0 (8)
15	1.0	−3	7.74	45.8	4	> 0.01	0	4 (1)	0 (7)

a temperature-dependent viscosity option, which I have not used; this option uses viscosities that are off by two orders of magnitude. I corrected this viscosity calculation in *breath* versions 1.1, 1.2, and 1.3 today.

The fix is to relabel all references to permeability to a value three orders of magnitude lower. The results are actually more comforting than the originally reported interpretations implied, since the actual range of permeabilities is in the range of silty sands through clean sands, rather than clean sands through gravels, and indeed are representative of the range of values reported for Yucca Mountain as was reported by various USGS papers. In fact, if my simulations were reported using saturated conductivities, the results would have been consistent and it is quite possible that the persistent error would not have been found. The simulations were incorrectly presented in Stothoff

et al. (1995), Stothoff and Bagtzoglou (1996), Bagtzoglou et al. (1995), Stothoff et al. (1996), and the poster used for both Stothoff and Bagtzoglou (1995) and the 1995 Kearney Conference. It may yet be possible to save the version of Stothoff and Bagtzoglou (1996) that will be widely distributed.

3/8/96 Update figures and results.

SAS

In preparing a series of slides for a Geological Society of America conference on 3/12/96, I am taking the opportunity to tabulate the results generated from a sequence of runs using a tight grid, as explained in the entry of 1/26/95. All hydraulic-property cases and the pressure and temperature cases were rerun for the 2-cm and 5-cm alluvium depths. The base case scenario was rerun for the 10-cm, 15-cm, 500-cm, and 1000-cm alluvium depths, as well as the semi-infinite alluvium case.

The results of the simulations are summarized in Table 1-2. The base-case weather is denoted by an "m"; perturbations in AAP and in AAT are denoted by "r" and "t", respectively. AAP is perturbed by multiplying all precipitation values by the noted perturbation; AAT is perturbed by adding (t+) or subtracting (t−) the noted perturbation. The alluvium and fracture codes both coalesce the permeability, porosity, and van Genuchten parameters into a 4-digit code. The codes are selected to allow one integer per parameter, and are translated in Table 1-3. The odd translation for fracture intrinsic permeability and van Genuchten scaling pressure are because saturated hydraulic conductivity and van Genuchten α created better codes. Note that the -3 factor in the intrinsic permeability codes is the correction for the improperly specified viscosity in earlier runs, so all runs are consistently labelled.

4/16/96 Update results and interpret.

SAS

Over the past month, I've been running simulations with fairly extreme climatic change in order to examine what would be expected at Yucca Mountain. So far, only 2-cm and 5-cm alluvium depths have been run, since the deeper cases take much longer. The climatic change is accomplished by multiplying all precipitation by a constant factor and/or adding a constant temperature. For both 2-cm and 5-cm cases, all combinations of rain and temperature have been completed with rain multiplied by 2/3, 1, or 3/2, and -5, 0, or $+5$ degrees C added to the temperature. A similar sequence is underway for rain multiplied by 1/2, 1, or 2, and -10, 0, or $+10$ degrees C added to the temperature. I should probably run a 15-cm and semi-infinite sequence as well for completeness, but these would take a *long* time. The results are summarized in **af_cli.result** in

Table 1-2: Summary of tight-grid infiltration simulation results

Code	Weather Perturbation	Alluvium Depth (cm)	Alluvium Code	Fracture Code	Moisture Content	Flux (cm/yr)
m	0	2	5223	2713	0.0331	5.82
m	0	2	5223	2712	0.0331	5.89
m	0	2	5223	2714	0.0328	3.29
m	0	2	5223	2703	0.0328	7.32
m	0	2	5223	2723	0.0331	5.75
m	0	2	5223	2613	0.0331	5.90
m	0	2	5223	2813	0.0331	5.77
m	0	2	5223	0713	0.0330	5.19
m	0	2	5223	4713	0.0331	5.86
m	0	2	5222	2713	0.0218	7.05
m	0	2	5225	2713	0.0548	4.43
m	0	2	5213	2713	0.0324	5.92
m	0	2	5253	2713	0.0352	5.87
m	0	2	5123	2713	0.1015	6.17
m	0	2	5323	2713	0.0151	6.51
m	0	2	4223	2713	0.0293	6.20
m	0	2	6223	2713	0.0397	5.43
m	0	5	5223	2713	0.0484	3.10
m	0	5	5223	2712	0.0486	3.18
m	0	5	5223	2714	0.0484	1.72
m	0	5	5223	2703	0.0483	3.32
m	0	5	5223	2723	0.0486	3.08
m	0	5	5223	2613	0.0485	3.15
m	0	5	5223	2813	0.0486	3.07
m	0	5	5223	0713	0.0485	2.69
m	0	5	5223	4713	0.0486	3.17
m	0	5	5222	2713	0.0331	4.30
m	0	5	5225	2713	0.0750	1.56
m	0	5	5213	2713	0.0505	3.22
m	0	5	5253	2713	0.0469	2.93
m	0	5	5123	2713	0.1219	3.69
m	0	5	5323	2713	0.0251	3.28
m	0	5	4223	2713	0.0380	3.37
m	0	5	6223	2713	0.0625	3.05
t−	3.0	2	5223	2713	0.0381	6.87
t+	3.0	2	5223	2713	0.0294	5.06
r*	0.9	2	5223	2713	0.0324	4.81
r*	1.1	2	5223	2713	0.0338	6.90
t−	3.0	5	5223	2713	0.0562	3.87
t+	3.0	5	5223	2713	0.0423	2.53
r*	0.9	5	5223	2713	0.0465	2.37
r*	1.1	5	5223	2713	0.0503	3.86

Table 1-3: Summary of alluvium ($abcd$) and fracture ($efgh$) parameter codes

Code	Parameter	Translation
a	Intrinsic permeability k (cm^2)	$k = 10^{-a-3}$
b	van Genuchten m	$m = b/10$
c	van Genuchten scaling pressure P_0 (gm/cm-s^2)	$P_0 = c \times 10^4$
d	Porosity ε	$\varepsilon = d/10$
e	Intrinsic permeability k (cm^2)	$k = 1.14694 \times 10^{-e-3}$
f	van Genuchten m	$m = f/10$
g	van Genuchten scaling pressure P_0 (gm/cm-s^2)	$P_0 = 980 \times 10^{-g}$
h	Porosity ε	$\varepsilon = 10^{-h}$

***$HOME1/RunCliFrac** (correction (dated 12/7/96): **$BREATH1/RunCliFrac**).*

Doubling rain and subtracting 10 degrees C from the temperature yields the most infiltration of all cases considered. For the 2-cm case, a factor of 4.3 increase is generated; for the 5-cm case, a factor of 6.6 increase is generated. Overall, this suggests that roughly a factor of 5 to 6 increase should be expected for this climatic condition, taking into account the importance of shallow covers relative to deeper covers. This increase could be quantified better using the newly developed colluvium-balance model discussed in the Geomorphology chapter.

4/17/96 Thoughts on creating an infiltration PDF.

SAS

The original motivation for examining shallow infiltration was to provide a PDF for the deep percolation fluxes past the repository. Ross and I planned to have my shallow infiltration fluxes feed into his deep percolation models. At the time, my idea was to construct a response surface for shallow infiltration as a function of whatever parameters were found to be important. It is now years later, but my work is reaching a point where construction of such a PDF is in sight.

An infiltration PDF is not a particularly well-defined concept. Ideally, one would construct many realizations of the entire mountain, from the surface to the water table, and pass in the appropriate boundary fluxes. The TSPA approach breaks the mountain into representative columns, each with its own infiltration flux. I believe that the PDF of interest is actually the PDF describing fluxes in each column, and presumably the fluxes in the columns are correlated. Accordingly, the shallow infiltration work can only be step one in the process, albeit a critical link between climate and deep percolation.

If the infiltration work is split into shallow and deep components, I believe that the best that the shallow infiltration work can do is to pass off plausible realizations of shallow fluxes to the deep percolation model, which in turn uses realizations of the stratigraphy and hydraulic properties to calculate fluxes through the repository. If indeed the fluxes at the repository in the deep model are insensitive to the degree of spatial variability in the shallow distributions, as I suspect, the smoothest distributions yielding minimal deviation at the repository should be used. A grid of spatially averaged infiltrations would be appropriate, perhaps on a 10-pixel spacing.

Ross' deep percolation work (Bagtzoglou et al., 1995) suggests that the repository is rather insensitive to focused recharge. Another approach that might be taken is to calculate the average infiltration over the area "upstream" of the repository. Unfortunately, the upstream area would be different for each realization, so that some representative area would need to be designated. The entire DEM feels excessive, while the repository footprint is too small. Perhaps the channel in Solitario Canyon to east of the footprint, extending a total of twice the north-south extent of the footprint?

The response surface idea can come into play at a second level in the average-infiltration approach. The first level is the construction of infiltration at a pixel as a function of parameter values. The second level is the construction of the average upstream infiltration as a function of parameter values. The response surface would assume that a single value of each hydraulic property is sampled and applied to the entire domain. Alternatively, it is possible to randomly assign properties to each pixel from an appropriate distribution and generate many realizations, calculating the average infiltration for each realization. Both of the approaches should be performed, using corresponding property PDFs, in order to see if important differences appear. I suspect that the two approaches will give essentially identical PDFs for shallow infiltration (some sort of law of large numbers), even if correlation between parameters is present.

In my model, the spatio-temporal distribution of shallow infiltration can be captured with 8 parameters: (i) four alluvium hydraulic properties (K_{sat}, porosity, and two van Genuchten parameters); (ii) two alluvium-depth properties; and (iii) average temperature and precipitation. The alluvium hydraulic properties could easily be functions of space. The average temperature and precipitation may be available from the geologic and other records (e.g., the Devil's Hole data, packrat middens). The alluvium-depth properties, however, are big unknowns; I feel these should be constants for a realization. The Yucca Mountain field trip planned for the near future will aid in constraining the alluvium-depth properties.

Given that the alluvium-depth properties and the climatic properties are constants for a

realization, there is no reason to suspect that the two average-infiltration approaches would yield a different PDF unless there is some systematic bias for hydraulic properties as a function of colluvium depth. Consider the environment of deposition. Shallow covers tend to be cobbly, with outcrops of rock. There may be some trend towards low spatial-average porosity, high permeability, and coarser grains in the shallower cover. Are shallow covers coarser? Something to check on the field trip, but how? Perhaps portable grain-size distributions, timing infiltration rates. Upon second thought, such ideas are silly – it would be very difficult to find discernable trends in the 2-cm through 15-cm regimes. It doesn't matter once the depths are greater than 0.5 m, since there is no infiltration to speak of anyway for such cases.

Since the two average-infiltration approaches should yield consistent PDFs, it makes sense to construct the response surface. I suspect that a reasonably detailed 8-dimensional surface could be calculated in hours; setting up the software could take a day or two, since the software should take advantage of new information from additional simulations as they might become available. Enforcing consistency between various simulations with various degrees of reliability may be a headache, as I have migrated to tighter and tighter numerical standards over time.

One issue that should be addressed is the issue of climatic change. I've talked to Dave Turner and Mike Miklas about retrieving climatic records. The idea would be to generate a series of plausible climatic-change realizations based on available data and feed it through the response surface to generate plausible traces of average infiltration. The resultant trace could be compared to TSPA traces. The deep percolation model really needs to be flogged to get the response of the repository horizon to infiltration rates for this to be most useful, but a nice paper could come out of the work.

4/23/96 Watershed modelling. SAS

Dr. David Woolhiser will be consulting to CNWRA on the subject of watershed modelling. A number of discussions have taken place between Woolhiser, Gordon, Ross, and myself, with the intent of scoping out the work to be performed. After these discussions, we have decided to break out the work into several packages of roughly $10 k apiece. The first package will be simulation of a representative wash feeding into Solitario Canyon from the west, which would be a surrogate for wash-scale modelling of easterly of Yucca Crest. The first package will test the methodology and feasibility of future work. Further packages would include the full Solitario Canyon watershed, and perhaps some detailed side-slope simulations with lateral subsurface flow.

To date, we have sent Woolhiser relatively limited information on the site. He has requested additional information including

- a large contour map of the Solitario Canyon watershed;
- a contour map of slopes in the Solitario Canyon watershed;
- available information on infiltration;
- available information on saturated conductivity;
- channel cross-sections; and
- photographs of the channel cross-sections (for roughness estimates).

A field trip to Yucca Mountain is being planned for the near future, at which time channel cross-sections and photographs can be obtained. In addition, I will obtain measurements of alluvium depths to compare with my geomorphology model, and perhaps some limited infiltration sampling using a falling-head permeameter can be performed as well. According to Woolhiser, a representative channel section or two midway between incoming washes would probably be sufficient for his needs, with 3 or 4 sections in representative washes. Photographs of each section should be taken, roughly 50 feet downstream.

Woolhiser has software available that should be able to generate the weather conditions at the resolution required for his model.

5/18/96 Summary of field trip observations. SAS

This past week, Ross Bagtzoglou, Gordon Wittmeyer, and I went to Solitario Canyon to obtain field measurements and observations. Ross and Gordon concentrated on surveying wash cross-sections for the mid- to lower-canyon reaches, while I concentrated on walking the mid- to lower-canyon from rim to rim taking spot measurements of colluvium depths and trying to make observations useful for comparison with computational models. My field observations are documented in a field book, CNWRA Controlled Copy number 175.

The first field day, May 13, we spent basically getting together procedures and familiarizing ourselves with the site and equipment. Ross and Gordon wrestled with the surveying equipment and data logger all day, finally becoming comfortable with the equipment after successfully surveying a

motel room that evening. During the day, they located well USW H-7 (on the other side of the road from Plug Hill) as a benchmark and made one cross-section at a stream-gage station adjacent to Plug Hill. Additional cross-sections were stymied by a recalcitrant data logger, apparently confused by a mixup in coordinates input for the first two locations.

I spent part of the first field day making measurements of alluvium to the west and northwest of the USW H-7 pad, walking up a sideslope to the crest and returning down a small wash. Wherever I took alluvium depth measurements, I marked a nearby bush with surveyor's tape with the idea of having the points surveyed in subsequently. As it turned out, we did not get a chance to survey the points due to delays caused by unfamiliarity with the equipment.

In order to estimate shallow alluvium/colluvium depths, I brought a tile probe with the idea of poking a hole into the alluvium until further advances were rejected. The tile probe is a metal rod with a diameter of 1/2 in, with a metal tip 4 cm long and a padded handle. The base of the adapter attached to the handle is 124 cm from the tip. I brought a 10-lb hammer attachment to replace the handle, in order to help drive the tile probe. I scored the probe, creating very distinctive grooves at 10, 20, 30, 40, and 50 cm distances from the tip, for quick depth and length estimates.

Proceeding up the slope from the USW H-7 pad to the west crest, point measurements ranged up to 44 cm. At one representative mid-slope location, depths were 27, 36, and 42 cm within 2 m; at another, depths were 17, 21, and 37 cm. At the crest, depths were typically 2 to 4 cm in places, at others 6 to 8 cm. Just below the crest, pockets of 12 to 18 cm colluvium were found, increasing with distance below crest to at least 37 cm. Walking down the rill, the channel was found to consist of bare rock in places, particularly at narrow and/or steep reaches. As the channel flattened, the scoured zones disappeared. Judging from the walls of the channel in scoured zones, alluvium depths could be as much as 2 m in places, but it is difficult to tell for sure. Certainly ridges between subwashes are up to 2 m.

It quickly became obvious that the idea of the tile probe was not going to work in alluvium over a certain depth or in regions with numerous chunks of rock, since rejection due to rubble was so likely compared to rejection due to bedrock. Accordingly, I concentrated use of the probe in shallow zones generally less than 40 cm in depth. These zones are of the most interest for infiltration estimates anyway.

The second part of the first day, I walked north along the bottom of Solitario Canyon further than well USW H-6. The stream channel morphology is rather confused in the entire stretch I walked north from Plug Hill. It appears that there are typically two channels, one for the eastern side of Solitario Canyon and one for the western side, but the channels are not strongly distinct and tend

to braid. The bottom of the channel is not uniform, with patches of similar materials ranging from very fine through gravel. There is brush in most of the channel, with somewhat less brush in the most active portions of the channel. There is a great deal of variability at a scale less than the 30 m x 30 m resolution provided by the DEMs we've been using, so that the cross-sections are essential. Unfortunately, in order to fully capture the stream channels, cross-sections would be required at a much higher density (every 20 to 50 m, I estimate) than Gordon and Ross set out to perform. Gordon and Ross were going by Woolhiser's estimates of one cross-section per side wash.

The second field day, I walked or crossed each of the washes in the watershed draining to the north of the USW H-7 pad. The watershed consists of 6 or 7 washes to the north and west of the pad. Proceeding to the north, I walked the Boomerang Point crestline, crossed to near the Jet Ridge crestline, and dropped back into the USW H-6 watershed. This day, I used Global Position System (GPS) pack to provide approximate latitude and longitude at selected locations. The GPS equipment is supposed to place one within 100 m of the correct location; if a second station is used, differential methods are supposed to yield sub-meter accuracy. Our original intent was to use a reference station and a rover station; however, we found that the supplied batteries were only good for 4-1/2 to 5 hours and we did not have four batteries to cover the full day. Upon return, I hear that motorcycle batteries might do the trick for a reference station.

The third field day, I was in Las Vegas and received a NTS badge and GET training.

The fourth (and my last) field day, I walked up the east part of Solitario Canyon to Yucca Crest, arriving not far from USW-UZ6. Again I used the GPS equipment without a reference station. I started at a trench apparently dug to expose the Solitario Canyon fault, and passed some terracing exposing the upper half of the PTn outcrop. Once at the Crest, I proceeded down the wash north of Highway Ridge to the first of two sets of trenches scraping away the alluvium cover from bedrock. The trenches extend from ridgetop to ridgetop. Due to time constraints, I only examined the southerly trench closely. This trench shows very little alluvial cover at the channel bottom, increasing to 1 or 1.5 m within 10 m of the bottom, and gradually thins to less than 10 cm at the top. Returning to the crest on the southern side of the roadway, I was able to observe the wash to the south as well. I returned to Solitario Canyon slightly north of USW H-3. Upon my return, judging from aerial photographs I was able to observe terrain typical of the western and central portions of the repository footprint; further to the east, the wash channels become wider and have little in the way of scouring in the channel bottoms.

During the four field days, Gordon and Ross completed on the order of 15 cross-sections, extending up Solitario Canyon most of the way from Plug Hill to USW H-6. The original plans to

survey the entire canyon channel were discarded due to the messy nature of the channel above this point and due to time constraints. The day after I left, Gordon and Ross visited the ESF.

Based on the three days of walking around and poking colluvium, it is clear that there are some problems with the colluvium model hooked together with the infiltration response surface, although the basic approach is sound. In general, even on ridgetops there are very few places that have less than 3 or 4 cm colluvium cover, and these places are usually exfoliation shards overlying bedrock. TC caprock boulders are generally massive and unfractured. Along crestlines, TC caprock exposures cover 50 to 90 percent of the surface (visually estimated). Moving downhill easterly from the crests, TC caprock boulders on the order of meters in length appear, get smaller and sparser, then disappear. In the cracks between TC caprock outcrops at the crestlines, it is typical for fine sand through loess to be present with depths at least 3 cm and less than 6 cm. Depths increase with distance from the crestline, averaging 10 cm or so between the larger boulders and increasing to 15 to 20 cm as the boulders decrease in size. There are occasional pockets with deeper colluvium, typically less than twice the average depths for the area. I saw few washes cutting directly into the caprock, aside from the western portions of crestlines, although it was not uncommon for caprock boulders to be sliding along other TC units into washes to the east.

Most of the exposures east of crestlines are TC units. Generally these are not highly fractured near the caprock but increase with depth. Any TC units below the caprock do not appear distinctive to my admittedly untrained eye. Chunks of the lower TC tend to be much smaller than the TC caprock boulders, generally being less than 50 cm. In the steepest portions of washes cutting TC units, bare country rock may be exposed, particularly in wash channels and up to 10 m above the channels in places. The washes on the west of Solitario Canyon tend to be steeper and shorter than the washes on Yucca Mountain proper. The Yucca Mountain washes tend to develop long regular reaches with uniform sideslopes, very nice for modelling. Based on a trench north of Highway Ridge, maximum alluvium depth on sideslopes should not be much more than 1 to 2 m, near the channel bottom. It appears that the long regular slopes are steepened at the base, due to removal of colluvium due to stream action during rainfall. It may be possible to estimate the depth of alluvium by projecting sideslopes out to midchannel in the upper portions of the washes.

All along the steep portions to the west of Yucca Crest, pockets may be as much as 40 cm, but generally are in the 5 to 15 cm range. A considerable amount of bare outcrop is present, as much as 50 percent or more of the surface area. Even partway down the flatter slopes, depths may not be more than 50 to 100 cm.

There are distinctive stripes of dark, highly varnished scree alternating with light, clean

scree on many of the wash slopes. Stripes may be as little as 1 to 2 m on center and may be tens of meters on center. Invariably the dark scree is raised relative to the clean scree, suggesting that runoff is focused on the clean scree and washes it. It may be safe to assume that the darker the scree, the higher it is relative to the adjacent light scree.

Two difficulties arise when comparing the infiltration conceptual model work with field observations. The first difficulty is in treating the regions near the crestlines. Although colluvium depths, where present, are generally greater than I've been assuming, the areal average might not be too bad. However, the flow modelling assumes that there is uniform depths of colluvium everywhere, while the actual situation is patchier and deeper. An obvious way of treating the actual situation is to decrease the porosity to account for the proportion of surficial area that is impermeable boulder. It may be that reducing porosity is essentially equivalent to reducing depth, since the volume available for flow is reduced by either approach. If so, accounting for boulder size and area may not be tremendously important in the colluvium model.

The second difficulty is in treatment of wash channels. The colluvium model breaks down when factors other than gravity become important, such as overland water flow. It should not be difficult to include a factor increasing colluvium fluxes due to streamflow, which will get rid of the (arbitrary) 20 m depths in upper channels. Unfortunately, all of the action is on a scale that is subgrid compared to the DEM measurements. The channels are only 1 to 2 m wide where the rock is bare, yet the grid is 30 m on a side. It may be necessary to overlay a refined grid on wash bottoms to properly capture infiltration, at least in upper portions of the washes. As the channel bottoms are relatively narrow, there may not be a great deal of infiltration relative to ridgetops.

5/28/96 Summary of second field trip observations. SAS

As an adjunct to a Technical Exchange on the NRC audit of the DOE TSPA-95 performance assessment document, which was held in Las Vegas, a group of 8 NRC/CNWRA/consultant personnel took a tour of the ESF at Yucca Mountain(myself, C. Glenn, B. Behlke, M. Bell, A. Campbell, R. Manteufel, J. Walton, G. Stirewalt). The tour took place May 24, 1996. The tour was led by Alan ? of the DOE mapping team and hydrologic input was provided by Alan Flint of the USGS.

One of the more important observations that Alan Flint made regards lateral diversion in and near the PTn bedded tuffs. Previous TSPA analyses have assumed that lateral diversion may be strongly impacted by a very low permeability unfractured layer just below the PTn. However, the ESF borehole exposes a section of PTn that appears to be rather frequently, on the order of

every 10 to 20 m by my observation, punctuated by small-offset faults. The offsets tend to be less than a meter, and may easily have been missed in boreholes. The following day, I took a walk up from Solitario Canyon to Yucca Crest and noticed some small (10 to 20 cm) offsets at one PTn exposure. Alan Flint's observation is that lateral diversion is probably not going to be very significant, because the frequent offsets in the low-permeability unit should minimize the most significant source of lateral flow.

Along the way in the ESF tour, various chlorine-36 sampling locations were pointed out by A. Flint and A. Campbell from the Fabryka-Martin et al. (1996) draft report. We also saw the heavily fractured zone, 1 km in length and still being encountered by the TBM. The fractures seemed to alternate between zones of fracture spacings less than 10 cm to zones where the spacing is more on the order of 30 to 40 cm.

As it rained (fairly heavily in spots) on May 24, I was inspired to take another walking tour of Yucca Mountain on May 25. Based on wetting front observations, which penetrated roughly 3.5 to 6.5 cm in various representative areas, and on water in exposed lithophysae, I estimate 1 to 2 cm of rain took place. I noticed that on Yucca Crest, enhanced wetting took place in the gaps between outcrops (10 cm and larger in spots), while under rubble scree on sideslopes less wetting took place (dry soil was not uncommon). While walking about, a storm cell drifted overhead and roughly a half hour of rain occurred. A total of no more than 5 minutes of reasonably heavy rain occurred, with most of the interval light to nearly non-existent. Exposed rubble faces were definitely wet; however, vertical sides tended to be dry with wetting fronts occurring at the top of perhaps 1 to 3 cm. Fifteen minutes after rain ceased, little or no trace of the event could be detected.

I also examined four of the trenches that are exposed in what I think is Split Wash or the next wash north (the wash with the Ghost Dance pavement and the wash immediately north of this wash). Each of these are sufficiently downstream that the wash bottom is at least 10 m wide. In this region, what I believe Alan Flint refers to as channel terraces are exposed. It appears that currently active wash channels are cutting into the terraces. Depth to bedrock at the deepest point in the trenches ranged from 2.5 to 4 m, as best as I could estimate. However, once the slope of the ground increased from the relatively flat terrace to side slope, cover decreased to the more typical 10 to 50 cm. It should be possible to identify these deeper zones simply by the slope or break in slope.

I also had the opportunity to talk with Alan Flint about his site-scale modelling work. He demonstrated time-traces of moisture content in various neutron-probe boreholes. In one channel terrace probe, lateral subsurface flow was clearly evident. He is currently using a 3-event (upgrading

to 5-event) Markov-chain model to generate daily precipitation and daily mean temperature readings. Each rainfall event is redistributed to essentially perch on the colluvium/bedrock interface at the end of the day, where it infiltrates according to matrix and fracture properties. Each Scott and Bonk (1984) layer has matrix properties assigned, either from direct measurement or from analog. Fractures are grouped into 3 size classes, and further subdivided into filled/unfilled areal fractions. Pixel size is 90 m on a side; no lateral diversion is considered. Evapotranspiration is a part of the model.

Pondering the site visit, it seems that the DEM is somewhat unwieldy for colluvium-flow calculations, as it completely misses meter-scale features such as wash channels. Ideas of quasi-1D flow-tube analyses occurred to me as being particularly appropriate for Yucca Mountain. Each flow tube would carry along local information on topography, width, depth, shape, vegetation, etc., in the form of integer categories or classes. Accordingly, the information could be encoded very compactly in the form of bit substrings within a few integers. Vegetation is another tricky topic inspired by discussions with Alan Flint, which it would be very nice to have a better handle on.

8/27/96 Pondering questions relevant to performance. SAS

In brief, work to date has focused on

- 1D simulations
- bare soil (no vegetation)
- no matrix-fracture interaction
- instantaneous lateral redistribution
- long-term average impacts due to
  - hydraulic properties
  - meteorologic input
- spatial distribution of surface cover
- spatial distribution of AAI
- to a minor extent, response to climatic change

Most of the work is documented in a journal article currently in preparation. The text and figures for the article will be included in this notebook upon submission to the journal and internally documented.

After the completion of work to date, it is my opinion that numerical modelling can give reasonable estimates of spatial distributions for relative AAI, the relative response of AAI to climatic change, but not absolute magnitudes for AAI. Since almost all precipitation ends up returning to the atmosphere, small errors in evaporation estimates may yield large errors in AAI estimates. Thus, the large area of interest with associated high heterogeneity levels and complex physical behavior preclude more than bounding estimates for AAI.

A number of future investigation directions can be considered.

- The validity and conservativism of the 1D approach could be examined using 3D simulations with discrete fractures on the grid-block scale for the DEM (roughly 30 m x 30 m). A 2D or 3D code would need to be assembled, presumably with the additional processes of vegetation and snow considered. Studies on the grid-block scale would be aimed at ascertaining the impact of heterogeneity and fracture spacings.
- Hillslope- and watershed-scale studies can be examined to see if lateral redistribution would significantly alter the predicted spatial distributions for AAI. Again a 2D or 3D code would need to be assembled, similar or identical to the code for the grid-block-scale simulations.
- Detailed process-level simulations, on the scale of a single fracture, could be undertaken to see how the matrix might affect infiltration magnitudes and timings. Code development is required.
- Additional 1D simulations could be undertaken to see how vegetation and snow might affect infiltration magnitudes and timings. Code development is required.
- The simulations performed to date can be squeezed to obtain the most information possible. Perhaps the most important additional information regards the timing and magnitude of infiltration pulses. The weekly trace of fluxes for each simulation can be examined relative to the rainfall input to determine the pulse description as a function of precipitation description. Perhaps comparison to the bucket approach would be in order. Analysis and *Matlab* code development required.
- Given infiltration-pulse information, the spatial distribution and timings of fluxes through the PTn can be estimated. The important question is what time-scale pulses through the PTn

have and how uniform the distribution of fluxes at the bottom of the PTn would end up being, so that the representativeness of quasi-steady-state approaches can perhaps be assessed. A logical first step might be 1D simulations using the output from one or more of the 10-yr shallow simulations. Again, some sort of 3D simulator may be in order. Predictions of travel times through the PTn could be made prior to tests in the ESF.

A key point in nearly all of these future directions is the common thread of required code development. Even in 1D, additional refinements to *breath* are necessary, while 3D codes are not available at CNWRA that have the proper capabilities.

8/28/96 Data bibliography. SAS

As discussed above, my studies examining the spatial distribution of AAI may be extended to below the PTn layer. If this is the case, it is extremely useful to collect all data pertaining to ambient unsaturated-zone hydrology at Yucca Mountain. I started collecting this type of information last month, as I needed to verify some of the information regarding alluvium depths measured in boreholes and trenches collected by Hannah Castellaw almost a year previously in order to double-check predictions of depths from DEM slopes. It took some time to find her sources, and in the interim I located additional information nestled in the CNWRA library. The current entry summarizes some of the information available.

Flint and Flint (1995) provide a summary of 99 neutron-probe boreholes, including locations, elevations, classifications, dates, alluvium depths, and lithology, as well as some analysis of the data. The entire moisture-content data set for all boreholes has been ordered from the DOE and should be arriving within the week, on tape. Attempts to email the data set were stymied due to the CNWRA inability to receive email greater than 1 Mb in size (the data set consists of two files of 12+ and 14.5+ Mb, respectively). The DOE system manager was not available to set up an anonymous ftp site.

The Flint and Flint (1995) neutron-probe locations are provided in Nevada State Plane (NSP) coordinates, not the CNWRA standard of Universal Transverse Mercator (UTM). Information on the locations and elevations of most of the Yucca Mountain boreholes are also specified in a data file obtained from the DOE in January, 1994, with specifications for 243 boreholes. Alluvium depths are not specified, although various other sources of information are available including Fernandez et al. (1994), Schenker et al. (1995), and numerous drilling log reports and summaries. Some of the most recent boreholes are not in the DOE tape and locations are available from

other sources and are only specified in NSP coordinates. I have collected the available information in directory ***$HOME2/Matlab/3Ddata***, with **neutron_hole.dat** containing the most complete information.

Flint and Flint (1990) provide data from 73 samples in 9 boreholes, all in nonwelded and bedded tuffs (i.e., PTn, Calico Hills). Each sample is precisely located within the respective borehole. The emphasis is on studying data-determination methods in relatively permeable and porous Yucca Mountain cores, presumably because these are faster to analyse. Porosity, grain density, bulk density, intrinsic permeability (measured 4 ways), relative permeability versus saturation (measured 2 ways), and potential versus water content (measured 3 ways) are tabulated. Some analysis comparing the measurement techniques for the intrinsic permeability values is performed. No attempt to estimate van Genuchten parameters is made, and it seems to me that the data is not of sufficiently high quality to make the attempt.

Rautman et al. (1995) provide data obtained from a sampling grid along 1.4 km of the PTn outcrop in Solitario Canyon, with a total of about 330 core samples obtained from 26 vertical transects. Bulk properties (porosity, bulk density, and particle density) are presented for all samples; sorptivity and saturated hydraulic conductivity are presented for almost all samples (except where handling damaged the sample). Locations of vertical (upslope) transects are specified as a northward offset to a transect reported by Flint et al. (1996), with core samples located relative to the base of the sampled sequence. Distinct vertical trends in the properties are shown in plots, and high r^2 values ($r^2 > 0.824$) were obtained between the 4 bulk properties.

Flint et al. (1996) provide data obtained from 5 vertical and 3 horizontal sampling transects, with a total of 656 core samples. Bulk properties (porosity, bulk density, and particle density) are presented for all samples; either measured or estimated saturated hydraulic conductivity is presented for most samples; and sorptivity is presented for some samples for two horizontal transects. In addition, moisture retention information is obtained for 41 of the samples, with estimated van Genuchten and Brooks-Corey parameters. Relative-permeability information was not determined. Regression equations are presented for properties as a function of porosity. Arguments were made that porosity values can be used to estimate van Genuchten parameters; perhaps additional information can be gleaned from the sorptivity information. The report appears to be the best current source for property data suitable for modelling.

The five vertical transects presented by Flint et al. (1996) are further analyzed by McKenna and Rautman (1995) to examine correlation information. The correlation structure appears to be nonstationary horizontally. Appropriate downhole sampling strategies are suggested.

Schenker et al. (1995) collect and reference a large number of data sets and impose PDF descriptions on them. Most of the data are from cores extracted from boreholes; transect sampling information from Rautman et al. (1995) and Flint et al. (1996) does not appear. Porosity and bulk density have 1234 and 2173 measurements, respectively. There are 257 saturated hydraulic conductivity values from 8 boreholes. The matrix van Genuchten parameters are reportedly determined from the original pressure/saturation data sets by the authors, yielding 211 property estimates; however, the set of estimates is not directly available. Fracture properties are estimated using fracture spacing and orientation data from four boreholes (G-1, G-4, a #1, and GU-3), saturated bulk conductivity data from the saturated zone in 7 boreholes (G-4, H-1, H-3, H-4, b #1, p #1, and J-13) and bulk gas permeabilities from barometric fluctuations observed in 2 boreholes (UZ-1 and a #4). Lots of extrapolation is required due to the sparseness of the fracture data.

8/29/96 Revisiting PTn modelling ideas. SAS

Further discussions with English and Sitakanta suggest that examining the behavior of the PTn layer may be of the most direct use to PA. For example, the appropriateness of the various models for flow in the subsurface can be examined (i.e., ECM versus dual-permeability versus weeps) by examining the time behavior of pulses reaching the top of the PTn layer. If extremely long time scales at the bottom of the PTn are observed, the ECM model may be in order. If extremely short time scales are observed, the weeps model is in order. Intermediate cases presumably would require the dual-permeability model).

A second question that can be examined is the issue of the spatial distribution of fluxes leaving the PTn layer. There are direct implications for the distribution of fluxes at the drift scale, since the TSw units are relatively homogeneous from the PTn to the repository. My conceptual model of drift-scale processes under ambient conditions has high relative humidity at all flow packages and relatively few packages contact a dripping fracture (i.e., dripping fractures are widely spaced). In this case, the drips are a strong focussing mechanism, shielding most surrounding packages. Studying the behavior of the PTn layer may shed some light on the relative spacing of dripping fractures.

9/21/96 Setting up 1D PTn modelling. SAS

Two detailed sources of information are available for unsaturated-zone tuff properties, Rautman et al. (1995) and Flint et al. (1996). The Rautman et al. (1995) data set is finely resolved in

both the lateral and vertical directions, but only covers part of the PTn layer and does not provide van Genuchten properties for the samples. The Flint et al. (1996) data set consists of 8 transects, covering the full range of layers in less detail. The Flint et al. (1996) data set does provide several measurements of van Genuchten properties, however.

The Flint et al. (1996) data set will be used to test the behavior of wetting pulses, since it provides a much longer vertical transect (the Solitario Canyon transect, in particular) and some van Genuchten information. Two approaches are immediately obvious: (i) use average layer thicknesses and properties, based on Tables 2, 5, and I-1; and (ii) use Table I-1 for fullest spatial resolution but supplement properties as necessary. The idea would be to assume fracture flow with the wetting pulses translated undamped from surface conditions as a top boundary condition, with the top boundary at the top of the shardy base of the Tiva Canyon Tuff, and use gravity drainage bottom conditions in fractures to correspond to the Topopah Spring Tuff vitric caprock and lower layers. There are between 20 and 25 measured K_{sat} values within the roughly 35 m section of the transect of interest, with perhaps 35 additional core samples that do not have K_{sat} values. It is not clear whether the reported transect distance is vertical distance, horizontal distance, or along-ground distance, but assuming that the slope is roughly 30 degrees in this region, the vertical section of nonwelded tuff is about 20 m, about twice the thickness considered by Rautman et al. (1995).

As a first cut, the detailed stratigraphy implied by Table I-1 of Flint et al. (1996) will be assembled into detailed layering. For points where K_{sat} and van Genuchten properties are missing, the regressions provided by Tables 3 and 6 will be used. Between each data reading, K_{sat} and van Genuchten α will be loglinearly interpolated and van Genuchten n will be linearly interpolated. Initial conditions will be provided by using the steady-state vertical ODE approach discussed in the PA Research and Ambient Hydrology projects.

The regression equation for K_{sat} as a function of porosity for the welded and nonwelded portions of the Solitario Canyon transect in Table 3 of Flint et al. (1996), based on 36 samples and with an r^2 value of 0.90, is:

$$K_{sat} = -13.9 + 33.1\varepsilon - 30.8\varepsilon^2, \tag{1-1}$$

where K_{sat} is in m/s. Based on Figure 11, it appears that the regressed equation is actually for $\log_{10}(K_{sat})$, which makes much more sense.

From Table 6 of Flint et al. (1996), based on 10 samples and with r^2 values of 0.01 and 0.44

for van Genuchten α and n, respectively, the regression relationships are:

$$\alpha = 0.49 + 0.31\varepsilon, \tag{1-2}$$

$$n = 0.95 + 1.94\varepsilon, \tag{1-3}$$

where α is in units of MPa^{-1}.

Parenthetical note:

My suspicion is that the van Genuchten regression relationships could be significantly improved by solving for all samples simultaneously, since there is considerable latitude in changing the α and n parameters without greatly affecting the fit between data and formula. The simultaneous-solution procedure minimizes the least-squares sum of squares,

$$Y = \sum_{i=1}^{N} [\theta_i - \hat{\theta}(P_i)]^2, \tag{1-4}$$

where θ_i is a measured saturation value and $\hat{\theta}$ is the corresponding predicted saturation value for measured pressure P_i. The prediction formula is

$$\hat{\theta} = \hat{\theta}(\alpha, n, \theta_{res}, P), \tag{1-5}$$

$$\alpha = C_0 + C_1\varepsilon, \tag{1-6}$$

$$n = C_2 + C_3\varepsilon, \tag{1-7}$$

$$\theta_{res} = C_4 + C_5\varepsilon. \tag{1-8}$$

The minimization takes place when the gradients of Y are zero, or

$$F = \frac{dY}{dC_j} = -2\sum_{i=1}^{N} [\theta_i - \hat{\theta}(P_i)] \frac{d\hat{\theta}_i}{dC_j} = 0. \tag{1-9}$$

Newton's method is convenient for this minimization, which simply states that for each iteration k,

$$J(\mathbf{x}_k)s_k = -F(\mathbf{x}_k), \tag{1-10}$$

$$\mathbf{x}_{k+1} = \mathbf{x}_k + s_k, \tag{1-11}$$

where $J(\mathbf{x}_k)$ is the Jacobian and $\mathbf{x}$ is the vector of unknowns C_j. It shouldn't be too difficult to check this out on the data presented by Flint et al. (1996).

9/24/96 First results from 1D PTn modelling. SAS

After a good deal of putting together *Matlab* code and some *breath* debugging, the first set of PTn simulations were run using the base-case infiltration traces for 2-cm and 5-cm colluvium over a

fracture continuum. The 2-cm case has weekly outputs of flux, while the 5-cm case has daily flux outputs; both cases have fluxes that are higher than almost any pixel value would show, so the simulations are probably more extreme than will be observed in future work.

All work is done in ***/home2/sierra/stothoff/Matlab/PTnCheck***. The input files for *breath* are created using **fix_FFRI_dat.m**, which in turn uses **extract_qw.m**, **pre_ydot_setup.m**, and **ydot_setup.m**. The built-in *Matlab* ODE solver ode23s is used to create initial conditions for the temporal average of the input flux, using **ydot_setup.m**. Output is examined using **show_stuff.m** and **new_show_seq('t', 'nf\1;col\co;plot\pl;nseq\1;last\10')**.

Several cases were tried, varying (i) the assumption for the continuum underlying the PTn layer and (ii) the input flux case. The 2-cm input-flux case was run using 2 m of fracture continuum, 2 m of TS58 material, and 20 m of TS58 material. The last material case was also run using the 5-cm input-flux case. All cases use 5-cm nodal spacing.

Several observations were made:

- The fracture continuum below the PTn causes time steps on the order of 3 seconds, while simulations using the matrix below complete in minutes of CPU time.
- The steady-state moisture profile is very different for fractures underlying the matrix and for tuff underlying; the fractures cause the PTn to be essentially saturated in locations, while the tuff allows much drier profiles *even with the same flux.*
- The flux distribution is very peaky. Over the period of a day, fluxes can jump by 4 orders of magnitude, then decay exponentially.
- The flux pulse propagates essentially instantaneously (less than a day) through the PTn layer, but the pulse magnitude decreases exponentially with depth.
- The moisture content responds by a few percent in the same timeframe.
- The gravity drainage condition 2 m below the bottom dampens the peakiness significantly relative to the 20-m depth.
- There are roughly 2 pulses a year, although the pulses are clumped. As the colluvium depth increases further, the number of pulses will decrease.

There are several implications to the work:

- Capturing flux pulses with moisture-content readings may be a hopeless endeavor.
- Steady-state assumptions may be appropriate for calculating moisture contents.
- Using the gravity-drainage assumption with moisture contents must be examined carefully, since structural features and heterogeneity can modify moisture contents without modifying fluxes.
- It may not be that bad to use the ECM assumptions below the PTn, as there is indeed strong damping in the input signal.

The current *breath* approach must be augmented to provide more realistic simulations. In particular, it is still not possible to check the ECM assumptions since there is no possibility for more than one continuum below the PTn. Also, the saturation profile in the PTn is strongly impacted by the lower-layer assumptions. An approach that may bear fruit is to allow several continua to dangle off the bottom of the PTn, each independent except that the same pressure exists in each one at the bottom of the PTn. One continuum might be the matrix, with the rest being fracture sets. Occasional lower cross-links between the fracture continua might okay.

The augmented approach would allow the investigation of which fracture set(s) kick in, if any. In addition, the saturation in each set may be able to be translated into an equivalent wetted length, which can than be used to intersect with the drifts.

It may be considerably more difficult to construct a steady-state solver for this case, since there are multiple threads of flux joining at a middle node. Shooting may be necessary.

10/5/96 ACNW, change in PI. SAS

I attended the ACNW meeting in Las Vegas on September 26 and 27, 1996. My impressions are discussed in the trip report. However, there are a few important issues in particular that should be examined.

- Five independent estimates of infiltration (surface modeling by A. Flint, isotopic tracers, fracture coatings, thermal profiles, and core-sample moisture contents and pressures) all point to fluxes on the order of 1 to 10 mm/yr.
- Fault zones are considered highly permeable (1000 Darcy) horizontally, but less so vertically.
- In general, gas bulk permeabilities are on the order of 2 to 10 Darcy.

- Inverse modeling pulls the TSw matrix permeabilities up 1 or 2 orders of magnitude above core information.
- First-cut drift-scale 2D heterogenous-matrix simulations are underway with dripping requiring a transient pulse of 280 mm/yr.
- G. Bodvarsson claims that the ECM and the dual-permeability models must be identical at steady state. *Note: I think this is not correct and may explain the shift in TSw permeabilities he is obtaining.*

Last week, I became PI for the Unsaturated and Saturated Flow under Isothermal Conditions (USFIC) KTI, as I have the most hours allocated and Gordon has relatively few hours. Upcoming duties include a presentation on the USFIC KTI work at the Annual Program Review on November 13, 1996, and on December 5, 1996. The first (45 min + 15 min) presentation is to focus on technical and programmatic aspects, with subtopics including

- Status of subissue(s) resolution
- Integration with other KTIs
- Analysis of infiltration/percolation
- Results of sensitivity analyses
- Work priorities for 1997-98

The second (60 min) presentation is to focus on technical, programmatic, and managerial aspects, with subtopics including

- Infiltration/percolation rates
- Preferred conceptual model for fracture-matrix flow
- Future climate scenario and formation of perched water
- Relationship to total system performance
- Strategy for review of viability analysis

Issues involving infiltration and percolation should be straightforward to discuss. The two technical issues that will be difficult to discuss will be the preferred conceptual model for fracture-matrix flow and the future climate scenario related to the formation of perched water. I take these topics as spurs to perform some quick calculations and have discussions with Ross and others. In particular, testing Bodvarsson's opinion on the steady-state equivalence of the ECM and dual-permeability approaches is in order, as is coming up with a contour plot of areal AAI as a function of precipitation and temperature.

10/16/96 Start of alluvium/bedrock simulations. SAS

The approach that Alan Flint is taking to estimating shallow infiltration, as he has described it to me, essentially fills the alluvium pore space with as much water as will fit and runs off the excess (i.e., infinite alluvium conductivity), then using evapotranspiration to mine water back to the atmosphere. A perched-water system is assumed to exist above the bedrock due to the infiltration events. Water moves into the bedrock assuming gravity drainage within the bedrock. Three classes of fracture sizes, fractions of filled and unfilled fractures, and matrix permeability are combined to yield an equivalent conductivity for the 7 classes. In contrast, I have completely neglected the matrix, filled fractures, and transpiration, and have used highly resolved simulations to capture the dynamics of flow in detail.

I have observed that in simulations with bedrock exposed (i.e., alluvium with permeability less than 10^{-8} cm^2), essentially no infiltration occurs. I have not considered the case of alluvium overlying bedrock, however. I hypothesize that little or no infiltration will occur until several meters of alluvium cover the bedrock. When the alluvium/matrix interface is below the active zone, flow should be essentially steady through the bedrock at the bedrock K_{sat} or the semi-infinite infiltration rate for the alluvium, whichever is smaller. When the active zone interacts with the matrix/bedrock interface, I suspect that the low-permeability bedrock will prevent significant infiltration. As verification of this hypothesis, I am setting up several simulations to probe the behavior of alluvium overlying unfractured bedrock.

The Tiva Canyon tuff microstratigraphy is of primary interest. According to Flint et al. (1996), the shardy base has a mean K_{sat} of 1.6×10^{-6} m/s ($k = 1.6 \times 10^{-9}$ cm^2= 5.0×10^4 mm/yr), while the remaining Tiva Canyon layers have K_{sat} ranging from 3.1×10^{-9} to 3.0×10^{-12} m/s (k ranges from 3.1×10^{-12} to 3.0×10^{-15} cm^2, or 98 to 0.95 mm/yr). None of these should exhibit bare-soil infiltration if the low-permeability matrix-only results can be extrapolated.

Table 1-4: Summary of colluvium and matrix properties used in simulations.

Material	K_{sat} m/s	ε	θ_r	van Genuchten α MPa^{-1}	van Genuchten m	van Genuchten P_0 ($\times 10^6$) gm cm^{-1}s^{-2}
Colluvium	9.8×10^{-6}	0.300	0.000	50.0[1]	0.200	0.2[2]
Caprock	3.1×10^{-9}	0.105	0.002	5.00	0.301	2.0
Upper lithophysal	8.9×10^{-12}	0.108	0.001	2.90	0.310	3.4
Shardy base	1.6×10^{-6}	0.235	0.035	3.01	0.237	3.3
Fracture	0.011	0.001	0.000	10^5	0.700	9.8×10^{-5}

[1] Correct value is 500 (2/26/97) SAS

[2] Correct value is 0.02 (2/26/97) SAS

To test the hypothesis, the base-case colluvium over three material cases will be examined: (i) shardy base, (ii) caprock, and (iii) upper lithophysal. These cases are representative of the range of k and are of interest in their own right. Samples BT26Hs, PW19s, and TPC52s will be used to determine van Genuchten properties, using the 2-parameter estimates. A summary of properties is shown in Table 1-4, with the colluvium and base-case fracture properties shown for reference. Initially, a 10-cm and a 25-cm depth-of-cover case will be run for each, as representative cases. Further examination may suggest additional cases.

10/19/96 First results for alluvium/bedrock simulations. SAS

Four of the six runs have completed 3 cycles of boundary conditions: both shardy-base cases, the 10-cm caprock case, and the 25-cm upper-lithophysal case. Each of the cases erroneously used colluvium permeabilities 1000 times larger than desired, due to incompletely correcting the viscosity value in the new input-file generation routine **ingen_am.m** in ***$BREATH2/Subreg/-MakekmpoKmao***. The input and output cases are renamed correctly to reflect this error, and **ingen_am.m** was corrected. The matrix properties are correct.

None of the cases are particularly near cyclic steady state, but some conclusions can already be drawn from the first results. The shardy base is permeable enough that significant infiltration can occur, perhaps 10 mm/yr or more. Interestingly, there are indications that deeper cover provides more infiltration for the shardy base, opposite to the alluvium/fracture case. The caprock case shows some indications of infiltration as well, perhaps on the order of 1 mm/yr. The upper

lithophysal case is drying out from the initial condition of 0.25 mm/yr.

Based on this rather limited set of runs, a few conclusions are presenting themselves to me:

- The capillary barrier effect is turned around for the case of matrix underlying alluvium, so that water is preferentially drawn into the matrix.
- The conclusions regarding alluvium cases that allow and disallow infiltration may not be far off for a shallow cover over bedrock.
- There may be some additional infiltration due to cover protection.
- Materials as permeable as the caprock are probably dominated by fracture flow for shallow covers and matrix flow for deeper covers.
- As the permeability increases from the caprock, matrix flow dominates.
- As the permeability decreases from the caprock, fracture flow dominates.

The only microstratigraphic layers more permeable than the caprock, according to Flint et al. (1996), are located in the sequence including the Tiva Canyon shardy base through the nonwelded units of the Yucca Mountain and Pah Canyon Tuffs to above the Topopah Spring upper lithophysal zone. These microstratigraphic layers are essentially the PTn layer addressed in my previous analyses, perhaps a little larger, which only is about 5 percent of the total subregional outcrop area. Accordingly, I expect that the alluvium/fracture results considered before would not be significantly modified for most of the subregional area.

A much more definitive modeling approach can be conceived with some modification to *breath*. The idea is to have multiple interacting continua throughout the bedrock, all with a common pressure in the alluvium. The multiple-continuum approach will allow partitioning between the fractures and matrix to be examined, particularly since separate continua can be defined for various fracture-aperature size classes. The approach is also essential for considering deep-percolation processes.

12/7/96 Updated results for alluvium/bedrock simulations.

SAS

A new file was created in ***$BREATH1/RunTightAM*** entitled **am_all.result** to document the results of alluvium/matrix simulations. The file follows a generic standard with many entries not used. The columns of the result file are, in order:

- Depth of soil (cm),
- Alluvium code (see Table 1-3),
- Bedrock code (Table 1-4 for properties),
- Perturbation code

  b0 Base case (precipitation and temperature may vary),

  e0 Longwave radiation is scaled,

  s0 Shortwave radiation is scaled,

  v0 Vapor density is scaled,

  w0 Windspeed is scaled,

  ge Solar aspect is rotated east (perturbation in degrees),

  gw Solar aspect is rotated west (perturbation in degrees),

  gn Solar aspect is rotated north (perturbation in degrees),

  gs Solar aspect is rotated south (perturbation in degrees),
- Perturbation,
- Precipitation multiplier,
- Temperature shift,
- Average soil moisture content at the interface, and
- Average net infiltration (cm/yr).

Most of the values in the file should be viewed as order of magnitude results rather than fully converged, as more cycles are required for full convergence in almost all cases. The runs are primarily useful for screening where fracture flow would dominate. From the runs, it appears that significant matrix infiltration can occur for the Tiva Canyon caprock and shardy units, while fracture flow should dominate in Tiva Canyon upper lithophysal and Topopah Springs lower nonlithophysal units.

The shardy unit is considered part of the PTn, has large infiltration, and is the most permeable unit of any of the microstratigraphic layers considered. The 10-cm case has AAI approximately 24 percent of AAP, while the 25-cm case has AAI approximately 16 percent of AAP. The remainder of the PTn should have smaller AAI. Assuming that the PTn as a whole yields AAI roughly

equivalent to 10 to 20 percent of AAP is probably justified based on these simulations. Note that in the FY96 Annual Progress Report (Bagtzoglou et al., 1996), my assumption was that 10 percent of AAP enters the PTn, and I found that the overall sensitivity to the PTn unit is quite low.

The Tiva Canyon caprock matrix shows behavior unlike any other unit considered, as AAI *increases* with soil depth for the two soil depths considered. Experience from early semi-infinite experiments suggests that essentially no infiltration should occur for exposed materials with this permeability. A cover of soil appears to provide a permeable zone to allow water to penetrate the subsurface while protecting caprock from evaporative processes, and the difference in bubbling pressure between soil and caprock preferentially sucks water into the bedrock. The caprock is laterally extensive over the repository, primarily in regions where my colluvium/fracture models predict high AAI, so revisiting this material with ***breath*** modified to consider both bedrock and fractures simultaneously would be appropriate. Note that one would expect that the caprock should never have much more than 50 cm of cover.

Today I tried to finalize the table of atmospheric influences on infiltration for a colluvium/fracture system. The table is in ***$BREATH1/RunCliFrac*** and is called **af_egsvw.result**, abstracting the results of simulations run over the period from July through November. The simulations do not consider changes in precipitation or temperature. The columns of the result file are, in order:

- Depth of soil (cm),
- Alluvium code (see Table 1-3),
- Fracture code (see Table 1-3),
- Perturbation code

  b0 Base case (precipitation and temperature do not vary),

  e0 Longwave radiation is scaled,

  s0 Shortwave radiation is scaled,

  v0 Vapor density is scaled,

  w0 Windspeed is scaled,

  ge Solar aspect is rotated east (perturbation in degrees),

  gw Solar aspect is rotated west (perturbation in degrees),

  gn Solar aspect is rotated north (perturbation in degrees),

gs Solar aspect is rotated south (perturbation in degrees),

- Perturbation,
- Average soil moisture content at the interface, and
- Average net infiltration (cm/yr).

The values in the file have reliably reached cyclic steady state.

An important observation was made during the finalization process. The final simulations in the colluvium/fracture set of simulations overlapped the first soil/bedrock simulations. I had previously noticed that there are cases where the combination of soil and underlying material require such small time steps during a large infiltration event that a simulated hour may not complete within the 10000-time-step limit. For the last simulation, I imposed a 50000-time-step limit for each hour; during large infiltration events even this limit might be reached before the hour was up, but more than half of the events exceeding 10000 time steps completed before 50000 time steps were finished. For the case with the larger limit on the number of time steps, larger net infiltration was obtained than would have been expected (5.5 mm/yr rather than roughly 1 mm/yr). The implication is that my estimates of AAI are too low in some (but not all) cases. I suspect that the error is generally additive, on the order of several mm/yr, rather than being a multiplicative error. Unfortunately, it is not possible to untangle which simulations yield underpredictions without rerunning the simulations. I believe that sensitivity predictions may be relatively unaffected, but there is some question regarding the appropriate decay in infiltration with soil depth.

12/8/96 Estimating regression relationships for AAI.

SAS

As part of estimating regression relationships between hydraulic properties, climatic variables, and AAI, I fit the data to predicted values using a least-squares fit. Say, for example, that the relationship is

$$\log_{10}\left(\frac{AAI}{AAP}k^{1/2}\right) = \alpha_0 + \alpha_1\left[\left(\frac{m}{m_0}\right)^2 - 1\right] + \alpha_2\left[\left(\frac{P_0}{P}\right)^{1/2} - 1\right] + \alpha_3\left[\left(\frac{\varepsilon}{\varepsilon_0}\right) - 1\right], \tag{1-12}$$

where k is intrinsic permeability, m is van Genuchten $m = 1 - 1/n$, P is bubbling pressure (the reciprocal of van Genuchten α in the units used here), ε is porosity, a subscript 0 represents a reference value for the parameter, and the α values are hydraulic-parameter sensitivity constants.

For any particular simulation, the only unknowns in the relationship are the α values. Thus, for a simulation, one can write the equation as

$$C_0 = \alpha_0 + \alpha_1 C_1 + \alpha_2 C_2 + \alpha_3 C_3, \tag{1-13}$$

where the C values result from evaluating the hydraulic-property functions. Combining all simulations results in the matrix relationships

$$\left[\mathbf{C}_1\ \mathbf{C}_2\ \mathbf{C}_3\right]\{\alpha\} = \{\mathbf{C}_0\}, \tag{1-14}$$

where bold-face represents a vector. When provided with linear equations having a matrix that is not square, *Matlab* solves the equations using least squares (exactly the appropriate behavior). Any reported regressions are coded using *Matlab* to take advantage of this feature.

1/7/97 Documenting plots for ANS-1997 submission.

SAS

Budhi was invited to give an invited talk at the American Nuclear Society (ANS) convention in June, 1997. A summary of the talk is required for the conference, consisting of 450 to 900 words. The summary presents the methodology for creating infiltration maps and sensitivity maps, in an extremely schematic fashion. Included in the summary are two plots, one of my latest base infiltration map and a newly created sensitivity plot for sensitivity of infiltration to soil depth.

The plots were generated with a master *Matlab* driver called **do_sens_eval.m**, which in turn calls a number of other routines. The current versions of required files and concommitant input were stored in a subdirectory of ***$HOME2/Matlab/YMInfil*** entitled ***ANS96***. The directory was stored in a tar file entitled **ANS96_plotgen_tar**, which was in turn compressed using the gzip command (appending ".gz" to the file name).

Sensitivity S_k of areal-average AAI to generic parameter α_k can be calculated using normalized sensitivity coefficients (Sykes et al., 1985)

$$S_k = \frac{\alpha_k}{AAI}\frac{\mathrm{d}AAI}{\mathrm{d}\alpha_k} \tag{1-15}$$

$$S_k = \alpha_k \frac{\mathrm{d}\ln AAI}{\mathrm{d}\alpha_k} \tag{1-16}$$

The sensitivity coefficients are calculated by using first-order derivatives between a high and low perturbation, normalized by a reference value. In general, sensitivity coefficients will change as the set of base input values change. For the example problem, the base-case soil depth was uniformly multiplied by 0.9 and 1.1 to provide perturbations. Values of S_k less than or equal to 0 were

arbitrarily set to 10^{-32} for plotting purposes (the most-negative value was on the order of -10^{-16}). Note that sensitivities are largest on sideslopes and are zero wherever depth does not change infiltration (e.g., deep soil, PTn outcrops under current modeling shortcuts).

1/8/97 Documenting 1996 annual report work.

SAS

An archive file was created in both ***$HOME2/Matlab/YMInfil*** and in ***$HOME2/Matlab/-ColluvWaste*** documenting the input files and limited output files used to generate figure 10-4 and tables 10-1 and 10-2 in chapter 10 of the NRC High-Level Radioactive Waste Program Annual Progress Report, Fiscal Year 1996. Both archive files are called **AnnRep96_tar**; both are compressed. The file in ***$HOME2/Matlab/YMInfil*** includes all of the files from ***$HOME2/Matlab/ColluvWaste***, for completeness, and is submitted to QA as formal documentation of the results. A couple of files were added or fixed up for readability and reproducibility of results. Description of the process is in a ReadMe file in the archive.

1/13/97 Documenting alluvium regression.

SAS

Alluvium depths are not well captured by the equilibrium mass-wasting scheme in areas of deep alluvium, partly due to the irregular topography of the washes. In order to have a reasonable representation for deep alluvium, in August, 1995, Ross Bagtzoglou developed a regression for alluvium depth b as a function of slope s:

$$b = 47\exp(-0.32s). \tag{1-17}$$

The regression was based on borehole information for b and the nearest-neighbor values from the DEM for s. No borehole classification was performed, and ad-hoc data censoring was used for the regression. Due to time constraints, the work was performed very quickly.

I revisited the regression expression last summer, and decided that it is probably better to use an expression of the form

$$\ln(b) = a + b\ln(s). \tag{1-18}$$

I pulled together as much available information on alluvium depths as I could find and sorted it into a file called **neutron_hole.dat** in ***$HOME2/Matlab/3Ddata***. Neutron-borehole data is reported by Flint and Flint (1995); other data sources are noted in **neutron_hole.dat**. I pulled neutron-borehole data from channels and terraces into separate files (**chan.dat**, and **st.dat**, respectively);

other boreholes with reported alluvium depths were pulled into file **well.dat**. A total of 110 boreholes are included in these three classes; an additional 64 boreholes are not considered.

Boreholes with shallow covers (i.e., ridgetops, sideslopes) are not considered further, as I feel that alluvium depths for these boreholes are not reported with sufficient accuracy and are in a range of depth that should be handled by the mass-wasting approach anyway.

For the regression, each of the boreholes was assigned the slope of the nearest-neighbor pixel in the DEM. An additional censoring process eliminated all boreholes with unreported soil depths or having soil depths less than 1 m, leaving a total of 37 boreholes, conveniently grouped as 9 channel boreholes and 28 deep-alluvium boreholes. The data points and regression lines are shown in Figure 1-1, manually generated by regressing all data using **regress_set.m** and further processing with the **show_regress.m** routine. I feel that it is questionable whether the overall regression should use the channel data, as the pixels are larger than the channel width. Even if the channel data is included, the regression line is not tremendously changed. As a note, the correlation coefficient with the original formulation is 0.59 and 0.58 for the channel and terrace, respectively; using the new formulation the correlation coefficient is 0.66 and 0.69, respectively.

1/15/97 Documenting infiltration abstractions. SAS

In ***$HOME2/Matlab/YMInfil/SubregSpaceDist***, abstractions for AAI as a function of material and meteorologic properties are examined using **find_best_regress.m**. Abstractions for AAI as a function of material properties were originally developed in the summer of 1996. The abstractions were developed "by eye" and are more formally documented here.

The deep-alluvium abstraction originally developed is in the form

$$\log_{10}\left(\frac{AAI}{AAP}k^{1/2}\right) = \alpha_0 + \alpha_1\left[\left(\frac{m}{m_0}\right)^2 - 1\right] + \alpha_2\left[\left(\frac{P_0}{P}\right)^{1/2} - 1\right] + \alpha_3\left[\left(\frac{\varepsilon}{\varepsilon_0}\right) - 1\right], \tag{1-19}$$

where

- k is intrinsic permeability,
- m is van Genuchten $m = 1 - 1/n$,
- P is bubbling pressure (the reciprocal of van Genuchten α in the units used here), and
- ε is porosity.

A subscript 0 represents a reference value for the parameter ($m_0 = 0.2$, $P_0 = 2000$ Pa, and $\varepsilon_0 = 0.3$), and the α values are hydraulic-parameter sensitivity constants. Equation 1-19 was

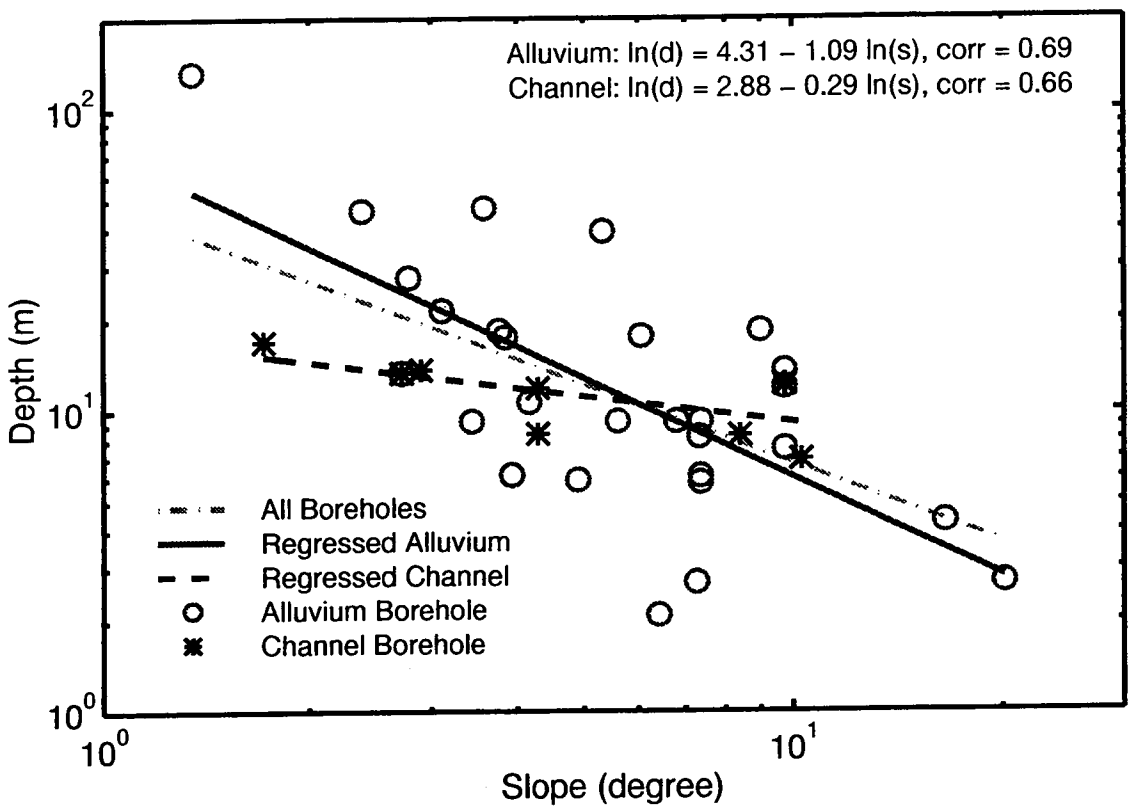

Figure 1-1: 1/13/97. Regression of borehole alluvium depths with nearest-neighbor DEM slopes.

originally reported by Bagtzoglou et al. (1996).

Using **find_best_regress.m** and **f_deep_hyd_fit.m**, a best-fit exponent was determined using the 28 material-property-variation simulations in **alluv.result** that have non-negative infiltration. Also, the impact of assuming a $\log_{10}$ relationship instead of a scaling relationship can be determined. These are performed by flipping switches at the top of **find_best_regress.m**.

Using the more formal abstraction process, a better regression is

$$\log_{10}\left[\frac{AAI}{AAP}\left(\frac{k}{k_0}\right)^{1/2}\right] = \alpha_0 + \alpha_1\left[\left(\frac{m}{m_0}\right)^{\beta_1} - 1\right] + \alpha_2\left[\left(\frac{P}{P_0}\right)^{\beta_2} - 1\right] + \alpha_3\left[\left(\frac{\varepsilon}{\varepsilon_0}\right)^{\beta_3} - 1\right], \tag{1-20}$$

where k_0 is 10^{-8} cm^2 and the β values are fitting exponents. A plot of the least-squares fit for the exponents is shown in Figure 1-2, where the fit for each curve only uses simulations with the parameter varying. Note that there is more noise in the value for P than in the other parameters.

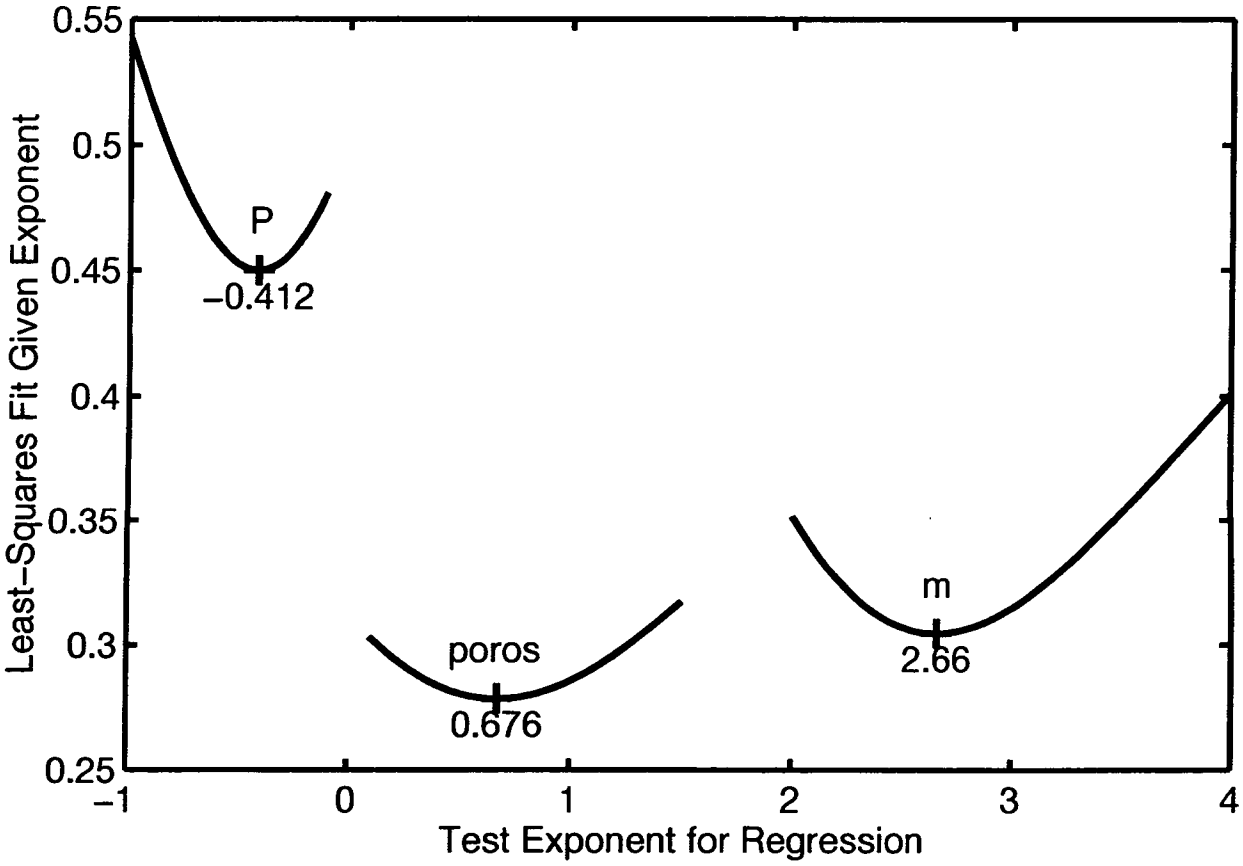

Figure 1-2: 1/15/97. Least-squares fit of simulation prediction to abstraction prediction for various exponents in Equation 1-20.

The best-fit coefficients are shown in Table 1-5. The least-squares fit is also shown for the counterpart of the formal abstraction equation using logarithms,

$$\log_{10}\left[\frac{AAI}{AAP}\left(\frac{k}{k_0}\right)^{1/2}\right] = \alpha_0 + \alpha_1 \log_{10}\left(\frac{m}{m_0}\right) + \alpha_2 \log_{10}\left(\frac{P}{P_0}\right) + \alpha_3 \log_{10}\left(\frac{\varepsilon}{\varepsilon_0}\right). \tag{1-21}$$

The best scaling fit is better than the logarithm fit for each parameter. If the logarithm of k is examined, however, the associated α coefficient is -0.495 and associated logarithm fit is 0.258, strongly supporting pulling k into the left-hand side as is done in Equation 1-20.

Table 1-5: Best-fit abstractions to material properties in deep alluvium.

Parameter	α	β	Fit	Log Fit
Scaling Constant	-1.38165	—	0.587745	1.09475
van Genuchten m	0.42505	2.6576	0.304383	0.821475
P	2.05672	-0.41248	0.449886	0.50599
ε	-1.39944	0.67568	0.278631	0.633175

1/20/97 Documenting infiltration abstractions. SAS

In ***$HOME2/Matlab/YMInfil/SubregSpaceDist***, abstractions for AAI as a function of material and meteorologic properties are examined using **find_best_regress.m**. Abstractions for AAI as a function of material properties were originally developed in the summer of 1996. The abstractions were developed "by eye" and are more formally documented here.

A routine called **f_deep_met_fit.m** was developed to check out the appropriateness of abstractions in the form of a scaling or a logarithmic representation, identical to the approach followed for material properties. Some trial-and-error runs were followed to pick reasonable base values for exponents, varying one parameter at a time. The value of the sought exponent was observed to shift about, depending on the values of the remaining exponents. Accordingly, the *Matlab* routine **fmins** was used to perform a global minimization for all meteorologic-variable exponents simultaneously. A modified version of **f_deep_met_fit.m** entitled **f_deep_met_reg.m** was created to follow the format required by **fmins**.

Two sets of regression results are presented in Table 1-6, for simultaneously determined exponents and for logarithmic regression, labelled Scale Fit and Log Fit, respectively. Each reported fit only uses simulations where the variable of interest is perturbed (including the base value of the variable). The column entitled Curvature represents the second derivative of the scale fit with respect to the variable, and is a measure of sensitivity; the larger the value of curvature, the better the exponent is determined. The logarithmic fit does not admit this measure. The best fit is to AAP; the worst fit is to AAT. The exponent for AAL, AAV, and AAW is roughly within a value of ± 1; the exponent for AAP is better determined and the exponent for AAT is much more poorly determined.

Based on comparing the fits reported in Table 1-6, it can be concluded that a logarithmic representation should be used for AAL and AAW and a scaled representation should be used for the remaining variables. The best-fit coefficients for this representation are shown in Table 1-

Table 1-6: Regression values for deep-alluvium meteorologic abstraction.

Parameter	Exponent	Scale Fit	Curvature	Log Fit
AAL	-0.03723	0.308036	0.0284408	0.289575
AAP	-0.2889	0.419721	0.486325	0.440836
AAT	-15.96	0.648594	0.000370696	0.700391
AAV	2.075	0.323644	0.0174236	0.357603
AAW	0.2412	0.304608	0.0112994	0.28684

Table 1-7: Regression coefficients for deep-alluvium meteorologic abstraction. *Correction dated 1/23/97: Two curvature numbers were incorrectly transcribed. Correct numbers are italicized in the table.* SAS

Parameter	Exponent	Coefficient	Fit	Curvature
AAL	—	-1.52051	0.312029	—
AAP	-0.2416	-5.56806	0.420087	0.4858
AAT	-16.67	0.945489	0.649914	0.700391 *0.000366185*
AAV	2.138	0.281891	0.326738	0.357603 *0.0171413*
AAW	—	-0.321916	0.307231	—

7. The parameters without a reported value for exponent are represented using a logarithmic representation.

1/22/97 Documentation of USGS data acquisition.

SAS

I set up ***$HOME2/AmbientKTI/3Ddata*** as an archive for site-specific data acquired from or reported by DOE or subcontractors, such as core-sample data. Today A. Ramos typed in the moisture-retention data from Appendix II of Flint et al. (1996). He double-checked his typing and I confirmed each number. I noticed that the original report is missing a number for sample TPC27s and for sample TPC15s. The original wordperfect file is called **usgs_ofr95-280_app2.wp** and an ASCII version is called **usgs_ofr95-280_app2.asc**. File **Sources** in the same directory documents this procedure.

Sources also documents previously obtained data residing in the same directory. The complete neutron-probe data discussed by Flint and Flint (1995) was obtained from the DOE office in September, 1996. Table 4 from Rautman et al. (1995) was obtained from C. Rautman on

November 6, 1996, using email. Tables I-1 through I-8 from Flint et al. (1996) were obtained directly from L. Flint on November 4, 1996, also by email.

1/24/97 Deep-alluvium meteorology regressions. SAS

I have noticed an increasing sensitivity of AAI to meteorologic properties as AAI decreases. Work to date has used the deep-alluvium regression equation the form

$$\log_{10}(H) = \alpha_0 + \sum_i \alpha_i U_i, \tag{1-22}$$

where $H = (AAI/AAP)U_k$, U_i represents a normalized value for parameter i, and the α values are constants. Two forms of U_i are considered, (i) the scaling fit (e.g., $U_{AAV} = [(AAV/AAV_0)^\beta - 1]$), and (ii) the logarithmic fit (e.g., $U_{AAL} = \log_{10}(AAL/AAL_0)$). Note that both forms are zero for the base case of the parameter. Results for the two forms are discussed in the entry for 1/20/97, in which it was determined that AAL and AAW are probably better fit using the logarithmic form and AAP, AAT, and AAV are probably better fit using the scaling form.

In order to account for this sensitivity, I postulate that the deep-alluvium regression equation for meteorologic properties is in the form

$$\log_{10}(H) = \alpha_0 + \sum_i \alpha_i U_i + [a_0 + a_1 \log_{10}(H)] \sum_j \alpha_j U_j \tag{1-23}$$

$$= \frac{\alpha_0 + \sum_i \alpha_i U_i + a_0 \sum_j \alpha_j U_j}{(1 - a_1) \sum_j \alpha_j U_j}, \tag{1-24}$$

where index i represents a parameter that is insensitive to H and index j represents a parameter that is sensitive to H. Note that a_0 is arbitrarily set to 1 if there are no parameters considered insensitive to H. Again using *Matlab* routine fmins, I created a file to evaluate the least-squares fit of the simulation data to the regression equation with **f_deep_met_eval.m**. Although thousands of iterations are required to reach convergence, the new formulation significantly improves the data fit. For example, overall least-square-fits from 1/20/97 for simultaneous fits of AAP, AAT, and AAV are about 1.5 times larger than the new formulation provides. The form in Equation 1-24 is more general than a similar equation that uses $[a_0 + a_1 U_(k)]$ as the scale, although the latter form should work as well.

Hint for the future: the solution procedure appears to really benefit from periodic restarts. Perhaps the solution steps get too small and the restart enlarges them.

2/14/97 Daily-averaged meteorology. SAS

Insofar as A. Flint typically uses daily meteorologic values when simulating infiltration, and I have been using hourly values in the vicinity of rainfall events and monthly values otherwise, and as daily simulations run faster than hourly simulations, I'm starting a few test cases to check on whether it actually makes a significant difference. I had looked at this years ago and found that averaging makes a relatively small difference, most important near precipitation events, and precipitation is the most important variable to capture. The simulations used 2-cm grids rather than the 1-mm grids I currently am using, so perhaps the conclusion may be altered.

Met files are generated in ***$HOME2/AuxRain/Climate***. A meteorology file with daily inputs averaged from the Desert Rock data, **dr_0d0d_24as.met**, was generated using **make_ave_metseq('dr_0d0d_24as.met', 24)**. The met file was created by averaging all fair-day met values in a window of 30 days around each day, then overwriting the days with precipitation with the original, unaveraged, values for those days. It is possible to change the size of the window for averaging and the window for not averaging by changing hard-coded numbers in the call to **move_metave.m**.

The met file was copied to ***$SubRegBreath/RunTightAM*** and a sequence of simulations was started with 50 cm of alluvium over porous bedrock. These simulations took on the order of 3 days with hourly values.

2/27/97 Daily-averaged meteorology results and calcite. SAS

Directory ***$SubRegBreath/RunTightAM/ResultDir*** holds the results of ten simulations of daily meteorology compared to hourly meteorology. The simulations are designated by **_ds** following both **reg07** and **reg08**. These designators represent bedrock cases 1 and 2, respectively, derived from regressed relationships by Flint et al. (1996). The comparable cases with hourly meteorology are missing the **_ds** designator.

The *Matlab* routine **make_DH_Plot** was created to plot the results as shown in Figure 1-3. The plots show convergence over repeated input cycles to a constant value of decadal-average flux with depth; complete convergence occurs when the decadal-average flux is constant over all depths. Perturbations from the base meteorology are labeled $2/3P$, $3/2P$, $T+5$, and $T-5$, for multipliers in precipitation (P) and shifts of temperature (T) uniformly applied to all values.

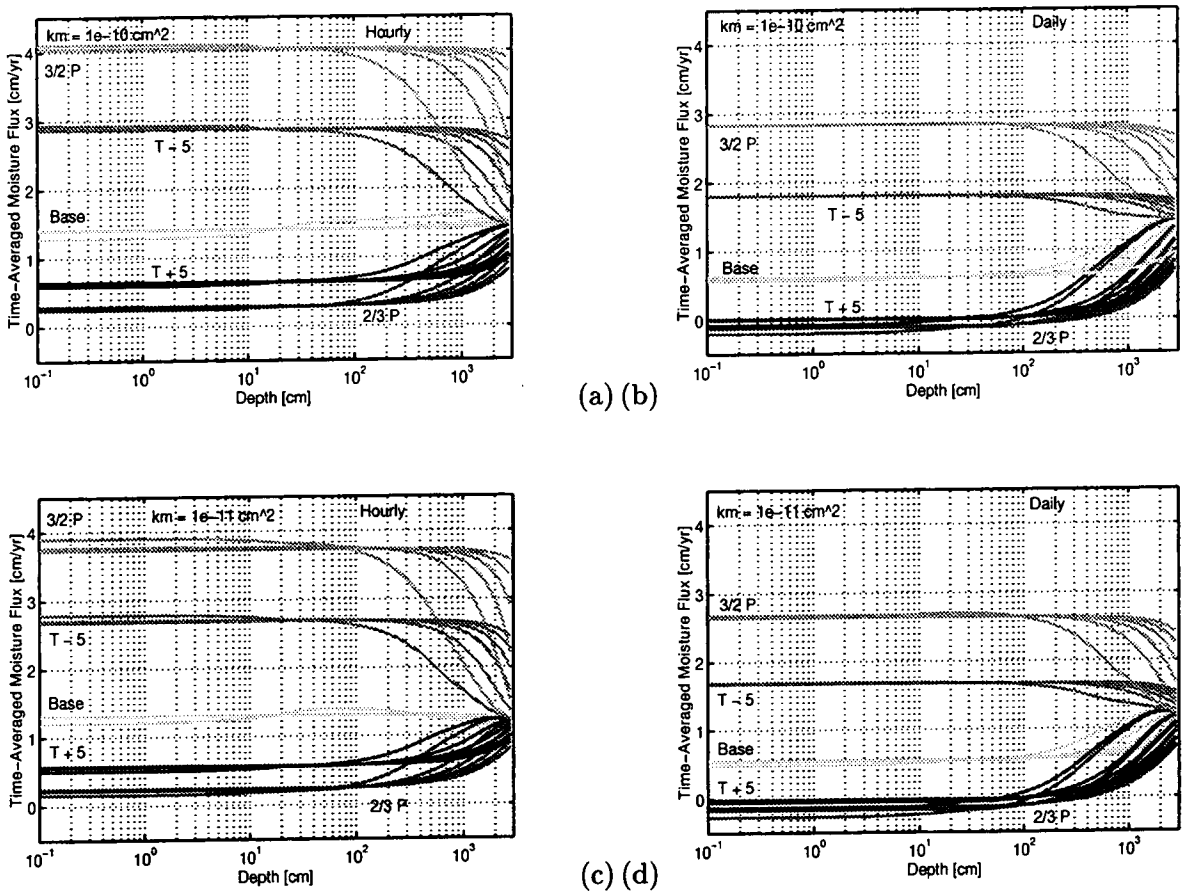

Figure 1-3: 2/27/97. Time history of decadal-average moisture flux after each of 6 decades, as a function of AAP and AAT, for (a) hourly meteorologic input and bedrock 1, (b) daily meteorologic input and bedrock 1, (c) hourly meteorologic input and bedrock 2, and (d) daily meteorologic input and bedrock 2.

Two items are of particular interest in Figure 1-3. First, although the two bedrocks have permeabilities different by an order of magnitude, AAI remains essentially unchanged. More importantly, there is significant difference between the hourly and daily meteorologic inputs, with the hourly values yielding significantly higher infiltration. With the current procedure for handling evaporation, I conclude that the simulator cannot be trusted to yield reliable results with daily inputs.

I have thus far examined the behavior of deep soil, soil overlying open fractures, and soil overlying bedrock. The one related case that remains to be investigated is the behavior of soil

overlying fractures filled with calcite. It is reported by Flint et al. (1996) that measured values for saturated hydraulic conductivity on fracture-fill materials averages 43.2 mm/day (5×10^{-7} m/s or approximately 5×10^{-10} cm^2). No van Genuchten properties are reported. The fracture-filling permeability is almost as large as the most permeable bedrock. After consulting with Gordon Wittmeyer, it is probably not unreasonable to have fracture fillings with $\varepsilon = 0.1$, van Genuchten $\alpha = 100$ MPa^{-1}, and van Genuchten $n = 2$ (van Genuchten $m = 0.5$).

In ***$SubRegBreath/RunTightAM***, I am setting off a set of simulations assuming that the matrix is impermeable, fracture pore space is representative of the fracture classes in TCw as reported by Flint et al. (1996), and the fracture-filling properties are as above. The three classes have reported fracture pore volume of 2.6×10^{-5}, 2.6×10^{-4}, and 2.6×10^{-3}, for 2.5 μm, 25 μm, and 250 μm fractures, respectively. Since porosity must also account for fracture pore space, filling porosity will be 2.6×10^{-4} (rounded to 10^{-4}). Precasting behavior suggests that infiltration will increase with increasing soil depth (to the order of 1 m), due to the capillary attraction that calcite has relative to soil, but infiltration should be relatively small due to the rather small net porosity. Files with **cal3**, **cal4**, and **cal5** for fracture properties represent fracture pore volumes of 10^{-3}, 10^{-4}, and 10^{-5}, respectively.

In conversations with L. Flint (USGS) today, she clarified the weighting schemes that were used by Flint et al. (1996) assign the values of 0.09, 0.055, 0.005, 0.025, 0.8, and 0.025 as the weights for open 2.5 μm, open 25 μm, open 250 μm, filled 2.5 μm, filled 25 μm, and filled 250 μm fractures, respectively. She also will send me data packets with the full set measured values, Without having the data in front of her, Lorrie independently used the thinking that Gordon used to suggest how the filling properties would be different from matrix properties.

3/1/97 Preliminary calcite simulations. SAS

Three simulations have completed, each with 10 cm of soil over fillings with total porosity of 10^{-4}, 10^{-5}, and 10^{-6}, respectively. Interestingly, the three porosity cases do not appear to yield total infiltrations that are significantly different. The fractures respond very quickly, due to the small pore volume and high permeability, so it is adequate to use 2 decades for simulations. Partial results for deeper soils show decreases in infiltration with depth, similar to open fractures. A sequence of simulations for **cal3** and **cal4** were fired with the standard set of climate variations (AAP and AAT). A similar set of simulations, varying filling properties, will be run subsequently.

An error was found in the UZFLOW module converting meters to feet. The error came

directly from the *Matlab* routine that calculates AAP, AAT, and AAT on each pixel of a DEM. Accordingly, all previous reported predictions for AAI are slightly incorrect, and should be slightly increased. Over the range of Yucca Mountain elevations (1100 to 1500 m), corrected values of AAP are 8 to 13 mm/yr larger, AAT are 0.65 to 0.9 °C cooler, and AAT are 1.2×10^{-7} to 1.4×10^{-7} drier.

3/23/97 Data from DOE.

SAS

A CD-ROM disk was received from L. Flint about two weeks ago that contains the entire set of matrix-property core-sample measurements from 31 boreholes, including 23 neutron-probe boreholes and 8 deeper boreholes. A total of nearly 5000 samples have properties reported. The CD-ROM disk is entitled "Matrix Properties" and is dated 3/2/97. The CD-ROM disk has one file, entitled **database.wk4**, which is a file in Lotus 1-2-3 version 4.0 format. The CNWRA does not have software current enough to be capable of reading this format; however, the Net Force contractors to the CNWRA were able to convert the file to Lotus 1-2-3 version 3.0 format, which is capable of being read. E. Pearcy was able to pull this into Excel and output it in tab-delimited ASCII form. I stored both the Lotus 1-2-3 version 3.0 file, entitled **database.wk4**, and the tab-delimited ASCII form, entitled **usgs_borehole_db.asc**, in ***$HOME2/AmbientKTI/3Ddata***. The original CD-ROM will be delivered to B. Mabrito and stored in the QA vault.

A second set of data was obtained from the NRC, which consists of a 8-mm tape that copies a CD-ROM with numerous ARC-VIEW coverages stored as 99 themes. The themes range from base-map information (e.g., Nellis Air Force Range boundaries, roads) through contour maps, borehole locations, ecological study plots, a digitized version of the Scott and Bonk stratigraphy, and various other information. The files take up roughly 31 Mb. The original CD-ROM resides at the NRC offices. The CD-ROM was accompanied by a user's guide dated May 1, 1996, with 18 pages plus 3 appendices. I am maintaining the tape in my office until the information can be transferred to disk in an accessible location.

4/10/97 Trip report for Yucca Mountain fieldwork.

SAS

The remainder of this entry is adapted from the trip report for a two-day trip to Yucca Mountain to perform characterization field work. Field documentation for the trip is in CNWRA notebooks 175 (soils and vegetation) and 217 (Solitario Canyon measurements).

Persons Present

The trip to Yucca Mountain (YM), on March 26 28, 1997 was undertaken by S. Stothoff and J. Winterle (CNWRA), D. Groeneveld and J. Thompson (Natural Resources, Inc.), and D. Or (Utah State University).

Background and Purpose of Trip

CNWRA is working with D. Groeneveld, D. Or, and J. Thompson to aid in characterizing the impact of vegetation upon shallow infiltration. Transpiration is a process included in DOE models but not considered in CNWRA modeling efforts to date. The intent of the CNWRA work is to incorporate vegetation into infiltration-modeling efforts in a plausible and defensible manner, with appropriate modeling of soil-moisture uptake by plants of particular interest. The trip was inspired by the need for field-checking hypothesized relationships between vegetation and bedrock type, soil cover, slope, and solar loading. In a parallel effort, watershed-scale modeling is being performed by D. Woolhiser. Soil permeability in the wash channels is one of the critical parameters in the watershed-scale model. J. Winterle accompanied the group to obtain soil permeabilities in Solitario Canyon channels, which will be used in the watershed-scale model.

Summary of Activities

The field work was split into three activities: (i) a spot-check vegetation survey verifying the more-detailed TRW vegetation work and examining factors governing the distribution of individual species (D. Groeneveld and J. Thompson); (ii) a spot-check of soil-permeability measurements to verify more-detailed United States Geological Survey (USGS) work, as well as examination of plant rooting distributions (D. Or and S. Stothoff); and (iii) channel permeability measurements in Solitario Canyon (J. Winterle). The vegetation survey was conducted over four days while the remaining work was performed over two days. Prior to the main trip, D. Groeneveld flew a photographic airborne survey of plant distributions, augmenting a collection of coarser-scale photographs taken previously by EG&G.

Overall Impressions

The trip was extremely useful in orienting Or to the YM site and to identifying and refining hypotheses regarding the spatial distribution of plants and plant uptake patterns. Soil measurements taken during field activities will provide direct input into modeling activities. The trip was also useful in planning future activities with Groeneveld and Or.

Interpretations Based on Field Observations

Prior to the field excursion, aerial photographs were examined and it was noticed that linear vegetation features could be identified, particularly along Yucca Crest. As a working hypothesis, it was felt that these linear features represent fissures in the bedrock that the plants were able to take advantage of for water uptake. To verify this hypothesis, several pits were dug adjacent to flourishing plants. Two pits were dug along an apparent linear feature in the Tiva Canyon caprock. Bedrock was reached at a depth of approximately 30 to 40 cm under the plants and in both pits a fissure of approximately 5 to 15 cm was identified, aligned with the vegetation feature, that was densely populated with roots. In one of the pits, a carbonate layer was identified within the fissure at a depth of roughly 5 cm below soil/bedrock contact; in the other, no distinct carbonate layer was identified to a depth of about 20 to 30 cm but there did appear to be increasing carbonate concentrations in the soil with depth.

Plant roots were exposed at three additional sites with shallower soil. At one site, in caprock, both plants exposed had roots predominantly within fissures or extending to fissures. At the second site, in caprock, the plant selected was in the center of a pocket of soil several meters across, with bedrock cropping out on three sides and a soil depth of at least 30 to 40 cm directly under the plant. Although a fissure existed, the plant did not appear to take special advantage of the fissure but appeared to take advantage of runoff from the surrounding bedrock. Nearby plants in fissures between bedrock outcrops appeared more verdant. At the third site, on a side slope in the upper lithophysal unit of the Tiva Canyon formation, the plants were rooted in rubble with 30 cm of cover. For these locations, typical of ridgetops and side slopes, the use of unrestricted rooting systems reported in the literature is precluded due to the strong influence of bedrock.

In all locations examined, the soil cover was sandy loam to loam with bedrock fragments, and was rather permeable. The fine portion of the soil appears to be eolian in nature wherever it was examined. Although permeabilities and soil depths were only determined at a few locations,

soil samples were collected at scattered locations (including each vegetation transect). Roughly two dozen soil samples were obtained. The similarity of the samples suggests that it would be reasonable to assume that soils are reasonably similar over the entire mountainside (except perhaps in areas with sorting due to overland flow such as washes and wash channels), consistent with Flint et al. (1996).

Four ponded-head permeameter measurements were made at three sites with relatively shallow slopes along Yucca Crest and Highway Ridge. Measured saturated conductivity values ranged from 1.2×10^{-3} to 4.9×10^{-3} cm/s. The smallest reading occurred at a site where a large rock was subsequently found to lie directly under the disk; the next-largest reading was 2.9×10^{-3} cm/s. For comparison, Flint et al. (1996) reported soil conductivities in the YM area of 5.6×10^{-4} to 3.8×10^{-3} cm/s based on soil-texture analysis. Three tension-head measurements (two readings with different suctions at one site, one reading at another site) were also obtained, indicating consistent values. The measured values are remarkably similar.

Rock particles found in the soil ranged from small pebbles through cobble-sized blocks. In the pits and in trenches with bedrock exposed, the bedrock was considerably more irregular than the soil surface implying that vegetation may be preferentially located in locally deeper pockets of soil where water can be stored for longer periods after precipitation.

The welded Tiva Canyon units do not exhibit gullying along the side slopes of the washes over the proposed repository footprint, suggesting that erosional processes are not dominated by overland flow. The high permeability of the shallow soils and the dense carbonates existing in fractures exposed by trenches in the TCw units below the caprock further suggest that lateral flow is likely to be primarily along the soil/bedrock interface rather than as overland flow. The distribution of vegetation suggests that lateral flow may be significant; vegetation is relatively sparse at the top of slopes and relatively dense at points where slopes flatten. Note that the existence of subsurface lateral flow is also suggested by neutron-probe measurements.

Based on topography, soil depth, and bedrock materials, the ground surface over the repository footprint can be divided into four categories:

Tiva Canyon caprock on ridgetops. Slopes are generally moderate (less than 10 degrees) with shallow soils (0 to 40 cm with pockets greater than 60 cm). The bedrock is generally massive with fissures spaced sufficiently far apart in places to provide significant organization to vegetation. The fissures are typically 5 to 15 cm in aperture, and appear to form by eolian soils filling between boulders. Bedrock is irregular in topography, with at least 40 cm variation

possible within the space of 2 m. The bedrock is sufficiently permeable that moisture may interact significantly with it over periods of days to weeks. Soil fills the fissures to a depth of at least 5 to 30 cm, with carbonate fillings possible. Roots are common, almost ubiquitous, within fractures. Net infiltration may be quite significant due to shallow soils. Several vegetation transects were taken in this environment, 4 soil-permeability and 2 bedrock-permeability measurements were made, and 5 bedrock-exposure pits were dug.

Tiva Canyon welded units (i.e., lithophysal units) below the caprock. Slopes are generally moderate to steep (10 to 45 degrees). Scree exists where slopes are greater than roughly 40 degrees. Bedrock is irregular in topography, although perhaps less so than for the caprock. There is some evidence of stairstepping in the bedrock surface that is not echoed in the soil profile, which may provide localized pockets for vegetation. Fractures are typically narrow in aperture (less than 1 cm) but closely spaced. The fractures appear to be filled with carbonates as a rule, and generally not penetrated by roots except for perhaps a few localized zones with wider apertures. Vegetation is predominantly Great Basin on the north-facing slopes and Mojavian on the south-facing slopes, with vegetation densities about twice as large on the north-facing slopes. Vegetation increases in density downslope. Net infiltration may be significant due to shallow soils. Lateral redistribution along the soil/bedrock interface may also be significant. Several vegetation transects were taken in this environment, a pair of soil-permeability measurements were taken, and several trenches and pavements were examined in detail.

Alluvium-filled washes. Slopes are shallow and soils tend to be greater than 1 m in depth. Net infiltration may not be significant, due to the large storage capacity of the soils and the presence of vegetation. This environment was not examined in detail, aside from one or two vegetation transects.

The west face of Yucca Crest. Slopes are quite steep, as much as 50 degrees. Numerous strata are exposed, ranging from densely welded to nonwelded. Soil pockets exist of as much as 50 cm even in the steepest slopes. Vegetation is dominated by crack-dwelling species. Overland flow should be significant, as evidenced by gully formation. Of the four environments this environment is by far the most complex to model however, relatively little of the repository footprint is overlain by this category. The environment was not examined in detail, aside from daily hikes up and down to Yucca Crest.

Hydraulic Conductivity Measurements in Solitario Canyon

J. Winterle obtained 13 hydraulic conductivity measurements for the stream beds in Solitario Canyon and its side canyons. These measurements were obtained using a Guelph Permeameter which is used by augering a hole 20 to 40 cm deep into the sediments and measuring infiltration of water out of the bottom of this hole while a constant water level is maintained in the hole. There were problems with this technique involving difficulty in augering holes due to the presence of large cobbles, and a tendency for the holes to collapse due to the lack of cohesiveness of the sediments. Nevertheless, 13 measurements were obtained with hydraulic conductivities on the order of 10^{-3} to 10^{-1} cm/s. These values are consistent with published values for silty sands and gravels. It should be noted that 10^{-2} cm/s is the upper limit of the range of hydraulic conductivities for which the Guelph permeameter is designed, thus the values outside of this range may not be as accurate as the lower values; however, they do represent a good order-of-magnitude estimate. Samples of sediments were obtained from the auger holes and their hydraulic conductivities are currently being measured in the laboratory. Locations of each of the conductivity measurements was recorded using a GPS unit. The GPS measurements are accurate to the nearest 100 m. Table 1-8 summarizes the data collected.

Problems Encountered

The real-time differential GPS did not function properly, almost certainly due to operator error. Reported measurements are therefore only accurate to within 100 m.

4/27/97 Conversion of neutron-probe data to matlab format.

SAS

The complete set of neutron-probe readings from the 98 neutron-probe boreholes plus UZ-7 (described by Flint and Flint (1995)), obtained September, 1996, from the DOE office, were converted to *Matlab* format. An awk script (**reduce_neut.awk**) converted the ASCII file to a reduced format, and a *Matlab* script converted it to a binary format for fast reads. Two additional *Matlab* scripts were created to examine the plots as a time history, **plot_neut.m** and **plot_neut_set.m**. Borehole UZ-7 is designated as neutron-probe borehole number 99. The scripts are stored in ***$HOME2/AmbientKTI/3Ddata***.

The awk conversion uses the csh sequence "`zcat neutron_* | nawk -f reduce_neut.awk`

Table 1-8: Hydraulic conductivity measurements in Solitario Canyon on March 27 and 28, 1997.

Sample #	UTM (m) N	UTM (m) E	Hydraulic Conductivity (cm/s)	Notes
1	546637	4077467	0.04	silty coarse gravels; many large cobbles
2	546517	4077632	0.02	coarse gravel with fine silty sand
3	546794	4077389	0.07	sandy coarse gravel
4	546826	4077651	0.05	well-sorted, pea-sized gravel
5	546772	4077250	0.002	silty, sandy gravel; large cobbles
6	546667	4077103	0.007	silty, sandy gravel; a few large cobbles
7	546612	4076972	0.002	silty coarse gravel
8	546593	4076710	0.012	sandy gravel; a few large cobbles
9	546597	4076410	0.02	sandy gravel
10	547186	4079275	0.1	coarse sand and gravel
11	547135	4078848	0.04	well-sorted pea-gravel with coarse sand
12	547121	4078681	0.01	well-sorted pea-gravel with coarse sand
13	547021	4078283	0.002	silty overbank sediments stream channel well-sorted pea-gravel

> `neut.date_num_dep_mc`".

There appears to have been some adjustment of elevations in late 1985, judging from offsets in all boreholes with records that early.

5/9/97 Documentation of upper-bound infiltration estimates.

SAS

If the temperature and thermal conductivity profiles of a rock mass are known, one can calculate the energy flux due to conduction. If the actual energy flux through the rock mass differs from the conductive flux, it must be due to advection (i.e., energy transported through liquid or vapor fluxes). When a vertical column has smaller conductive fluxes than actual fluxes, it may be due to cool infiltrating water warming while moving to depth or upward vapor transport with an associated large latent-heat transport. In order to estimate infiltration fluxes when moisture movement is predominantly vertical, one can use an analytic solution or a numerical simulator accounting for both conductive and advective fluxes, and adjust the infiltration flux until the measured temperature profile is obtained. Lachenbruch and Sass (1977) presented a relationship that indicates that the reduction in apparent heat flux is roughly proportional to the volume of infiltrating water, the

thermal gradient, and the distance considered. Typically it is assumed that vapor flux is negligible, although this assumption is not necessary if the vapor flux can be accounted for. Implicit in the approach is the assumption that the liquid and rock remain in thermal equilibrium.

One of the advantages of the method is the lack of necessity for knowing details of how the liquid moves within the rock. On the other hand, it is necessary to have an independent estimate for the thermal flux, which can be difficult to obtain. It is also necessary to know thermal conductivities, but these are typically quite well constrained.

Estimates of thermal and liquid fluxes throughout the NTS are presented by Sass et al. (1980) and Sass and Lachenbruch (1982), with the results summarized by Sass et al. (1988). Sass et al. (1988) analyzed a set of boreholes in the Yucca Mountain area, with resulting estimates of conductive and total heat fluxes from the saturated zone (SZ) into the unsaturated zone (UZ) of 40±9 and 49±8 mW/m^2, respectively, with an average heat flux in the UZ of about 41 mW/m^2. Sass et al. (1988) contour conductive heat fluxes in the Yucca Mountain area (Figure 15 by Sass et al., 1988), which indicates that conductive fluxes are 70 to 74 mW/m^2 southeast through southwest of Yucca Mountain; roughly 60 mW/m^2 in the southwest part of Midway Valley; roughly 50 mW/m^2 in and near Fortymile Wash, Dune Wash, Yucca Wash, and Solitario Canyon; and roughly 30 to 40 mW/m^2 over the repository footprint and north past Drillhole Wash. Sass et al. (1988) suggest that there may be an apparent reduction of heat flow from the SZ to the UZ of 5 to 10 mW/m^2, and calculate that this apparent reduction of heat flow could be achieved by 2 to 5 mm/yr net infiltration and about 8 mW/m^2 reduction would be achieved if 0.1 mm/yr of water were vaporized. Lateral flow in the shallow SZ is also considered a possible source of local anomalies. Sass et al. (1988) also note (without further comment) that apparent heat flux is negatively correlated with elevation; one might infer that lateral diversion to lower topographic areas may be occurring, although the study by Rousseau et al. (1996), discussed below, would suggest the opposite due to the insulating properties of alluvium.

An implication of the analysis by Sass et al. (1988) is that, at least locally over the repository block and Drillhole Wash, deficits in the apparent heat flux that occur in the UZ may be as much as 20 mW/m^2[assuming that 10 mW/m^2 is roughly equivalent to 5 mm/yr infiltration, as calculated by Sass et al. (1988)], so that locally about 10 mm/yr infiltration might be estimated. When estimating infiltration, it may be better to estimate the vertical heat flux from boreholes that are unlikely to have significant infiltration. Infiltration fluxes in deep alluvium and not close to channels are likely to be quite small, so that the boreholes in Midway Valley and south of Yucca Mountain in deep alluvium may be more representative of regional vertical heat flux. If so, vertical heat flux could be as much as 60 to 75 mW/m^2 and local deficits at Yucca Mountain could be as much

as 45 mW/m^2, implying that locally more than 20 mm/yr infiltration could be inferred from the thermal data. Assuming that the UZ heat flux is 60 mW/m^2, heat-flux deficits on the order of 15 to 30 mW/m^2in the area of the repository block and Drillhole Wash could be justified, implying that local infiltration rates may be 7 through 15 mm/yr in this area.

One significant advantage of the heat-flux method is that it can yield upper-bound estimates for infiltration rates. Assuming that the regional heat flux is 85 mW/m^2, neglecting all other sources of reduction in apparent heat flux such as lateral flow in the SZ and vapor fluxes, using a value of 35 mW/m^2 as the average apparent heat flux over the repository block, and using the rule-of-thumb that 10 mW/m^2 reduction in apparent flux is equivalent to 5 mm/yr infiltration, one finds that the maximum average infiltration over the repository block is about 25 mm/yr.

The chloride mass balance technique, as applied by Fabryka-Martin et al. (1996), assumes that average Cl^- concentration multiplied by total flux is conserved, or

$$C_o P = CI, \tag{1-25}$$

where

- P is average precipitation rate,
- C_o is the Cl^- concentration corresponding to the average Cl^- deposition rate,
- C is the Cl^- concentration in a well-mixed reservoir at depth, and
- I is the net infiltration.

Knowing the average precipitation rate, Cl^- concentration corresponding to the average Cl^- deposition rate, and Cl^- concentration in a well-mixed reservoir at depth, the percolation flux at depth can be determined. Yang et al. (1996) report Cl^- concentrations in perched water of 4.1 to 15.5 mg/L, with 15 of the 17 reported values no greater than 8.3 mg/L and a Cl^- concentration of 7 mg/L at NRG-7a (the nearest borehole to UZ-4 and UZ-5 with a reported perched-water sample). Using the same precipitation rate (170 mm/yr) and Cl^- concentration (0.62 mg/L) as Fabryka-Martin et al. (1996), and assuming that the perched water is well mixed with the matrix waters, calculated net infiltration is 25.7, 12.7, and 6.8 mm/yr for concentrations of 4.1, 8.3, and 15.5 mg/L, respectively.

An infiltration value of about 26 mm/yr would represent an upper bound based upon the perched-water chloride data; if the matrix waters do not mix completely with the perched water, infiltration values may be lower. The estimated infiltration values are more consistent with the shallow infiltration estimates than the estimates from the PTn, however, suggesting that a considerable portion of the infiltrating water may bypass the PTn matrix. The upper-bound value

obtained by chloride mass balance on perched water, 26 mm/yr, is remarkably consistent with the upper-bound value obtained by geothermal heat-flux calculations.

5/19/97 Revisiting alluvium regression.

SAS

Since the discussion of 1/13/97, additional information on alluvium depths, borehole location, and borehole geomorphic classification (e.g., channel, sideslope) has been gleaned from the literature and the data file obtained with the site atlas. I incorporated the new information to obtain regression coefficients.

As it turns out, I was not able to reproduce the original slopes calculated by Hannah Castellaw in August, 1995. Apparently she used the slope at the nearest neighbor of the DEM, with all calculations performed in ArcInfo. I tried to use: (i) the slope at the nearest neighbor, (ii) the interpolated slope from the slope at the four nearest neighbors, and (iii) the interpolated slope from the elevations at the four nearest neighbors. None of these matched the previous slopes, although some were close. Unfortunately, the regressions exhibit poorer fits than before, particularly for the channels (although the channels have many more points now). It may be that Hannah used a different DEM coordinate grid; she has not worked at CNWRA for a year or two, so it will be difficult or impossible to retrace the exact calculations. There does seem to be quite a bit of scatter.

I revised the set of files used to estimate regression coefficients in ***$HOME2/Matlab/-3Ddata***. New data files were created in the format that the load_well file expects, and the other load routines call load_well. The original data and *Matlab* files all have ".1" appended. The routine that calculates the slope at the borehole locations is called calc_pt_slope; internally there are switches to calculate the slope according to the three options mentioned above.

5/25/97 Results of 1D simulations.

SAS

Over the last several months, a series of *breath* version 1.2 simulations were run examining the impact of alluvium-filled fissures and calcite-filled fractures. These simulations used the same strategy as was used for the open fractures, in that the bedrock was assumed impermeable and the porosity of the filling was lowered to account for the fracture porosity. The alluvium simulations use kmpo5223_aKmao5222 as the base case, while the calcite simulations use kmpo5223_cKmao7554 as the base case. The alluvium simulations used soil depths of 10, 25, and 50 cm; the calcite simulations

Table 1-9: Summary of alluvium (*abcd*) and fracture (*efgh*) parameter codes

Code	Parameter	Translation
Soil cover (kmpo*abcd*_aKmao*efgh*)		
a	Intrinsic permeability k (cm^2)	$k = 10^{-a-3}$
b	van Genuchten m	$m = b/10$
c	van Genuchten scaling pressure P_0 (gm/cm-s^2)	$P_0 = c \times 10^4$
d	Porosity ε	$\varepsilon = d/10$
Soil-filled fissure (kmpo*abcd*_aKmao*efgh*)		
e	Intrinsic permeability k (cm^2)	$k = 10^{-a-3}$
f	van Genuchten m	$m = f/10$
g	van Genuchten scaling pressure P_0 (gm/cm-s^2)	$P_0 = c \times 10^4$
h	Porosity ε	$\varepsilon = 10^{-h}$
Calcite-filled fracture (kmpo*abcd*_cKmao*efgh*)		
e	Saturated hydraulic conductivity K_{sat} (cm^2)	$K_{sat} = 10^{-e}$
f	van Genuchten m	$m = f/10$
g	van Genuchten scaling pressure P_0 (gm/cm-s^2)	$P_0 = 10^g$
h	Porosity ε	$\varepsilon = 10^{-h}$

used soil depths of 10, 25, 50, 100, and 150 cm. The alluvium simulations used fracture-alluvium porosity values of 10^{-2}, 10^{-3}, and 10^{-4}. The calcite simulations had a nearly full suite of calcite perturbations for soil depths of 10, 25, 50, 100, and 150 cm (2 perturbations calcite permeability, and calcite van Genuchten m; 1 perturbation for calcite P_0 and porosity) and a full suite of 2 perturbations for all soil properties with a soil depth of 10, 25, or 50 cm. The codes for the output files are discussed in Table 1-9. Note that the code for alluvium-filled should have been kmpo*abcd*_akmpo*efgh* and the code for calcite-filled should have been kmpo*abcd*_cKmpo*efgh* for clarity.

The average flux over the second decade, averaged over the depths of 1 to 10 m, were extracted using extract_qstate.m (coded in *Matlab*) for all simulations. Similarly, the decadal average moisture content in the node above the soil/fracture interface was extracted for each case. All values were stored in **af_allcli.result** in ***$BREATH2/Subreg***. The net-infiltration results are summarized in Table 1-10.

Several conclusions can drawn from the simulation results. The alluvium results suggest that as the fracture aperture decreases, net infiltration increases. The effect decreases as the soil depth increases, and is not tremendously large in any case. The calcite results suggest that the

Table 1-10: Net infiltration (mm/yr) for various cases with soil- and calcite-filled fractures

Code	10-cm	25-cm	50-cm
kmpo5223_aKmao5222	17.2	7.13	4.44
kmpo5223_aKmao5223	21.4	8.30	4.92
kmpo5223_aKmao5224	22.4	8.53	4.99
kmpo5223_cKmao7554	17.4	8.55	4.85
kmpo4223_cKmao7554	14.7	2.70	0.42
kmpo6223_cKmao7554	21.6	13.8	10.7
kmpo5123_cKmao7554	18.2	12.9	8.66
kmpo5323_cKmao7554	21.5	12.0	8.24
kmpo5213_cKmao7554	26.3	17.6	12.7
kmpo5253_cKmao7554	10.3	1.25	0.13
kmpo5222_cKmao7554	23.0	15.8	11.6
kmpo5225_cKmao7554	9.48	1.80	0.29
kmpo5223_cKmao6554	33.1	14.8	8.08
kmpo5223_cKmao8554	3.31	1.81	1.43
kmpo5223_cKmao7454	15.2	7.50	4.78
kmpo5223_cKmao7654	19.2	9.21	4.70
kmpo5223_cKmao7564	42.6	23.6	14.2
kmpo5223_cKmao7555	17.5	8.57	4.87

alluvium properties are not important relative to calcite properties when soil is 10 cm, but dominate when soil is 50 cm. Variation in calcite properties yields largest change in net infiltration when soils are shallow and are muted somewhat when soils are deep. The calcite property having strongest impact on net infiltration appears to be P_0, followed by K_{sat}.

The capillary properties of alluvium and calcite may be the most important parameters for calculating bare-soil infiltration. It appears that the ratio of alluvium P_0 to calcite P_0 is a controlling factor on infiltration. As the ratio gets smaller (calcite has finer pores relative to alluvium) net infiltration increases. One can attribute this to the propensity of calcite to imbibe moisture and not release it back to the soil to satisfy evaporation.

The variation of moisture content with net infiltration for the bottom node of the soil follows the general patterns ascertained before. There is a clear trend for drier soil with increasing net infiltration when the fracture-filling properties are changed, however, whether the filling is calcite or soil (note that only soil porosity was varied).

6/11/97 Documentation of soil sample analysis.

SAS

During the annual CNWRA QA audit, in which the USFIC KTI was audited, an issue of data collection was raised. During the Yucca Mountain field trip examining shallow infiltration processes in caprock, documented in the entry dated 4/10/97, 23 soil samples were collected and analyzed for electrical conductivity and percent hydrometer estimates of grain size and texture, by Utah State University Analytical Laboratories (Utah State University, Logan, UT 84322-4830, 801/797-2217). The reported analysis is dated 17 April, 1997; I have filed a copy of the results in my file cabinet. These samples were collected at various locations around Yucca Mountain at the suggestion of David Groeneveld and Dani Or (consultants hired for their expertise in characterizing shallow flow processes).

Typically our QA program requires that such analyses be planned prior to data collection and that verification of the analysis procedure be performed in order to be fully complient with QA requirements. I was made aware of their recommendation while we were in the field and did not realize that an external agency (albeit an agency at the same university that Dani Or is an employee of) was to perform the analyses. Note that the soil samples are only intended for qualitative verification of our observations that all of the fine materials at the site are remarkably similar and are not intended for numerical estimates or to provide data for regulatory positions. We will have to note that data was not collected under CNWRA QA procedures if and when we use the information.

6/30/97 Root growth simulations for caprock paper.

SAS

I am writing a paper documenting our investigations of hydrologic issues regarding the interaction of vegetation with fissures in TCw caprock environments with Dani Or and David Groeneveld (consultants). The paper consists of three major components: (i) a description of field observations, (ii) simulation of the impact of vegetation on hydrologic behavior in the presence of fissures, and (iii) simulation of root growth in the presence of fissures. David has been writing the description of the fieldwork. Dani has been performing 2D simulations of a vertical cross-section with 5 fissures overlain by soil using HYDRUS-2D, which is an enhancement of SWMS-2D (Šimůnek et al., 1992), in order to examine the hydrologic behavior component. I have been attempting to use Version 2.0 of a 3D code developed at UC-Davis by Jan Hopmans, Volker Clausnitzer, and Francesca Somma that explicitly models individual roots and distributes uptake to the surrounding nodes.

The root-growth code does not have a name; I will refer to it as Root-Growth Simulation

Model (RootSim) from now on. RootSim is a research-level code, so it has a number of shortcomings that would not be expected in a production code and that make it difficult to use for our purposes. Some shortcomings include:

- Every element must be the same size and rectangular shape.
- Properties are defined by node rather than element.
- Boundary conditions are restricted to a mixture of:
  - one (time-varying) flux value (as many nodes as desired),
  - one (time-varying) head value (as many nodes as desired).
- Gravity drainage is not allowed.
- The code relies on a non-portable random-number generator.

The code was run through a FORTRAN static analyzer code, for_study (called fstudy on bashful), provided by Cobalt Blue. SPARC version 2.0.1 was used for the test. A number of errors and warnings were identified, either through compilation messages, fstudy, or tracking down errors in simulation behavior, including:

- 24 overlength lines
- a branch into a block
- variable *init* used before being initialized
- calling subroutine ChInit when chemistry is disabled (thereby changing *dtMaxC*)
- 9 unused common blocks in routines
- 13 changes in common blocks between routines (different variable names)
- 21 instances where precision was lost (real to integer or double precision to single precision)
- rand is system-dependent (and does not work for SGI)

The common-block and lost-precision messages were ignored; the remaining messages were fixed. The rand problem was accommodated by writing a short C routine to use the rand48 routine provided as part of the SGI library. In addition, a modification was made so that the **outfem**

output files also include *cAvg*, so that the output file can be reused as a restart file without modification. Modifications and suggested modifications are further documented in file **Errors** in ***$HOME2/AmbientKTI/Root***.

Several tests have been run trying to get appropriate simulations for the paper. The physical problem entails a shallow soil atop a soil-filled fissure next to a matrix block, with a plant starting either directly over the fissure or starting at some distance, with the idea being to compare some measure (e.g., total plant mass) at the end of the simulation. Dani set up the original input files based on the documentation, and some properties were not totally appropriate for Yucca Mountain. Some of the plant properties have never even been measured.

Through a process of trial and error, I've modified the problem from the original set up by Dani. Problem setup and changes include:

- A relatively small domain is being modeled (an 11x12x36 grid, 25 mm on an element side). This represents a tradeoff between computational speed and grid refinement.
- Soil depth is about 10 cm and the fissure is about 15 cm wide (only half is modeled). The "about" is due to the node-defined material properties.
- Bedrock material properties are TCw cuc, with retention parameters for sample PW19s, composite-sample caprock K_{sat} (Flint et al., 1996).
- Soil retention parameters are for a loamy soil (Dani refers to a Carsel and Parrish, 1988) and K_{sat} is texture-estimated for Yucca Mountain soil (Schmidt, 1989).
- Soil strength has caused difficulties in simulations. Soil strength is defined in the code to be $(1-\theta)^3 S_{smax}$, where θ is effective saturation and S_{smax} is soil strength at residual saturation (with apparently arbitrary units). The **root.in** input file defines a soil strength at which growth ceases for each type of material. Dani changed the bedrock retention properties to artificially maintain very dry (very strong) conditions. I put realistic retention properties, and the roots acted as though the bedrock was clay. Changing the bedrock strength to an extremely large value (10^{32}) caused numerical problems (NaN for root-tip location), which I interpret as due to overenthusiastic adjustment to strength gradients, so I cut it back to 10^8 and gradually increased to 10^{11}. Results are not totally satisfactory due to the transition zone between nodes where properties change in an uncontrolled manner. I also had problems by making maximum soil strength too large (14) compared to the plant-growth cutoff at residual saturation (6), which I fixed by making the maximum soil strength 6 as well.

- Appropriate boundary and initial conditions are difficult to provide with the version of the code we have available. One can provide either a constant-head or constant-flux bottom condition and both tend to misrepresent the available water. Either a no-flow or specified-head (representing equilibrium with the atmosphere) top condition may work. I have been running into problems with balancing available water with rock availability. The latest solution is to provide wetting events every 15 or 30 days and have no-flow boundaries at the bottom. I initially used initial conditions at 50 cm suction head.

- The current conditions have been changed to 300 cm suction head in soil (field capacity of 0.3 bar) and 3000 cm (3 bar) suction head in the rock, redistributed with 15 days of evaporation (15 bar) at the top and no flow at the bottom. Rain (7.5 mm) is applied at 15, 30, 45, and 75 days, and evaporation continues throughout at 5 bar.

- When very wet conditions occur, the plant over bedrock develops more biomass than the plant over the fissure, even though the fissure plant has much greater penetration. The bedrock plant is apparently using the bedrock as an additional source of moisture and developing along the bedrock interface. I am not totally convinced that this is not an artifact of the slushy material-property zone, but the caprock *is* quite permeable.

7/8/97 Modification of Scott and Bonk electronic version. SAS

An electronic ARC/INFO coverage of Scott and Bonk (1984) geology is one of the data sets included on the DOE tape discussed in the 3/23/97 entry. There are 118 polygons that do not have a lithologic attribute and one alluvium polygon that is mislabeled as ym. Jim Prikryl extracted the coverage in UTM format last week and I have started entering the missing coverages by visual inspection. All work is in ***$HOME2/Matlab/YMGeology***. The updated coverage information is listed as **scotbonu.wat**; the original coverage is stored in subdirectory ***Orig***.

7/11/97 Regression for TPA shallow infiltration. SAS

It was brought to my attention that the UZFLOW module of the TPA3 code, which predicts infiltration on a pixel-by-pixel basis over Yucca Mountain, was predicting far more mean annual infiltration (MAI) than mean annual precipitation (MAP) under full glacial conditions. The regression formula features bicubics in both MAP and mean annual temperature (MAT), and apparently these cause problems outside the range of interpolation. The formulation is for soil over an open-fracture continuum.

I revisited the form of the regression equation and have come up with a more robust (and simpler) formulation that appears to work well even through 4× current *MAP* and -15 °C cooler than current *MAT*. The formulation fails for soil depths greater than 25 cm, but these depths should have negligible infiltration for the system considered and can be set to zero. For very shallow soils (< 10 cm) and extremely cool and wet conditions (beyond the range simulated), the formulation predicts *MAI* in excess of *MAP*. These cases should have *MAI* set to equal *MAP*.

The regression equation is intended to account for several facets of *MAI* behavior in this system: (i) *MAI* generally changes logarithmically with changing inputs; (ii) *MAI* is more sensitive to changing inputs when soil depths are larger; and (iii) *MAI* is more sensitive to changing inputs when *MAI* is small. The simplest form of an equation satisfying these conditions is

$$H = B^{b_1}[\sum_{i=1}^{N} a_i f_i(u_i)](1 + b_2 H), \tag{1-26}$$

where

- H is $\log_{10}(MAI/MAP)$
- a_i is a regressed constant
- b_i is a regressed constant
- u_i is a normalized regression variable (e.g., *MAP*, *MAT*)
- $f_i(u_i)$ is a regression relationship for variable u_i
- B is $(b\varepsilon)/(b_0\varepsilon_0)$
- b is soil depth
- b_0 is base-case soil depth
- ε is porosity
- ε_0 is base-case porosity

In ***$HOME2/Matlab/YMInfil/SubregSpaceDist*** I created two new *Matlab* routines, **run_sreg.m** and **f_regshal2.m**, that perform the regression using the formulation.

7/14/97 More regression for TPA shallow infiltration. SAS

In ***$HOME2/Matlab/YMInfil/SubregSpaceDist*** I created a new *Matlab* routine, **eval_TPA_fun.m**, that evaluates the function in Equation 1-26 (with best-fit constants) for every pixel in the standard Yucca Mountain DEM with soil depths given in **basecaseDepth.mat**. The areal-average *MAI* resulting from the formula, both as *MAI* and as normalized, is shown in Figure 1-4(a) and (b), respectively.

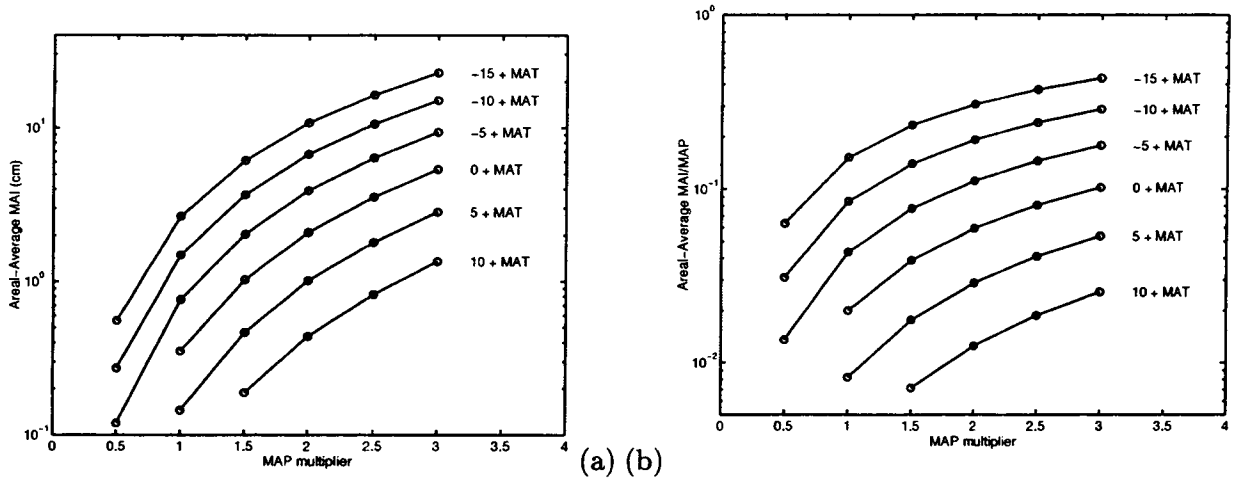

Figure 1-4: 7/14/97. Areal-average *MAI* for Yucca Mountain area, using regression formula based on soil/open-fracture system, (a) in dimensional form, and (b) in nondimensional form.

Following up on the incentive to examine the results in detail, I collected the simulations performed to date in **am_all.result** in ***$BREATH1/RunTightAM***. I modified the format of the file to include the date that the simulation was completed. I cursorily examined the soil-over-calcite simulations to check on the sensitivity to depth and climate. By plotting the simulations with the fracture code of **cal3** against the areal-average simulations, it appears that even thought the calcite simulations do not span the same range as the soil-over-fracture simulations, the change in infiltration with climate should have similar trends. Overall infiltration may be greater with the calcite due to the lesser sensitivity to soil depth (e.g., 10 cm soil depth has 29 mm/yr while 50 cm soil depth has 7 mm/yr *MAI*). Fracture properties have a much greater impact on *MAI* for the calcite simulations than for the open-fracture simulations; permeability and bubbling pressure are the two big players, along with soil porosity.

A cursory check of simulations with base-case alluvium filling fissures with various soil depths and fissure porosities suggests that the falloff of *MAI* with soil depth has a characteristic slope, as the **cal3** simulations have about 1.5 times as much *MAI* for a given soil depth. Interestingly, *MAI* increases slightly as fissure porosity decreases.

References

Bagtzoglou, A. C., N. M. Coleman, E. C. Pearcy, S. A. Stothoff, and G. W. Wittmeyer. 1996.

Unsaturated and Saturated Flow Under Isothermal Conditions. In B. Sagar (Ed.), *NRC High-Level Radioactive Waste Program FY96 Annual Progress Report*, Volume NUREG/CR-6513, No. 1, Washington, DC, pp. 10–1–10–28. Nuclear Regulatory Commission.

Bagtzoglou, A. C., S. A. Stothoff, and M. A. Muller. 1995. *Progress Towards Estimating Infiltration and Deep Percolation at the Yucca Mountain Site.* , Center for Nuclear Waste Regulatory Analyses, San Antonio, TX.

Fabryka-Martin, J. T., P. R. Dixon, S. Levy, B. Liu, H. J. Turin, and A. V. Wolfsberg. 1996. *Systematic Sampling for Chlorine-36 in the Exploratory Studies Facility.* LA-CST-TIP-96-001, Los Alamos National Laboratory, Los Alamos, NM.

Fabryka-Martin, J. T., H. J. Turin, A. V. Wolfsberg, D. Brenner, P. R. Dixon, and J. A. Musgrave. 1996. *Summary Report of Chlorine-36 Studies.* LA-CST-TIP-96-003, Los Alamos National Laboratory, Los Alamos, NM.

Fernandez, J. A., J. B. Case, C. A. Givens, and B. C. Carney. 1994. *A Strategy to Seal Exploratory Boreholes in Unsaturated Tuff.* SAND93-1184, Sandia National Laboratories, Albuquerque, NM.

Flint, A. L., J. A. Hevesi, and L. E. Flint. 1996. *Conceptual and Numerical Model of Infiltration for the Yucca Mountain Area, Nevada.* Water-Resources Investigations Report xx-xxx, United States Geological Survey, Denver, CO. Draft dated September 20, 1996.

Flint, L. E. and A. L. Flint. 1990. *Preliminary Permeability and Water-Retention Data for Nonwelded and Bedded Tuff Samples, Yucca Mountain Area, Nye County, Nevada.* Open-File Report 90-569, United States Geological Survey, Denver, CO.

Flint, L. E. and A. L. Flint. 1995. *Shallow Infiltration Processes at Yucca Mountain, Nevada – Neutron Logging Data 1984-93.* Water-Resources Investigations Report 95-4035, United States Geological Survey, Denver, CO.

Flint, L. E., A. L. Flint, C. A. Rautman, and J. D. Istok. 1996. *Physical and Hydrologic Properties of Rock Outcrop Samples at Yucca Mountain, Nevada.* Open-File Report 95-280, United States Geological Survey, Denver, CO.

Lachenbruch, A. H. and J. H. Sass. 1977. Heat Flow in the United States and the Thermal Regime of the Crust. In H. G. Heacock (Ed.), *The Earth's Crust*, Volume Geophysical Monograph 20, pp. 626–675. Washington, DC: American Geophysical Union.

McKenna, S. A. and C. A. Rautman. 1995. *Summary Evaluation of Yucca Mountain Surface Transects with Implications for Downhole Sampling.* SAND94-2038, Sandia National Laboratories, Albuquerque, NM.

Rautman, C. A., L. E. Flint, A. L. Flint, and J. D. Istok. 1995. *Physical and Hydrologic Properties of Rock Outcrop Samples From a Nonwelded to Welded Tuff Transition, Yucca Mountain, Nevada.* Water-Resources Investigations Report 95-4061, United States Geological Survey, Denver, CO.

Rousseau, J. P., E. M. Kwicklis, and D. C. Gillies (Eds.). 1996. *Hydrogeology of the Unsaturated Zone, North Ramp Area of the Exploratory Studies Facility, Yucca Mountain, Nevada*, Water-Resources Investigations Report 96-????, Denver, CO. United States Geological Survey. Draft dated 8/29/96.

Sass, J. H. and A. H. Lachenbruch. 1982. *Preliminary Interpretations of Thermal Data from the Nevada Test Site.* Open-File Report 82-973, United States Geological Survey, Reston, VA.

Sass, J. H., A. H. Lachenbruch, W. W. Dudley, Jr., S. S. Priest, and R. J. Munroe. 1988. *Temperature, thermal conductivity, and heat flow near Yucca Mountain, Nevada: Some tectonic and hydrologic implications.* Open-File Report 87-649, United States Geological Survey, Denver, CO.

Sass, J. H., A. H. Lachenbruch, and C. W. Mase. 1980. *Analysis of Thermal Data From Drill Holes UE25a-3 and UE25a-1, Calico Hills and Yucca Mountain, Nevada Test Site.* Open-File Report 80-826, United States Geological Survey, Menlo Park, CA.

Schenker, A. R., D. C. Guerin, T. H. Robey, C. A. Rautman, and R. W. Barnard. 1995. *Stochastic Hydrogeologic Units and Hydrogeologic Properties Development for Total-System Performance Assessments.* SAND94-0244, Sandia National Laboratories, Albuquerque, NM.

Schmidt, M. R. 1989. Classification of Upland Soils by Geomorphic and Physical Properties Affecting Infiltration at Yucca Mountain, Nevada. Master's thesis, Colorado State University, Fort Collins, CO.

Scott, R. B. and J. Bonk. 1984. *Preliminary Geologic Map (1:12,000 scale) of Yucca Mountain, Nye County, Nevada, with Geologic Cross Sections.* Open-File Report 84-494, United States Geological Survey, Denver, CO.

Šimůnek, J., T. Vogel, and M. T. van Genuchten. 1992. *The SWMS_2D code for simulating water flow and solute transport in two-dimensional variably saturated media V. 1.1.* Research Report No. 126, U. S. Salinity Laboratory, ARS USDA, Riverside, CA.

Stothoff, S. A. and A. C. Bagtzoglou. 1995. Estimation of Recharge at Yucca Mountain, Nevada. In *Supplement to Eos, Transactions*, Volume 76, Washington, DC, pp. F242. American Geophysical Union.

Stothoff, S. A. and A. C. Bagtzoglou. 1996. Subregional Hydrogeologic Flow and Transport Processes. In B. Sagar (Ed.), *NRC High-Level Radioactive Waste Research at CNWRA, July-*

December 1995, Volume CNWRA 95-02S, San Antonio, TX, pp. 9–1–9–20. Center for Nuclear Waste Regulatory Analyses.

Stothoff, S. A., A. C. Bagtzoglou, and H. Castellaw. 1996. Estimation of Spatial Distribution of Recharge Factors at Yucca Mountain, NV. In *Proceedings of the International Conference on Application of Geographic Information Systems in Hydrology and Water Resources Management*, Vienna, Austria. International Association of Hydrological Sciences.

Stothoff, S. A., H. M. Castellaw, and A. C. Bagtzoglou. 1995. Estimation of Spatial Distribution of Recharge Factors at Yucca Mountain. In B. Sagar (Ed.), *NRC High-Level Radioactive Waste Research at CNWRA, January–June 1995*, Volume CNWRA 95-01S, San Antonio, TX, pp. 9–5–9–12. Center for Nuclear Waste Regulatory Analyses.

Sykes, J. F., J. L. Wilson, and R. W. Andrews. 1985. Sensitivity Analysis for Steady State Groundwater Flow Using Adjoint Operators. *Water Resources Research 21*(3), 359–371.

Yang, I. C., G. W. Rattray, and P. Yu. 1996. *Interpretations of Chemical and Isotopic Data From Boreholes in the Unsaturated Zone at Yucca Mountain, Nevada.* Water-Resources Investigations Report 96-4058, United States Geological Survey, Denver, CO.

2. Thermal Hydrology KTI

Account Number: **20-5708-663**
Collaborators: **Ronald T. Green**
Directories: **As noted**

4/10/97 Printout entry. SAS

I performed no work on this project during the period covered by this printout.

3. Iterative Performance KTI

Account Number: **20-5708-761**
Collaborators: **Robert Baca, Gordon Wittmeyer**
Directories: **As noted**

4/10/97 Printout entry.

SAS

I performed no work on this project during the period covered by this printout.

4. Iterative Performance KTI - Total Performance Assessment Phase 3

Account Number: **20-5708-761**
Collaborators: **Robert Baca**
Directories: **$HOME2/Matlab/TPA3, $HOME2/IPA/Phase3, as noted**

Objective: Providing input and analyses for Total Performance Assessment (TPA) Phase 3 exercises. The emphasis under this project is on abstracting detailed process-level simulations into forms that are more amenable to performance assessment needs (e.g., probability distributions).

1/10/97 Software requirements for UZFLOW.

In ***$HOME2/IPA/Phase3***, I developed a first-cut description of proposed software requirements for the UZFLOW module and supplied it to R. Manteufel. The description is included below in italics.

UZFLOW Module Technical Description

Introduction

The UZFLOW module is to provide time-dependent percolation-flux boundary conditions for the NFENV module, based on climatic change. As the module considers climatic change, it could easily be modified to provide other climate-dependent values such as water table elevations and irrigation rates.

Two modes should exist for the UZFLOW module, in which mean annual infiltration (MAI) is (i) directly specified as a randomly sampled variable, and (ii) mechanistically varied according to current interpretations of the linkage between climate and infiltration.

The first UZFLOW mode reproduces the IPA2 procedure, taking advantage of the generality of random-parameter sampling strategies that can be employed in the IPA3 code.

The second UZFLOW mode consists of (i) a climate simulator and (ii) a shallow-infiltration simulator. The climate simulator generates a series of mean-annual precipitation and temperature values at discrete intervals, based on expert elicitation within 10 ky and Milankovich cycles for

longer intervals. The shallow-infiltration simulator uses these mean-annual values to predict mean-annual infiltration in a highly abstracted manner, using a DEM containing elevation, soil depth, and bedrock characteristics in conjunction with abstracted transfer functions.

The shallow-infiltration simulator should be considered as representative of the spatial distribution of the *MAI* signal; however, the results should be normalized to a user-specified value to reflect calibration from other lines of evidence.

Climate Simulation

A standard auto-regressive time-series generation process will be used to generate a climatic record. At particular time instants, mean, standard deviation, and correlation matrix for mean annual precipitation (MAP) and mean annual temperature (MAT) will be provided, either as a data file or as block data. The time instants will be sufficient to define climatic variation. Linear interpolation of the statistical parameters will be used to define the parameters at intermediate times.

A time series for MAP and MAT will be generated using the equation (Matalas, 1967)

$$\chi_k = A\chi_{k-1} + B\epsilon_i, \tag{4-1}$$

$$A = M_1 M_0^{-1}, \tag{4-2}$$

$$B = M_0 - M_1 M_0^{-1} M_1^T, \tag{4-3}$$

where the superscripts -1 and T denote the inverse and transpose of the matrix and ϵ is a random signal drawn from a normal distribution with zero mean and unit standard deviation. The matrices are defined as

$$M_0 = [\rho_0(i,j)], \tag{4-4}$$

$$M_1 = [\rho_1(i,j)], \tag{4-5}$$

where $\rho_0(i,j)$ is the correlation coefficient between variables i and j at the same time and $\rho_1(i,j)$ is the lag-1 correlation between variables i and j. Note that $\rho_0(i,i) = 1$, M_0 is symmetric, and M_1 is not necessarily symmetric. Variables MAP and MAT will be recovered from the deviation variable χ by taking into account the time-varying mean and standard deviation,

$$v_k = \chi_k s_k + m_k, \tag{4-6}$$

where

v_k *is the value of MAP or MAT at time k*

s_k *is the standard deviation of MAP or MAT at time k*

m_k *is the mean of MAP or MAT at time k*

A total of 9 parameters are provided as a function of time: m, s, and $\rho_1(i,i)$ *for both MAP and MAT (6 parameters);* $\rho_0(1,2)$*; and both* $\rho_1(1,2)$ *and* $\rho_1(2,1)$*. The* ρ *parameters can probably be time-independent. The m and s parameters will be derived from the expert elicitation (DeWispelare et al., 1993) for the first 10 ky. Beyond 10 ky, both m and s will be functions of orbital mechanics (i.e., the Milankovich cycle):*

$$m = \alpha(t)m_{current} + (1 - \alpha(t))m_{pluvial} \tag{4-7}$$

$$s = \alpha(t)s_{current} + (1 - \alpha(t))s_{pluvial} \tag{4-8}$$

where $\alpha(t)$ *is a time-varying signal based on solar loading, further based on orbital mechanics. Parameters* $m_{current}$*,* $m_{pluvial}$*,* $s_{current}$*, and* $s_{pluvial}$ *for both MAP and MAT will come from interpretations of Devils Hole data and other sources.*

Time steps will be on the order of decades to hundreds of years. Correlation between time steps may be zero at sufficiently long time intervals, in which case the values for ρ_1 *are all 0 and the model simplifies considerably to*

$$v_k = B\epsilon_k s_k + m_k. \tag{4-9}$$

Shallow Infiltration Transfer Functions

Transfer relationships have been developed for predicting MAI as a function of soil properties, soil depth, and meteorologic parameters such as MAP and MAT (Stothoff et al., 1996). Each of the soil properties is unknown; MAP and MAT are also unknown but will be provided from the climate simulator.

The hydraulic-property transfer relationships for deep soil is

$$\log_{10}\left(\frac{MAI}{MAP}k^{1/2}\right) = \alpha_0 + \alpha_1\left[\left(\frac{m}{m_0}\right)^2 - 1\right] + \alpha_2\left[\left(\frac{P_0}{P}\right)^{1/2} - 1\right] + \alpha_3\left[\left(\frac{\varepsilon}{\varepsilon_0}\right) - 1\right], \tag{4-10}$$

where k is intrinsic permeability, m is van Genuchten $m = 1 - 1/n$*, P is bubbling pressure (the reciprocal of van Genuchten* α *in the units used here),* ε *is porosity, a subscript 0 represents a reference value for the parameter (*$m_0 = 0.2$*,* $P_0 = 2000$ *Pa, and* $\varepsilon_0 = 0.3$*), and the* α *values are hydraulic-parameter sensitivity constants. If k is less than* 10^{-8} cm^2*, MAI is zero.*

The meteorologic-property transfer function for deep soil, neglecting longwave and shortwave radiation and windspeed, is

$$\log_{10}\left(\frac{MAI}{MAP}k^{1/2}\right) = J_{fit} \tag{4-11}$$

$$\begin{aligned} J_{fit} = \beta_0 + \beta_1 &\left[\left(\frac{MAV}{MAV_0}\right)^2 - 1\right] \\ &+ j_1 M + j_2 T + j_3 M^2 + j_4 MT \\ &+ j_5 T^2 + j_6 M^3 + j_7 M^2 T + j_8 M T^2 + j_9 T^3, \end{aligned} \tag{4-12}$$

$$T = (MAT - MAT_0)/MAT_0, \tag{4-13}$$

$$M = \log_{10}(MAP/MAP_0), \tag{4-14}$$

where the β_i and j_i values are fitting coefficients, T is the relative change in MAT and M is the change in the base-10 log of the MAP multiplier. Base-case mean-annual values are used for normalizing: (i) $MAP_0 = 163$ mm/yr, (ii) $MAT_0 = 290$ K, and (iii) $MAV_0 = 4.5 \times 10^{-6}$ gm/cm^3.

The transfer function for shallow soil over fractured welded bedrock, neglecting longwave and shortwave radiation and windspeed, is

$$\log_{10}\left[\frac{(MAI/MAP)}{I_{D0}}\right] = B^{\sqrt{1/2}}(J_{fit} - C_I) \tag{4-15}$$

$$B = \varepsilon\frac{b}{b_r} \tag{4-16}$$

where C_I, I_{D0}, and b_r values are all fitting coefficients. The β_i values and the j_i values are different in Equation 4-11 and Equation 4-15.

In addition, the transfer functions have corrections to account for solar aspect. Modification of the base-case MAI by solar radiation is estimated by calculating the north-south and east-west rotations of the ground surface, and interpolating within a table obtained from simulations using solar loads appropriate to surface rotations 30 degrees to the east, west, north, and south. The impact should be considered part of J_{fit}, so the sensitivity increases with depth.

A blending of the deep and shallow equations are required. I use the shallow equation for depths less than 5 m, the deep equation for depths greater than 10 m, and interpolate between the two for intermediate depths.

Formulae for predicting base meteorologic-property distributions under current climate are

$$MAP = \exp(4.26 + 0.000646Z) \tag{4-17}$$

$$MAT = 25.83 - 0.00840Z \tag{4-18}$$

$$MAV = \exp(-11.96 - 0.000341Z) \tag{4-19}$$

where Z is ground-surface elevation in meters, MAP is in mm/yr, MAT is in $^\circ C$, and mean annual vapor density (MAV) is in gm/cm^3. It should be adequate to ignore temporal variation in MAV and solar aspect.

Soil Depth

Three equilibrium balance equations are solved to calculate the equilibrium depth of alluvium over the Yucca Mountain region; (i) an overall alluvium mass balance, (ii) a sediment mass balance, and (iii) a hydraulic mass balance or stream-flow model. The overall mass balance for alluvium, the first equation, is

$$\nabla \cdot \mathbf{q}_{alluv} + Q_{wea} + \overline{Q_{str}} = 0, \tag{4-20}$$

where $\mathbf{q}_{alluv}$ is the flux of alluvium, Q_{wea} is the source of alluvium due to weathering, and $\overline{Q_{str}}$ is the time-averaged flux due to stream action. The erosion-balance model assumes that all processes are at equilibrium. Thus, the stream-flow model assumes that a representative spatially uniform rainfall rate is applied over the entire mountain, and the resulting equilibrium hydraulic flux distribution is used to calculate equilibrium sediment transport. As streamflow is actually highly episodic at Yucca Mountain, the equilibrium sediment-transport velocities and erosion/deposition rates must be adjusted to account for the time with no streamflow. Time averaged stream-action flux is approximated here by

$$\overline{Q_{str}} \approx F_{str} Q_{str}, \tag{4-21}$$

where F_{str} is the fraction of time stream flow occurs. The procedure is likely to under-represent the time average in headwater and overland-flow areas, and over-represent the time average in deep washes and downstream areas.

Flux of alluvium, other than through sediment transport, is assumed to occur through creep and is gravity-driven,

$$\mathbf{q}_{alluv} = -Kb\nabla Z, \tag{4-22}$$

where b is the depth of alluvium, Z is the ground surface elevation, and K is a creep conductance (assumed spatially constant here). The alluvium-flux term is similar to the short-range transport model used by Beaumont et al. (1992), except that here b varies with time and Z is constant, while in the Beaumont et al. (1992) application, b is assumed constant and Z is allowed to vary over time.

A simple source term representing weathering is used here. It is assumed that alluvium protects the bedrock from weathering, so that weathering decreases exponentially with alluvial depth:

$$Q_{wea} = Q_0 \exp(-b/b_0) \tag{4-23}$$

where Q_0 is the source strength, and b_0 represents a weathering-protection alluvium depth. The weathering model has two fitting parameters, Q_0 and b_0, which can be used to match observed alluvium depths.

Erosion and deposition through stream action is calculated using the second equilibrium balance equation, a sediment-balance equation,

$$\nabla \cdot c_s \mathbf{q}_w - Q_{str} = 0, \tag{4-24}$$

where c_s is the concentration of the sediment in water and $\mathbf{q}_w$ is the flux of water. Following standard practices in the literature (e.g., Woolhiser et al. (1990)), a simple kinetic rate law is used to characterize erosion and deposition,

$$Q_{str} = C_g(c_s - c_{eq}), \tag{4-25}$$

where c_{eq} is the equilibrium sediment concentration for a reach along a stream bed and C_g is an equilibrium constant.

Numerous equilibrium sediment concentration capacity relationships exist in the literature (e.g., Yang (1973), Kilinc and Richardson (1973), Ackers and White (1973), Yalin (1963)). A particularly simple relationship is used herein (Meyer and Wischmeier, 1969), based on tractive force:

$$c_{eq} = C_s \frac{v^4}{h}, \tag{4-26}$$

where C_s is a constant, v is water velocity, and h is hydraulic depth.

For erosion, C_g is a constant describing the erodibility of the alluvium or bedrock. For deposition ($c_s > c_{eq}$), C_g assumes that particles have fall velocities and drag characteristics similar to spheres (Fair and Geyer, 1954), and a coupled set of equations are used to calculate C_g:

$$v_s^2 = \frac{4}{3}\frac{g(S_s - 1)d}{C_D}, \tag{4-27}$$

$$C_D = \frac{24}{R} + \frac{3}{\sqrt{R}} + 0.34, \tag{4-28}$$

$$R = v_s d/\nu, \tag{4-29}$$

$$C_g = \frac{v_s}{h}\left(1 - \frac{c_{eq}}{c_s}\right), \tag{4-30}$$

where v_s is the particle settling velocity, g is the acceleration due to gravity, S_s is the particle specific gravity, d is the particle diameter, C_D is the drag coefficient, R is the Reynold's number, and ν is the kinematic viscosity.

The final equilibrium balance equation required to complete the alluvium-balance system is the water-balance equation,

$$\nabla \cdot \mathbf{q}_w + Q_{rain} = 0, \tag{4-31}$$

where Q_{rain} is the net rainfall. A standard practice in the literature is to use a kinematic-wave approximation for hydraulic flux in conjunction with the Manning hydraulic resistance law, so that (in metric units)

$$\mathbf{q}_w = \frac{S^{1/2} h^{5/3}}{n}, \tag{4-32}$$

where S is the slope and n is Manning's roughness coefficient.

Each of the three balance equations is solved using the same general finite-volume flow-routing approach. The DEM grid is discretized into square boxes, or nodes, with 1D connections to the nearest eight nodes. Taking advantage of the hyperbolic nature of the equations by assuming that upstream variables uniquely determine fluxes to downstream nodes, the nodes in the grid can be processed in order from highest to lowest elevation in one pass.

The water-balance equation is solved independently of the sediment- and alluvium-balance equations. In the water-balance equation, each node is processed using the algebraic equation,

$$A_i q_{rain} + \sum_{j=up} \frac{w_{ij} h_j^{5/3}}{n} \left(\frac{Z_j - Z_i}{\Delta_{ij}} \right)^{1/2} - \sum_{j=down} \frac{w_{ij} h_i^{5/3}}{n} \left(\frac{Z_i - Z_j}{\Delta_{ij}} \right)^{1/2} = 0, \tag{4-33}$$

where node i is the node being processed, node j is a neighboring node, A_i is the area associated with node i, q_{rain} is the rainfall rate minus infiltration, w_{ij} is the width of the 1D connection between nodes i and j, and Δ_{ij} is the distance between nodes i and j. Summing over upstream nodes is denoted by $j = up$, and summing over downstream nodes is denoted by $j = down$. On a square grid with constant node spacing Δ, w_{ij} is $\Delta/2$ for nearest-neighbor connections and $\sqrt{2}\Delta/3$ for diagonal connections.

The sediment- and alluvium-balance equations are solved simultaneously, by requiring that each nodal alluvium depth and sediment concentration is compatible with outflow from the node. The algebraic balance equations are:

$$\sum_{j=up} c_{sj} Q_{wij} - \sum_{j=down} c_{si} Q_{wij} + \frac{A_i}{8} \sum_{j=down} \overline{C_{gij}(c_{eqij} - c_{si})} = 0, \tag{4-34}$$

$$\sum_{j=1}^{8} w_{ij} K_{ij} b_{up} \left(\frac{Z_j - Z_i}{\Delta_{ij}} \right) + A_i Q_0 \exp(-b_i/b_0) - \frac{A_i}{8} \sum_{j=down} \overline{C_{gij}(c_{eqij} - c_{si})} = 0, \tag{4-35}$$

where b_{up} is the upstream alluvium depth. Alluvium depths are solved by bisection between a minimum depth of 0 m and a maximum depth (arbitrarily assumed to be 20 m here). The equilibrium sediment concentration is found during each bisection step.

The flow-routing approach works well when there are no local minima in the domain, so that there is a route from every node to the boundary. A physical local minimum cannot exist at equilibrium unless there is a physical mechanism for removing alluvium (e.g., wind transport). Typically, however, local minima are artifacts of the DEM resolution, as elevations are only reported to the nearest meter. Also, narrow features such as upstream wash channels, which are on the order of a meter wide, cannot be resolved with the 30-m DEM grid. About 0.5 percent of the nodes in the DEM are local minima, almost all occurring in wash bottoms but a few occurring along ridgetops. For these minimum nodes, a preprocessing step is performed to eliminate artificial local minima, by artificially raising minima nodes at least 10 cm above the lowest of the surrounding nodes. A number of passes are required to eliminate multinode basins.

There are a total of 11 adjustable parameters in the set of coupled balance equations, The 11 parameters, and values found to result in reasonable predictions of colluvium depths, are shown in Table 4-1. As F_{str}, K, and Q_0 control the relative importance of stream processes, colluvial diffusion, and weathering. These three parameters are not completely independent, so scaling the three parameters by the same constant does not modify the predicted colluvium distribution.

Within the mapped alluvium outline, a post-processing step is performed to provide more realistic alluvium depths. An exponential relationship of alluvial depth to surface slope was determined by regression,

$$b = 47 \exp(-0.32s) \tag{4-36}$$

where s is the slope, in degrees, of the ground surface at the nearest grid point in the DEM. The coefficient of determination is 0.61 for the relationship, using information from 56 of the boreholes discussed by Fernandez et al. (1994). Wherever the slope is less than 10 degrees within the Scott and Bonk (1984) alluvium outline, the alluvium depths are calculated using Equation 4-36; otherwise, the colluvium-routing model predictions are used. Note that in the near future Equation 4-36 will be replaced with a slightly better relationship of the form

$$b = as^{-c}, \tag{4-37}$$

where a and c are constants.

Table 4-1: Adjustable parameters for creating colluvium distributions.

Name	Symbol	Base Value
Net rainfall rate	q_{rain}	5 cm/hr
Manning's roughness coefficient	n	0.1
Kinetic coefficient for alluvium scour	C_g	0.1 s^{-1}
Kinetic coefficient for bedrock scour	C_g	0.002 s^{-1}
Traction coefficient for sediment equilibrium	C_s	10^{-3}
Particle diameter	d	1 mm
Particle specific gravity	S_s	2.5
Alluvium creep conductance	K	10^{-12} m/s
Alluvium weathering rate	Q_0	10^{-9} m^3/m^2s
Alluvium weathering depth	b_0	1 cm
Fraction of time in streamflow	F_{str}	30 min/100 yr

Application of the Transfer-Function Model

The transfer-function model has the general flow of

- *Map pixels to subareas, either one pixel per subarea or all pixels per subarea, depending on the analyst.*
- *Create a base map for soil depth, either once or for each realization, depending on the analyst.*
- *Step through the sequence of meteorology time steps, saving MAP and MAT at each output step.*
- *Run the transfer functions for the mapped pixels corresponding to the subareas for each output step.*
- *Normalize the transfer functions by the user-defined value.*

Data Needs

Two DEM input files must be provided, one for elevation control and one for pixel classification (i.e., mapped alluvium, welded, nonwelded). For each classification, appropriate parameters need to be provided for the hydraulic and erosional relationships.

Sensitivity analyses will probably center on

- *Mean and standard deviation of climatic parameters,*
- *Soil depth, and*
- *Soil hydraulic properties.*

Accordingly, these variables should be able to be tweaked. Ideally, each variable should be able to be tweaked. I suggest that an auxillary file be read in with parameter tweaks, in the form

```
parname1: value1 # comment
parname2: value2 # comment
/ # End of Input Signal
```

The parameters should have a default value. If the tweak file does not exist, the defaults should be used.

2/17/97 Software description for UZFLOW.

SAS

In ***$HOME2/Matlab/TPA3***, I prototyped a version of the UZFLOW module in *Matlab* to test out functionality and ideas. The prototype is driven from **uzflow_test.m** and calls several additional routines.

Based on this mockup, I redefined the software description for UZFLOW, which is copied below in italics.

UZFLOW Module Technical Description

Introduction

The UZFLOW module provides time-dependent percolation fluxes at and below the repository level, based on climatic change. Primary clients for this information are the NFENV and UZFT modules. As UZFLOW considers climatic change, it might easily be modified to provide other climate-dependent values such as water table elevations and irrigation rates.

UZFLOW consists of (i) a climate simulator and (ii) a shallow-infiltration simulator. The climate simulator generates a series of mean-annual precipitation (MAP) and mean-annual temperature (MAT) values at uniform time intervals. The shallow-infiltration simulator uses these mean-annual values to predict mean-annual infiltration (MAI) in a highly abstracted manner, using abstracted transfer functions on each pixel of a digital elevation model (DEM) containing elevation, soil depth, and bedrock characteristics. The pixels within each subarea (SA) are averaged to provide one MAI value for the SA. The SA values are then averaged in time to supply MAI at the output times requested by the user.

The mean values of MAP and MAT over the period of simulation are supplied from an input data file. It is suggested that these values are based on expert elicitation within 10 ky and Milankovich cycles or Devils Hole data for longer intervals.

The user specifies 7 parameters that are provided by the LHS sampler: (i) and (ii) change in the mean of MAP and MAT, respectively, at full glacial maximum; (iii) and (iv) standard deviation of MAP and MAT, respectively, about the mean over each sample period; (v) correlation between MAP and MAT perturbations about the mean; (vi) areally averaged MAI for the initial climate; and (vii) an index into a file containing normally distributed perturbations. IPA Phase 2 behavior is obtained by specifying that parameters (i) through (iv) are constant and zero.

Climate Simulation

A time-series generation process is used to generate a climatic record. An input file specifying mean values of MAP and MAT at particular points in the future is supplied, with enough points to define climatic variation. Linear interpolation of the statistical parameters is used to define the parameters at intermediate times. The values in the time history are normalized to LHS-sampled values for full-glacial conditions.

It is assumed that there is no correlation between perturbations in successive time periods. For a time period k, perturbations are generated using

$$\chi_{kj} = [\rho_{ij}]\epsilon_i \tag{4-38}$$

where

j *represents MAP or MAT*
χ_{kj} *is a vector of correlated perturbations*
ϵ_i *is a vector of independent normally distributed perturbations*
ρ_{ij} *is a correlation matrix*

Variables MAP and MAT are calculated from χ by taking into account the time-varying mean and standard deviation,

$$v_{kj} = \chi_{kj} s_j + m_{kj}, \tag{4-39}$$

where

j *represents MAP or MAT*
v_{kj} *is the value of variable j at time k*
s_j *is the standard deviation of variable j (constant in time)*
m_{kj} *is the mean of variable j at time k*

Shallow Infiltration Transfer Functions

Transfer relationships have been developed for predicting MAI as a function of soil properties, soil depth, and meteorologic parameters such as MAP and MAT (Stothoff et al., 1996). Each of the soil properties is unknown; MAP and MAT are also unknown but will be provided from the climate simulator.

Transfer relationships are in the form of perturbations about a mean value for MAI, in the form

$$\log_{10}\left(\frac{MAI}{MAP}\right) = \alpha_0 + \sum_{i=1}^{N} \alpha_i N(u_i) + \sum_{j=1}^{M} \beta_j N(v_j)\left[1 + \gamma \log_{10}\left(\frac{MAI}{MAP}\right)\right] \tag{4-40}$$

where

N *is a normalizing function appropriate for each variable*
u_i, v_j *represent hydraulic and meteorologic variables*
$\alpha_i, \beta_j, \gamma$ *are fitting constants*

Soil properties and soil depths must be supplied for each pixel of the DEM. This information is uncertain. More than one realization for the properties could be provided by the user and LHS-sampled, as might be done for sensitivity analyses, but the typical user would probably not gain a great deal of benefit by having more than one realization for soil properties.

Formulae for predicting base meteorologic-property distributions under current climate are

$$MAP = \exp(4.26 + 0.000646Z) \tag{4-41}$$

$$MAT = 25.83 - 0.00840Z \tag{4-42}$$

$$MAV = \exp(-11.96 - 0.000341Z) \tag{4-43}$$

where Z is ground-surface elevation in feet, MAP is in mm/yr, MAT is in $^\circ C$, and mean annual vapor density (MAV) is in gm/cm^3. Solar aspect is calculated from the surface slope.

Application of the Transfer-Function Model

The transfer-function model has the general flow of

- *Map DEM pixels to subareas.*
- *Sample one or more base maps for soil depth and soil properties.*
- *Step through the sequence of uniform time steps, saving MAP and MAT at each step.*
- *Normalize MAP and MAT using the sampled full-glacial value.*
- *Run the transfer functions for the mapped pixels in the SAs.*
- *Average the pixel values within each SA.*
- *Normalize MAI by the user-defined initial value.*
- *Output average MAI over each output time step.*

3/1/97 UZFLOW module.

SAS

The UZFLOW module was converted from a *Matlab* prototype into FORTRAN, by S. Stothoff, over the period from 2/22/97 through 2/23/97. Debugging and testing began 2/24/97, immediately linking to the TPA modules (i.e., there is no test driver routine). S. Stothoff verified that inputs were received from the sampler and data files as expected, and reasonable outputs were generated. Each function and subroutine was exercised, using the default tpa.inp data file provided for testing, except for the subroutine qclimate (23 lines of FORTRAN code plus comments). Total lines of code with comments are 1371, comprising the main UZFLOW module, uzflow.f, and a file included

into each subroutine, uzflow.i. There are 572 total lines of code, not including comments, for the two files, so that approximately 58 percent of the two files represent comments or white space.

The UZFLOW departs from the Software Requirement Description (SRD) in a few ways. The most significant change is introduced by modifying the future history of climate specified from the input file **climate.inp** to refer to the fraction of full glacial for AAP and AAT, rather than absolute values of AAP and AAT. Also, an additional parameter is required for sampling, 'TimeStepForClimate[yr]'. In addition, a query routine, qclimate, was provided to enable other modules to get AAP, AAT, and fraction of full glacial at specified time instants.

A. Armstrong went through the code line by line on 2/27/97, checking that the code met specifications. An incorrect conversion factor for feet to meters was identified and corrected. Also, a number of FORTRAN-usage questions were raised and explained, regarding the use of double-precision constants, indexing into character strings, and undefined parameters. These questions were explained satisfactorily. Several usages that are extensions to standard FORTRAN-77 were also identified (e.g., do-enddo loops, do-while loops, character*(*) dimension statements). Each usage was justified as being consistent with standards set in previously coded modules.

3/14/97 NFENV and UZFLOW modules.

SAS

During the past week I developed and modified several subroutines involved with the NFENV module, and tested both the NFENV and UZFLOW modules.

The NFENV module work was associated with adding reflux capabilities, encapsulated in the nfhydro subroutine in the **nfenv.f** file, and calculating dripping flux onto WPs, encapsulated in the nfdrip subroutine in the **nfenv.f** file.

The reflux module uses the following parameters in the **tpa.inp** file:

- ThermalConductivityofYMRock[W/(m-K)]
- BoilingPointofWater[C]
- ArealMassLoading[MTU/acre]
- LengthOfRefluxZone[m]
- MaximumFluxInRefluxZone[m/s]

- ReleaseFractionForPerchedBucket
- PerchedBucketVolumePerSAarea[m3/m2]

Each parameter (except for the boiling point of water and areal mass loading) are sampled.

The logic for handling the reflux zone is based on using a bucket that continually fills through deep percolation and partially empties whenever it fills. The bucket also continually drains while the reflux zone is intersecting the drift horizon. The balance equation for the bucket is

$$\frac{\partial V}{\partial t} = q_{perc} - q_{reflux}(z_{repos}), \tag{4-44}$$

where

V is the volume of the bucket per unit area [L^3/L^2]
q_{perc} is the percolation flux [L^3/TL^2]
$q_{reflux}(z_{repos})$ is the liquid reflux at the repository horizon [L^3/TL^2]

It is assumed that if while the reflux zone intersects the repository, the liquid flux at the repository continues past the repository. Liquid reflux, q_{reflux}, is assumed to be linearly varying from a maximum value at the boiling isotherm to zero at a specified distance below the isotherm. If the isotherm is farther above the repository horizon than the thickness of the reflux zone, $q_{reflux}(z_{repos})$ is assumed to be zero.

While the repository is below boiling, the bucket drains with a flux equal to q_{perc}. In addition, half of the existing water stored in the bucket is assumed to drain at each time step. When the repository is above boiling, the bucket fills at the rate of $q_{perc} - q_{reflux}(z_{repos})$ until it exceeds capacity within a time step. A loop releases a user-specified fraction of the bucket volume until the stored volume is than a full bucket.

A reasonable size of the bucket might be the difference between saturated moisture content and ambient moisture content, multiplied by 10 to 100 m. For TSw, this criterion corresponds to a range of roughly 0.1 to 1 m^3/m^2.

The dripping module simply calculates the volumetric flux across the cross-sectional area of a waste package given the volumetric flux across the repository. Additional calculations for localization and diversion is handled in the EBSPAC modules; for clarity, this should be moved to NFENV in the next iteration.

I tested the NFENV module by using inputs that generate constant q_{perc} over the length of the simulation and verifying that the magnitude of fluxes output from the module were consistent.

I then used standard climatic inputs and again verified that the resulting flux magnitudes were consistent and reasonable compared to the constant-q_{perc} case.

I also tested the UZFLOW module, to a greater extent than previously, verifying that the IPA2 approach could be reproduced. Several bugs were found in subroutine get_climean, which reads in the mean values for the climate from the disk. These were fixed. I identified one additional bug tonight in subroutine get_climean that will need to be rectified in the next version – it is assumed that the start of the climatic history (i.e., current conditions) must have a fraction of full glacial maximum equal to zero. In actuality it might be different from zero, so that the weighting schemes should take this into account.

3/15/97 Thoughts on NFHYDRO module.

SAS

There are a couple of weaknesses in the NFHYDRO portion of the NFENV module that should be rectified for the next version of the TPA code.

It is assumed that the bucket drains half of its volume per time step once the temperature drops below boiling at the repository; this procedure should be replaced with a decay constant

$$\frac{\partial V}{\partial t} = \lambda V + q_{perc} \tag{4-45}$$

where λ is a decay constant.

It is assumed that the bucket flushes a multiple of a fixed volume if it overflows. It may be more realistic to simply pass the excess on directly (steady-state assumption), particularly for typical time steps.

Some accounting for the moisture in the dry-out zone needs to be done. A more realistic model provides three saturation levels, θ_{amb}, θ_{buck}, and θ_{dry}, corresponding to ambient, bucket, and dryout-zone saturations. Presumably $\theta_{buck} > \theta_{amb} > \theta_{dry}$. As the boiling isotherm moves up, the moisture in the new part of the dryout zone should be put into the bucket. The governing mass balance equation is

$$\varepsilon \left[\theta_{dry} \frac{\partial L_{dry}}{\partial t} + \theta_{buck} \frac{\partial L_{buck}}{\partial t} + \theta_{amb} \frac{\partial L_{amb}}{\partial t} \right] = q_{perc} - q_{reflux}(z_{repos}) - q_{flush}, \tag{4-46}$$

where L represents the height of a bucket, q_{flush} is the overflow flushed from a full bucket, and subscripts *dry*, *buck*, and *amb* represent the dryout-zone, perched-zone, and ambient-zone buckets, respectively. Note that $L_{amb} + L_{buck} + L_{dry} = L_{tot}$ is a constant, where L_{tot} is the maximum

thickness for the calculation (perhaps TSw layer thickness) and L_{dry} is the height of the boiling isotherm above the repository level. Accordingly,

$$L_{amb} = L_{tot} - L_{dry} - L_{buck} \tag{4-47}$$

and

$$\varepsilon \left[\theta_{dry} \frac{\partial L_{dry}}{\partial t} + \theta_{buck} \frac{\partial L_{buck}}{\partial t} - \theta_{amb} \frac{\partial (L_{dry} + L_{buck})}{\partial t} \right] = q_{perc} - q_{reflux}(z_{repos}) - q_{flush}, \tag{4-48}$$

(noting that $\partial L_{tot}/\partial t = 0$), yielding

$$\varepsilon \left[(\theta_{dry} - \theta_{amb}) \frac{\partial L_{dry}}{\partial t} + (\theta_{buck} - \theta_{amb}) \frac{\partial L_{buck}}{\partial t} \right] = q_{perc} - q_{reflux}(z_{repos}) - q_{flush}. \tag{4-49}$$

With the adjusted mass balance equation, the height of the perched-zone bucket is tracked. As the repository heats up, L_{buck} remains zero until $q_{reflux}(z_{repos}) < q_{perc}$. A period of time exists, while $L_{buck} + L_{dry} < L_{tot}$, where $q_{reflux}(z_{repos}) + q_{flush} = 0$. While $L_{buck} + L_{dry} = L_{tot}$,

$$q_{flush} = q_{perc} - \varepsilon(\theta_{dry} - \theta_{buck}) \frac{\partial L_{dry}}{\partial t}. \tag{4-50}$$

As the temperature drops, there may be another period of zero flux. Finally, as the boiling isotherm returns to the repository level, reflux kicks in to drain the perched-zone bucket.

A potential pitfall arises if the perched-zone bucket tries to generate negative thickness. Two obvious approaches can handle this situation: (i) collapse the perched-zone bucket and track the ambient-dry interface explicitly, or (ii) add a separate fracture-rewetting front accounting for sorption into the matrix. The first approach would tend to delay the arrival of rewetting at the repository, while the second approach promotes arrival of rewetting.

7/15/97 Documenting changes to UZFLOW module.

SAS

Over the course of testing, it became apparent that the regression formula for *MAI* used in the UZFLOW module was seriously in error beyond the range of values used for the regression. As documented in the 7/11/97 entry of the Ambient Hydrology KTI, a modified regression equation was proposed that extrapolates reasonably to the wet and cool extremes demanded by the TPA code.

As per a telecon with Tim McCartin, Dick Codell, and Neil Coleman, I have changed one constant in the regression equation to represent a fudge factor for all the unsampled parameters.

The original practice was to calculate *MAI* under current conditions, using my formula, and scale the calculated *MAI* including climate change by the factor required to match the user-specified *MAI* under current conditions. The problem is that the regressed relationships are not linear, so that under climatic extremes excessive *MAI* may result. By adjusting the regression equation so that initial conditions are exactly matched, conditions under climatic extremes are also matched.

In order to match the condition, *MAI* is tabulated for various values of the fudge factor. Given the initial *MAI* to match, the matching fudge factor is found through interpolation within the table.

I implemented the equation in the last version of the UZFLOW module that I had been working on. A practice has been implemented in the interim with the rationale of eliminating warning and error messages, so as not to upset NRC, but is instead a poor coding practice that fosters modification errors. The one included file that I had created, with all parameter statements, dimensioning information, and common blocks, has been replaced with 6 included files (one for each common block) and all other information has been copied into each subroutine that it is used in. The module is about 1/3 larger, is unwieldy to read, and subject to modification errors due to the redundant statements. **I strongly deprecate this practice as cutting off one's nose to spite one's face.**

References

Ackers, P. and W. R. White. 1973. Sediment Transport: New Approach and Analysis. *Journal of the Hydraulics Division, American Society of Civil Engineers 99*(HY11), 2041–2060.

Beaumont, C., P. Fullsack, and J. Hamilton. 1992. Erosional control of active compressional orogens. In K. R. McClay (Ed.), *Thrust Tectonics*, London, pp. 1–18. Chapman & Hall.

DeWispelare, A. R., L. T. Herren, M. P. Miklas, and R. T. Clemen. 1993. *Expert Elicitation of Future Climate in the Yucca Mountain Vicinity.* CNWRA 93-016, Center for Nuclear Waste Regulatory Analyses, San Antonio, TX.

Fair, G. M. and J. C. Geyer. 1954. *Water Supply and Wastewater Disposal.* New York, NY: John Wiley & Sons.

Fernandez, J. A., J. B. Case, C. A. Givens, and B. C. Carney. 1994. *A Strategy to Seal Exploratory Boreholes in Unsaturated Tuff.* SAND93-1184, Sandia National Laboratories, Albuquerque, NM.

Kilinc, M. and E. V. Richardson. 1973. *Mechanics of Soil Erosion From Overland Flow Generated*

by Simulated Rainfall. Hydrology Paper 63, Colorado State University, Fort Collins, CO.

Matalas, N. C. 1967. Mathematical Assessment of Synthetic Hydrology. *Water Resources Research 3*(4), 937–945.

Meyer, L. D. and W. H. Wischmeier. 1969. Mathematical Simulation of the Process of Soil Erosion by Water. *Transactions of the American Society of Agricultural Engineers 12*(6), 754–762.

Scott, R. B. and J. Bonk. 1984. *Preliminary Geologic Map (1:12,000 scale) of Yucca Mountain, Nye County, Nevada, with Geologic Cross Sections.* Open-File Report 84-494, United States Geological Survey, Denver, CO.

Stothoff, S. A., H. M. Castellaw, and A. C. Bagtzoglou. 1996. Simulating the Spatial Distribution of Infiltration at Yucca Mountain, Nevada. *Water Resources Research ?*(?), ? In preparation.

Woolhiser, D. A., R. E. Smith, and D. C. Goodrich. 1990. *KINEROS, A Kinematic Runoff and Erosion Model: Documentation and User Manual.* ARS-77, United States Department of Agriculture, Agricultural Research Service.

Yalin, Y. S. 1963. An Expression for Bed-Load Transportation. *Journal of the Hydraulics Division, American Society of Civil Engineers 89*(HY3), 221–250.

Yang, C. T. 1973. Incipient Motion and Sediment Transport. *Journal of the Hydraulics Division, American Society of Civil Engineers 99*(HY10), 1679–1704.

5. Breath code development

Account Number: **20-5708-863**
Collaborators: **As noted**
Directories: **Subdirectories of $HOME2/Unsat_1D/Breath as noted**

Objective: Perform modifications to the *breath* code as required for infiltration analyses. Each version of the code is in a subdirectory labelled ***V1.1***, ***V1.2***, etc., located off of the main *breath* directory, ***$HOME2/Unsat_1D/Breath***.

2/17/96 Initial entry.

SAS

A bug was found in the calculation of temperature-dependent water viscosity. The fviscw2 routine calculated viscosity in centipoise, rather than poise, which is then converted to user units. Version 1.1, and beta versions of 1.2 and 1.3, had the correction made.

8/24/96 Planning for additional enhancements to *breath*.

SAS

breath has been used essentially without modification for numerous production runs over the last year, primarily investigating shallow infiltration processes with one or two layers. Although *breath* has performed reasonably well for these purposes, there are several significant areas that require enhancement for future planned studies at Yucca Mountain, including

- snow and snowmelt dynamics (important for future-climate studies),
- vegetation dynamics,
- atmospheric-pressure dynamics,
- discrete-fracture interactions,
- weather simulation,
- weather averaging,
- tracer pulses, and
- overland- and lateral-flow dynamics.

Most of these studies could be performed by enhancing the current 1D *breath* simulator; others require extending the 1D formulation to 2D and 3D.

During the production runs, some dissatisfaction with performance cropped up due to extremely long simulation times (i.e., several weeks to complete a 20-yr simulation). It became painfully clear that a restart capability was highly desirable, due to the inability to maintain computers up and running for such extended periods. In addition, speed of calculation continues to be an issue. It has been determined that roughly half of the computational effort is involved with function evaluations. For such long simulations, which may involve 10 to 100 million function evaluations, tabulated functions may drastically cut the function evaluation effort.

In the simulations, mass balance is also a critical issue, which has required that extremely refined grids be employed, both near the ground surface and at material interfaces. Two possible changes have been identified that may allow considerably coarser meshes to be used, at least for some time intervals: (i) using a finite-element approach at material interfaces, and (ii) using adaptive gridding. The change from a finite-volume approach, in which material interfaces are between nodes, to a true finite-element approach, in which material interfaces are between elements, will presumably cut the refinement requirements at the interfaces since a very small element at the interface has been used to minimize the impacts of improperly approximating fluxes across the interface. Using adaptive gridding is perhaps more problematical, since mass balance issues will be involved in regridding, and will be more useful in 1D than 2D or 3D. Also, adaptive gridding requires that material properties be specified by zone, as opposed to the current practice of specifying properties individually by element.

Based on the set of enhancements and extensions that have been identified, it appears that a generic multiphase, multicomponent, multicontinuum mass and energy transport simulator might be appropriate, developed in such a way that adding and subtracting simulation modules is extremely straightforward. The generic mass-component balance equation includes a storage term, an advective-transport term, a diffusive-transport term, and terms accounting for (i) decay, (ii) transfer across phase boundaries, (iii) transfer due to phase change, (iv) reaction with other components, and (v) external sources/sinks. In addition to such terms, the energy balance equation may consider radiation.

In general, a generic code consists of modules responsible for

- data input,
- mesh description and maintenance,

- discretization operations,
- functional relationships,
- state maintenance,
- balance-equation description,
- balance-equation assembly,
- matrix solvers,
- result analysis,
- output routines, and
- restart/debug routines.

It is highly desirable that these modules be as logically independent as possible, so that code maintenance can be localized. Although *breath* was originally coded in Fortran, modularity would be considerably enhanced using C or C++, as would maintenance of data structure and sophistication of input/output. As the computational portion of the code is typically on the order of 10 percent of total coding, and for many computer systems the computational speed of the two languages is comparable, recoding *breath* in C or C++ would be appropriate, particularly since much of this work can be done using a Fortran-to-C converter.

The organization of a generic code depends on the use to which the code will be put. At one extreme, a code may be used for extremely straightforward problems, with homogeneous properties and simple geometries. At the other extreme, extremely complex situations may also be encountered, with layering, embedded discontinuities, and random properties. In the first case, it is desirable to have strong data generation capabilities with minimalist input and global storage structure. In the second case, powerful input is required and each node/element may need individual data storage. These situations are further complicated by the possibility of different parameterization needs for different parts of the domain (e.g., a snow layer has different requirements than a Brooks-Corey medium or a dual-continuum medium).

The internal data structure must be suited both to sophisticated input facilities and to computational efficiency in matrix assembly. Three types of computer architecture are available, each with particular strengths and weaknesses: (i) serial machines (e.g., PCs, workstations), (ii) vector machines (e.g., Crays), and (iii) data-parallel machines (e.g., Connection machines). Appropriate assembly algorithms are considerably different for the three architectures. In general, though,

element-by-element or node-by-node assembly is most appropriate, since information regarding element discretization can be rather voluminous to store in RAM for 2D and 3D. From the standpoint of data input, however, it would be most efficient to assemble by using a process-level assembly process, thereby allowing several data storage schemes to be accommodated simultaneously.

8/25/96 Further planning. SAS

An attractive approach to reconciling efficiency requirements is to maintain data by separate computational zones. With adaptive gridding in 1D, such a zone might be an individual layer. Transition nodes cause a problem – they might be stored independently or might be duplicated as necessary. In higher dimensions, a zone might consist of all triangles, or all dual-permeability elements. Adaptive and non-adaptive zones should be stored separately.

For peak performance in matrix assembly, all potentially state-dependent coefficients should be calculated and separated out to convenient storage before element-discretization operations are performed. Typically, such coefficients are more interesting to look at than element-discretization variables and storage should be smaller as well. Coefficients include capacitance terms, phase mobilities, diffusion coefficients, and derived state variables (e.g., density, viscosity, saturation, enthalpy).

8/26/96 Function handling ideas. SAS

Each of the different types of coefficients discussed yesterday are typically calculated with functions. Ideally, three types of functions should be available: (i) internal hard-coded functions, (ii) tabular functions, and (iii) external user-defined functions. To minimize overhead of identifying pointers, variable names, etc., each function should perform processing in a vector manner (e.g., all nodes can be processed with one call to the function). The strategy has the drawback of requiring additional memory for temporary storage and perhaps some temporary pointer lists as well. The strategy is not suited to Fortran-77 (Fortran-90 may be better), but can be straight-forwardly implemented in C or C++.

Internal hard-coded functions may typically have several arguments, and the arguments may arbitrarily be vectors or constants depending on the user. This multiplicity of options can be handled by restricting internal functions to the straight-forward protocol outlined below. For simplicity of handling facilities, three variables should be passed into each function, (i) an array

handling the list of arguments, (ii) the number of arguments passed in (length of the array), and (iii) the number of vector entries to process. The argument-handling array is actually an array of structures, with each structure containing variables

- pointing to the data vector structure,
- pointing to the index vector structure, and
- maintaining pointers into the index vector.

Since these structures are cumbersome to address, predefined functions should be provided for common manipulations (i.e., pointer initialization, pointer increment, vector addressing). In addition, each function might define shorthand names for the variables, so that the function could end up looking like a normal scalar function with somewhat different interface and an internal loop.

Tabular functions should behave like internal hard-coded functions, with function parameters replaced by the table itself. In addition, a setup routine may be needed to define the table. A somewhat novel idea may be useful for highly heterogeneous systems for some functions, where the expense of function evaluations can be amortized in a partial table with perhaps 4 entries per node. Only when the nodal value goes out of bounds is it necessary to recalculate table entries, and it is expected that most nodes would need to recalculate entries only infrequently.

User-defined functions should assume that vector protocols are in use. The function has the number of arguments and their names predefined, as for the other types of functions, but this time a pair of variables are passed for each argument; (i) the vector/scalar of interest, and (ii) an index vector/scalar. The user-defined functions could utilize the Jacquard vector-C software that I developed at Vermont. Converting these routines to the new use should be straightforward. Alternatively, *Matlab* might be used instead.

9/4/96 Discretization handling ideas.

SAS

There are many different physical systems that may be considered. There are also numerous philosophies for discretizing the physical systems, ranging from several flavors of finite element methods, finite difference methods, finite volume methods, and boundary integral methods. Various numerical methods are more appropriate depending on whether the underlying PDE is elliptic, parabolic, or hyperbolic in character. In addition, one can use static grids or adaptive grids. For

1D problems, quite sophisticated adaptive gridding can be performed; as the dimensionality of the problem increases, adaptive gridding becomes increasingly difficult.

Ideally, one would like the structure of the program to allow for generic discretization schemes, so that a scheme can be selected based on the special characteristics of the problem at hand. In order to do this, each general scheme should be modularized with an identical interface structure. Module categories include:

- mesh maintenance (adaptive gridding),
- mesh description (connectivity lists),
- mesh-independent parameters,
- mesh-dependent parameters and state variables,
- discretization description:
  - capacitance term,
  - flux terms,
  - source term,
  - cross-source term, and
  - boundary condition terms,
- matrix assembly, and
- matrix solution.

I envision the mesh-related module categories as separate categories, while the description modules are linked according to the discretization scheme. The various schemes require different levels of information–for example, finite volume schemes consist of 1D pipes and require no spatial information other than distances, while finite element schemes need information on the connections for each element, finite difference schemes implicitly handle the connection information and boundary element schemes also need information on the interfaces between regions. The matrix assembly modules should provide a uniform interface for each of the matrix solution schemes that might be available.

9/17/96 Documentation of version 1.2 for TOP-018. SAS

A file called **Changes** in the subdirectory ***V1.2/Src*** of the main *breath* directory has been maintained since June, 1995. The file is quoted below (in slightly prettier format) for completeness of documentation, in order to comply with the requirements of TOP-018 for version 1.2.

5/12/96 Fixed bug in boundary condition for specified energy flux. Variable bcenet had incorrect reference for second boundary in thrm1bc.

2/17/96 Fixed bug in the calculation of temperature-dependent water viscosity. The fviscw2 routine calculated viscosity in centipoise, rather than poise, which is then converted to user units. Version 1.1, and beta versions of 1.2 and 1.3, had the correction made.

8/10/95 Fixed bug in evaporation calculations. Added time-averaging of pressure, pressure perturbations, and vapor density perturbations.

8/6/95 Fixed bug in routine calculating d(mobility)/d(mc), which divides by zero when saturated. Added evaporation calculations within domain.

8/5/95 Implemented signal catch routines in C to gracefully shut down when floating point error or interrupt signal thrown.

8/4/95 Fixed bug in time-averaging of perturbations of moisture content times gradient in temperature perturbation.

8/3/95 Added upstream weighting of conductivities to tracking routine for first-type flow boundary conditions. Added capability for tracking partial of vapor density wrt pressure and temperature, perturbations of moisture content times gradient in temperature perturbation.

7/28/95 Fixed error in upstream mobility coding and added option for upstream weighting of conductivities.

7/27/95 Fixed index problem for range output in real restart. Included upstream weighting of mobilities as an option a la TOUGH. Also included dptmax and dtemax checks, which are maximum changes for pressure and temperature in an iteration. Defaults are 100 and 2. An abort occurs as soon as a node hits one of these barriers.

7/25/95 Made floating-point constants and character variables tracked by name array in restart and set/echo calls.

7/23/95 Cleaned up boundary conditions for flux in flow equation. Now the elemental mobility is used, rather than the interface mobility between the two elements nearest the boundary.

7/16/95 Added grid peclet and grid courant calculations. All floating point variables are now tracked by name, just like arrays.

7/15/95 Reorganized common blocks further for binary output. Began work on summary output for time-averaging variables.

7/8/95 Added a few variables tracking averaged quantities.

7/4/95 All real variables dimensioned with mnnd/mnel/mnbc tracked in an equivalenced array, so that trace/snap/restart/set/echo all automatically get each variable.

6/27/95 Added capability for arithmetic/geometric/harmonic means for hydraulic conductivity and for vapor dispersion coefficient.

6/15/95 Added iovar variable and input command to specify the output file for restart variable dumps.

6/14/95 Added a const and a linear option to met command to define whether met variables are piecewise linear or piecewise constant.

6/13/95 Added a scale and a shift option to met command to change met variables from file values at runtime.

6/9/95 Added restart capabilities (actually just echo all variables in a format that *breath* can read). Dump to unit 6.

9/24/96 Bug fix in met command.

SAS

I tracked down several bugs in handling the maximum-time-step input from the met command. There was no problem when the boundary conditions were for side 0, as I usually assume, but the time step information was lost when boundary conditions were for side 1. The problem was that the t0bc and t1bc arrays had the time information put in the same array slot as the boundary conditions on reads, while otherwise it was assumed that timmax was in the array slot for side 0. This was fixed by generalizing the code to use the proper slot.

5/23/97 Check using fstudy and corrective actions. SAS

Version 1.2 of *breath* was checked using a FORTRAN static analyzer code, for_study (called fstudy on bashful), provided by Cobalt Blue. SPARC version 2.0.1 was used for the test. A total of 3 syntax errors, 15 semantic errors, and 1181 warnings were reported by fstudy.

The vast majority of the warnings (700) were due to including file brecom.h, which contains specifications for all common blocks, into routines that did not use all common blocks. These warnings should be disregarded.

A total of 340 warnings dealt with subroutine initname, with 141 due to passing an array rather than the anticipated scalar, and an additional 199 due to mixing strings and arithmetic objects. Although it is generally deprecated, this behavior was specifically required during coding, and each of these warnings can be disregarded. One additional warning was due to not explicitly converting character to double precision. Although it is generally deprecated, this behavior was specifically required during coding, and the warning can be disregarded. This set of warnings are all generated by the scheme for providing a pointer and a name for all arrays, which is not handled gracefully in FORTRAN.

A total of 67 warnings dealt with passing the address of functions to subroutines, which apparently confuses fstudy. An additional 22 warnings dealt with passing a constant into a subroutine rather than a variable. These warnings can be disregarded.

A total of 28 warnings dealt with loss of precision (double precision to integer). In each case, the loss of precision was anticipated during coding, so each of these warnings can be disregarded.

A total of 12 warnings dealt with passing a scalar instead of an array. In each case, the dimension of the array passed to the subroutine is 1, so each of these warnings can be disregarded.

A total of 10 warnings dealt with including brecom.h into routines where it is not used. The included file defines implicit variable-name types, as well as providing common blocks; fstudy does not account for this. These do not have any impact on performance, so each of these warnings can be disregarded. In cases there were no repercussions, the statement was removed.

One warning is due to a missing function, initsig, which is a C routine for catching system signals. This warning can be disregarded.

A total of 8 reported syntax errors were generated by passing a DO-loop index into a sub-

routine, which potentially could change the value of the index. These messages can be disregarded, as in each case the subroutine treats the value as a flag and does not change its value.

The 3 reported syntax errors were due to extra commas in write statements in brvresty and brvrestz. These commas were removed.

A total of 7 reported syntax errors were due to variables being referenced before being set. These errors were each remedied. In richlbc, variables a2, c1, and c2 were defined; the error was not encountered during simulations to date. In richbal, the test "kmobder .eq. 0" was replaced by already-defined logical variable ymbder; the error affects output of the Peclet number and was not encountered during simulations to date. In tmstep, variable conve0 was replaced by the correct variable (econv0); the error may modify time step sizes. In brvsnap, the section of code referring to variables kset and ksqe was obsolete and therefore was commented out; the error is harmless.

5/31/97 Implementation of unique header. SAS

One of the TOP-018 requirements is that output files are uniquely identified by run. The requirement is typically fulfilled by putting a time stamp in a header line. This requirement had not been implemented in *breath*, except that there is a capability to echo character strings that are defined in the input file. Part of my reluctance to implement headers was due to the non-portability of FORTRAN calls to get the current time, and part was due to the use of *Matlab* routines that scan the output for further processing and that are more conveniently implemented without a header line.

In order to complete an acceptable version of the code, I added two character-string variables (ztime and zversion) that hold the time at the start of the simulation and a version identifier, respectively. The time is obtained using a small routine in C that is coded within the brcatch.c module. By default, the headers are not output; variables are defined for each output stream that enable output. The changes were documented in the version 1.2 user's guide.

A fully compliant release was placed on a diskette and will become part of the QA documentation.

6. Ambient KTI – Vertical ODE Solver

Account Number: **20-5708-861**
Collaborators: **Sitakanta Mohanty, Gordon Wittmeyer**
Directories: **$HOME2/Matlab/ODE → $ODE**

4/10/97 Printout entry.

SAS

I performed no work on this project during the period covered by this printout.

7. Boundary Element Methods for Steady-State Unsaturated Fractured Media

Account Number: **As noted**
Collaborators: **As noted**
Directories: **$HOME2/Matlab/ExpToVG**

4/10/97 Printout entry. SAS

I performed no work on this project during the period covered by this printout.

8. Geomorphology of Mountain Erosion

Account Number:	**20-5704-166 and 20-5704-174**
Collaborators:	**David Farrell**
Directories:	**$HOME2/Matlab/MassWaste → $MassWaste**

4/10/97 Printout entry. SAS

I performed no work on this project during the period covered by this printout.

9. Environ - Evaluation of Mass Balance Errors in PTC

Account Number: **20-7614-007**
Collaborators: **None**
Directories: **$HOME2/WFO/Environ → $Environ**

4/10/97 Printout entry.

SAS

I performed no work on this project during the period covered by this printout.

10. Quick Looks

Account Number:	**As noted**
Collaborators:	**As noted**
Directories:	**As noted**

Objective: Perform quick looks at technical questions that arise in brainstorming sessions and document the results. Each quick look should take a few hours to no more than a day.

4/10/97 Printout entry.

SAS

I performed no work on this project during the period covered by this printout.

308 --- 0199712150007
Ambient Hydrology KTI -
Infltration
8 of 20

SCIENTIFIC NOTEBOOK

by

Stuart A. Stothoff

SCIENTIFIC NOTEBOOK

by

Stuart A. Stothoff

Southwest Research Institute
Center for Nuclear Waste Regulatory Analyses
San Antonio, Texas

October 8, 1997

Initial Entries

Scientific NoteBook: # 163

Issued to: S. A. Stothoff

Issue Date: Tuesday, November 16, 1993

By agreement with the CNWRA QA this NoteBook is to be printed at approximate quarterly intervals. This computerized Scientific NoteBook is intended to address the criteria of CNWRA QAP–001.

Table 0-1: Computing Equipment

Machine Name	Type	OS	Location
sierra.cnwra.swri.edu	Sun SPARC 20	SUNOS 4.1.3_U1	desk Rm A-212, Bldg. 189
sisyphus.cnwra.swri.edu	Sun SPARC 20	SUNOS 4.1.3_U1	network
dopey.cnwra.swri.edu	Sun SPARC 10	SUNOS 4.1.3_U1	network
performer.cnwra.swri.edu	SGI Onyx	IRIX 5.3	network
yosemite.cnwra.swri.edu	SGI Onyx	IRIX 5.3	network
bemore.cnwra.swri.edu	SGI Onyx	IRIX 6.2	network
redwood.cnwra.swri.edu	SGI Indy	IRIX 6.2	network
bigbend.cnwra.swri.edu	Sun Ultra-2	SUNOS 5.5.1	network
scratchy1.cnwra.swri.edu	Sun Ultra-2	SUNOS 5.5.1	network
hornet.cnwra.swri.edu	Sun Ultra-2	SUNOS 5.5.1	network

Contents

Initial Entries ii

List of Figures xii

List of Tables xiii

1 Ambient Hydrology KTI – Infiltration 1

2 Thermal Hydrology KTI 165

3 Iterative Performance KTI 166

4 Iterative Performance KTI - Total Performance Assessment Phase 3 167

5 Breath code development 168

6 Ambient KTI – Vertical ODE Solver 169

7 Boundary Element Methods for Steady-State Unsaturated Fractured Media 170

8 Geomorphology of Mountain Erosion 171

9 Environ - Evaluation of Mass Balance Errors in PTC 172

10 Quick Looks 173

List of Figures

1-1 1/13/97. Regression of borehole alluvium depths with nearest-neighbor DEM slopes. 34

1-2 1/15/97. Least-squares fit of simulation prediction to abstraction prediction for various exponents in Equation 1-20. 35

1-3 2/27/97. Time history of decadal-average moisture flux after each of 6 decades, as a function of AAP and AAT, for (a) hourly meteorologic input and bedrock 1, (b) daily meteorologic input and bedrock 1, (c) hourly meteorologic input and bedrock 2, and (d) daily meteorologic input and bedrock 2. 40

1-4 7/14/97. Areal-average MAI for Yucca Mountain area, using regression formula based on soil/open-fracture system, (a) in dimensional form, and (b) in nondimensional form. 59

1-5 8/31/97. The complete set of measured K_{sat} values in the USGS database. 63

1-6 9/9/97. Comparison of best-estimate K_{sat} and measured K_{sat} using (a) the USGS database, (b) the best 1-parameter regression, (c) the best 2-parameter regression, and (d) the best 3-parameter regression. 66

1-7 9/9/97. **BHprofile_NRG6_c.eps**. Porosity, saturation, change in particle density, and measured and estimated values for K_{sat} in borehole NRG6. 68

1-8 9/9/97. **BHprofile_NRG77a_c.eps**. Porosity, saturation, change in particle density, and measured and estimated values for K_{sat} in borehole NRG7/7a. 69

1-9 9/9/97. **BHprofile_SD12_c.eps**. Porosity, saturation, change in particle density, and measured and estimated values for K_{sat} in borehole SD-12. 70

1-10 9/9/97. **BHprofile_SD7_c.eps**. Porosity, saturation, change in particle density, and measured and estimated values for K_{sat} in borehole SD-7. 71

1-11 9/9/97. **BHprofile_SD9_c.eps**. Porosity, saturation, change in particle density, and measured and estimated values for K_{sat} in borehole SD-9. 72

1-12 9/9/97. **BHprofile_UZ14_c.eps**. Porosity, saturation, change in particle density, and measured and estimated values for K_{sat} in borehole UZ-14. 73

1-13 9/9/97. **BHprofile_UZ16_c.eps**. Porosity, saturation, change in particle density, and measured and estimated values for K_{sat} in borehole UZ-16. 74

1-14 9/9/97. **BHprofile_UZ7a_c.eps**. Porosity, saturation, change in particle density, and measured and estimated values for K_{sat} in borehole UZ-7a. 75

1-15 9/9/97. **BHprofile_UZN11_c.eps**. Porosity, saturation, change in particle density, and measured and estimated values for K_{sat} in borehole N11. 76

1-16 9/9/97. **BHprofile_UZN15_c.eps**. Porosity, saturation, change in particle density, and measured and estimated values for K_{sat} in borehole N15. 77

1-17 9/9/97. **BHprofile_UZN16_c.eps**. Porosity, saturation, change in particle density, and measured and estimated values for K_{sat} in borehole N16. 78

1-18 9/9/97. **BHprofile_UZN17_c.eps**. Porosity, saturation, change in particle density, and measured and estimated values for K_{sat} in borehole N17. 79

1-19 9/9/97. **BHprofile_UZN27_c.eps**. Porosity, saturation, change in particle density, and measured and estimated values for K_{sat} in borehole N27. 80

1-20 9/9/97. **BHprofile_UZN31_c.eps**. Porosity, saturation, change in particle density, and measured and estimated values for K_{sat} in borehole N31. 81

1-21 9/9/97. **BHprofile_UZN32_c.eps**. Porosity, saturation, change in particle density, and measured and estimated values for K_{sat} in borehole N32. 82

1-22 9/9/97. **BHprofile_UZN33_c.eps**. Porosity, saturation, change in particle density, and measured and estimated values for K_{sat} in borehole N33. 83

1-23 9/9/97. **BHprofile_UZN34_c.eps**. Porosity, saturation, change in particle density, and measured and estimated values for K_{sat} in borehole N34. 84

1-24 9/9/97. **BHprofile_UZN35_c.eps**. Porosity, saturation, change in particle density, and measured and estimated values for K_{sat} in borehole N35. 85

1-25 9/9/97. **BHprofile_UZN36_c.eps**. Porosity, saturation, change in particle density, and measured and estimated values for K_{sat} in borehole N36. 86

1-26 9/9/97. **BHprofile_UZN37_c.eps**. Porosity, saturation, change in particle density, and measured and estimated values for K_{sat} in borehole N37. 87

1-27 9/9/97. **BHprofile_UZN38_c.eps**. Porosity, saturation, change in particle density, and measured and estimated values for K_{sat} in borehole N38. 88

1-28 9/9/97. **BHprofile_UZN53_c.eps**. Porosity, saturation, change in particle density, and measured and estimated values for K_{sat} in borehole N53. 89

1-29 9/9/97. **BHprofile_UZN54_c.eps**. Porosity, saturation, change in particle density, and measured and estimated values for K_{sat} in borehole N54. 90

1-30 9/9/97. **BHprofile_UZN55_c.eps**. Porosity, saturation, change in particle density, and measured and estimated values for K_{sat} in borehole N55. 91

1-31 9/9/97. **BHprofile_UZN57_c.eps**. Porosity, saturation, change in particle density, and measured and estimated values for K_{sat} in borehole N57. 92

1-32 9/9/97. **BHprofile_UZN58_c.eps**. Porosity, saturation, change in particle density, and measured and estimated values for K_{sat} in borehole N58. 93

1-33 9/9/97. **BHprofile_UZN59_c.eps**. Porosity, saturation, change in particle density, and measured and estimated values for K_{sat} in borehole N59. 94

1-34 9/9/97. **BHprofile_UZN61_c.eps**. Porosity, saturation, change in particle density, and measured and estimated values for K_{sat} in borehole N61. 95

1-35 9/9/97. **BHprofile_UZN62_c.eps**. Porosity, saturation, change in particle density, and measured and estimated values for K_{sat} in borehole N62. 96

1-36 9/9/97. **BHprofile_UZN63_c.eps**. Porosity, saturation, change in particle density, and measured and estimated values for K_{sat} in borehole N63. 97

1-37 9/9/97. **BHprofile_UZN64_c.eps**. Porosity, saturation, change in particle density, and measured and estimated values for K_{sat} in borehole N64. 98

1-38 9/17/97. All CNWRA-estimated and USGS-measured K_{sat} values in formation: (a) Tpcrn4 (**FormK_Tpcrn4_c.eps**), and (b) Tpcrn3 (**FormK_Tpcrn3_c.eps**). 100

1-39 9/17/97. All CNWRA-estimated and USGS-measured K_{sat} values in formation: (a) Tpcrn2 (**FormK_Tpcrn2_c.eps**), and (b) Tpcrn1 (**FormK_Tpcrn1_c.eps**). 101

1-40 9/17/97. All CNWRA-estimated and USGS-measured K_{sat} values in formation: (a) Tpcrl2 (**FormK_Tpcrl2_c.eps**), and (b) Tpcrl1 (**FormK_Tpcrl1_c.eps**). 102

1-41 9/17/97. All CNWRA-estimated and USGS-measured K_{sat} values in formation: (a) Tpcpul (**FormK_Tpcpul_c.eps**), and (b) Tpcpmn (**FormK_Tpcpmn_c.eps**). . . . 103

1-42 9/17/97. All CNWRA-estimated and USGS-measured K_{sat} values in formation: (a) Tpcpll (**FormK_Tpcpll_c.eps**), and (b) Tpcplnh (**FormK_Tpcplnh_c.eps**). . . . 104

1-43 9/17/97. All CNWRA-estimated and USGS-measured K_{sat} values in formation: (a) Tpcplnc (**FormK_Tpcplnc_c.eps**), and (b) Tpcpv2 (**FormK_Tpcpv2_c.eps**). . . 105

1-44 9/17/97. All CNWRA-estimated and USGS-measured K_{sat} values in formation: (a) Tpcpv1 (**FormK_Tpcpv1_c.eps**), and (b) Tpbt4 (**FormK_Tpbt4_c.eps**). 106

1-45 9/17/97. All CNWRA-estimated and USGS-measured K_{sat} values in formation: (a) Tpy (**FormK_Tpy_c.eps**), and (b) Tpbt3 (**FormK_Tpbt3_c.eps**). 107

1-46 9/17/97. All CNWRA-estimated and USGS-measured K_{sat} values in formation: (a) Tpp (**FormK_Tpp_c.eps**), and (b) Tpbt2 (**FormK_Tpbt2_c.eps**). 108

1-47 9/17/97. All CNWRA-estimated and USGS-measured K_{sat} values in formation: (a) Tptrv3 (**FormK_Tptrv3_c.eps**), and (b) Tptrv2 (**FormK_Tptrv2_c.eps**). 109

1-48 9/17/97. All CNWRA-estimated and USGS-measured K_{sat} values in formation: (a) Tptrv1 (**FormK_Tptrv1_c.eps**), and (b) Tptrn (**FormK_Tptrn_c.eps**). 110

1-49 9/17/97. All CNWRA-estimated and USGS-measured K_{sat} values in formation: (a) Tptrn2 (**FormK_Tptrn2_c.eps**), and (b) Tptrl (**FormK_Tptrl_c.eps**). 111

1-50 9/17/97. All CNWRA-estimated and USGS-measured K_{sat} values in formation: (a) Tptrl2 (**FormK_Tptrl2_c.eps**), and (b) Tptrl1 (**FormK_Tptrl1_c.eps**). 112

1-51 9/17/97. All CNWRA-estimated and USGS-measured K_{sat} values in formation: (a) Tptpul (**FormK_Tptpul_c.eps**), and (b) Tptpul2 (**FormK_Tptpul2_c.eps**). . . . 113

1-52 9/17/97. All CNWRA-estimated and USGS-measured K_{sat} values in formation: (a) Tptpul1 (**FormK_Tptpul1_c.eps**), and (b) Tptpmn (**FormK_Tptpmn_c.eps**). . . 114

1-53 9/17/97. All CNWRA-estimated and USGS-measured K_{sat} values in formation: (a) Tptpmn3 (**FormK_Tptpmn3_c.eps**), and (b) Tptpmn2 (**FormK_Tptpmn2_c.eps**).115

1-54 9/17/97. All CNWRA-estimated and USGS-measured K_{sat} values in formation: (a) Tptpmn1 (**FormK_Tptpmn1_c.eps**), and (b) Tptpll (**FormK_Tptpll_c.eps**). . . 116

1-55 9/17/97. All CNWRA-estimated and USGS-measured K_{sat} values in formation: (a) Tptpln (**FormK_Tptpln_c.eps**), and (b) Tptpv3 (**FormK_Tptpv3_c.eps**). 117

1-56 9/17/97. All CNWRA-estimated and USGS-measured K_{sat} values in formation: (a) Tptpv2 (**FormK_Tptpv2_c.eps**), and (b) Tptpv1 (**FormK_Tptpv1_c.eps**). 118

1-57 9/17/97. All CNWRA-estimated and USGS-measured K_{sat} values in formation: (a) Tpbt1 (**FormK_Tpbt1_c.eps**), and (b) Tac (**FormK_Tac_c.eps**). 119

1-58 9/17/97. All CNWRA-estimated and USGS-measured K_{sat} values in formation: (a) TacUnit4 (**FormK_TacUnit4_c.eps**), and (b) TacUnit3NW (**FormK_TacUnit3NW-_c.eps**). 120

1-59 9/17/97. All CNWRA-estimated and USGS-measured K_{sat} values in formation: (a) TacUnit2NW (**FormK_TacUnit2NW_c.eps**), and (b) TacUnit1NW (**FormK-_TacUnit1NW_c.eps**). 121

1-60 9/17/97. All CNWRA-estimated and USGS-measured K_{sat} values in formation: (a) TacbtNW (**FormK_TacbtNW_c.eps**), and (b) TacbsNW (**FormK_TacbsNW-_c.eps**). 122

1-61 9/17/97. All CNWRA-estimated and USGS-measured K_{sat} values in formation: (a) TcpUnit4 (**FormK_TcpUnit4_c.eps**), and (b) TcpUnit4NW (**FormK_TcpUnit4NW-_c.eps**). 123

1-62 9/17/97. All CNWRA-estimated and USGS-measured K_{sat} values in formation: (a) TcpUnit4sub3 (**FormK_TcpUnit4sub3_c.eps**), and (b) TcpUnit4sub2 (**FormK-_TcpUnit4sub2_c.eps**). 124

1-63 9/17/97. All CNWRA-estimated and USGS-measured K_{sat} values in formation: (a) TcpUnit4sub1 (**FormK_TcpUnit4sub1_c.eps**), and (b) TcpUnit3 (**FormK_TcpUnit3_c.eps**). 125

1-64 9/17/97. All CNWRA-estimated and USGS-measured K_{sat} values in formation: (a) TcpUnit2 (**FormK_TcpUnit2_c.eps**), and (b) TcpUnit1 (**FormK_TcpUnit1_c.eps**). 126

1-65 9/17/97. All CNWRA-estimated and USGS-measured K_{sat} values in formation: (a) Tcpbt (**FormK_Tcpbt_c.eps**), and (b) TcbUnit4NW (**FormK_TcbUnit4NW_c.eps**). 127

1-66 9/17/97. All CNWRA-estimated and USGS-measured K_{sat} values in formation: (a) TcbUnit4MW (**FormK_TcbUnit4MW_c.eps**), and (b) TcbUnit3MW (**FormK_TcbUnit3MW_c.eps**). 128

1-67 9/17/97. All CNWRA-estimated and USGS-measured K_{sat} values in formation: (a) TcbUnit3PW (**FormK_TcbUnit3PW_c.eps**), and (b) TcbUnit2NW (**FormK_TcbUnit2NW_c.eps**). 129

1-68 9/17/97. All CNWRA-estimated and USGS-measured K_{sat} values in formation: (a) TcbUnit1NW (**FormK_TcbUnit1NW_c.eps**), and (b) Tcbbs (**FormK_Tcbbs_c.eps**). 130

1-69 9/17/97. All CNWRA-estimated and USGS-measured K_{sat} values in formation TctNW (**FormK_TctNW_c.eps**). 131

1-70 10/7/97. **Disp_DBstat_CCR_c.eps**. Measured and generated formation values for (a) saturation and porosity, (b) saturation and estimated saturated hydraulic conductivity, and (c) porosity and estimated saturated hydraulic conductivity. 147

1-71 10/7/97. **Disp_DBstat_CUC_c.eps**. Measured and generated formation values for (a) saturation and porosity, (b) saturation and estimated saturated hydraulic conductivity, and (c) porosity and estimated saturated hydraulic conductivity. 147

1-72 10/7/97. **Disp_DBstat_CUL_c.eps**. Measured and generated formation values for (a) saturation and porosity, (b) saturation and estimated saturated hydraulic conductivity, and (c) porosity and estimated saturated hydraulic conductivity. 148

1-73 10/7/97. **Disp_DBstat_CW_c.eps**. Measured and generated formation values for (a) saturation and porosity, (b) saturation and estimated saturated hydraulic conductivity, and (c) porosity and estimated saturated hydraulic conductivity. 148

1-74 10/7/97. **Disp_DBstat_CMW_c.eps**. Measured and generated formation values for (a) saturation and porosity, (b) saturation and estimated saturated hydraulic conductivity, and (c) porosity and estimated saturated hydraulic conductivity. 149

1-75 10/7/97. **Disp_DBstat_CNW_c.eps**. Measured and generated formation values for (a) saturation and porosity, (b) saturation and estimated saturated hydraulic conductivity, and (c) porosity and estimated saturated hydraulic conductivity. 149

1-76 10/7/97. **Disp_DBstat_BT4_c.eps**. Measured and generated formation values for (a) saturation and porosity, (b) saturation and estimated saturated hydraulic conductivity, and (c) porosity and estimated saturated hydraulic conductivity. 150

1-77 10/7/97. **Disp_DBstat_TPY_c.eps**. Measured and generated formation values for (a) saturation and porosity, (b) saturation and estimated saturated hydraulic conductivity, and (c) porosity and estimated saturated hydraulic conductivity. 150

1-78 10/7/97. **Disp_DBstat_BT3_c.eps**. Measured and generated formation values for (a) saturation and porosity, (b) saturation and estimated saturated hydraulic conductivity, and (c) porosity and estimated saturated hydraulic conductivity. 151

1-79 10/7/97. **Disp_DBstat_TPP_c.eps**. Measured and generated formation values for (a) saturation and porosity, (b) saturation and estimated saturated hydraulic conductivity, and (c) porosity and estimated saturated hydraulic conductivity. 151

1-80 10/7/97. **Disp_DBstat_BT2_c.eps**. Measured and generated formation values for (a) saturation and porosity, (b) saturation and estimated saturated hydraulic conductivity, and (c) porosity and estimated saturated hydraulic conductivity. 152

1-81 10/7/97. **Disp_DBstat_TC_c.eps**. Measured and generated formation values for (a) saturation and porosity, (b) saturation and estimated saturated hydraulic conductivity, and (c) porosity and estimated saturated hydraulic conductivity. 152

1-82 10/7/97. **Disp_DBstat_TR_c.eps**. Measured and generated formation values for (a) saturation and porosity, (b) saturation and estimated saturated hydraulic conductivity, and (c) porosity and estimated saturated hydraulic conductivity. 153

1-83 10/7/97. **Disp_DBstat_TUL_c.eps**. Measured and generated formation values for (a) saturation and porosity, (b) saturation and estimated saturated hydraulic conductivity, and (c) porosity and estimated saturated hydraulic conductivity. 153

1-84 10/7/97. **Disp_DBstat_TMN_c.eps**. Measured and generated formation values for (a) saturation and porosity, (b) saturation and estimated saturated hydraulic conductivity, and (c) porosity and estimated saturated hydraulic conductivity. 154

1-85 10/7/97. **Disp_DBstat_TLL_c.eps**. Measured and generated formation values for (a) saturation and porosity, (b) saturation and estimated saturated hydraulic conductivity, and (c) porosity and estimated saturated hydraulic conductivity. 154

1-86 10/7/97. **Disp_DBstat_TM2_c.eps**. Measured and generated formation values for (a) saturation and porosity, (b) saturation and estimated saturated hydraulic conductivity, and (c) porosity and estimated saturated hydraulic conductivity. 155

1-87 10/7/97. **Disp_DBstat_TM1_c.eps**. Measured and generated formation values for (a) saturation and porosity, (b) saturation and estimated saturated hydraulic conductivity, and (c) porosity and estimated saturated hydraulic conductivity. 155

1-88 10/7/97. **Disp_DBstat_PV3_c.eps**. Measured and generated formation values for (a) saturation and porosity, (b) saturation and estimated saturated hydraulic conductivity, and (c) porosity and estimated saturated hydraulic conductivity. 156

1-89 10/7/97. **Disp_DBstat_PV2_c.eps**. Measured and generated formation values for (a) saturation and porosity, (b) saturation and estimated saturated hydraulic conductivity, and (c) porosity and estimated saturated hydraulic conductivity. 156

1-90 10/7/97. **Disp_DBstat_BT1_c.eps**. Measured and generated formation values for (a) saturation and porosity, (b) saturation and estimated saturated hydraulic conductivity, and (c) porosity and estimated saturated hydraulic conductivity. 157

1-91 10/7/97. **Disp_DBstat_CHV_c.eps**. Measured and generated formation values for (a) saturation and porosity, (b) saturation and estimated saturated hydraulic conductivity, and (c) porosity and estimated saturated hydraulic conductivity. 157

1-92 10/7/97. **Disp_DBstat_CHZ_c.eps**. Measured and generated formation values for (a) saturation and porosity, (b) saturation and estimated saturated hydraulic conductivity, and (c) porosity and estimated saturated hydraulic conductivity. 158

1-93 10/7/97. **Disp_DBstat_BT_c.eps**. Measured and generated formation values for (a) saturation and porosity, (b) saturation and estimated saturated hydraulic conductivity, and (c) porosity and estimated saturated hydraulic conductivity. 158

1-94 10/7/97. **Disp_DBstat_PP4_c.eps**. Measured and generated formation values for (a) saturation and porosity, (b) saturation and estimated saturated hydraulic conductivity, and (c) porosity and estimated saturated hydraulic conductivity. 159

1-95 10/7/97. **Disp_DBstat_PP3_c.eps**. Measured and generated formation values for (a) saturation and porosity, (b) saturation and estimated saturated hydraulic conductivity, and (c) porosity and estimated saturated hydraulic conductivity. 159

1-96 10/7/97. **Disp_DBstat_PP2_c.eps**. Measured and generated formation values for (a) saturation and porosity, (b) saturation and estimated saturated hydraulic conductivity, and (c) porosity and estimated saturated hydraulic conductivity. 160

1-97 10/7/97. **Disp_DBstat_PP1_c.eps**. Measured and generated formation values for (a) saturation and porosity, (b) saturation and estimated saturated hydraulic conductivity, and (c) porosity and estimated saturated hydraulic conductivity. 160

1-98 10/7/97. **Disp_DBstat_BF3_c.eps**. Measured and generated formation values for (a) saturation and porosity, (b) saturation and estimated saturated hydraulic conductivity, and (c) porosity and estimated saturated hydraulic conductivity. 161

1-99 10/7/97. **Disp_DBstat_BF2_c.eps**. Measured and generated formation values for (a) saturation and porosity, (b) saturation and estimated saturated hydraulic conductivity, and (c) porosity and estimated saturated hydraulic conductivity. 161

List of Tables

0-1 Computing Equipment ii

1-1 Statistical behavior of net infiltration (AAI in mm/yr). 3

1-2 Summary of tight-grid infiltration simulation results 5

1-3 Summary of alluvium ($abcd$) and fracture ($efgh$) parameter codes 6

1-4 Summary of colluvium and matrix properties used in simulations. 26

1-5 Best-fit abstractions to material properties in deep alluvium. 36

1-6 Regression values for deep-alluvium meteorologic abstraction. 37

1-7 Regression coefficients for deep-alluvium meteorologic abstraction. 37

1-8 Hydraulic conductivity measurements in Solitario Canyon on March 27 and 28, 1997. 48

1-9 Summary of alluvium ($abcd$) and fracture ($efgh$) parameter codes 52

1-10 Net infiltration (mm/yr) for various cases with soil- and calcite-filled fractures 53

1-11 Statistical description of $Y = \log_{10}[K_{sat}\ (m/s)]$ in TCw. 131

1-12 Statistical description of $Y = \log_{10}[K_{sat}\ (m/s)]$ in PTn. 132

1-13 Statistical description of $Y = \log_{10}[K_{sat}\ (m/s)]$ in TSw. 132

1-14 Statistical description of $Y = \log_{10}[K_{sat}\ (m/s)]$ below TSw (CHnv, CHnz, PP, UCF, UBF). 133

1-15 Statistical properties of regression on K_{sat}. 143

1-16 Layerwise estimates of K_{sat} (m/s). 10^{-10} m/s is equal to 3.16 mm/yr. 146

1. Ambient Hydrology KTI – Infiltration

Account Number: **20-5708-861**
Collaborators: **Amvrossios Bagtzoglou, Gordon Wittmeyer**
Directories: **$SubRegBreath and as noted**

Objective: Perform detailed analysis of the spatial and temporal distribution of infiltration at Yucca Mountain. A good deal of previous work is documented in the Scientific Notebook for the Subregional Flow and Transport Processes Research Project (subregional project) and various publications under the subregional project and the umbrella of the Iterative Performance Assessment and Performance Assessment Research projects. The research projects were closed out due to reorganization of the NRC and consequently CNWRA; infiltration work is largely being subsumed under the Ambient Hydrology KTI, with some applications possible under the Thermal Effects on Flow KTI in order to examine heating effects on infiltration. Initial efforts in the new project are to be directed towards documenting the work already completed in journal articles. Future work will depend very much on funding and time availability, but several avenues that may be explored include: (i) the impact of matrix-fracture interactions; (ii) watershed-scale modelling, with vegetation and lateral flow accounted for; (iii) geochemical tracer verification; and (iv) "shallow" diversion of infiltration due to the PTn layer.

1/26/96 Initial entry. SAS

Work on infiltration under the subregional project and IPA is currently being documented in two journal articles. The first article deals with the impacts of hydraulic properties on 1D infiltration; the second looks at meteorology, documents the alluvium flow model, and estimates spatial and temporal distributions of infiltration. All simulations to date have been 1D; the first sets examined semi-infinite alluvium columns, with later sets looking at a shallow alluvium layer over a fracture continuum. It is quite clear that the fracture continuum will allow far more water to infiltrate than the alluvium columns; a relatively thin alluvium coating (less than 50 cm) will shut off fracture flow entirely, but sufficiently deep alluvium (greater than 5 m) will allow the flow to resume; hillslopes and ridgetops are the most important infiltration areas; micrometeorology is not a great factor, nor is the fracture description if there is enough fracture porosity; alluvium hydraulic properties have a significant influence, increasing with depth, but the depth of alluvium is the single most important parameter; detailed hourly description of meteorology is only important near precipitation events; and it is critical to use arithmetic averaging or upstream weighting for conductivities in the fracture

continuum.

In the process of creating traces of infiltration rates, it became apparent that several of the cases with very shallow alluvium covers (2 cm and 5 cm) spuriously created mass for one or more storms. Increasing the resolution in the top layer from roughly 1 cm per element to 1 mm per element fixed the problem for the simulations that were rerun this week (temperature and precipitation perturbations). Unfortunately, even though the new results show excellent self-consistency, there is significant deviation between the coarse and fine cases (roughly 50 percent less infiltration for 2-cm cases). A revised set were set off today for the hydraulic properties, but it takes roughly a day per simulation so it will be several weeks before all are completed.

1/30/96 Data Analysis. SAS

Created matlab files to analyze the lowest flux trace from a set of breath runs. The workhorse file, **stat_infil.m**, is in ***$HOME2/Matlab/BreathUtil***. Copies of the driver routine, **eval_all_stat.m**, must be put in the result directory of interest. Filled out a table for temporal behavior of infiltration in the paper on the spatial/temporal distribution of infiltration, aside from the 10-cm case which must be rerun due to accidental erasure of the trace files. The table is included here as Table 1-1. Also tracked down many of the figures to be included and rearranged the directory structure below ***$HOME2/Subreg*** to have better segregation of figures. New directories containing figures now are listed as ***FigureXxxx***, where ***Xxxx*** is one of ***Paper*** or ***YMElev***.

2/17/96 Error in viscosity units. SAS

A persistent mistake was found in the specification of viscosity, dating from the earliest runs using *breath*. *breath* uses consistent units for all variables; however, the *Matlab* files used to create inputs for *breath* consistently uses viscosities three orders of magnitude too large. There is no net impact on the results when saturated conductivity is provided as data, as *breath* requires intrinsic permeability rather than saturated conductivity and intrinsic permeability is obtained by scaling hydraulic conductivity with the incorrect viscosity, which in turn is scaled back internally to *breath*. Accordingly, test problems based on saturated conductivity have been correctly calculated, since intrinsic permeability and viscosity are incorrect in compensating ways. Many other simulations are perfectly valid. Unfortunately, all sequences of infiltration experiments performed with alluvium and fractures have alluvium permeability specified (fracture saturated conductivity is specified), so that the reported permeabilities are actually off by three orders of magnitude. The *breath* code has

Table 1-1: Statistical behavior of net infiltration (AAI in mm/yr).

Depth (cm)	Multiple of AAP	°C Added to AAT	AAI	Wettest Year AAI	Wettest Year Events	Driest Year AAI	Driest Year Events	Events Max	Events Min
2	1.0	0	58.2	172.5	5	9.5	1	7 (1)	1 (1)
2	0.9	0	48.1	149.5	5	7.9	1	6 (2)	1 (1)
2	1.1	0	67.0	196.5	5	11.16	1	10 (1)	1 (1)
2	1.0	+3	50.6	158.2	5	8.79	1	6 (2)	1 (2)
2	1.0	−3	68.7	191.2	5	10.34	1	10 (1)	1 (1)
5	1.0	0	31.0	124.7	7	0.29	0	7 (1)	0 (1)
5	0.9	0	23.7	101.2	5	> 0.01	0	7 (1)	0 (2)
5	1.1	0	38.6	147.9	5	2.98	1	5 (2)	1 (3)
5	1.0	+3	25.3	108.3	5	0.59	0	5 (1)	0 (1)
5	1.0	−3	38.7	148.3	5	2.18	1	6 (1)	1 (3)
10	1.0	0	12.5	60.1	4	> 0.01	0	4 (1)	0 (3)
10	0.9	0	8.73	42.8	4	> 0.01	0	4 (1)	0 (5)
10	1.1	0	TBD	TBD	TBD	TBD	TBD	TBD	TBD
10	1.0	+3	9.68	49.9	4	> 0.01	0	4 (1)	0 (4)
10	1.0	−3	16.8	81.8	4	> 0.01	0	4 (1)	0 (3)
15	1.0	0	4.61	26.7	2	> 0.01	0	2 (2)	0 (7)
15	0.9	0	2.65	13.9	1	> 0.01	0	2 (1)	0 (8)
15	1.1	0	6.26	33.3	3	> 0.01	0	3 (1)	0 (6)
15	1.0	+3	3.18	17.3	2	> 0.01	0	2 (1)	0 (8)
15	1.0	−3	7.74	45.8	4	> 0.01	0	4 (1)	0 (7)

a temperature-dependent viscosity option, which I have not used; this option uses viscosities that are off by two orders of magnitude. I corrected this viscosity calculation in *breath* versions 1.1, 1.2, and 1.3 today.

The fix is to relabel all references to permeability to a value three orders of magnitude lower. The results are actually more comforting than the originally reported interpretations implied, since the actual range of permeabilities is in the range of silty sands through clean sands, rather than clean sands through gravels, and indeed are representative of the range of values reported for Yucca Mountain as was reported by various USGS papers. In fact, if my simulations were reported using saturated conductivities, the results would have been consistent and it is quite possible that the persistent error would not have been found. The simulations were incorrectly presented in Stothoff

et al. (1995), Stothoff and Bagtzoglou (1996), Bagtzoglou et al. (1995), Stothoff et al. (1996), and the poster used for both Stothoff and Bagtzoglou (1995) and the 1995 Kearney Conference. It may yet be possible to save the version of Stothoff and Bagtzoglou (1996) that will be widely distributed.

3/8/96 Update figures and results.

SAS

In preparing a series of slides for a Geological Society of America conference on 3/12/96, I am taking the opportunity to tabulate the results generated from a sequence of runs using a tight grid, as explained in the entry of 1/26/95. All hydraulic-property cases and the pressure and temperature cases were rerun for the 2-cm and 5-cm alluvium depths. The base case scenario was rerun for the 10-cm, 15-cm, 500-cm, and 1000-cm alluvium depths, as well as the semi-infinite alluvium case.

The results of the simulations are summarized in Table 1-2. The base-case weather is denoted by an "m"; perturbations in AAP and in AAT are denoted by "r" and "t", respectively. AAP is perturbed by multiplying all precipitation values by the noted perturbation; AAT is perturbed by adding (t+) or subtracting (t−) the noted perturbation. The alluvium and fracture codes both coalesce the permeability, porosity, and van Genuchten parameters into a 4-digit code. The codes are selected to allow one integer per parameter, and are translated in Table 1-3. The odd translation for fracture intrinsic permeability and van Genuchten scaling pressure are because saturated hydraulic conductivity and van Genuchten α created better codes. Note that the -3 factor in the intrinsic permeability codes is the correction for the improperly specified viscosity in earlier runs, so all runs are consistently labelled.

4/16/96 Update results and interpret.

SAS

Over the past month, I've been running simulations with fairly extreme climatic change in order to examine what would be expected at Yucca Mountain. So far, only 2-cm and 5-cm alluvium depths have been run, since the deeper cases take much longer. The climatic change is accomplished by multiplying all precipitation by a constant factor and/or adding a constant temperature. For both 2-cm and 5-cm cases, all combinations of rain and temperature have been completed with rain multiplied by 2/3, 1, or 3/2, and −5, 0, or +5 degrees C added to the temperature. A similar sequence is underway for rain multiplied by 1/2, 1, or 2, and −10, 0, or +10 degrees C added to the temperature. I should probably run a 15-cm and semi-infinite sequence as well for completeness, but these would take a *long* time. The results are summarized in **af_cli.result** in

Table 1-2: Summary of tight-grid infiltration simulation results

Code	Weather Perturbation	Alluvium Depth (cm)	Alluvium Code	Fracture Code	Moisture Content	Flux (cm/yr)
m	0	2	5223	2713	0.0331	5.82
m	0	2	5223	2712	0.0331	5.89
m	0	2	5223	2714	0.0328	3.29
m	0	2	5223	2703	0.0328	7.32
m	0	2	5223	2723	0.0331	5.75
m	0	2	5223	2613	0.0331	5.90
m	0	2	5223	2813	0.0331	5.77
m	0	2	5223	0713	0.0330	5.19
m	0	2	5223	4713	0.0331	5.86
m	0	2	5222	2713	0.0218	7.05
m	0	2	5225	2713	0.0548	4.43
m	0	2	5213	2713	0.0324	5.92
m	0	2	5253	2713	0.0352	5.87
m	0	2	5123	2713	0.1015	6.17
m	0	2	5323	2713	0.0151	6.51
m	0	2	4223	2713	0.0293	6.20
m	0	2	6223	2713	0.0397	5.43
m	0	5	5223	2713	0.0484	3.10
m	0	5	5223	2712	0.0486	3.18
m	0	5	5223	2714	0.0484	1.72
m	0	5	5223	2703	0.0483	3.32
m	0	5	5223	2723	0.0486	3.08
m	0	5	5223	2613	0.0485	3.15
m	0	5	5223	2813	0.0486	3.07
m	0	5	5223	0713	0.0485	2.69
m	0	5	5223	4713	0.0486	3.17
m	0	5	5222	2713	0.0331	4.30
m	0	5	5225	2713	0.0750	1.56
m	0	5	5213	2713	0.0505	3.22
m	0	5	5253	2713	0.0469	2.93
m	0	5	5123	2713	0.1219	3.69
m	0	5	5323	2713	0.0251	3.28
m	0	5	4223	2713	0.0380	3.37
m	0	5	6223	2713	0.0625	3.05
t−	3.0	2	5223	2713	0.0381	6.87
t+	3.0	2	5223	2713	0.0294	5.06
r*	0.9	2	5223	2713	0.0324	4.81
r*	1.1	2	5223	2713	0.0338	6.90
t−	3.0	5	5223	2713	0.0562	3.87
t+	3.0	5	5223	2713	0.0423	2.53
r*	0.9	5	5223	2713	0.0465	2.37
r*	1.1	5	5223	2713	0.0503	3.86

Table 1-3: Summary of alluvium ($abcd$) and fracture ($efgh$) parameter codes

Code	Parameter	Translation
a	Intrinsic permeability k (cm^2)	$k = 10^{-a-3}$
b	van Genuchten m	$m = b/10$
c	van Genuchten scaling pressure P_0 (gm/cm-s^2)	$P_0 = c \times 10^4$
d	Porosity ε	$\varepsilon = d/10$
e	Intrinsic permeability k (cm^2)	$k = 1.14694 \times 10^{-e-3}$
f	van Genuchten m	$m = f/10$
g	van Genuchten scaling pressure P_0 (gm/cm-s^2)	$P_0 = 980 \times 10^{-g}$
h	Porosity ε	$\varepsilon = 10^{-h}$

$HOME1/RunCliFrac *(correction (dated 12/7/96):* ***$BREATH1/RunCliFrac****).*

Doubling rain and subtracting 10 degrees C from the temperature yields the most infiltration of all cases considered. For the 2-cm case, a factor of 4.3 increase is generated; for the 5-cm case, a factor of 6.6 increase is generated. Overall, this suggests that roughly a factor of 5 to 6 increase should be expected for this climatic condition, taking into account the importance of shallow covers relative to deeper covers. This increase could be quantified better using the newly developed colluvium-balance model discussed in the Geomorphology chapter.

4/17/96 Thoughts on creating an infiltration PDF. SAS

The original motivation for examining shallow infiltration was to provide a PDF for the deep percolation fluxes past the repository. Ross and I planned to have my shallow infiltration fluxes feed into his deep percolation models. At the time, my idea was to construct a response surface for shallow infiltration as a function of whatever parameters were found to be important. It is now years later, but my work is reaching a point where construction of such a PDF is in sight.

An infiltration PDF is not a particularly well-defined concept. Ideally, one would construct many realizations of the entire mountain, from the surface to the water table, and pass in the appropriate boundary fluxes. The TSPA approach breaks the mountain into representative columns, each with its own infiltration flux. I believe that the PDF of interest is actually the PDF describing fluxes in each column, and presumably the fluxes in the columns are correlated. Accordingly, the shallow infiltration work can only be step one in the process, albeit a critical link between climate and deep percolation.

If the infiltration work is split into shallow and deep components, I believe that the best that the shallow infiltration work can do is to pass off plausible realizations of shallow fluxes to the deep percolation model, which in turn uses realizations of the stratigraphy and hydraulic properties to calculate fluxes through the repository. If indeed the fluxes at the repository in the deep model are insensitive to the degree of spatial variability in the shallow distributions, as I suspect, the smoothest distributions yielding minimal deviation at the repository should be used. A grid of spatially averaged infiltrations would be appropriate, perhaps on a 10-pixel spacing.

Ross' deep percolation work (Bagtzoglou et al., 1995) suggests that the repository is rather insensitive to focused recharge. Another approach that might be taken is to calculate the average infiltration over the area "upstream" of the repository. Unfortunately, the upstream area would be different for each realization, so that some representative area would need to be designated. The entire DEM feels excessive, while the repository footprint is too small. Perhaps the channel in Solitario Canyon to east of the footprint, extending a total of twice the north-south extent of the footprint?

The response surface idea can come into play at a second level in the average-infiltration approach. The first level is the construction of infiltration at a pixel as a function of parameter values. The second level is the construction of the average upstream infiltration as a function of parameter values. The response surface would assume that a single value of each hydraulic property is sampled and applied to the entire domain. Alternatively, it is possible to randomly assign properties to each pixel from an appropriate distribution and generate many realizations, calculating the average infiltration for each realization. Both of the approaches should be performed, using corresponding property PDFs, in order to see if important differences appear. I suspect that the two approaches will give essentially identical PDFs for shallow infiltration (some sort of law of large numbers), even if correlation between parameters is present.

In my model, the spatio-temporal distribution of shallow infiltration can be captured with 8 parameters: (i) four alluvium hydraulic properties (K_{sat}, porosity, and two van Genuchten parameters); (ii) two alluvium-depth properties; and (iii) average temperature and precipitation. The alluvium hydraulic properties could easily be functions of space. The average temperature and precipitation may be available from the geologic and other records (e.g., the Devil's Hole data, packrat middens). The alluvium-depth properties, however, are big unknowns; I feel these should be constants for a realization. The Yucca Mountain field trip planned for the near future will aid in constraining the alluvium-depth properties.

Given that the alluvium-depth properties and the climatic properties are constants for a

realization, there is no reason to suspect that the two average-infiltration approaches would yield a different PDF unless there is some systematic bias for hydraulic properties as a function of colluvium depth. Consider the environment of deposition. Shallow covers tend to be cobbly, with outcrops of rock. There may be some trend towards low spatial-average porosity, high permeability, and coarser grains in the shallower cover. Are shallow covers coarser? Something to check on the field trip, but how? Perhaps portable grain-size distributions, timing infiltration rates. Upon second thought, such ideas are silly – it would be very difficult to find discernable trends in the 2-cm through 15-cm regimes. It doesn't matter once the depths are greater than 0.5 m, since there is no infiltration to speak of anyway for such cases.

Since the two average-infiltration approaches should yield consistent PDFs, it makes sense to construct the response surface. I suspect that a reasonably detailed 8-dimensional surface could be calculated in hours; setting up the software could take a day or two, since the software should take advantage of new information from additional simulations as they might become available. Enforcing consistency between various simulations with various degrees of reliability may be a headache, as I have migrated to tighter and tighter numerical standards over time.

One issue that should be addressed is the issue of climatic change. I've talked to Dave Turner and Mike Miklas about retrieving climatic records. The idea would be to generate a series of plausible climatic-change realizations based on available data and feed it through the response surface to generate plausible traces of average infiltration. The resultant trace could be compared to TSPA traces. The deep percolation model really needs to be flogged to get the response of the repository horizon to infiltration rates for this to be most useful, but a nice paper could come out of the work.

4/23/96 Watershed modelling. SAS

Dr. David Woolhiser will be consulting to CNWRA on the subject of watershed modelling. A number of discussions have taken place between Woolhiser, Gordon, Ross, and myself, with the intent of scoping out the work to be performed. After these discussions, we have decided to break out the work into several packages of roughly $10 k apiece. The first package will be simulation of a representative wash feeding into Solitario Canyon from the west, which would be a surrogate for wash-scale modelling of easterly of Yucca Crest. The first package will test the methodology and feasibility of future work. Further packages would include the full Solitario Canyon watershed, and perhaps some detailed side-slope simulations with lateral subsurface flow.

To date, we have sent Woolhiser relatively limited information on the site. He has requested additional information including

- a large contour map of the Solitario Canyon watershed;
- a contour map of slopes in the Solitario Canyon watershed;
- available information on infiltration;
- available information on saturated conductivity;
- channel cross-sections; and
- photographs of the channel cross-sections (for roughness estimates).

A field trip to Yucca Mountain is being planned for the near future, at which time channel cross-sections and photographs can be obtained. In addition, I will obtain measurements of alluvium depths to compare with my geomorphology model, and perhaps some limited infiltration sampling using a falling-head permeameter can be performed as well. According to Woolhiser, a representative channel section or two midway between incoming washes would probably be sufficient for his needs, with 3 or 4 sections in representative washes. Photographs of each section should be taken, roughly 50 feet downstream.

Woolhiser has software available that should be able to generate the weather conditions at the resolution required for his model.

5/18/96 Summary of field trip observations. SAS

This past week, Ross Bagtzoglou, Gordon Wittmeyer, and I went to Solitario Canyon to obtain field measurements and observations. Ross and Gordon concentrated on surveying wash cross-sections for the mid- to lower-canyon reaches, while I concentrated on walking the mid- to lower-canyon from rim to rim taking spot measurements of colluvium depths and trying to make observations useful for comparison with computational models. My field observations are documented in a field book, CNWRA Controlled Copy number 175.

The first field day, May 13, we spent basically getting together procedures and familiarizing ourselves with the site and equipment. Ross and Gordon wrestled with the surveying equipment and data logger all day, finally becoming comfortable with the equipment after successfully surveying a

motel room that evening. During the day, they located well USW H-7 (on the other side of the road from Plug Hill) as a benchmark and made one cross-section at a stream-gage station adjacent to Plug Hill. Additional cross-sections were stymied by a recalcitrant data logger, apparently confused by a mixup in coordinates input for the first two locations.

I spent part of the first field day making measurements of alluvium to the west and northwest of the USW H-7 pad, walking up a sideslope to the crest and returning down a small wash. Wherever I took alluvium depth measurements, I marked a nearby bush with surveyor's tape with the idea of having the points surveyed in subsequently. As it turned out, we did not get a chance to survey the points due to delays caused by unfamiliarity with the equipment.

In order to estimate shallow alluvium/colluvium depths, I brought a tile probe with the idea of poking a hole into the alluvium until further advances were rejected. The tile probe is a metal rod with a diameter of 1/2 in, with a metal tip 4 cm long and a padded handle. The base of the adapter attached to the handle is 124 cm from the tip. I brought a 10-lb hammer attachment to replace the handle, in order to help drive the tile probe. I scored the probe, creating very distinctive grooves at 10, 20, 30, 40, and 50 cm distances from the tip, for quick depth and length estimates.

Proceeding up the slope from the USW H-7 pad to the west crest, point measurements ranged up to 44 cm. At one representative mid-slope location, depths were 27, 36, and 42 cm within 2 m; at another, depths were 17, 21, and 37 cm. At the crest, depths were typically 2 to 4 cm in places, at others 6 to 8 cm. Just below the crest, pockets of 12 to 18 cm colluvium were found, increasing with distance below crest to at least 37 cm. Walking down the rill, the channel was found to consist of bare rock in places, particularly at narrow and/or steep reaches. As the channel flattened, the scoured zones disappeared. Judging from the walls of the channel in scoured zones, alluvium depths could be as much as 2 m in places, but it is difficult to tell for sure. Certainly ridges between subwashes are up to 2 m.

It quickly became obvious that the idea of the tile probe was not going to work in alluvium over a certain depth or in regions with numerous chunks of rock, since rejection due to rubble was so likely compared to rejection due to bedrock. Accordingly, I concentrated use of the probe in shallow zones generally less than 40 cm in depth. These zones are of the most interest for infiltration estimates anyway.

The second part of the first day, I walked north along the bottom of Solitario Canyon further than well USW H-6. The stream channel morphology is rather confused in the entire stretch I walked north from Plug Hill. It appears that there are typically two channels, one for the eastern side of Solitario Canyon and one for the western side, but the channels are not strongly distinct and tend

to braid. The bottom of the channel is not uniform, with patches of similar materials ranging from very fine through gravel. There is brush in most of the channel, with somewhat less brush in the most active portions of the channel. There is a great deal of variability at a scale less than the 30 m x 30 m resolution provided by the DEMs we've been using, so that the cross-sections are essential. Unfortunately, in order to fully capture the stream channels, cross-sections would be required at a much higher density (every 20 to 50 m, I estimate) than Gordon and Ross set out to perform. Gordon and Ross were going by Woolhiser's estimates of one cross-section per side wash.

The second field day, I walked or crossed each of the washes in the watershed draining to the north of the USW H-7 pad. The watershed consists of 6 or 7 washes to the north and west of the pad. Proceeding to the north, I walked the Boomerang Point crestline, crossed to near the Jet Ridge crestline, and dropped back into the USW H-6 watershed. This day, I used Global Position System (GPS) pack to provide approximate latitude and longitude at selected locations. The GPS equipment is supposed to place one within 100 m of the correct location; if a second station is used, differential methods are supposed to yield sub-meter accuracy. Our original intent was to use a reference station and a rover station; however, we found that the supplied batteries were only good for 4-1/2 to 5 hours and we did not have four batteries to cover the full day. Upon return, I hear that motorcycle batteries might do the trick for a reference station.

The third field day, I was in Las Vegas and received a NTS badge and GET training.

The fourth (and my last) field day, I walked up the east part of Solitario Canyon to Yucca Crest, arriving not far from USW-UZ6. Again I used the GPS equipment without a reference station. I started at a trench apparently dug to expose the Solitario Canyon fault, and passed some terracing exposing the upper half of the PTn outcrop. Once at the Crest, I proceeded down the wash north of Highway Ridge to the first of two sets of trenches scraping away the alluvium cover from bedrock. The trenches extend from ridgetop to ridgetop. Due to time constraints, I only examined the southerly trench closely. This trench shows very little alluvial cover at the channel bottom, increasing to 1 or 1.5 m within 10 m of the bottom, and gradually thins to less than 10 cm at the top. Returning to the crest on the southern side of the roadway, I was able to observe the wash to the south as well. I returned to Solitario Canyon slightly north of USW H-3. Upon my return, judging from aerial photographs I was able to observe terrain typical of the western and central portions of the repository footprint; further to the east, the wash channels become wider and have little in the way of scouring in the channel bottoms.

During the four field days, Gordon and Ross completed on the order of 15 cross-sections, extending up Solitario Canyon most of the way from Plug Hill to USW H-6. The original plans to

survey the entire canyon channel were discarded due to the messy nature of the channel above this point and due to time constraints. The day after I left, Gordon and Ross visited the ESF.

Based on the three days of walking around and poking colluvium, it is clear that there are some problems with the colluvium model hooked together with the infiltration response surface, although the basic approach is sound. In general, even on ridgetops there are very few places that have less than 3 or 4 cm colluvium cover, and these places are usually exfoliation shards overlying bedrock. TC caprock boulders are generally massive and unfractured. Along crestlines, TC caprock exposures cover 50 to 90 percent of the surface (visually estimated). Moving downhill easterly from the crests, TC caprock boulders on the order of meters in length appear, get smaller and sparser, then disappear. In the cracks between TC caprock outcrops at the crestlines, it is typical for fine sand through loess to be present with depths at least 3 cm and less than 6 cm. Depths increase with distance from the crestline, averaging 10 cm or so between the larger boulders and increasing to 15 to 20 cm as the boulders decrease in size. There are occasional pockets with deeper colluvium, typically less than twice the average depths for the area. I saw few washes cutting directly into the caprock, aside from the western portions of crestlines, although it was not uncommon for caprock boulders to be sliding along other TC units into washes to the east.

Most of the exposures east of crestlines are TC units. Generally these are not highly fractured near the caprock but increase with depth. Any TC units below the caprock do not appear distinctive to my admittedly untrained eye. Chunks of the lower TC tend to be much smaller than the TC caprock boulders, generally being less than 50 cm. In the steepest portions of washes cutting TC units, bare country rock may be exposed, particularly in wash channels and up to 10 m above the channels in places. The washes on the west of Solitario Canyon tend to be steeper and shorter than the washes on Yucca Mountain proper. The Yucca Mountain washes tend to develop long regular reaches with uniform sideslopes, very nice for modelling. Based on a trench north of Highway Ridge, maximum alluvium depth on sideslopes should not be much more than 1 to 2 m, near the channel bottom. It appears that the long regular slopes are steepened at the base, due to removal of colluvium due to stream action during rainfall. It may be possible to estimate the depth of alluvium by projecting sideslopes out to midchannel in the upper portions of the washes.

All along the steep portions to the west of Yucca Crest, pockets may be as much as 40 cm, but generally are in the 5 to 15 cm range. A considerable amount of bare outcrop is present, as much as 50 percent or more of the surface area. Even partway down the flatter slopes, depths may not be more than 50 to 100 cm.

There are distinctive stripes of dark, highly varnished scree alternating with light, clean

scree on many of the wash slopes. Stripes may be as little as 1 to 2 m on center and may be tens of meters on center. Invariably the dark scree is raised relative to the clean scree, suggesting that runoff is focused on the clean scree and washes it. It may be safe to assume that the darker the scree, the higher it is relative to the adjacent light scree.

Two difficulties arise when comparing the infiltration conceptual model work with field observations. The first difficulty is in treating the regions near the crestlines. Although colluvium depths, where present, are generally greater than I've been assuming, the areal average might not be too bad. However, the flow modelling assumes that there is uniform depths of colluvium everywhere, while the actual situation is patchier and deeper. An obvious way of treating the actual situation is to decrease the porosity to account for the proportion of surficial area that is impermeable boulder. It may be that reducing porosity is essentially equivalent to reducing depth, since the volume available for flow is reduced by either approach. If so, accounting for boulder size and area may not be tremendously important in the colluvium model.

The second difficulty is in treatment of wash channels. The colluvium model breaks down when factors other than gravity become important, such as overland water flow. It should not be difficult to include a factor increasing colluvium fluxes due to streamflow, which will get rid of the (arbitrary) 20 m depths in upper channels. Unfortunately, all of the action is on a scale that is subgrid compared to the DEM measurements. The channels are only 1 to 2 m wide where the rock is bare, yet the grid is 30 m on a side. It may be necessary to overlay a refined grid on wash bottoms to properly capture infiltration, at least in upper portions of the washes. As the channel bottoms are relatively narrow, there may not be a great deal of infiltration relative to ridgetops.

5/28/96 Summary of second field trip observations. SAS

As an adjunct to a Technical Exchange on the NRC audit of the DOE TSPA-95 performance assessment document, which was held in Las Vegas, a group of 8 NRC/CNWRA/consultant personnel took a tour of the ESF at Yucca Mountain(myself, C. Glenn, B. Behlke, M. Bell, A. Campbell, R. Manteufel, J. Walton, G. Stirewalt). The tour took place May 24, 1996. The tour was led by Alan ? of the DOE mapping team and hydrologic input was provided by Alan Flint of the USGS.

One of the more important observations that Alan Flint made regards lateral diversion in and near the PTn bedded tuffs. Previous TSPA analyses have assumed that lateral diversion may be strongly impacted by a very low permeability unfractured layer just below the PTn. However, the ESF borehole exposes a section of PTn that appears to be rather frequently, on the order of

every 10 to 20 m by my observation, punctuated by small-offset faults. The offsets tend to be less than a meter, and may easily have been missed in boreholes. The following day, I took a walk up from Solitario Canyon to Yucca Crest and noticed some small (10 to 20 cm) offsets at one PTn exposure. Alan Flint's observation is that lateral diversion is probably not going to be very significant, because the frequent offsets in the low-permeability unit should minimize the most significant source of lateral flow.

Along the way in the ESF tour, various chlorine-36 sampling locations were pointed out by A. Flint and A. Campbell from the Fabryka-Martin et al. (1996) draft report. We also saw the heavily fractured zone, 1 km in length and still being encountered by the TBM. The fractures seemed to alternate between zones of fracture spacings less than 10 cm to zones where the spacing is more on the order of 30 to 40 cm.

As it rained (fairly heavily in spots) on May 24, I was inspired to take another walking tour of Yucca Mountain on May 25. Based on wetting front observations, which penetrated roughly 3.5 to 6.5 cm in various representative areas, and on water in exposed lithophysae, I estimate 1 to 2 cm of rain took place. I noticed that on Yucca Crest, enhanced wetting took place in the gaps between outcrops (10 cm and larger in spots), while under rubble scree on sideslopes less wetting took place (dry soil was not uncommon). While walking about, a storm cell drifted overhead and roughly a half hour of rain occurred. A total of no more than 5 minutes of reasonably heavy rain occurred, with most of the interval light to nearly non-existent. Exposed rubble faces were definitely wet; however, vertical sides tended to be dry with wetting fronts occurring at the top of perhaps 1 to 3 cm. Fifteen minutes after rain ceased, little or no trace of the event could be detected.

I also examined four of the trenches that are exposed in what I think is Split Wash or the next wash north (the wash with the Ghost Dance pavement and the wash immediately north of this wash). Each of these are sufficiently downstream that the wash bottom is at least 10 m wide. In this region, what I believe Alan Flint refers to as channel terraces are exposed. It appears that currently active wash channels are cutting into the terraces. Depth to bedrock at the deepest point in the trenches ranged from 2.5 to 4 m, as best as I could estimate. However, once the slope of the ground increased from the relatively flat terrace to side slope, cover decreased to the more typical 10 to 50 cm. It should be possible to identify these deeper zones simply by the slope or break in slope.

I also had the opportunity to talk with Alan Flint about his site-scale modelling work. He demonstrated time-traces of moisture content in various neutron-probe boreholes. In one channel terrace probe, lateral subsurface flow was clearly evident. He is currently using a 3-event (upgrading

to 5-event) Markov-chain model to generate daily precipitation and daily mean temperature readings. Each rainfall event is redistributed to essentially perch on the colluvium/bedrock interface at the end of the day, where it infiltrates according to matrix and fracture properties. Each Scott and Bonk (1984) layer has matrix properties assigned, either from direct measurement or from analog. Fractures are grouped into 3 size classes, and further subdivided into filled/unfilled areal fractions. Pixel size is 90 m on a side; no lateral diversion is considered. Evapotranspiration is a part of the model.

Pondering the site visit, it seems that the DEM is somewhat unwieldy for colluvium-flow calculations, as it completely misses meter-scale features such as wash channels. Ideas of quasi-1D flow-tube analyses occurred to me as being particularly appropriate for Yucca Mountain. Each flow tube would carry along local information on topography, width, depth, shape, vegetation, etc., in the form of integer categories or classes. Accordingly, the information could be encoded very compactly in the form of bit substrings within a few integers. Vegetation is another tricky topic inspired by discussions with Alan Flint, which it would be very nice to have a better handle on.

8/27/96 Pondering questions relevant to performance. SAS

In brief, work to date has focused on

- 1D simulations
- bare soil (no vegetation)
- no matrix-fracture interaction
- instantaneous lateral redistribution
- long-term average impacts due to
  - hydraulic properties
  - meteorologic input
- spatial distribution of surface cover
- spatial distribution of AAI
- to a minor extent, response to climatic change

Most of the work is documented in a journal article currently in preparation. The text and figures for the article will be included in this notebook upon submission to the journal and internally documented.

After the completion of work to date, it is my opinion that numerical modelling can give reasonable estimates of spatial distributions for relative AAI, the relative response of AAI to climatic change, but not absolute magnitudes for AAI. Since almost all precipitation ends up returning to the atmosphere, small errors in evaporation estimates may yield large errors in AAI estimates. Thus, the large area of interest with associated high heterogeneity levels and complex physical behavior preclude more than bounding estimates for AAI.

A number of future investigation directions can be considered.

- The validity and conservativism of the 1D approach could be examined using 3D simulations with discrete fractures on the grid-block scale for the DEM (roughly 30 m x 30 m). A 2D or 3D code would need to be assembled, presumably with the additional processes of vegetation and snow considered. Studies on the grid-block scale would be aimed at ascertaining the impact of heterogeneity and fracture spacings.
- Hillslope- and watershed-scale studies can be examined to see if lateral redistribution would significantly alter the predicted spatial distributions for AAI. Again a 2D or 3D code would need to be assembled, similar or identical to the code for the grid-block-scale simulations.
- Detailed process-level simulations, on the scale of a single fracture, could be undertaken to see how the matrix might affect infiltration magnitudes and timings. Code development is required.
- Additional 1D simulations could be undertaken to see how vegetation and snow might affect infiltration magnitudes and timings. Code development is required.
- The simulations performed to date can be squeezed to obtain the most information possible. Perhaps the most important additional information regards the timing and magnitude of infiltration pulses. The weekly trace of fluxes for each simulation can be examined relative to the rainfall input to determine the pulse description as a function of precipitation description. Perhaps comparison to the bucket approach would be in order. Analysis and *Matlab* code development required.
- Given infiltration-pulse information, the spatial distribution and timings of fluxes through the PTn can be estimated. The important question is what time-scale pulses through the PTn

have and how uniform the distribution of fluxes at the bottom of the PTn would end up being, so that the representativeness of quasi-steady-state approaches can perhaps be assessed. A logical first step might be 1D simulations using the output from one or more of the 10-yr shallow simulations. Again, some sort of 3D simulator may be in order. Predictions of travel times through the PTn could be made prior to tests in the ESF.

A key point in nearly all of these future directions is the common thread of required code development. Even in 1D, additional refinements to *breath* are necessary, while 3D codes are not available at CNWRA that have the proper capabilities.

8/28/96 Data bibliography. SAS

As discussed above, my studies examining the spatial distribution of AAI may be extended to below the PTn layer. If this is the case, it is extremely useful to collect all data pertaining to ambient unsaturated-zone hydrology at Yucca Mountain. I started collecting this type of information last month, as I needed to verify some of the information regarding alluvium depths measured in boreholes and trenches collected by Hannah Castellaw almost a year previously in order to double-check predictions of depths from DEM slopes. It took some time to find her sources, and in the interim I located additional information nestled in the CNWRA library. The current entry summarizes some of the information available.

Flint and Flint (1995) provide a summary of 99 neutron-probe boreholes, including locations, elevations, classifications, dates, alluvium depths, and lithology, as well as some analysis of the data. The entire moisture-content data set for all boreholes has been ordered from the DOE and should be arriving within the week, on tape. Attempts to email the data set were stymied due to the CNWRA inability to receive email greater than 1 Mb in size (the data set consists of two files of 12+ and 14.5+ Mb, respectively). The DOE system manager was not available to set up an anonymous ftp site.

The Flint and Flint (1995) neutron-probe locations are provided in Nevada State Plane (NSP) coordinates, not the CNWRA standard of Universal Transverse Mercator (UTM). Information on the locations and elevations of most of the Yucca Mountain boreholes are also specified in a data file obtained from the DOE in January, 1994, with specifications for 243 boreholes. Alluvium depths are not specified, although various other sources of information are available including Fernandez et al. (1994), Schenker et al. (1995), and numerous drilling log reports and summaries. Some of the most recent boreholes are not in the DOE tape and locations are available from

other sources and are only specified in NSP coordinates. I have collected the available information in directory ***$HOME2/Matlab/3Ddata***, with **neutron_hole.dat** containing the most complete information.

Flint and Flint (1990) provide data from 73 samples in 9 boreholes, all in nonwelded and bedded tuffs (i.e., PTn, Calico Hills). Each sample is precisely located within the respective borehole. The emphasis is on studying data-determination methods in relatively permeable and porous Yucca Mountain cores, presumably because these are faster to analyse. Porosity, grain density, bulk density, intrinsic permeability (measured 4 ways), relative permeability versus saturation (measured 2 ways), and potential versus water content (measured 3 ways) are tabulated. Some analysis comparing the measurement techniques for the intrinsic permeability values is performed. No attempt to estimate van Genuchten parameters is made, and it seems to me that the data is not of sufficiently high quality to make the attempt.

Rautman et al. (1995) provide data obtained from a sampling grid along 1.4 km of the PTn outcrop in Solitario Canyon, with a total of about 330 core samples obtained from 26 vertical transects. Bulk properties (porosity, bulk density, and particle density) are presented for all samples; sorptivity and saturated hydraulic conductivity are presented for almost all samples (except where handling damaged the sample). Locations of vertical (upslope) transects are specified as a northward offset to a transect reported by Flint et al. (1996), with core samples located relative to the base of the sampled sequence. Distinct vertical trends in the properties are shown in plots, and high r^2 values ($r^2 > 0.824$) were obtained between the 4 bulk properties.

Flint et al. (1996) provide data obtained from 5 vertical and 3 horizontal sampling transects, with a total of 656 core samples. Bulk properties (porosity, bulk density, and particle density) are presented for all samples; either measured or estimated saturated hydraulic conductivity is presented for most samples; and sorptivity is presented for some samples for two horizontal transects. In addition, moisture retention information is obtained for 41 of the samples, with estimated van Genuchten and Brooks-Corey parameters. Relative-permeability information was not determined. Regression equations are presented for properties as a function of porosity. Arguments were made that porosity values can be used to estimate van Genuchten parameters; perhaps additional information can be gleaned from the sorptivity information. The report appears to be the best current source for property data suitable for modelling.

The five vertical transects presented by Flint et al. (1996) are further analyzed by McKenna and Rautman (1995) to examine correlation information. The correlation structure appears to be nonstationary horizontally. Appropriate downhole sampling strategies are suggested.

Schenker et al. (1995) collect and reference a large number of data sets and impose PDF descriptions on them. Most of the data are from cores extracted from boreholes; transect sampling information from Rautman et al. (1995) and Flint et al. (1996) does not appear. Porosity and bulk density have 1234 and 2173 measurements, respectively. There are 257 saturated hydraulic conductivity values from 8 boreholes. The matrix van Genuchten parameters are reportedly determined from the original pressure/saturation data sets by the authors, yielding 211 property estimates; however, the set of estimates is not directly available. Fracture properties are estimated using fracture spacing and orientation data from four boreholes (G-1, G-4, a #1, and GU-3), saturated bulk conductivity data from the saturated zone in 7 boreholes (G-4, H-1, H-3, H-4, b #1, p #1, and J-13) and bulk gas permeabilities from barometric fluctuations observed in 2 boreholes (UZ-1 and a #4). Lots of extrapolation is required due to the sparseness of the fracture data.

8/29/96 Revisiting PTn modelling ideas. SAS

Further discussions with English and Sitakanta suggest that examining the behavior of the PTn layer may be of the most direct use to PA. For example, the appropriateness of the various models for flow in the subsurface can be examined (i.e., ECM versus dual-permeability versus weeps) by examining the time behavior of pulses reaching the top of the PTn layer. If extremely long time scales at the bottom of the PTn are observed, the ECM model may be in order. If extremely short time scales are observed, the weeps model is in order. Intermediate cases presumably would require the dual-permeability model).

A second question that can be examined is the issue of the spatial distribution of fluxes leaving the PTn layer. There are direct implications for the distribution of fluxes at the drift scale, since the TSw units are relatively homogeneous from the PTn to the repository. My conceptual model of drift-scale processes under ambient conditions has high relative humidity at all flow packages and relatively few packages contact a dripping fracture (i.e., dripping fractures are widely spaced). In this case, the drips are a strong focussing mechanism, shielding most surrounding packages. Studying the behavior of the PTn layer may shed some light on the relative spacing of dripping fractures.

9/21/96 Setting up 1D PTn modelling. SAS

Two detailed sources of information are available for unsaturated-zone tuff properties, Rautman et al. (1995) and Flint et al. (1996). The Rautman et al. (1995) data set is finely resolved in

both the lateral and vertical directions, but only covers part of the PTn layer and does not provide van Genuchten properties for the samples. The Flint et al. (1996) data set consists of 8 transects, covering the full range of layers in less detail. The Flint et al. (1996) data set does provide several measurements of van Genuchten properties, however.

The Flint et al. (1996) data set will be used to test the behavior of wetting pulses, since it provides a much longer vertical transect (the Solitario Canyon transect, in particular) and some van Genuchten information. Two approaches are immediately obvious: (i) use average layer thicknesses and properties, based on Tables 2, 5, and I-1; and (ii) use Table I-1 for fullest spatial resolution but supplement properties as necessary. The idea would be to assume fracture flow with the wetting pulses translated undamped from surface conditions as a top boundary condition, with the top boundary at the top of the shardy base of the Tiva Canyon Tuff, and use gravity drainage bottom conditions in fractures to correspond to the Topopah Spring Tuff vitric caprock and lower layers. There are between 20 and 25 measured K_{sat} values within the roughly 35 m section of the transect of interest, with perhaps 35 additional core samples that do not have K_{sat} values. It is not clear whether the reported transect distance is vertical distance, horizontal distance, or along-ground distance, but assuming that the slope is roughly 30 degrees in this region, the vertical section of nonwelded tuff is about 20 m, about twice the thickness considered by Rautman et al. (1995).

As a first cut, the detailed stratigraphy implied by Table I-1 of Flint et al. (1996) will be assembled into detailed layering. For points where K_{sat} and van Genuchten properties are missing, the regressions provided by Tables 3 and 6 will be used. Between each data reading, K_{sat} and van Genuchten α will be loglinearly interpolated and van Genuchten n will be linearly interpolated. Initial conditions will be provided by using the steady-state vertical ODE approach discussed in the PA Research and Ambient Hydrology projects.

The regression equation for K_{sat} as a function of porosity for the welded and nonwelded portions of the Solitario Canyon transect in Table 3 of Flint et al. (1996), based on 36 samples and with an r^2 value of 0.90, is:

$$K_{sat} = -13.9 + 33.1\varepsilon - 30.8\varepsilon^2, \tag{1-1}$$

where K_{sat} is in m/s. Based on Figure 11, it appears that the regressed equation is actually for $\log_{10}(K_{sat})$, which makes much more sense.

From Table 6 of Flint et al. (1996), based on 10 samples and with r^2 values of 0.01 and 0.44

for van Genuchten α and n, respectively, the regression relationships are:

$$\alpha = 0.49 + 0.31\varepsilon, \tag{1-2}$$

$$n = 0.95 + 1.94\varepsilon, \tag{1-3}$$

where α is in units of MPa^{-1}.

Parenthetical note:

My suspicion is that the van Genuchten regression relationships could be significantly improved by solving for all samples simultaneously, since there is considerable latitude in changing the α and n parameters without greatly affecting the fit between data and formula. The simultaneous-solution procedure minimizes the least-squares sum of squares,

$$Y = \sum_{i=1}^{N} [\theta_i - \hat{\theta}(P_i)]^2, \tag{1-4}$$

where θ_i is a measured saturation value and $\hat{\theta}$ is the corresponding predicted saturation value for measured pressure P_i. The prediction formula is

$$\hat{\theta} = \hat{\theta}(\alpha, n, \theta_{res}, P), \tag{1-5}$$

$$\alpha = C_0 + C_1\varepsilon, \tag{1-6}$$

$$n = C_2 + C_3\varepsilon, \tag{1-7}$$

$$\theta_{res} = C_4 + C_5\varepsilon. \tag{1-8}$$

The minimization takes place when the gradients of Y are zero, or

$$F = \frac{dY}{dC_j} = -2\sum_{i=1}^{N} [\theta_i - \hat{\theta}(P_i)] \frac{d\hat{\theta}_i}{dC_j} = 0. \tag{1-9}$$

Newton's method is convenient for this minimization, which simply states that for each iteration k,

$$J(\mathbf{x}_k)s_k = -F(\mathbf{x}_k), \tag{1-10}$$

$$\mathbf{x}_{k+1} = \mathbf{x}_k + s_k, \tag{1-11}$$

where $J(\mathbf{x}_k)$ is the Jacobian and $\mathbf{x}$ is the vector of unknowns C_j. It shouldn't be too difficult to check this out on the data presented by Flint et al. (1996).

9/24/96 First results from 1D PTn modelling. SAS

After a good deal of putting together *Matlab* code and some *breath* debugging, the first set of PTn simulations were run using the base-case infiltration traces for 2-cm and 5-cm colluvium over a

fracture continuum. The 2-cm case has weekly outputs of flux, while the 5-cm case has daily flux outputs; both cases have fluxes that are higher than almost any pixel value would show, so the simulations are probably more extreme than will be observed in future work.

All work is done in ***/home2/sierra/stothoff/Matlab/PTnCheck***. The input files for *breath* are created using **fix_FFRI_dat.m**, which in turn uses **extract_qw.m**, **pre_ydot_setup.m**, and **ydot_setup.m**. The built-in *Matlab* ODE solver ode23s is used to create initial conditions for the temporal average of the input flux, using **ydot_setup.m**. Output is examined using **show_stuff.m** and **new_show_seq('t', 'nf\1;col\co;plot\pl;nseq\1;last\10')**.

Several cases were tried, varying (i) the assumption for the continuum underlying the PTn layer and (ii) the input flux case. The 2-cm input-flux case was run using 2 m of fracture continuum, 2 m of TS58 material, and 20 m of TS58 material. The last material case was also run using the 5-cm input-flux case. All cases use 5-cm nodal spacing.

Several observations were made:

- The fracture continuum below the PTn causes time steps on the order of 3 seconds, while simulations using the matrix below complete in minutes of CPU time.
- The steady-state moisture profile is very different for fractures underlying the matrix and for tuff underlying; the fractures cause the PTn to be essentially saturated in locations, while the tuff allows much drier profiles *even with the same flux.*
- The flux distribution is very peaky. Over the period of a day, fluxes can jump by 4 orders of magnitude, then decay exponentially.
- The flux pulse propagates essentially instantaneously (less than a day) through the PTn layer, but the pulse magnitude decreases exponentially with depth.
- The moisture content responds by a few percent in the same timeframe.
- The gravity drainage condition 2 m below the bottom dampens the peakiness significantly relative to the 20-m depth.
- There are roughly 2 pulses a year, although the pulses are clumped. As the colluvium depth increases further, the number of pulses will decrease.

There are several implications to the work:

- Capturing flux pulses with moisture-content readings may be a hopeless endeavor.
- Steady-state assumptions may be appropriate for calculating moisture contents.
- Using the gravity-drainage assumption with moisture contents must be examined carefully, since structural features and heterogeneity can modify moisture contents without modifying fluxes.
- It may not be that bad to use the ECM assumptions below the PTn, as there is indeed strong damping in the input signal.

The current *breath* approach must be augmented to provide more realistic simulations. In particular, it is still not possible to check the ECM assumptions since there is no possibility for more than one continuum below the PTn. Also, the saturation profile in the PTn is strongly impacted by the lower-layer assumptions. An approach that may bear fruit is to allow several continua to dangle off the bottom of the PTn, each independent except that the same pressure exists in each one at the bottom of the PTn. One continuum might be the matrix, with the rest being fracture sets. Occasional lower cross-links between the fracture continua might okay.

The augmented approach would allow the investigation of which fracture set(s) kick in, if any. In addition, the saturation in each set may be able to be translated into an equivalent wetted length, which can than be used to intersect with the drifts.

It may be considerably more difficult to construct a steady-state solver for this case, since there are multiple threads of flux joining at a middle node. Shooting may be necessary.

10/5/96 ACNW, change in PI. SAS

I attended the ACNW meeting in Las Vegas on September 26 and 27, 1996. My impressions are discussed in the trip report. However, there are a few important issues in particular that should be examined.

- Five independent estimates of infiltration (surface modeling by A. Flint, isotopic tracers, fracture coatings, thermal profiles, and core-sample moisture contents and pressures) all point to fluxes on the order of 1 to 10 mm/yr.
- Fault zones are considered highly permeable (1000 Darcy) horizontally, but less so vertically.
- In general, gas bulk permeabilities are on the order of 2 to 10 Darcy.

- Inverse modeling pulls the TSw matrix permeabilities up 1 or 2 orders of magnitude above core information.
- First-cut drift-scale 2D heterogenous-matrix simulations are underway with dripping requiring a transient pulse of 280 mm/yr.
- G. Bodvarsson claims that the ECM and the dual-permeability models must be identical at steady state. *Note: I think this is not correct and may explain the shift in TSw permeabilities he is obtaining.*

Last week, I became PI for the Unsaturated and Saturated Flow under Isothermal Conditions (USFIC) KTI, as I have the most hours allocated and Gordon has relatively few hours. Upcoming duties include a presentation on the USFIC KTI work at the Annual Program Review on November 13, 1996, and on December 5, 1996. The first (45 min + 15 min) presentation is to focus on technical and programmatic aspects, with subtopics including

- Status of subissue(s) resolution
- Integration with other KTIs
- Analysis of infiltration/percolation
- Results of sensitivity analyses
- Work priorities for 1997-98

The second (60 min) presentation is to focus on technical, programmatic, and managerial aspects, with subtopics including

- Infiltration/percolation rates
- Preferred conceptual model for fracture-matrix flow
- Future climate scenario and formation of perched water
- Relationship to total system performance
- Strategy for review of viability analysis

Issues involving infiltration and percolation should be straightforward to discuss. The two technical issues that will be difficult to discuss will be the preferred conceptual model for fracture-matrix flow and the future climate scenario related to the formation of perched water. I take these topics as spurs to perform some quick calculations and have discussions with Ross and others. In particular, testing Bodvarsson's opinion on the steady-state equivalence of the ECM and dual-permeability approaches is in order, as is coming up with a contour plot of areal AAI as a function of precipitation and temperature.

10/16/96 Start of alluvium/bedrock simulations. SAS

The approach that Alan Flint is taking to estimating shallow infiltration, as he has described it to me, essentially fills the alluvium pore space with as much water as will fit and runs off the excess (i.e., infinite alluvium conductivity), then using evapotranspiration to mine water back to the atmosphere. A perched-water system is assumed to exist above the bedrock due to the infiltration events. Water moves into the bedrock assuming gravity drainage within the bedrock. Three classes of fracture sizes, fractions of filled and unfilled fractures, and matrix permeability are combined to yield an equivalent conductivity for the 7 classes. In contrast, I have completely neglected the matrix, filled fractures, and transpiration, and have used highly resolved simulations to capture the dynamics of flow in detail.

I have observed that in simulations with bedrock exposed (i.e., alluvium with permeability less than 10^{-8} cm^2), essentially no infiltration occurs. I have not considered the case of alluvium overlying bedrock, however. I hypothesize that little or no infiltration will occur until several meters of alluvium cover the bedrock. When the alluvium/matrix interface is below the active zone, flow should be essentially steady through the bedrock at the bedrock K_{sat} or the semi-infinite infiltration rate for the alluvium, whichever is smaller. When the active zone interacts with the matrix/bedrock interface, I suspect that the low-permeability bedrock will prevent significant infiltration. As verification of this hypothesis, I am setting up several simulations to probe the behavior of alluvium overlying unfractured bedrock.

The Tiva Canyon tuff microstratigraphy is of primary interest. According to Flint et al. (1996), the shardy base has a mean K_{sat} of 1.6×10^{-6} m/s ($k = 1.6 \times 10^{-9}$ cm^2= 5.0×10^{4} mm/yr), while the remaining Tiva Canyon layers have K_{sat} ranging from 3.1×10^{-9} to 3.0×10^{-12} m/s (k ranges from 3.1×10^{-12} to 3.0×10^{-15} cm^2, or 98 to 0.95 mm/yr). None of these should exhibit bare-soil infiltration if the low-permeability matrix-only results can be extrapolated.

Table 1-4: Summary of colluvium and matrix properties used in simulations.

Material	K_{sat} m/s	ε	θ_r	van Genuchten α MPa^{-1}	m	P_0 ($\times 10^6$) gm cm^{-1}s^{-2}
Colluvium	9.8×10^{-6}	0.300	0.000	50.0[1]	0.200	0.2[2]
Caprock	3.1×10^{-9}	0.105	0.002	5.00	0.301	2.0
Upper lithophysal	8.9×10^{-12}	0.108	0.001	2.90	0.310	3.4
Shardy base	1.6×10^{-6}	0.235	0.035	3.01	0.237	3.3
Fracture	0.011	0.001	0.000	10^5	0.700	9.8×10^{-5}

[1] Correct value is 500 (2/26/97) SAS

[2] Correct value is 0.02 (2/26/97) SAS

To test the hypothesis, the base-case colluvium over three material cases will be examined: (i) shardy base, (ii) caprock, and (iii) upper lithophysal. These cases are representative of the range of k and are of interest in their own right. Samples BT26Hs, PW19s, and TPC52s will be used to determine van Genuchten properties, using the 2-parameter estimates. A summary of properties is shown in Table 1-4, with the colluvium and base-case fracture properties shown for reference. Initially, a 10-cm and a 25-cm depth-of-cover case will be run for each, as representative cases. Further examination may suggest additional cases.

10/19/96 First results for alluvium/bedrock simulations. SAS

Four of the six runs have completed 3 cycles of boundary conditions: both shardy-base cases, the 10-cm caprock case, and the 25-cm upper-lithophysal case. Each of the cases erroneously used colluvium permeabilities 1000 times larger than desired, due to incompletely correcting the viscosity value in the new input-file generation routine **ingen_am.m** in ***$BREATH2/Subreg/-MakekmpoKmao***. The input and output cases are renamed correctly to reflect this error, and **ingen_am.m** was corrected. The matrix properties are correct.

None of the cases are particularly near cyclic steady state, but some conclusions can already be drawn from the first results. The shardy base is permeable enough that significant infiltration can occur, perhaps 10 mm/yr or more. Interestingly, there are indications that deeper cover provides more infiltration for the shardy base, opposite to the alluvium/fracture case. The caprock case shows some indications of infiltration as well, perhaps on the order of 1 mm/yr. The upper

lithophysal case is drying out from the initial condition of 0.25 mm/yr.

Based on this rather limited set of runs, a few conclusions are presenting themselves to me:

- The capillary barrier effect is turned around for the case of matrix underlying alluvium, so that water is preferentially drawn into the matrix.
- The conclusions regarding alluvium cases that allow and disallow infiltration may not be far off for a shallow cover over bedrock.
- There may be some additional infiltration due to cover protection.
- Materials as permeable as the caprock are probably dominated by fracture flow for shallow covers and matrix flow for deeper covers.
- As the permeability increases from the caprock, matrix flow dominates.
- As the permeability decreases from the caprock, fracture flow dominates.

The only microstratigraphic layers more permeable than the caprock, according to Flint et al. (1996), are located in the sequence including the Tiva Canyon shardy base through the nonwelded units of the Yucca Mountain and Pah Canyon Tuffs to above the Topopah Spring upper lithophysal zone. These microstratigraphic layers are essentially the PTn layer addressed in my previous analyses, perhaps a little larger, which only is about 5 percent of the total subregional outcrop area. Accordingly, I expect that the alluvium/fracture results considered before would not be significantly modified for most of the subregional area.

A much more definitive modeling approach can be conceived with some modification to *breath*. The idea is to have multiple interacting continua throughout the bedrock, all with a common pressure in the alluvium. The multiple-continuum approach will allow partitioning between the fractures and matrix to be examined, particularly since separate continua can be defined for various fracture-aperature size classes. The approach is also essential for considering deep-percolation processes.

12/7/96 Updated results for alluvium/bedrock simulations. SAS

A new file was created in ***$BREATH1/RunTightAM*** entitled **am_all.result** to document the results of alluvium/matrix simulations. The file follows a generic standard with many entries not used. The columns of the result file are, in order:

- Depth of soil (cm),
- Alluvium code (see Table 1-3),
- Bedrock code (Table 1-4 for properties),
- Perturbation code

  b0 Base case (precipitation and temperature may vary),

  e0 Longwave radiation is scaled,

  s0 Shortwave radiation is scaled,

  v0 Vapor density is scaled,

  w0 Windspeed is scaled,

  ge Solar aspect is rotated east (perturbation in degrees),

  gw Solar aspect is rotated west (perturbation in degrees),

  gn Solar aspect is rotated north (perturbation in degrees),

  gs Solar aspect is rotated south (perturbation in degrees),
- Perturbation,
- Precipitation multiplier,
- Temperature shift,
- Average soil moisture content at the interface, and
- Average net infiltration (cm/yr).

Most of the values in the file should be viewed as order of magnitude results rather than fully converged, as more cycles are required for full convergence in almost all cases. The runs are primarily useful for screening where fracture flow would dominate. From the runs, it appears that significant matrix infiltration can occur for the Tiva Canyon caprock and shardy units, while fracture flow should dominate in Tiva Canyon upper lithophysal and Topopah Springs lower nonlithophysal units.

The shardy unit is considered part of the PTn, has large infiltration, and is the most permeable unit of any of the microstratigraphic layers considered. The 10-cm case has AAI approximately 24 percent of AAP, while the 25-cm case has AAI approximately 16 percent of AAP. The remainder of the PTn should have smaller AAI. Assuming that the PTn as a whole yields AAI roughly

equivalent to 10 to 20 percent of AAP is probably justified based on these simulations. Note that in the FY96 Annual Progress Report (Bagtzoglou et al., 1996), my assumption was that 10 percent of AAP enters the PTn, and I found that the overall sensitivity to the PTn unit is quite low.

The Tiva Canyon caprock matrix shows behavior unlike any other unit considered, as AAI *increases* with soil depth for the two soil depths considered. Experience from early semi-infinite experiments suggests that essentially no infiltration should occur for exposed materials with this permeability. A cover of soil appears to provide a permeable zone to allow water to penetrate the subsurface while protecting caprock from evaporative processes, and the difference in bubbling pressure between soil and caprock preferentially sucks water into the bedrock. The caprock is laterally extensive over the repository, primarily in regions where my colluvium/fracture models predict high AAI, so revisiting this material with *breath* modified to consider both bedrock and fractures simultaneously would be appropriate. Note that one would expect that the caprock should never have much more than 50 cm of cover.

Today I tried to finalize the table of atmospheric influences on infiltration for a colluvium/fracture system. The table is in ***$BREATH1/RunCliFrac*** and is called **af_egsvw.result**, abstracting the results of simulations run over the period from July through November. The simulations do not consider changes in precipitation or temperature. The columns of the result file are, in order:

- Depth of soil (cm),
- Alluvium code (see Table 1-3),
- Fracture code (see Table 1-3),
- Perturbation code

  b0 Base case (precipitation and temperature do not vary),

  e0 Longwave radiation is scaled,

  s0 Shortwave radiation is scaled,

  v0 Vapor density is scaled,

  w0 Windspeed is scaled,

  ge Solar aspect is rotated east (perturbation in degrees),

  gw Solar aspect is rotated west (perturbation in degrees),

  gn Solar aspect is rotated north (perturbation in degrees),

gs Solar aspect is rotated south (perturbation in degrees),

- Perturbation,
- Average soil moisture content at the interface, and
- Average net infiltration (cm/yr).

The values in the file have reliably reached cyclic steady state.

An important observation was made during the finalization process. The final simulations in the colluvium/fracture set of simulations overlapped the first soil/bedrock simulations. I had previously noticed that there are cases where the combination of soil and underlying material require such small time steps during a large infiltration event that a simulated hour may not complete within the 10000-time-step limit. For the last simulation, I imposed a 50000-time-step limit for each hour; during large infiltration events even this limit might be reached before the hour was up, but more than half of the events exceeding 10000 time steps completed before 50000 time steps were finished. For the case with the larger limit on the number of time steps, larger net infiltration was obtained than would have been expected (5.5 mm/yr rather than roughly 1 mm/yr). The implication is that my estimates of AAI are too low in some (but not all) cases. I suspect that the error is generally additive, on the order of several mm/yr, rather than being a multiplicative error. Unfortunately, it is not possible to untangle which simulations yield underpredictions without rerunning the simulations. I believe that sensitivity predictions may be relatively unaffected, but there is some question regarding the appropriate decay in infiltration with soil depth.

12/8/96 Estimating regression relationships for AAI. SAS

As part of estimating regression relationships between hydraulic properties, climatic variables, and AAI, I fit the data to predicted values using a least-squares fit. Say, for example, that the relationship is

$$\log_{10}\left(\frac{AAI}{AAP}k^{1/2}\right) = \alpha_0 + \alpha_1\left[\left(\frac{m}{m_0}\right)^2 - 1\right] + \alpha_2\left[\left(\frac{P_0}{P}\right)^{1/2} - 1\right] + \alpha_3\left[\left(\frac{\varepsilon}{\varepsilon_0}\right) - 1\right], \tag{1-12}$$

where k is intrinsic permeability, m is van Genuchten $m = 1 - 1/n$, P is bubbling pressure (the reciprocal of van Genuchten α in the units used here), ε is porosity, a subscript 0 represents a reference value for the parameter, and the α values are hydraulic-parameter sensitivity constants.

For any particular simulation, the only unknowns in the relationship are the α values. Thus, for a simulation, one can write the equation as

$$C_0 = \alpha_0 + \alpha_1 C_1 + \alpha_2 C_2 + \alpha_3 C_3, \tag{1-13}$$

where the C values result from evaluating the hydraulic-property functions. Combining all simulations results in the matrix relationships

$$\left[\mathbf{C}_1\ \mathbf{C}_2\ \mathbf{C}_3\right]\{\alpha\} = \{\mathbf{C}_0\}, \tag{1-14}$$

where bold-face represents a vector. When provided with linear equations having a matrix that is not square, *Matlab* solves the equations using least squares (exactly the appropriate behavior). Any reported regressions are coded using *Matlab* to take advantage of this feature.

1/7/97 Documenting plots for ANS-1997 submission.

SAS

Budhi was invited to give an invited talk at the American Nuclear Society (ANS) convention in June, 1997. A summary of the talk is required for the conference, consisting of 450 to 900 words. The summary presents the methodology for creating infiltration maps and sensitivity maps, in an extremely schematic fashion. Included in the summary are two plots, one of my latest base infiltration map and a newly created sensitivity plot for sensitivity of infiltration to soil depth.

The plots were generated with a master *Matlab* driver called **do_sens_eval.m**, which in turn calls a number of other routines. The current versions of required files and concommitant input were stored in a subdirectory of ***$HOME2/Matlab/YMInfil*** entitled ***ANS96***. The directory was stored in a tar file entitled **ANS96_plotgen_tar**, which was in turn compressed using the gzip command (appending ".gz" to the file name).

Sensitivity S_k of areal-average AAI to generic parameter α_k can be calculated using normalized sensitivity coefficients (Sykes et al., 1985)

$$S_k = \frac{\alpha_k}{AAI}\frac{\mathrm{d}AAI}{\mathrm{d}\alpha_k} \tag{1-15}$$

$$S_k = \alpha_k \frac{\mathrm{d}\ln AAI}{\mathrm{d}\alpha_k} \tag{1-16}$$

The sensitivity coefficients are calculated by using first-order derivatives between a high and low perturbation, normalized by a reference value. In general, sensitivity coefficients will change as the set of base input values change. For the example problem, the base-case soil depth was uniformly multiplied by 0.9 and 1.1 to provide perturbations. Values of S_k less than or equal to 0 were

arbitrarily set to 10^{-32} for plotting purposes (the most-negative value was on the order of -10^{-16}). Note that sensitivities are largest on sideslopes and are zero wherever depth does not change infiltration (e.g., deep soil, PTn outcrops under current modeling shortcuts).

1/8/97 Documenting 1996 annual report work.

SAS

An archive file was created in both ***$HOME2/Matlab/YMInfil*** and in ***$HOME2/Matlab/-ColluvWaste*** documenting the input files and limited output files used to generate figure 10-4 and tables 10-1 and 10-2 in chapter 10 of the NRC High-Level Radioactive Waste Program Annual Progress Report, Fiscal Year 1996. Both archive files are called **AnnRep96_tar**; both are compressed. The file in ***$HOME2/Matlab/YMInfil*** includes all of the files from ***$HOME2/Matlab/ColluvWaste***, for completeness, and is submitted to QA as formal documentation of the results. A couple of files were added or fixed up for readability and reproducibility of results. Description of the process is in a ReadMe file in the archive.

1/13/97 Documenting alluvium regression.

SAS

Alluvium depths are not well captured by the equilibrium mass-wasting scheme in areas of deep alluvium, partly due to the irregular topography of the washes. In order to have a reasonable representation for deep alluvium, in August, 1995, Ross Bagtzoglou developed a regression for alluvium depth b as a function of slope s:

$$b = 47\exp(-0.32s). \tag{1-17}$$

The regression was based on borehole information for b and the nearest-neighbor values from the DEM for s. No borehole classification was performed, and ad-hoc data censoring was used for the regression. Due to time constraints, the work was performed very quickly.

I revisited the regression expression last summer, and decided that it is probably better to use an expression of the form

$$\ln(b) = a + b\ln(s). \tag{1-18}$$

I pulled together as much available information on alluvium depths as I could find and sorted it into a file called **neutron_hole.dat** in ***$HOME2/Matlab/3Ddata***. Neutron-borehole data is reported by Flint and Flint (1995); other data sources are noted in **neutron_hole.dat**. I pulled neutron-borehole data from channels and terraces into separate files (**chan.dat**, and **st.dat**, respectively);

other boreholes with reported alluvium depths were pulled into file **well.dat**. A total of 110 boreholes are included in these three classes; an additional 64 boreholes are not considered.

Boreholes with shallow covers (i.e., ridgetops, sideslopes) are not considered further, as I feel that alluvium depths for these boreholes are not reported with sufficient accuracy and are in a range of depth that should be handled by the mass-wasting approach anyway.

For the regression, each of the boreholes was assigned the slope of the nearest-neighbor pixel in the DEM. An additional censoring process eliminated all boreholes with unreported soil depths or having soil depths less than 1 m, leaving a total of 37 boreholes, conveniently grouped as 9 channel boreholes and 28 deep-alluvium boreholes. The data points and regression lines are shown in Figure 1-1, manually generated by regressing all data using **regress_set.m** and further processing with the **show_regress.m** routine. I feel that it is questionable whether the overall regression should use the channel data, as the pixels are larger than the channel width. Even if the channel data is included, the regression line is not tremendously changed. As a note, the correlation coefficient with the original formulation is 0.59 and 0.58 for the channel and terrace, respectively; using the new formulation the correlation coefficient is 0.66 and 0.69, respectively.

1/15/97 Documenting infiltration abstractions.

SAS

In ***$HOME2/Matlab/YMInfil/SubregSpaceDist***, abstractions for AAI as a function of material and meteorologic properties are examined using **find_best_regress.m**. Abstractions for AAI as a function of material properties were originally developed in the summer of 1996. The abstractions were developed "by eye" and are more formally documented here.

The deep-alluvium abstraction originally developed is in the form

$$\log_{10}\left(\frac{AAI}{AAP}k^{1/2}\right) = \alpha_0 + \alpha_1\left[\left(\frac{m}{m_0}\right)^2 - 1\right] + \alpha_2\left[\left(\frac{P_0}{P}\right)^{1/2} - 1\right] + \alpha_3\left[\left(\frac{\varepsilon}{\varepsilon_0}\right) - 1\right], \tag{1-19}$$

where

- k is intrinsic permeability,
- m is van Genuchten $m = 1 - 1/n$,
- P is bubbling pressure (the reciprocal of van Genuchten α in the units used here), and
- ε is porosity.

A subscript 0 represents a reference value for the parameter ($m_0 = 0.2$, $P_0 = 2000$ Pa, and $\varepsilon_0 = 0.3$), and the α values are hydraulic-parameter sensitivity constants. Equation 1-19 was

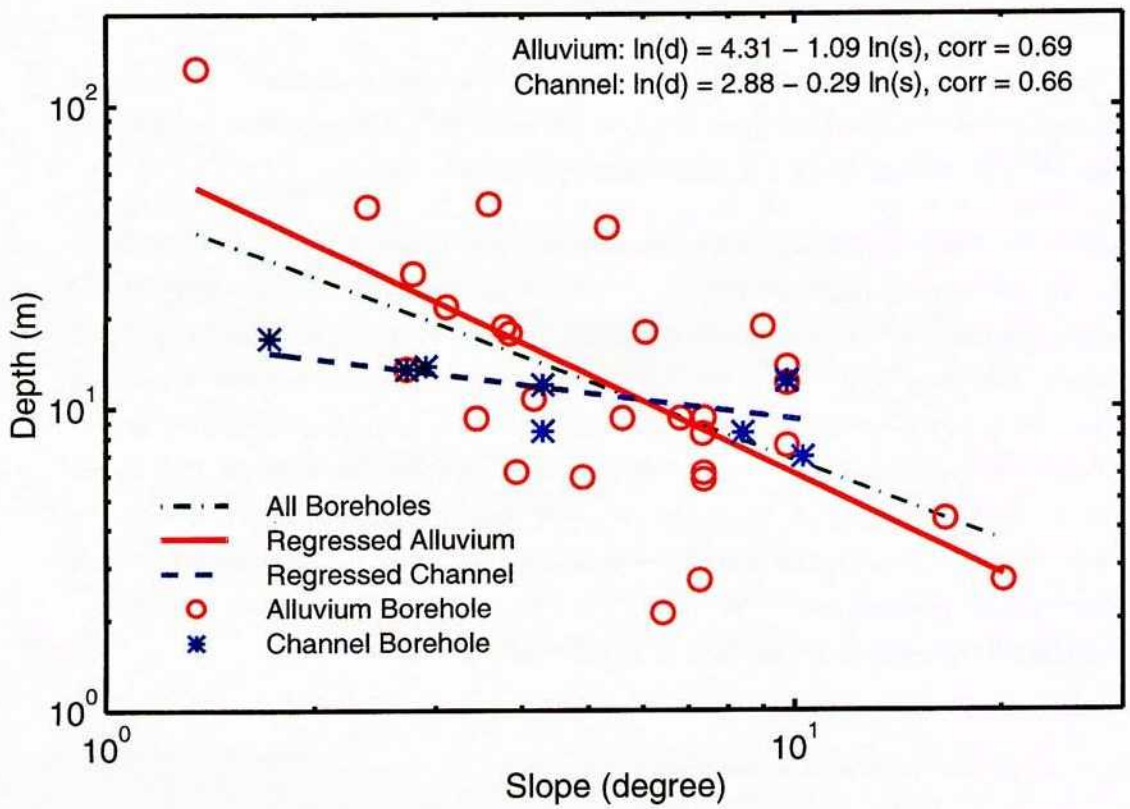

Figure 1-1: 1/13/97. Regression of borehole alluvium depths with nearest-neighbor DEM slopes.

originally reported by Bagtzoglou et al. (1996).

Using **find_best_regress.m** and **f_deep_hyd_fit.m**, a best-fit exponent was determined using the 28 material-property-variation simulations in **alluv.result** that have non-negative infiltration. Also, the impact of assuming a $\log_{10}$ relationship instead of a scaling relationship can be determined. These are performed by flipping switches at the top of **find_best_regress.m**.

Using the more formal abstraction process, a better regression is

$$\log_{10}\left[\frac{AAI}{AAP}\left(\frac{k}{k_0}\right)^{1/2}\right] = \alpha_0 + \alpha_1\left[\left(\frac{m}{m_0}\right)^{\beta_1} - 1\right] + \alpha_2\left[\left(\frac{P}{P_0}\right)^{\beta_2} - 1\right] + \alpha_3\left[\left(\frac{\varepsilon}{\varepsilon_0}\right)^{\beta_3} - 1\right], \tag{1-20}$$

where k_0 is 10^{-8} cm^2 and the β values are fitting exponents. A plot of the least-squares fit for the exponents is shown in Figure 1-2, where the fit for each curve only uses simulations with the parameter varying. Note that there is more noise in the value for P than in the other parameters.

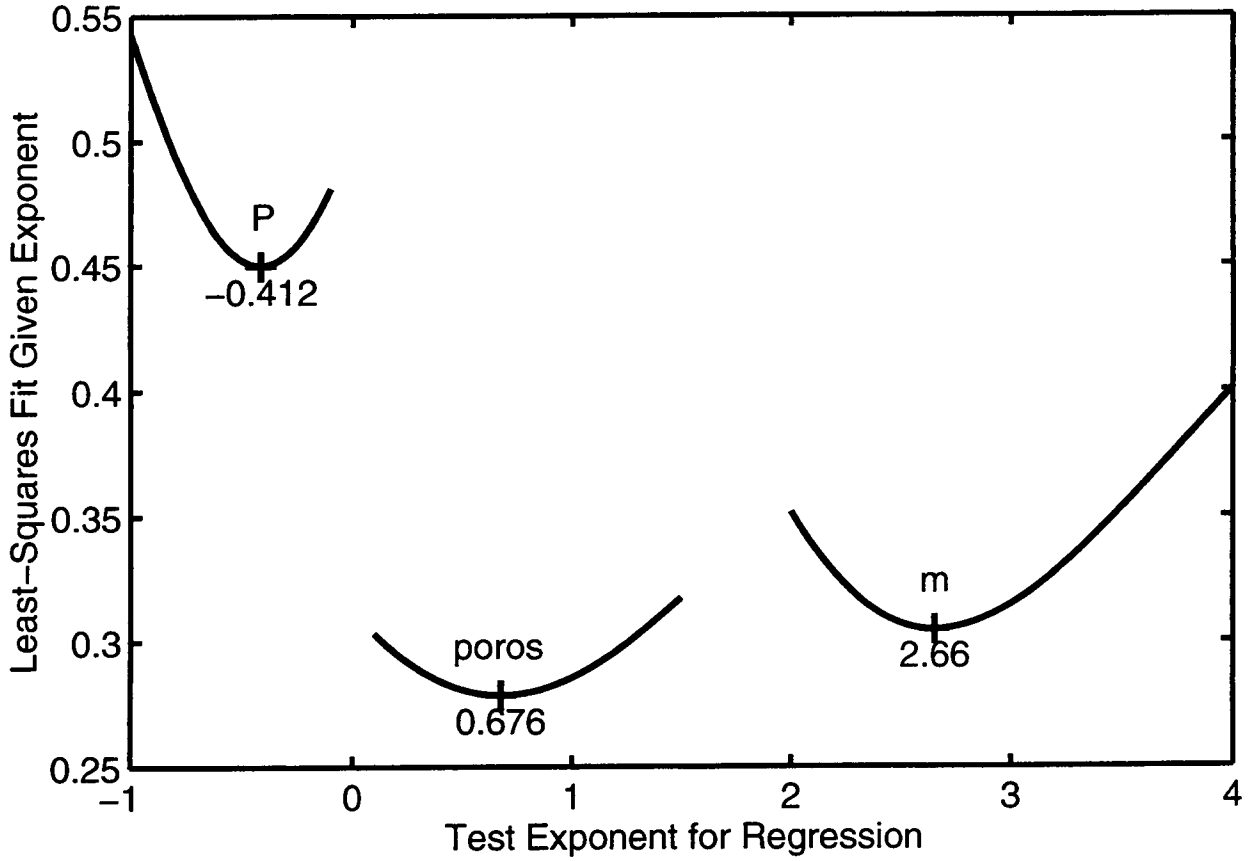

Figure 1-2: 1/15/97. Least-squares fit of simulation prediction to abstraction prediction for various exponents in Equation 1-20.

The best-fit coefficients are shown in Table 1-5. The least-squares fit is also shown for the counterpart of the formal abstraction equation using logarithms,

$$\log_{10}\left[\frac{AAI}{AAP}\left(\frac{k}{k_0}\right)^{1/2}\right] = \alpha_0 + \alpha_1 \log_{10}\left(\frac{m}{m_0}\right) + \alpha_2 \log_{10}\left(\frac{P}{P_0}\right) + \alpha_3 \log_{10}\left(\frac{\varepsilon}{\varepsilon_0}\right). \tag{1-21}$$

The best scaling fit is better than the logarithm fit for each parameter. If the logarithm of k is examined, however, the associated α coefficient is -0.495 and associated logarithm fit is 0.258, strongly supporting pulling k into the left-hand side as is done in Equation 1-20.

Table 1-5: Best-fit abstractions to material properties in deep alluvium.

Parameter	α	β	Fit	Log Fit
Scaling Constant	-1.38165	—	0.587745	1.09475
van Genuchten m	0.42505	2.6576	0.304383	0.821475
P	2.05672	-0.41248	0.449886	0.50599
ε	-1.39944	0.67568	0.278631	0.633175

1/20/97 Documenting infiltration abstractions. SAS

In ***$HOME2/Matlab/YMInfil/SubregSpaceDist***, abstractions for AAI as a function of material and meteorologic properties are examined using **find_best_regress.m**. Abstractions for AAI as a function of material properties were originally developed in the summer of 1996. The abstractions were developed "by eye" and are more formally documented here.

A routine called **f_deep_met_fit.m** was developed to check out the appropriateness of abstractions in the form of a scaling or a logarithmic representation, identical to the approach followed for material properties. Some trial-and-error runs were followed to pick reasonable base values for exponents, varying one parameter at a time. The value of the sought exponent was observed to shift about, depending on the values of the remaining exponents. Accordingly, the *Matlab* routine **fmins** was used to perform a global minimization for all meteorologic-variable exponents simultaneously. A modified version of **f_deep_met_fit.m** entitled **f_deep_met_reg.m** was created to follow the format required by **fmins**.

Two sets of regression results are presented in Table 1-6, for simultaneously determined exponents and for logarithmic regression, labelled Scale Fit and Log Fit, respectively. Each reported fit only uses simulations where the variable of interest is perturbed (including the base value of the variable). The column entitled Curvature represents the second derivative of the scale fit with respect to the variable, and is a measure of sensitivity; the larger the value of curvature, the better the exponent is determined. The logarithmic fit does not admit this measure. The best fit is to AAP; the worst fit is to AAT. The exponent for AAL, AAV, and AAW is roughly within a value of ± 1; the exponent for AAP is better determined and the exponent for AAT is much more poorly determined.

Based on comparing the fits reported in Table 1-6, it can be concluded that a logarithmic representation should be used for AAL and AAW and a scaled representation should be used for the remaining variables. The best-fit coefficients for this representation are shown in Table 1-

Table 1-6: Regression values for deep-alluvium meteorologic abstraction.

Parameter	Exponent	Scale Fit	Curvature	Log Fit
AAL	-0.03723	0.308036	0.0284408	0.289575
AAP	-0.2889	0.419721	0.486325	0.440836
AAT	-15.96	0.648594	0.000370696	0.700391
AAV	2.075	0.323644	0.0174236	0.357603
AAW	0.2412	0.304608	0.0112994	0.28684

Table 1-7: Regression coefficients for deep-alluvium meteorologic abstraction. *Correction dated 1/23/97: Two curvature numbers were incorrectly transcribed. Correct numbers are italicized in the table.* SAS

Parameter	Exponent	Coefficient	Fit	Curvature
AAL	—	-1.52051	0.312029	—
AAP	-0.2416	-5.56806	0.420087	0.4858
AAT	-16.67	0.945489	0.649914	0.700391 *0.000366185*
AAV	2.138	0.281891	0.326738	0.357603 *0.0171413*
AAW	—	-0.321916	0.307231	—

7. The parameters without a reported value for exponent are represented using a logarithmic representation.

1/22/97 Documentation of USGS data acquisition.

SAS

I set up ***$HOME2/AmbientKTI/3Ddata*** as an archive for site-specific data acquired from or reported by DOE or subcontractors, such as core-sample data. Today A. Ramos typed in the moisture-retention data from Appendix II of Flint et al. (1996). He double-checked his typing and I confirmed each number. I noticed that the original report is missing a number for sample TPC27s and for sample TPC15s. The original wordperfect file is called **usgs_ofr95-280_app2.wp** and an ASCII version is called **usgs_ofr95-280_app2.asc**. File **Sources** in the same directory documents this procedure.

Sources also documents previously obtained data residing in the same directory. The complete neutron-probe data discussed by Flint and Flint (1995) was obtained from the DOE office in September, 1996. Table 4 from Rautman et al. (1995) was obtained from C. Rautman on

November 6, 1996, using email. Tables I-1 through I-8 from Flint et al. (1996) were obtained directly from L. Flint on November 4, 1996, also by email.

1/24/97 Deep-alluvium meteorology regressions. SAS

I have noticed an increasing sensitivity of AAI to meteorologic properties as AAI decreases. Work to date has used the deep-alluvium regression equation the form

$$\log_{10}(H) = \alpha_0 + \sum_i \alpha_i U_i, \tag{1-22}$$

where $H = (AAI/AAP)U_k$, U_i represents a normalized value for parameter i, and the α values are constants. Two forms of U_i are considered, (i) the scaling fit (e.g., $U_{AAV} = [(AAV/AAV_0)^\beta - 1]$), and (ii) the logarithmic fit (e.g., $U_{AAL} = \log_{10}(AAL/AAL_0)$). Note that both forms are zero for the base case of the parameter. Results for the two forms are discussed in the entry for 1/20/97, in which it was determined that AAL and AAW are probably better fit using the logarithmic form and AAP, AAT, and AAV are probably better fit using the scaling form.

In order to account for this sensitivity, I postulate that the deep-alluvium regression equation for meteorologic properties is in the form

$$\log_{10}(H) = \alpha_0 + \sum_i \alpha_i U_i + [a_0 + a_1 \log_{10}(H)] \sum_j \alpha_j U_j \tag{1-23}$$

$$= \frac{\alpha_0 + \sum_i \alpha_i U_i + a_0 \sum_j \alpha_j U_j}{(1 - a_1) \sum_j \alpha_j U_j}, \tag{1-24}$$

where index i represents a parameter that is insensitive to H and index j represents a parameter that is sensitive to H. Note that a_0 is arbitrarily set to 1 if there are no parameters considered insensitive to H. Again using *Matlab* routine fmins, I created a file to evaluate the least-squares fit of the simulation data to the regression equation with **f_deep_met_eval.m**. Although thousands of iterations are required to reach convergence, the new formulation significantly improves the data fit. For example, overall least-square-fits from 1/20/97 for simultaneous fits of AAP, AAT, and AAV are about 1.5 times larger than the new formulation provides. The form in Equation 1-24 is more general than a similar equation that uses $[a_0 + a_1 U_(k)]$ as the scale, although the latter form should work as well.

Hint for the future: the solution procedure appears to really benefit from periodic restarts. Perhaps the solution steps get too small and the restart enlarges them.

2/14/97 Daily-averaged meteorology. SAS

Insofar as A. Flint typically uses daily meteorologic values when simulating infiltration, and I have been using hourly values in the vicinity of rainfall events and monthly values otherwise, and as daily simulations run faster than hourly simulations, I'm starting a few test cases to check on whether it actually makes a significant difference. I had looked at this years ago and found that averaging makes a relatively small difference, most important near precipitation events, and precipitation is the most important variable to capture. The simulations used 2-cm grids rather than the 1-mm grids I currently am using, so perhaps the conclusion may be altered.

Met files are generated in ***$HOME2/AuxRain/Climate***. A meteorology file with daily inputs averaged from the Desert Rock data, **dr_0d0d_24as.met**, was generated using **make_ave_metseq('dr_0d0d_24as.met', 24)**. The met file was created by averaging all fair-day met values in a window of 30 days around each day, then overwriting the days with precipitation with the original, unaveraged, values for those days. It is possible to change the size of the window for averaging and the window for not averaging by changing hard-coded numbers in the call to **move_metave.m**.

The met file was copied to ***$SubRegBreath/RunTightAM*** and a sequence of simulations was started with 50 cm of alluvium over porous bedrock. These simulations took on the order of 3 days with hourly values.

2/27/97 Daily-averaged meteorology results and calcite. SAS

Directory ***$SubRegBreath/RunTightAM/ResultDir*** holds the results of ten simulations of daily meteorology compared to hourly meteorology. The simulations are designated by **_ds** following both **reg07** and **reg08**. These designators represent bedrock cases 1 and 2, respectively, derived from regressed relationships by Flint et al. (1996). The comparable cases with hourly meteorology are missing the **_ds** designator.

The *Matlab* routine **make_DH_Plot** was created to plot the results as shown in Figure 1-3. The plots show convergence over repeated input cycles to a constant value of decadal-average flux with depth; complete convergence occurs when the decadal-average flux is constant over all depths. Perturbations from the base meteorology are labeled $2/3P$, $3/2P$, $T+5$, and $T-5$, for multipliers in precipitation (P) and shifts of temperature (T) uniformly applied to all values.

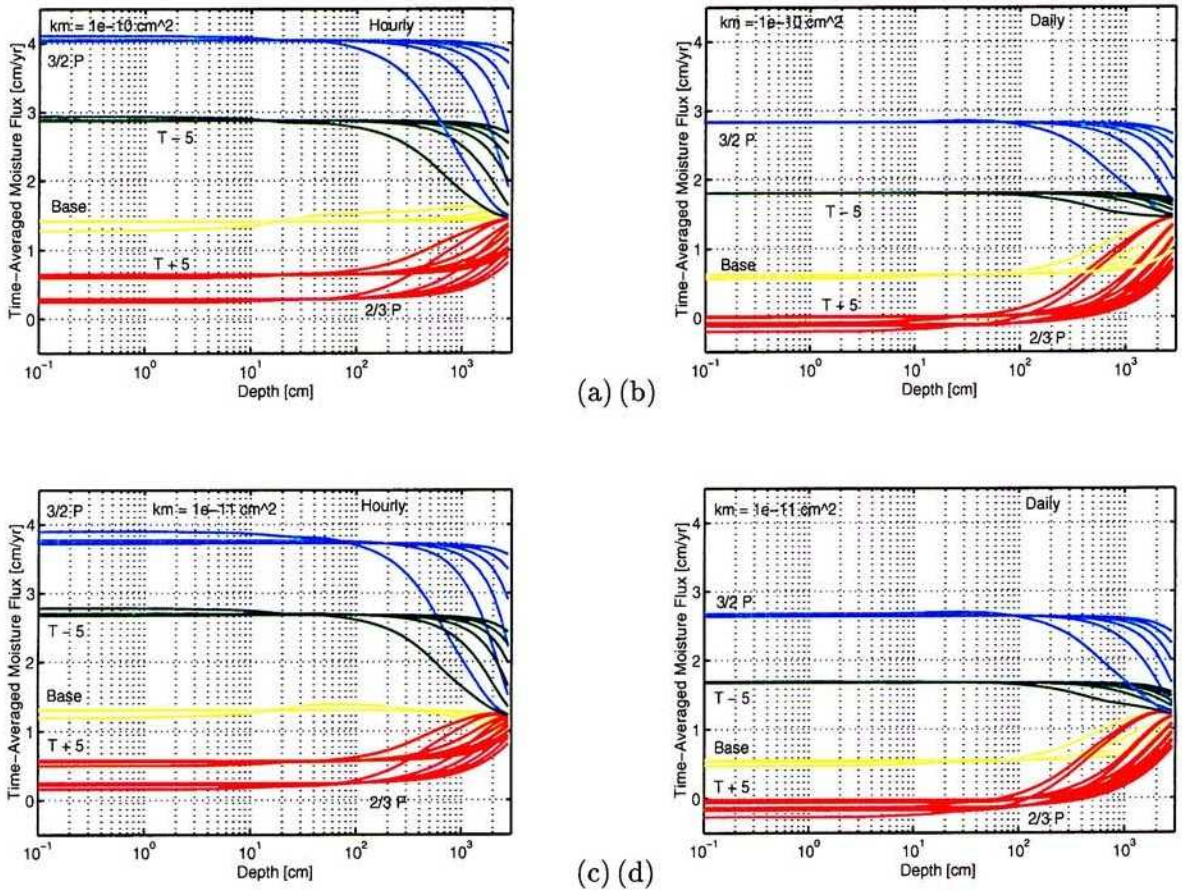

Figure 1-3: 2/27/97. Time history of decadal-average moisture flux after each of 6 decades, as a function of AAP and AAT, for (a) hourly meteorologic input and bedrock 1, (b) daily meteorologic input and bedrock 1, (c) hourly meteorologic input and bedrock 2, and (d) daily meteorologic input and bedrock 2.

Two items are of particular interest in Figure 1-3. First, although the two bedrocks have permeabilities different by an order of magnitude, AAI remains essentially unchanged. More importantly, there is significant difference between the hourly and daily meteorologic inputs, with the hourly values yielding significantly higher infiltration. With the current procedure for handling evaporation, I conclude that the simulator cannot be trusted to yield reliable results with daily inputs.

I have thus far examined the behavior of deep soil, soil overlying open fractures, and soil overlying bedrock. The one related case that remains to be investigated is the behavior of soil

overlying fractures filled with calcite. It is reported by Flint et al. (1996) that measured values for saturated hydraulic conductivity on fracture-fill materials averages 43.2 mm/day (5×10^{-7} m/s or approximately 5×10^{-10} cm^2). No van Genuchten properties are reported. The fracture-filling permeability is almost as large as the most permeable bedrock. After consulting with Gordon Wittmeyer, it is probably not unreasonable to have fracture fillings with $\varepsilon = 0.1$, van Genuchten $\alpha = 100$ MPa^{-1}, and van Genuchten $n = 2$ (van Genuchten $m = 0.5$).

In ***$SubRegBreath/RunTightAM***, I am setting off a set of simulations assuming that the matrix is impermeable, fracture pore space is representative of the fracture classes in TCw as reported by Flint et al. (1996), and the fracture-filling properties are as above. The three classes have reported fracture pore volume of 2.6×10^{-5}, 2.6×10^{-4}, and 2.6×10^{-3}, for 2.5 μm, 25 μm, and 250 μm fractures, respectively. Since porosity must also account for fracture pore space, filling porosity will be 2.6×10^{-4} (rounded to 10^{-4}). Precasting behavior suggests that infiltration will increase with increasing soil depth (to the order of 1 m), due to the capillary attraction that calcite has relative to soil, but infiltration should be relatively small due to the rather small net porosity. Files with **cal3**, **cal4**, and **cal5** for fracture properties represent fracture pore volumes of 10^{-3}, 10^{-4}, and 10^{-5}, respectively.

In conversations with L. Flint (USGS) today, she clarified the weighting schemes that were used by Flint et al. (1996) assign the values of 0.09, 0.055, 0.005, 0.025, 0.8, and 0.025 as the weights for open 2.5 μm, open 25 μm, open 250 μm, filled 2.5 μm, filled 25 μm, and filled 250 μm fractures, respectively. She also will send me data packets with the full set measured values, Without having the data in front of her, Lorrie independently used the thinking that Gordon used to suggest how the filling properties would be different from matrix properties.

3/1/97 Preliminary calcite simulations. SAS

Three simulations have completed, each with 10 cm of soil over fillings with total porosity of 10^{-4}, 10^{-5}, and 10^{-6}, respectively. Interestingly, the three porosity cases do not appear to yield total infiltrations that are significantly different. The fractures respond very quickly, due to the small pore volume and high permeability, so it is adequate to use 2 decades for simulations. Partial results for deeper soils show decreases in infiltration with depth, similar to open fractures. A sequence of simulations for **cal3** and **cal4** were fired with the standard set of climate variations (AAP and AAT). A similar set of simulations, varying filling properties, will be run subsequently.

An error was found in the UZFLOW module converting meters to feet. The error came

directly from the *Matlab* routine that calculates AAP, AAT, and AAT on each pixel of a DEM. Accordingly, all previous reported predictions for AAI are slightly incorrect, and should be slightly increased. Over the range of Yucca Mountain elevations (1100 to 1500 m), corrected values of AAP are 8 to 13 mm/yr larger, AAT are 0.65 to 0.9 °C cooler, and AAT are 1.2×10^{-7} to 1.4×10^{-7} drier.

3/23/97 Data from DOE. SAS

A CD-ROM disk was received from L. Flint about two weeks ago that contains the entire set of matrix-property core-sample measurements from 31 boreholes, including 23 neutron-probe boreholes and 8 deeper boreholes. A total of nearly 5000 samples have properties reported. The CD-ROM disk is entitled "Matrix Properties" and is dated 3/2/97. The CD-ROM disk has one file, entitled **database.wk4**, which is a file in Lotus 1-2-3 version 4.0 format. The CNWRA does not have software current enough to be capable of reading this format; however, the Net Force contractors to the CNWRA were able to convert the file to Lotus 1-2-3 version 3.0 format, which is capable of being read. E. Pearcy was able to pull this into Excel and output it in tab-delimited ASCII form. I stored both the Lotus 1-2-3 version 3.0 file, entitled **database.wk4**, and the tab-delimited ASCII form, entitled **usgs_borehole_db.asc**, in ***$HOME2/AmbientKTI/3Ddata***. The original CD-ROM will be delivered to B. Mabrito and stored in the QA vault.

A second set of data was obtained from the NRC, which consists of a 8-mm tape that copies a CD-ROM with numerous ARC-VIEW coverages stored as 99 themes. The themes range from base-map information (e.g., Nellis Air Force Range boundaries, roads) through contour maps, borehole locations, ecological study plots, a digitized version of the Scott and Bonk stratigraphy, and various other information. The files take up roughly 31 Mb. The original CD-ROM resides at the NRC offices. The CD-ROM was accompanied by a user's guide dated May 1, 1996, with 18 pages plus 3 appendices. I am maintaining the tape in my office until the information can be transferred to disk in an accessible location.

4/10/97 Trip report for Yucca Mountain fieldwork. SAS

The remainder of this entry is adapted from the trip report for a two-day trip to Yucca Mountain to perform characterization field work. Field documentation for the trip is in CNWRA notebooks 175 (soils and vegetation) and 217 (Solitario Canyon measurements).

Persons Present

The trip to Yucca Mountain (YM), on March 26 28, 1997 was undertaken by S. Stothoff and J. Winterle (CNWRA), D. Groeneveld and J. Thompson (Natural Resources, Inc.), and D. Or (Utah State University).

Background and Purpose of Trip

CNWRA is working with D. Groeneveld, D. Or, and J. Thompson to aid in characterizing the impact of vegetation upon shallow infiltration. Transpiration is a process included in DOE models but not considered in CNWRA modeling efforts to date. The intent of the CNWRA work is to incorporate vegetation into infiltration-modeling efforts in a plausible and defensible manner, with appropriate modeling of soil-moisture uptake by plants of particular interest. The trip was inspired by the need for field-checking hypothesized relationships between vegetation and bedrock type, soil cover, slope, and solar loading. In a parallel effort, watershed-scale modeling is being performed by D. Woolhiser. Soil permeability in the wash channels is one of the critical parameters in the watershed-scale model. J. Winterle accompanied the group to obtain soil permeabilities in Solitario Canyon channels, which will be used in the watershed-scale model.

Summary of Activities

The field work was split into three activities: (i) a spot-check vegetation survey verifying the more-detailed TRW vegetation work and examining factors governing the distribution of individual species (D. Groeneveld and J. Thompson); (ii) a spot-check of soil-permeability measurements to verify more-detailed United States Geological Survey (USGS) work, as well as examination of plant rooting distributions (D. Or and S. Stothoff); and (iii) channel permeability measurements in Solitario Canyon (J. Winterle). The vegetation survey was conducted over four days while the remaining work was performed over two days. Prior to the main trip, D. Groeneveld flew a photographic airborne survey of plant distributions, augmenting a collection of coarser-scale photographs taken previously by EG&G.

Overall Impressions

The trip was extremely useful in orienting Or to the YM site and to identifying and refining hypotheses regarding the spatial distribution of plants and plant uptake patterns. Soil measurements taken during field activities will provide direct input into modeling activities. The trip was also useful in planning future activities with Groeneveld and Or.

Interpretations Based on Field Observations

Prior to the field excursion, aerial photographs were examined and it was noticed that linear vegetation features could be identified, particularly along Yucca Crest. As a working hypothesis, it was felt that these linear features represent fissures in the bedrock that the plants were able to take advantage of for water uptake. To verify this hypothesis, several pits were dug adjacent to flourishing plants. Two pits were dug along an apparent linear feature in the Tiva Canyon caprock. Bedrock was reached at a depth of approximately 30 to 40 cm under the plants and in both pits a fissure of approximately 5 to 15 cm was identified, aligned with the vegetation feature, that was densely populated with roots. In one of the pits, a carbonate layer was identified within the fissure at a depth of roughly 5 cm below soil/bedrock contact; in the other, no distinct carbonate layer was identified to a depth of about 20 to 30 cm but there did appear to be increasing carbonate concentrations in the soil with depth.

Plant roots were exposed at three additional sites with shallower soil. At one site, in caprock, both plants exposed had roots predominantly within fissures or extending to fissures. At the second site, in caprock, the plant selected was in the center of a pocket of soil several meters across, with bedrock cropping out on three sides and a soil depth of at least 30 to 40 cm directly under the plant. Although a fissure existed, the plant did not appear to take special advantage of the fissure but appeared to take advantage of runoff from the surrounding bedrock. Nearby plants in fissures between bedrock outcrops appeared more verdant. At the third site, on a side slope in the upper lithophysal unit of the Tiva Canyon formation, the plants were rooted in rubble with 30 cm of cover. For these locations, typical of ridgetops and side slopes, the use of unrestricted rooting systems reported in the literature is precluded due to the strong influence of bedrock.

In all locations examined, the soil cover was sandy loam to loam with bedrock fragments, and was rather permeable. The fine portion of the soil appears to be eolian in nature wherever it was examined. Although permeabilities and soil depths were only determined at a few locations,

soil samples were collected at scattered locations (including each vegetation transect). Roughly two dozen soil samples were obtained. The similarity of the samples suggests that it would be reasonable to assume that soils are reasonably similar over the entire mountainside (except perhaps in areas with sorting due to overland flow such as washes and wash channels), consistent with Flint et al. (1996).

Four ponded-head permeameter measurements were made at three sites with relatively shallow slopes along Yucca Crest and Highway Ridge. Measured saturated conductivity values ranged from 1.2×10^{-3} to 4.9×10^{-3} cm/s. The smallest reading occurred at a site where a large rock was subsequently found to lie directly under the disk; the next-largest reading was 2.9×10^{-3} cm/s. For comparison, Flint et al. (1996) reported soil conductivities in the YM area of 5.6×10^{-4} to 3.8×10^{-3} cm/s based on soil-texture analysis. Three tension-head measurements (two readings with different suctions at one site, one reading at another site) were also obtained, indicating consistent values. The measured values are remarkably similar.

Rock particles found in the soil ranged from small pebbles through cobble-sized blocks. In the pits and in trenches with bedrock exposed, the bedrock was considerably more irregular than the soil surface implying that vegetation may be preferentially located in locally deeper pockets of soil where water can be stored for longer periods after precipitation.

The welded Tiva Canyon units do not exhibit gullying along the side slopes of the washes over the proposed repository footprint, suggesting that erosional processes are not dominated by overland flow. The high permeability of the shallow soils and the dense carbonates existing in fractures exposed by trenches in the TCw units below the caprock further suggest that lateral flow is likely to be primarily along the soil/bedrock interface rather than as overland flow. The distribution of vegetation suggests that lateral flow may be significant; vegetation is relatively sparse at the top of slopes and relatively dense at points where slopes flatten. Note that the existence of subsurface lateral flow is also suggested by neutron-probe measurements.

Based on topography, soil depth, and bedrock materials, the ground surface over the repository footprint can be divided into four categories:

Tiva Canyon caprock on ridgetops. Slopes are generally moderate (less than 10 degrees) with shallow soils (0 to 40 cm with pockets greater than 60 cm). The bedrock is generally massive with fissures spaced sufficiently far apart in places to provide significant organization to vegetation. The fissures are typically 5 to 15 cm in aperture, and appear to form by eolian soils filling between boulders. Bedrock is irregular in topography, with at least 40 cm variation

possible within the space of 2 m. The bedrock is sufficiently permeable that moisture may interact significantly with it over periods of days to weeks. Soil fills the fissures to a depth of at least 5 to 30 cm, with carbonate fillings possible. Roots are common, almost ubiquitous, within fractures. Net infiltration may be quite significant due to shallow soils. Several vegetation transects were taken in this environment, 4 soil-permeability and 2 bedrock-permeability measurements were made, and 5 bedrock-exposure pits were dug.

Tiva Canyon welded units (i.e., lithophysal units) below the caprock. Slopes are generally moderate to steep (10 to 45 degrees). Scree exists where slopes are greater than roughly 40 degrees. Bedrock is irregular in topography, although perhaps less so than for the caprock. There is some evidence of stairstepping in the bedrock surface that is not echoed in the soil profile, which may provide localized pockets for vegetation. Fractures are typically narrow in aperture (less than 1 cm) but closely spaced. The fractures appear to be filled with carbonates as a rule, and generally not penetrated by roots except for perhaps a few localized zones with wider apertures. Vegetation is predominantly Great Basin on the north-facing slopes and Mojavian on the south-facing slopes, with vegetation densities about twice as large on the north-facing slopes. Vegetation increases in density downslope. Net infiltration may be significant due to shallow soils. Lateral redistribution along the soil/bedrock interface may also be significant. Several vegetation transects were taken in this environment, a pair of soil-permeability measurements were taken, and several trenches and pavements were examined in detail.

Alluvium-filled washes. Slopes are shallow and soils tend to be greater than 1 m in depth. Net infiltration may not be significant, due to the large storage capacity of the soils and the presence of vegetation. This environment was not examined in detail, aside from one or two vegetation transects.

The west face of Yucca Crest. Slopes are quite steep, as much as 50 degrees. Numerous strata are exposed, ranging from densely welded to nonwelded. Soil pockets exist of as much as 50 cm even in the steepest slopes. Vegetation is dominated by crack-dwelling species. Overland flow should be significant, as evidenced by gully formation. Of the four environments this environment is by far the most complex to model however, relatively little of the repository footprint is overlain by this category. The environment was not examined in detail, aside from daily hikes up and down to Yucca Crest.

Hydraulic Conductivity Measurements in Solitario Canyon

J. Winterle obtained 13 hydraulic conductivity measurements for the stream beds in Solitario Canyon and its side canyons. These measurements were obtained using a Guelph Permeameter which is used by augering a hole 20 to 40 cm deep into the sediments and measuring infiltration of water out of the bottom of this hole while a constant water level is maintained in the hole. There were problems with this technique involving difficulty in augering holes due to the presence of large cobbles, and a tendency for the holes to collapse due to the lack of cohesiveness of the sediments. Nevertheless, 13 measurements were obtained with hydraulic conductivities on the order of 10^{-3} to 10^{-1} cm/s. These values are consistent with published values for silty sands and gravels. It should be noted that 10^{-2} cm/s is the upper limit of the range of hydraulic conductivities for which the Guelph permeameter is designed, thus the values outside of this range may not be as accurate as the lower values; however, they do represent a good order-of-magnitude estimate. Samples of sediments were obtained from the auger holes and their hydraulic conductivities are currently being measured in the laboratory. Locations of each of the conductivity measurements was recorded using a GPS unit. The GPS measurements are accurate to the nearest 100 m. Table 1-8 summarizes the data collected.

Problems Encountered

The real-time differential GPS did not function properly, almost certainly due to operator error. Reported measurements are therefore only accurate to within 100 m.

4/27/97 Conversion of neutron-probe data to matlab format.

SAS

The complete set of neutron-probe readings from the 98 neutron-probe boreholes plus UZ-7 (described by Flint and Flint (1995)), obtained September, 1996, from the DOE office, were converted to *Matlab* format. An awk script (**reduce_neut.awk**) converted the ASCII file to a reduced format, and a *Matlab* script converted it to a binary format for fast reads. Two additional *Matlab* scripts were created to examine the plots as a time history, **plot_neut.m** and **plot_neut_set.m**. Borehole UZ-7 is designated as neutron-probe borehole number 99. The scripts are stored in ***$HOME2/AmbientKTI/3Ddata***.

The awk conversion uses the csh sequence "`zcat neutron_* | nawk -f reduce_neut.awk`

Table 1-8: Hydraulic conductivity measurements in Solitario Canyon on March 27 and 28, 1997.

Sample #	UTM (m) N	UTM (m) E	Hydraulic Conductivity (cm/s)	Notes
1	546637	4077467	0.04	silty coarse gravels; many large cobbles
2	546517	4077632	0.02	coarse gravel with fine silty sand
3	546794	4077389	0.07	sandy coarse gravel
4	546826	4077651	0.05	well-sorted, pea-sized gravel
5	546772	4077250	0.002	silty, sandy gravel; large cobbles
6	546667	4077103	0.007	silty, sandy gravel; a few large cobbles
7	546612	4076972	0.002	silty coarse gravel
8	546593	4076710	0.012	sandy gravel; a few large cobbles
9	546597	4076410	0.02	sandy gravel
10	547186	4079275	0.1	coarse sand and gravel
11	547135	4078848	0.04	well-sorted pea-gravel with coarse sand
12	547121	4078681	0.01	well-sorted pea-gravel with coarse sand
13	547021	4078283	0.002	silty overbank sediments stream channel well-sorted pea-gravel

> `neut.date_num_dep_mc`".

There appears to have been some adjustment of elevations in late 1985, judging from offsets in all boreholes with records that early.

5/9/97 Documentation of upper-bound infiltration estimates. SAS

If the temperature and thermal conductivity profiles of a rock mass are known, one can calculate the energy flux due to conduction. If the actual energy flux through the rock mass differs from the conductive flux, it must be due to advection (i.e., energy transported through liquid or vapor fluxes). When a vertical column has smaller conductive fluxes than actual fluxes, it may be due to cool infiltrating water warming while moving to depth or upward vapor transport with an associated large latent-heat transport. In order to estimate infiltration fluxes when moisture movement is predominantly vertical, one can use an analytic solution or a numerical simulator accounting for both conductive and advective fluxes, and adjust the infiltration flux until the measured temperature profile is obtained. Lachenbruch and Sass (1977) presented a relationship that indicates that the reduction in apparent heat flux is roughly proportional to the volume of infiltrating water, the

thermal gradient, and the distance considered. Typically it is assumed that vapor flux is negligible, although this assumption is not necessary if the vapor flux can be accounted for. Implicit in the approach is the assumption that the liquid and rock remain in thermal equilibrium.

One of the advantages of the method is the lack of necessity for knowing details of how the liquid moves within the rock. On the other hand, it is necessary to have an independent estimate for the thermal flux, which can be difficult to obtain. It is also necessary to know thermal conductivities, but these are typically quite well constrained.

Estimates of thermal and liquid fluxes throughout the NTS are presented by Sass et al. (1980) and Sass and Lachenbruch (1982), with the results summarized by Sass et al. (1988). Sass et al. (1988) analyzed a set of boreholes in the Yucca Mountain area, with resulting estimates of conductive and total heat fluxes from the saturated zone (SZ) into the unsaturated zone (UZ) of 40±9 and 49±8 mW/m^2, respectively, with an average heat flux in the UZ of about 41 mW/m^2. Sass et al. (1988) contour conductive heat fluxes in the Yucca Mountain area (Figure 15 by Sass et al., 1988), which indicates that conductive fluxes are 70 to 74 mW/m^2 southeast through southwest of Yucca Mountain; roughly 60 mW/m^2 in the southwest part of Midway Valley; roughly 50 mW/m^2 in and near Fortymile Wash, Dune Wash, Yucca Wash, and Solitario Canyon; and roughly 30 to 40 mW/m^2 over the repository footprint and north past Drillhole Wash. Sass et al. (1988) suggest that there may be an apparent reduction of heat flow from the SZ to the UZ of 5 to 10 mW/m^2, and calculate that this apparent reduction of heat flow could be achieved by 2 to 5 mm/yr net infiltration and about 8 mW/m^2 reduction would be achieved if 0.1 mm/yr of water were vaporized. Lateral flow in the shallow SZ is also considered a possible source of local anomalies. Sass et al. (1988) also note (without further comment) that apparent heat flux is negatively correlated with elevation; one might infer that lateral diversion to lower topographic areas may be occurring, although the study by Rousseau et al. (1996), discussed below, would suggest the opposite due to the insulating properties of alluvium.

An implication of the analysis by Sass et al. (1988) is that, at least locally over the repository block and Drillhole Wash, deficits in the apparent heat flux that occur in the UZ may be as much as 20 mW/m^2[assuming that 10 mW/m^2 is roughly equivalent to 5 mm/yr infiltration, as calculated by Sass et al. (1988)], so that locally about 10 mm/yr infiltration might be estimated. When estimating infiltration, it may be better to estimate the vertical heat flux from boreholes that are unlikely to have significant infiltration. Infiltration fluxes in deep alluvium and not close to channels are likely to be quite small, so that the boreholes in Midway Valley and south of Yucca Mountain in deep alluvium may be more representative of regional vertical heat flux. If so, vertical heat flux could be as much as 60 to 75 mW/m^2 and local deficits at Yucca Mountain could be as much

as 45 mW/m^2, implying that locally more than 20 mm/yr infiltration could be inferred from the thermal data. Assuming that the UZ heat flux is 60 mW/m^2, heat-flux deficits on the order of 15 to 30 mW/m^{2}in the area of the repository block and Drillhole Wash could be justified, implying that local infiltration rates may be 7 through 15 mm/yr in this area.

One significant advantage of the heat-flux method is that it can yield upper-bound estimates for infiltration rates. Assuming that the regional heat flux is 85 mW/m^2, neglecting all other sources of reduction in apparent heat flux such as lateral flow in the SZ and vapor fluxes, using a value of 35 mW/m^2 as the average apparent heat flux over the repository block, and using the rule-of-thumb that 10 mW/m^2 reduction in apparent flux is equivalent to 5 mm/yr infiltration, one finds that the maximum average infiltration over the repository block is about 25 mm/yr.

The chloride mass balance technique, as applied by Fabryka-Martin et al. (1996), assumes that average Cl^- concentration multiplied by total flux is conserved, or

$$C_o P = CI, \tag{1-25}$$

where

- P is average precipitation rate,
- C_o is the Cl^- concentration corresponding to the average Cl^- deposition rate,
- C is the Cl^- concentration in a well-mixed reservoir at depth, and
- I is the net infiltration.

Knowing the average precipitation rate, Cl^- concentration corresponding to the average Cl^- deposition rate, and Cl^- concentration in a well-mixed reservoir at depth, the percolation flux at depth can be determined. Yang et al. (1996) report Cl^- concentrations in perched water of 4.1 to 15.5 mg/L, with 15 of the 17 reported values no greater than 8.3 mg/L and a Cl^- concentration of 7 mg/L at NRG-7a (the nearest borehole to UZ-4 and UZ-5 with a reported perched-water sample). Using the same precipitation rate (170 mm/yr) and Cl^- concentration (0.62 mg/L) as Fabryka-Martin et al. (1996), and assuming that the perched water is well mixed with the matrix waters, calculated net infiltration is 25.7, 12.7, and 6.8 mm/yr for concentrations of 4.1, 8.3, and 15.5 mg/L, respectively.

An infiltration value of about 26 mm/yr would represent an upper bound based upon the perched-water chloride data; if the matrix waters do not mix completely with the perched water, infiltration values may be lower. The estimated infiltration values are more consistent with the shallow infiltration estimates than the estimates from the PTn, however, suggesting that a considerable portion of the infiltrating water may bypass the PTn matrix. The upper-bound value

obtained by chloride mass balance on perched water, 26 mm/yr, is remarkably consistent with the upper-bound value obtained by geothermal heat-flux calculations.

5/19/97 Revisiting alluvium regression. SAS

Since the discussion of 1/13/97, additional information on alluvium depths, borehole location, and borehole geomorphic classification (e.g., channel, sideslope) has been gleaned from the literature and the data file obtained with the site atlas. I incorporated the new information to obtain regression coefficients.

As it turns out, I was not able to reproduce the original slopes calculated by Hannah Castellaw in August, 1995. Apparently she used the slope at the nearest neighbor of the DEM, with all calculations performed in ArcInfo. I tried to use: (i) the slope at the nearest neighbor, (ii) the interpolated slope from the slope at the four nearest neighbors, and (iii) the interpolated slope from the elevations at the four nearest neighbors. None of these matched the previous slopes, although some were close. Unfortunately, the regressions exhibit poorer fits than before, particularly for the channels (although the channels have many more points now). It may be that Hannah used a different DEM coordinate grid; she has not worked at CNWRA for a year or two, so it will be difficult or impossible to retrace the exact calculations. There does seem to be quite a bit of scatter.

I revised the set of files used to estimate regression coefficients in ***$HOME2/Matlab/-3Ddata***. New data files were created in the format that the load_well file expects, and the other load routines call load_well. The original data and *Matlab* files all have ".1" appended. The routine that calculates the slope at the borehole locations is called calc_pt_slope; internally there are switches to calculate the slope according to the three options mentioned above.

5/25/97 Results of 1D simulations. SAS

Over the last several months, a series of *breath* version 1.2 simulations were run examining the impact of alluvium-filled fissures and calcite-filled fractures. These simulations used the same strategy as was used for the open fractures, in that the bedrock was assumed impermeable and the porosity of the filling was lowered to account for the fracture porosity. The alluvium simulations use kmpo5223_aKmao5222 as the base case, while the calcite simulations use kmpo5223_cKmao7554 as the base case. The alluvium simulations used soil depths of 10, 25, and 50 cm; the calcite simulations

Table 1-9: Summary of alluvium (*abcd*) and fracture (*efgh*) parameter codes

Code	Parameter	Translation
Soil cover (kmpo*abcd*_aKmao*efgh*)		
a	Intrinsic permeability k (cm^2)	$k = 10^{-a-3}$
b	van Genuchten m	$m = b/10$
c	van Genuchten scaling pressure P_0 (gm/cm-s^2)	$P_0 = c \times 10^4$
d	Porosity ε	$\varepsilon = d/10$
Soil-filled fissure (kmpo*abcd*_aKmao*efgh*)		
e	Intrinsic permeability k (cm^2)	$k = 10^{-a-3}$
f	van Genuchten m	$m = f/10$
g	van Genuchten scaling pressure P_0 (gm/cm-s^2)	$P_0 = c \times 10^4$
h	Porosity ε	$\varepsilon = 10^{-h}$
Calcite-filled fracture (kmpo*abcd*_cKmao*efgh*)		
e	Saturated hydraulic conductivity K_{sat} (cm^2)	$K_{sat} = 10^{-e}$
f	van Genuchten m	$m = f/10$
g	van Genuchten scaling pressure P_0 (gm/cm-s^2)	$P_0 = 10^g$
h	Porosity ε	$\varepsilon = 10^{-h}$

used soil depths of 10, 25, 50, 100, and 150 cm. The alluvium simulations used fracture-alluvium porosity values of 10^{-2}, 10^{-3}, and 10^{-4}. The calcite simulations had a nearly full suite of calcite perturbations for soil depths of 10, 25, 50, 100, and 150 cm (2 perturbations calcite permeability, and calcite van Genuchten m; 1 perturbation for calcite P_0 and porosity) and a full suite of 2 perturbations for all soil properties with a soil depth of 10, 25, or 50 cm. The codes for the output files are discussed in Table 1-9. Note that the code for alluvium-filled should have been kmpo*abcd*_akmpo*efgh* and the code for calcite-filled should have been kmpo*abcd*_cKmpo*efgh* for clarity.

The average flux over the second decade, averaged over the depths of 1 to 10 m, were extracted using extract_qstate.m (coded in *Matlab*) for all simulations. Similarly, the decadal average moisture content in the node above the soil/fracture interface was extracted for each case. All values were stored in **af_allcli.result** in ***$BREATH2/Subreg***. The net-infiltration results are summarized in Table 1-10.

Several conclusions can drawn from the simulation results. The alluvium results suggest that as the fracture aperture decreases, net infiltration increases. The effect decreases as the soil depth increases, and is not tremendously large in any case. The calcite results suggest that the

Table 1-10: Net infiltration (mm/yr) for various cases with soil- and calcite-filled fractures

Code	10-cm	25-cm	50-cm
kmpo5223_aKmao5222	17.2	7.13	4.44
kmpo5223_aKmao5223	21.4	8.30	4.92
kmpo5223_aKmao5224	22.4	8.53	4.99
kmpo5223_cKmao7554	17.4	8.55	4.85
kmpo4223_cKmao7554	14.7	2.70	0.42
kmpo6223_cKmao7554	21.6	13.8	10.7
kmpo5123_cKmao7554	18.2	12.9	8.66
kmpo5323_cKmao7554	21.5	12.0	8.24
kmpo5213_cKmao7554	26.3	17.6	12.7
kmpo5253_cKmao7554	10.3	1.25	0.13
kmpo5222_cKmao7554	23.0	15.8	11.6
kmpo5225_cKmao7554	9.48	1.80	0.29
kmpo5223_cKmao6554	33.1	14.8	8.08
kmpo5223_cKmao8554	3.31	1.81	1.43
kmpo5223_cKmao7454	15.2	7.50	4.78
kmpo5223_cKmao7654	19.2	9.21	4.70
kmpo5223_cKmao7564	42.6	23.6	14.2
kmpo5223_cKmao7555	17.5	8.57	4.87

alluvium properties are not important relative to calcite properties when soil is 10 cm, but dominate when soil is 50 cm. Variation in calcite properties yields largest change in net infiltration when soils are shallow and are muted somewhat when soils are deep. The calcite property having strongest impact on net infiltration appears to be P_0, followed by K_{sat}.

The capillary properties of alluvium and calcite may be the most important parameters for calculating bare-soil infiltration. It appears that the ratio of alluvium P_0 to calcite P_0 is a controlling factor on infiltration. As the ratio gets smaller (calcite has finer pores relative to alluvium) net infiltration increases. One can attribute this to the propensity of calcite to imbibe moisture and not release it back to the soil to satisfy evaporation.

The variation of moisture content with net infiltration for the bottom node of the soil follows the general patterns ascertained before. There is a clear trend for drier soil with increasing net infiltration when the fracture-filling properties are changed, however, whether the filling is calcite or soil (note that only soil porosity was varied).

6/11/97 Documentation of soil sample analysis. SAS

During the annual CNWRA QA audit, in which the USFIC KTI was audited, an issue of data collection was raised. During the Yucca Mountain field trip examining shallow infiltration processes in caprock, documented in the entry dated 4/10/97, 23 soil samples were collected and analyzed for electrical conductivity and percent hydrometer estimates of grain size and texture, by Utah State University Analytical Laboratories (Utah State University, Logan, UT 84322-4830, 801/797-2217). The reported analysis is dated 17 April, 1997; I have filed a copy of the results in my file cabinet. These samples were collected at various locations around Yucca Mountain at the suggestion of David Groeneveld and Dani Or (consultants hired for their expertise in characterizing shallow flow processes).

Typically our QA program requires that such analyses be planned prior to data collection and that verification of the analysis procedure be performed in order to be fully complient with QA requirements. I was made aware of their recommendation while we were in the field and did not realize that an external agency (albeit an agency at the same university that Dani Or is an employee of) was to perform the analyses. Note that the soil samples are only intended for qualitative verification of our observations that all of the fine materials at the site are remarkably similar and are not intended for numerical estimates or to provide data for regulatory positions. We will have to note that data was not collected under CNWRA QA procedures if and when we use the information.

6/30/97 Root growth simulations for caprock paper. SAS

I am writing a paper documenting our investigations of hydrologic issues regarding the interaction of vegetation with fissures in TCw caprock environments with Dani Or and David Groeneveld (consultants). The paper consists of three major components: (i) a description of field observations, (ii) simulation of the impact of vegetation on hydrologic behavior in the presence of fissures, and (iii) simulation of root growth in the presence of fissures. David has been writing the description of the fieldwork. Dani has been performing 2D simulations of a vertical cross-section with 5 fissures overlain by soil using HYDRUS-2D, which is an enhancement of SWMS-2D (Šimůnek et al., 1992), in order to examine the hydrologic behavior component. I have been attempting to use Version 2.0 of a 3D code developed at UC-Davis by Jan Hopmans, Volker Clausnitzer, and Francesca Somma that explicitly models individual roots and distributes uptake to the surrounding nodes.

The root-growth code does not have a name; I will refer to it as Root-Growth Simulation

Model (RootSim) from now on. RootSim is a research-level code, so it has a number of shortcomings that would not be expected in a production code and that make it difficult to use for our purposes. Some shortcomings include:

- Every element must be the same size and rectangular shape.
- Properties are defined by node rather than element.
- Boundary conditions are restricted to a mixture of:
  - one (time-varying) flux value (as many nodes as desired),
  - one (time-varying) head value (as many nodes as desired).
- Gravity drainage is not allowed.
- The code relies on a non-portable random-number generator.

The code was run through a FORTRAN static analyzer code, for_study (called fstudy on bashful), provided by Cobalt Blue. SPARC version 2.0.1 was used for the test. A number of errors and warnings were identified, either through compilation messages, fstudy, or tracking down errors in simulation behavior, including:

- 24 overlength lines
- a branch into a block
- variable *init* used before being initialized
- calling subroutine ChInit when chemistry is disabled (thereby changing *dtMaxC*)
- 9 unused common blocks in routines
- 13 changes in common blocks between routines (different variable names)
- 21 instances where precision was lost (real to integer or double precision to single precision)
- rand is system-dependent (and does not work for SGI)

The common-block and lost-precision messages were ignored; the remaining messages were fixed. The rand problem was accommodated by writing a short C routine to use the rand48 routine provided as part of the SGI library. In addition, a modification was made so that the **outfem**

output files also include *cAvg*, so that the output file can be reused as a restart file without modification. Modifications and suggested modifications are further documented in file **Errors** in ***$HOME2/AmbientKTI/Root***.

Several tests have been run trying to get appropriate simulations for the paper. The physical problem entails a shallow soil atop a soil-filled fissure next to a matrix block, with a plant starting either directly over the fissure or starting at some distance, with the idea being to compare some measure (e.g., total plant mass) at the end of the simulation. Dani set up the original input files based on the documentation, and some properties were not totally appropriate for Yucca Mountain. Some of the plant properties have never even been measured.

Through a process of trial and error, I've modified the problem from the original set up by Dani. Problem setup and changes include:

- A relatively small domain is being modeled (an 11x12x36 grid, 25 mm on an element side). This represents a tradeoff between computational speed and grid refinement.
- Soil depth is about 10 cm and the fissure is about 15 cm wide (only half is modeled). The "about" is due to the node-defined material properties.
- Bedrock material properties are TCw cuc, with retention parameters for sample PW19s, composite-sample caprock K_{sat} (Flint et al., 1996).
- Soil retention parameters are for a loamy soil (Dani refers to a Carsel and Parrish, 1988) and K_{sat} is texture-estimated for Yucca Mountain soil (Schmidt, 1989).
- Soil strength has caused difficulties in simulations. Soil strength is defined in the code to be $(1-\theta)^3 S_{smax}$, where θ is effective saturation and S_{smax} is soil strength at residual saturation (with apparently arbitrary units). The **root.in** input file defines a soil strength at which growth ceases for each type of material. Dani changed the bedrock retention properties to artificially maintain very dry (very strong) conditions. I put realistic retention properties, and the roots acted as though the bedrock was clay. Changing the bedrock strength to an extremely large value (10^{32}) caused numerical problems (NaN for root-tip location), which I interpret as due to overenthusiastic adjustment to strength gradients, so I cut it back to 10^8 and gradually increased to 10^{11}. Results are not totally satisfactory due to the transition zone between nodes where properties change in an uncontrolled manner. I also had problems by making maximum soil strength too large (14) compared to the plant-growth cutoff at residual saturation (6), which I fixed by making the maximum soil strength 6 as well.

- Appropriate boundary and initial conditions are difficult to provide with the version of the code we have available. One can provide either a constant-head or constant-flux bottom condition and both tend to misrepresent the available water. Either a no-flow or specified-head (representing equilibrium with the atmosphere) top condition may work. I have been running into problems with balancing available water with rock availability. The latest solution is to provide wetting events every 15 or 30 days and have no-flow boundaries at the bottom. I initially used initial conditions at 50 cm suction head.

- The current conditions have been changed to 300 cm suction head in soil (field capacity of 0.3 bar) and 3000 cm (3 bar) suction head in the rock, redistributed with 15 days of evaporation (15 bar) at the top and no flow at the bottom. Rain (7.5 mm) is applied at 15, 30, 45, and 75 days, and evaporation continues throughout at 5 bar.

- When very wet conditions occur, the plant over bedrock develops more biomass than the plant over the fissure, even though the fissure plant has much greater penetration. The bedrock plant is apparently using the bedrock as an additional source of moisture and developing along the bedrock interface. I am not totally convinced that this is not an artifact of the slushy material-property zone, but the caprock *is* quite permeable.

7/8/97 Modification of Scott and Bonk electronic version.

SAS

An electronic ARC/INFO coverage of Scott and Bonk (1984) geology is one of the data sets included on the DOE tape discussed in the 3/23/97 entry. There are 118 polygons that do not have a lithologic attribute and one alluvium polygon that is mislabeled as ym. Jim Prikryl extracted the coverage in UTM format last week and I have started entering the missing coverages by visual inspection. All work is in ***$HOME2/Matlab/YMGeology***. The updated coverage information is listed as **scotbonu.wat**; the original coverage is stored in subdirectory ***Orig***.

7/11/97 Regression for TPA shallow infiltration.

SAS

It was brought to my attention that the UZFLOW module of the TPA3 code, which predicts infiltration on a pixel-by-pixel basis over Yucca Mountain, was predicting far more mean annual infiltration (MAI) than mean annual precipitation (MAP) under full glacial conditions. The regression formula features bicubics in both MAP and mean annual temperature (MAT), and apparently these cause problems outside the range of interpolation. The formulation is for soil over an open-fracture continuum.

I revisited the form of the regression equation and have come up with a more robust (and simpler) formulation that appears to work well even through 4× current *MAP* and -15 °C cooler than current *MAT*. The formulation fails for soil depths greater than 25 cm, but these depths should have negligible infiltration for the system considered and can be set to zero. For very shallow soils (< 10 cm) and extremely cool and wet conditions (beyond the range simulated), the formulation predicts *MAI* in excess of *MAP*. These cases should have *MAI* set to equal *MAP*.

The regression equation is intended to account for several facets of *MAI* behavior in this system: (i) *MAI* generally changes logarithmically with changing inputs; (ii) *MAI* is more sensitive to changing inputs when soil depths are larger; and (iii) *MAI* is more sensitive to changing inputs when *MAI* is small. The simplest form of an equation satisfying these conditions is

$$H = B^{b_1}[\sum_{i=1}^{N} a_i f_i(u_i)](1 + b_2 H), \tag{1-26}$$

where

- H is $\log_{10}(MAI/MAP)$
- a_i is a regressed constant
- b_i is a regressed constant
- u_i is a normalized regression variable (e.g., *MAP*, *MAT*)
- $f_i(u_i)$ is a regression relationship for variable u_i
- B is $(b\varepsilon)/(b_0\varepsilon_0)$
- b is soil depth
- b_0 is base-case soil depth
- ε is porosity
- ε_0 is base-case porosity

In ***$HOME2/Matlab/YMInfil/SubregSpaceDist*** I created two new *Matlab* routines, **run_sreg.m** and **f_regshal2.m**, that perform the regression using the formulation.

7/14/97 More regression for TPA shallow infiltration. SAS

In ***$HOME2/Matlab/YMInfil/SubregSpaceDist*** I created a new *Matlab* routine, **eval_TPA_fun.m**, that evaluates the function in Equation 1-26 (with best-fit constants) for every pixel in the standard Yucca Mountain DEM with soil depths given in **basecaseDepth.mat**. The areal-average *MAI* resulting from the formula, both as *MAI* and as normalized, is shown in Figure 1-4(a) and (b), respectively.

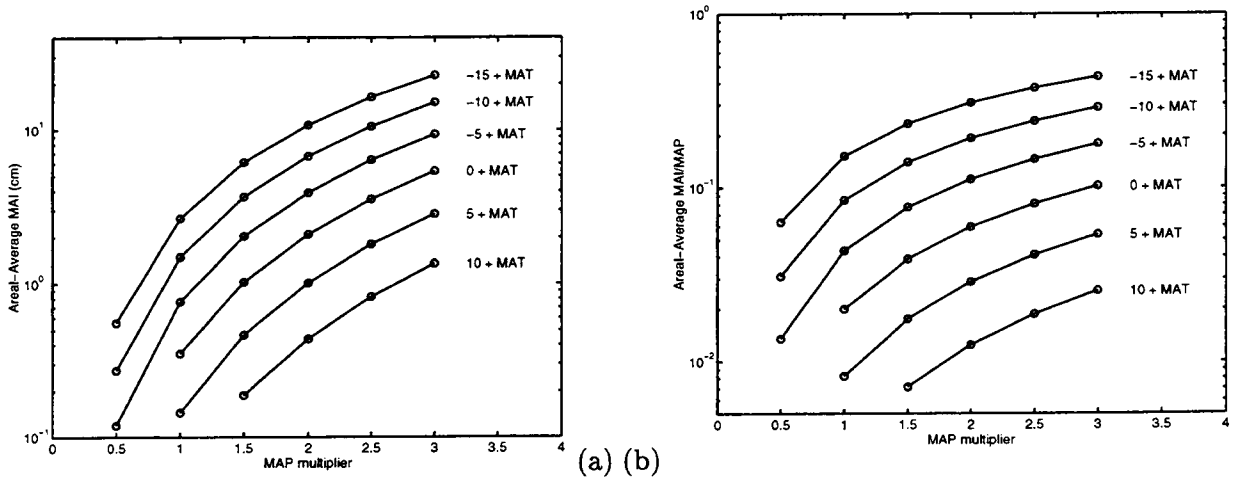

Figure 1-4: 7/14/97. Areal-average *MAI* for Yucca Mountain area, using regression formula based on soil/open-fracture system, (a) in dimensional form, and (b) in nondimensional form.

Following up on the incentive to examine the results in detail, I collected the simulations performed to date in **am_all.result** in ***$BREATH1/RunTightAM***. I modified the format of the file to include the date that the simulation was completed. I cursorily examined the soil-over-calcite simulations to check on the sensitivity to depth and climate. By plotting the simulations with the fracture code of **cal3** against the areal-average simulations, it appears that even thought the calcite simulations do not span the same range as the soil-over-fracture simulations, the change in infiltration with climate should have similar trends. Overall infiltration may be greater with the calcite due to the lesser sensitivity to soil depth (e.g., 10 cm soil depth has 29 mm/yr while 50 cm soil depth has 7 mm/yr *MAI*). Fracture properties have a much greater impact on *MAI* for the calcite simulations than for the open-fracture simulations; permeability and bubbling pressure are the two big players, along with soil porosity.

A cursory check of simulations with base-case alluvium filling fissures with various soil depths and fissure porosities suggests that the falloff of *MAI* with soil depth has a characteristic slope, as the **cal3** simulations have about 1.5 times as much *MAI* for a given soil depth. Interestingly, *MAI* increases slightly as fissure porosity decreases.

8/31/97 Investigation of USGS UZ properties.

SAS

Files for the following investigations can be found in ***$HOME2/AmbientKTI/3Ddata***.

On 8/28, Amit Armstrong requested that I provide estimates of the layer properties for the TPA sensitivity exercises. The idea is to use the microstratigraphy property information (including porosity, particle density, and K_{sat}) provided by Flint (1996), in conjunction with the layer microstratigraphy thicknesses extracted from the recently obtained DOE Earthvision model, to estimate the equivalent thicknesses of the TPA subareas. Amit provided layer thicknesses and a mapping of the sublayers into the TPA layers.

In Table 7 of the Flint (1996) report, K_{sat} for the individual sublayers is reported as a mean and a standard deviation. The K_{sat} mean statistics are reported for three cases: (i) geometric mean of raw K_{sat} values, (ii) power-law mean of raw K_{sat} values, and (iii) geometric mean of K_{sat} values derived from regression equations applied to all measured porosities. In each case, the standard deviation is reported on the raw values. The combination of log-10 mean and base-10 standard deviation renders these statistics unsuitable for coming up with a distribution.

This spring, Lorrie Flint sent me the database used in the Flint (1996) report. The database includes UZ core properties from 31 boreholes. I have not had a chance to examine the database in detail, but this represents a good opportunity to digest it. I created two *Matlab* routines (extract_k.m and show_pdk.m) to extract information from the database and to show results. A total of 589 K_{sat} measurements were made, of which 188 were less than 5×10^{-12} m/s (0.16 mm/yr). At first blush, the raw K_{sat} statistics would be best to use for estimating layer properties; however, as the numerous low-K_{sat} measurements are not considered in the statistics for the raw values, second thought suggests that it may be appropriate to use the far more numerous porosity samples to estimate properties.

There have been a number of UZ formation classification schemes at Yucca Mountain. In Table 1 by Flint (1996), correspondences between the classification scheme of Buesch et al. (1996), Scott and Bonk (1984), and Montazer and Wilson (1984) are shown. For the most part, correspondences are clearly denoted, although based on comparing Figure 12 by Flint (1996) and a direct plot, it appears that there may be discrepancies in the assignment of units:

- Although apparently assigned to the TC hydrogeologic unit in Table 1, all of the Tptrn unit with porosity less than a cutoff value (perhaps 9 percent?) seemed to have been assigned to the TR hydrogeologic unit in Figure 12.
- There are two high-porosity, low-K_{sat} outliers not shown in Figure 12 (from the BT2 and BT4 units, respectively).

Flint (1996) provides regression relationships between porosity and the remaining hydraulic

properties, as porosity is far easier to measure than most other properties. Three categories are identified: (i) microfractured, (ii) altered, and vitric/crystallized.

The microfractured category has samples from vitrophyres assigned to it (i.e., Tptrv1 and Tptrv3 from the Topopah Spring Tuff). The microfractured category reportedly includes the TC and PV3 hydrogeologic units. In addition, one sample each from the crystallized and welded Tptrn, Tptpul, and Tptpln units is assigned to the microfractured category due to visible microfractures.

The altered category includes all lithostratigraphic units below the vitric/zeolitic boundary (BT1, CHZ, BT, PP4, PP3, PP2, PP1, BF3, and BF2) plus the CMW (an altered portion at the base of the Tiva Canyon formation). As Flint (1996) notes, there are crystallized and vitric units within the "altered" category, but the assignment was done for simplicity in developing predictive equations.

The vitric/crystallized category includes everything left over after the other categories are considered.

Although one can wish that the hydrogeologic layers would be relatively homogeneous within each layer, unfortunately the properties are not necessarily homogeneous. As can be seen in the section of borehole SD7 displayed in Figure 10 by Flint (1996), zeolites occur in samples from the CHV, CHZ, BT, PP4, PP2, and PP1 hydrogeologic layers, while zeolites are missing from samples in the BT1, CHV, PP3, PP2, and BF3 hydrogeologic layers. Flint (1996) suggest that the presence of alteration can be estimated by a significant change in porosity after drying at elevated temperatures. Two porosity measurements were obtained for each sample: (i) dried at a temperature of 60 °C and a relative humidity of 65 percent, and (ii) dried at 105 °C and an ambient relative humidity (< 20 percent). Flint (1996) suggests that if the two porosity measurements differ by 0.05, the sample is altered. Areas in SD7 with the 5-percent differential porosity but not having zeolites (in the form of clinoptilolite) are reported to have vapor-phase minerals tridymite and cristobalite, although elevated cristobalite without tridymite does not exhibit the differential porosity.

Other areas with the 5-percent differential are pointed out as occurring at the base of the Tiva Canyon Tuff, and are attributed to alteration to clay (such as smectite). It is pointed out that the extent of alteration appears to be related to the topographic location of the borehole. Boreholes in narrow upwash channels may receive more frequent runoff, hence infiltration maintains higher water contents. Flint (1996) implies that alteration to clay is due to wet conditions. Despite the presence of the differential, these altered high-porosity samples tend to also have high K_{sat}.

A method for discriminating between alteration to zeolites and alteration to clays is offered

by Flint (1996) using measurements of particle density obtained in two ways: (i) calculated from bulk density and porosity, and (ii) directly measuring the volume of the solid particles using helium pycnometry. Approximately 180 samples from UZ16 (judging from Figure 11 by Flint (1996)) were analyzed using the two techniques. For zeolitic samples, the calculated particle density almost invariably was greater than the measured density, by an average of about 0.07 g/cm^3 (my estimate), and the measured particle density was always less than 2.5 g/cm^3. For nonwelded vitric samples, the calculated particle density was less than the measured density when the calculated density was less than 2.35 g/cm^3 and gradually switches above that value; however, the zeolitic samples tend to have a larger differential. The nonwelded vitric samples tend to have somewhat larger particle densities than the zeolitic.

The welded crystallized samples had calculated particle densities uniformly greater than 2.45 g/cm^3, while the densely welded vitric samples had calculated particle densities uniformly less than 2.45 g/cm^3. Three classes could be distinguished from these samples: (i) welded/crystallized, (ii) nonwelded vitric, and (iii) nonwelded zeolitic or densely welded vitric. Despite the usefulness of the technique, helium-pycnometric measurements did not appear to be made on the majority of Yucca Mountain samples.

The complete set of measured K_{sat} values in the database reported on by Flint (1996) are shown in Figure 1-5. The database reports three microstratigraphic classifications for each sample, corresponding to the Buesch et al. (1996) nomenclature: (i) formation (e.g., Tpc, Tpt); (ii) zone, where applicable (e.g., pul, rn); and (ii) subzone, where applicable (e.g., pv2, rv2). Where the formation has no subzones, the database repeats the zone identification for the subzone. The generating routine is *Matlab* show_pdk.m.arch091097.

In Figure 1-5, the microstratigraphic zones are grouped into the nomenclature of Montazer and Wilson (1984) according to Table 1 of Flint (1996).

The samples considered microfractured are the TC and PV3 units (denoted with small circles), and obviously microfractured samples (denoted with black asterisks). For consistency with Figure 12 of Flint (1996), the TC unit consists of only the Tptrv1 subzone in Figure 1-5, even though the Tptrn subzone appears to be classified as TC in Table 1 of Flint (1996).

The remaining samples are color-coded, broadly by formation. Outlying samples are labeled according to unit. Classification into the BT1a and BT1 hydrogeologic units is not clear from Table 1 by Flint (1996); the one Tpbt1 sample was placed into the BT1 hydrogeologic unit. As alteration is a key component of the property-classification scheme proposed by Flint (1996), any sample meeting the 5-percent porosity-change criterion is circled.

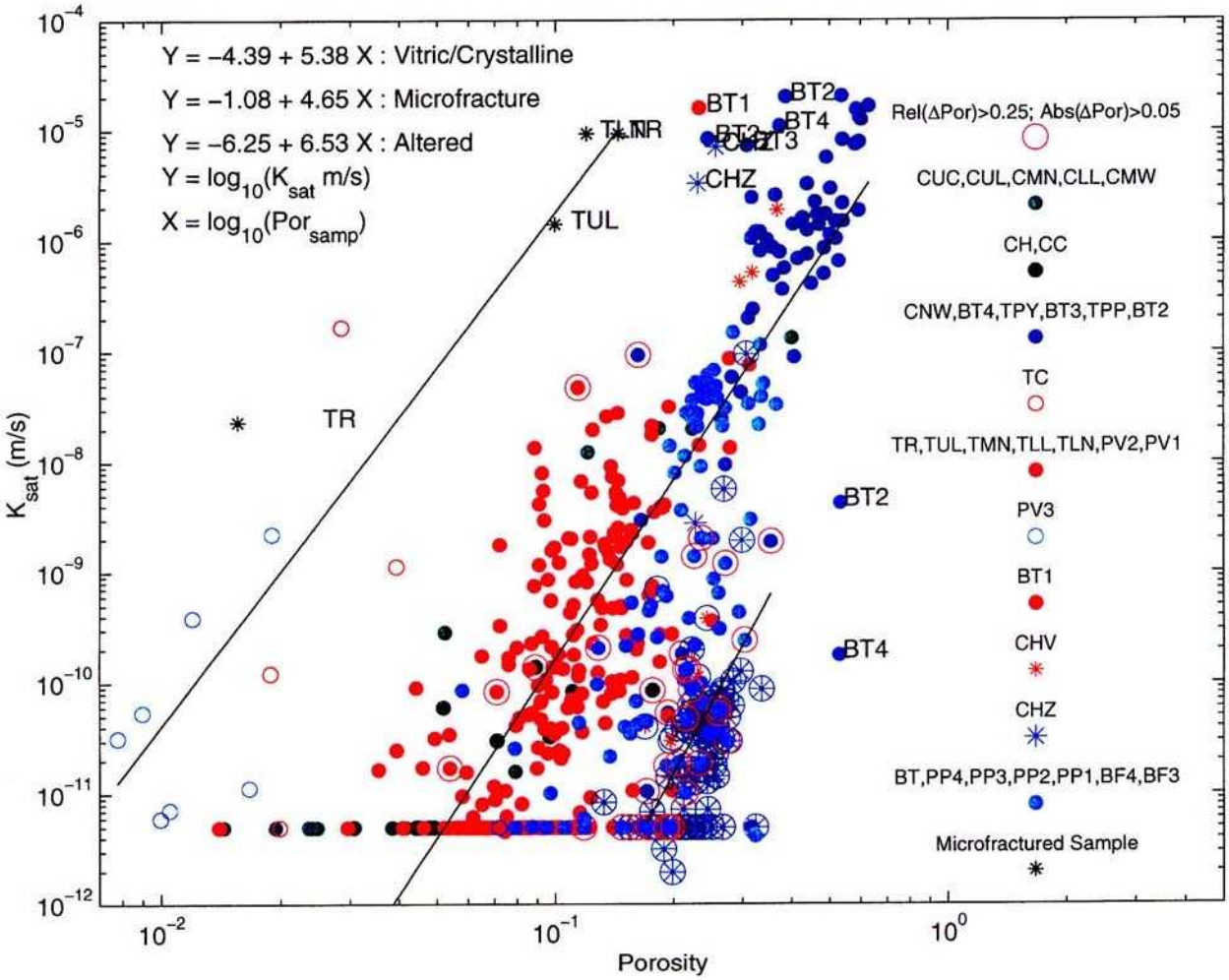

Figure 1-5: 8/31/97. The complete set of measured K_{sat} values in the USGS database.

Based on Figure 1-5, it can be argued that five general categories exist for the samples:

- Microfractured, low (< 0.05) porosity
- Microfractured, high (> 0.05) porosity
- Zeolitic
- Vitric/crystallized
- Inexplicably high (> 0.5) porosity, low-permeability

Flint (1996) lumps the first two categories, and never presents data in the last category. It is not clear where the high-porosity microfractured category turns into the vitric/crystallized category; some of the high-permeability bedded-tuff samples may fall into the microfractured category due to handling difficulties. It is also not clear where the zeolitic and the vitric/crystallized categories turn into each other; many of the "altered" samples in Figure 12 by Flint (1996) appear to fall squarely into the vitric/crystallized category.

9/9/97 Further investigation of USGS UZ properties. SAS

It is my feeling that a successful use of matrix properties to predict matrix K_{sat} should have one formula for all cases (except, perhaps, for the microfractured cases). Accordingly, I played with various forms of a predictive relationship and have come up with a set of formulae that better match the non-microfractured data than the estimates in the database provided by L. Flint. I used a least-squares measure to make quantitative evaluations of the fit of the prediction to the measured data:

$$\log_{10}(M) = \left[\sum_{i=1}^{N}(Y_i - Y_{mi})^2\right]^{1/2}, \tag{1-27}$$

where M is the performance measure, Y_i is the ith predicted value of $\log_{10}(K_{sat})$, and Y_{mi} is the ith measured value of $\log_{10}(K_{sat})$.

There are a number of properties measured for each core sample, including:

- Bulk density (at 65 and 105 °C)
- Porosity (at 65 and 105 °C)
- Particle density (at 65 and 105 °C)
- Volumetric water content (at 65 and 105 °C)
- Saturation (at 65 and 105 °C)
- Tuff unit, zone, and subzone

In addition, some of the core samples have subsamples for which porosity and K_{sat} are measured.

I systematically tested all sets of 1-, 2-, 3-, and 4-parameter regression equations. The linear and loglinear predictions for each of the parameters were tested, as well as calculated absolute

and relative change in particle density, bulk density, and porosity. In order to systematically test regression equations, I created a *Matlab* routine (test_usgs_regr.m) that ran through all possible combinations using all vitric/crystalline and altered samples with measured K_{sat} above the measurement limit (5×10^{-12} m/s) and porosity greater than 0.05. The samples denoted microfractured were not used, although I think that some of the samples retained could be classified microfractured.

For reference, performance measure M is 15.7 when using the estimated K_{sat} values in the database and is 19.1 when using a linear regression on subsample porosity (23.9 for $\log_{10}$ regression). The estimated K_{sat} values are thus off by a mean value of more than an order of magnitude (i.e., a factor of 16 for the USGS regression). The USGS regression also has 6 coefficients: two for the altered, three for the unaltered, and an exponent in the unaltered equation.

The best single regression fit (13.1) occurs, rather surprisingly, for $\log_{10}$ saturation at 65 °C. Saturation provides the single best predictor; all 4 values of M, for the 65 and 105 °C pairs (i.e., linear and $\log_{10}$), are better than the USGS estimate, which is based on classifying samples into bins and using two regression equations). Even better, only 2 coefficients are used.

A significant improvement occurs with one more variable, porosity. In this case, the best match occurs with saturation at 65 °C and the subsample porosity, with M dropping to 8.22. Considering three variables, the best match occurs with $\log_{10}$ of the subsample porosity, porosity at 65 °C, and volumetric water content at 105 °C, yielding an M value of 7.62. The case with four variables yields the same set as the 3-variable case, with the saturation at 65 °C added, and M drops to 7.46. Clearly the parsimonious selection would use two variables, a saturation and a porosity, with a total of 3 coefficients. Note that there is not a tremendous difference between predictions using different types of porosity measurement or water content measurement. Also note that the difference between the USGS estimate and the 2-parameter estimate in log space is $1.196 - 0.914 = 0.28$, which is a significant but not outstanding improvement.

The estimated K_{sat} using the best-fit 1-, 2-, and 3-parameter equations, as well as the USGS-estimated K_{sat}, are plotted as a function of the measured K_{sat} in Figure 1-6. The closer a point lies to the diagonal line, the better the fit. The *Matlab* routine generating the plots is archived as test_usgs_regr.m.arch091097 in ***$HOME2/AmbientKTI/3Ddata***.

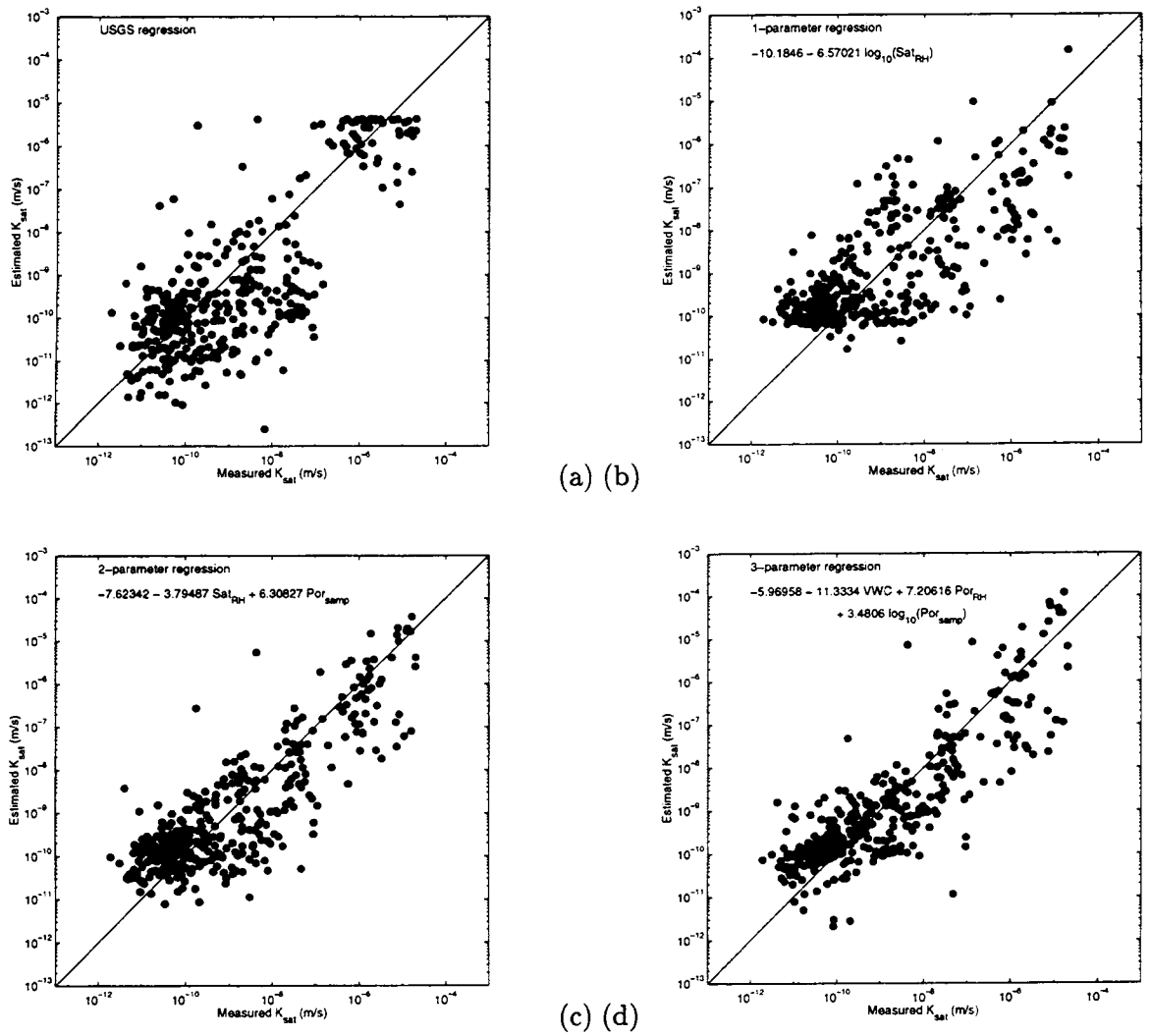

Figure 1-6: 9/9/97. Comparison of best-estimate K_{sat} and measured K_{sat} using (a) the USGS database, (b) the best 1-parameter regression, (c) the best 2-parameter regression, and (d) the best 3-parameter regression.

The best-fit regression equations are:

$$\log_{10}(K) = -10.1846 - 6.57021 \log 10(\theta_{65}), \tag{1-28}$$

$$= -7.62342 - 3.79487\theta_{65} + 6.30827\varepsilon_{sample}, \tag{1-29}$$

$$= -5.96958 - 11.3334VWC_{105} + 7.20616\varepsilon_{65} + 3.4806 \log_{10}(\varepsilon_{sample}), \tag{1-30}$$

where a subscript of 65 denotes the measurement at 65 °C, a subscript of 105 denotes the measurement at 105 °C, a subscript of *sample* denotes the subsample measurement, θ is saturation, ε is porosity, and VWC is volumetric water content.

In the following plots, important components of the regression equations are shown graphically for each borehole. Components include: (i) porosity at 65 °C (shown both as a bar height and a color); (ii) saturation at 65 °C; (iii) particle-density difference (absolute density by bar height, relative density by color); (iv) measured K_{sat} where available (blue dots); (v) estimated K_{sat} (USGS are green dots, best 2-parameter regression are red dots); (vi) formation identification. The *Matlab* routine generating the plots is archived as show_usgs_db.m.arch091797 in ***$HOME2/-AmbientKTI/3Ddata***. The *Matlab* routine converting the ASCII database into a *Matlab* binary (".mat") file is archived as make_flint_db_to_mat.m.arch091797, and the resulting file is archived as usgs_bhdb.mat.arch091797.

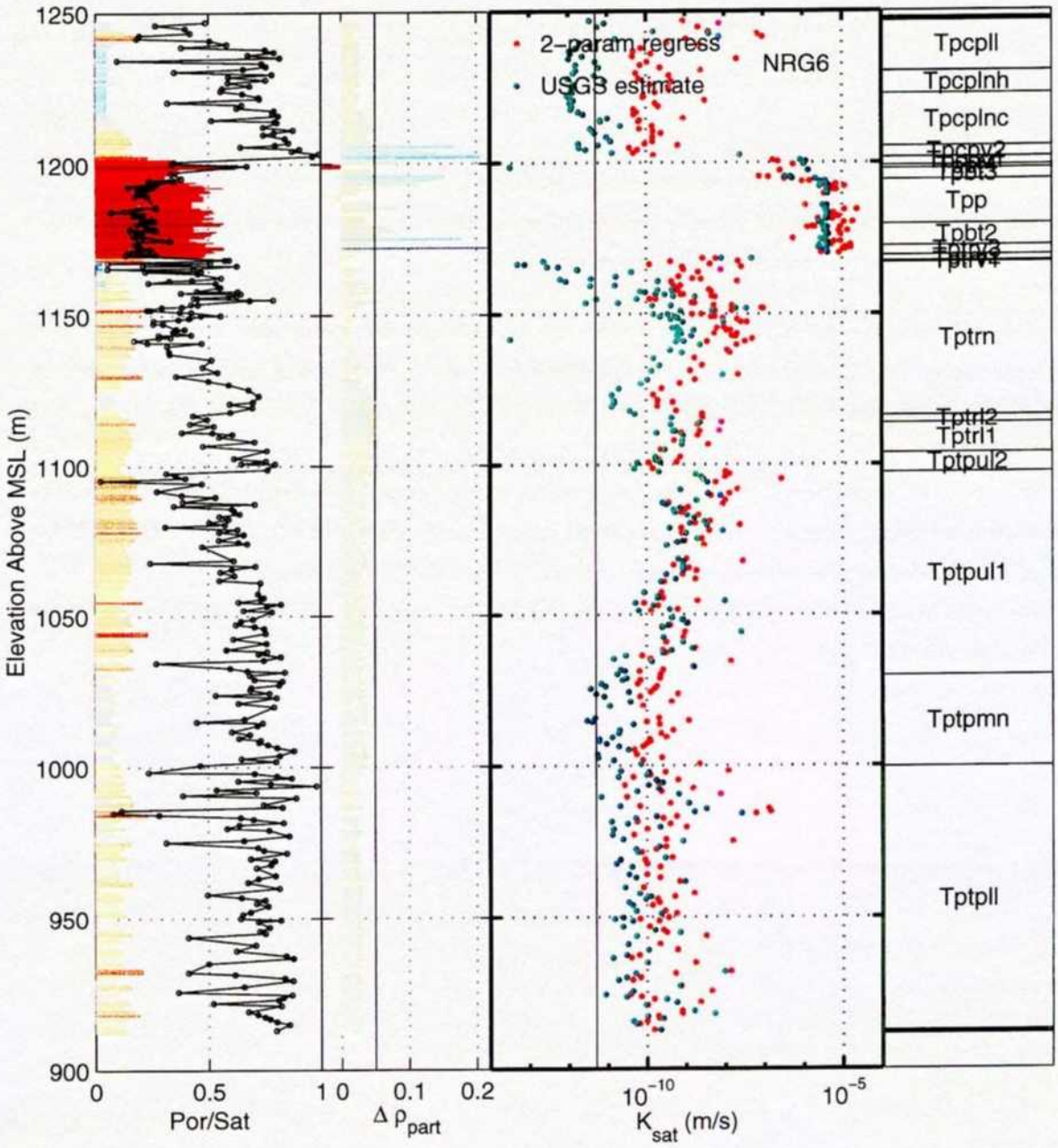

Figure 1-7: 9/9/97. **BHprofile_NRG6_c.eps**. Porosity, saturation, change in particle density, and measured and estimated values for K_{sat} in borehole NRG6.

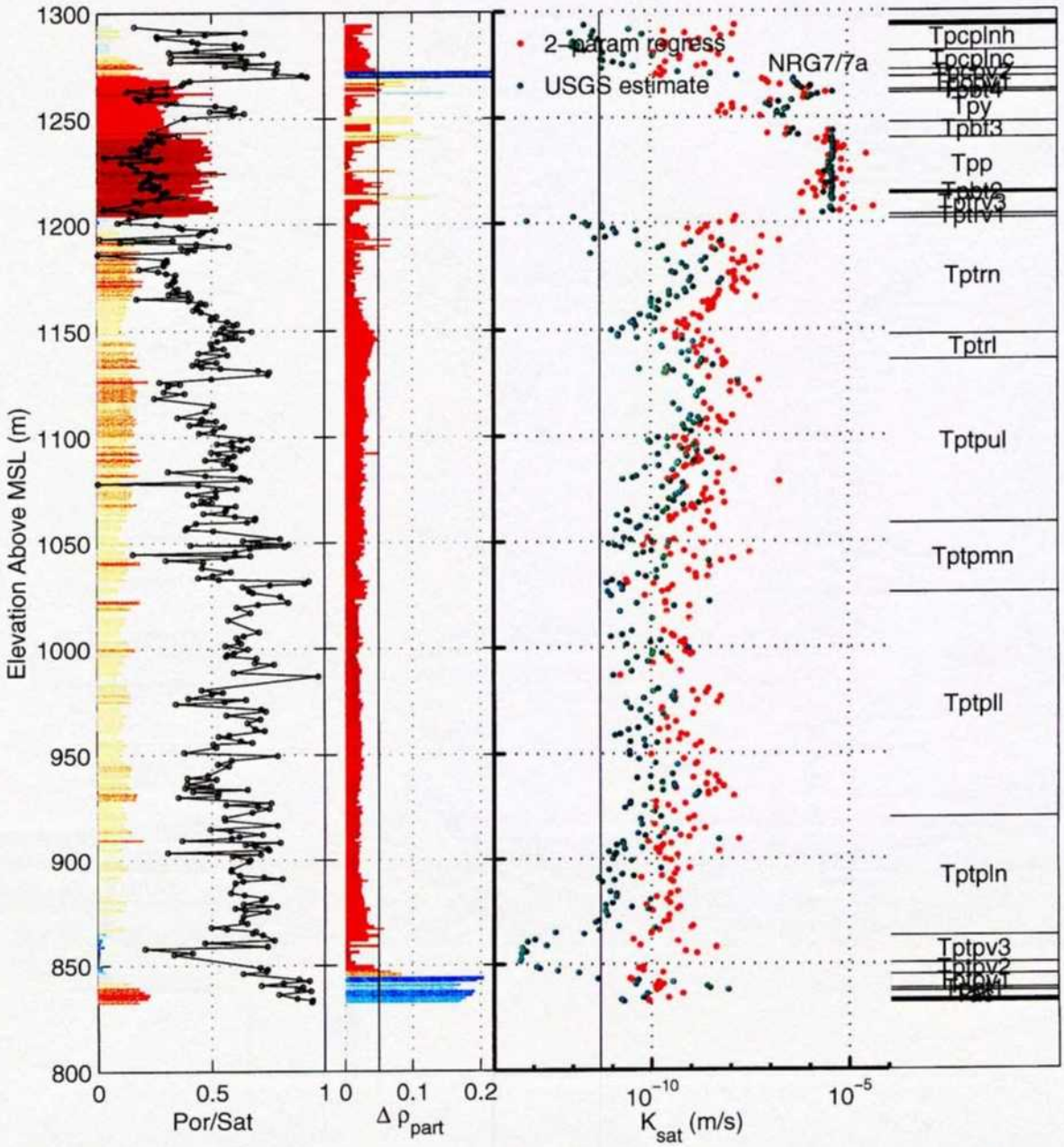

Figure 1-8: 9/9/97. **BHprofile_NRG77a_c.eps**. Porosity, saturation, change in particle density, and measured and estimated values for K_{sat} in borehole NRG7/7a.

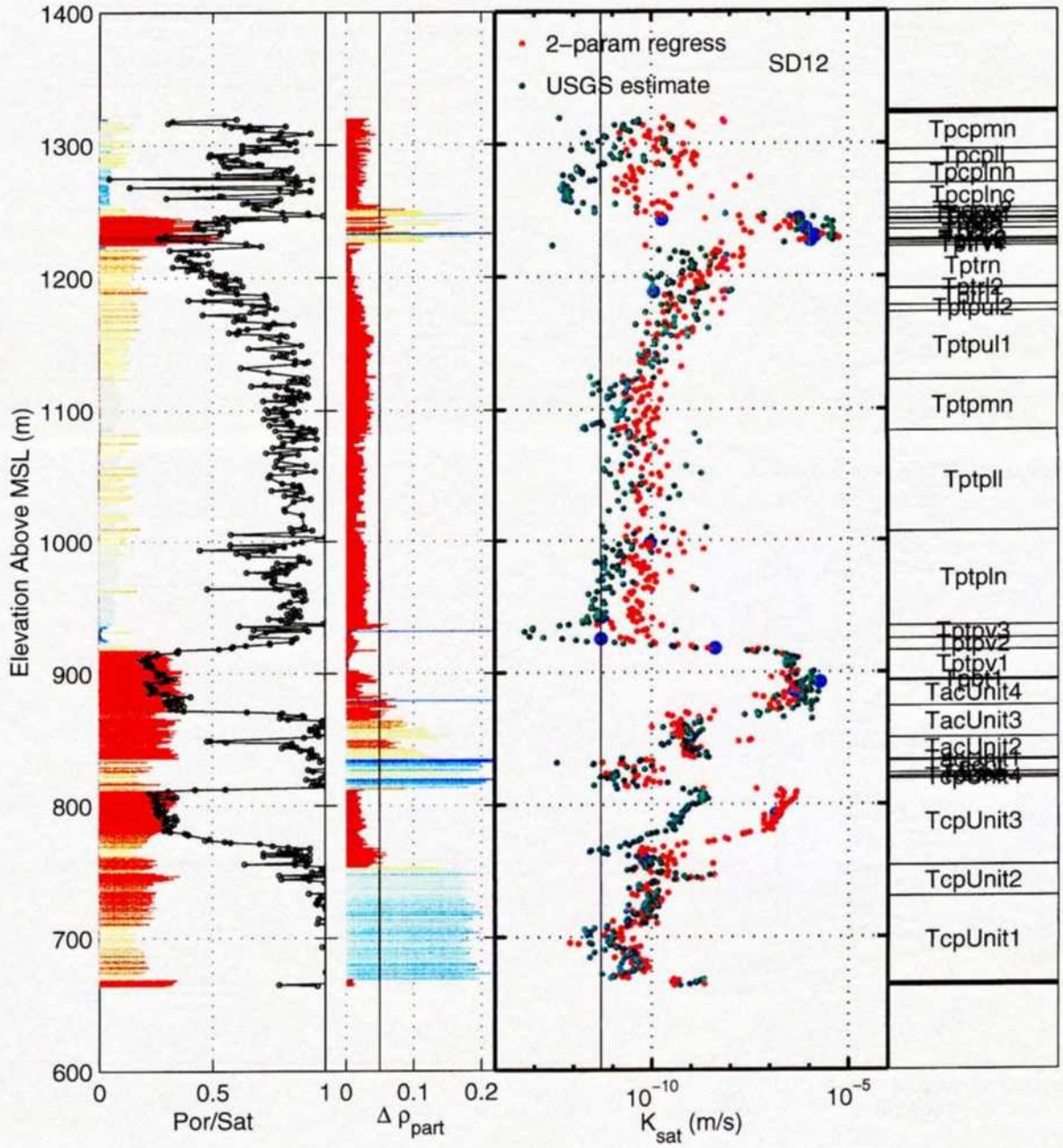

Figure 1-9: 9/9/97. **BHprofile_SD12_c.eps**. Porosity, saturation, change in particle density, and measured and estimated values for K_{sat} in borehole SD-12.

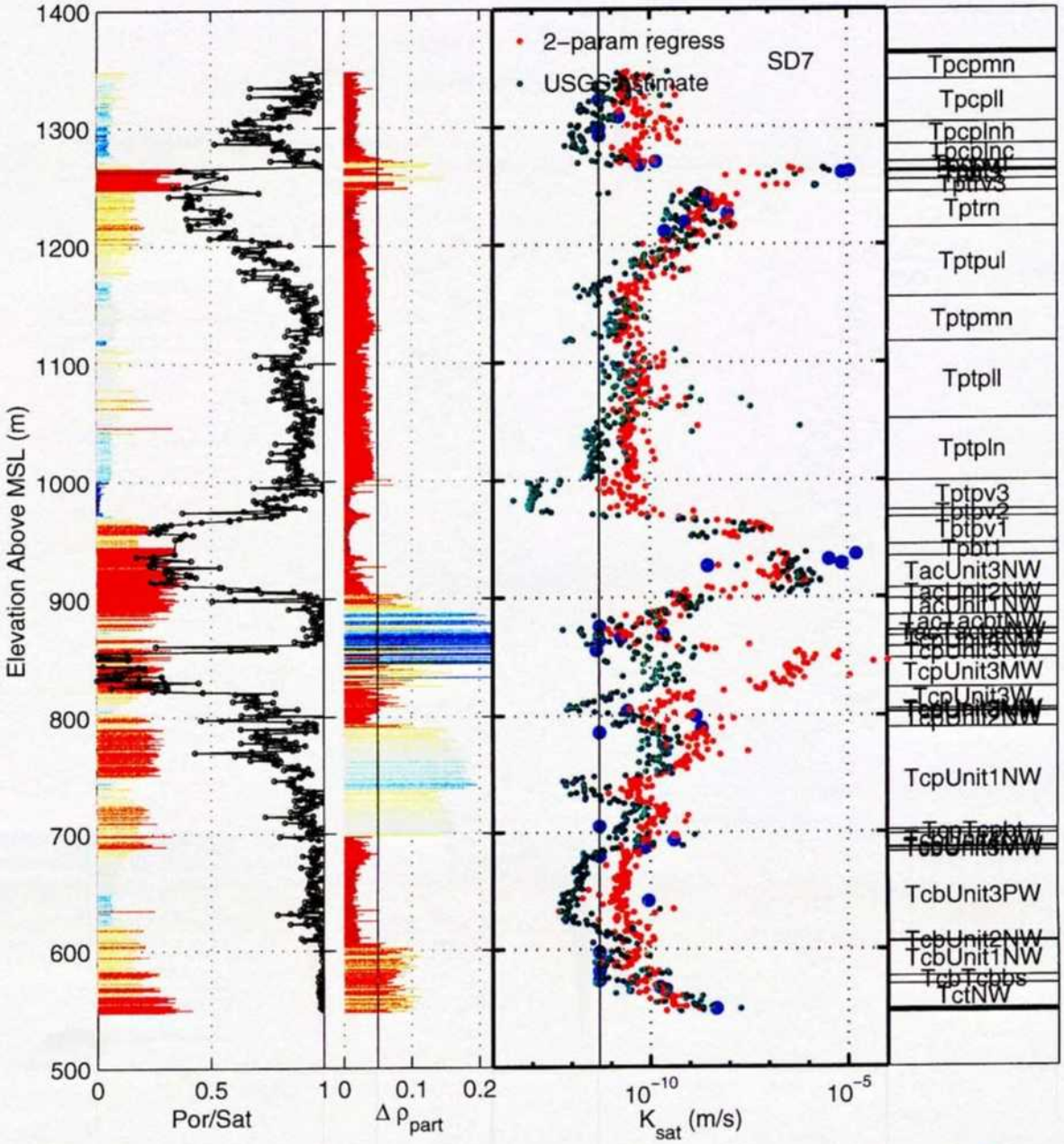

Figure 1-10: 9/9/97. **BHprofile_SD7_c.eps**. Porosity, saturation, change in particle density, and measured and estimated values for K_{sat} in borehole SD-7.

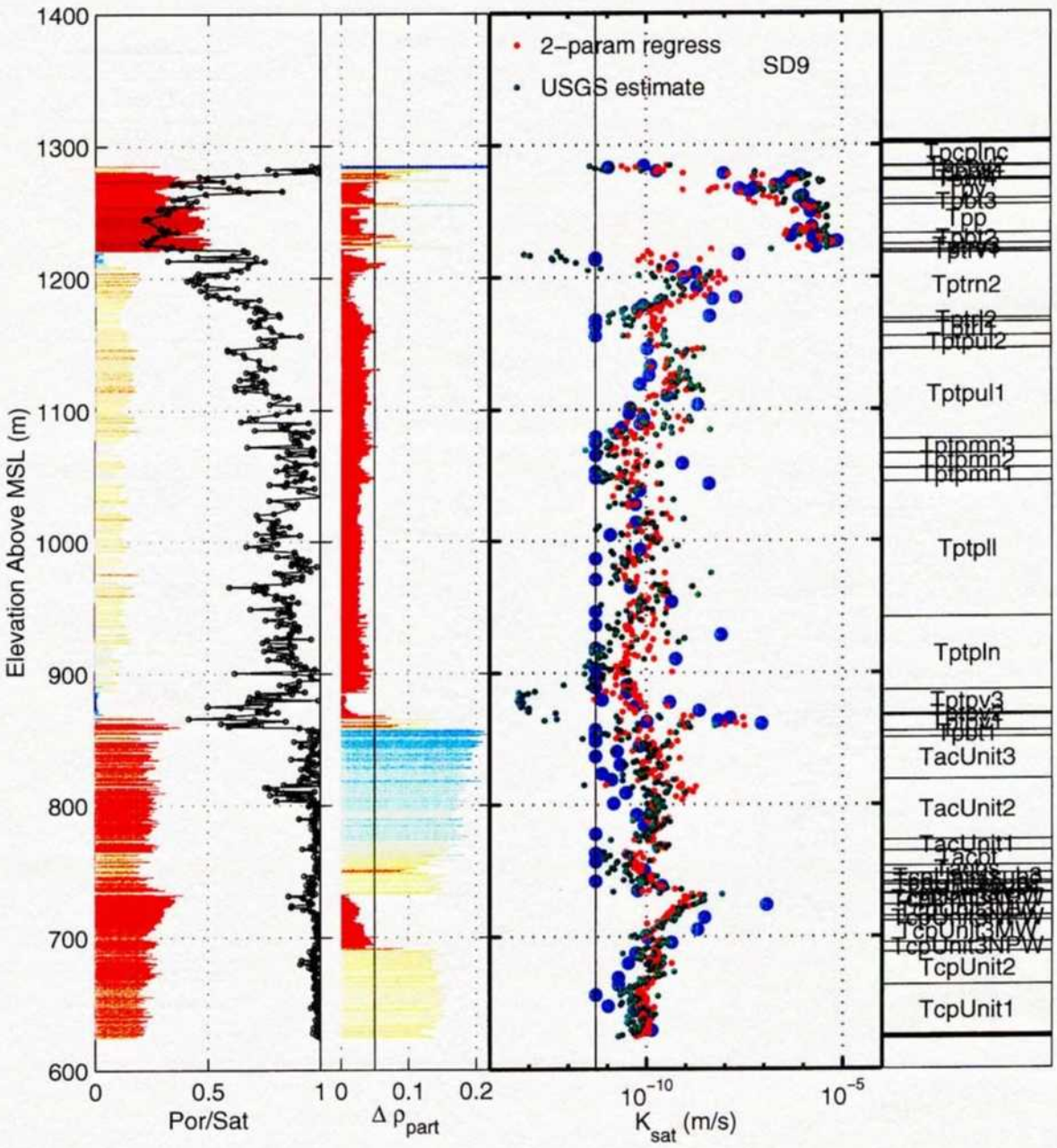

Figure 1-11: 9/9/97. **BHprofile_SD9_c.eps**. Porosity, saturation, change in particle density, and measured and estimated values for K_{sat} in borehole SD-9.

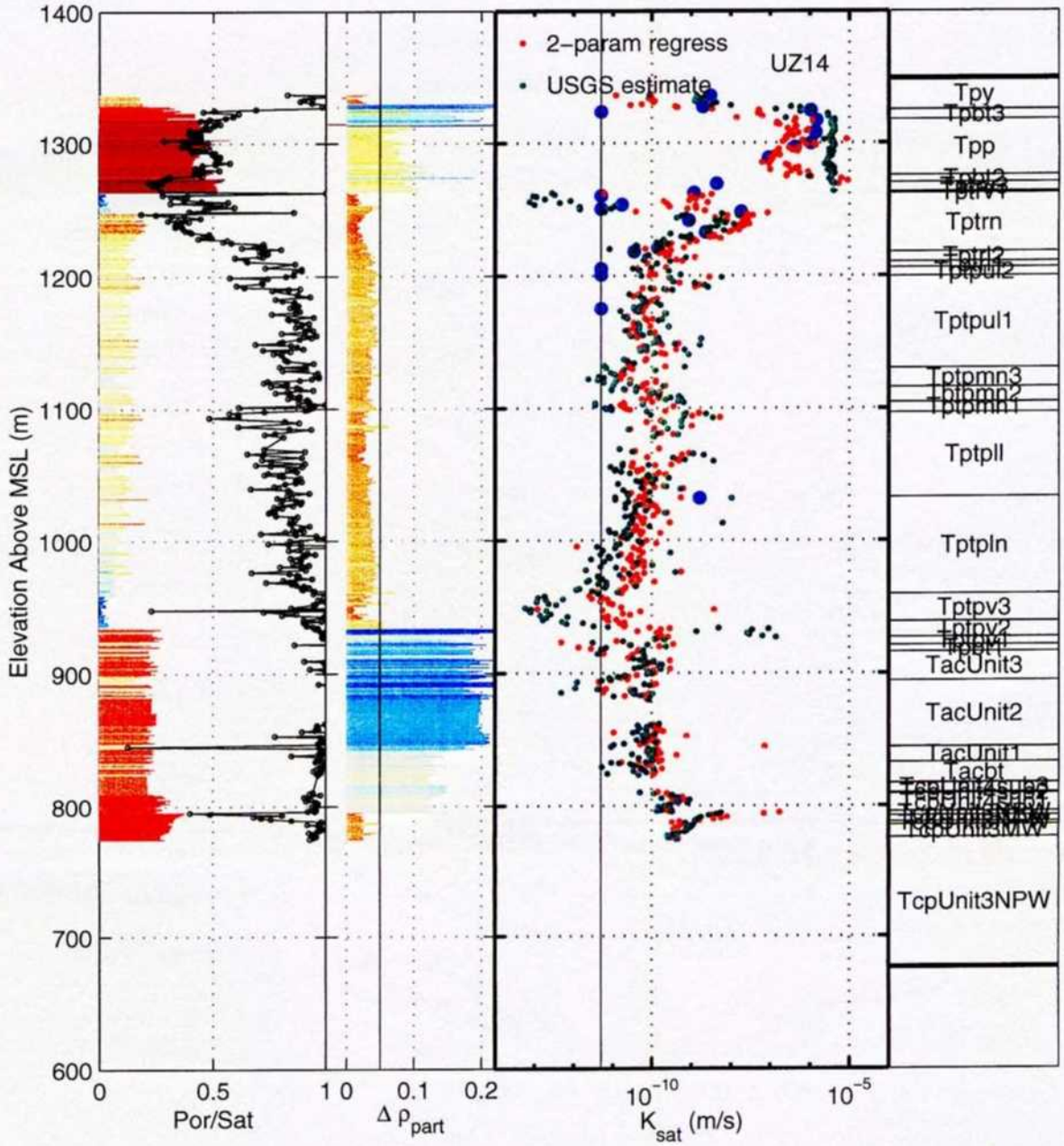

Figure 1-12: 9/9/97. **BHprofile_UZ14_c.eps**. Porosity, saturation, change in particle density, and measured and estimated values for K_{sat} in borehole UZ-14.

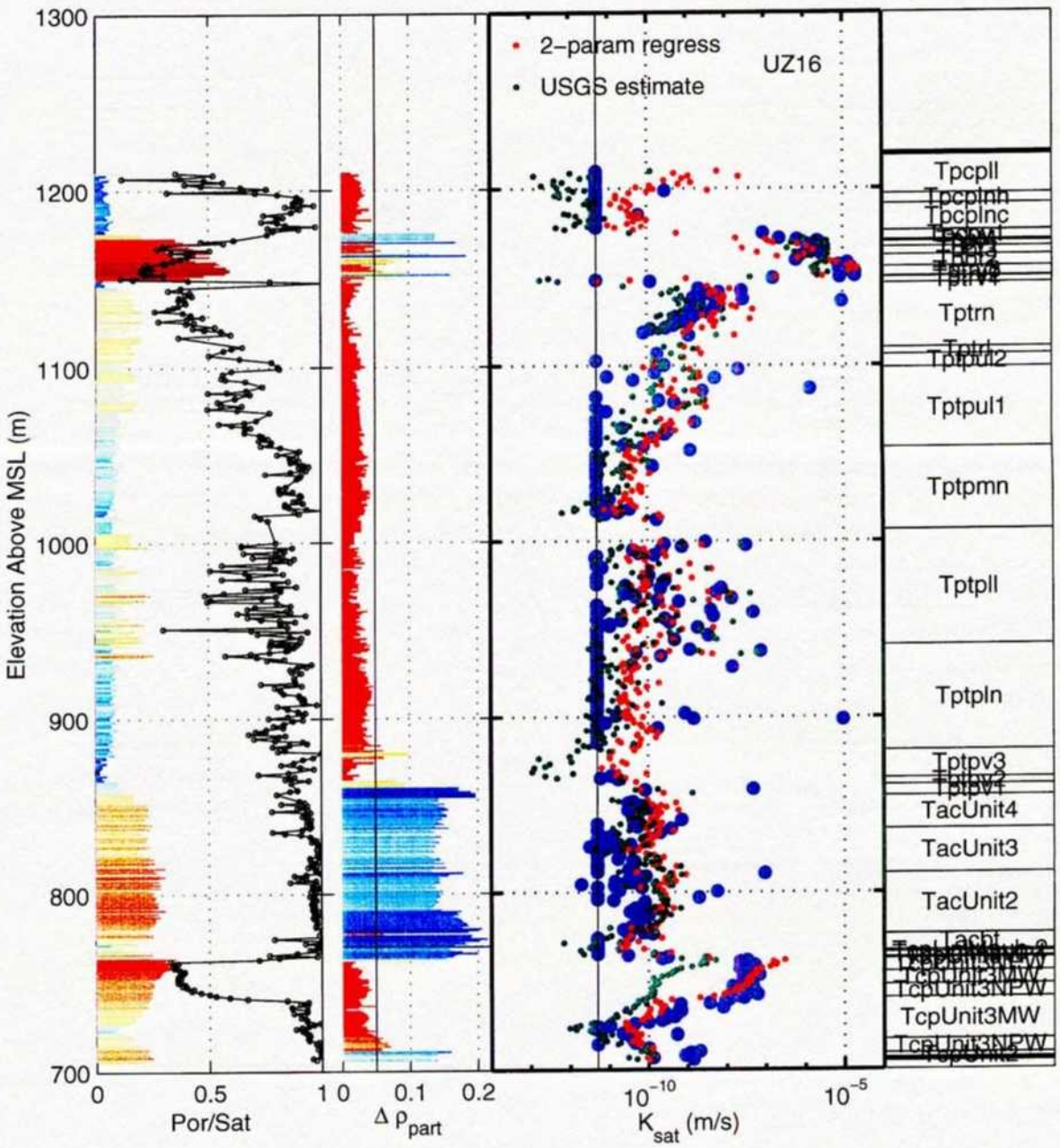

Figure 1-13: 9/9/97. **BHprofile_UZ16_c.eps**. Porosity, saturation, change in particle density, and measured and estimated values for K_{sat} in borehole UZ-16.

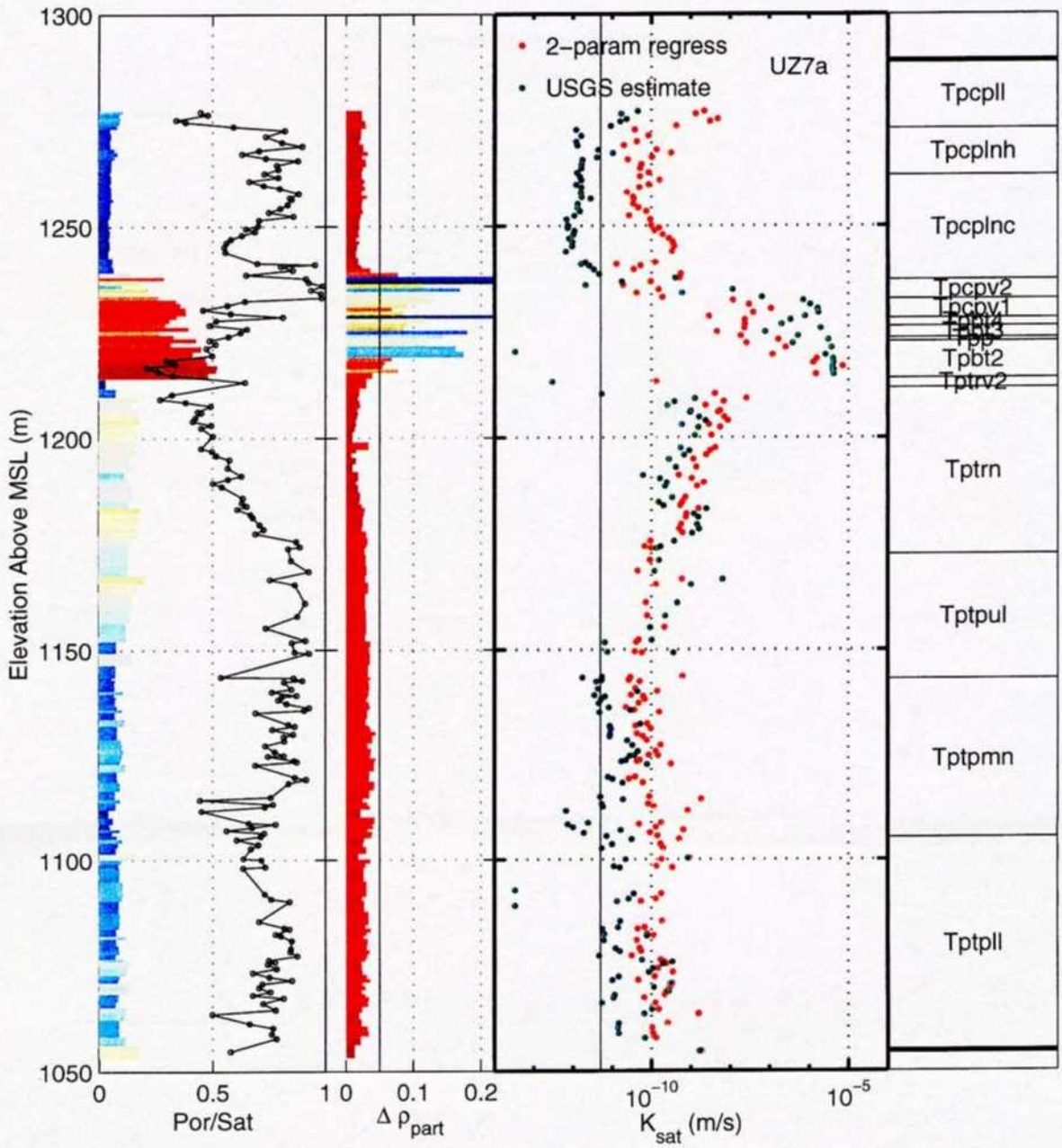

Figure 1-14: 9/9/97. **BHprofile_UZ7a_c.eps**. Porosity, saturation, change in particle density, and measured and estimated values for K_{sat} in borehole UZ-7a.

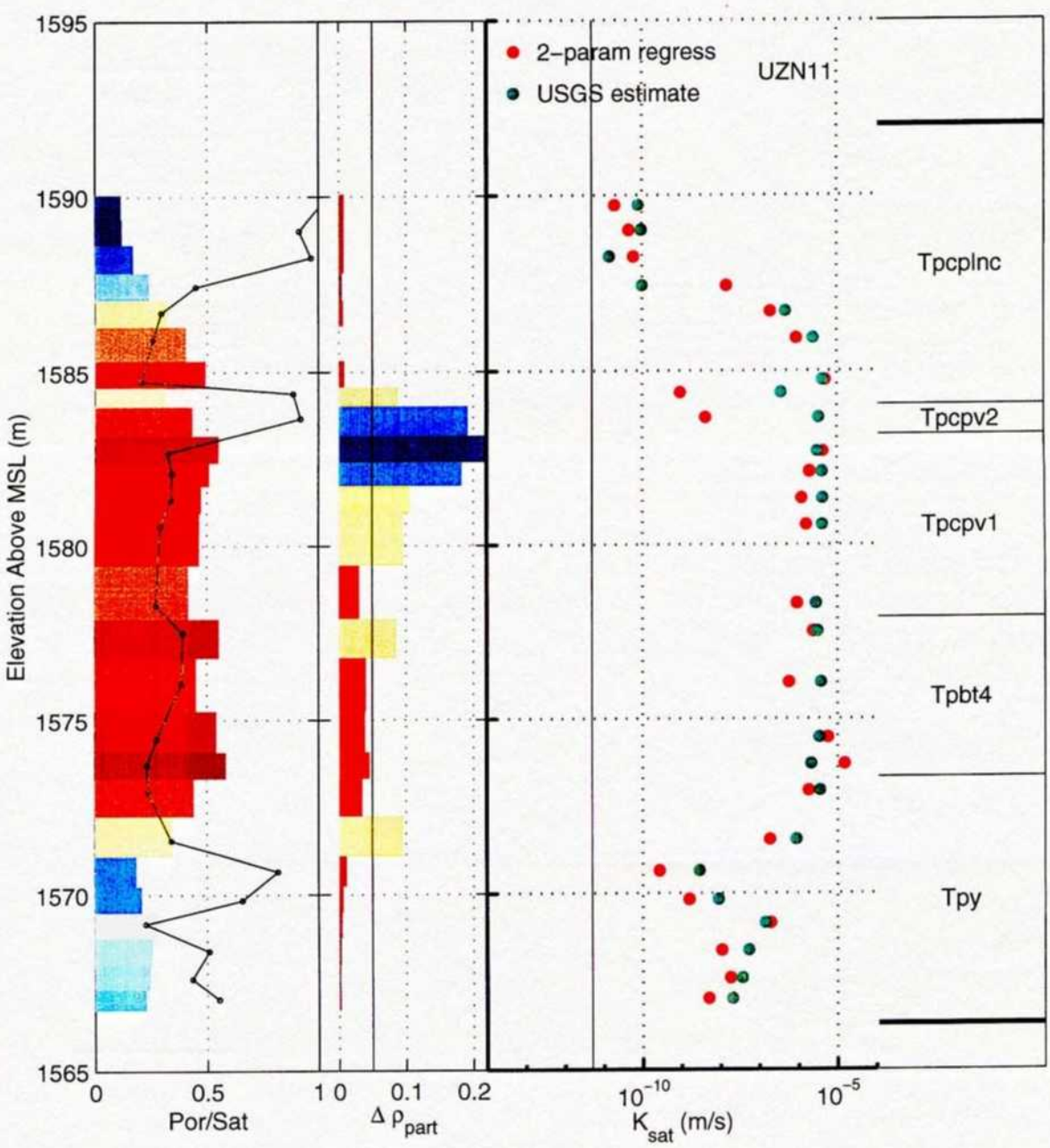

Figure 1-15: 9/9/97. **BHprofile_UZN11_c.eps**. Porosity, saturation, change in particle density, and measured and estimated values for K_{sat} in borehole N11.

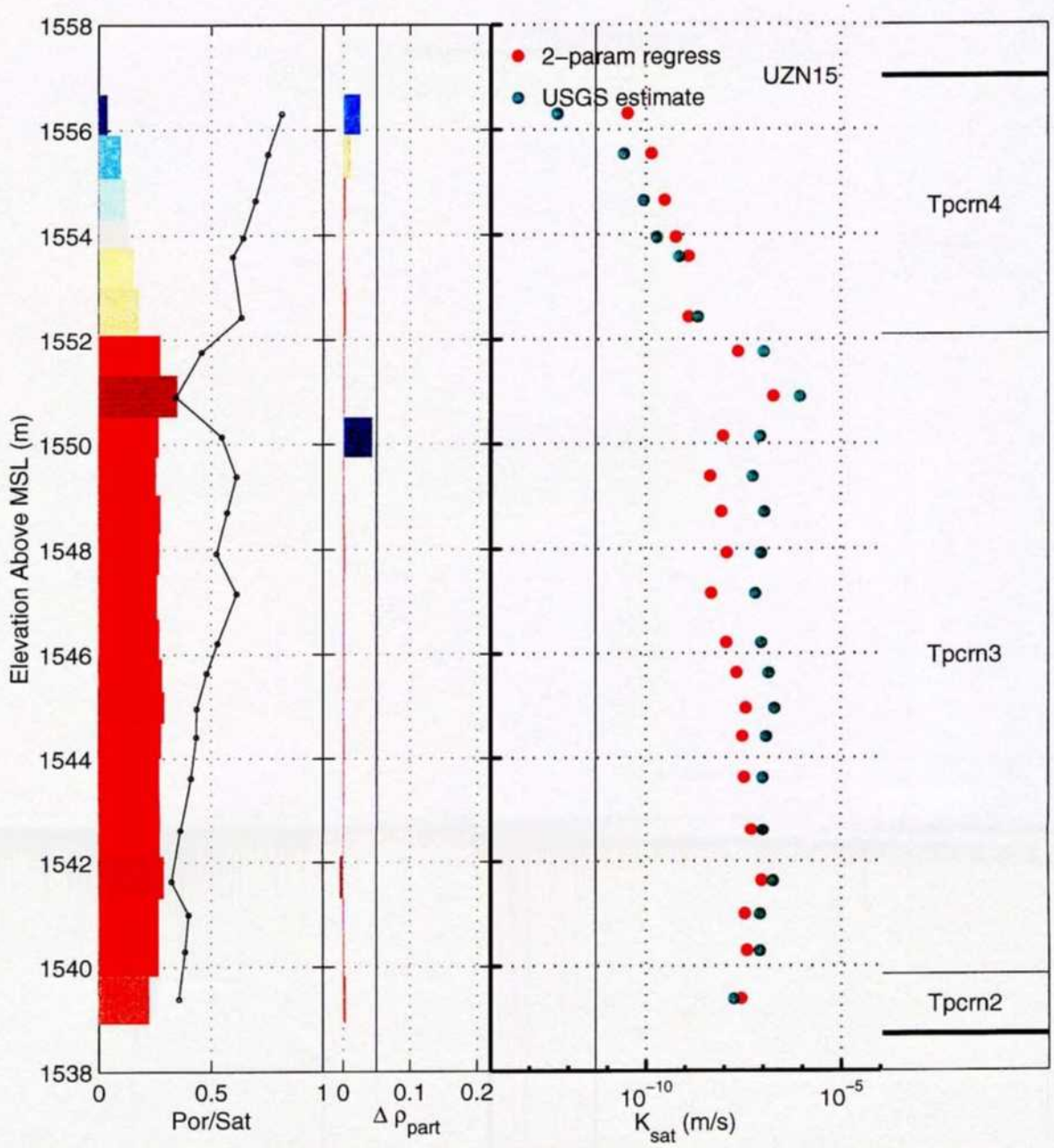

Figure 1-16: 9/9/97. **BHprofile_UZN15_c.eps**. Porosity, saturation, change in particle density, and measured and estimated values for K_{sat} in borehole N15.

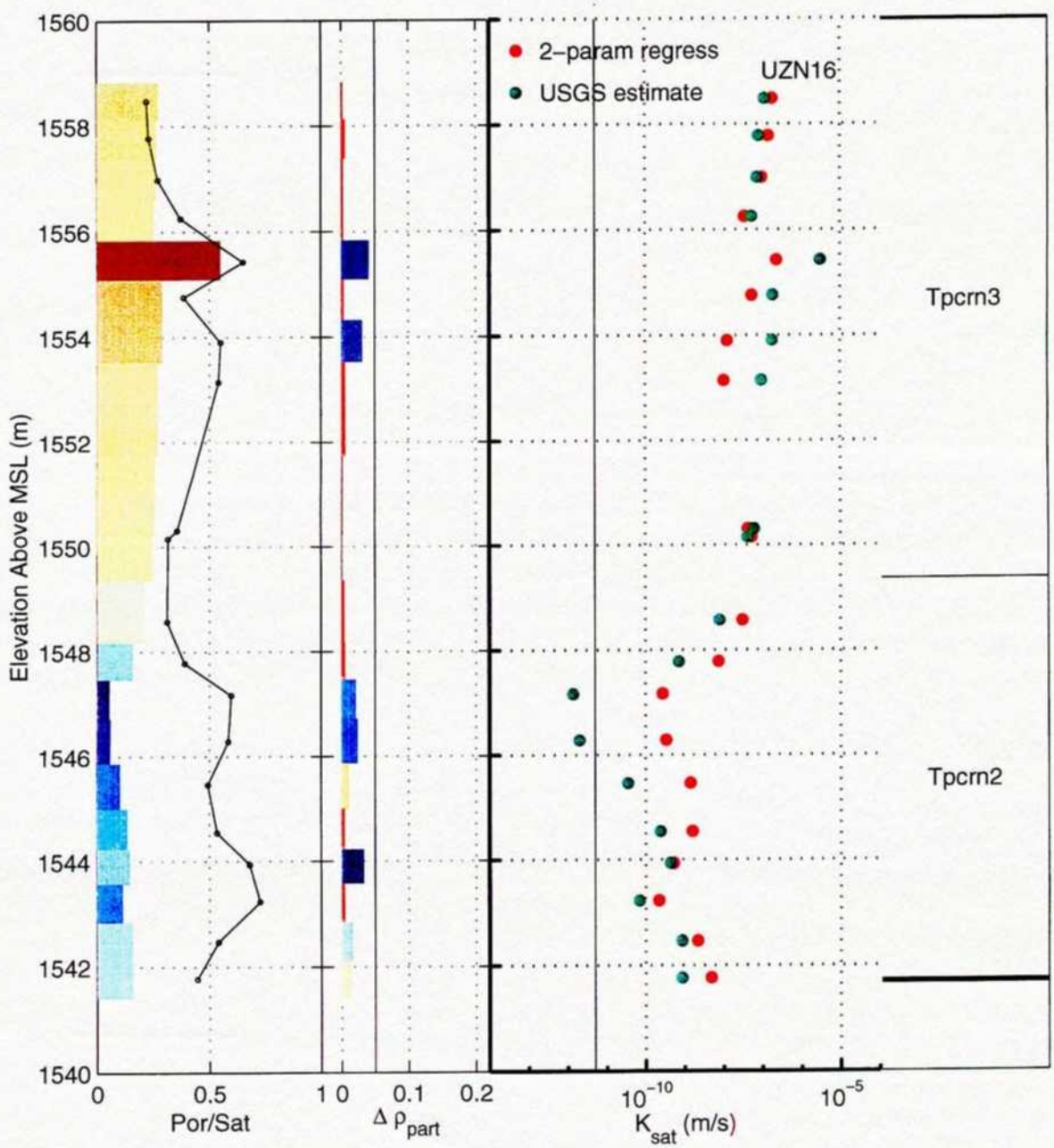

Figure 1-17: 9/9/97. **BHprofile_UZN16_c.eps**. Porosity, saturation, change in particle density, and measured and estimated values for K_{sat} in borehole N16.

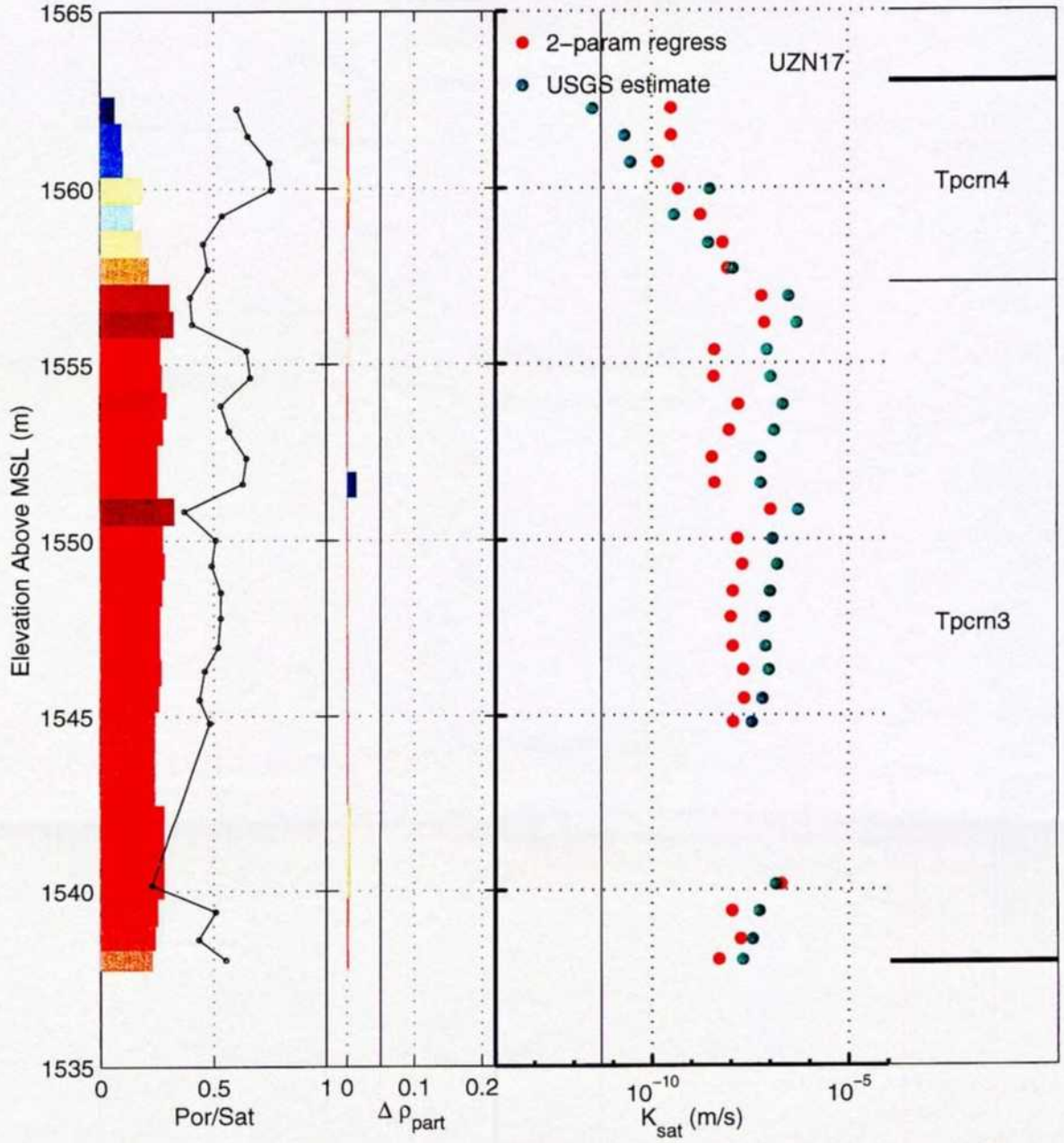

Figure 1-18: 9/9/97. **BHprofile_UZN17_c.eps**. Porosity, saturation, change in particle density, and measured and estimated values for K_{sat} in borehole N17.

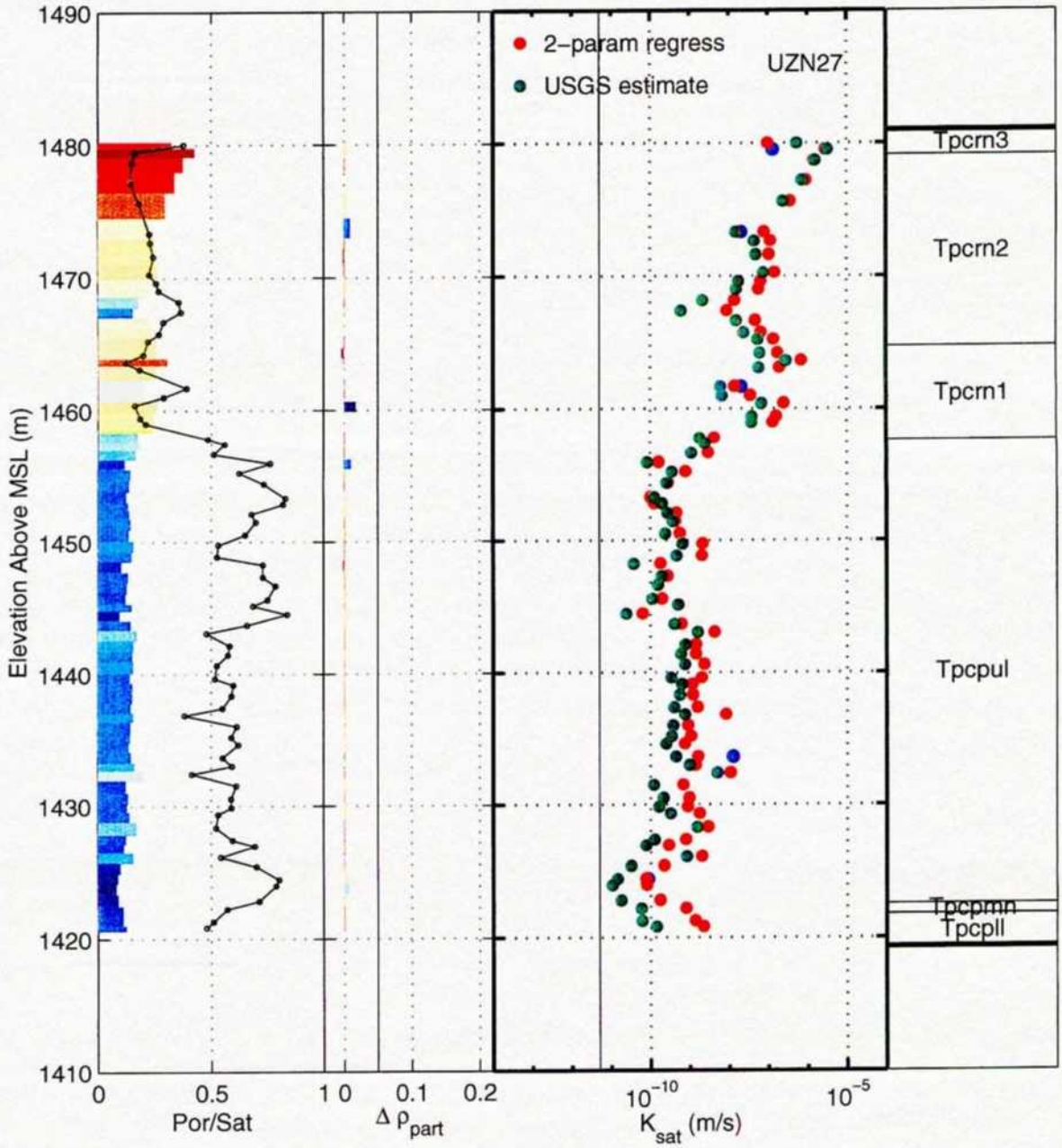

Figure 1-19: 9/9/97. **BHprofile_UZN27_c.eps**. Porosity, saturation, change in particle density, and measured and estimated values for K_{sat} in borehole N27.

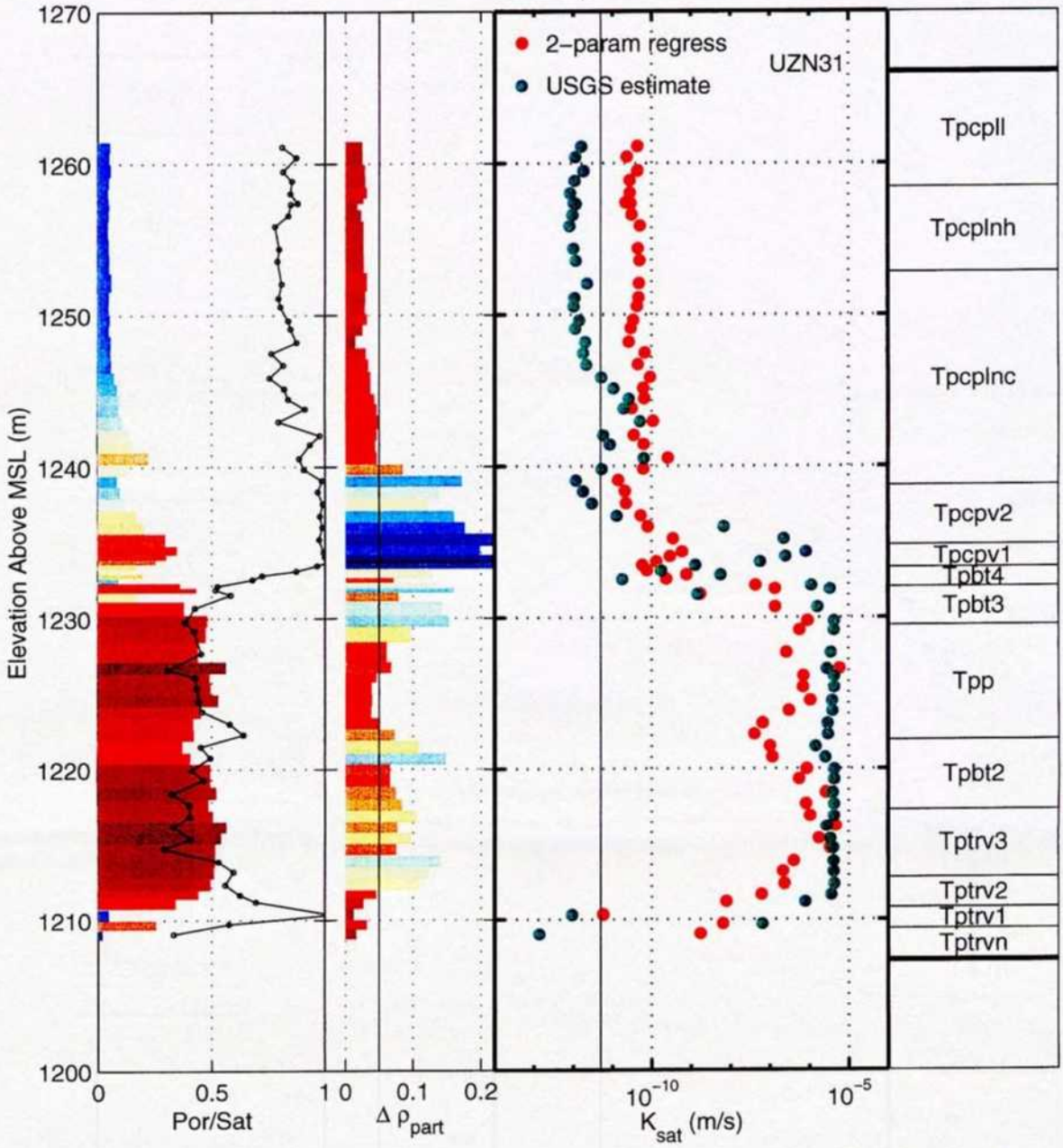

Figure 1-20: 9/9/97. **BHprofile_UZN31_c.eps**. Porosity, saturation, change in particle density, and measured and estimated values for K_{sat} in borehole N31.

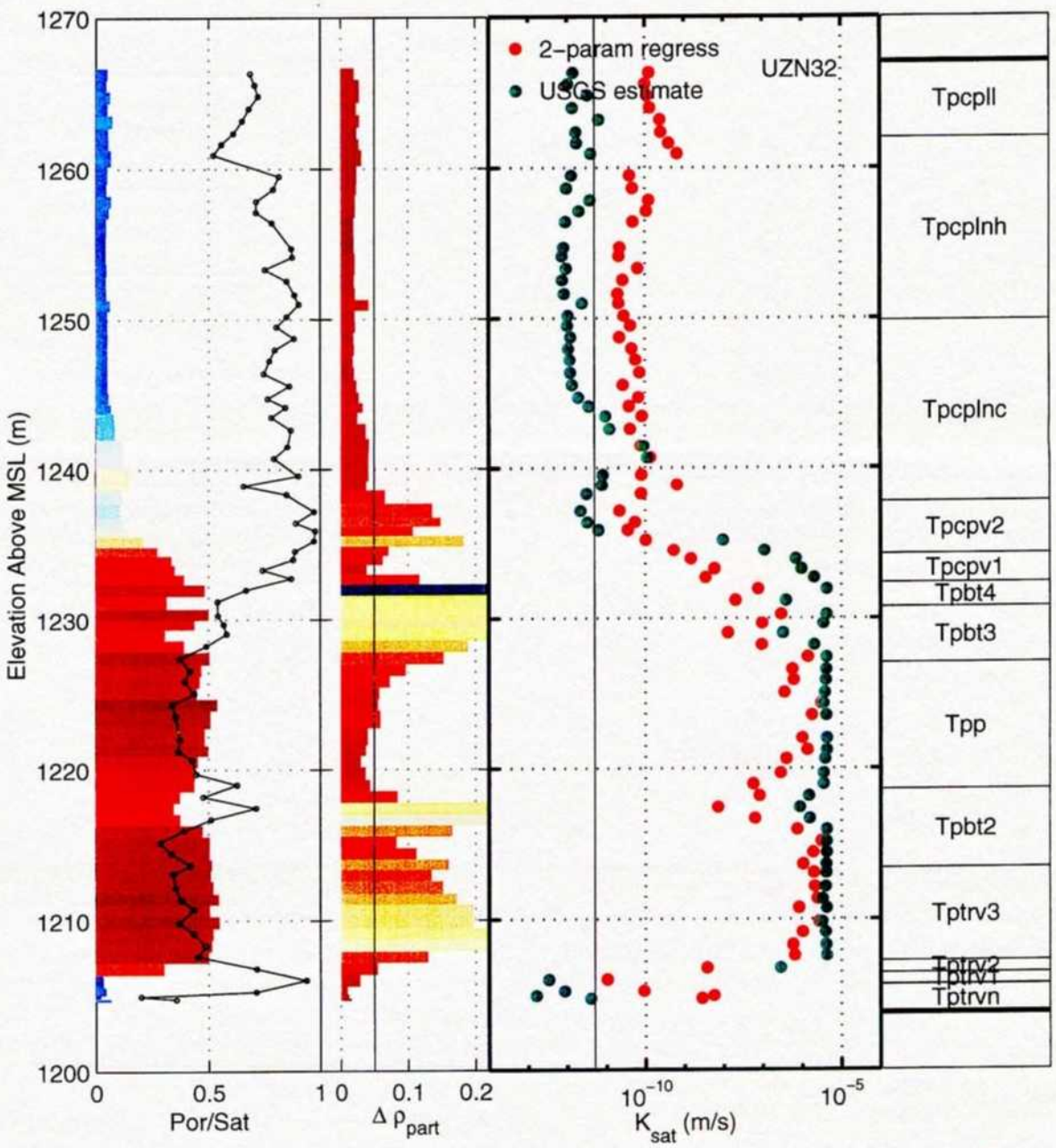

Figure 1-21: 9/9/97. **BHprofile_UZN32_c.eps**. Porosity, saturation, change in particle density, and measured and estimated values for K_{sat} in borehole N32.

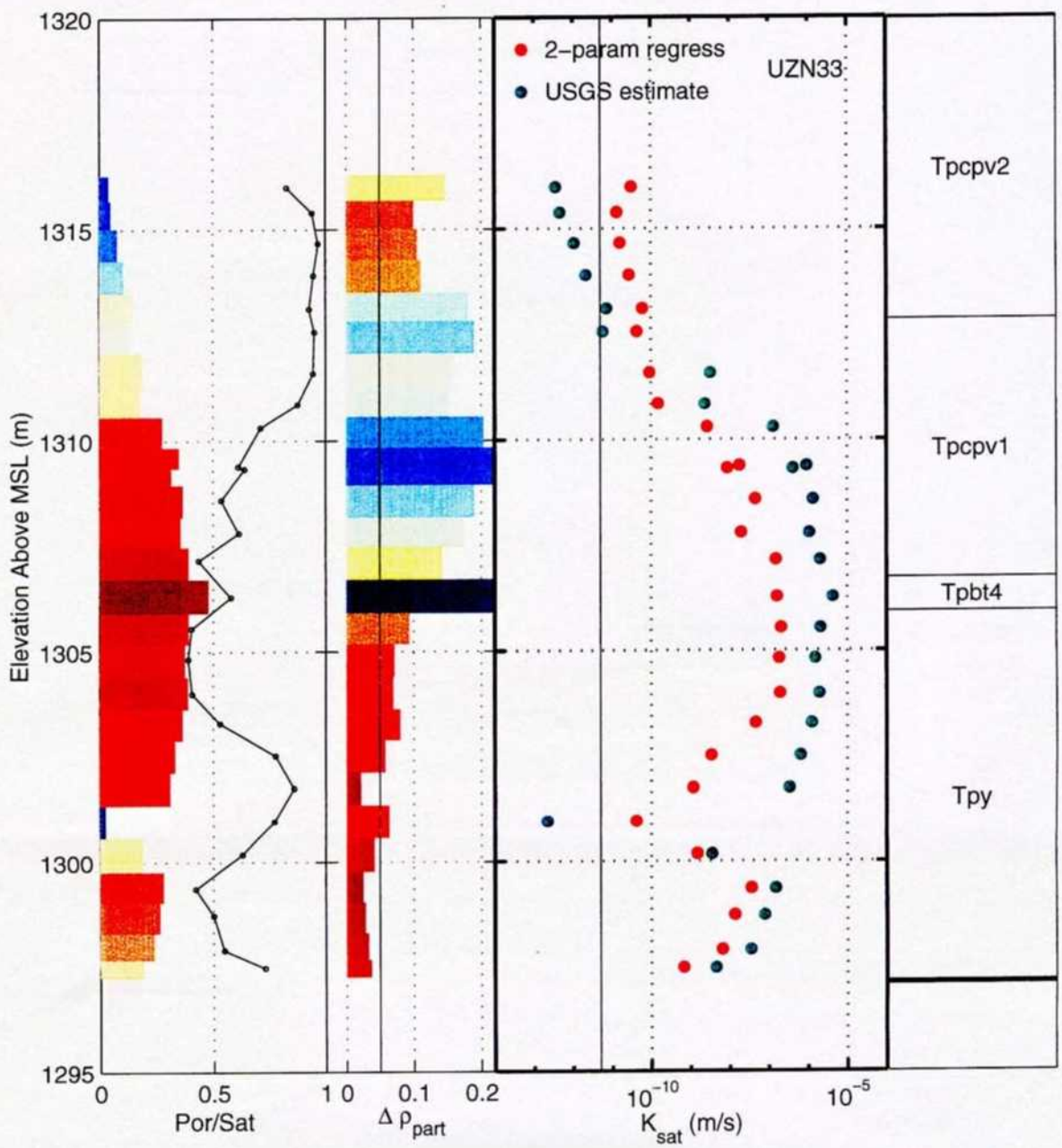

Figure 1-22: 9/9/97. **BHprofile_UZN33_c.eps**. Porosity, saturation, change in particle density, and measured and estimated values for K_{sat} in borehole N33.

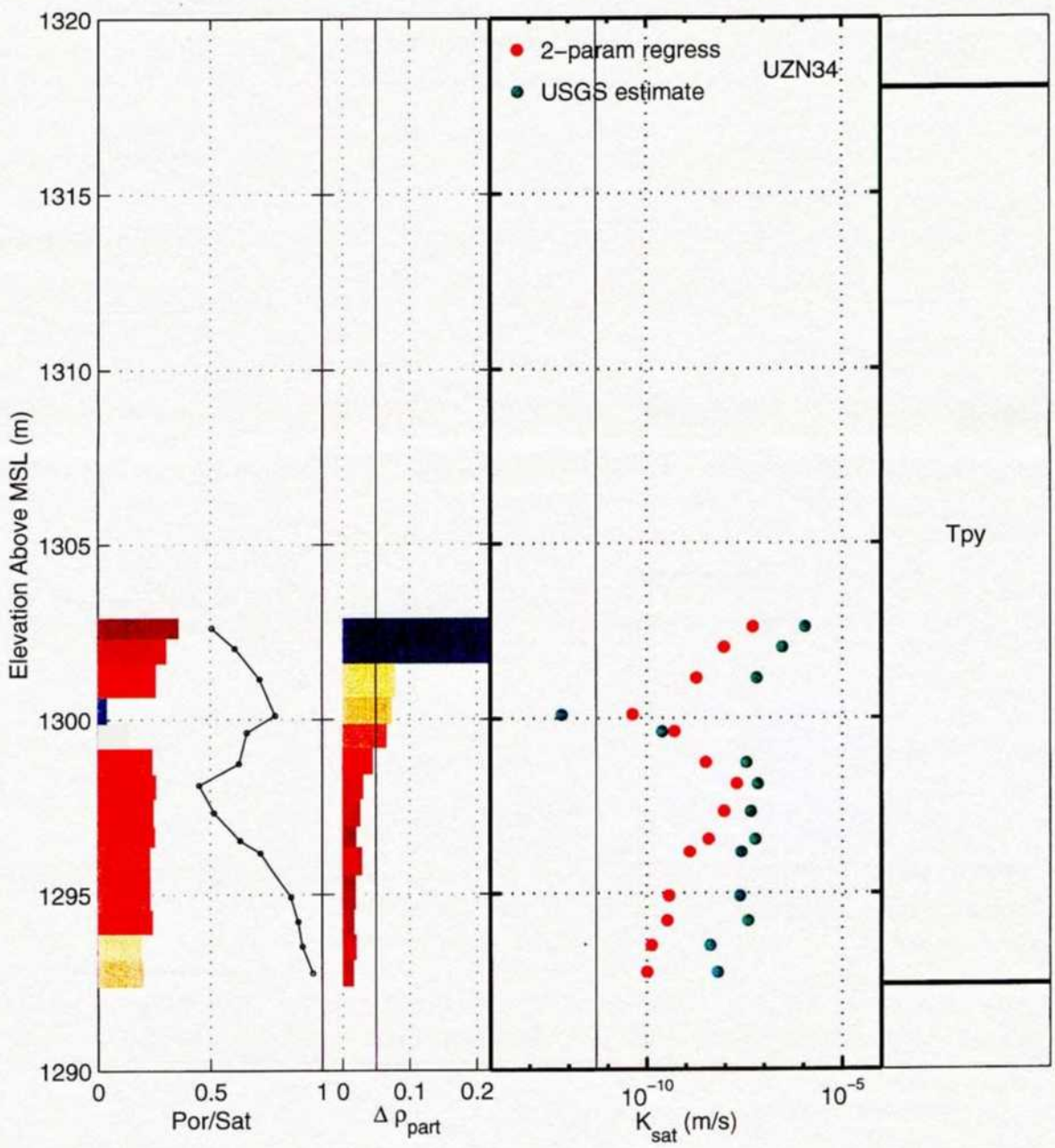

Figure 1-23: 9/9/97. **BHprofile_UZN34_c.eps**. Porosity, saturation, change in particle density, and measured and estimated values for K_{sat} in borehole N34.

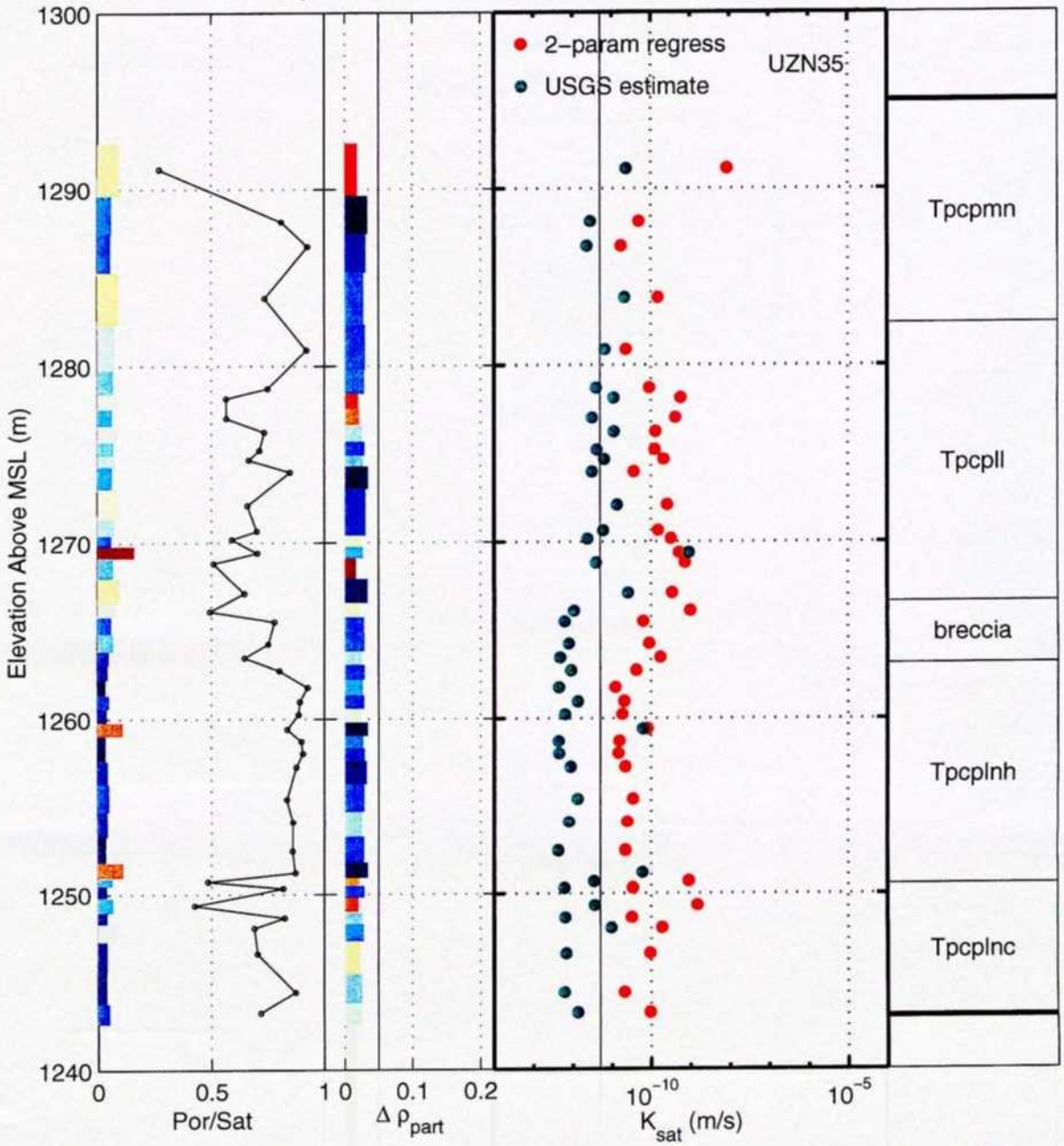

Figure 1-24: 9/9/97. **BHprofile_UZN35_c.eps**. Porosity, saturation, change in particle density, and measured and estimated values for K_{sat} in borehole N35.

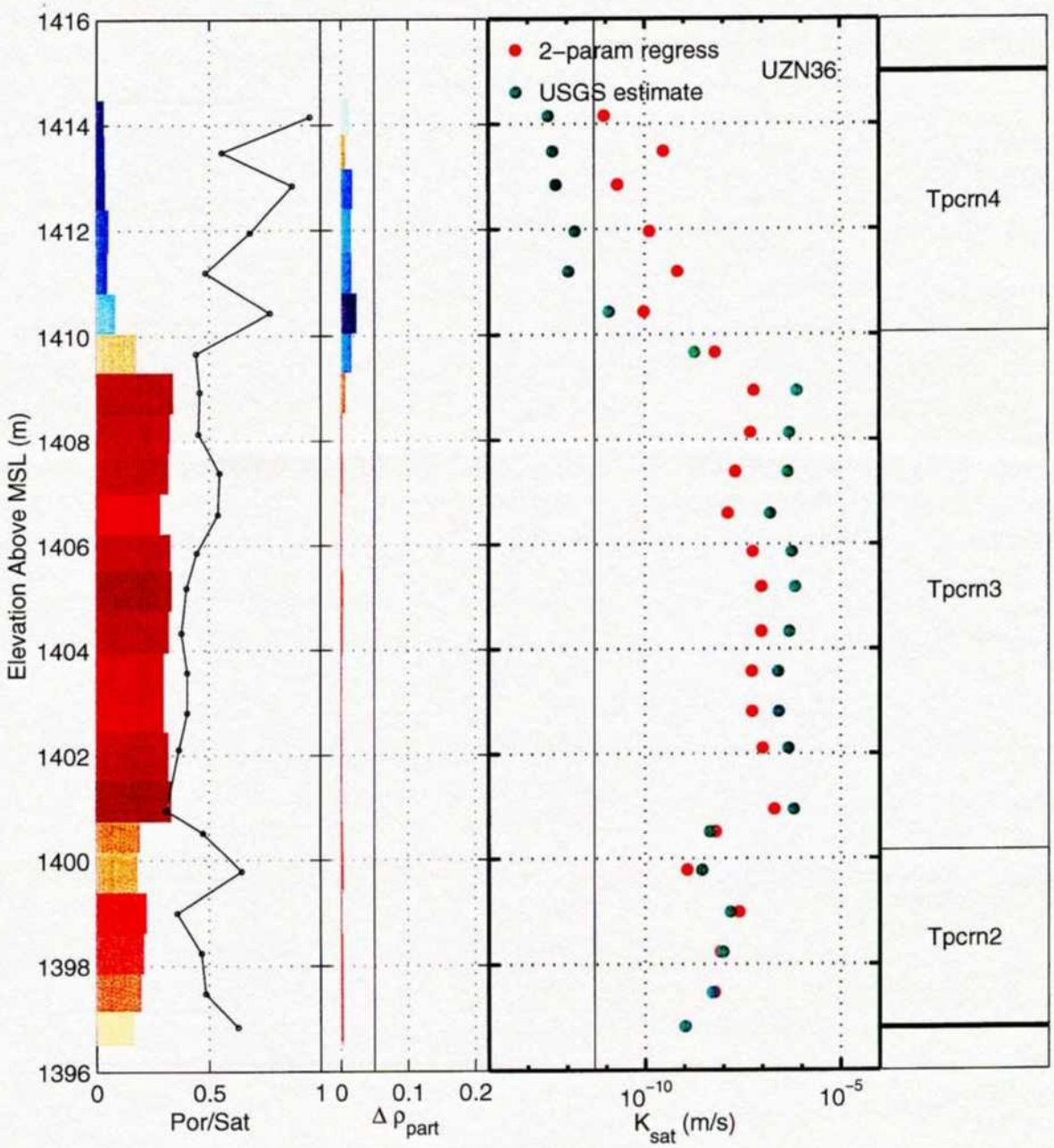

Figure 1-25: 9/9/97. **BHprofile_UZN36_c.eps**. Porosity, saturation, change in particle density, and measured and estimated values for K_{sat} in borehole N36.

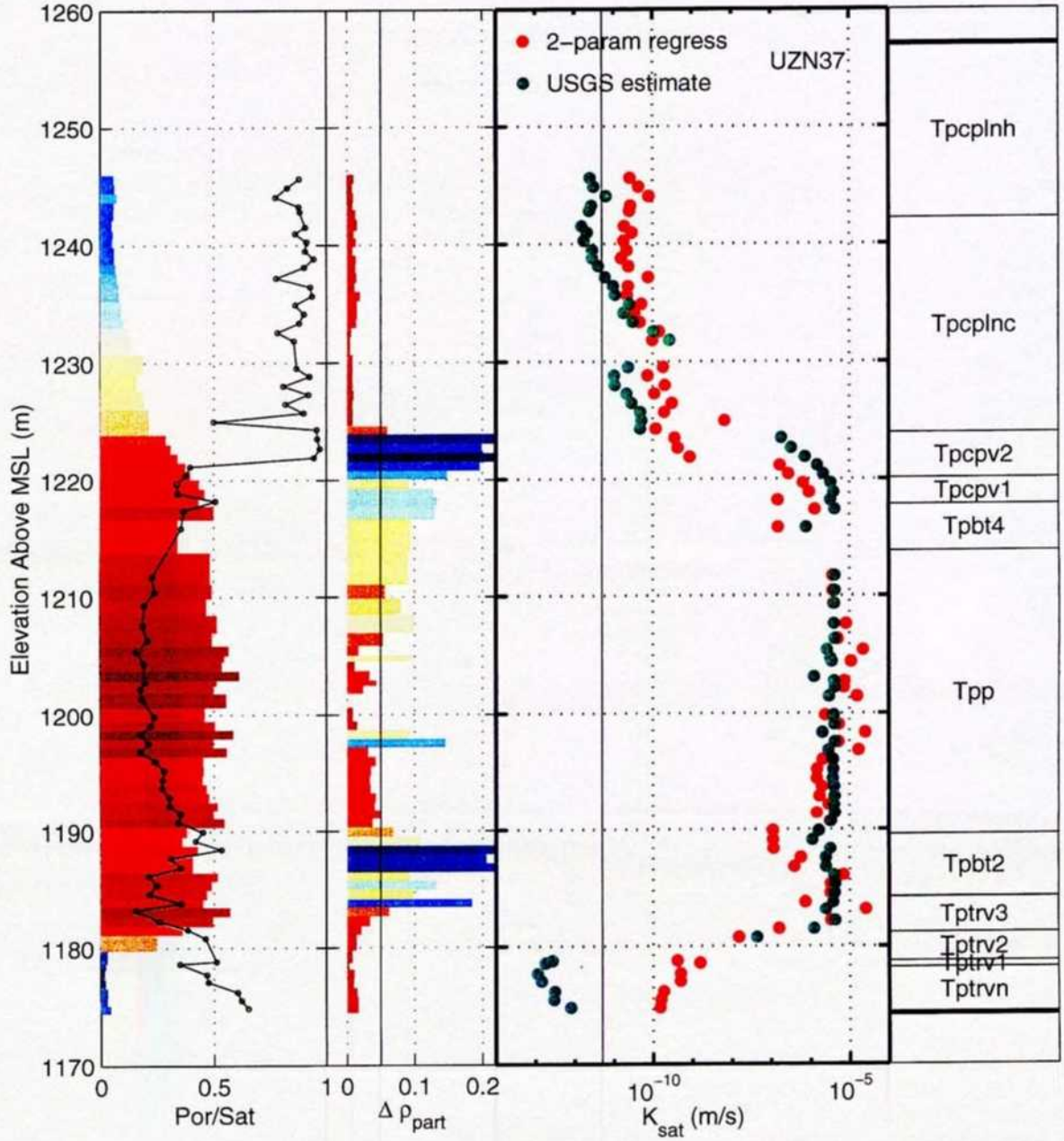

Figure 1-26: 9/9/97. **BHprofile_UZN37_c.eps**. Porosity, saturation, change in particle density, and measured and estimated values for K_{sat} in borehole N37.

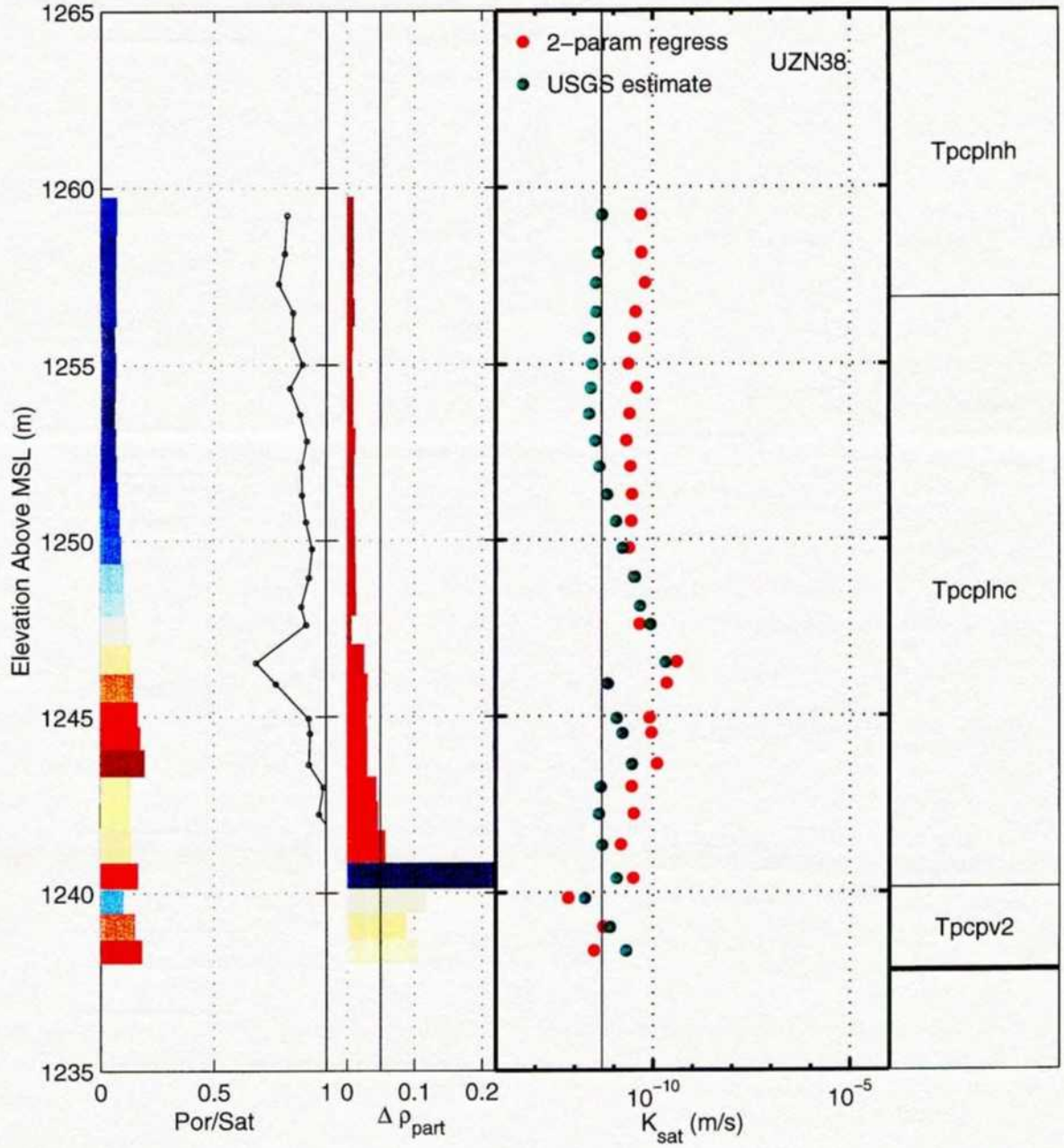

Figure 1-27: 9/9/97. **BHprofile_UZN38_c.eps.** Porosity, saturation, change in particle density, and measured and estimated values for K_{sat} in borehole N38.

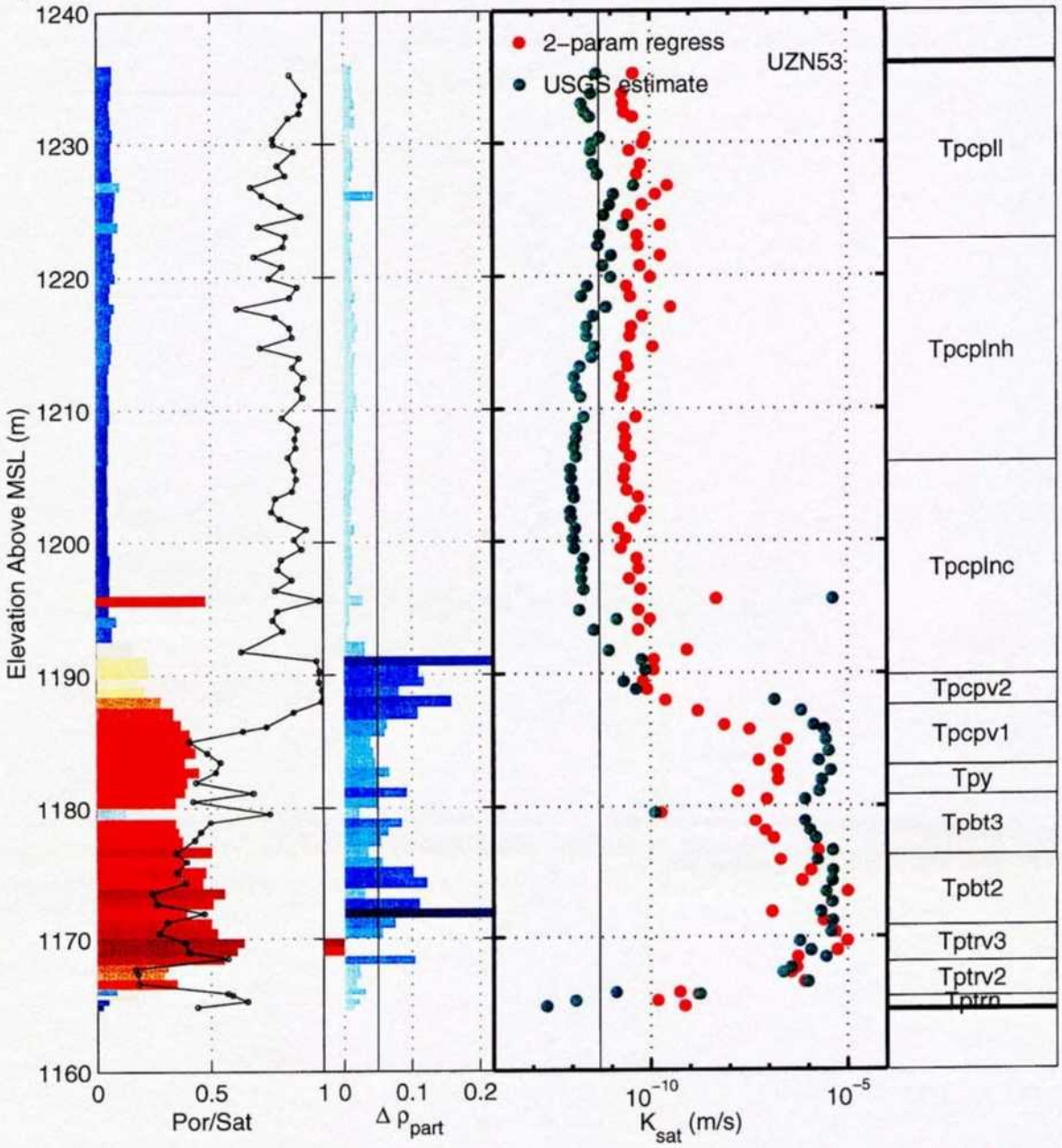

Figure 1-28: 9/9/97. **BHprofile_UZN53_c.eps**. Porosity, saturation, change in particle density, and measured and estimated values for K_{sat} in borehole N53.

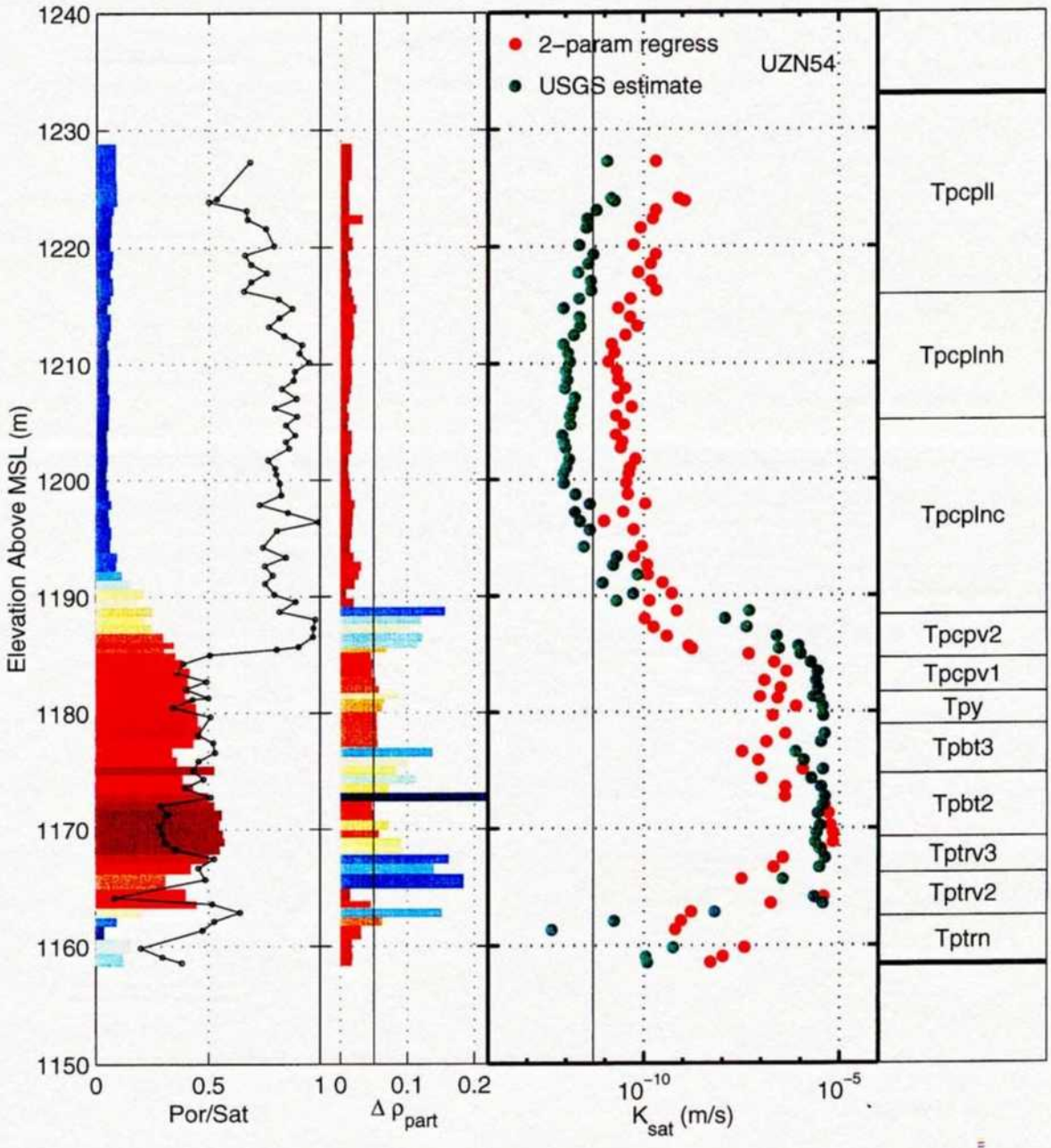

Figure 1-29: 9/9/97. **BHprofile_UZN54_c.eps**. Porosity, saturation, change in particle density, and measured and estimated values for K_{sat} in borehole N54.

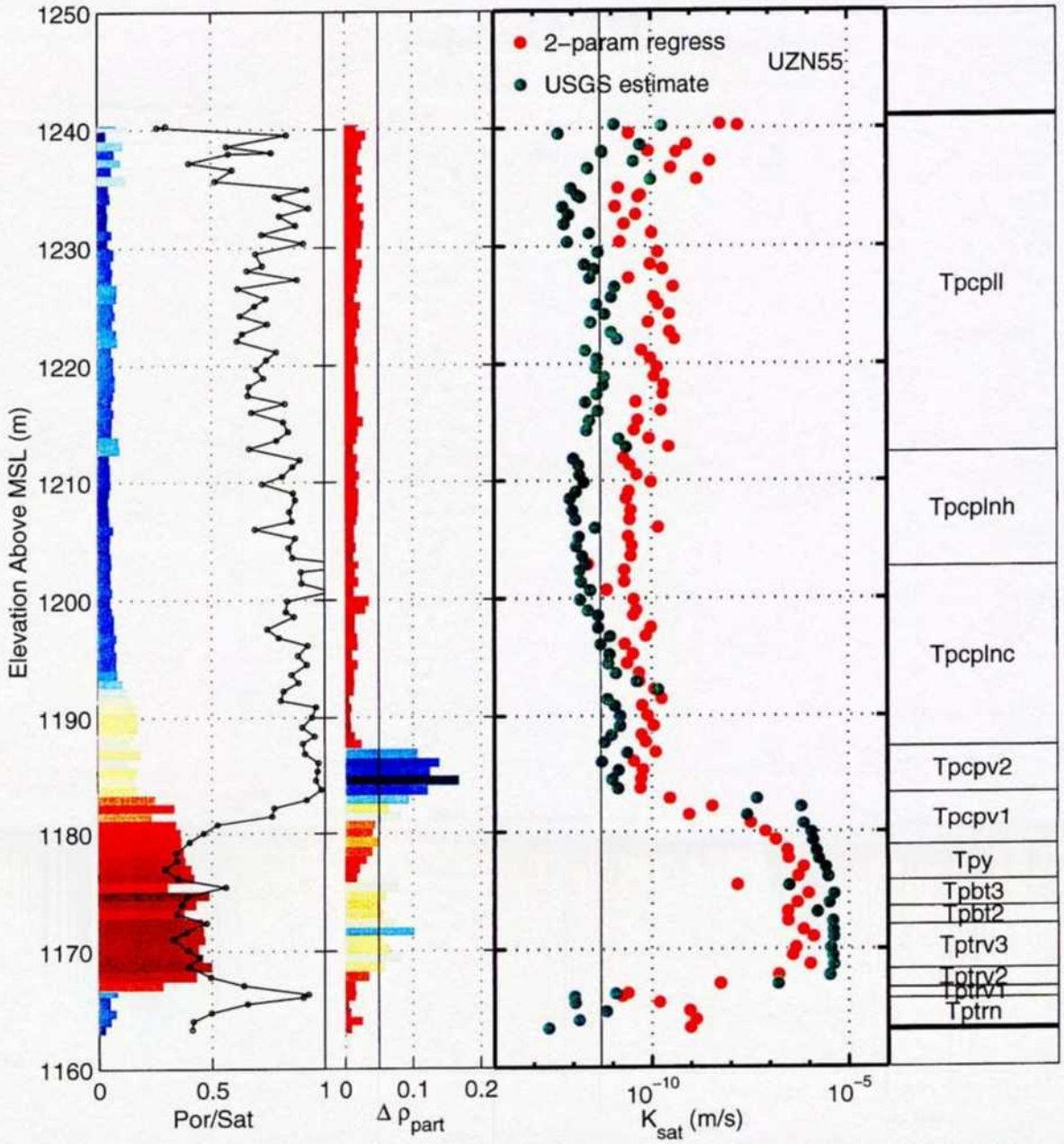

Figure 1-30: 9/9/97. **BHprofile_UZN55_c.eps**. Porosity, saturation, change in particle density, and measured and estimated values for K_{sat} in borehole N55.

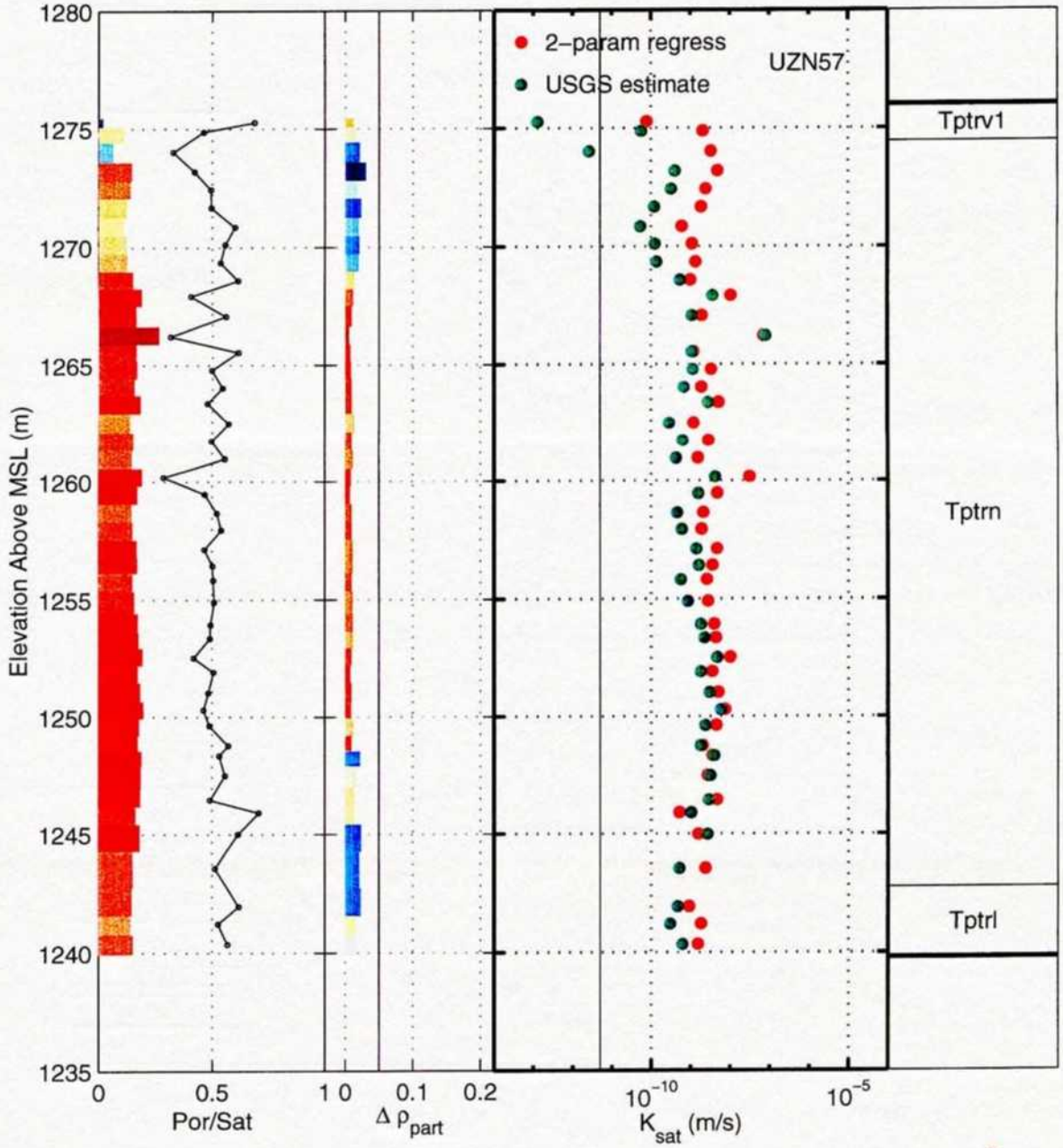

Figure 1-31: 9/9/97. **BHprofile_UZN57_c.eps**. Porosity, saturation, change in particle density, and measured and estimated values for K_{sat} in borehole N57.

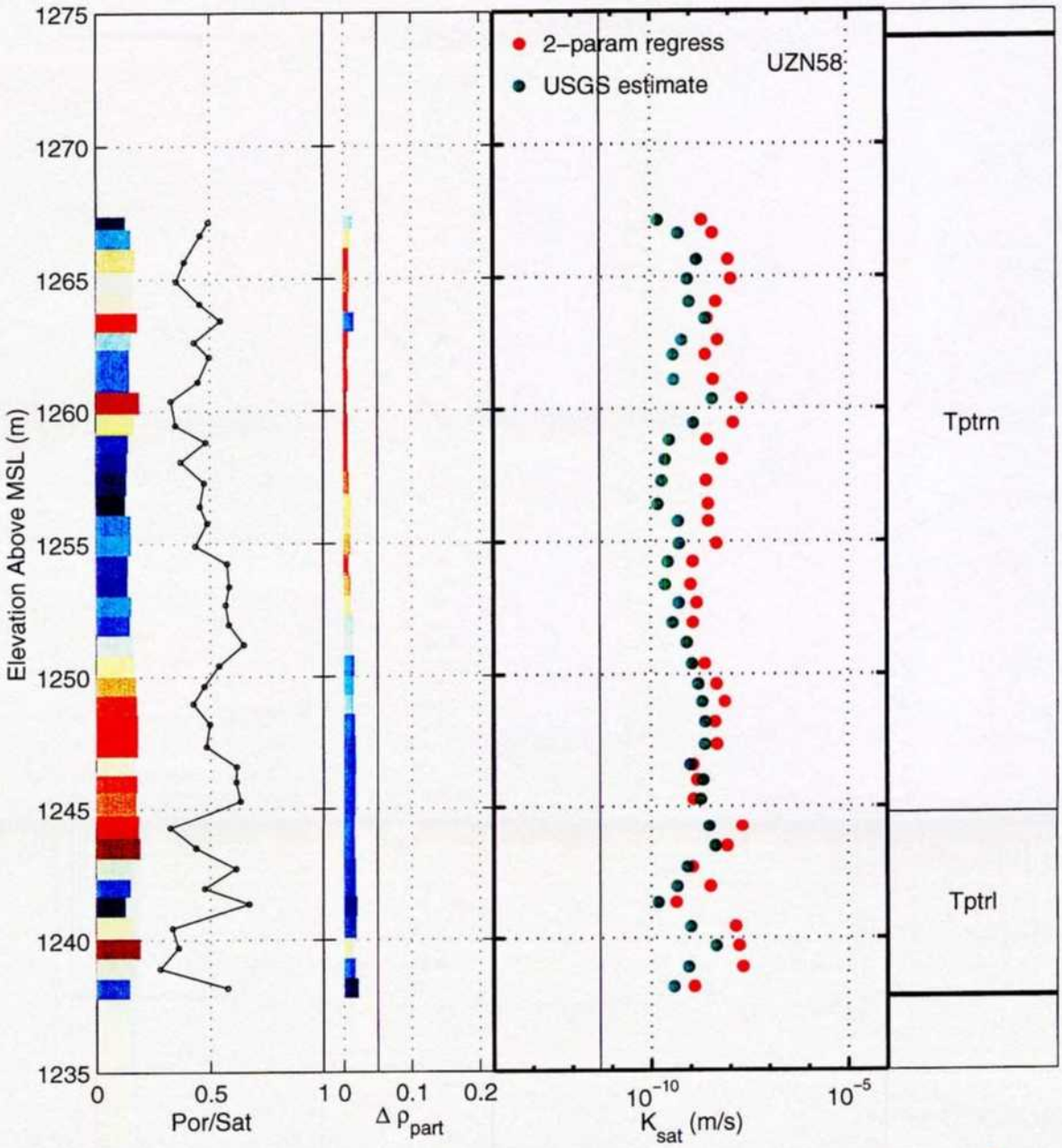

Figure 1-32: 9/9/97. **BHprofile_UZN58_c.eps**. Porosity, saturation, change in particle density, and measured and estimated values for K_{sat} in borehole N58.

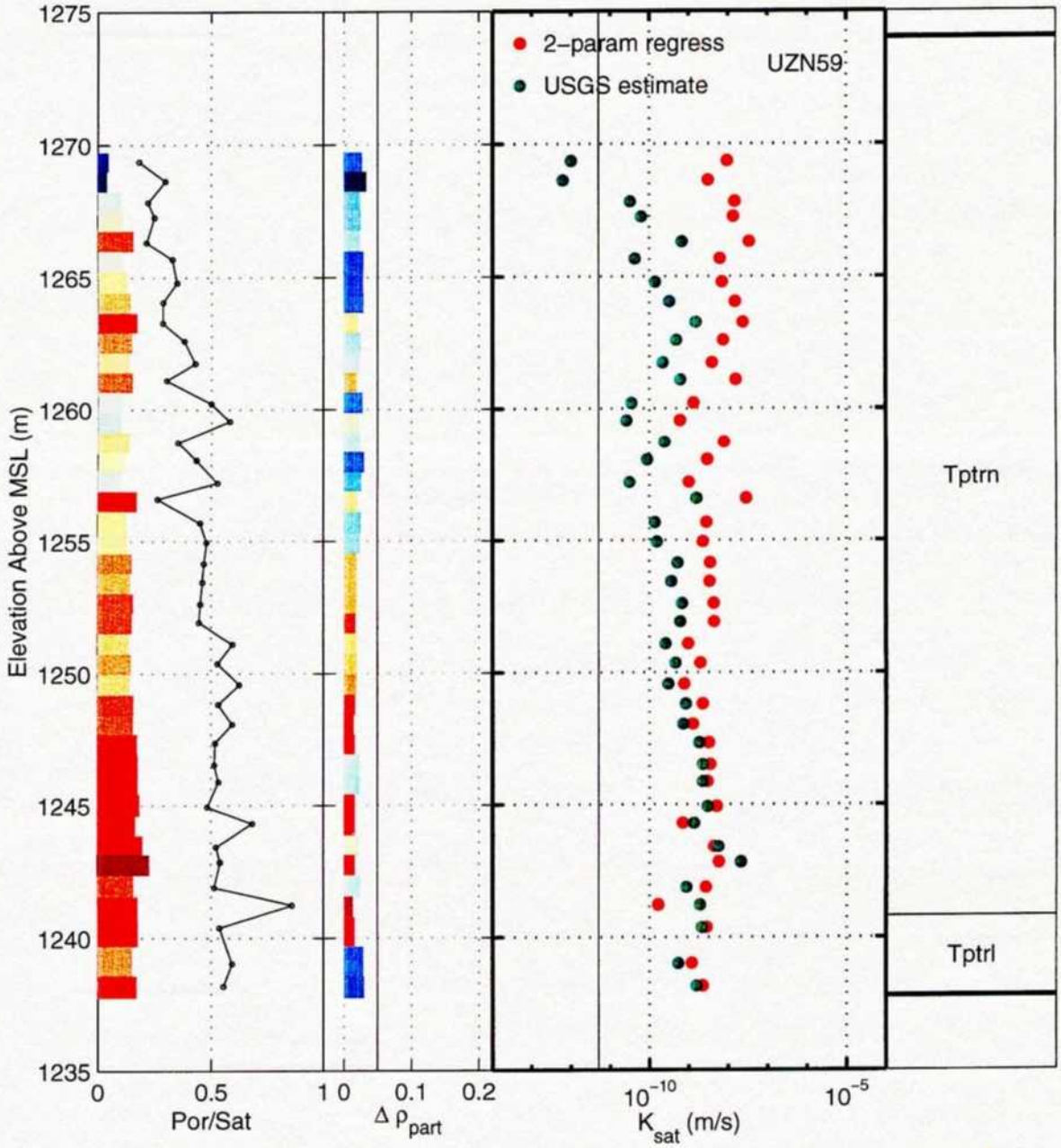

Figure 1-33: 9/9/97. **BHprofile_UZN59_c.eps**. Porosity, saturation, change in particle density, and measured and estimated values for K_{sat} in borehole N59.

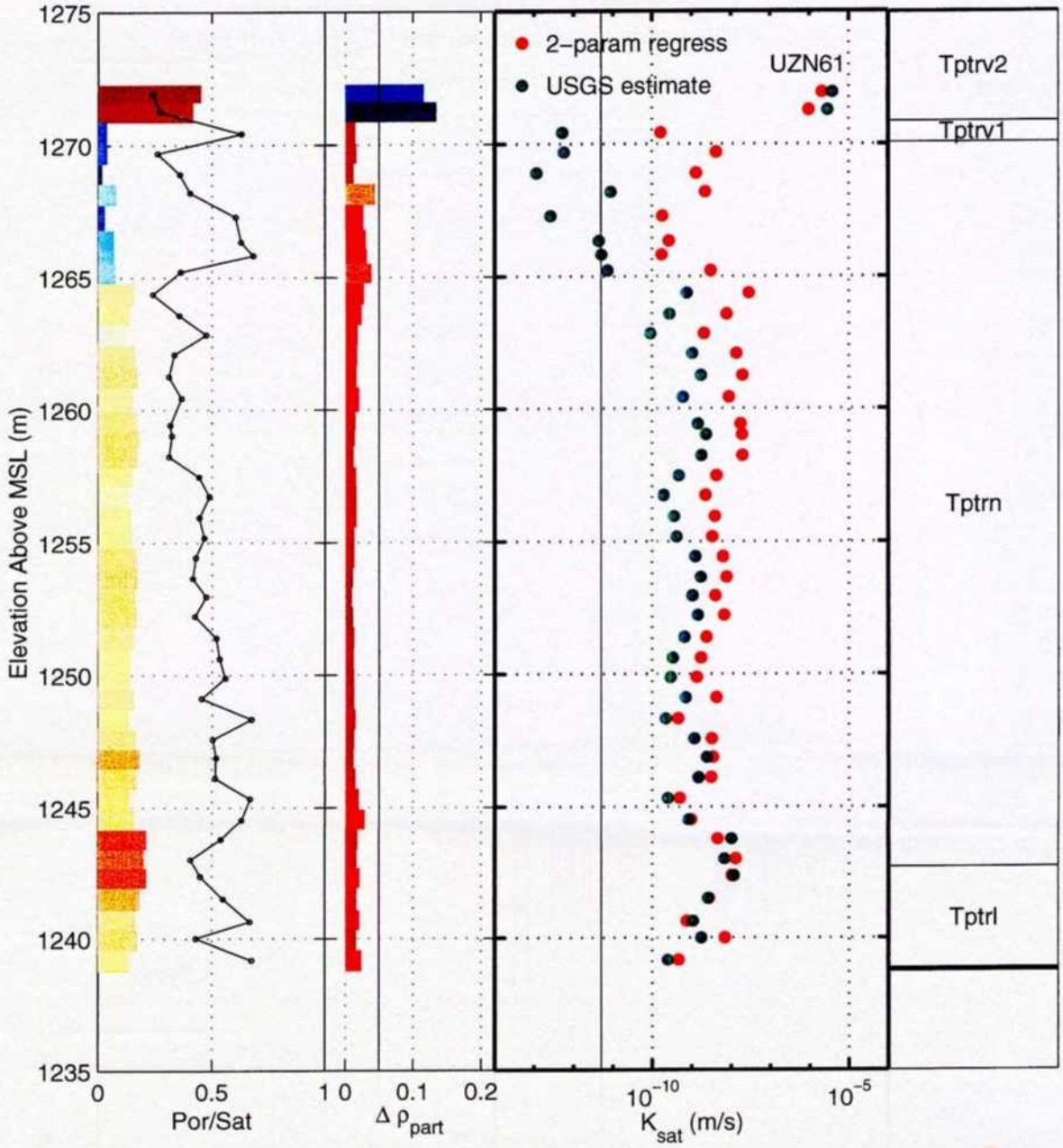

Figure 1-34: 9/9/97. **BHprofile_UZN61_c.eps**. Porosity, saturation, change in particle density, and measured and estimated values for K_{sat} in borehole N61.

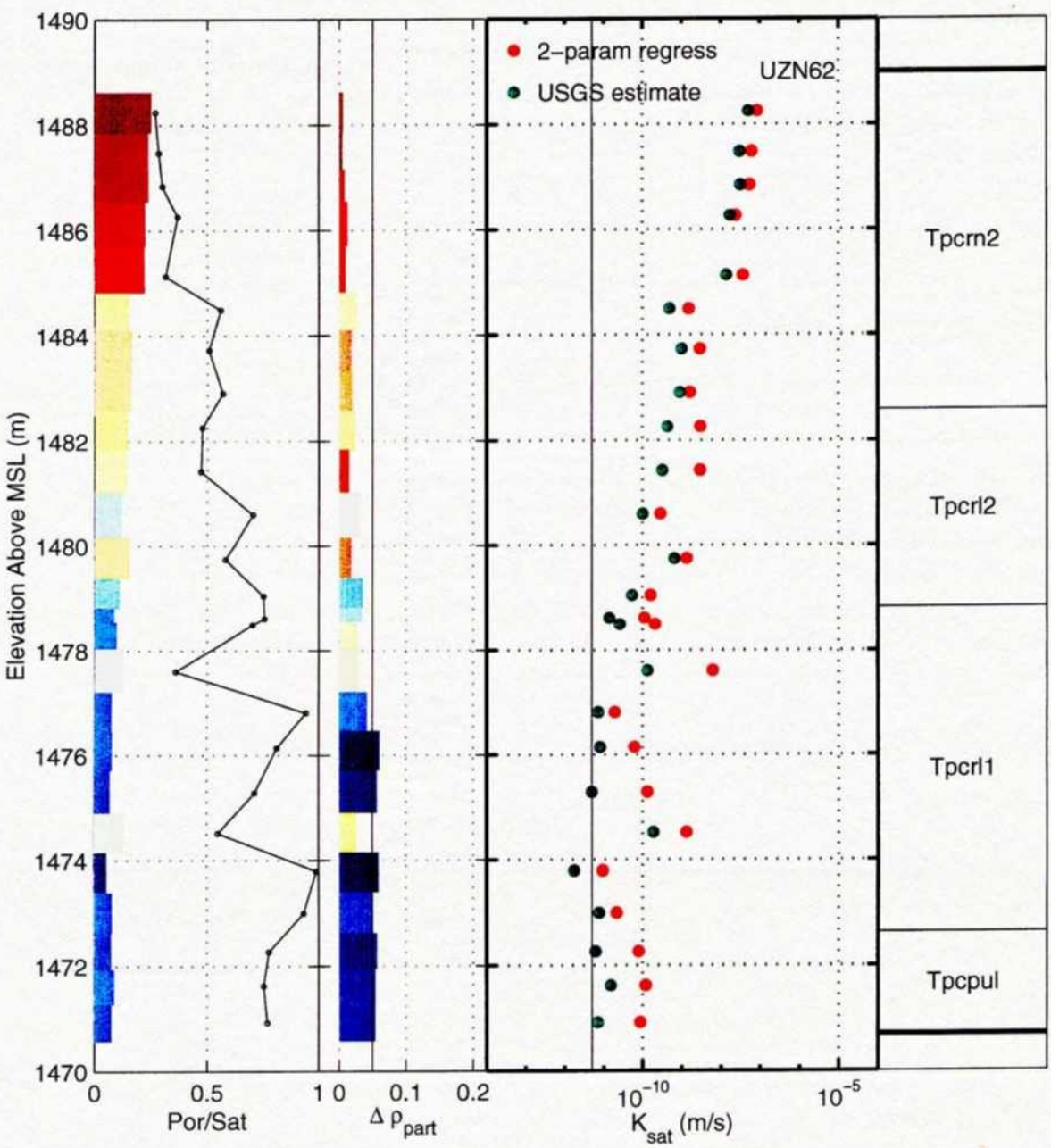

Figure 1-35: 9/9/97. **BHprofile_UZN62_c.eps**. Porosity, saturation, change in particle density, and measured and estimated values for K_{sat} in borehole N62.

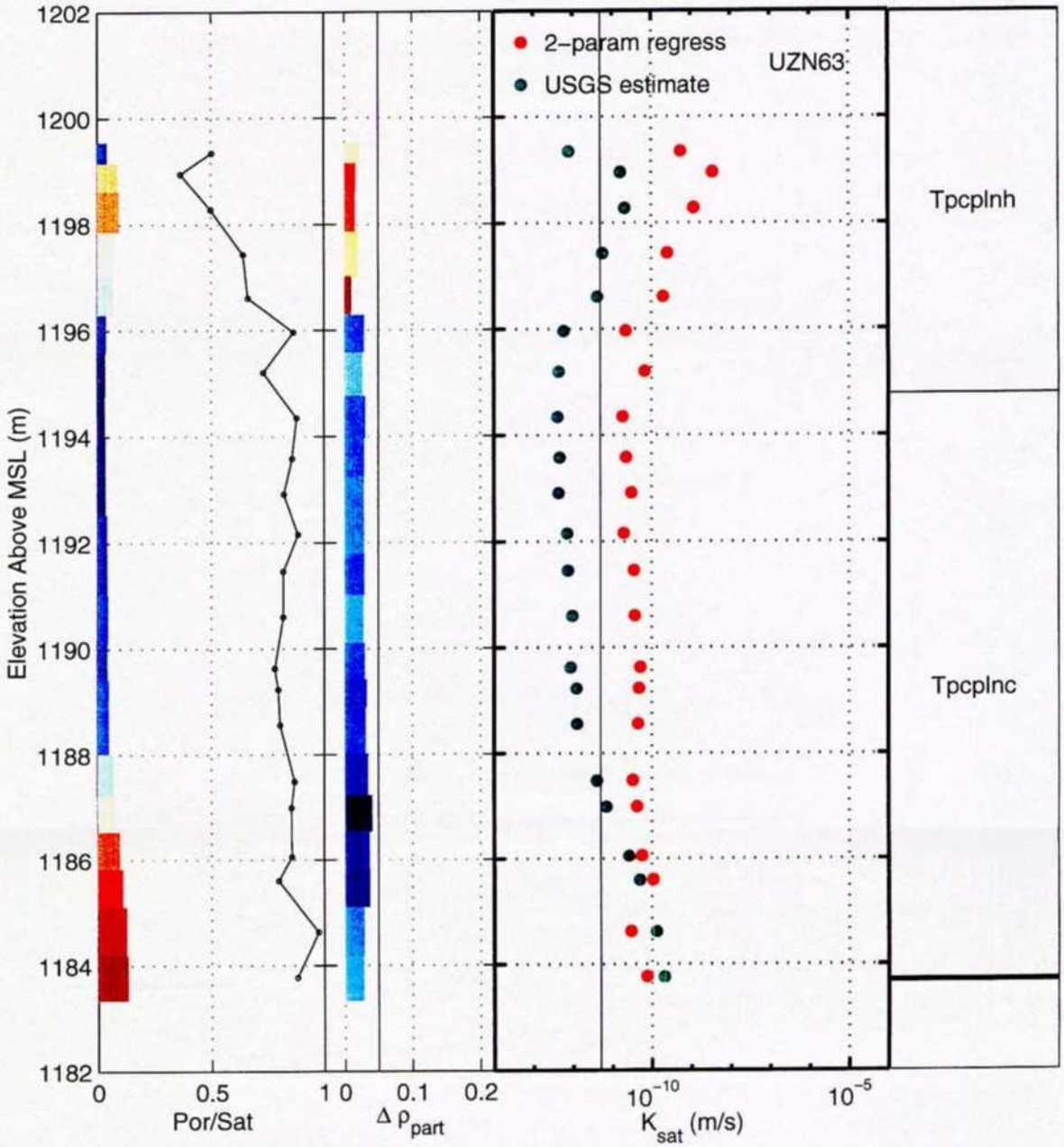

Figure 1-36: 9/9/97. **BHprofile_UZN63_c.eps**. Porosity, saturation, change in particle density, and measured and estimated values for K_{sat} in borehole N63.

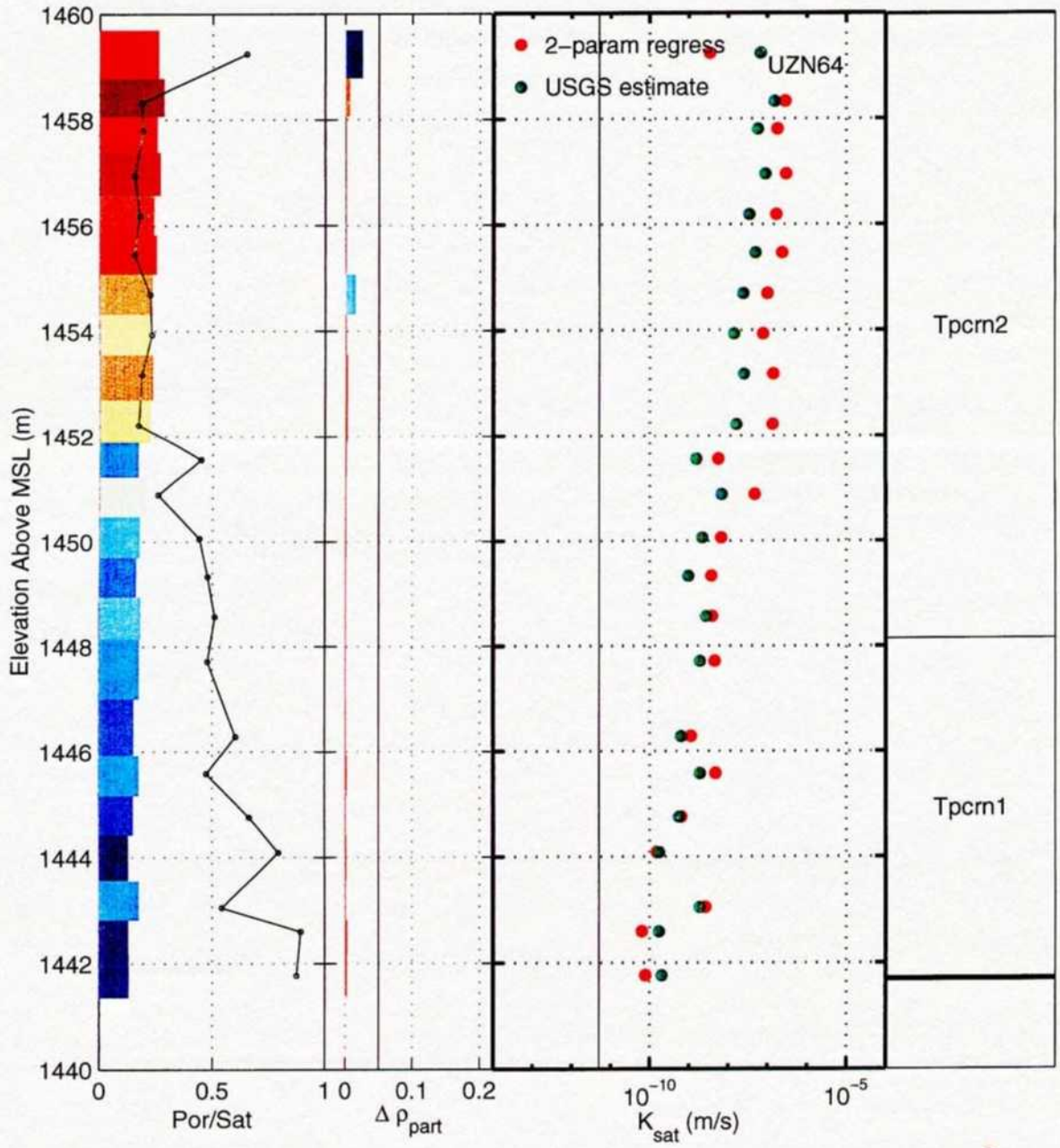

Figure 1-37: 9/9/97. **BHprofile_UZN64_c.eps**. Porosity, saturation, change in particle density, and measured and estimated values for K_{sat} in borehole N64.

9/17/97 Further investigation of USGS UZ properties. SAS

In ***$HOME2/AmbientKTI/3Ddata***, I created a *Matlab* routine, show_usgs_db_ksat.m, that plots the K_{sat} values for each formation using all boreholes having K_{sat} values for the formation, either measured or estimated using my regression. A small location map, idealized formation map, and statistical information are part of each plot. The creating routine is saved with a .arch091697 appended.

The plots are shown in the following pages. The statistical descriptions are summarized in the tables following the plots.

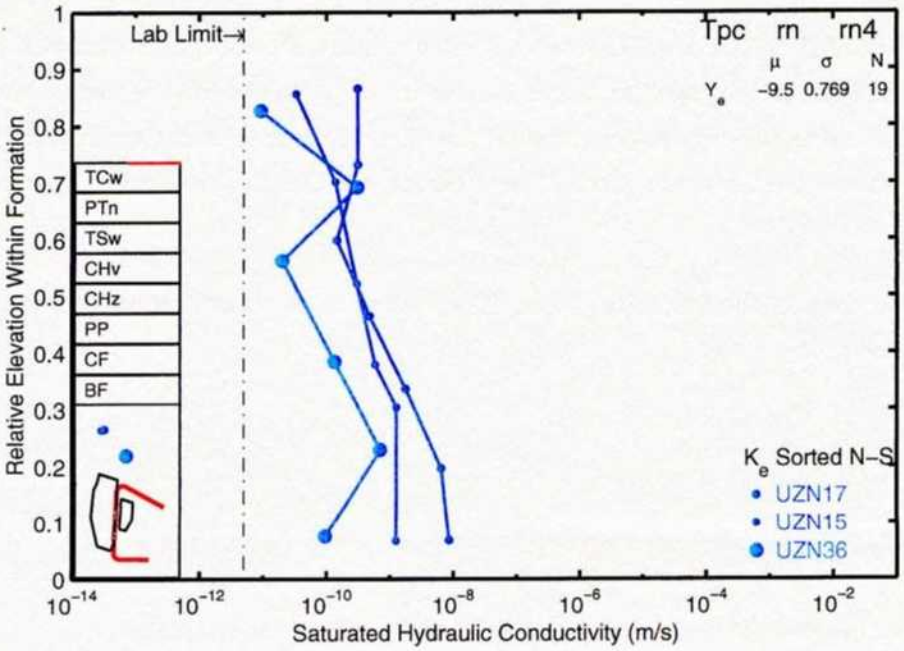

(a)

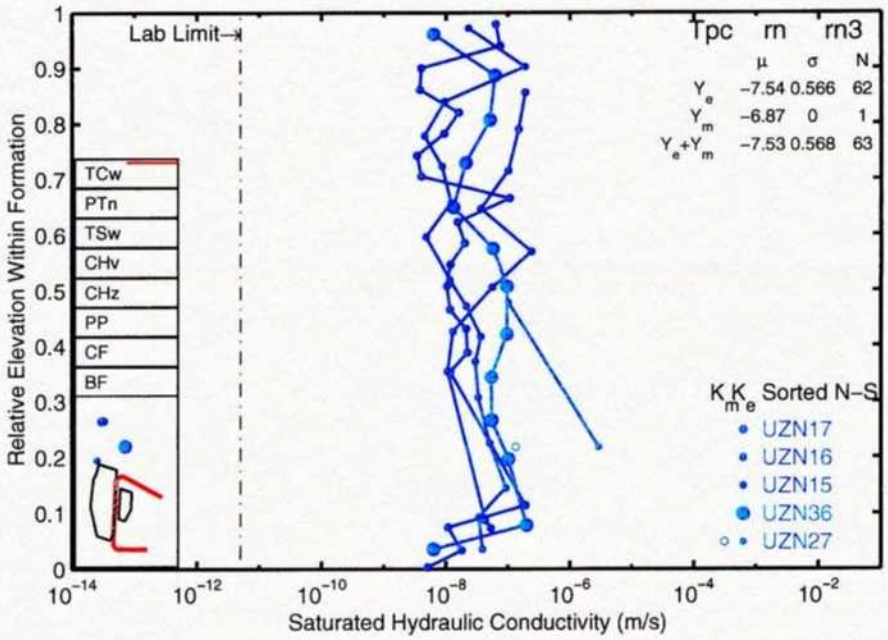

(b)

Figure 1-38: 9/17/97. All CNWRA-estimated and USGS-measured K_{sat} values in formation: (a) Tpcrn4 (**FormK_Tpcrn4_c.eps**), and (b) Tpcrn3 (**FormK_Tpcrn3_c.eps**).

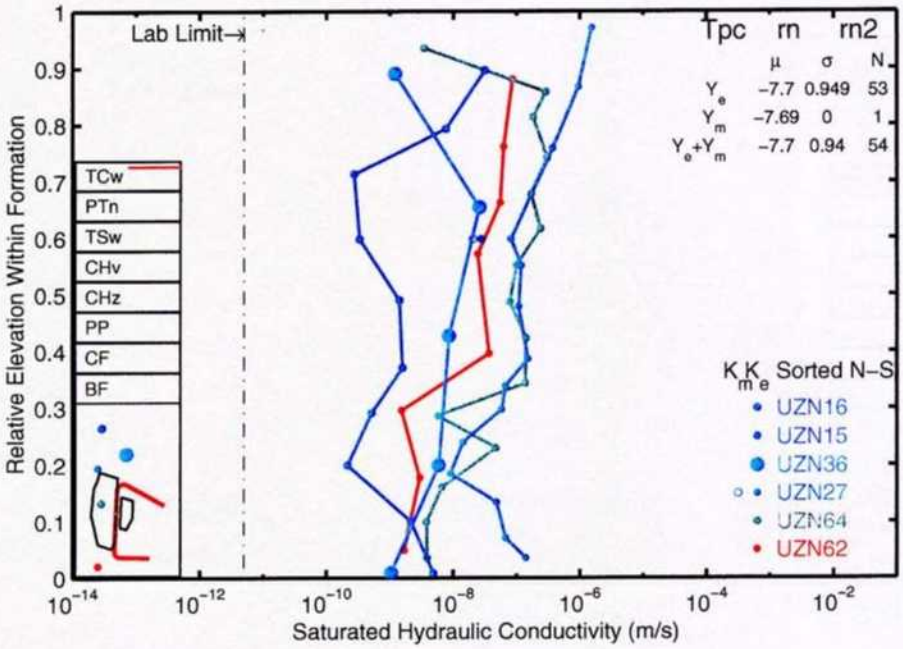

(a)

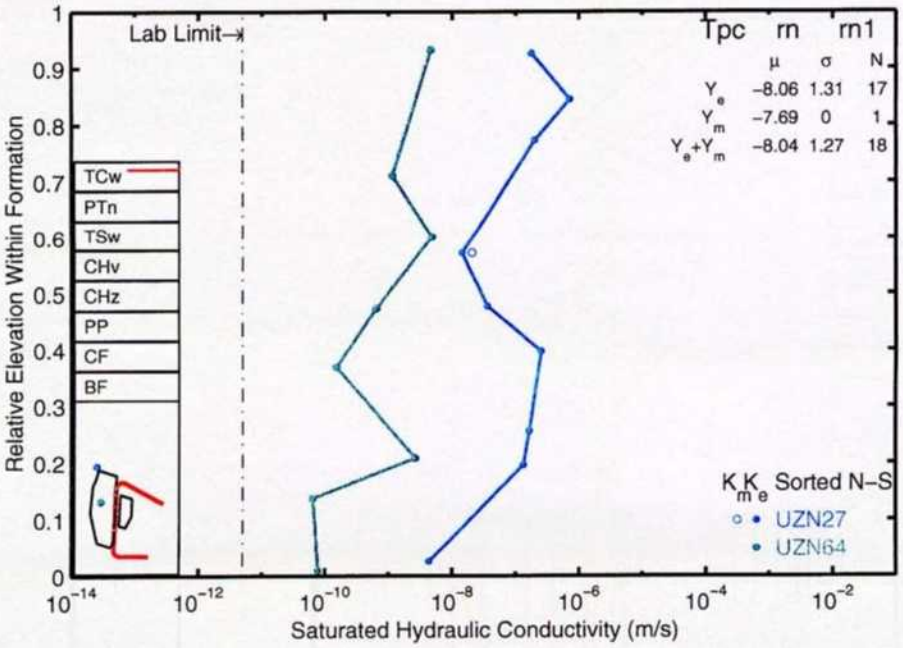

(b)

Figure 1-39: 9/17/97. All CNWRA-estimated and USGS-measured K_{sat} values in formation: (a) Tpcrn2 (**FormK_Tpcrn2_c.eps**), and (b) Tpcrn1 (**FormK_Tpcrn1_c.eps**).

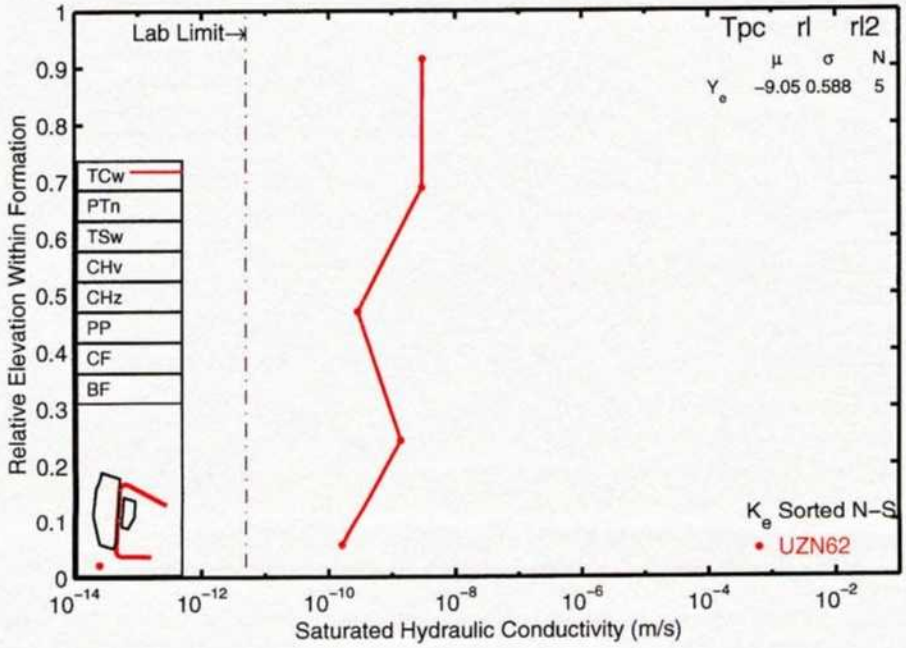

(a)

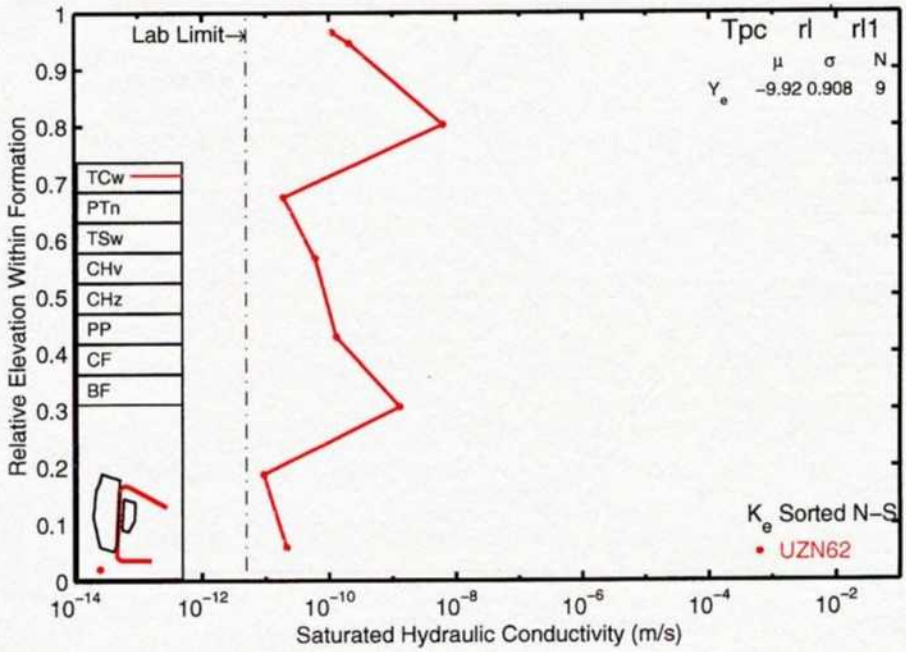

(b)

Figure 1-40: 9/17/97. All CNWRA-estimated and USGS-measured K_{sat} values in formation: (a) Tpcrl2 (**FormK_Tpcrl2_c.eps**), and (b) Tpcrl1 (**FormK_Tpcrl1_c.eps**).

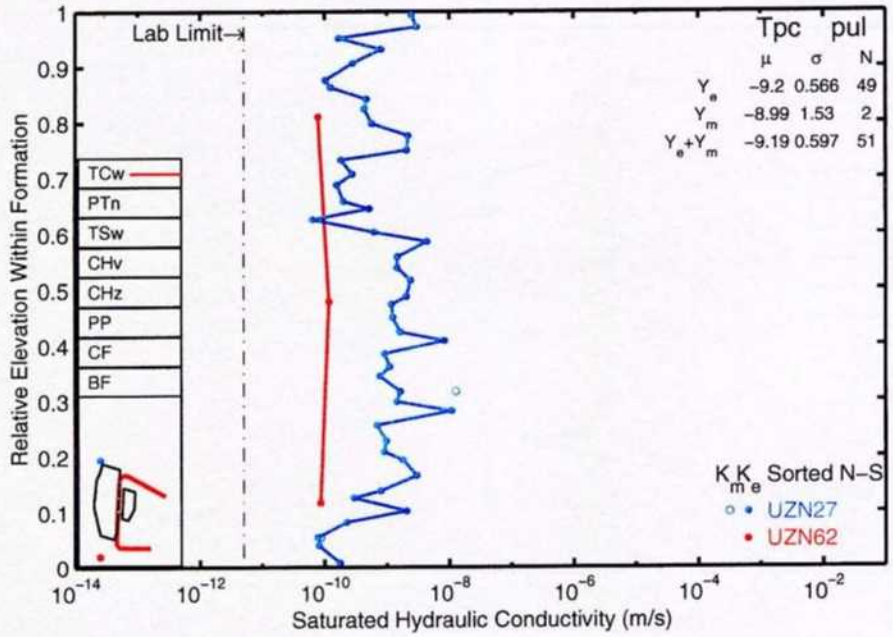

(a)

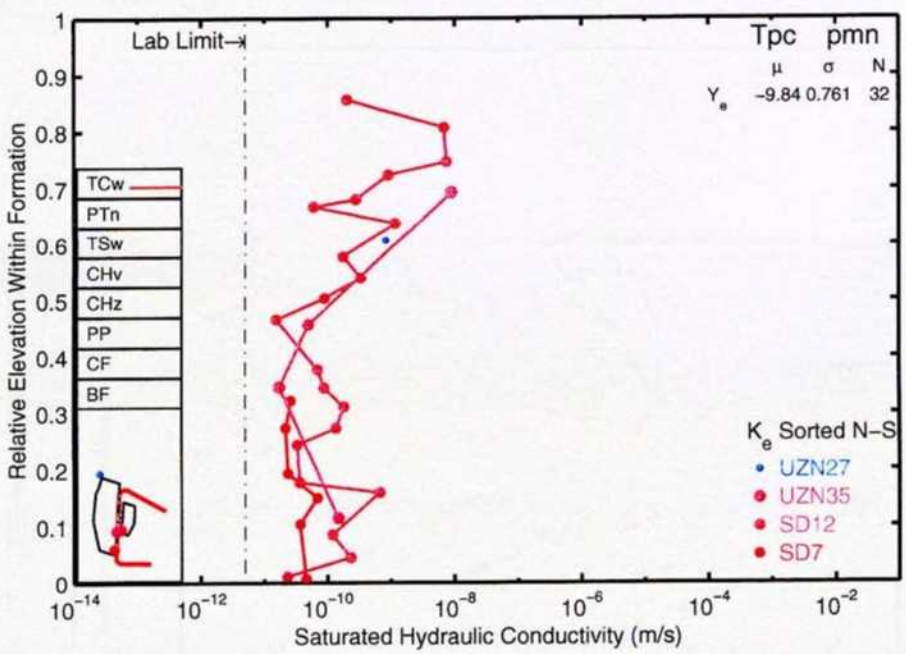

(b)

Figure 1-41: 9/17/97. All CNWRA-estimated and USGS-measured K_{sat} values in formation: (a) Tpcpul (**FormK_Tpcpul_c.eps**), and (b) Tpcpmn (**FormK_Tpcpmn_c.eps**).

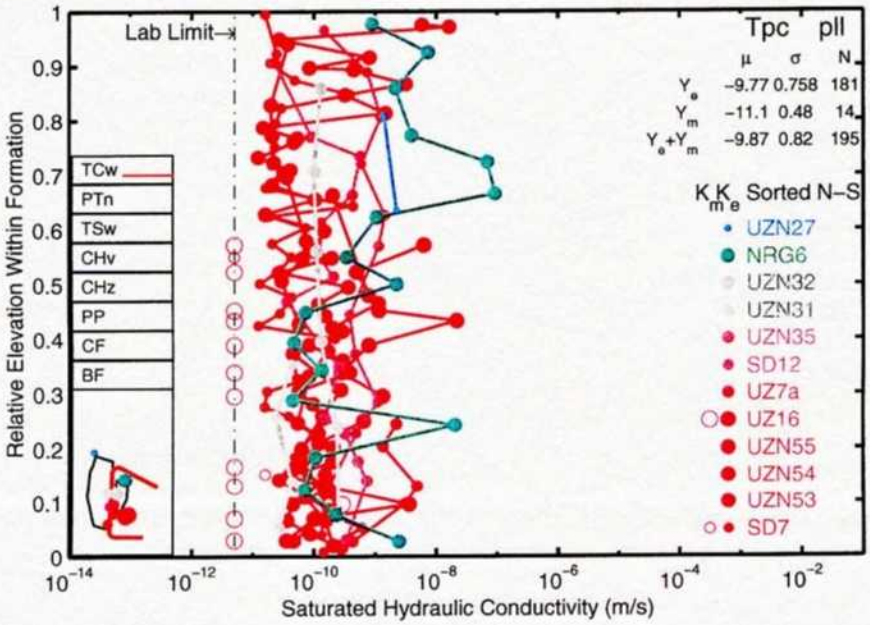

(a)

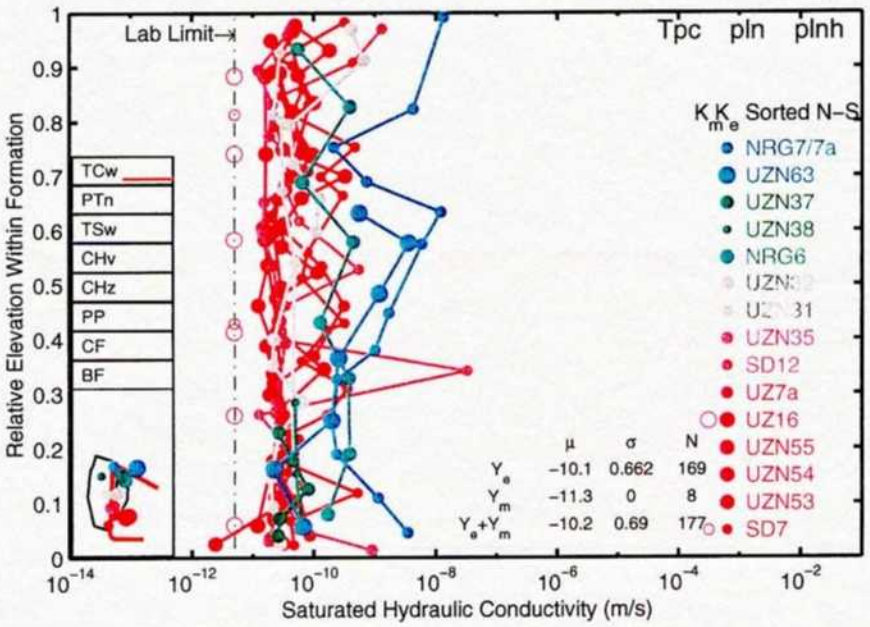

(b)

Figure 1-42: 9/17/97. All CNWRA-estimated and USGS-measured K_{sat} values in formation: (a) Tpcpll (**FormK_Tpcpll_c.eps**), and (b) Tpcplnh (**FormK_Tpcplnh_c.eps**).

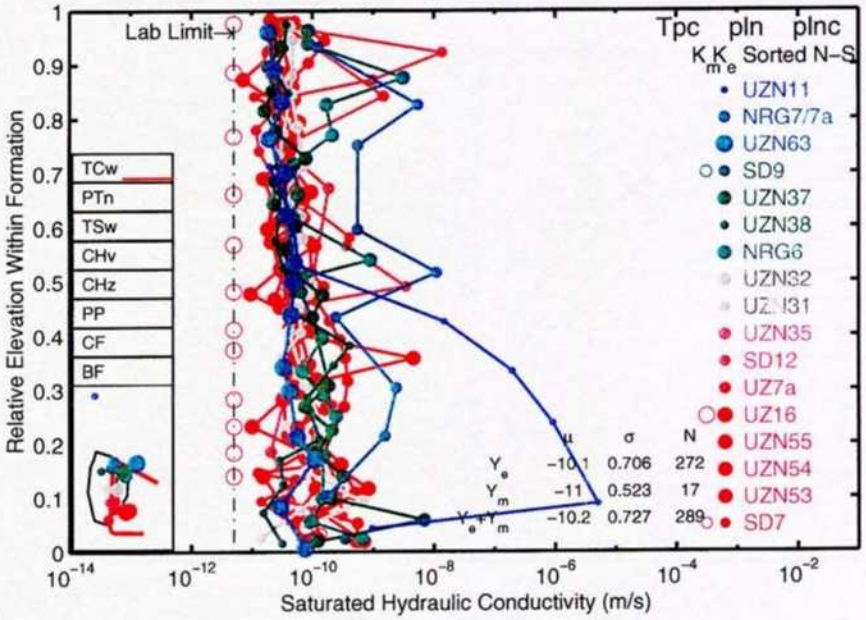

(a)

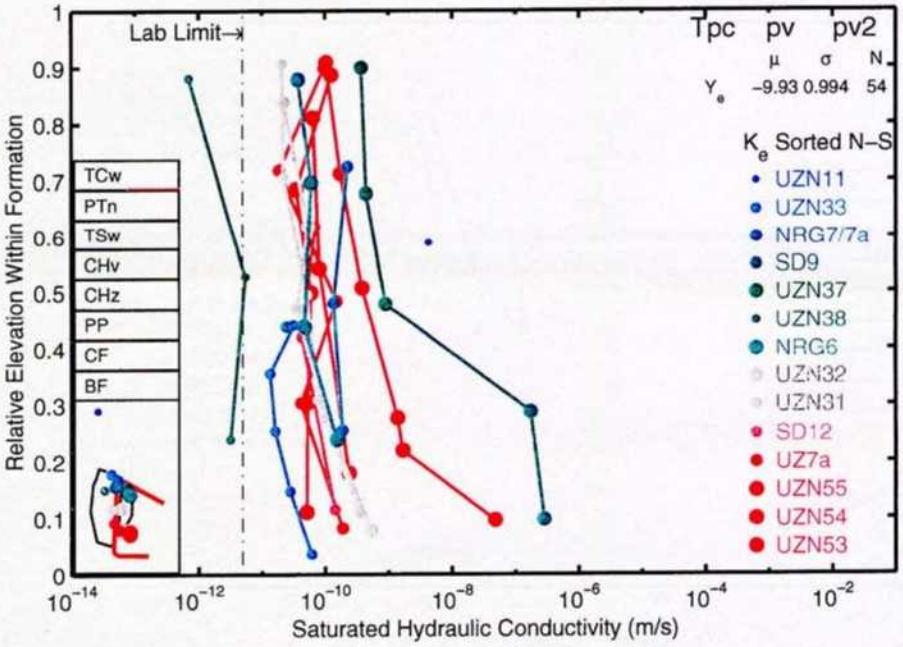

(b)

Figure 1-43: 9/17/97. All CNWRA-estimated and USGS-measured K_{sat} values in formation: (a) Tpcplnc (**FormK_Tpcplnc_c.eps**), and (b) Tpcpv2 (**FormK_Tpcpv2_c.eps**).

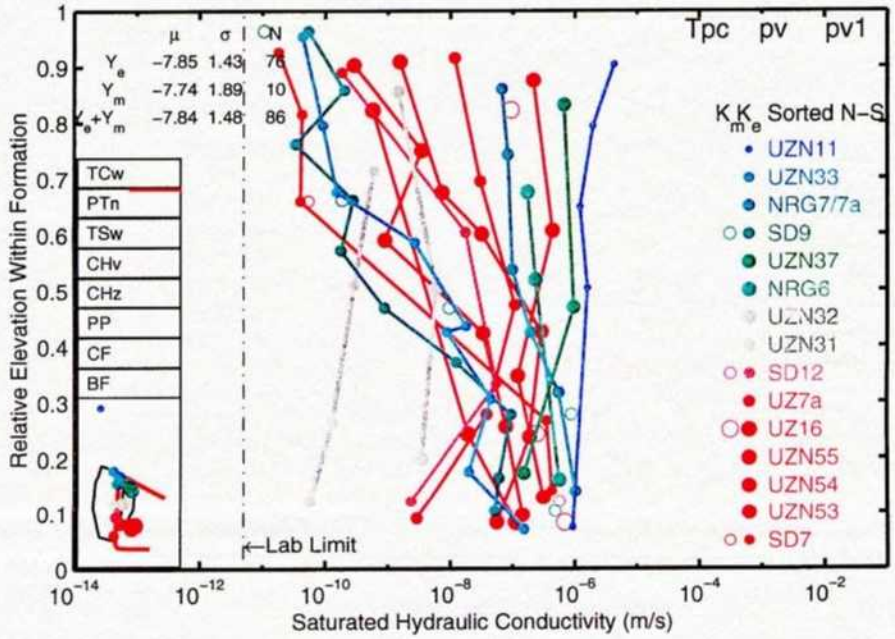

(a)

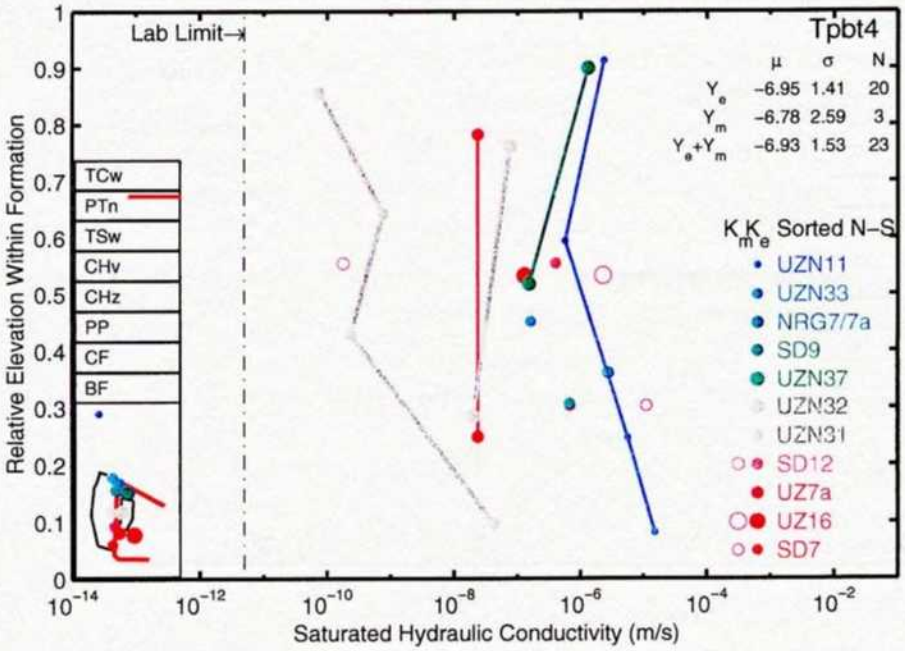

(b)

Figure 1-44: 9/17/97. All CNWRA-estimated and USGS-measured K_{sat} values in formation: (a) Tpcpv1 (**FormK_Tpcpv1_c.eps**), and (b) Tpbt4 (**FormK_Tpbt4_c.eps**).

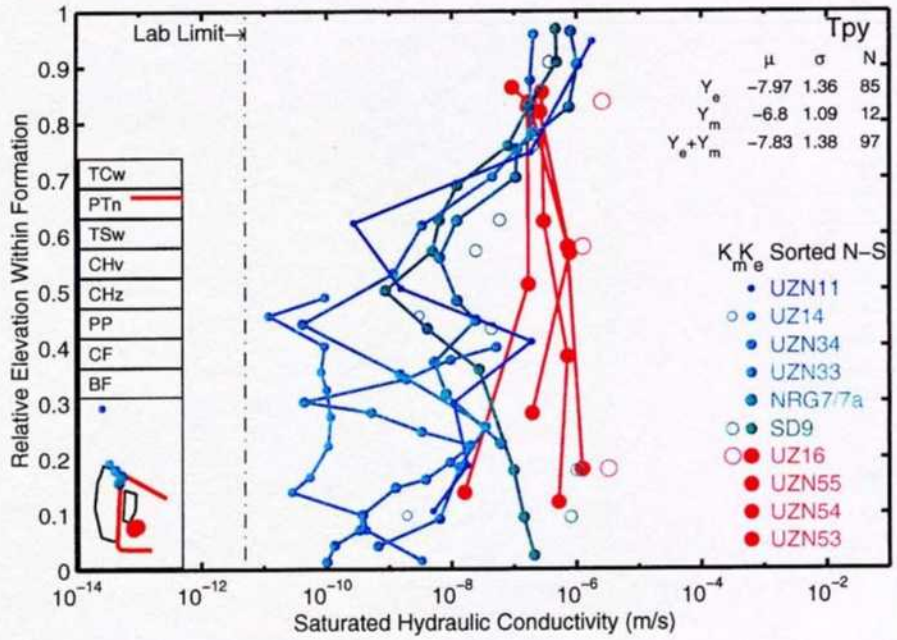

(a)

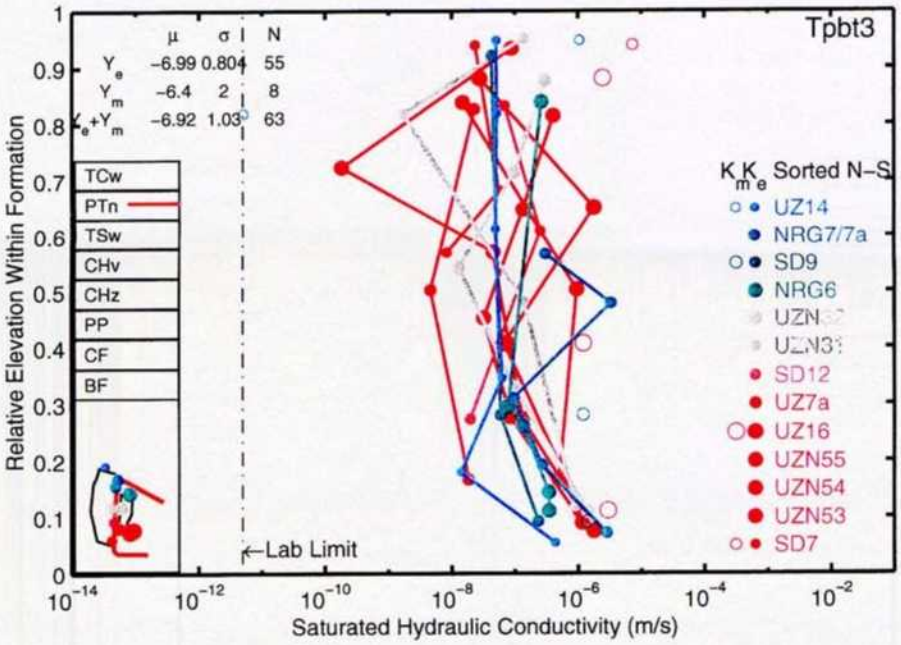

(b)

Figure 1-45: 9/17/97. All CNWRA-estimated and USGS-measured K_{sat} values in formation: (a) Tpy (**FormK_Tpy_c.eps**), and (b) Tpbt3 (**FormK_Tpbt3_c.eps**).

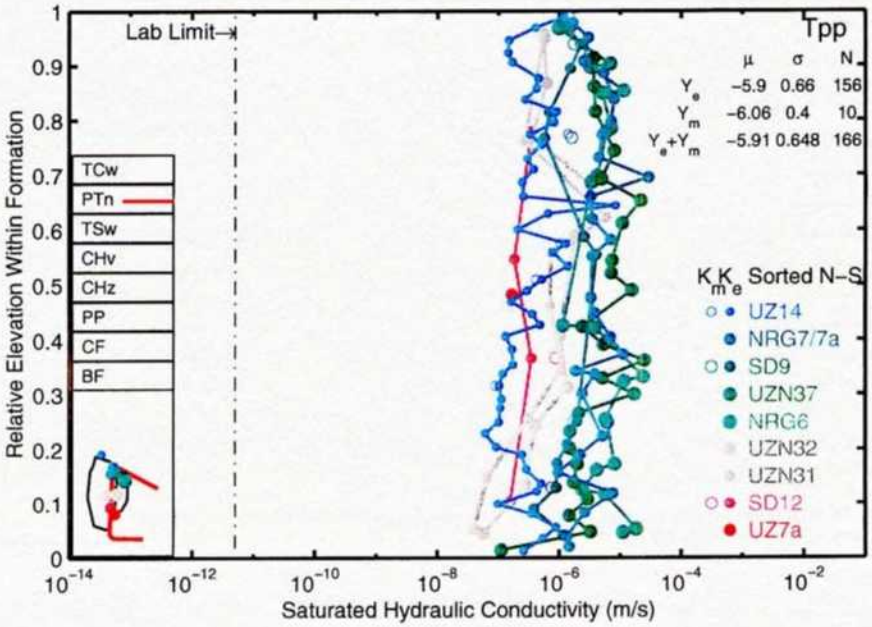

(a)

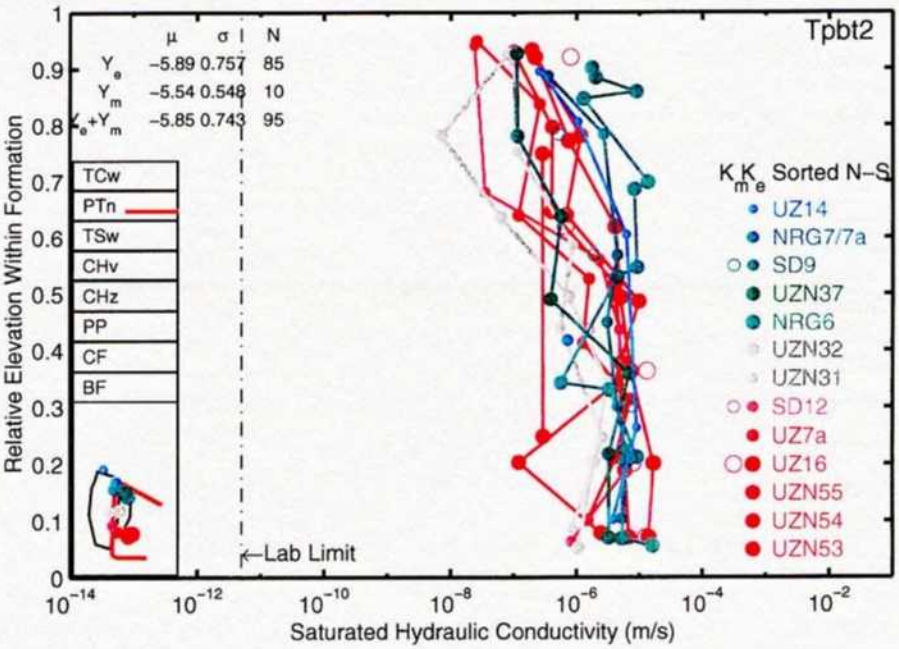

(b)

Figure 1-46: 9/17/97. All CNWRA-estimated and USGS-measured K_{sat} values in formation: (a) Tpp (**FormK_Tpp_c.eps**), and (b) Tpbt2 (**FormK_Tpbt2_c.eps**).

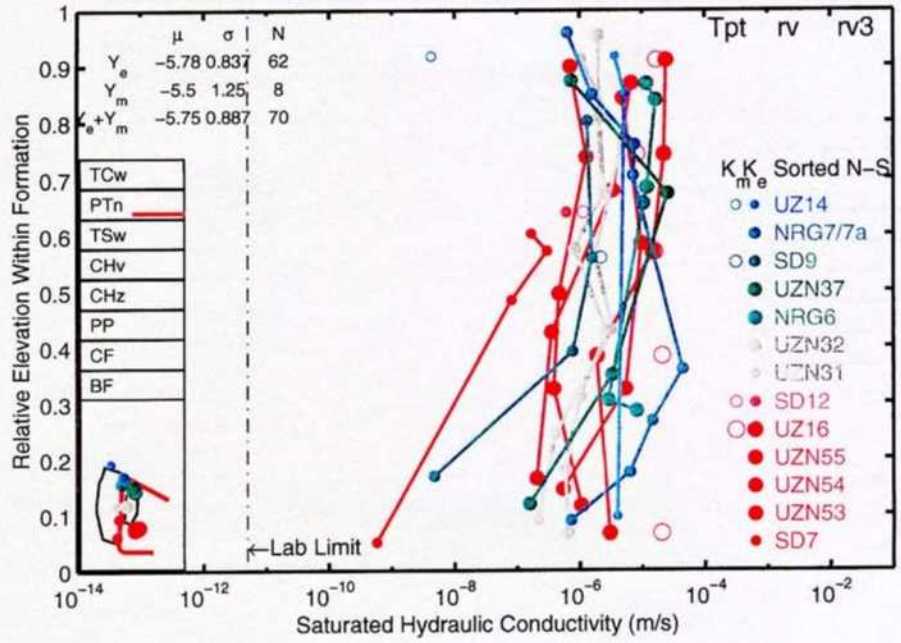

(a)

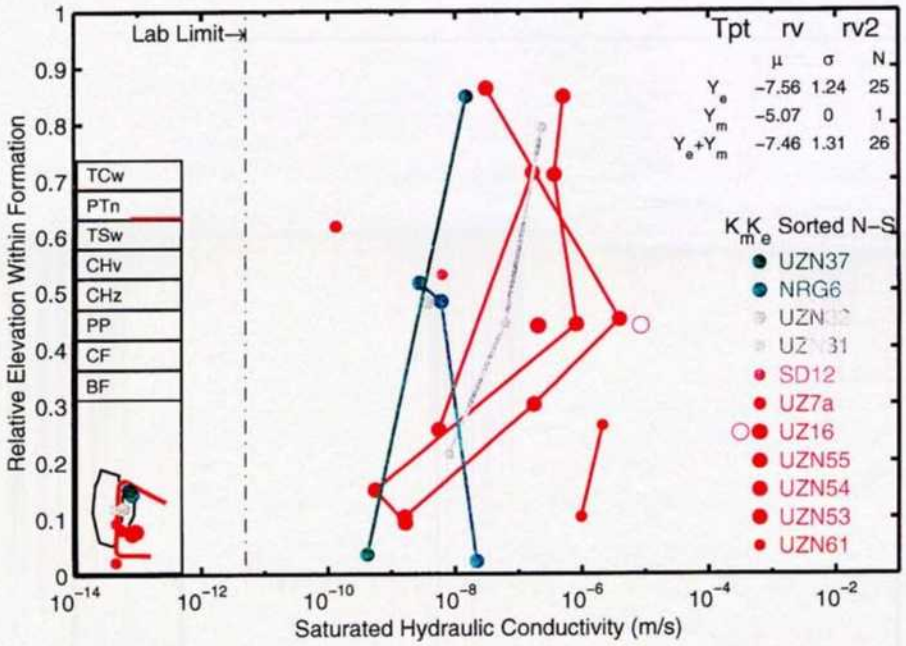

(b)

Figure 1-47: 9/17/97. All CNWRA-estimated and USGS-measured K_{sat} values in formation: (a) Tptrv3 (**FormK_Tptrv3_c.eps**), and (b) Tptrv2 (**FormK_Tptrv2_c.eps**).

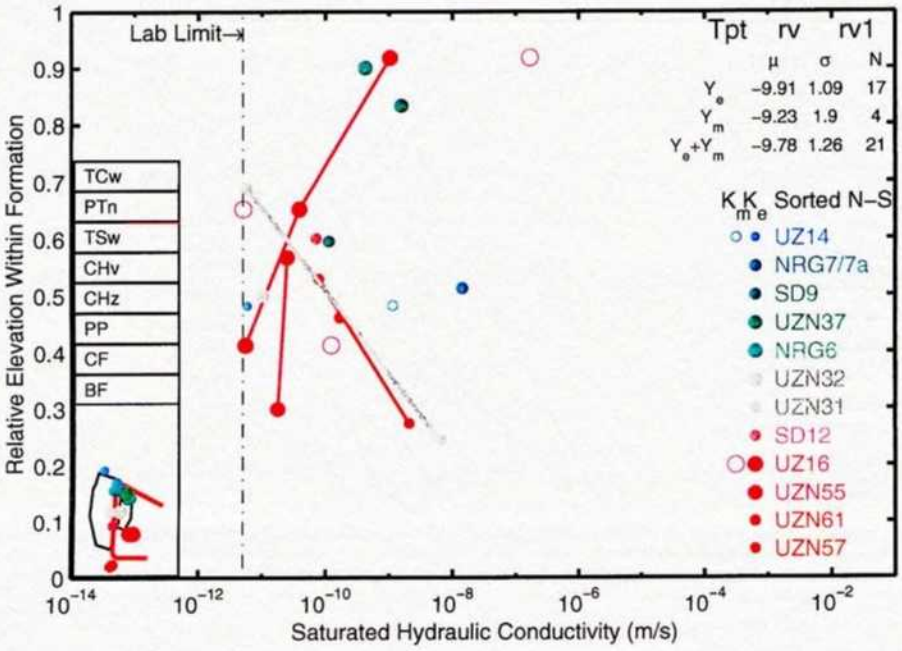

(a)

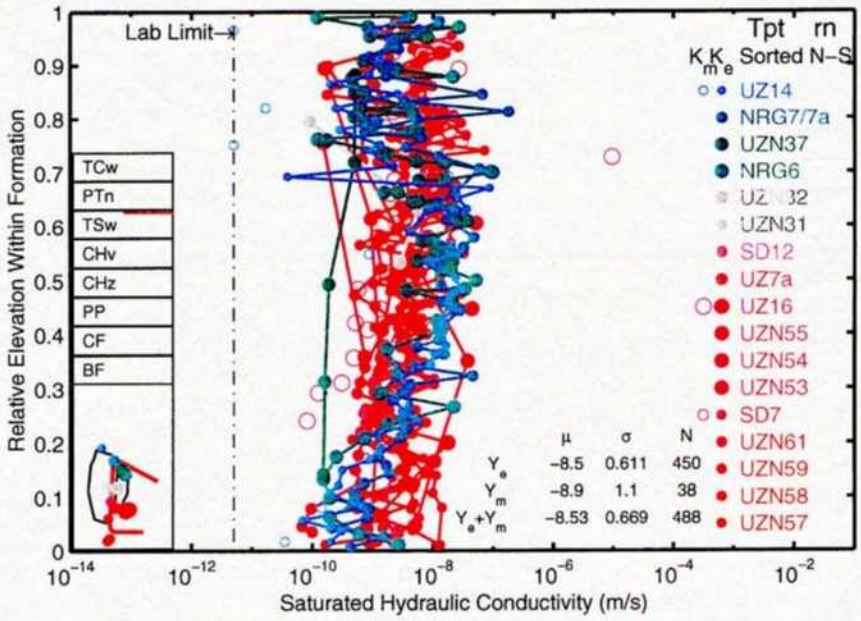

(b)

Figure 1-48: 9/17/97. All CNWRA-estimated and USGS-measured K_{sat} values in formation: (a) Tptrv1 (**FormK_Tptrv1_c.eps**), and (b) Tptrn (**FormK_Tptrn_c.eps**).

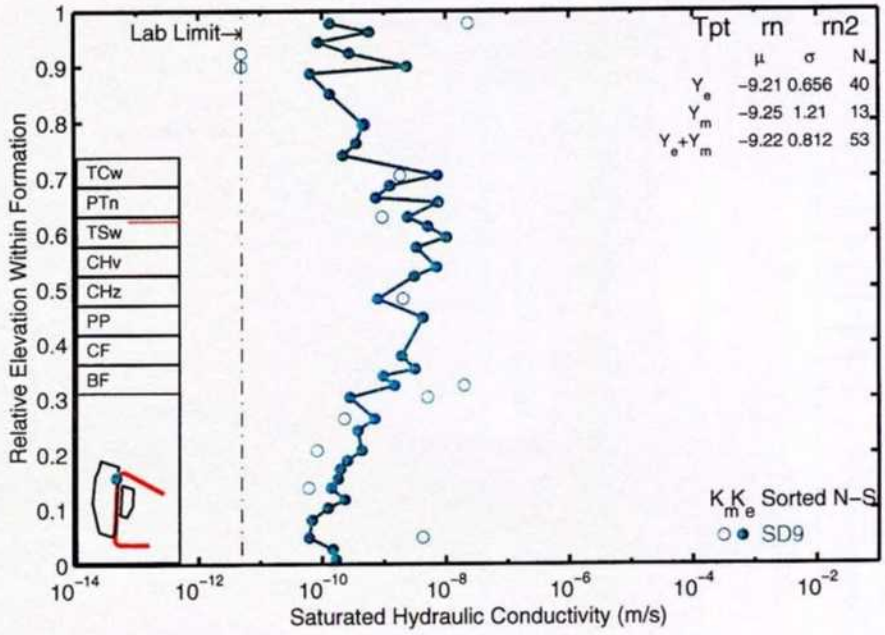

(a)

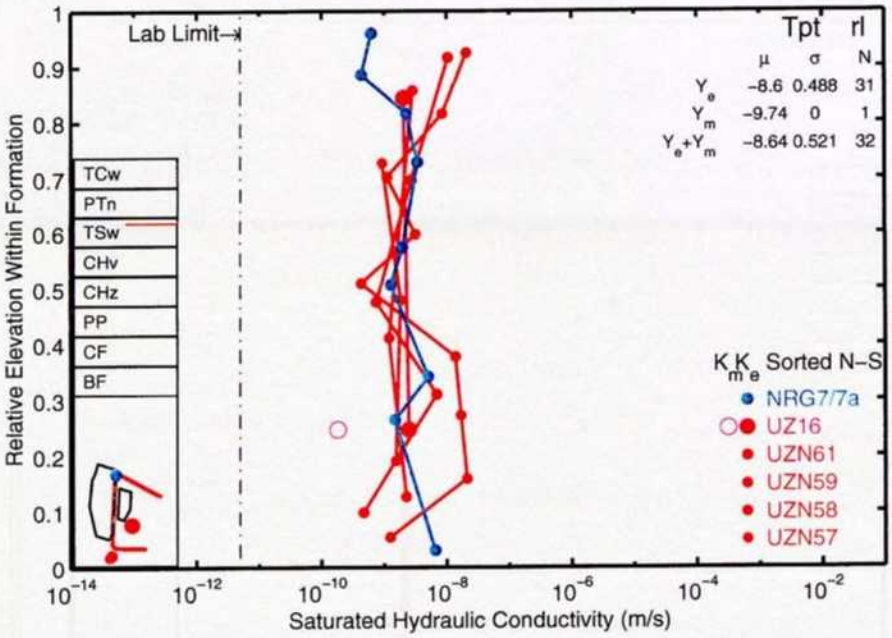

(b)

Figure 1-49: 9/17/97. All CNWRA-estimated and USGS-measured K_{sat} values in formation: (a) Tptrn2 (**FormK_Tptrn2_c.eps**), and (b) Tptrl (**FormK_Tptrl_c.eps**).

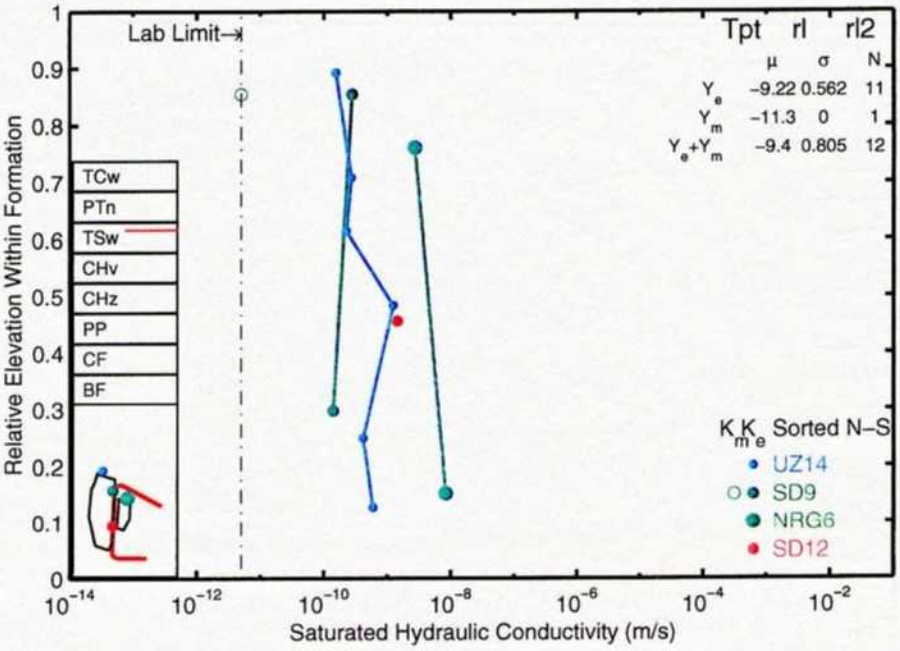

(a)

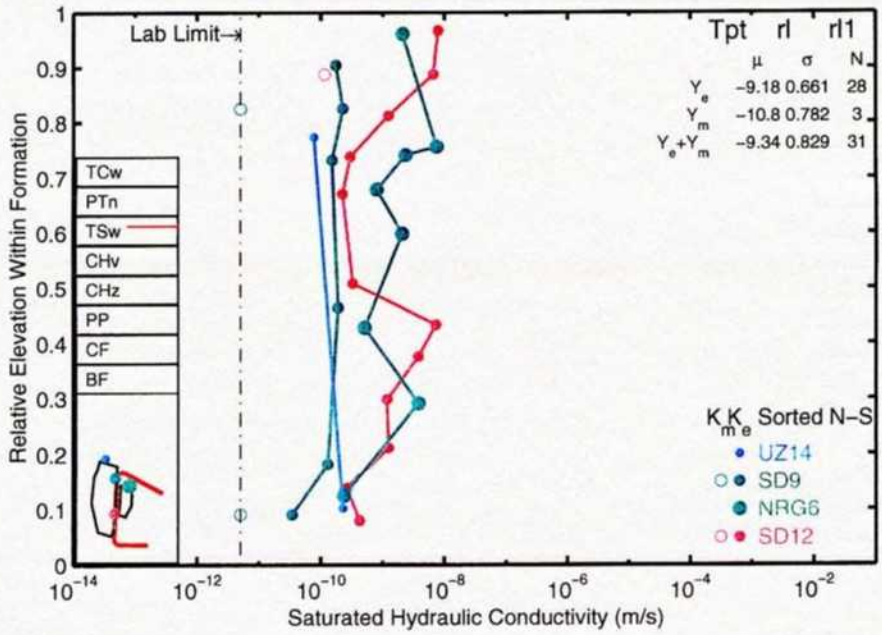

(b)

Figure 1-50: 9/17/97. All CNWRA-estimated and USGS-measured K_{sat} values in formation: (a) Tptrl2 (**FormK_Tptrl2_c.eps**), and (b) Tptrl1 (**FormK_Tptrl1_c.eps**).

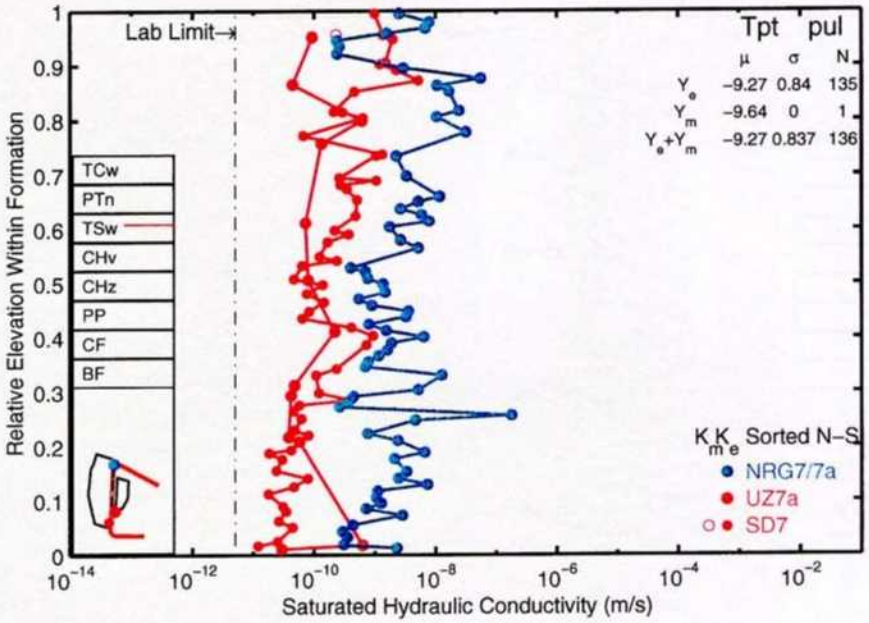

(a)

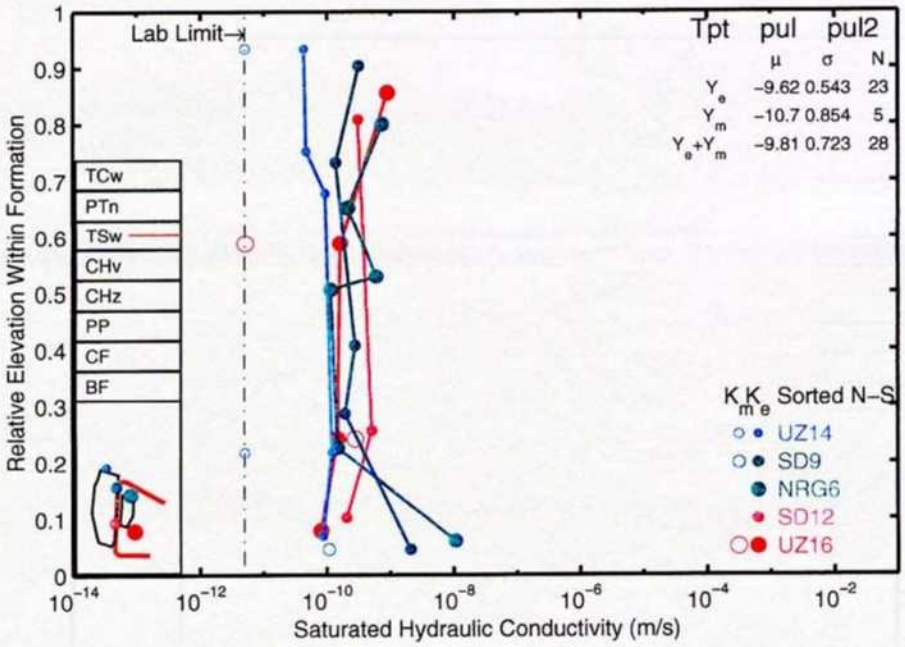

(b)

Figure 1-51: 9/17/97. All CNWRA-estimated and USGS-measured K_{sat} values in formation: (a) Tptpul (**FormK_Tptpul_c.eps**), and (b) Tptpul2 (**FormK_Tptpul2_c.eps**).

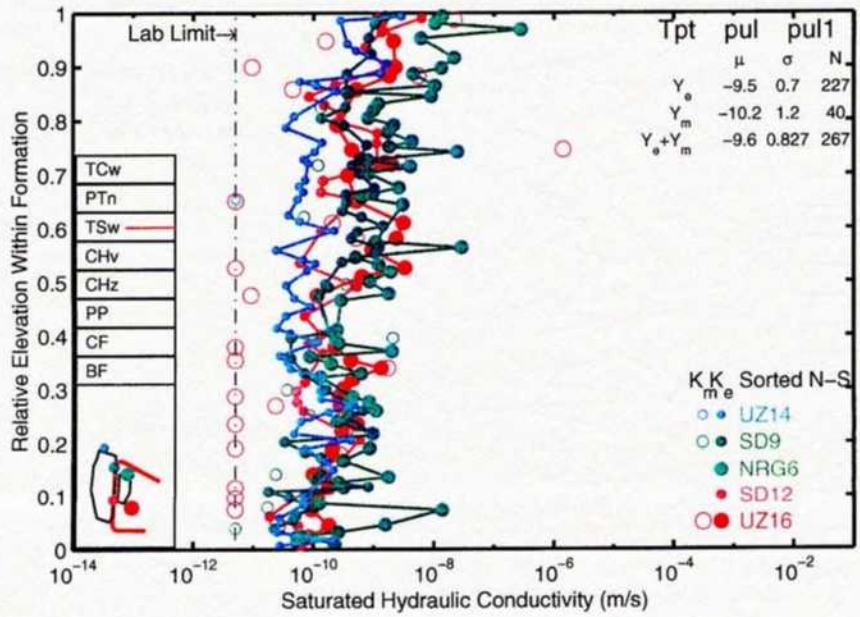

(a)

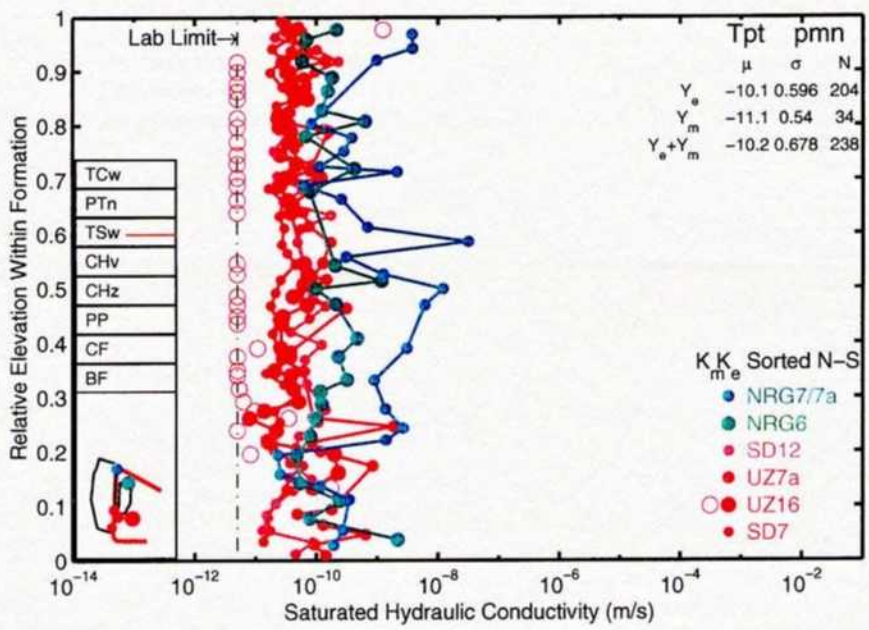

(b)

Figure 1-52: 9/17/97. All CNWRA-estimated and USGS-measured K_{sat} values in formation: (a) Tptpul1 (**FormK_Tptpul1_c.eps**), and (b) Tptpmn (**FormK_Tptpmn_c.eps**).

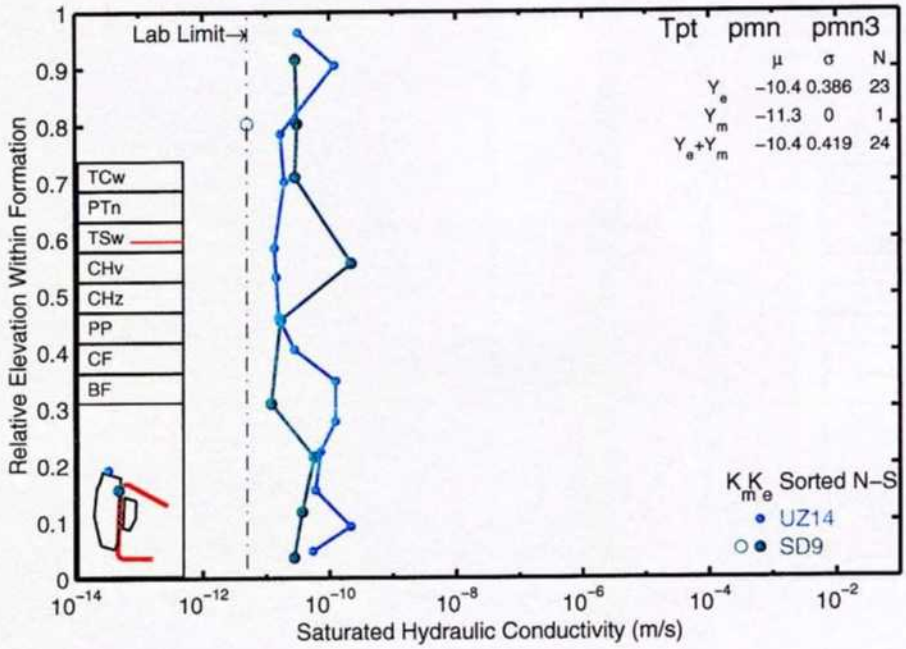

(a)

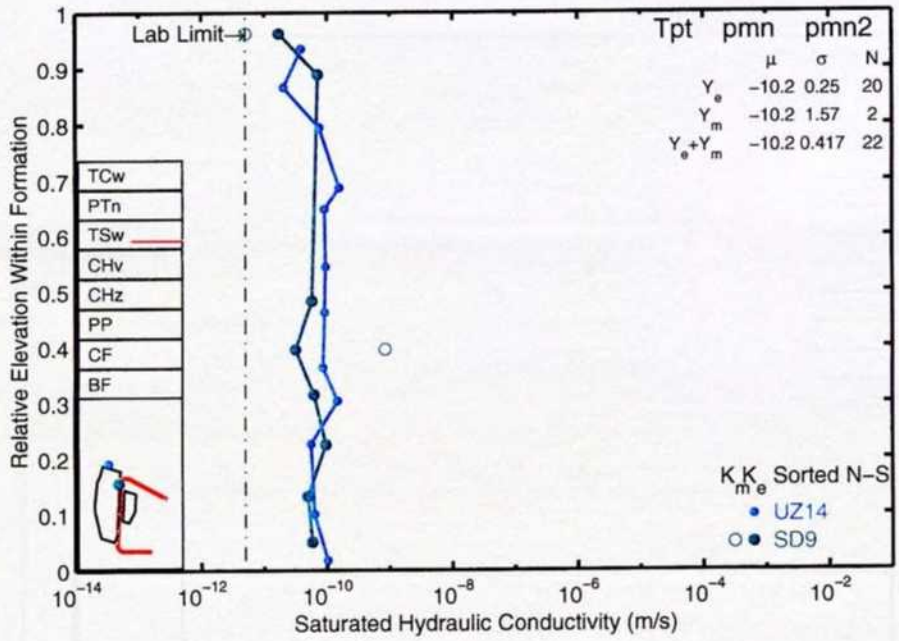

(b)

Figure 1-53: 9/17/97. All CNWRA-estimated and USGS-measured K_{sat} values in formation: (a) Tptpmn3 (**FormK_Tptpmn3_c.eps**), and (b) Tptpmn2 (**FormK_Tptpmn2_c.eps**).

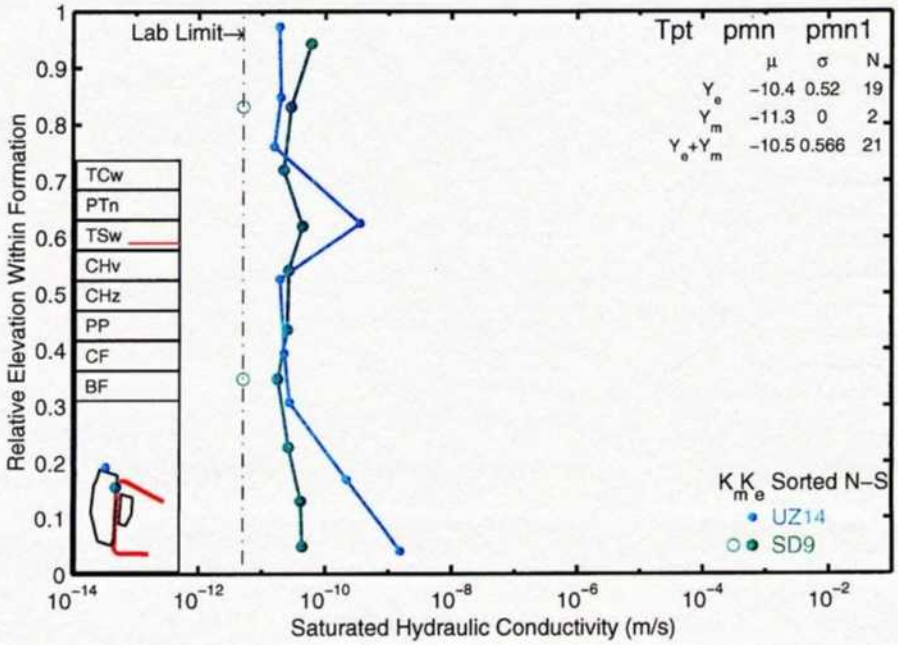

(a)

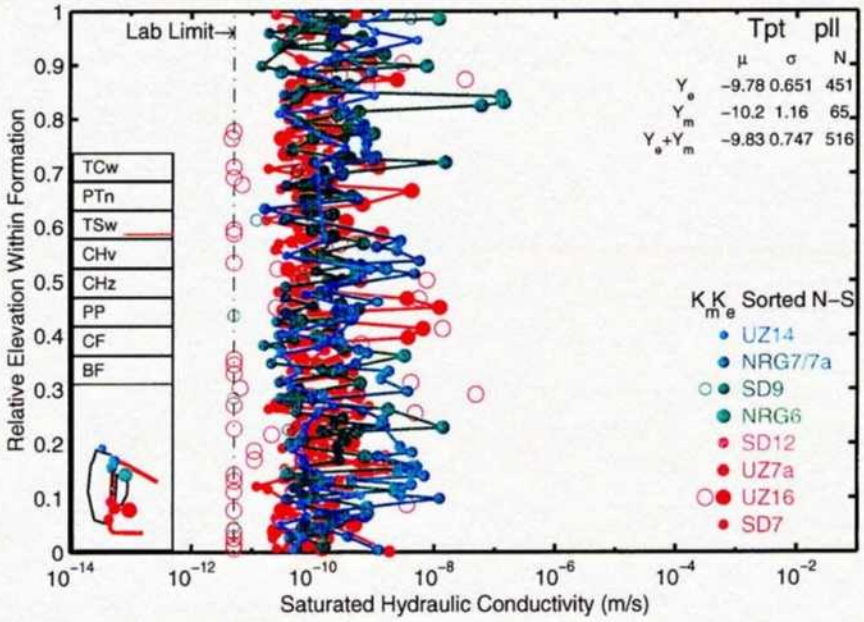

(b)

Figure 1-54: 9/17/97. All CNWRA-estimated and USGS-measured K_{sat} values in formation: (a) Tptpmn1 (**FormK_Tptpmn1_c.eps**), and (b) Tptpll (**FormK_Tptpll_c.eps**).

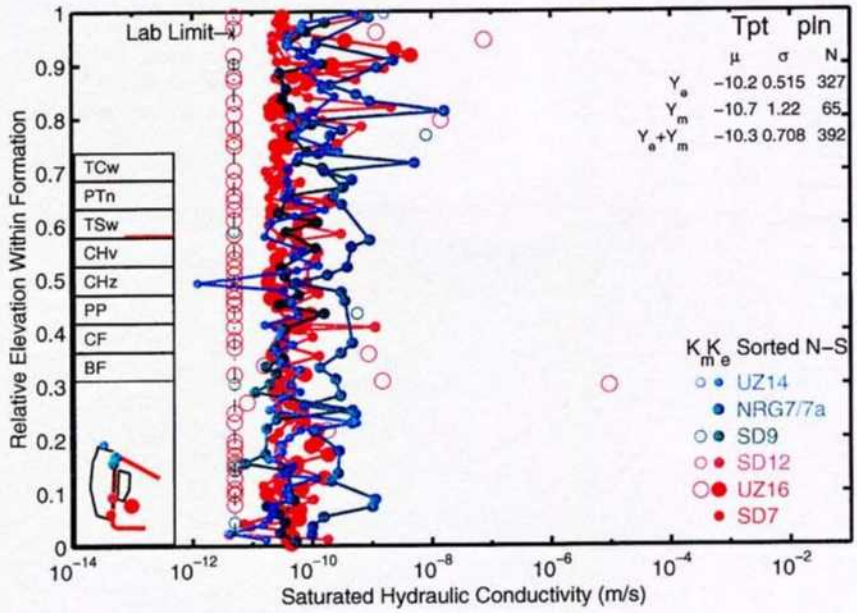

(a)

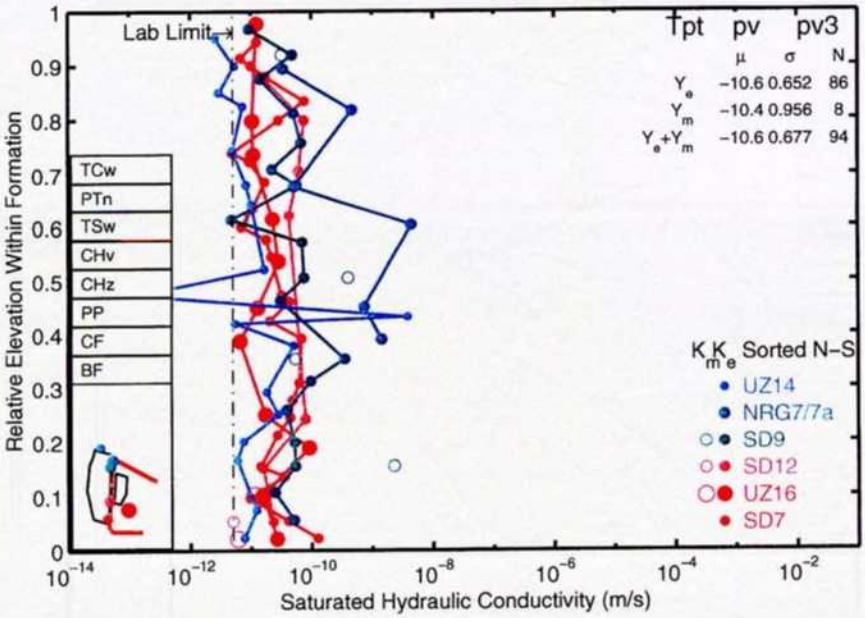

(b)

Figure 1-55: 9/17/97. All CNWRA-estimated and USGS-measured K_{sat} values in formation: (a) Tptpln (**FormK_Tptpln_c.eps**), and (b) Tptpv3 (**FormK_Tptpv3_c.eps**).

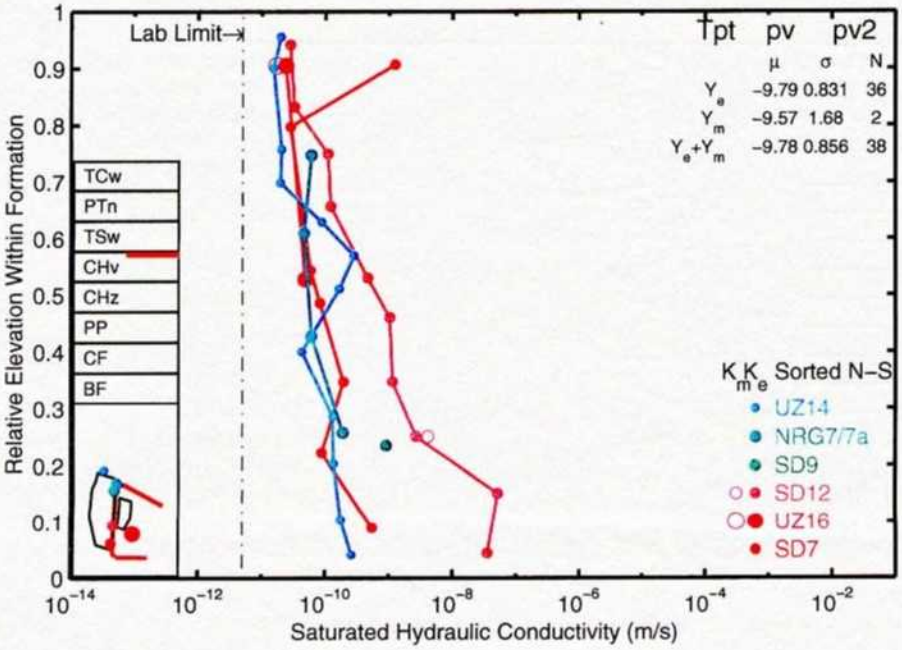

(a)

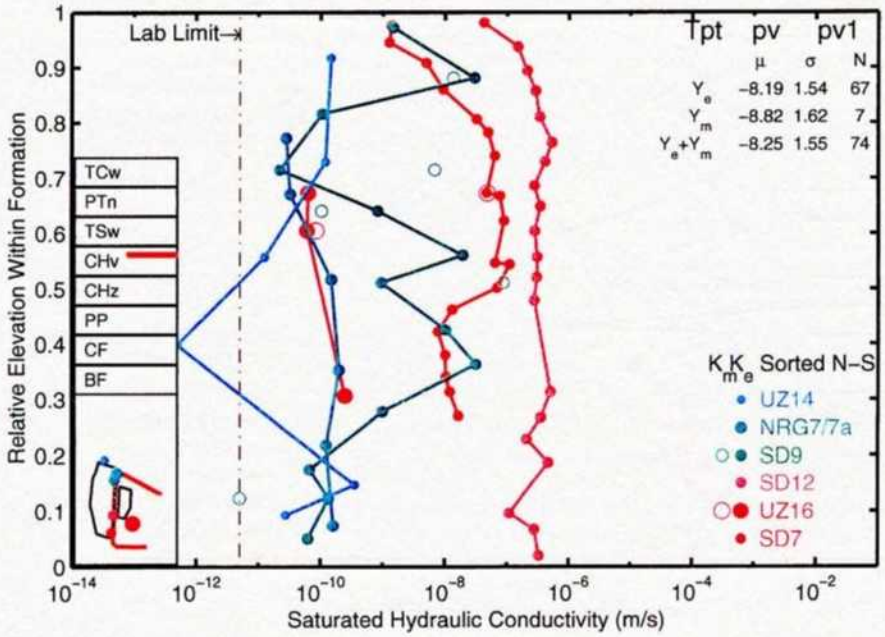

(b)

Figure 1-56: 9/17/97. All CNWRA-estimated and USGS-measured K_{sat} values in formation: (a) Tptpv2 (**FormK_Tptpv2_c.eps**), and (b) Tptpv1 (**FormK_Tptpv1_c.eps**).

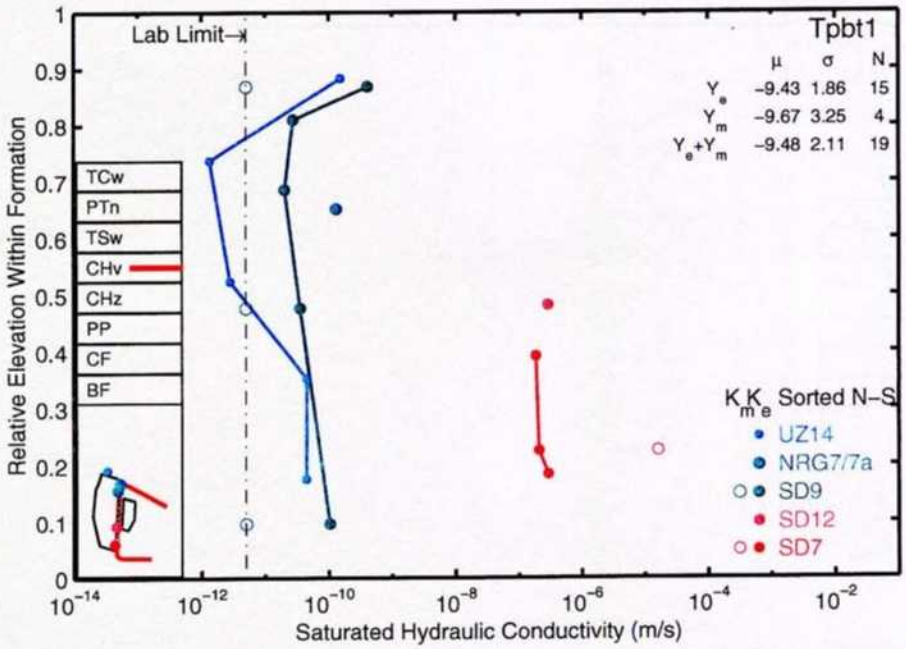

(a)

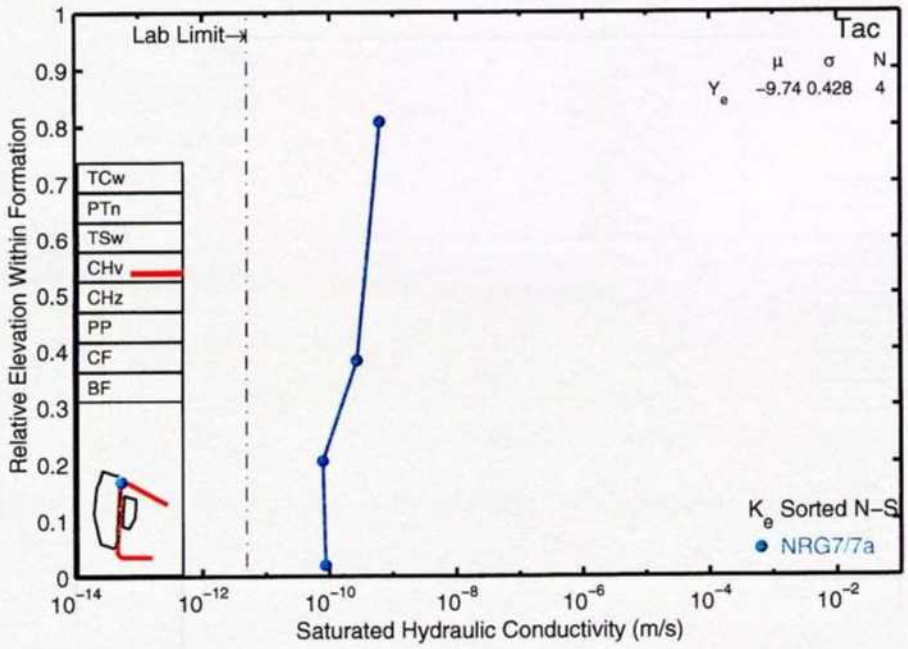

(b)

Figure 1-57: 9/17/97. All CNWRA-estimated and USGS-measured K_{sat} values in formation: (a) Tpbt1 (**FormK_Tpbt1_c.eps**), and (b) Tac (**FormK_Tac_c.eps**).

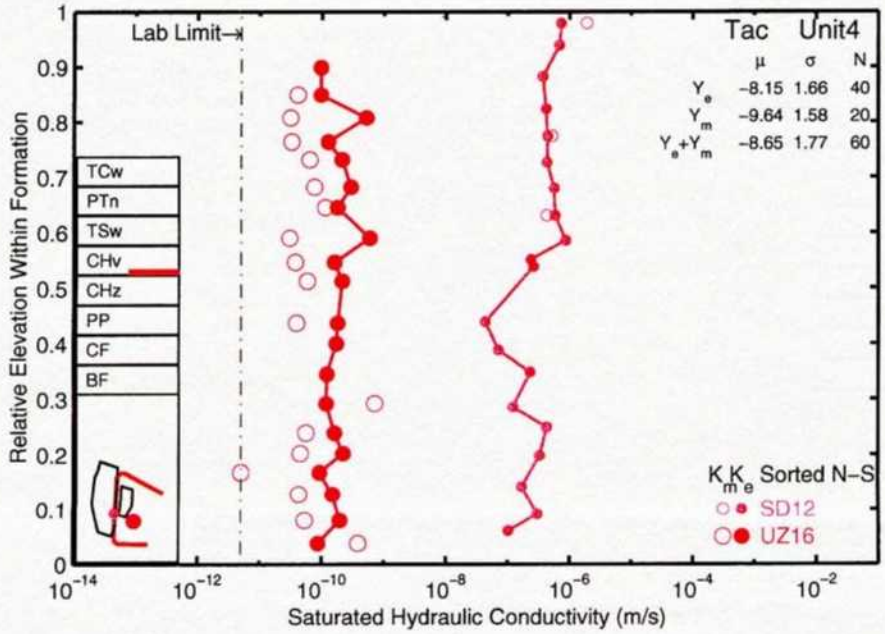

(a)

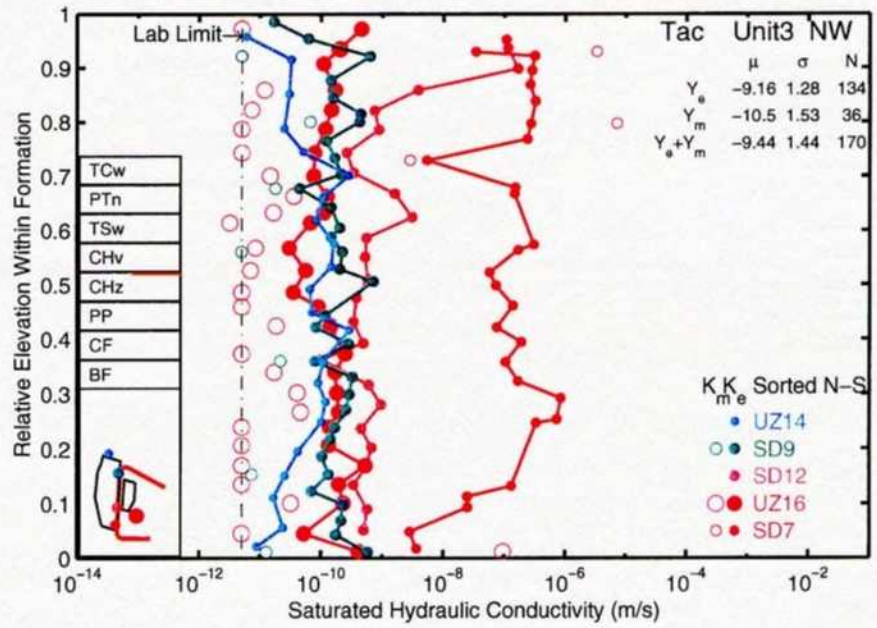

(b)

Figure 1-58: 9/17/97. All CNWRA-estimated and USGS-measured K_{sat} values in formation: (a) TacUnit4 (**FormK_TacUnit4_c.eps**), and (b) TacUnit3NW (**FormK_TacUnit3NW_c.eps**).

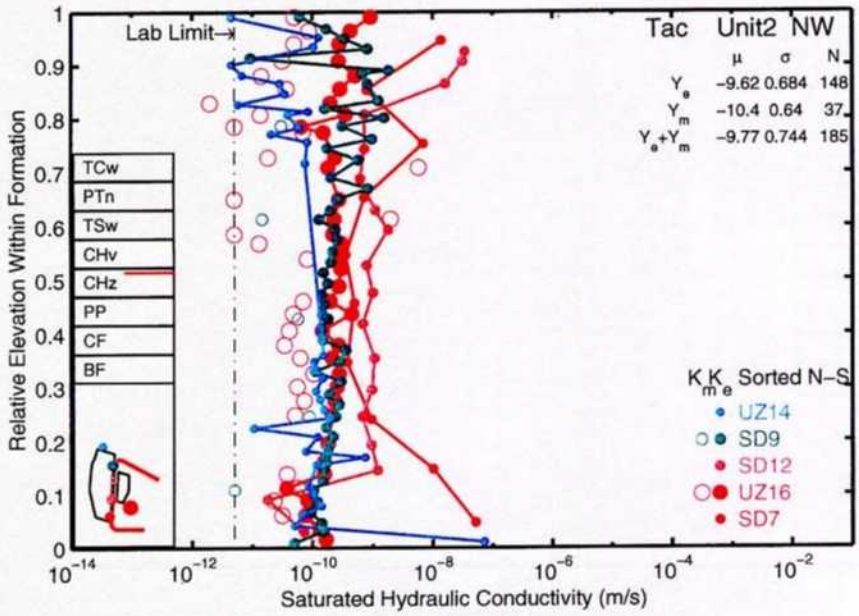

(a)

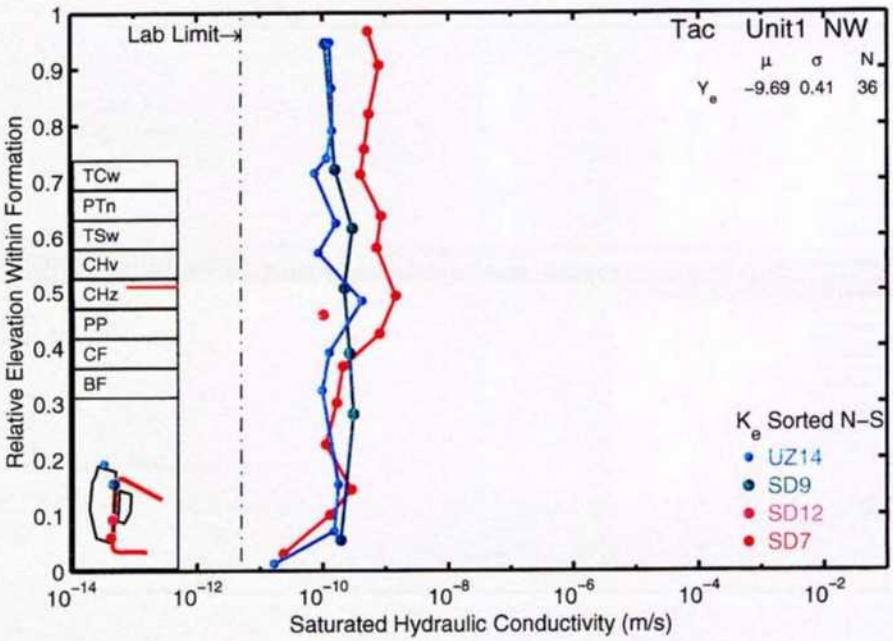

(b)

Figure 1-59: 9/17/97. All CNWRA-estimated and USGS-measured K_{sat} values in formation: (a) TacUnit2NW (**FormK_TacUnit2NW_c.eps**), and (b) TacUnit1NW (**FormK_TacUnit1NW-_c.eps**).

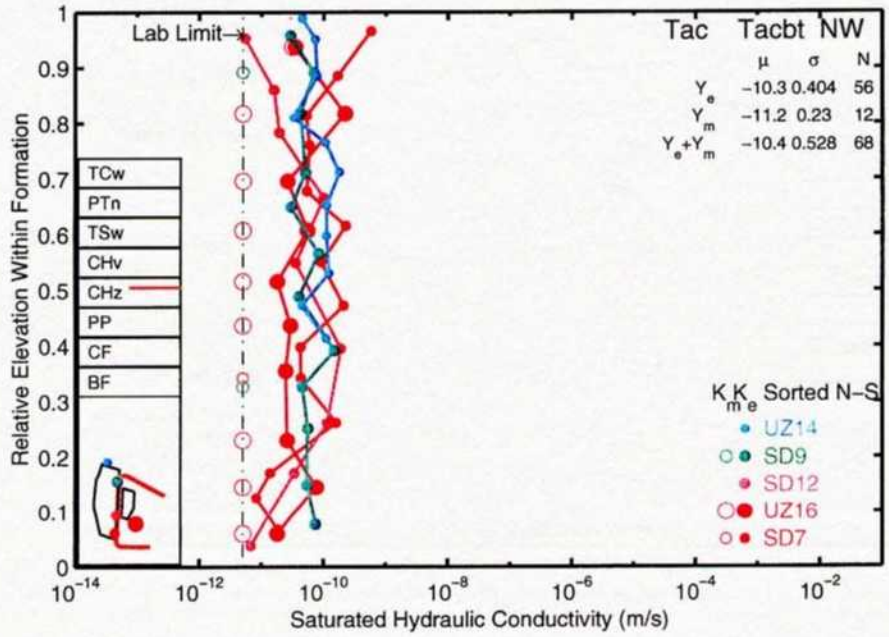

(a)

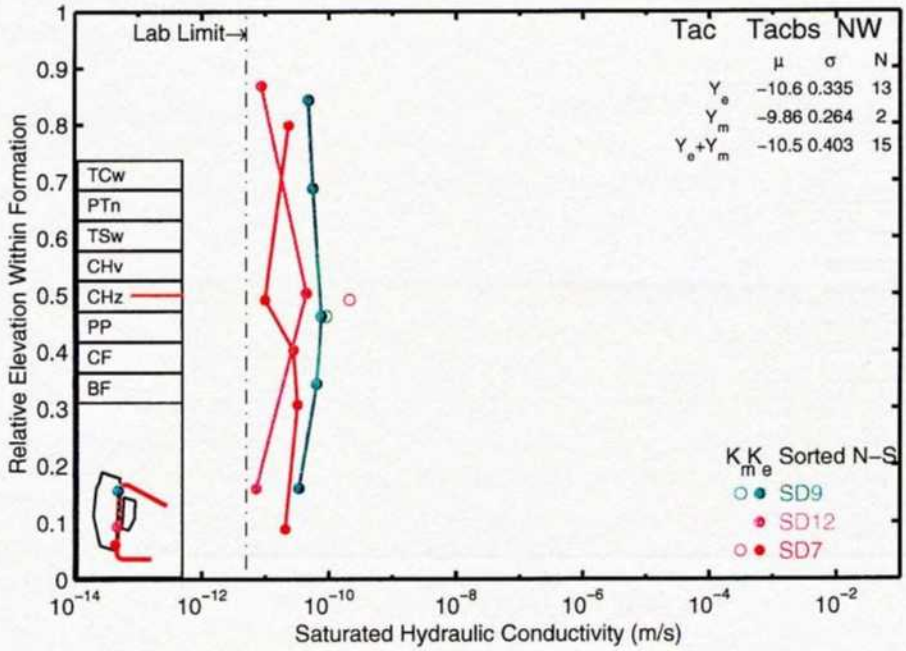

(b)

Figure 1-60: 9/17/97. All CNWRA-estimated and USGS-measured K_{sat} values in formation: (a) TacbtNW (**FormK_TacbtNW_c.eps**), and (b) TacbsNW (**FormK_TacbsNW_c.eps**).

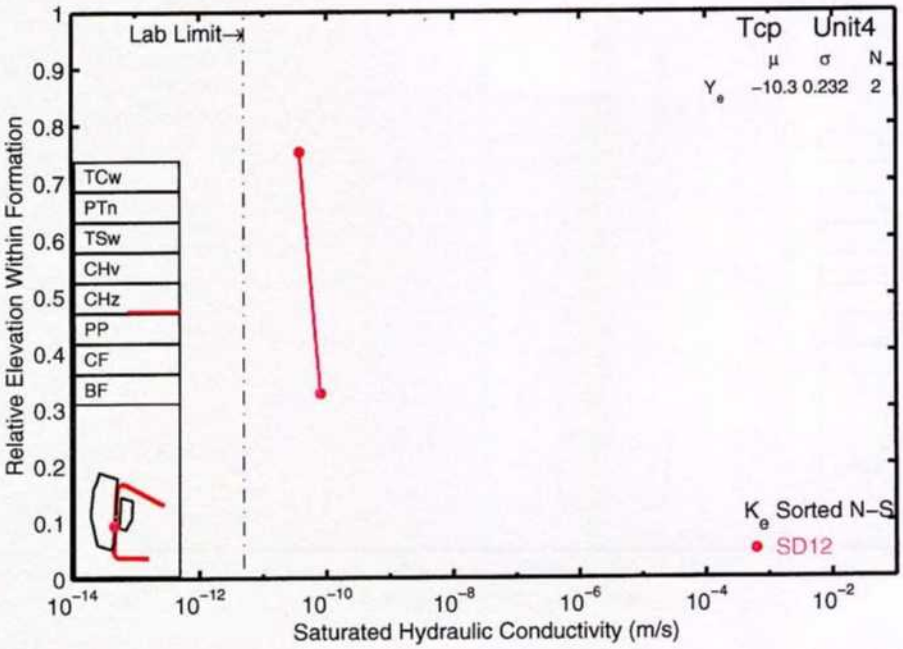

(a)

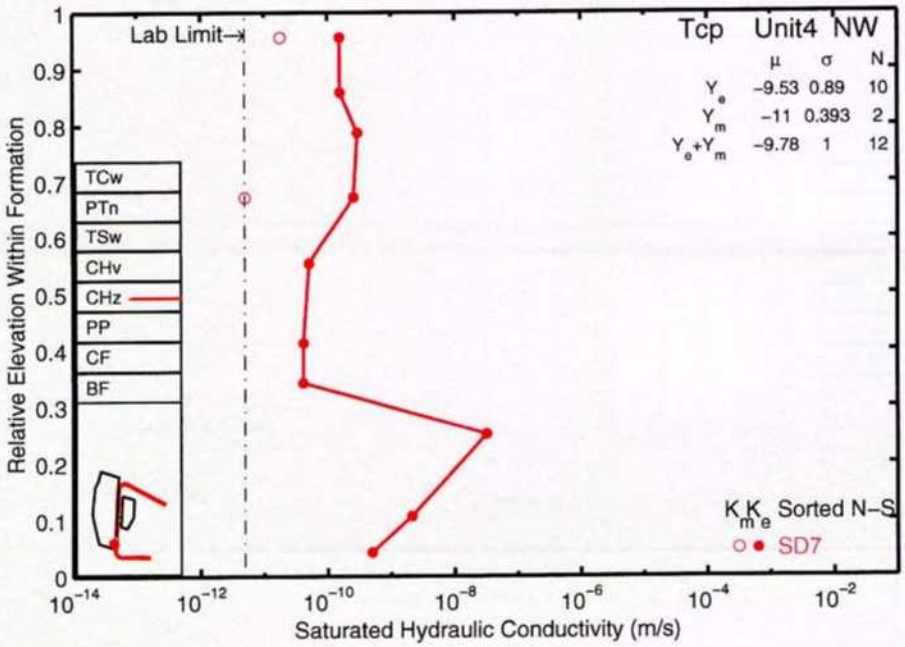

(b)

Figure 1-61: 9/17/97. All CNWRA-estimated and USGS-measured K_{sat} values in formation: (a) TcpUnit4 (**FormK_TcpUnit4_c.eps**), and (b) TcpUnit4NW (**FormK_TcpUnit4NW_c.eps**).

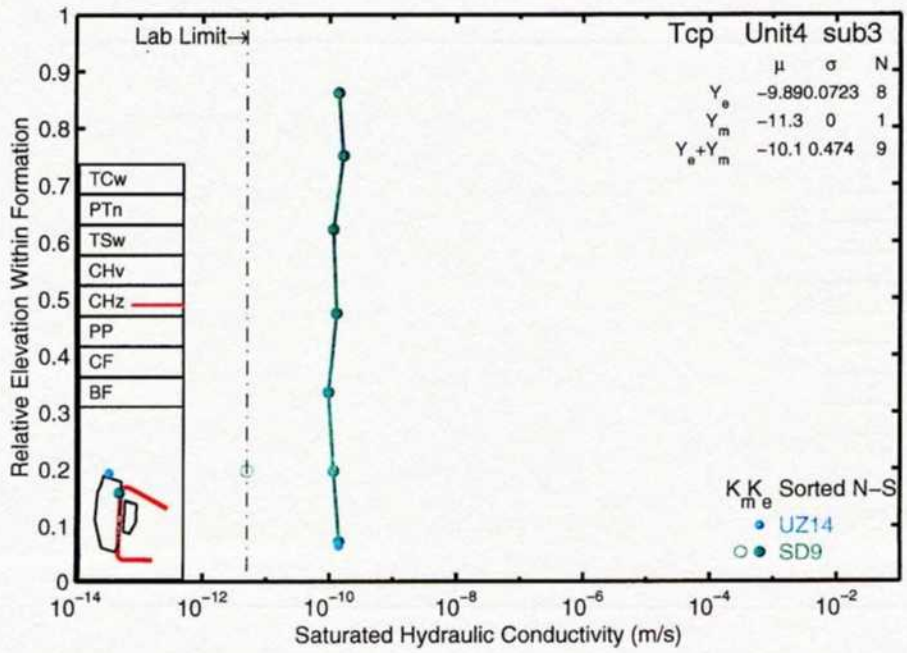

(a)

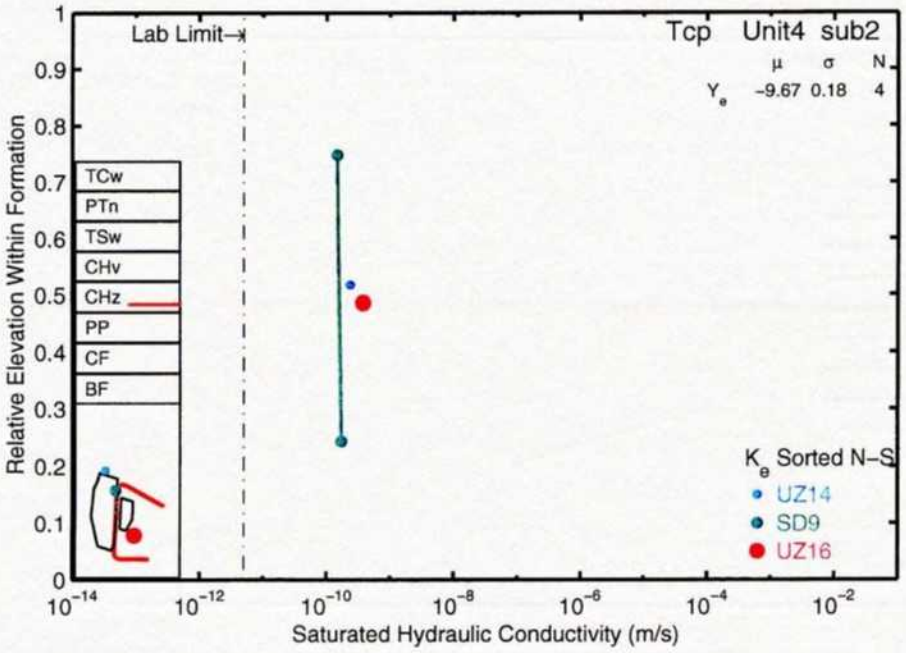

(b)

Figure 1-62: 9/17/97. All CNWRA-estimated and USGS-measured K_{sat} values in formation: (a) TcpUnit4sub3 (**FormK_TcpUnit4sub3_c.eps**), and (b) TcpUnit4sub2 (**FormK-_TcpUnit4sub2_c.eps**).

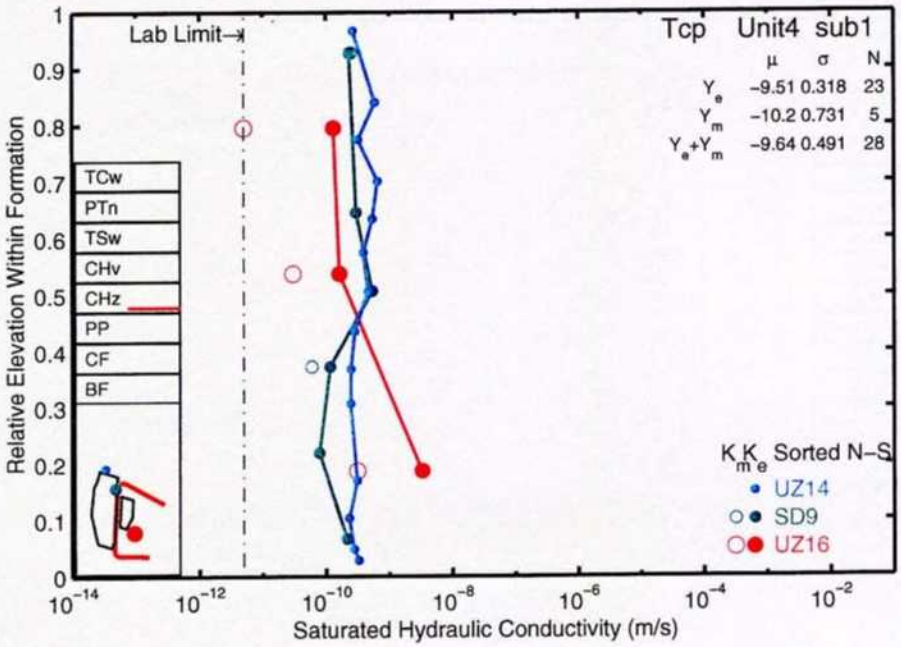

(a)

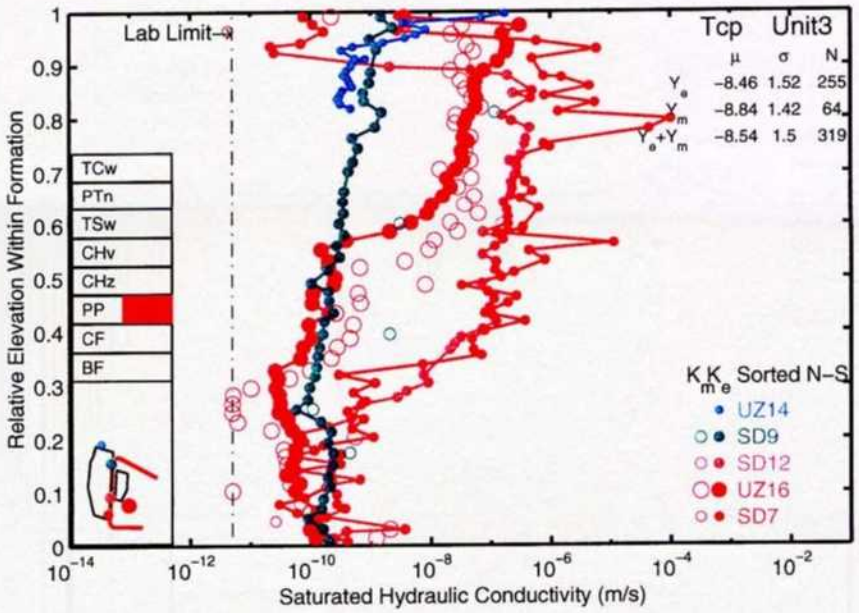

(b)

Figure 1-63: 9/17/97. All CNWRA-estimated and USGS-measured K_{sat} values in formation: (a) TcpUnit4sub1 (**FormK_TcpUnit4sub1_c.eps**), and (b) TcpUnit3 (**FormK_TcpUnit3_c.eps**).

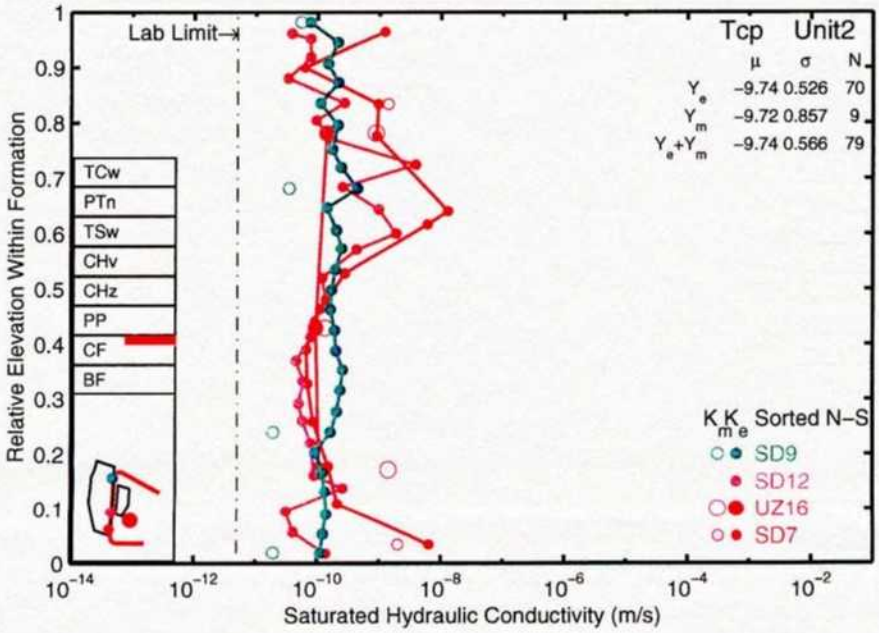

(a)

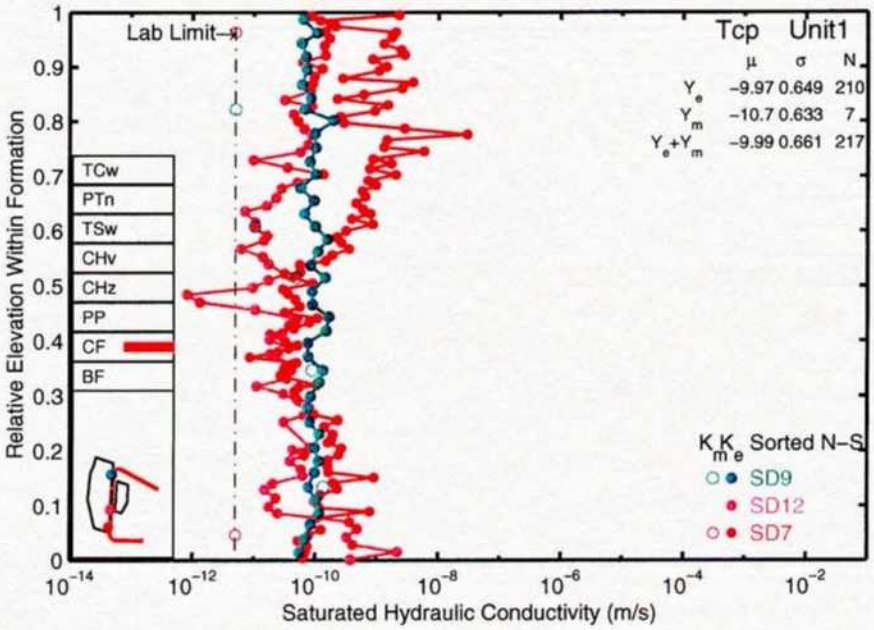

(b)

Figure 1-64: 9/17/97. All CNWRA-estimated and USGS-measured K_{sat} values in formation: (a) TcpUnit2 (**FormK_TcpUnit2_c.eps**), and (b) TcpUnit1 (**FormK_TcpUnit1_c.eps**).

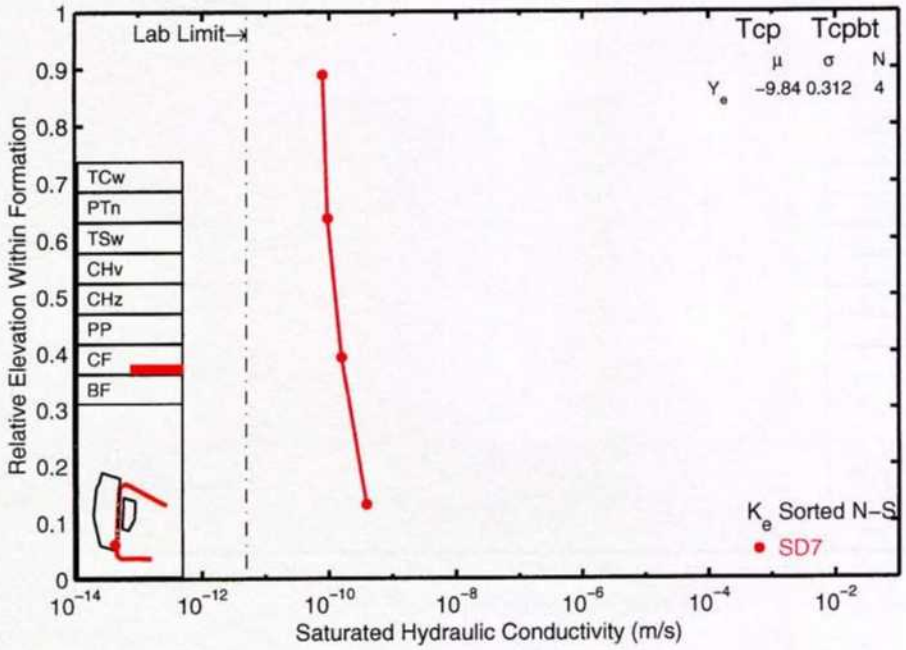

(a)

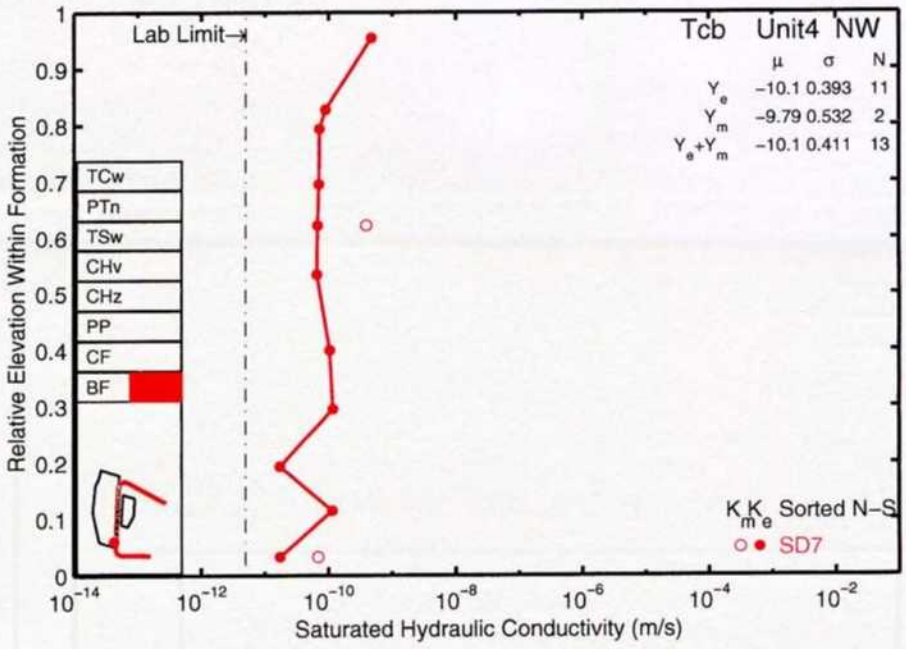

(b)

Figure 1-65: 9/17/97. All CNWRA-estimated and USGS-measured K_{sat} values in formation: (a) Tcpbt (**FormK_Tcpbt_c.eps**), and (b) TcbUnit4NW (**FormK_TcbUnit4NW_c.eps**).

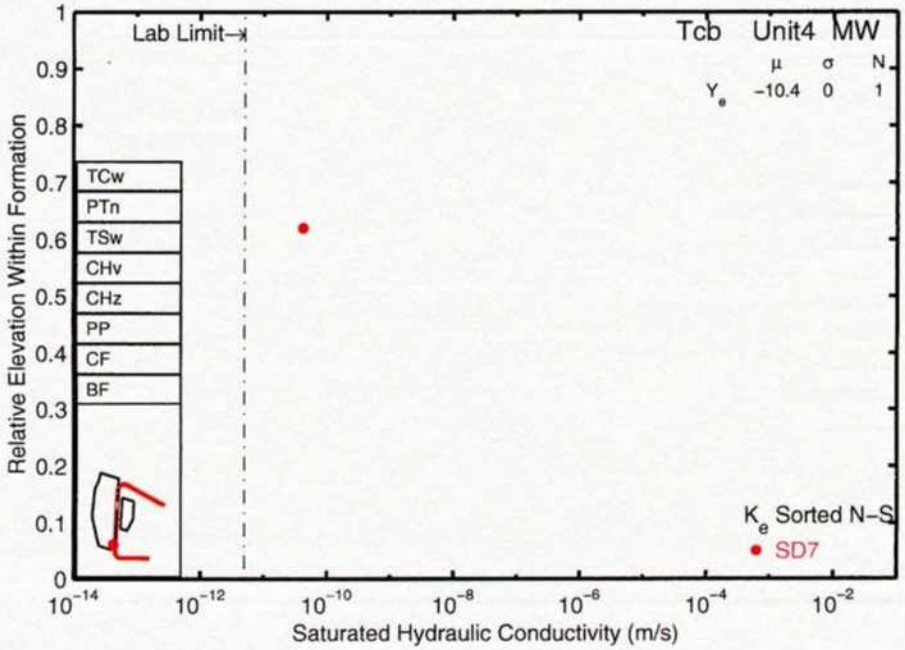

(a)

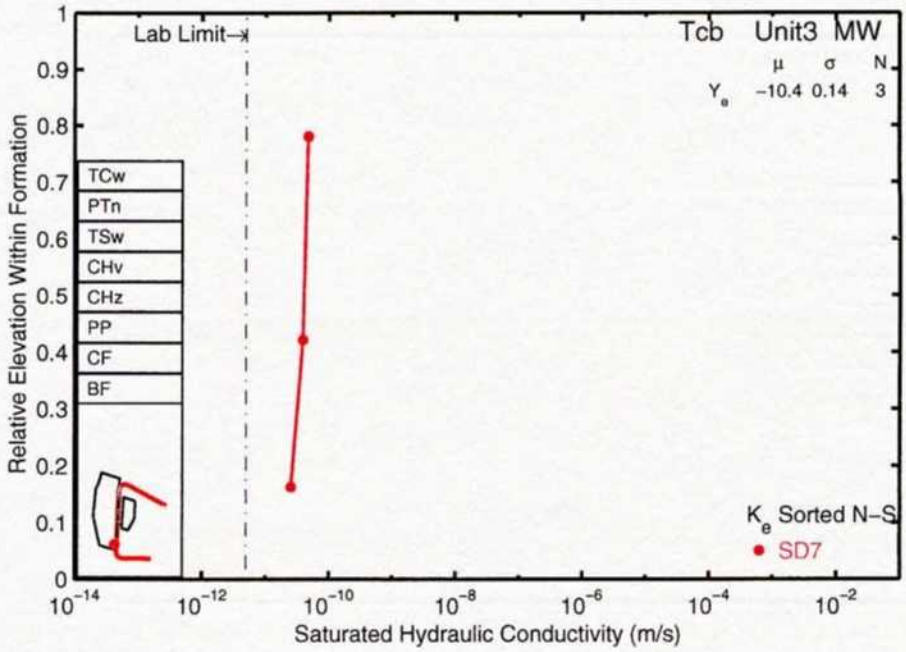

(b)

Figure 1-66: 9/17/97. All CNWRA-estimated and USGS-measured K_{sat} values in formation: (a) TcbUnit4MW (**FormK_TcbUnit4MW_c.eps**), and (b) TcbUnit3MW (**FormK-_TcbUnit3MW_c.eps**).

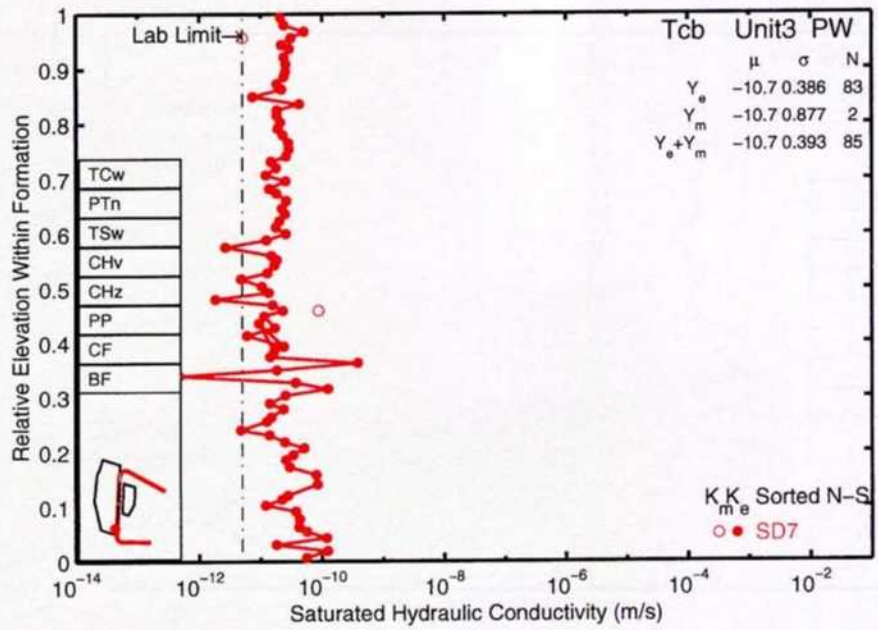

(a)

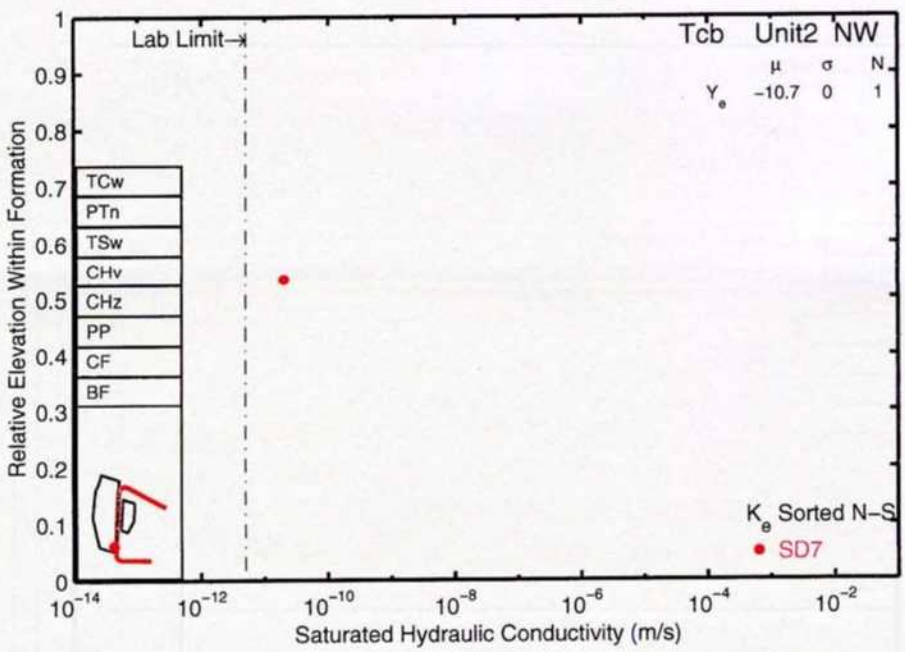

(b)

Figure 1-67: 9/17/97. All CNWRA-estimated and USGS-measured K_{sat} values in formation: (a) TcbUnit3PW (**FormK_TcbUnit3PW_c.eps**), and (b) TcbUnit2NW (**FormK_TcbUnit2NW-_c.eps**).

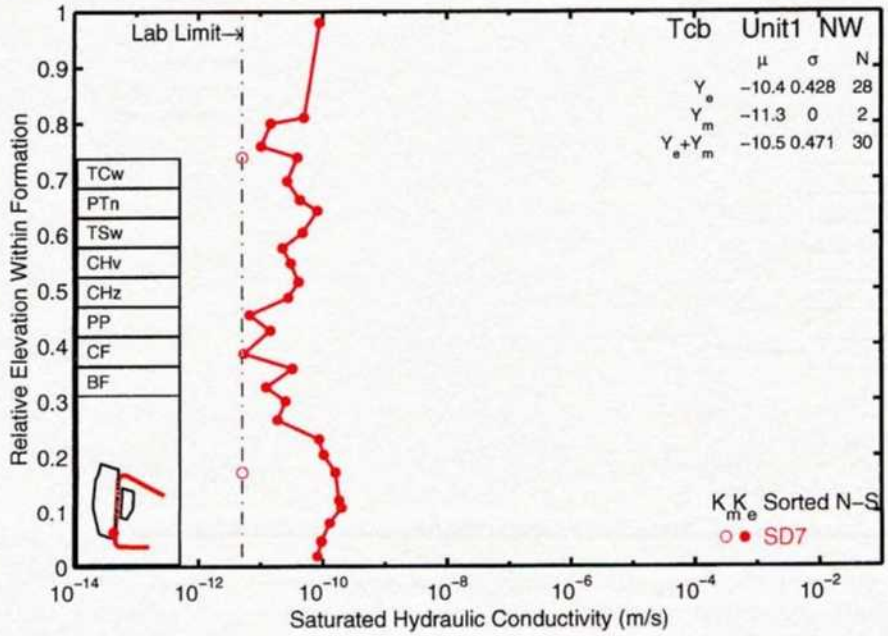

(a)

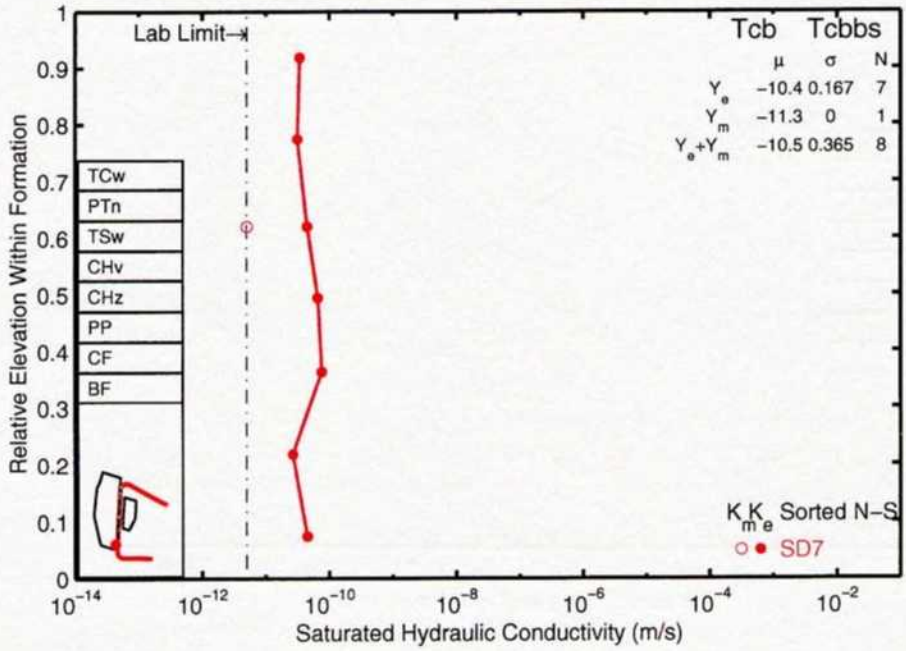

(b)

Figure 1-68: 9/17/97. All CNWRA-estimated and USGS-measured K_{sat} values in formation: (a) TcbUnit1NW (**FormK_TcbUnit1NW_c.eps**), and (b) Tcbbs (**FormK_Tcbbs_c.eps**).

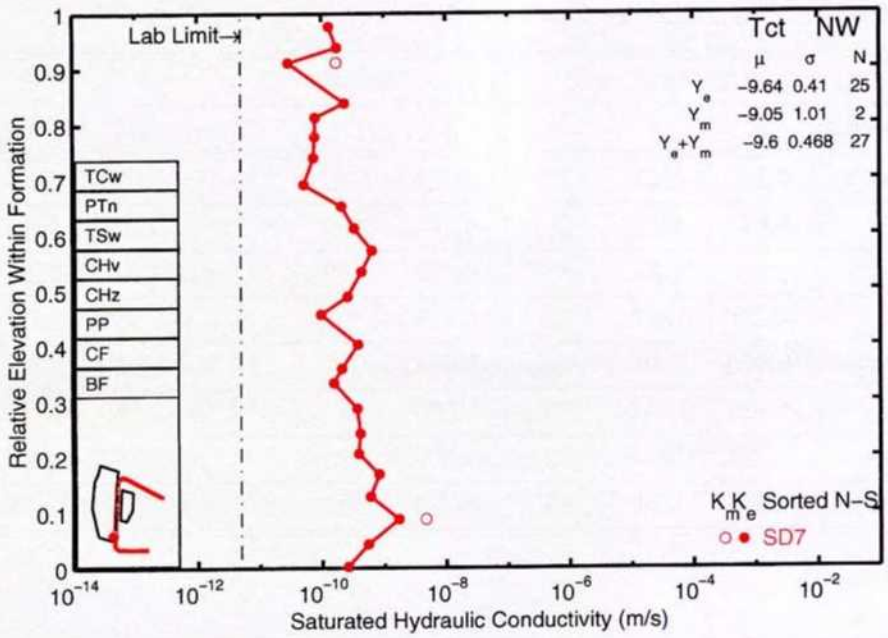

Figure 1-69: 9/17/97. All CNWRA-estimated and USGS-measured K_{sat} values in formation TctNW (**FormK_TctNW_c.eps**).

Table 1-11: Statistical description of $Y = \log_{10}[K_{sat}\ (m/s)]$ in TCw.

Formation			SAS Estimated			Measured			All		
Form	Zone1	Zone2	μ	σ	N	μ	σ	N	μ	σ	N
Tpc	rn	rn4	-9.497	0.769	19				-9.497	0.769	19
Tpc	rn	rn3	-7.541	0.566	62	-6.875	0	1	-7.53	0.568	63
Tpc	rn	rn2	-7.704	0.949	53	-7.693	0	1	-7.703	0.94	54
Tpc	rn	rn1	-8.064	1.31	17	-7.69	0	1	-8.043	1.27	18
Tpc	rl	rl2	-9.05	0.588	5				-9.05	0.588	5
Tpc	rl	rl1	-9.917	0.908	9				-9.917	0.908	9
Tpc	pul		-9.201	0.566	49	-8.985	1.53	2	-9.193	0.597	51
Tpc	pmn		-9.841	0.761	32				-9.841	0.761	32
Tpc	pll		-9.774	0.758	181	-11.14	0.48	14	-9.872	0.82	195
Tpc	pln	plnh	-10.15	0.662	169	-11.3	0	8	-10.2	0.69	177
Tpc	pln	plnc	-10.1	0.706	272	-10.99	0.523	17	-10.15	0.727	289
Tpc	pv	pv2	-9.93	0.994	54				-9.93	0.994	54

Table 1-12: Statistical description of $Y = \log_{10}[K_{sat}\ (m/s)]$ in PTn.

Formation			SAS Estimated			Measured			All		
Form	Zone1	Zone2	μ	σ	N	μ	σ	N	μ	σ	N
Tpc	pv	pv1	-7.851	1.43	76	-7.741	1.89	10	-7.839	1.48	86
Tpbt4			-6.947	1.41	20	-6.784	2.59	3	-6.925	1.53	23
Tpy			-7.97	1.36	85	-6.803	1.09	12	-7.826	1.38	97
Tpbt3			-6.99	0.804	55	-6.405	2	8	-6.915	1.03	63
Tpp			-5.903	0.66	156	-6.058	0.4	10	-5.913	0.648	166
Tpbt2			-5.885	0.757	85	-5.539	0.548	10	-5.849	0.743	95
Tpt	rv	rv3	-5.784	0.837	62	-5.503	1.25	8	-5.752	0.887	70
Tpt	rv	rv2	-7.556	1.24	25	-5.074	0	1	-7.46	1.31	26

Table 1-13: Statistical description of $Y = \log_{10}[K_{sat}\ (m/s)]$ in TSw.

Formation			SAS Estimated			Measured			All		
Form	Zone1	Zone2	μ	σ	N	μ	σ	N	μ	σ	N
Tpt	rv	rv1	-9.907	1.09	17	-9.233	1.9	4	-9.778	1.26	21
Tpt	rn		-8.5	0.611	450	-8.903	1.1	38	-8.532	0.669	488
Tpt	rn	rn2	-9.215	0.656	40	-9.255	1.21	13	-9.225	0.812	53
Tpt	rl		-8.603	0.488	31	-9.741	0	1	-8.639	0.521	32
Tpt	rl	rl2	-9.222	0.562	11	-11.3	0	1	-9.396	0.805	12
Tpt	rl	rl1	-9.178	0.661	28	-10.85	0.782	3	-9.339	0.829	31
Tpt	pul		-9.265	0.84	135	-9.638	0	1	-9.268	0.837	136
Tpt	pul	pul2	-9.617	0.543	23	-10.69	0.854	5	-9.808	0.723	28
Tpt	pul	pul1	-9.503	0.7	227	-10.17	1.2	40	-9.603	0.827	267
Tpt	pmn		-10.11	0.596	204	-11.07	0.54	34	-10.25	0.678	238
Tpt	pmn	pmn3	-10.41	0.386	23	-11.3	0	1	-10.44	0.419	24
Tpt	pmn	pmn2	-10.2	0.25	20	-10.19	1.57	2	-10.2	0.417	22
Tpt	pmn	pmn1	-10.38	0.52	19	-11.3	0	2	-10.47	0.566	21
Tpt	pll		-9.776	0.651	451	-10.21	1.16	65	-9.831	0.747	516
Tpt	pln		-10.22	0.515	327	-10.74	1.22	65	-10.31	0.708	392
Tpt	pv	pv3	-10.59	0.652	86	-10.43	0.956	8	-10.57	0.677	94

Table 1-14: Statistical description of $Y = \log_{10}[K_{sat}\ (m/s)]$ below TSw (CHnv, CHnz, PP, UCF, UBF).

Formation			SAS Estimated			Measured			All		
Form	Zone1	Zone2	μ	σ	N	μ	σ	N	μ	σ	N
Tpt	pv	pv2	-9.793	0.831	36	-9.574	1.68	2	-9.781	0.856	38
Tpt	pv	pv1	-8.193	1.54	67	-8.825	1.62	7	-8.253	1.55	74
Tpbt1			-9.426	1.86	15	-9.675	3.25	4	-9.479	2.11	19
Tac			-9.738	0.428	4				-9.738	0.428	4
Tac	Unit4		-8.153	1.66	40	-9.636	1.58	20	-8.648	1.77	60
Tac	Unit3	NW	-9.159	1.28	134	-10.47	1.53	36	-9.438	1.44	170
Tac	Unit2	NW	-9.615	0.684	148	-10.4	0.64	37	-9.772	0.744	185
Tac	Unit1	NW	-9.693	0.41	36				-9.693	0.41	36
Tac	Tacbt	NW	-10.27	0.404	56	-11.23	0.23	12	-10.44	0.528	68
Tac	Tacbs	NW	-10.56	0.335	13	-9.865	0.264	2	-10.47	0.403	15
Tcp	Unit4		-10.26	0.232	2				-10.26	0.232	2
Tcp	Unit4	NW	-9.528	0.89	10	-11.02	0.393	2	-9.777	1	12
Tcp	Unit4	sub3	-9.894	0.0723	8	-11.3	0	1	-10.05	0.474	9
Tcp	Unit4	sub2	-9.667	0.18	4				-9.667	0.18	4
Tcp	Unit4	sub1	-9.513	0.318	23	-10.23	0.731	5	-9.642	0.491	28
Tcp	Unit3		-8.465	1.52	255	-8.841	1.42	64	-8.54	1.5	319
Tcp	Unit2		-9.742	0.526	70	-9.723	0.857	9	-9.739	0.566	79
Tcp	Unit1		-9.965	0.649	210	-10.73	0.633	7	-9.99	0.661	217
Tcp	Tcpbt		-9.836	0.312	4				-9.836	0.312	4
Tcb	Unit4	NW	-10.13	0.393	11	-9.785	0.532	2	-10.08	0.411	13
Tcb	Unit4	MW	-10.38	0	1				-10.38	0	1
Tcb	Unit3	MW	-10.44	0.14	3				-10.44	0.14	3
Tcb	Unit3	PW	-10.68	0.386	83	-10.68	0.877	2	-10.68	0.393	85
Tcb	Unit2	NW	-10.7	0	1				-10.7	0	1
Tcb	Unit1	NW	-10.41	0.428	28	-11.3	0	2	-10.47	0.471	30
Tcb	Tcbbs		-10.37	0.167	7	-11.3	0	1	-10.48	0.365	8
Tct		NW	-9.641	0.41	25	-9.053	1.01	2	-9.598	0.468	27

Based on the set of figures, there appears to be little in the way of systematic spatial variability in the material properties, either vertically or horizontally. The systematic variability that is present is almost exclusively associated with the bedded units (e.g., PTn, CH). Examples of possible systematic spatial variability within a subzone include: (i) Tpy (north/south), (ii) Tpcpv1 (east/west), (iii) units transitional from nonzeolitic to zeolitic.

Bedded units also tend to have the largest unsystematic variability. This can be seen in the tables, in which most bedded units have standard deviations greater than 1 and most low-permeability units have standard deviations less than 1. Some of the lower variability in the low-permeability units is due to including those K_{sat} values at the laboratory limit for measured K_{sat} when calculating the statistical measures.

There is little point in breaking several of the zones into subzones, at least based on K_{sat}. Candidates for consolidation include:

- Tpcrn3 through Tpcrn1 (μ ranges from -7.53 through -8.04)
- Perhaps Tpcrl2 through Tpcpul (μ ranges from -9.05 through -9.92)
- Tpcmn through Tpcpv2 (μ ranges from -9.84 through -10.2)
- Tpp through Tptrv3 (μ ranges from -5.75 through -5.91)
- Tptrn through Tptrl1 (μ ranges from -8.53 through -9.40)
- Tptpul through Tptpul1 (μ ranges from -9.27 through -9.81)
- Tptpmn through Tptpv3 (μ ranges from -9.83 through -10.47)
- Tac Unit3 through Tac Unit1 (μ ranges from -9.44 through -9.77)
- Tacbt through Tacbs (μ ranges from -10.44 through -10.47)
- All Tcp Unit4 subzones (μ ranges from -9.64 through -10.26)
- Tcp Unit2 through Tcpbt (μ ranges from -9.74 through -9.99)
- All Tcb (μ ranges from -10.08 through -10.7)

9/23/97 Investigation of USGS retention properties.

The USGS has only presented data for retention properties on core samples obtained from outcrops (Flint et al., 1996), to the best of my knowledge. As documented in the 1/22/97 entry, these data were entered electronically by A. Ramos from Appendix II in the report by Flint et al. (1996). I created two *Matlab* files, show_reten.m and ss_logpcap_eval.m, in ***$HOME2/AmbientKTI/-3Ddata***, to investigate the retention properties.

The procedure Flint et al. (1996) followed was to use RETC for the data of each core sample individually, obtaining van Genuchten α and m, then regressing these into a global relationship. Thoughts on the Flint et al. (1996) procedure are discussed in the 9/21/96 entry, but in short my opinion is that it would be more fruitful to try to perform simultaneous regressions.

The idea behind today's investigation is to create a regression for all measured points simultaneously, using the intrinsic *Matlab* function fmins to minimize

$$u = \sum_{i=1}^{N} [\log_{10}(P_{mi}) - \log_{10}(P_{ei})]^2, \tag{1-31}$$

$$P_e = P_0(\theta^{-1/m} - 1)^{1-m}, \tag{1-32}$$

$$\log_{10}(P_{0i}) = a_0 + a_1 V_{1i} + a_2 V_{2i}, \tag{1-33}$$

$$m_i = b_0 + b_1 V_{3i} + b_2 V_{4i}. \tag{1-34}$$

where

- u is the objective function,
- P_m is measured capillary pressure,
- P_e is estimated capillary pressure,
- m is van Genuchten $m = 1 - 1/n$,
- P_0 is bubbling pressure (the reciprocal of van Genuchten α in the units used here),
- V_{ji} are the variables being regressed against, and
- a_j, b_j are the regression constants.

Flint et al. (1996) report pairs of volumetric water content (VWC) and capillary pressure (P_c) in their Appendix II. Data from two subsamples (TS47s, CH60s) were discarded, as properties (e.g., porosity) for the parent core samples were either not determined or were not reported in the electronic data set. Several VWC/P_c pairs had only one of the pair reported, or had a zero value for VWC; these pairs were also discarded.

The measured porosity of some core samples was not consistent with the VWC reported at

a P_c of 0.01 bar [note that Flint et al. (1996) assume full saturation at 0.01 bar]. Accordingly, for the purposes of regression, effective saturation was calculated by multiplying all VWC values for a sample by $0.999/VWC_0$, where VWC_0 is VWC at 0.01 bar; also, the porosity for each subsample was assumed to be VWC_0. Because of this inconsistency, the core-sample value for the difference between porosity at 65 and 105 °C was used as a candidate regression parameter, but not either porosity value individually.

All combinations of 1-parameter and 2-parameter fits for both P_0 and m were exhaustively checked for the best value of u. The 8 candidate regression variables, v, included VWC_0, bulk density at both 65 and 105 °C, particle density at both 65 and 105 °C, and change in porosity, bulk density, and particle density between 65 and 105 °C. The optimal fit provided by the best set and the worst set of parameters was not greatly different, differing by only about one-third, and all optimal fits were on the order of 10 (mean error for a measured/estimated P_0 pair is about one order of magnitude). The insensitivity to regression parameter is probably due to: (i) a high degree of correlation between the various parameters for each sample, and (ii) considerable noise in the data. A spot check for several combinations of parameters suggests that worse fits would be obtained for P_0 rather than $\log_{10}(P_0)$ and for $\log_{10}(m)$ rather than m.

9/24/97 Thoughts on assignment of layer properties. SAS

The actual flow path of a water particle in a heterogeneous medium is likely to be quite tortuous. Under certain restrictive conditions, a heterogeneous porous medium can be replaced with an equivalent homogeneous porous medium. When saturated flow is 1D, and the flow is perpendicular to the heterogeneity (like a bundle of tubes), the flow is in parallel and the equivalent K_{sat} is the area-weighted arithmetic average of K_{sat} for the individual tubes. When saturated flow is 1D, and the flow is parallel to the heterogeneity (layers), the flow is in series and the equivalent K_{sat} is the length-weighted harmonic average of the individual tube K_{sat}s. If the heterogeneity relationship is more complicated, or the flow is not saturated, the picture muddies considerably and a unique K_{sat} cannot be determined in general.

When dealing with unsaturated media, the actual task is to determine equivalent values of K_{sat}, ε, α, m, and dispersivity so that a box containing the equivalent porous medium behaves like a box containing the heterogeneous medium, over the range of fluxes of interest. For Yucca Mountain, there is a tremendous upscaling that must be accomplished, from the core scale (5 cm on a side) to the formation scale (1 to 100 m thick by km^2).

A method that is useful for upscaling, and I believe is used in the petroleum industry, involves repeatedly averaging stochastically generated blocks of material, with each averaging occurring at a larger scale. At each scale, one creates the equivalent medium for 2, 4, or 8 blocks (depending on dimensionality). Averaging is typically performed for steady state conditions.

In the most rigorous approach, one would create a series of simulations with the original medium. For Yucca Mountain conditions, each simulation would presumably have 8 or more blocks, pressure conditions imposed at top and bottom, and no-flow conditions on the vertical sides (allowing lateral flow within the domain but not between averaging blocks). The equivalent properties would then be found by matching the flux and travel time results for each of the boundary conditions. It seems to me that the best that one could hope for would be to end up with pressure matches for the top and bottom of the formation and arbitrary variation in between.

It seems that one might do well trying to obtain an equivalent porous medium composed of several distinct media with different volumetric fractions; the distinct media might be preselected, with the job becoming obtaining the volumetric fractions. A first approach to picking media might be to: (i) determine the porosity distribution (for example) of a layer, (ii) pick out say 8 quantiles for porosity, and (iii) assign mean values for the other properties in each quantile.

In the case of Yucca Mountain, my feeling is that heterogeneity has much smaller correlation lengths in the vertical than in the horizontal, particularly for bedded tuffs. Welded tuffs should be almost isotropic at a small scale.

I think that an approach with merit would be to create many short columns, perhaps a correlation length in vertical dimension, pick a set of values of the medium properties for each end, and assume that the properties vary linearly/loglinearly between ends. The sets of properties should be appropriately correlated. The equivalent-medium properties can be obtained from building up a retention curve and a relative-permeability curve for the equivalent medium by averaging the contributions from each of the columns.

Actually, using the theory that lateral redistribution of pressure is efficient enough that pressure everywhere at the same relative height within a layer is approximately equal and gravity drainage is the primary condition of interest, a better approach would be to simply generate the arithmetic-mean response curves for each layer by imposing a gravity-drainage assumption for a series of capillary pressures and abstracting the mean responses. Arithmetic means should be taken of $k(P_c)$ and $\theta(P_c)$. It should be relatively efficient to calculate K_{sat}, α, and m for the effective medium using this approach.

9/29/97 More thoughts on assignment of layer properties. SAS

A major component of generating layer properties by averaging core-sample properties is generating the set of random core-sample properties that are to be averaged. In order to generate properties, the statistical distribution of the properties must be known. However, these properties can only be estimated from the sampled values. According to Benjamin and Cornell (1970), in their section 4.1.2, the mean of a distribution estimated from samples is itself a random variable, normally distributed in the limit of many samples. Benjamin and Cornell (1970), in their section 4.3.2, further note that regression equations have uncertain coefficients as well.

The sample mean, $\bar{X}$, and sample variance, S^2, of n observations, X_i, from a random distibution are

$$\bar{X} = \frac{1}{n}\sum_{i=1}^{N} X_i, \tag{1-35}$$

$$S^2 = \frac{1}{n-1}\sum_{i=1}^{N}(X_i - \bar{X}). \tag{1-36}$$

The expected value and variance of $\bar{X}$ are

$$\mathrm{E}[\bar{X}] = m_X, \tag{1-37}$$

$$\mathrm{Var}[\bar{X}] = \frac{\sigma_X^2}{n}, \tag{1-38}$$

where m_X and σ_X are the true mean and standard deviation of the underlying physical process. Note that the variance of $\bar{X}$ would include correlation terms if the observations were not mutually independent. The expected value and variance of S^2 are

$$\mathrm{E}[S^2] = \sigma_X^2, \tag{1-39}$$

$$\mathrm{Var}[S^2] = \frac{2\sigma_X^4}{n-1}, \tag{1-40}$$

where it is assumed that X is normally distributed when deriving the expression for $\mathrm{Var}[S^2]$.

The regression equations have the form

$$y_j = a + \sum_{i=1}^{N} b_i x_{ij} + \epsilon_j, \tag{1-41}$$

where y_j is the jth observation of the predicted variable y, the x_{ij} values represent observations of N predictor variables, and ϵ_j represents a normally distributed zero-mean noise. To estimate the

a and b_i constants, one chooses $\hat{a}$ and $\hat{b}_i$ such that the sum of squares, or

$$\sum_{j=1}^{M}\left[y_j - \left(\hat{a} + \sum_{i=1}^{N}\hat{b}_i x_{ij}\right)\right]^2, \tag{1-42}$$

is minimized by taking the derivative with respect to the coefficients, yielding

$$\sum_{j=1}^{M} 2\left[y_j - \left(\hat{a} + \sum_{i=1}^{N}\hat{b}_i x_{ij}\right)\right](-1) = 0, \tag{1-43}$$

$$\sum_{j=1}^{M} 2\left[y_j - \left(\hat{a} + \sum_{i=1}^{N}\hat{b}_i x_{ij}\right)\right](-x_{kj}) = 0, \tag{1-44}$$

where $k = 1, 2, \ldots, N$. The equations reduce to

$$M\left(\bar{y} - \hat{a} - \sum_{i=1}^{N}\hat{b}_i\bar{x}_i\right) = 0, \tag{1-45}$$

$$\sum_{j=1}^{M} y_j x_{kj} - \hat{a}\bar{x}_k - \sum_{i=1}^{N}\hat{b}_i x_{ij} x_{kj} = 0, \tag{1-46}$$

$$\bar{y} = \frac{1}{n}\sum_{j=1}^{M} y_i, \tag{1-47}$$

$$\bar{x}_k = \frac{1}{n}\sum_{j=1}^{M} x_{kj}, \tag{1-48}$$

and finally to

$$\hat{a} = \bar{y} - \sum_{i=1}^{N}\hat{b}_i\bar{x}_i, \tag{1-49}$$

$$\sum_{j=1}^{M} y_j x_{kj} - M\hat{a}\bar{x}_k - \sum_{i=1}^{N}\hat{b}_i x_{ij} x_{kj} = 0, \tag{1-50}$$

$$\bar{y} = \frac{1}{M}\sum_{j=1}^{M} y_j, \tag{1-51}$$

$$\bar{x}_k = \frac{1}{M}\sum_{j=1}^{M} x_{kj}. \tag{1-52}$$

Benjamin and Cornell (1970) note that the obvious estimator for σ^2, the assumed-constant variance of Y given x, is the average of the squared residuals. This turns out to be

$$s^2 = \hat{\sigma^2} = \frac{1}{M-N-1}\sum_{j=1}^{M}\left[y_j - \left(\hat{a} + \sum_{i=1}^{N}\hat{b}_i x_{ij}\right)\right]^2. \tag{1-53}$$

Further, when the sample size is sufficiently large, $N = 1$, the values of y_i are uncorrelated, and the values of y_i have the same variance,

$$B = \sum_{j=1}^{M} c_j y_j, \tag{1-54}$$

$$c_j = \frac{x_j - \bar{x}}{\sum_{j=1}^{M}(x_j - \bar{x})^2}, \tag{1-55}$$

$$\mathrm{E}[B] = \mathrm{E}[\sum_{j=1}^{M} c_j y_j] = \sum_{j=1}^{M} c_j \mathrm{E}[y_j] = a\sum_{j=1}^{M} c_j + b\sum_{j=1}^{M} c_j x_j = b, \tag{1-56}$$

$$\mathrm{Var}[B] = \mathrm{Var}[\sum_{j=1}^{M} c_j y_j] = \sum_{j=1}^{M} c_j^2 \mathrm{Var}[y_j] = \mathrm{Var}[y_j]\frac{\sum_{j=1}^{M} x_j^2 - M\bar{x}}{(\sum_{j=1}^{M} x_j^2 - M\bar{x})^2} = \frac{s^2}{M s_X^2}, \tag{1-57}$$

$$\mathrm{Var}[A] = \mathrm{Var}[\bar{y} - b\bar{x}] = \frac{\mathrm{Var}[y_j]}{M} + \bar{x}^2\mathrm{Var}[B] = \frac{s^2}{M}\left(1 + \frac{\bar{x}^2}{s_X^2}\right). \tag{1-58}$$

Expanding upon the procedure outlined in section 4.3.2 by Benjamin and Cornell (1970), the corresponding estimators for two-variable regression equations are

$$B_1 = \frac{C_{10}C_{22} - C_{20}C_{12}}{C_{11}C_{22} - C_{12}C_{21}}, \tag{1-59}$$

$$B_2 = \frac{C_{20}C_{11} - C_{10}C_{21}}{C_{11}C_{22} - C_{12}C_{21}}, \tag{1-60}$$

$$C_{10} = \sum_{j=1}^{M}(x_{1j} - \bar{x}_1)y_j, \tag{1-61}$$

$$C_{20} = \sum_{j=1}^{M}(x_{2j} - \bar{x}_2)y_j, \tag{1-62}$$

$$C_{11} = \sum_{j=1}^{M}(x_{1j}^2 - \bar{x}_1^2) = M s_1^2, \tag{1-63}$$

$$C_{22} = \sum_{j=1}^{M}(x_{2j}^2 - \bar{x}_2^2) = M s_2^2, \tag{1-64}$$

$$C_{12} = C_{21} = \sum_{j=1}^{M}(x_{1j}x_{2j} - \bar{x}_1\bar{x}_2) = M s_{12} = M\rho s_1 s_2, \tag{1-65}$$

$$C_{11}C_{22} - C_{12}C_{21} = M^2 s_1^2 s_2^2(1 - \rho^2), \tag{1-66}$$

where ρ is the correlation coefficient. The equations can be arranged to yield

$$B_1 = \sum_{j=1}^{M} \beta_{1j} y_j, \tag{1-67}$$

$$B_2 = \sum_{j=1}^{M} \beta_{2j} y_j, \tag{1-68}$$

$$\beta_{1j} = \frac{C_{22}(x_{1j} - \bar{x}_1) - C_{12}(x_{2j} - \bar{x}_2)}{M^2 s_1^2 s_2^2 (1-\rho^2)}, \tag{1-69}$$

$$\beta_{2j} = \frac{C_{11}(x_{2j} - \bar{x}_2) - C_{21}(x_{1j} - \bar{x}_1)}{M^2 s_1^2 s_2^2 (1-\rho^2)}. \tag{1-70}$$

Noting that

$$\sum_{j=1}^{M} \beta_{1j} = 0, \tag{1-71}$$

$$\sum_{j=1}^{M} \beta_{1j} x_{1j} = 1, \tag{1-72}$$

$$\sum_{j=1}^{M} \beta_{1j} x_{2j} = 0, \tag{1-73}$$

the corresponding variances are

$$\begin{aligned} \mathrm{Var}[B_1] &= \mathrm{Var}[y_j] \sum_{j=1}^{M} \left(\frac{C_{22}(x_{1j} - \bar{x}_1) - C_{12}(x_{2j} - \bar{x}_2)}{C_{11}C_{22} - C_{12}C_{21}} \right)^2 \\ &= s^2 \frac{C_{22}}{C_{11}C_{22} - C_{12}C_{21}} = \frac{s^2}{M} \left[\frac{1}{s_1^2(1-\rho^2)} \right], \end{aligned} \tag{1-74}$$

$$\begin{aligned} \mathrm{Var}[B_2] &= \mathrm{Var}[y_j] \sum_{j=1}^{M} \left(\frac{C_{11}(x_{2j} - \bar{x}_2) - C_{21}(x_{1j} - \bar{x}_1)}{C_{11}C_{22} - C_{12}C_{21}} \right)^2 \\ &= s^2 \frac{C_{11}}{C_{11}C_{22} - C_{12}C_{21}} = \frac{s^2}{M} \left[\frac{1}{s_2^2(1-\rho^2)} \right], \end{aligned} \tag{1-75}$$

$$\begin{aligned} \mathrm{Var}[A] &= \mathrm{Var}[\bar{y} - b_1\bar{x}_1 - b_2\bar{x}_2] = \frac{\mathrm{Var}[y_j]}{M} + \bar{x}_1^2 \mathrm{Var}[B_1] + \bar{x}_2^2 \mathrm{Var}[B_2] \\ &= \frac{s^2}{M} \left[1 + \frac{\bar{x}_1^2}{s_1^2(1-\rho^2)} + \frac{\bar{x}_2^2}{s_2^2(1-\rho^2)} \right]. \end{aligned} \tag{1-76}$$

Note that when x_1 and x_2 are not correlated ($\rho = 0$), the expressions for the variances simplify.

These ideas can be generalized to be handled using matrix algebra, as listed by, for example, Lapin (1983). The set of observations,

$$\hat{y}_j = A + \sum_{i=1}^{N} B_i x_{ji} + \epsilon, \tag{1-77}$$

can be written in matrix form as

$$\mathbf{y} = \mathbf{X}\mathbf{b} + \epsilon, \tag{1-78}$$

where $\mathbf{y}$ is the column of observations, $\mathbf{X}$ is the matrix of individual-variable observations (each row is a data point and each column is a variable, with the first column all ones), $\mathbf{b}$ is the vector of unknown coefficients. Rewriting, the coefficients are found by solving

$$\mathbf{b} = (\mathbf{X}'\mathbf{X})^{-1}\mathbf{X}'\mathbf{y}. \tag{1-79}$$

The sum of squared residuals is

$$S^2_{Y\cdot 12\ldots} = \frac{1}{M-N-1}(\mathbf{y}'\mathbf{y} - \mathbf{b}'\mathbf{X}'\mathbf{y}), \tag{1-80}$$

and the sample variance-covariance pairs are provided by

$$S^2_{Y\cdot 12\ldots}(\mathbf{X}'\mathbf{X})^{-1} = \frac{1}{M-N-1}(\mathbf{y}'\mathbf{y} - \mathbf{b}'\mathbf{X}'\mathbf{y})(\mathbf{X}'\mathbf{X})^{-1}, \tag{1-81}$$

where the standard error for b_k is the square root of the kth diagonal element.

The above discussion relates to estimating K_{sat} in core samples using other measured properties (i.e., saturation, porosity). In previous entries, it was found that the best regression equation for predicting K_{sat} from measured properties is

$$\log_{10}(K_{sat}) = a + b_1\theta_{65} + b_2\varepsilon_{sample} + \epsilon. \tag{1-82}$$

The best-fit regression equations found before are:

$$\log_{10}(K_{sat}) = -10.1846 - 6.57021 \log 10(\theta_{65}), \tag{1-83}$$

$$= -7.62342 - 3.79487\theta_{65} + 6.30827\varepsilon_{sample}, \tag{1-84}$$

$$= -5.96958 - 11.3334VWC_{105} + 7.20616\varepsilon_{65} + 3.4806\log_{10}(\varepsilon_{sample}), \tag{1-85}$$

where a subscript of 65 denotes the measurement at 65 °C, a subscript of 105 denotes the measurement at 105 °C, a subscript of *sample* denotes the subsample measurement, θ is saturation, ε is porosity, and VWC is volumetric water content. For these equations, the sample coefficient of multiple determination, $R^2 = 1 - [\sum(Y - \hat{Y})]/[\sum(Y - \bar{Y})]$, total sum of squared error, S^2, and standard error of b_k (using Equation 1-81) are as shown in Table 1-15. The standard errors correspond to the coefficents listed as above. Notice that as the explained error increases, the uncertainty in the coefficients also increases.

Table 1-15: Statistical properties of regression on K_{sat}.

Source	R^2	S^2	Standard Error in Equation Coefficient			
			a	b_1	b_2	b_3
USGS database	0.512	–	–	–	–	–
1-Parameter	0.574	1.25	6.20×10^{-3}	8.31×10^{-2}	–	–
2-Parameter	0.715	0.84	4.03×10^{-2}	3.90×10^{-2}	1.81×10^{-1}	–
3-Parameter	0.735	0.78	3.17×10^{-1}	3.06×10^{-1}	7.97×10^{-1}	2.19×10^{-1}

There are uncertainties in the regression-equation coefficients as well as the underlying properties. In order to estimate layer-wide K_{sat} values given a statistical description of all relationships, first the underlying populations of θ and ε must be generated using the statistical descriptions of the two variables. Since the two variables are correlated, an appropriate procedure is to first generate the distribution for one, using sample statistics, then generate the distribution for the other using conditional mean and variance (Benjamin and Cornell, 1970, section 3.6.3). Assuming mutual normality,

$$\mu_{Y|X} = \mu_Y + \rho\frac{\sigma_Y}{\sigma_X}(x - \mu_x), \tag{1-86}$$

$$\sigma^2_{Y|X} = (1 - \rho^2)\sigma^2_Y. \tag{1-87}$$

Once the underlying population samples are determined, these are plugged into the regression equation for $\log_{10}(K_{sat})$ and random noise (ϵ) applied based on the standard deviation about the regression plane. The integrated value for K_{sat} can then be determined from the population.

Since each of the coefficients in the equations are themselves uncertain, the coefficients must also be sampled. The resulting distribution of average K_{sat} more fully reflects the underlying uncertainties than a single averaged value using the mean coefficients determined from regression analysis.

A difficulty arises when considering retention properties. The USGS procedure, in which retention properties are determined for each core sample individually and the regression coefficients are then determined, lends itself to the same kind of analysis discussed above for K_{sat}, although the variability in the individual saturation measurements is muted. The procedure I followed (using all core samples simultaneously to determine retention parameters) does not lend itself to the determination of regression-parameter uncertainties, even though the overall fit to the data is at least as good as obtained with the USGS procedure.

10/2/97 Layer properties. SAS

I created *Matlab* routine do_ksat_layerest.m to estimate K_{sat} for each layer. The idea is to generate many realizations of θ_{65} and ε_{sample}, use the regression equation for $\log_{10}(K_{sat})$ with ϵ added, and take the mean of the collection of realizations. I found that the underlying distributions for θ_{65} and ε_{sample} were sometimes quite skewed if they were near one end of their range (e.g., ε near 0 or θ near 1). The Type-I largest- and smallest-value distributions (Benjamin and Cornell, 1970, Section 3.3.3) conveniently describe shapes similar to the apparent skewed distributions. In cases where computed skew is less than half of the skew for the Type-I distribution, I assume that the distribution is normal; otherwise, the appropriate Type-I distribution is used.

There are difficulties in estimating bounded properties such as ε or θ using unbounded distributions. I made no attempt to resolve this problem, except for using the skewed distributions, primarily because some reported measured values fell outside the physically valid range and the regression is based on the full reported range of measured values. I do not believe that there should be a strong impact on estimated values for K_{sat}.

As it turns out, the linearity of the regression equation allows correlation between ε and θ to be ignored when calculating geometric mean. I verified this by comparing cases having normal distributions for both ε and θ. Identical geometric and means were obtained (to within the noise from 10^4 samples) considering correlation and neglecting correlation. However, correlation does appear to have an impact on arithmetic mean, as much as 2 orders of magnitude.

The comparison between data, USGS estimates, and my estimates are shown in Table 1-16. During repeated trials with the same number of realizations, the geometric mean of my estimated K_{sat} varies in the 3rd decimal place, while the arithmetic mean varies within a factor of about 1/3. In most cases, the geometric mean calculated using the many-realization approach was within a factor of 3 of the USGS estimate for the same layer. The USGS estimates are significantly different from my estimate (at least an order of magnitude) for 11 of the 30 layers; when there is a significant discrepancy my estimates usually honor the measured values somewhat better. Explanations for cases with estimates at least an order of magnitude difference include: (i) no measured K_{sat} values (CCR); (ii) measured K_{sat} is between the 2 estimates and K_{sat} subsamples are not representative (CW); (iii) measured K_{sat} values are between the 2 estimates (BT3, TR, TM1); and (iv) USGS estimates are significantly further from measured values (CMW, CNW, TC, PV3, PP3, BF3).

It is interesting to note that an arithmetic-mean layerwide K_{sat}, appropriate when gravity drainage is occurring and pressure is equalized horizontally within the layer, suggests that current

MAI estimates (<30 mm/yr or $<10^{-9}$ m/s) can be accommodated as deep percolation in the TSw without recourse to fracture flow. At and below the potential repository, only the TM1, BT, and BF3 units would perhaps require fracture flow to accommodate MAI rates.

10/7/97 Display of estimated fits. SAS

The *Matlab* routine do_ksat_layerest.m used to estimate layer properties was augmented to plot the ε, θ, and K_{sat} values for the core samples and generated realizations. The figures are displayed on the following pages. There were 10^6 realizations used to generate mean values; only 1 in 20 realizations are plotted. In each figure, the mean (arithmetic for ε and θ, geometric for K_{sat}) of each sample set is denoted with a large circle and crosshair; the crosshair has the same color as the corresponding data source.

Table 1-16: Layerwise estimates of K_{sat} (m/s). 10^{-10} m/s is equal to 3.16 mm/yr.

	Measured		USGS Estimate		SAS Estimate		
Unit	Number Obs.	Geom. Mean	Number Obs.	Geom. Mean	Number Obs.	Geom. Mean	Arith. Mean
CCR	0	–	9	1.55×10^{-12}	10^5	1.05×10^{-10}	2.27×10^{-9}
CUC	3	3.81×10^{-8}	101	3.86×10^{-8}	10^5	3.01×10^{-8}	2.09×10^{-5}
CUL	1	1.25×10^{-8}	98	5.72×10^{-10}	10^5	1.25×10^{-9}	3.06×10^{-6}
CW	38	7.27×10^{-12}	599	3.77×10^{-12}	10^5	8.88×10^{-11}	6.43×10^{-9}
CMW	4	4.98×10^{-10}	90	8.84×10^{-12}	10^5	9.48×10^{-11}	6.30×10^{-9}
CNW	8	3.06×10^{-8}	101	2.55×10^{-7}	10^5	8.84×10^{-9}	9.52×10^{-6}
BT4	3	1.64×10^{-7}	32	6.77×10^{-7}	10^5	1.22×10^{-7}	5.85×10^{-5}
TPY	2	3.31×10^{-8}	43	1.68×10^{-8}	10^5	2.39×10^{-9}	5.18×10^{-7}
BT3	18	2.81×10^{-7}	85	7.85×10^{-7}	10^5	6.80×10^{-8}	2.75×10^{-6}
TPP	10	8.75×10^{-7}	156	3.65×10^{-6}	10^5	1.26×10^{-6}	2.58×10^{-5}
BT2	19	3.17×10^{-6}	170	1.86×10^{-6}	10^5	8.54×10^{-7}	3.45×10^{-5}
TC	10	8.82×10^{-11}	71	6.15×10^{-13}	10^5	5.42×10^{-10}	2.55×10^{-8}
TR	45	1.67×10^{-9}	438	3.98×10^{-10}	10^5	3.20×10^{-9}	6.85×10^{-8}
TUL	51	5.44×10^{-11}	455	2.26×10^{-10}	10^5	4.50×10^{-10}	1.36×10^{-7}
TMN	39	8.98×10^{-12}	266	1.50×10^{-11}	10^5	6.91×10^{-11}	2.74×10^{-9}
TLL	65	6.22×10^{-11}	451	7.20×10^{-11}	10^5	1.69×10^{-10}	8.71×10^{-9}
TM2	48	2.59×10^{-11}	225	1.79×10^{-11}	10^5	6.82×10^{-11}	1.68×10^{-9}
TM1	17	6.88×10^{-12}	102	4.85×10^{-12}	10^5	4.63×10^{-11}	5.59×10^{-10}
PV3	8	3.73×10^{-11}	86	1.53×10^{-13}	10^5	2.61×10^{-11}	1.09×10^{-8}
PV2	4	7.32×10^{-10}	39	7.39×10^{-11}	10^5	1.56×10^{-10}	5.76×10^{-8}
BT1	9	5.87×10^{-10}	79	2.60×10^{-9}	10^5	4.40×10^{-9}	2.55×10^{-5}
CHV	6	5.51×10^{-7}	69	2.13×10^{-7}	10^5	4.29×10^{-8}	1.68×10^{-6}
CHZ	87	2.88×10^{-11}	293	1.08×10^{-10}	10^5	1.79×10^{-10}	3.40×10^{-9}
BT	14	9.14×10^{-12}	69	1.40×10^{-11}	10^5	4.70×10^{-11}	4.58×10^{-10}
PP4	8	2.72×10^{-11}	47	9.61×10^{-11}	10^5	2.37×10^{-10}	3.88×10^{-9}
PP3	30	2.00×10^{-8}	166	2.93×10^{-10}	10^5	1.79×10^{-8}	1.51×10^{-5}
PP2	25	2.84×10^{-10}	140	5.60×10^{-11}	10^5	1.89×10^{-10}	2.44×10^{-9}
PP1	27	4.88×10^{-11}	245	3.15×10^{-11}	10^5	1.01×10^{-10}	4.36×10^{-9}
BF3	2	2.09×10^{-11}	86	2.10×10^{-12}	10^5	2.12×10^{-11}	1.93×10^{-10}
BF2	5	3.96×10^{-11}	65	5.03×10^{-11}	10^5	8.53×10^{-11}	1.29×10^{-9}

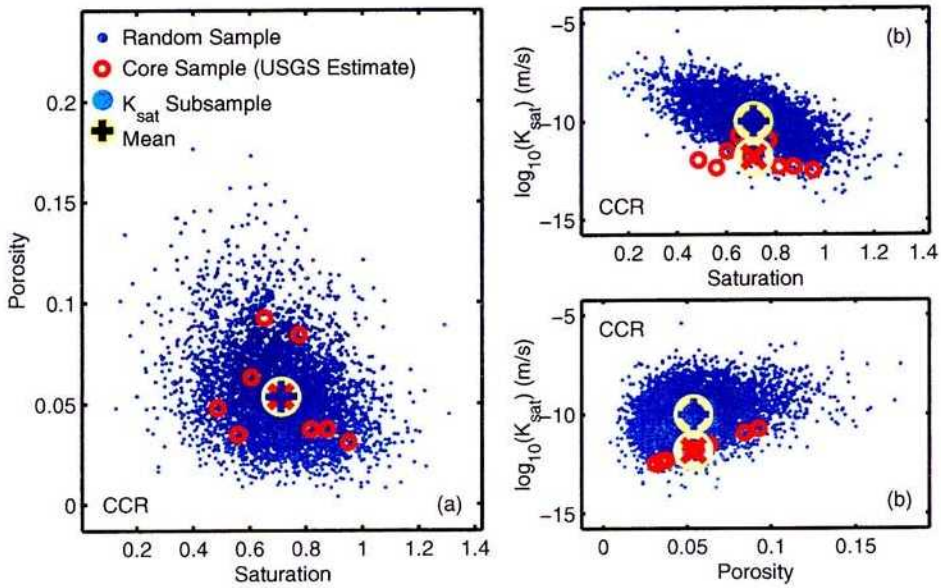

Figure 1-70: 10/7/97. **Disp_DBstat_CCR_c.eps**. Measured and generated formation values for (a) saturation and porosity, (b) saturation and estimated saturated hydraulic conductivity, and (c) porosity and estimated saturated hydraulic conductivity.

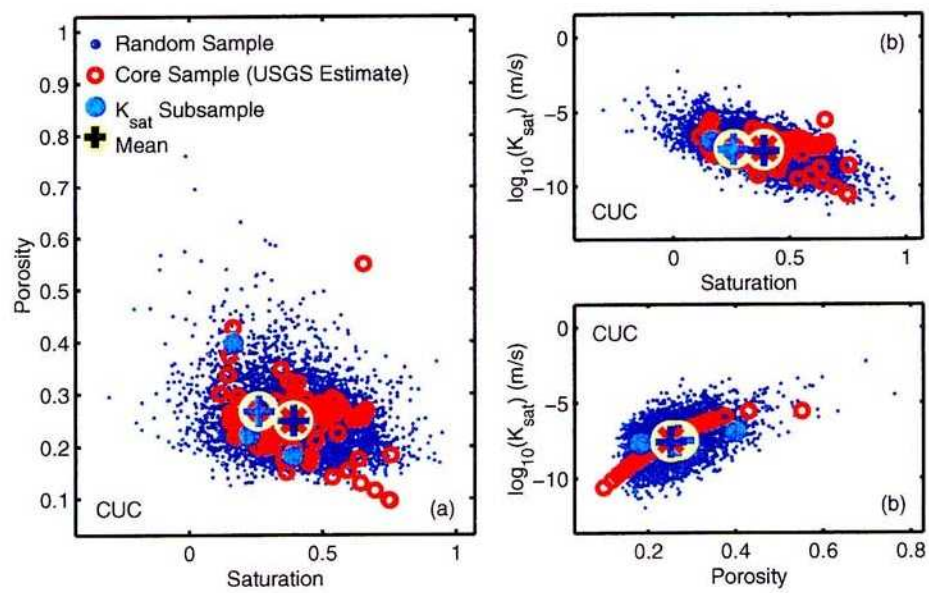

Figure 1-71: 10/7/97. **Disp_DBstat_CUC_c.eps**. Measured and generated formation values for (a) saturation and porosity, (b) saturation and estimated saturated hydraulic conductivity, and (c) porosity and estimated saturated hydraulic conductivity.

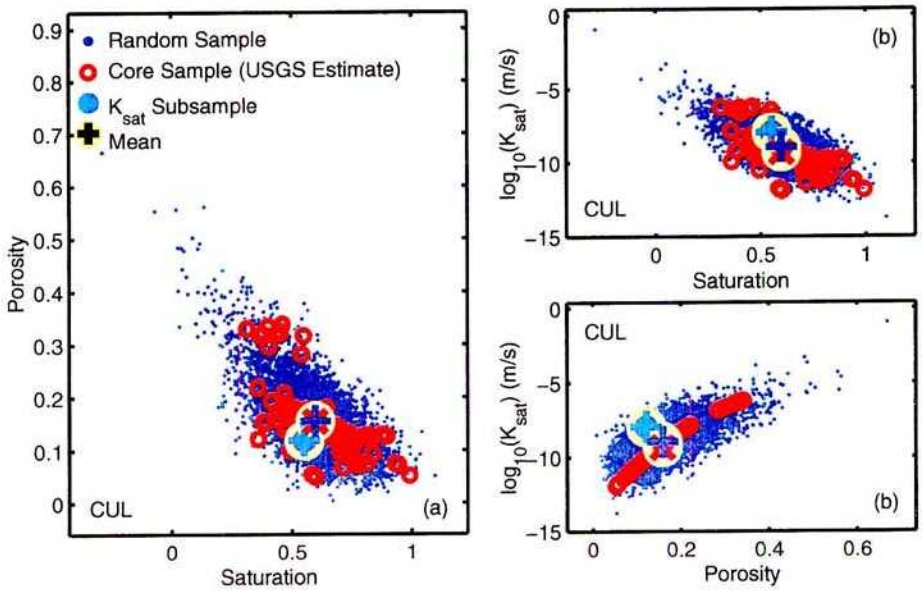

Figure 1-72: 10/7/97. **Disp_DBstat_CUL_c.eps**. Measured and generated formation values for (a) saturation and porosity, (b) saturation and estimated saturated hydraulic conductivity, and (c) porosity and estimated saturated hydraulic conductivity.

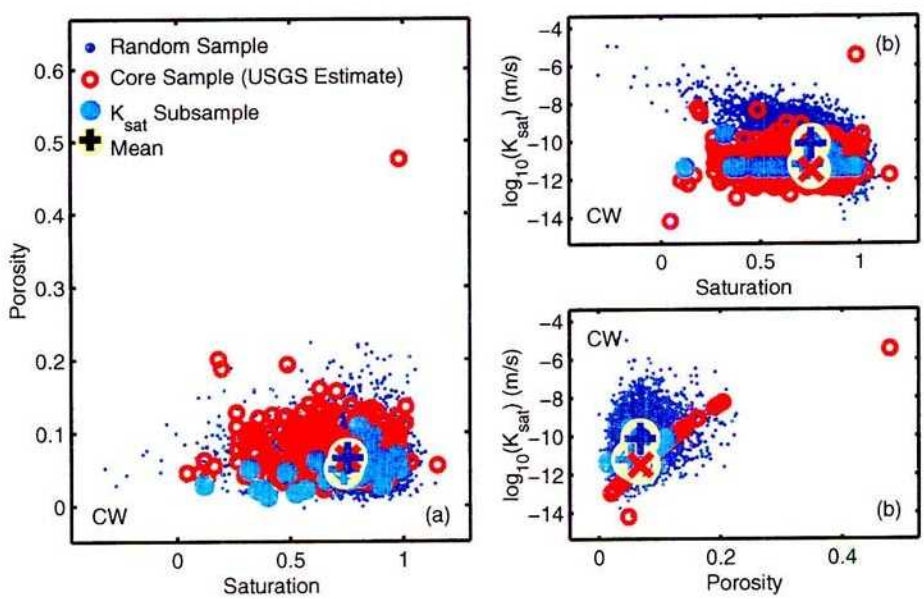

Figure 1-73: 10/7/97. **Disp_DBstat_CW_c.eps**. Measured and generated formation values for (a) saturation and porosity, (b) saturation and estimated saturated hydraulic conductivity, and (c) porosity and estimated saturated hydraulic conductivity.

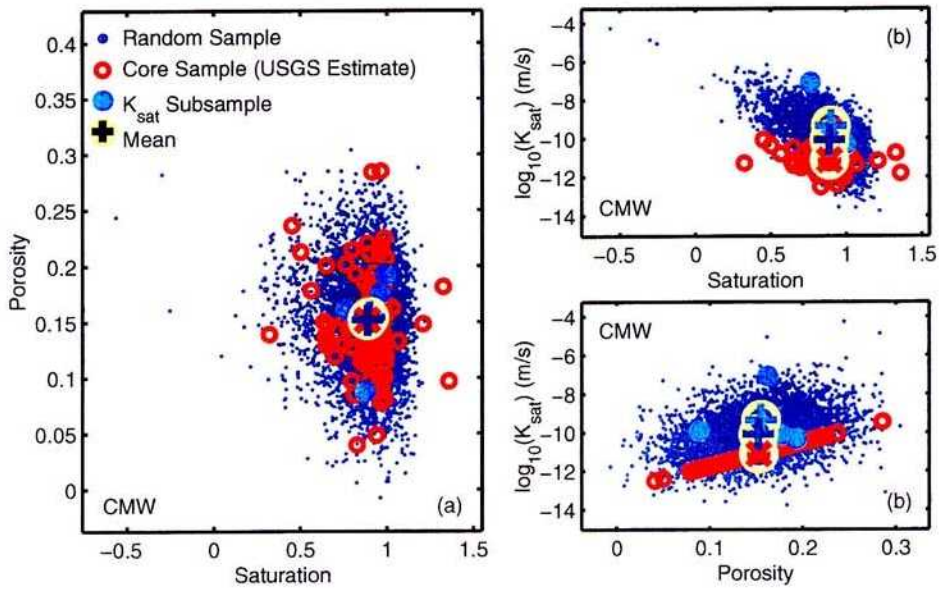

Figure 1-74: 10/7/97. **Disp_DBstat_CMW_c.eps**. Measured and generated formation values for (a) saturation and porosity, (b) saturation and estimated saturated hydraulic conductivity, and (c) porosity and estimated saturated hydraulic conductivity.

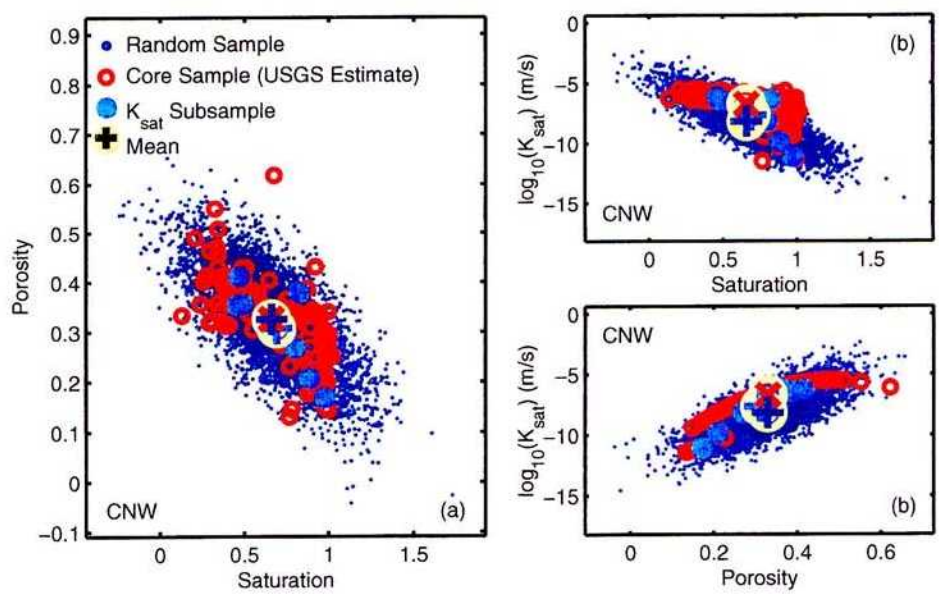

Figure 1-75: 10/7/97. **Disp_DBstat_CNW_c.eps**. Measured and generated formation values for (a) saturation and porosity, (b) saturation and estimated saturated hydraulic conductivity, and (c) porosity and estimated saturated hydraulic conductivity.

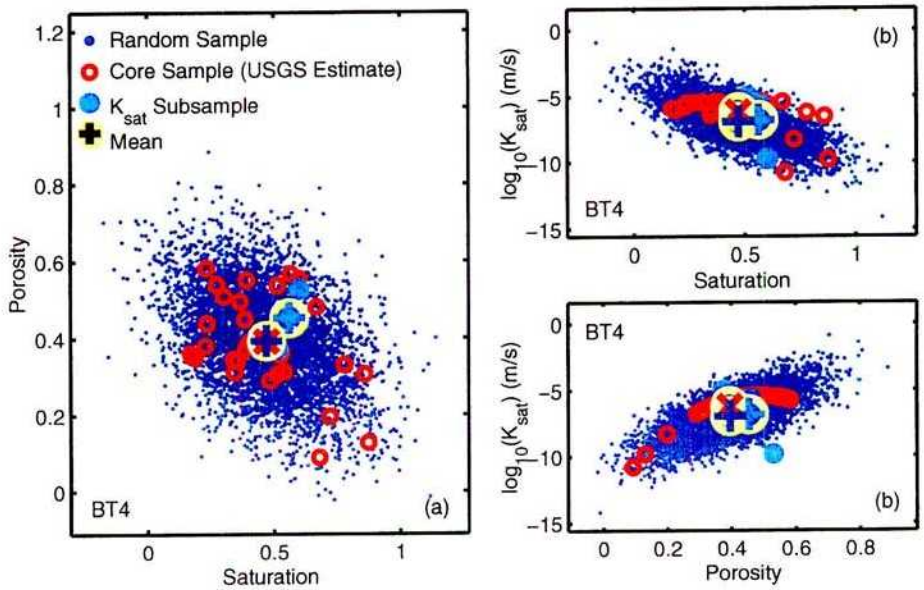

Figure 1-76: 10/7/97. **Disp_DBstat_BT4_c.eps**. Measured and generated formation values for (a) saturation and porosity, (b) saturation and estimated saturated hydraulic conductivity, and (c) porosity and estimated saturated hydraulic conductivity.

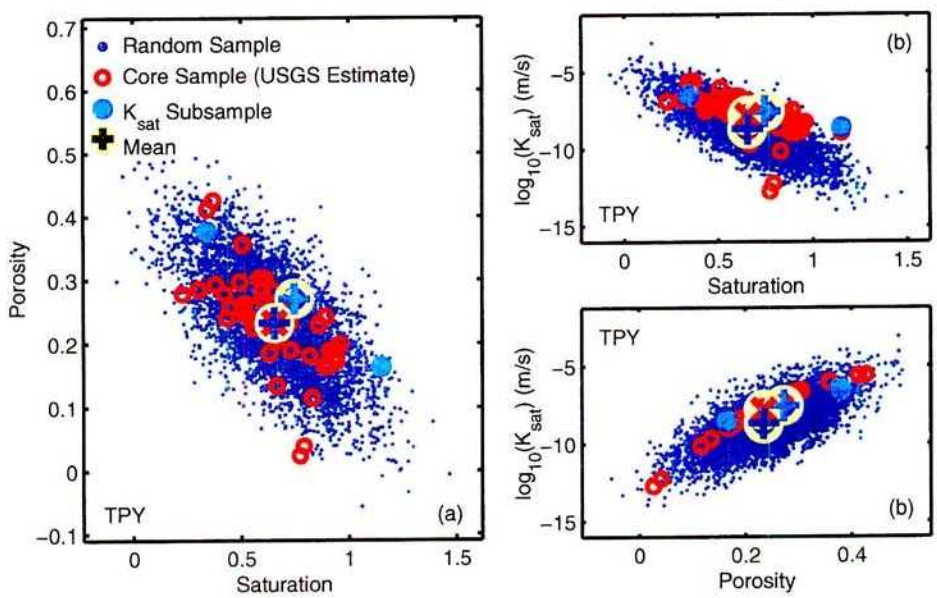

Figure 1-77: 10/7/97. **Disp_DBstat_TPY_c.eps**. Measured and generated formation values for (a) saturation and porosity, (b) saturation and estimated saturated hydraulic conductivity, and (c) porosity and estimated saturated hydraulic conductivity.

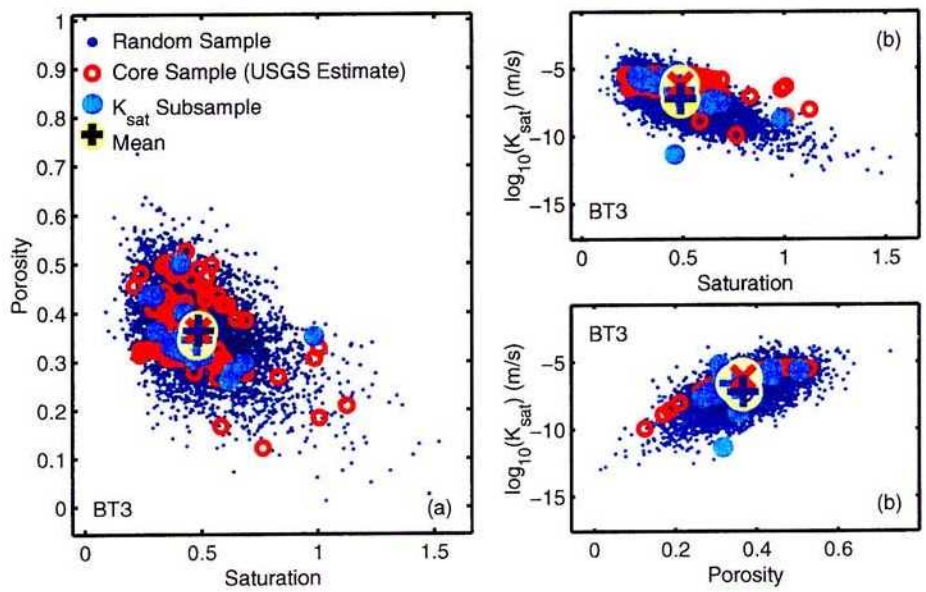

Figure 1-78: 10/7/97. **Disp_DBstat_BT3_c.eps**. Measured and generated formation values for (a) saturation and porosity, (b) saturation and estimated saturated hydraulic conductivity, and (c) porosity and estimated saturated hydraulic conductivity.

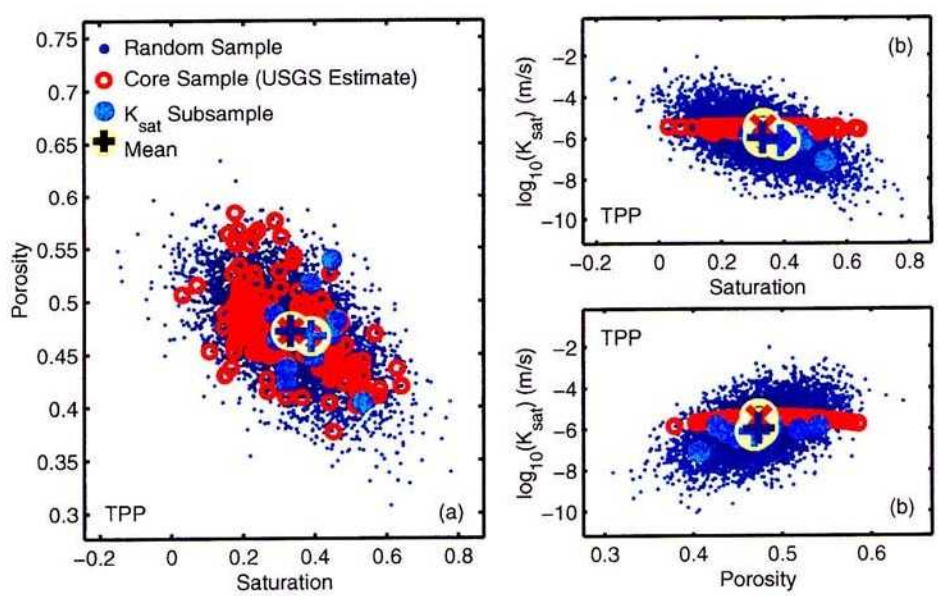

Figure 1-79: 10/7/97. **Disp_DBstat_TPP_c.eps**. Measured and generated formation values for (a) saturation and porosity, (b) saturation and estimated saturated hydraulic conductivity, and (c) porosity and estimated saturated hydraulic conductivity.

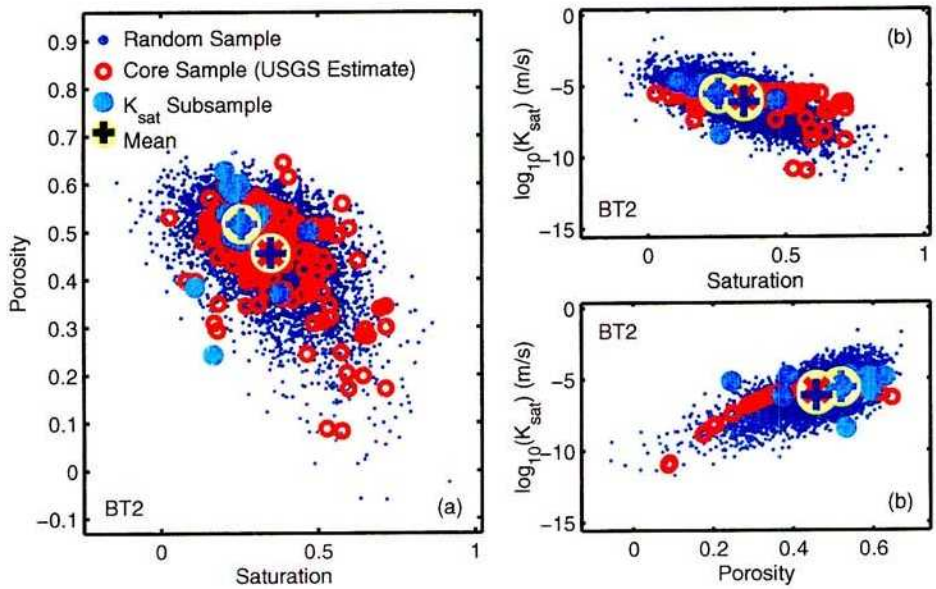

Figure 1-80: 10/7/97. **Disp_DBstat_BT2_c.eps**. Measured and generated formation values for (a) saturation and porosity, (b) saturation and estimated saturated hydraulic conductivity, and (c) porosity and estimated saturated hydraulic conductivity.

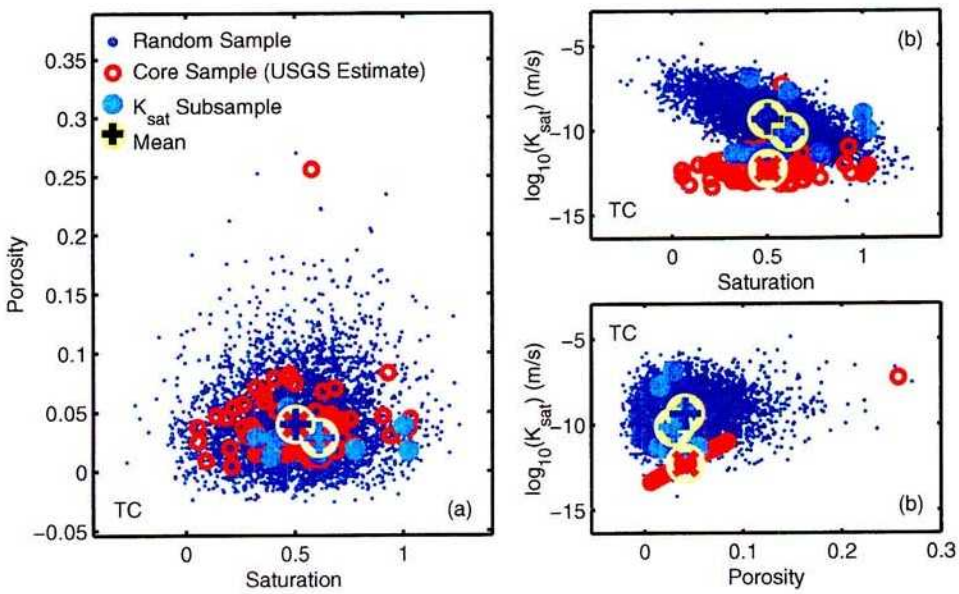

Figure 1-81: 10/7/97. **Disp_DBstat_TC_c.eps**. Measured and generated formation values for (a) saturation and porosity, (b) saturation and estimated saturated hydraulic conductivity, and (c) porosity and estimated saturated hydraulic conductivity.

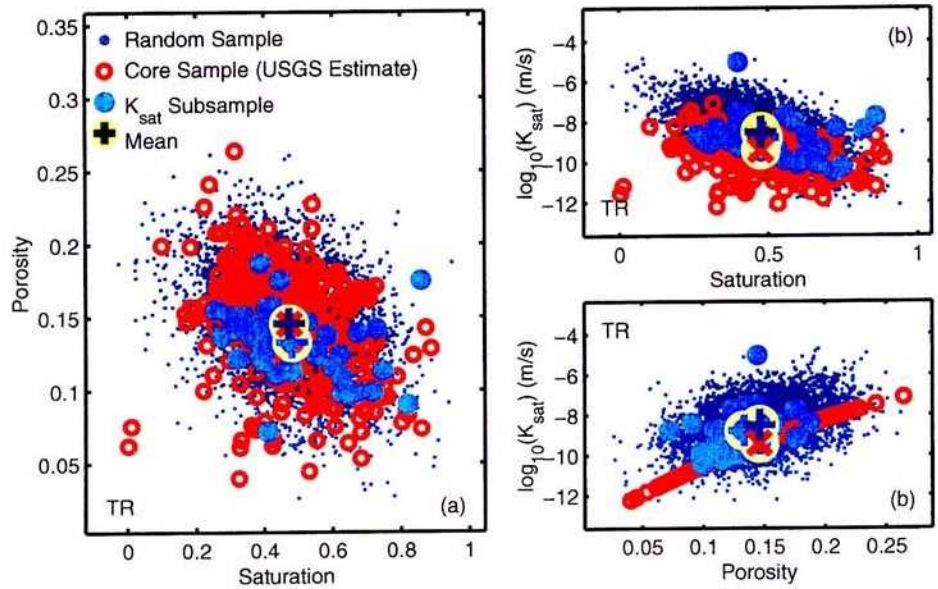

Figure 1-82: 10/7/97. **Disp_DBstat_TR_c.eps.** Measured and generated formation values for (a) saturation and porosity, (b) saturation and estimated saturated hydraulic conductivity, and (c) porosity and estimated saturated hydraulic conductivity.

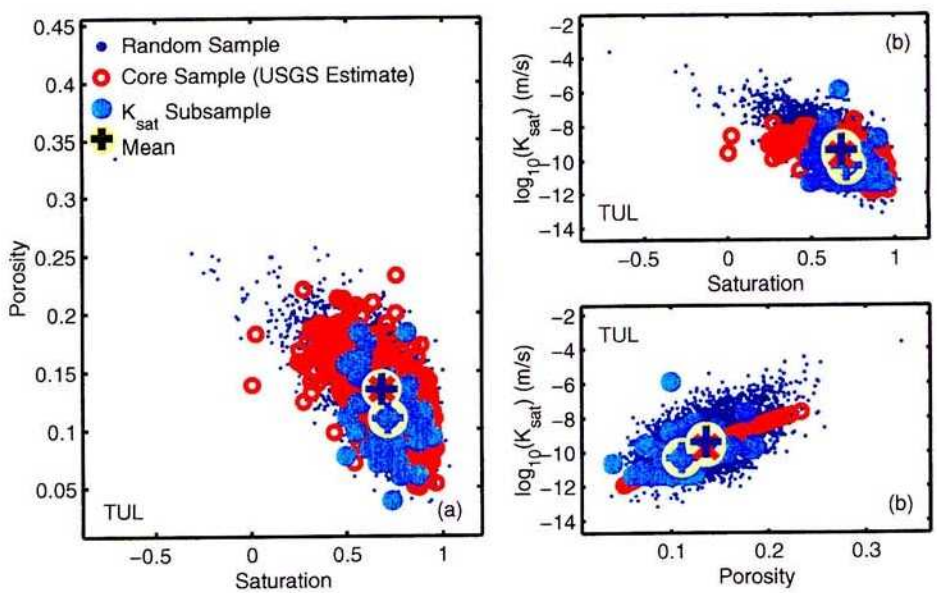

Figure 1-83: 10/7/97. **Disp_DBstat_TUL_c.eps.** Measured and generated formation values for (a) saturation and porosity, (b) saturation and estimated saturated hydraulic conductivity, and (c) porosity and estimated saturated hydraulic conductivity.

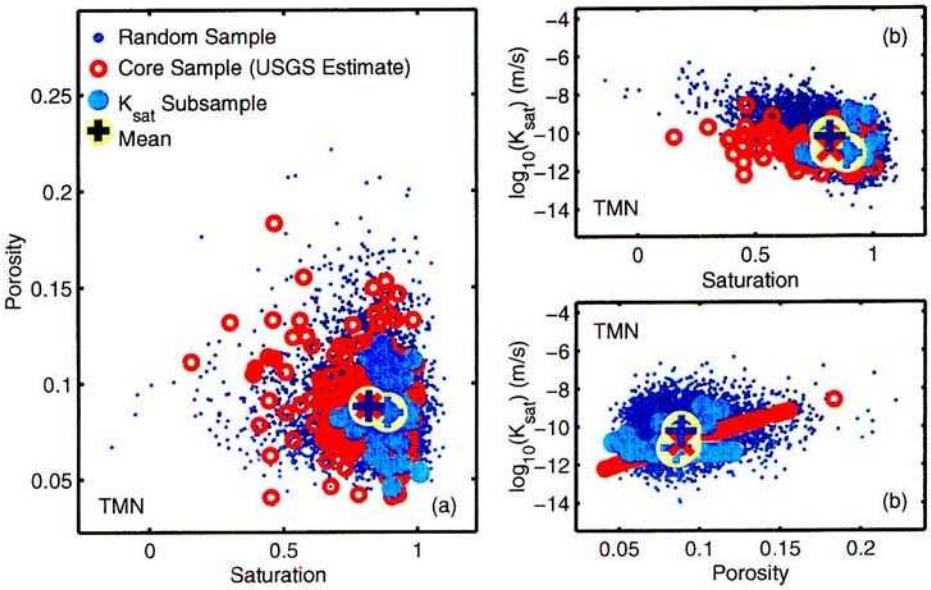

Figure 1-84: 10/7/97. **Disp_DBstat_TMN_c.eps**. Measured and generated formation values for (a) saturation and porosity, (b) saturation and estimated saturated hydraulic conductivity, and (c) porosity and estimated saturated hydraulic conductivity.

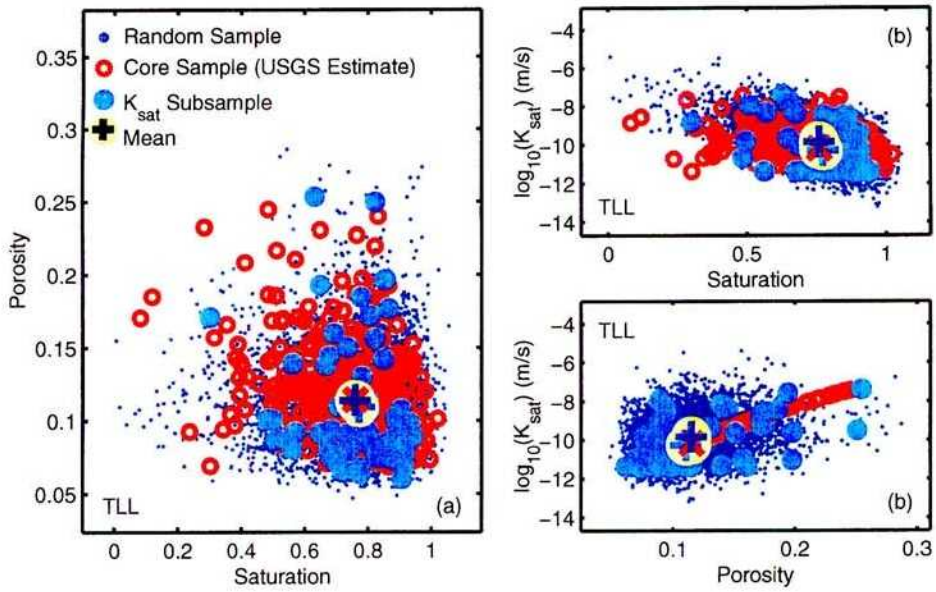

Figure 1-85: 10/7/97. **Disp_DBstat_TLL_c.eps**. Measured and generated formation values for (a) saturation and porosity, (b) saturation and estimated saturated hydraulic conductivity, and (c) porosity and estimated saturated hydraulic conductivity.

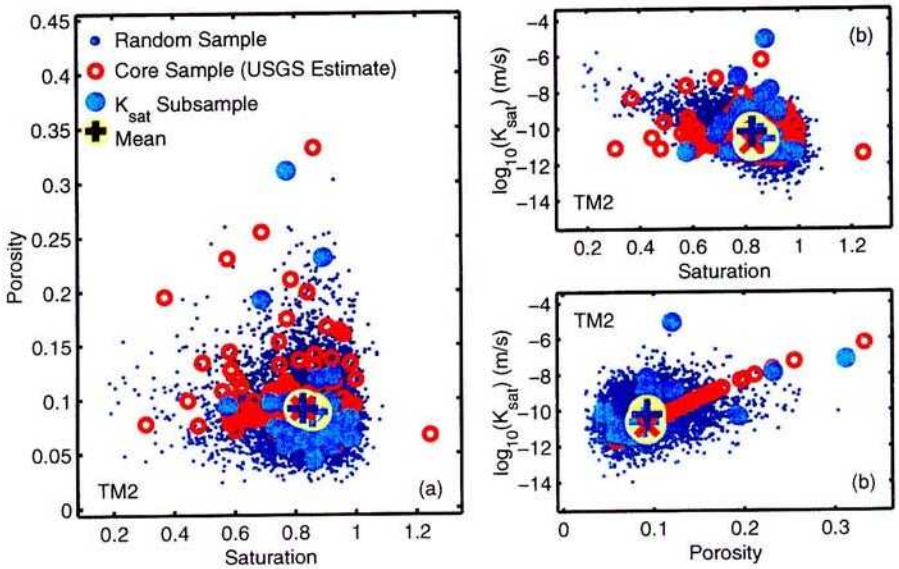

Figure 1-86: 10/7/97. **Disp_DBstat_TM2_c.eps**. Measured and generated formation values for (a) saturation and porosity, (b) saturation and estimated saturated hydraulic conductivity, and (c) porosity and estimated saturated hydraulic conductivity.

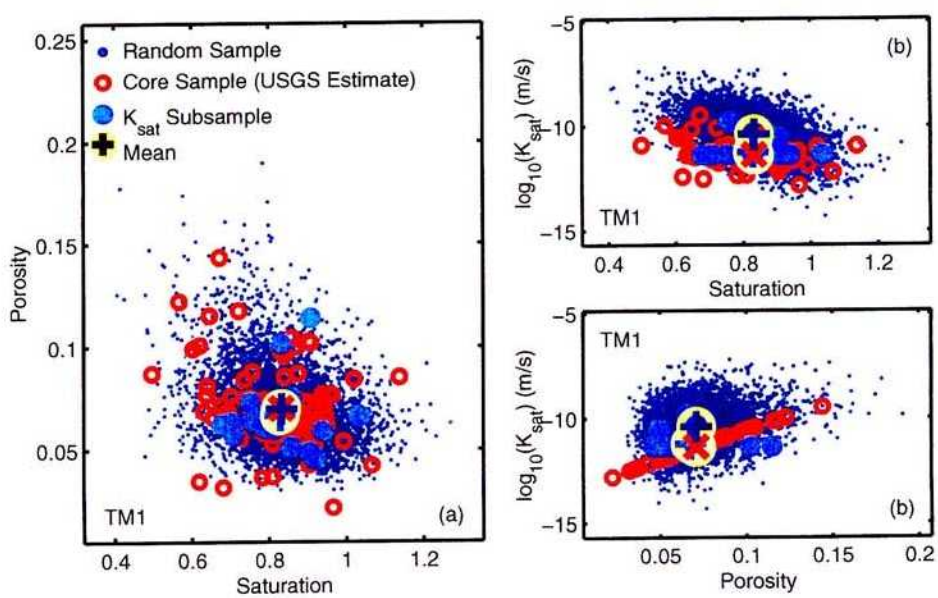

Figure 1-87: 10/7/97. **Disp_DBstat_TM1_c.eps**. Measured and generated formation values for (a) saturation and porosity, (b) saturation and estimated saturated hydraulic conductivity, and (c) porosity and estimated saturated hydraulic conductivity.

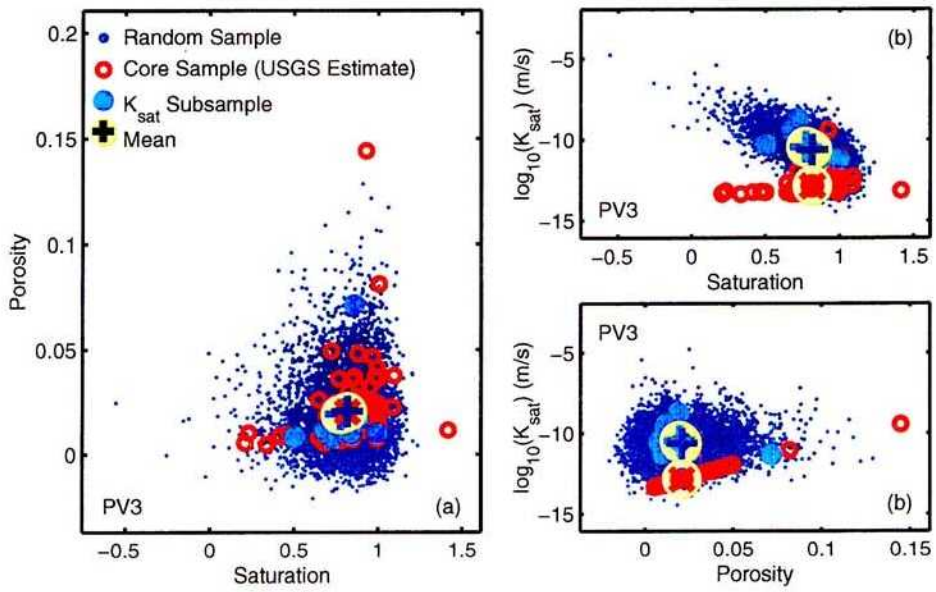

Figure 1-88: 10/7/97. **Disp_DBstat_PV3_c.eps**. Measured and generated formation values for (a) saturation and porosity, (b) saturation and estimated saturated hydraulic conductivity, and (c) porosity and estimated saturated hydraulic conductivity.

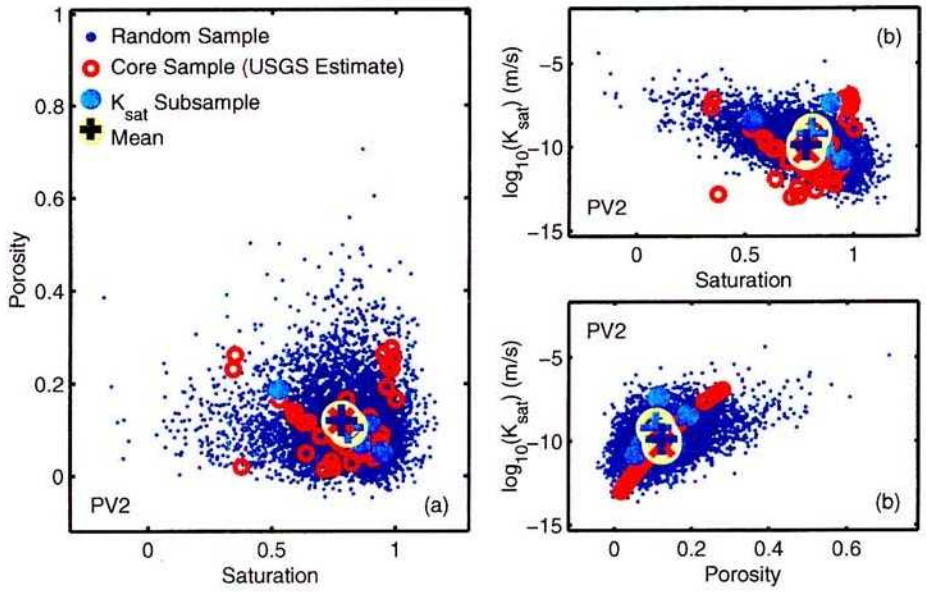

Figure 1-89: 10/7/97. **Disp_DBstat_PV2_c.eps**. Measured and generated formation values for (a) saturation and porosity, (b) saturation and estimated saturated hydraulic conductivity, and (c) porosity and estimated saturated hydraulic conductivity.

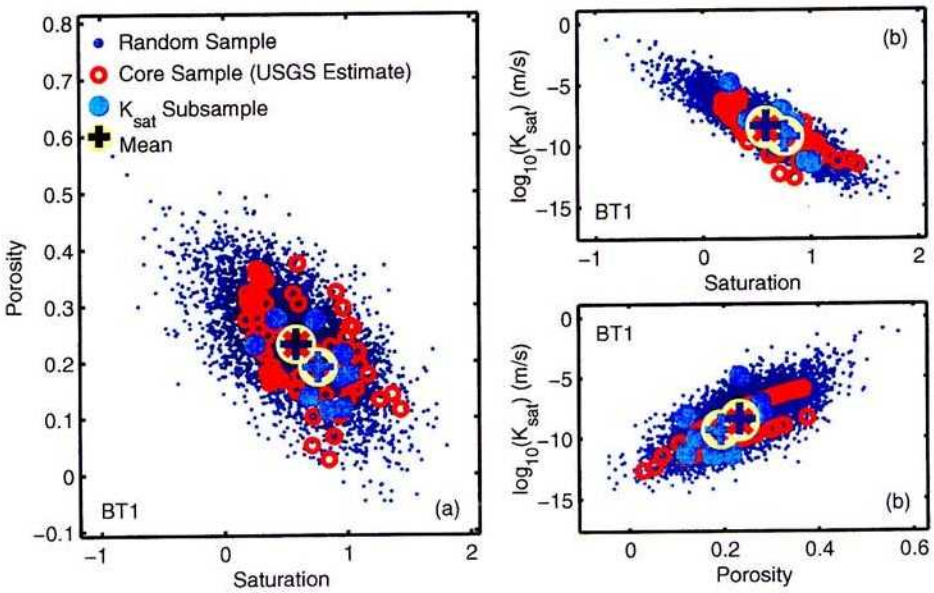

Figure 1-90: 10/7/97. **Disp_DBstat_BT1_c.eps**. Measured and generated formation values for (a) saturation and porosity, (b) saturation and estimated saturated hydraulic conductivity, and (c) porosity and estimated saturated hydraulic conductivity.

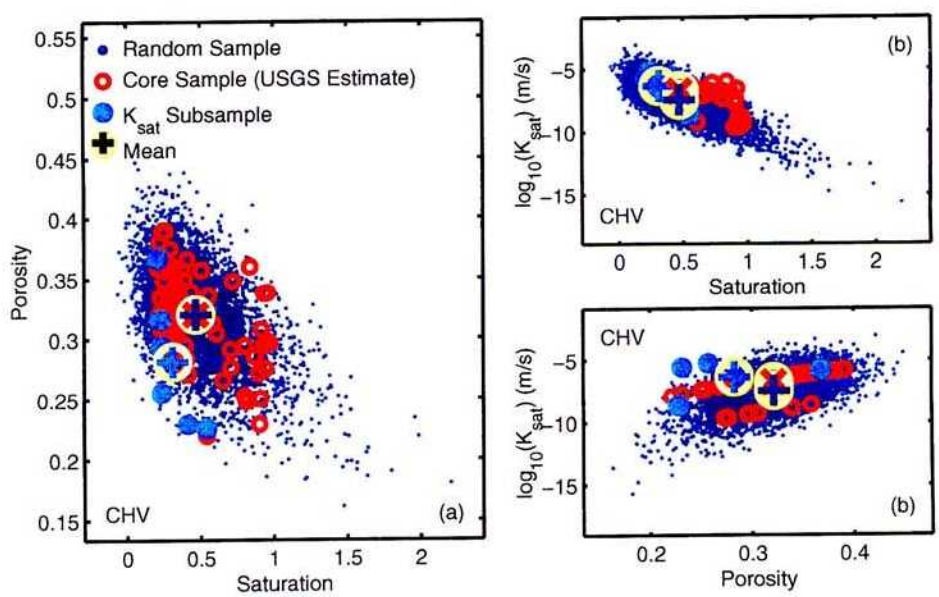

Figure 1-91: 10/7/97. **Disp_DBstat_CHV_c.eps**. Measured and generated formation values for (a) saturation and porosity, (b) saturation and estimated saturated hydraulic conductivity, and (c) porosity and estimated saturated hydraulic conductivity.

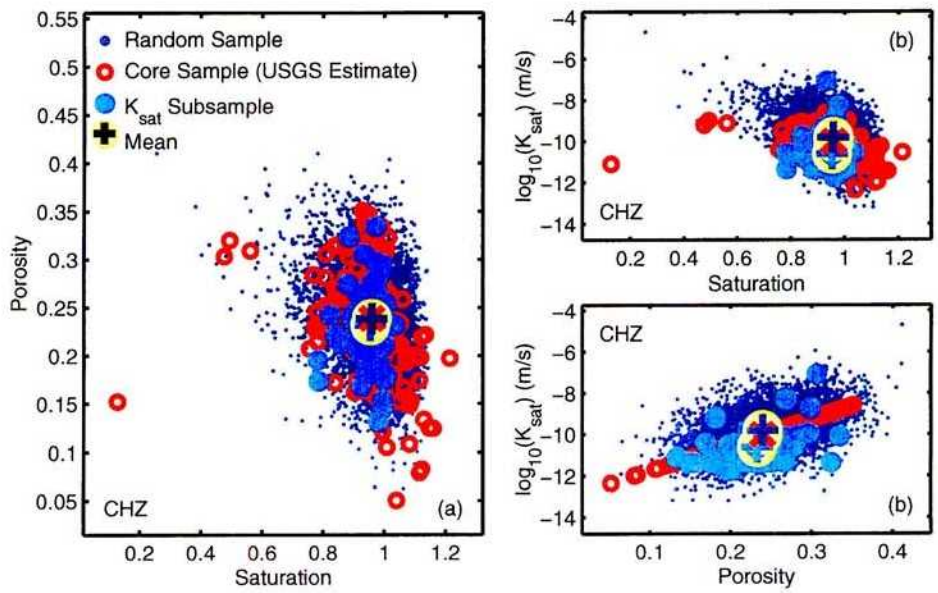

Figure 1-92: 10/7/97. **Disp_DBstat_CHZ_c.eps**. Measured and generated formation values for (a) saturation and porosity, (b) saturation and estimated saturated hydraulic conductivity, and (c) porosity and estimated saturated hydraulic conductivity.

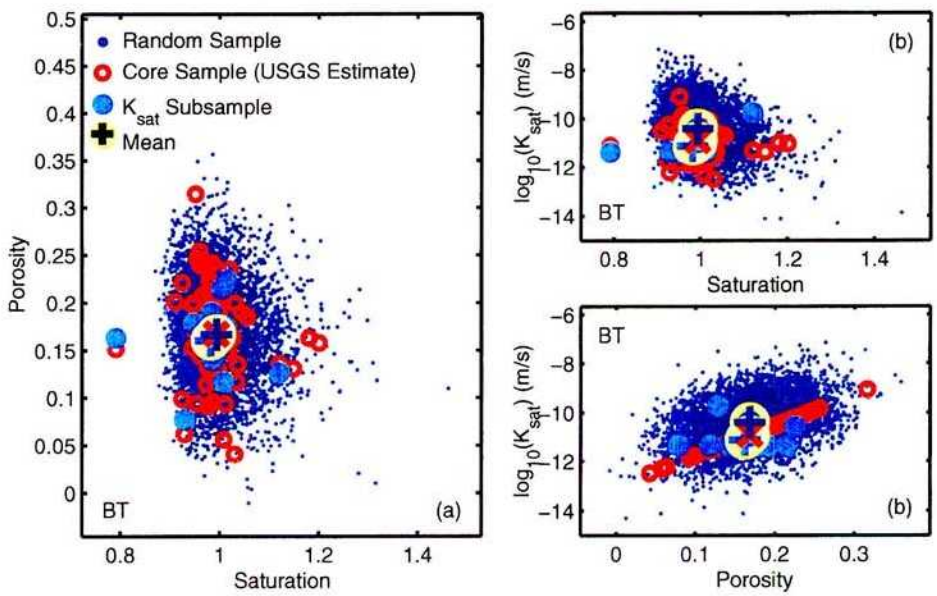

Figure 1-93: 10/7/97. **Disp_DBstat_BT_c.eps**. Measured and generated formation values for (a) saturation and porosity, (b) saturation and estimated saturated hydraulic conductivity, and (c) porosity and estimated saturated hydraulic conductivity.

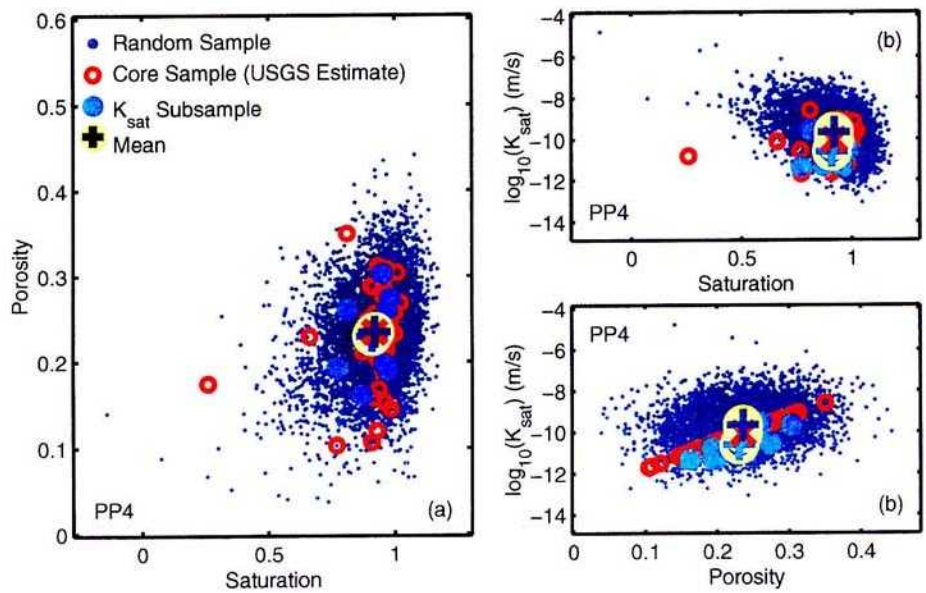

Figure 1-94: 10/7/97. **Disp_DBstat_PP4_c.eps**. Measured and generated formation values for (a) saturation and porosity, (b) saturation and estimated saturated hydraulic conductivity, and (c) porosity and estimated saturated hydraulic conductivity.

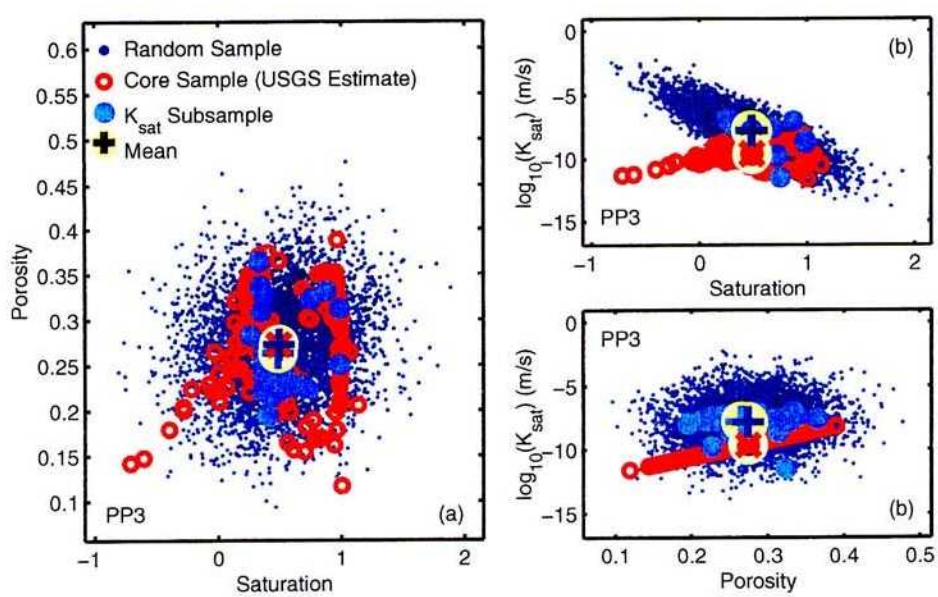

Figure 1-95: 10/7/97. **Disp_DBstat_PP3_c.eps**. Measured and generated formation values for (a) saturation and porosity, (b) saturation and estimated saturated hydraulic conductivity, and (c) porosity and estimated saturated hydraulic conductivity.

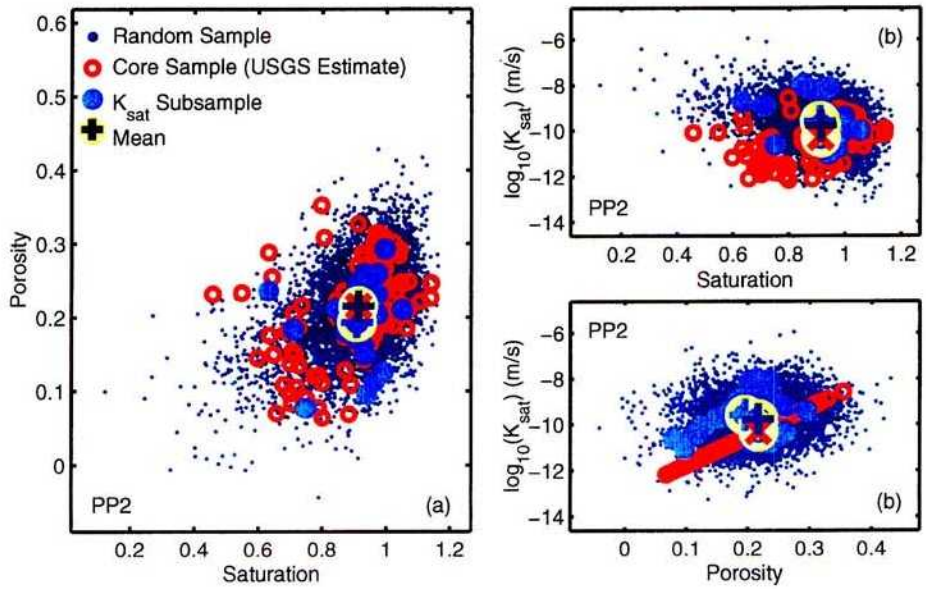

Figure 1-96: 10/7/97. **Disp_DBstat_PP2_c.eps**. Measured and generated formation values for (a) saturation and porosity, (b) saturation and estimated saturated hydraulic conductivity, and (c) porosity and estimated saturated hydraulic conductivity.

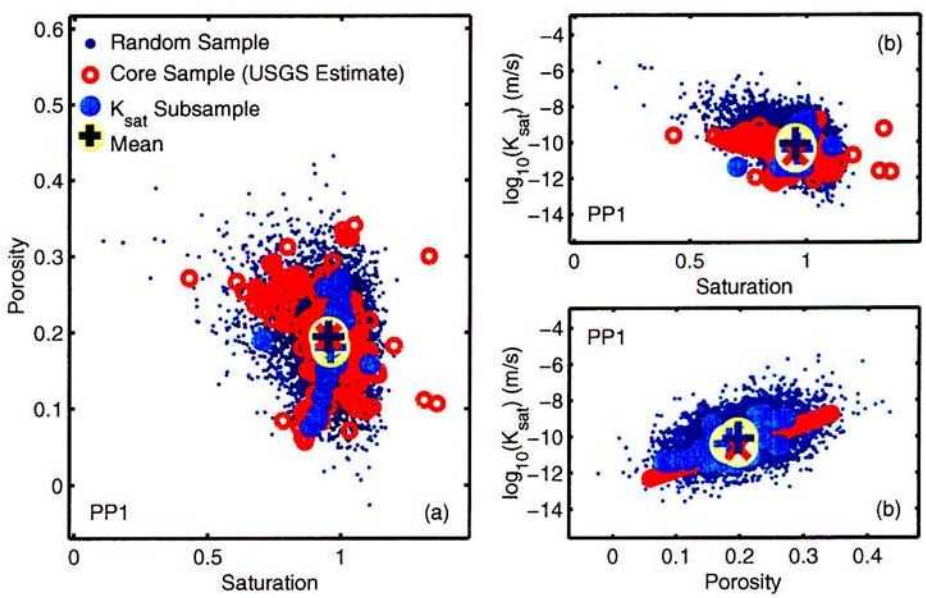

Figure 1-97: 10/7/97. **Disp_DBstat_PP1_c.eps**. Measured and generated formation values for (a) saturation and porosity, (b) saturation and estimated saturated hydraulic conductivity, and (c) porosity and estimated saturated hydraulic conductivity.

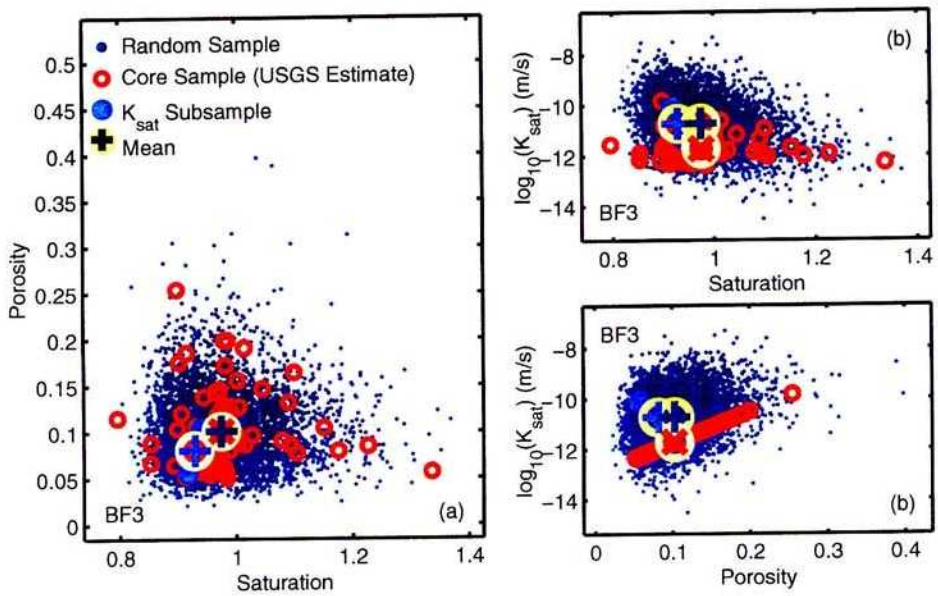

Figure 1-98: 10/7/97. **Disp_DBstat_BF3_c.eps.** Measured and generated formation values for (a) saturation and porosity, (b) saturation and estimated saturated hydraulic conductivity, and (c) porosity and estimated saturated hydraulic conductivity.

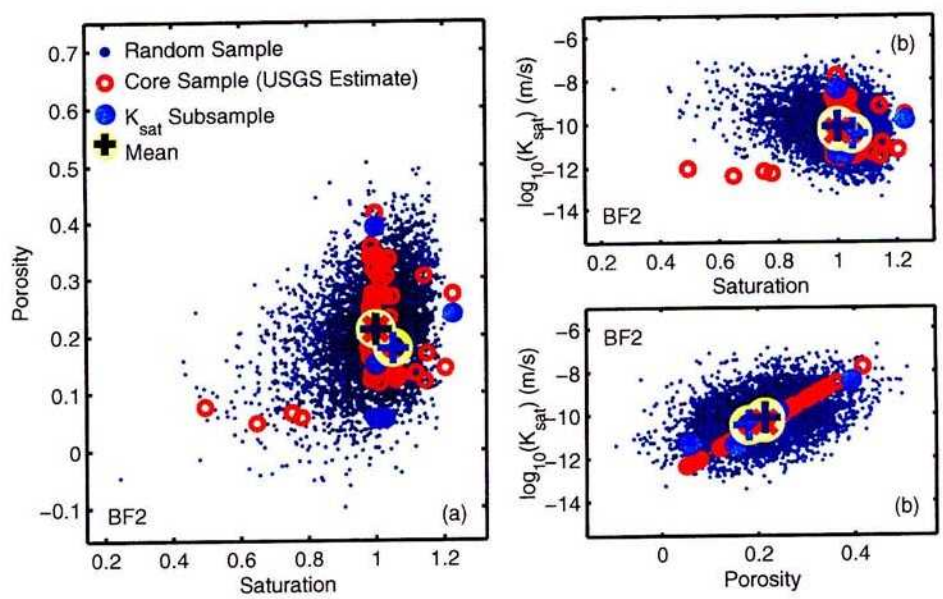

Figure 1-99: 10/7/97. **Disp_DBstat_BF2_c.eps.** Measured and generated formation values for (a) saturation and porosity, (b) saturation and estimated saturated hydraulic conductivity, and (c) porosity and estimated saturated hydraulic conductivity.

References

Bagtzoglou, A. C., N. M. Coleman, E. C. Pearcy, S. A. Stothoff, and G. W. Wittmeyer. 1996. Unsaturated and Saturated Flow Under Isothermal Conditions. In B. Sagar (Ed.), *NRC High-Level Radioactive Waste Program FY96 Annual Progress Report*, Volume NUREG/CR-6513, No. 1, Washington, DC, pp. 10–1–10–28. Nuclear Regulatory Commission.

Bagtzoglou, A. C., S. A. Stothoff, and M. A. Muller. 1995. *Progress Towards Estimating Infiltration and Deep Percolation at the Yucca Mountain Site.* , Center for Nuclear Waste Regulatory Analyses, San Antonio, TX.

Benjamin, J. R. and C. A. Cornell. 1970. *Probability, Statistics, and Decision for Civil Engineers.* New York, NY: McGraw-Hill.

Buesch, D. C., R. W. Spengler, T. C. Moyer, and J. K. Geslin. 1996. *Proposed Stratigraphic Nomenclature and Macroscopic Identification of Lithostratigraphic Units of the Paintbrush Group Exposed at Yucca Mountain, Nevada.* Open-File Report 94-469, United States Geological Survey, Denver, CO.

Fabryka-Martin, J. T., P. R. Dixon, S. Levy, B. Liu, H. J. Turin, and A. V. Wolfsberg. 1996. *Systematic Sampling for Chlorine-36 in the Exploratory Studies Facility.* LA-CST-TIP-96-001, Los Alamos National Laboratory, Los Alamos, NM.

Fabryka-Martin, J. T., H. J. Turin, A. V. Wolfsberg, D. Brenner, P. R. Dixon, and J. A. Musgrave. 1996. *Summary Report of Chlorine-36 Studies.* LA-CST-TIP-96-003, Los Alamos National Laboratory, Los Alamos, NM.

Fernandez, J. A., J. B. Case, C. A. Givens, and B. C. Carney. 1994. *A Strategy to Seal Exploratory Boreholes in Unsaturated Tuff.* SAND93-1184, Sandia National Laboratories, Albuquerque, NM.

Flint, A. L., J. A. Hevesi, and L. E. Flint. 1996. *Conceptual and Numerical Model of Infiltration for the Yucca Mountain Area, Nevada.* 3GUI623M, Department of Energy, Las Vegas, NV.

Flint, L. E. 1996. *Matrix Properties of Hydrogeologic Units at Yucca Mountain, Nevada.* Milestone 3GUP604M, Department of Energy, Las Vegas, NV.

Flint, L. E. and A. L. Flint. 1990. *Preliminary Permeability and Water-Retention Data for Nonwelded and Bedded Tuff Samples, Yucca Mountain Area, Nye County, Nevada.* Open-File Report 90-569, United States Geological Survey, Denver, CO.

Flint, L. E. and A. L. Flint. 1995. *Shallow Infiltration Processes at Yucca Mountain, Nevada – Neutron Logging Data 1984-93.* Water-Resources Investigations Report 95-4035, United States Geological Survey, Denver, CO.

Flint, L. E., A. L. Flint, C. A. Rautman, and J. D. Istok. 1996. *Physical and Hydrologic Properties of Rock Outcrop Samples at Yucca Mountain, Nevada.* Open-File Report 95-280, United States Geological Survey, Denver, CO.

Lachenbruch, A. H. and J. H. Sass. 1977. Heat Flow in the United States and the Thermal Regime of the Crust. In H. G. Heacock (Ed.), *The Earth's Crust*, Volume Geophysical Monograph 20, pp. 626–675. Washington, DC: American Geophysical Union.

Lapin, L. 1983. *Probability and Statistics for Modern Engineering.* Boston, MA: PWS Publishers.

McKenna, S. A. and C. A. Rautman. 1995. *Summary Evaluation of Yucca Mountain Surface Transects with Implications for Downhole Sampling.* SAND94-2038, Sandia National Laboratories, Albuquerque, NM.

Montazer, P. and W. E. Wilson. 1984. *Conceptual Hydrologic Model of Flow in the Unsaturated Zone, Yucca Mountain, Nevada.* Open-File Report 84-4345, United States Geological Survey, Lakewood, CO.

Rautman, C. A., L. E. Flint, A. L. Flint, and J. D. Istok. 1995. *Physical and Hydrologic Properties of Rock Outcrop Samples From a Nonwelded to Welded Tuff Transition, Yucca Mountain, Nevada.* Water-Resources Investigations Report 95-4061, United States Geological Survey, Denver, CO.

Rousseau, J. P., E. M. Kwicklis, and D. C. Gillies (Eds.). 1996. *Hydrogeology of the Unsaturated Zone, North Ramp Area of the Exploratory Studies Facility, Yucca Mountain, Nevada*, Water-Resources Investigations Report 96-????, Denver, CO. United States Geological Survey. Draft dated 8/29/96.

Sass, J. H. and A. H. Lachenbruch. 1982. *Preliminary Interpretations of Thermal Data from the Nevada Test Site.* Open-File Report 82-973, United States Geological Survey, Reston, VA.

Sass, J. H., A. H. Lachenbruch, W. W. Dudley, Jr., S. S. Priest, and R. J. Munroe. 1988. *Temperature, thermal conductivity, and heat flow near Yucca Mountain, Nevada: Some tectonic and hydrologic implications.* Open-File Report 87-649, United States Geological Survey, Denver, CO.

Sass, J. H., A. H. Lachenbruch, and C. W. Mase. 1980. *Analysis of Thermal Data From Drill Holes UE25a-3 and UE25a-1, Calico Hills and Yucca Mountain, Nevada Test Site.* Open-File Report 80-826, United States Geological Survey, Menlo Park, CA.

Schenker, A. R., D. C. Guerin, T. H. Robey, C. A. Rautman, and R. W. Barnard. 1995. *Stochastic Hydrogeologic Units and Hydrogeologic Properties Development for Total-System Performance Assessments.* SAND94-0244, Sandia National Laboratories, Albuquerque, NM.

Schmidt, M. R. 1989. Classification of Upland Soils by Geomorphic and Physical Properties Affecting Infiltration at Yucca Mountain, Nevada. Master's thesis, Colorado State University, Fort Collins, CO.

Scott, R. B. and J. Bonk. 1984. *Preliminary Geologic Map (1:12,000 scale) of Yucca Mountain, Nye County, Nevada, with Geologic Cross Sections.* Open-File Report 84-494, United States Geological Survey, Denver, CO.

Šimůnek, J., T. Vogel, and M. T. van Genuchten. 1992. *The SWMS_2D code for simulating water flow and solute transport in two-dimensional variably saturated media V. 1.1.* Research Report No. 126, U. S. Salinity Laboratory, ARS USDA, Riverside, CA.

Stothoff, S. A. and A. C. Bagtzoglou. 1995. Estimation of Recharge at Yucca Mountain, Nevada. In *Supplement to Eos, Transactions*, Volume 76, Washington, DC, pp. F242. American Geophysical Union.

Stothoff, S. A. and A. C. Bagtzoglou. 1996. Subregional Hydrogeologic Flow and Transport Processes. In B. Sagar (Ed.), *NRC High-Level Radioactive Waste Research at CNWRA, July–December 1995*, Volume CNWRA 95-02S, San Antonio, TX, pp. 9–1–9–20. Center for Nuclear Waste Regulatory Analyses.

Stothoff, S. A., A. C. Bagtzoglou, and H. Castellaw. 1996. Estimation of Spatial Distribution of Recharge Factors at Yucca Mountain, NV. In *Proceedings of the International Conference on Application of Geographic Information Systems in Hydrology and Water Resources Management*, Vienna, Austria. International Association of Hydrological Sciences.

Stothoff, S. A., H. M. Castellaw, and A. C. Bagtzoglou. 1995. Estimation of Spatial Distribution of Recharge Factors at Yucca Mountain. In B. Sagar (Ed.), *NRC High-Level Radioactive Waste Research at CNWRA, January–June 1995*, Volume CNWRA 95-01S, San Antonio, TX, pp. 9–5–9–12. Center for Nuclear Waste Regulatory Analyses.

Sykes, J. F., J. L. Wilson, and R. W. Andrews. 1985. Sensitivity Analysis for Steady State Groundwater Flow Using Adjoint Operators. *Water Resources Research 21*(3), 359–371.

Yang, I. C., G. W. Rattray, and P. Yu. 1996. *Interpretations of Chemical and Isotopic Data From Boreholes in the Unsaturated Zone at Yucca Mountain, Nevada.* Water-Resources Investigations Report 96-4058, United States Geological Survey, Denver, CO.

2. Thermal Hydrology KTI

Account Number: **20-5708-663**
Collaborators: **Ronald T. Green**
Directories: **As noted**

October 8, 1997 Printout entry. SAS

I performed no work on this project during the period covered by this printout.

3. Iterative Performance KTI

Account Number: **20-5708-761**
Collaborators: **Robert Baca, Gordon Wittmeyer**
Directories: **As noted**

October 8, 1997 Printout entry. SAS

I performed no work on this project during the period covered by this printout.

4. Iterative Performance KTI - Total Performance Assessment Phase 3

Account Number: **20-5708-761**
Collaborators: **Robert Baca**
Directories: **$HOME2/Matlab/TPA3, $HOME2/IPA/Phase3, as noted**

October 8, 1997 Printout entry. SAS

I performed no work on this project during the period covered by this printout.

5. Breath code development

Account Number:	**20-5708-863**
Collaborators:	**As noted**
Directories:	**Subdirectories of $HOME2/Unsat_1D/Breath as noted**

October 8, 1997 Printout entry. SAS

I performed no work on this project during the period covered by this printout.

6. Ambient KTI – Vertical ODE Solver

Account Number:	**20-5708-861**
Collaborators:	**Sitakanta Mohanty, Gordon Wittmeyer**
Directories:	**$HOME2/Matlab/ODE → $ODE**

October 8, 1997 Printout entry. SAS

I performed no work on this project during the period covered by this printout.

7. Boundary Element Methods for Steady-State Unsaturated Fractured Media

Account Number: **As noted**
Collaborators: **As noted**
Directories: **$HOME2/Matlab/ExpToVG**

October 8, 1997 Printout entry.

SAS

I performed no work on this project during the period covered by this printout.

8. Geomorphology of Mountain Erosion

Account Number: **20-5704-166 and 20-5704-174**
Collaborators: **David Farrell**
Directories: **$HOME2/Matlab/MassWaste → $MassWaste**

October 8, 1997 Printout entry. SAS

I performed no work on this project during the period covered by this printout.

9. Environ - Evaluation of Mass Balance Errors in PTC

Account Number: **20-7614-007**
Collaborators: **None**
Directories: **$HOME2/WFO/Environ → $Environ**

October 8, 1997 Printout entry. SAS

I performed no work on this project during the period covered by this printout.

10. Quick Looks

Account Number:	**As noted**
Collaborators:	**As noted**
Directories:	**As noted**

Objective: Perform quick looks at technical questions that arise in brainstorming sessions and document the results. Each quick look should take a few hours to no more than a day.

October 8, 1997 Printout entry. SAS

I performed no work on this project during the period covered by this printout.

3/8 --- 0199805280001
Scientific Notebook # 163

SCIENTIFIC NOTEBOOK

by

Stuart A. Stothoff

SCIENTIFIC NOTEBOOK

by

Stuart A. Stothoff

Southwest Research Institute
Center for Nuclear Waste Regulatory Analyses
San Antonio, Texas

April 12, 1998

Initial Entries

Scientific NoteBook: # 163

Issued to: S. A. Stothoff

Issue Date: Tuesday, November 16, 1993

By agreement with the CNWRA QA this NoteBook is to be printed at approximate quarterly intervals. This computerized Scientific NoteBook is intended to address the criteria of CNWRA QAP–001.

Table 0-1: Computing Equipment

Machine Name	Type	OS	Location
sierra.cnwra.swri.edu	Sun SPARC 20	SUNOS 4.1.3_U1	desk Rm A-212, Bldg. 189
sisyphus.cnwra.swri.edu	Sun SPARC 20	SUNOS 4.1.3_U1	network
dopey.cnwra.swri.edu	Sun SPARC 10	SUNOS 4.1.3_U1	network
performer.cnwra.swri.edu	SGI Onyx	IRIX 5.3	network
yosemite.cnwra.swri.edu	SGI Onyx	IRIX 5.3	network
bemore.cnwra.swri.edu	SGI Onyx	IRIX 6.2	network
redwood.cnwra.swri.edu	SGI Indy	IRIX 6.2	network
bigbend.cnwra.swri.edu	Sun Ultra-2	SUNOS 5.5.1	network
scratchy1.cnwra.swri.edu	Sun Ultra-2	SUNOS 5.5.1	network
hornet.cnwra.swri.edu	Sun Ultra-2	SUNOS 5.5.1	network

Contents

Initial Entries ii

List of Figures xiv

List of Tables xvi

1 Ambient Hydrology KTI – Infiltration 1

2 Ambient Hydrology KTI – Hydraulic Properties 66

3 Ambient Hydrology KTI – Model Development 213

4 Iterative Performance KTI 228

5 Iterative Performance KTI - Total Performance Assessment Phase 3 229

6 Breath code development 230

List of Figures

1-1 1/13/97. Regression of borehole alluvium depths with nearest-neighbor DEM slopes. 29

1-2 1/15/97. Least-squares fit of simulation prediction to abstraction prediction for various exponents in Equation 1-9. 31

1-3 2/27/97. Time history of decadal-average moisture flux after each of 6 decades, as a function of AAP and AAT, for (a) hourly meteorologic input and bedrock 1, (b) daily meteorologic input and bedrock 1, (c) hourly meteorologic input and bedrock 2, and (d) daily meteorologic input and bedrock 2. 36

1-4 7/14/97. Areal-average MAI for YM area, using regression formula based on soil/open-fracture system, (a) in dimensional form, and (b) in nondimensional form. 54

2-1 8/31/97. The complete set of measured K_{sat} values in the USGS database. 74

2-2 9/9/97. Comparison of best-estimate K_{sat} and measured K_{sat} using (a) the USGS database, (b) the best 1-parameter regression, (c) the best 2-parameter regression, and (d) the best 3-parameter regression. 78

2-3 9/9/97. **BHprofile_NRG6_c.eps**. Porosity, saturation, change in particle density, and measured and estimated values for K_{sat} in borehole NRG6. 80

2-4 9/9/97. **BHprofile_NRG77a_c.eps**. Porosity, saturation, change in particle density, and measured and estimated values for K_{sat} in borehole NRG7/7a. 81

2-5 9/9/97. **BHprofile_SD12_c.eps**. Porosity, saturation, change in particle density, and measured and estimated values for K_{sat} in borehole SD-12. 82

2-6 9/9/97. **BHprofile_SD7_c.eps**. Porosity, saturation, change in particle density, and measured and estimated values for K_{sat} in borehole SD-7. 83

2-7 9/9/97. **BHprofile_SD9_c.eps**. Porosity, saturation, change in particle density, and measured and estimated values for K_{sat} in borehole SD-9. 84

2-8 9/9/97. **BHprofile_UZ14_c.eps**. Porosity, saturation, change in particle density, and measured and estimated values for K_{sat} in borehole UZ-14. 85

2-9 9/9/97. **BHprofile_UZ16_c.eps**. Porosity, saturation, change in particle density, and measured and estimated values for K_{sat} in borehole UZ-16. 86

2-10 9/9/97. **BHprofile_UZ7a_c.eps**. Porosity, saturation, change in particle density, and measured and estimated values for K_{sat} in borehole UZ-7a. 87

2-11 9/9/97. **BHprofile_UZN11_c.eps**. Porosity, saturation, change in particle density, and measured and estimated values for K_{sat} in borehole N11. 88

2-12 9/9/97. **BHprofile_UZN15_c.eps**. Porosity, saturation, change in particle density, and measured and estimated values for K_{sat} in borehole N15. 89

2-13 9/9/97. **BHprofile_UZN16_c.eps**. Porosity, saturation, change in particle density, and measured and estimated values for K_{sat} in borehole N16. 90

2-14 9/9/97. **BHprofile_UZN17_c.eps**. Porosity, saturation, change in particle density, and measured and estimated values for K_{sat} in borehole N17. 91

2-15 9/9/97. **BHprofile_UZN27_c.eps**. Porosity, saturation, change in particle density, and measured and estimated values for K_{sat} in borehole N27. 92

2-16 9/9/97. **BHprofile_UZN31_c.eps**. Porosity, saturation, change in particle density, and measured and estimated values for K_{sat} in borehole N31. 93

2-17 9/9/97. **BHprofile_UZN32_c.eps**. Porosity, saturation, change in particle density, and measured and estimated values for K_{sat} in borehole N32. 94

2-18 9/9/97. **BHprofile_UZN33_c.eps**. Porosity, saturation, change in particle density, and measured and estimated values for K_{sat} in borehole N33. 95

2-19 9/9/97. **BHprofile_UZN34_c.eps**. Porosity, saturation, change in particle density, and measured and estimated values for K_{sat} in borehole N34. 96

2-20 9/9/97. **BHprofile_UZN35_c.eps**. Porosity, saturation, change in particle density, and measured and estimated values for K_{sat} in borehole N35. 97

2-21 9/9/97. **BHprofile_UZN36_c.eps**. Porosity, saturation, change in particle density, and measured and estimated values for K_{sat} in borehole N36. 98

2-22 9/9/97. **BHprofile_UZN37_c.eps**. Porosity, saturation, change in particle density, and measured and estimated values for K_{sat} in borehole N37. 99

2-23 9/9/97. **BHprofile_UZN38_c.eps**. Porosity, saturation, change in particle density, and measured and estimated values for K_{sat} in borehole N38. 100

2-24 9/9/97. **BHprofile_UZN53_c.eps**. Porosity, saturation, change in particle density, and measured and estimated values for K_{sat} in borehole N53. 101

2-25 9/9/97. **BHprofile_UZN54_c.eps**. Porosity, saturation, change in particle density, and measured and estimated values for K_{sat} in borehole N54. 102

2-26 9/9/97. **BHprofile_UZN55_c.eps**. Porosity, saturation, change in particle density, and measured and estimated values for K_{sat} in borehole N55. 103

2-27 9/9/97. **BHprofile_UZN57_c.eps**. Porosity, saturation, change in particle density, and measured and estimated values for K_{sat} in borehole N57. 104

2-28 9/9/97. **BHprofile_UZN58_c.eps**. Porosity, saturation, change in particle density, and measured and estimated values for K_{sat} in borehole N58. 105

2-29 9/9/97. **BHprofile_UZN59_c.eps**. Porosity, saturation, change in particle density, and measured and estimated values for K_{sat} in borehole N59. 106

2-30 9/9/97. **BHprofile_UZN61_c.eps**. Porosity, saturation, change in particle density, and measured and estimated values for K_{sat} in borehole N61. 107

2-31 9/9/97. **BHprofile_UZN62_c.eps**. Porosity, saturation, change in particle density, and measured and estimated values for K_{sat} in borehole N62. 108

2-32 9/9/97. **BHprofile_UZN63_c.eps**. Porosity, saturation, change in particle density, and measured and estimated values for K_{sat} in borehole N63. 109

2-33 9/9/97. **BHprofile_UZN64_c.eps**. Porosity, saturation, change in particle density, and measured and estimated values for K_{sat} in borehole N64. 110

2-34 9/17/97. All CNWRA-estimated and USGS-measured K_{sat} values in formation: (a) Tpcrn4 (**FormK_Tpcrn4_c.eps**), and (b) Tpcrn3 (**FormK_Tpcrn3_c.eps**). 112

2-35 9/17/97. All CNWRA-estimated and USGS-measured K_{sat} values in formation: (a) Tpcrn2 (**FormK_Tpcrn2_c.eps**), and (b) Tpcrn1 (**FormK_Tpcrn1_c.eps**). 113

2-36 9/17/97. All CNWRA-estimated and USGS-measured K_{sat} values in formation: (a) Tpcrl2 (**FormK_Tpcrl2_c.eps**), and (b) Tpcrl1 (**FormK_Tpcrl1_c.eps**). 114

2-37 9/17/97. All CNWRA-estimated and USGS-measured K_{sat} values in formation: (a) Tpcpul (**FormK_Tpcpul_c.eps**), and (b) Tpcpmn (**FormK_Tpcpmn_c.eps**). . . . 115

2-38 9/17/97. All CNWRA-estimated and USGS-measured K_{sat} values in formation: (a) Tpcpll (**FormK_Tpcpll_c.eps**), and (b) Tpcplnh (**FormK_Tpcplnh_c.eps**). . . . 116

2-39 9/17/97. All CNWRA-estimated and USGS-measured K_{sat} values in formation: (a) Tpcplnc (**FormK_Tpcplnc_c.eps**), and (b) Tpcpv2 (**FormK_Tpcpv2_c.eps**). . . 117

2-40 9/17/97. All CNWRA-estimated and USGS-measured K_{sat} values in formation: (a) Tpcpv1 (**FormK_Tpcpv1_c.eps**), and (b) Tpbt4 (**FormK_Tpbt4_c.eps**). 118

2-41 9/17/97. All CNWRA-estimated and USGS-measured K_{sat} values in formation: (a) Tpy (**FormK_Tpy_c.eps**), and (b) Tpbt3 (**FormK_Tpbt3_c.eps**). 119

2-42 9/17/97. All CNWRA-estimated and USGS-measured K_{sat} values in formation: (a) Tpp (**FormK_Tpp_c.eps**), and (b) Tpbt2 (**FormK_Tpbt2_c.eps**). 120

2-43 9/17/97. All CNWRA-estimated and USGS-measured K_{sat} values in formation: (a) Tptrv3 (**FormK_Tptrv3_c.eps**), and (b) Tptrv2 (**FormK_Tptrv2_c.eps**). 121

2-44 9/17/97. All CNWRA-estimated and USGS-measured K_{sat} values in formation: (a) Tptrv1 (**FormK_Tptrv1_c.eps**), and (b) Tptrn (**FormK_Tptrn_c.eps**). 122

2-45 9/17/97. All CNWRA-estimated and USGS-measured K_{sat} values in formation: (a) Tptrn2 (**FormK_Tptrn2_c.eps**), and (b) Tptrl (**FormK_Tptrl_c.eps**). 123

2-46 9/17/97. All CNWRA-estimated and USGS-measured K_{sat} values in formation: (a) Tptrl2 (**FormK_Tptrl2_c.eps**), and (b) Tptrl1 (**FormK_Tptrl1_c.eps**). 124

2-47 9/17/97. All CNWRA-estimated and USGS-measured K_{sat} values in formation: (a) Tptpul (**FormK_Tptpul_c.eps**), and (b) Tptpul2 (**FormK_Tptpul2_c.eps**). . . . 125

2-48 9/17/97. All CNWRA-estimated and USGS-measured K_{sat} values in formation: (a) Tptpul1 (**FormK_Tptpul1_c.eps**), and (b) Tptpmn (**FormK_Tptpmn_c.eps**). . . 126

2-49 9/17/97. All CNWRA-estimated and USGS-measured K_{sat} values in formation: (a) Tptpmn3 (**FormK_Tptpmn3_c.eps**), and (b) Tptpmn2 (**FormK_Tptpmn2_c.eps**).127

2-50 9/17/97. All CNWRA-estimated and USGS-measured K_{sat} values in formation: (a) Tptpmn1 (**FormK_Tptpmn1_c.eps**), and (b) Tptpll (**FormK_Tptpll_c.eps**). . . 128

2-51 9/17/97. All CNWRA-estimated and USGS-measured K_{sat} values in formation: (a) Tptpln (**FormK_Tptpln_c.eps**), and (b) Tptpv3 (**FormK_Tptpv3_c.eps**). 129

2-52 9/17/97. All CNWRA-estimated and USGS-measured K_{sat} values in formation: (a) Tptpv2 (**FormK_Tptpv2_c.eps**), and (b) Tptpv1 (**FormK_Tptpv1_c.eps**). 130

2-53 9/17/97. All CNWRA-estimated and USGS-measured K_{sat} values in formation: (a) Tpbt1 (**FormK_Tpbt1_c.eps**), and (b) Tac (**FormK_Tac_c.eps**). 131

2-54 9/17/97. All CNWRA-estimated and USGS-measured K_{sat} values in formation: (a) TacUnit4 (**FormK_TacUnit4_c.eps**), and (b) TacUnit3NW (**FormK_TacUnit3NW-_c.eps**). 132

2-55 9/17/97. All CNWRA-estimated and USGS-measured K_{sat} values in formation: (a) TacUnit2NW (**FormK_TacUnit2NW_c.eps**), and (b) TacUnit1NW (**FormK-_TacUnit1NW_c.eps**). 133

2-56 9/17/97. All CNWRA-estimated and USGS-measured K_{sat} values in formation: (a) TacbtNW (**FormK_TacbtNW_c.eps**), and (b) TacbsNW (**FormK_TacbsNW-_c.eps**). 134

2-57 9/17/97. All CNWRA-estimated and USGS-measured K_{sat} values in formation: (a) TcpUnit4 (**FormK_TcpUnit4_c.eps**), and (b) TcpUnit4NW (**FormK_TcpUnit4NW-_c.eps**). 135

2-58 9/17/97. All CNWRA-estimated and USGS-measured K_{sat} values in formation: (a) TcpUnit4sub3 (**FormK_TcpUnit4sub3_c.eps**), and (b) TcpUnit4sub2 (**FormK-_TcpUnit4sub2_c.eps**). 136

2-59 9/17/97. All CNWRA-estimated and USGS-measured K_{sat} values in formation: (a) TcpUnit4sub1 (**FormK_TcpUnit4sub1_c.eps**), and (b) TcpUnit3 (**FormK_TcpUnit3_c.eps**). 137

2-60 9/17/97. All CNWRA-estimated and USGS-measured K_{sat} values in formation: (a) TcpUnit2 (**FormK_TcpUnit2_c.eps**), and (b) TcpUnit1 (**FormK_TcpUnit1_c.eps**). 138

2-61 9/17/97. All CNWRA-estimated and USGS-measured K_{sat} values in formation: (a) Tcpbt (**FormK_Tcpbt_c.eps**), and (b) TcbUnit4NW (**FormK_TcbUnit4NW_c.eps**). 139

2-62 9/17/97. All CNWRA-estimated and USGS-measured K_{sat} values in formation: (a) TcbUnit4MW (**FormK_TcbUnit4MW_c.eps**), and (b) TcbUnit3MW (**FormK_TcbUnit3MW_c.eps**). 140

2-63 9/17/97. All CNWRA-estimated and USGS-measured K_{sat} values in formation: (a) TcbUnit3PW (**FormK_TcbUnit3PW_c.eps**), and (b) TcbUnit2NW (**FormK_TcbUnit2NW_c.eps**). 141

2-64 9/17/97. All CNWRA-estimated and USGS-measured K_{sat} values in formation: (a) TcbUnit1NW (**FormK_TcbUnit1NW_c.eps**), and (b) Tcbbs (**FormK_Tcbbs_c.eps**). 142

2-65 9/17/97. All CNWRA-estimated and USGS-measured K_{sat} values in formation TctNW (**FormK_TctNW_c.eps**). 143

2-66 10/7/97. **Disp_DBstat_CCR_c.eps**. Measured and generated formation values for (a) saturation and porosity, (b) saturation and estimated saturated hydraulic conductivity, and (c) porosity and estimated saturated hydraulic conductivity. 159

2-67 10/7/97. **Disp_DBstat_CUC_c.eps**. Measured and generated formation values for (a) saturation and porosity, (b) saturation and estimated saturated hydraulic conductivity, and (c) porosity and estimated saturated hydraulic conductivity. 159

2-68 10/7/97. **Disp_DBstat_CUL_c.eps**. Measured and generated formation values for (a) saturation and porosity, (b) saturation and estimated saturated hydraulic conductivity, and (c) porosity and estimated saturated hydraulic conductivity. 160

2-69 10/7/97. **Disp_DBstat_CW_c.eps**. Measured and generated formation values for (a) saturation and porosity, (b) saturation and estimated saturated hydraulic conductivity, and (c) porosity and estimated saturated hydraulic conductivity. 160

2-70 10/7/97. **Disp_DBstat_CMW_c.eps**. Measured and generated formation values for (a) saturation and porosity, (b) saturation and estimated saturated hydraulic conductivity, and (c) porosity and estimated saturated hydraulic conductivity. 161

2-71 10/7/97. **Disp_DBstat_CNW_c.eps**. Measured and generated formation values for (a) saturation and porosity, (b) saturation and estimated saturated hydraulic conductivity, and (c) porosity and estimated saturated hydraulic conductivity. 161

2-72 10/7/97. **Disp_DBstat_BT4_c.eps**. Measured and generated formation values for (a) saturation and porosity, (b) saturation and estimated saturated hydraulic conductivity, and (c) porosity and estimated saturated hydraulic conductivity. 162

2-73 10/7/97. **Disp_DBstat_TPY_c.eps**. Measured and generated formation values for (a) saturation and porosity, (b) saturation and estimated saturated hydraulic conductivity, and (c) porosity and estimated saturated hydraulic conductivity. 162

2-74 10/7/97. **Disp_DBstat_BT3_c.eps**. Measured and generated formation values for (a) saturation and porosity, (b) saturation and estimated saturated hydraulic conductivity, and (c) porosity and estimated saturated hydraulic conductivity. 163

2-75 10/7/97. **Disp_DBstat_TPP_c.eps**. Measured and generated formation values for (a) saturation and porosity, (b) saturation and estimated saturated hydraulic conductivity, and (c) porosity and estimated saturated hydraulic conductivity. 163

2-76 10/7/97. **Disp_DBstat_BT2_c.eps**. Measured and generated formation values for (a) saturation and porosity, (b) saturation and estimated saturated hydraulic conductivity, and (c) porosity and estimated saturated hydraulic conductivity. 164

2-77 10/7/97. **Disp_DBstat_TC_c.eps**. Measured and generated formation values for (a) saturation and porosity, (b) saturation and estimated saturated hydraulic conductivity, and (c) porosity and estimated saturated hydraulic conductivity. 164

2-78 10/7/97. **Disp_DBstat_TR_c.eps**. Measured and generated formation values for (a) saturation and porosity, (b) saturation and estimated saturated hydraulic conductivity, and (c) porosity and estimated saturated hydraulic conductivity. 165

2-79 10/7/97. **Disp_DBstat_TUL_c.eps.** Measured and generated formation values for (a) saturation and porosity, (b) saturation and estimated saturated hydraulic conductivity, and (c) porosity and estimated saturated hydraulic conductivity. 165

2-80 10/7/97. **Disp_DBstat_TMN_c.eps.** Measured and generated formation values for (a) saturation and porosity, (b) saturation and estimated saturated hydraulic conductivity, and (c) porosity and estimated saturated hydraulic conductivity. 166

2-81 10/7/97. **Disp_DBstat_TLL_c.eps.** Measured and generated formation values for (a) saturation and porosity, (b) saturation and estimated saturated hydraulic conductivity, and (c) porosity and estimated saturated hydraulic conductivity. 166

2-82 10/7/97. **Disp_DBstat_TM2_c.eps.** Measured and generated formation values for (a) saturation and porosity, (b) saturation and estimated saturated hydraulic conductivity, and (c) porosity and estimated saturated hydraulic conductivity. 167

2-83 10/7/97. **Disp_DBstat_TM1_c.eps.** Measured and generated formation values for (a) saturation and porosity, (b) saturation and estimated saturated hydraulic conductivity, and (c) porosity and estimated saturated hydraulic conductivity. 167

2-84 10/7/97. **Disp_DBstat_PV3_c.eps.** Measured and generated formation values for (a) saturation and porosity, (b) saturation and estimated saturated hydraulic conductivity, and (c) porosity and estimated saturated hydraulic conductivity. 168

2-85 10/7/97. **Disp_DBstat_PV2_c.eps.** Measured and generated formation values for (a) saturation and porosity, (b) saturation and estimated saturated hydraulic conductivity, and (c) porosity and estimated saturated hydraulic conductivity. 168

2-86 10/7/97. **Disp_DBstat_BT1_c.eps.** Measured and generated formation values for (a) saturation and porosity, (b) saturation and estimated saturated hydraulic conductivity, and (c) porosity and estimated saturated hydraulic conductivity. 169

2-87 10/7/97. **Disp_DBstat_CHV_c.eps.** Measured and generated formation values for (a) saturation and porosity, (b) saturation and estimated saturated hydraulic conductivity, and (c) porosity and estimated saturated hydraulic conductivity. 169

2-88 10/7/97. **Disp_DBstat_CHZ_c.eps.** Measured and generated formation values for (a) saturation and porosity, (b) saturation and estimated saturated hydraulic conductivity, and (c) porosity and estimated saturated hydraulic conductivity. 170

2-89 10/7/97. **Disp_DBstat_BT_c.eps**. Measured and generated formation values for (a) saturation and porosity, (b) saturation and estimated saturated hydraulic conductivity, and (c) porosity and estimated saturated hydraulic conductivity. 170

2-90 10/7/97. **Disp_DBstat_PP4_c.eps**. Measured and generated formation values for (a) saturation and porosity, (b) saturation and estimated saturated hydraulic conductivity, and (c) porosity and estimated saturated hydraulic conductivity. 171

2-91 10/7/97. **Disp_DBstat_PP3_c.eps**. Measured and generated formation values for (a) saturation and porosity, (b) saturation and estimated saturated hydraulic conductivity, and (c) porosity and estimated saturated hydraulic conductivity. 171

2-92 10/7/97. **Disp_DBstat_PP2_c.eps**. Measured and generated formation values for (a) saturation and porosity, (b) saturation and estimated saturated hydraulic conductivity, and (c) porosity and estimated saturated hydraulic conductivity. 172

2-93 10/7/97. **Disp_DBstat_PP1_c.eps**. Measured and generated formation values for (a) saturation and porosity, (b) saturation and estimated saturated hydraulic conductivity, and (c) porosity and estimated saturated hydraulic conductivity. 172

2-94 10/7/97. **Disp_DBstat_BF3_c.eps**. Measured and generated formation values for (a) saturation and porosity, (b) saturation and estimated saturated hydraulic conductivity, and (c) porosity and estimated saturated hydraulic conductivity. 173

2-95 10/7/97. **Disp_DBstat_BF2_c.eps**. Measured and generated formation values for (a) saturation and porosity, (b) saturation and estimated saturated hydraulic conductivity, and (c) porosity and estimated saturated hydraulic conductivity. 173

2-96 10/28/97. Estimated properties for layer TMN. Correlation between material properties (b), and quartiles for: (a) equivalent K_{sat}, P_0 using retention and conductivity (c and d, respectively); and m using retention and conductivity (e and f, respectively).191

2-97 10/28/97. Estimated properties for layer TLL. Correlation between material properties (b), and quartiles for: (a) equivalent K_{sat}, P_0 using retention and conductivity (c and d, respectively); and m using retention and conductivity (e and f, respectively).192

2-98 10/28/97. Estimated properties for layer TM2. Correlation between material properties (b), and quartiles for: (a) equivalent K_{sat}, P_0 using retention and conductivity (c and d, respectively); and m using retention and conductivity (e and f, respectively).193

2-99 10/28/97. Estimated properties for layer TM1. Correlation between material properties (b), and quartiles for: (a) equivalent K_{sat}, P_0 using retention and conductivity (c and d, respectively); and m using retention and conductivity (e and f, respectively).194

2-100 10/28/97. Estimated properties for layer PV3. Correlation between material properties (b), and quartiles for: (a) equivalent K_{sat}, P_0 using retention and conductivity (c and d, respectively); and m using retention and conductivity (e and f, respectively).195

2-101 10/28/97. Estimated properties for layer PV2. Correlation between material properties (b), and quartiles for: (a) equivalent K_{sat}, P_0 using retention and conductivity (c and d, respectively); and m using retention and conductivity (e and f, respectively).196

2-102 10/28/97. Estimated properties for layer BT1. Correlation between material properties (b), and quartiles for: (a) equivalent K_{sat}, P_0 using retention and conductivity (c and d, respectively); and m using retention and conductivity (e and f, respectively).197

2-103 10/28/97. Estimated properties for layer CHV. Correlation between material properties (b), and quartiles for: (a) equivalent K_{sat}, P_0 using retention and conductivity (c and d, respectively); and m using retention and conductivity (e and f, respectively).198

2-104 10/28/97. Estimated properties for layer CHZ. Correlation between material properties (b), and quartiles for: (a) equivalent K_{sat}, P_0 using retention and conductivity (c and d, respectively); and m using retention and conductivity (e and f, respectively).199

2-105 10/28/97. Estimated properties for layer BT. Correlation between material properties (b), and quartiles for: (a) equivalent K_{sat}, P_0 using retention and conductivity (c and d, respectively); and m using retention and conductivity (e and f, respectively).200

2-106 10/28/97. Estimated properties for layer PP4. Correlation between material properties (b), and quartiles for: (a) equivalent K_{sat}, P_0 using retention and conductivity (c and d, respectively); and m using retention and conductivity (e and f, respectively).201

2-107 10/28/97. Estimated properties for layer PP3. Correlation between material properties (b), and quartiles for: (a) equivalent K_{sat}, P_0 using retention and conductivity (c and d, respectively); and m using retention and conductivity (e and f, respectively).202

2-108 10/28/97. Estimated properties for layer PP2. Correlation between material properties (b), and quartiles for: (a) equivalent K_{sat}, P_0 using retention and conductivity (c and d, respectively); and m using retention and conductivity (e and f, respectively).203

2-10910/28/97. Estimated properties for layer PP1. Correlation between material properties (b), and quartiles for: (a) equivalent K_{sat}, P_0 using retention and conductivity (c and d, respectively); and m using retention and conductivity (e and f, respectively).204

2-11010/28/97. Estimated properties for layer BF3. Correlation between material properties (b), and quartiles for: (a) equivalent K_{sat}, P_0 using retention and conductivity (c and d, respectively); and m using retention and conductivity (e and f, respectively).205

2-11110/28/97. Estimated properties for layer BF2. Correlation between material properties (b), and quartiles for: (a) equivalent K_{sat}, P_0 using retention and conductivity (c and d, respectively); and m using retention and conductivity (e and f, respectively).206

List of Tables

0-1 Computing Equipment ii

1-1 Statistical behavior of net infiltration (AAI in mm/yr). 3

1-2 Summary of tight-grid infiltration simulation results 5

1-3 Summary of alluvium ($abcd$) and fracture ($efgh$) parameter codes 6

1-4 Summary of colluvium and matrix properties used in simulations. 22

1-5 Best-fit abstractions to material properties in deep alluvium. 31

1-6 Regression values for deep-alluvium meteorologic abstraction. 32

1-7 Regression coefficients for deep-alluvium meteorologic abstraction. 33

1-8 Hydraulic conductivity measurements in Solitario Canyon on March 27 and 28, 1997. 43

1-9 Summary of alluvium ($abcd$) and fracture ($efgh$) parameter codes 47

1-10 Net infiltration (mm/yr) for various cases with soil- and calcite-filled fractures 48

2-1 Statistical description of $Y = \log_{10}[K_{sat}\ (m/s)]$ in TCw. 143

2-2 Statistical description of $Y = \log_{10}[K_{sat}\ (m/s)]$ in PTn. 144

2-3 Statistical description of $Y = \log_{10}[K_{sat}\ (m/s)]$ in TSw. 144

2-4 Statistical description of $Y = \log_{10}[K_{sat}\ (m/s)]$ below TSw (CHnv, CHnz, PP, UCF, UBF). 145

2-5 Statistical properties of regression on K_{sat}. 155

2-6 Layerwise estimates of K_{sat} (m/s). 10^{-10} m/s is equal to 3.16 mm/yr. 158

2-7 Estimates of mean and standard deviation for average K_{sat} (m/s) over a layer, reported as $\log_{10}(K_{sat})$. Both geometric and arithmetic means are reported. 10^4 replicates of 10^4 realizations were used. 177

2-8 Best estimated fits to retention data using USGS outcrop data. 179

2-9 Restricted fits to retention data using USGS outcrop data. 180

2-10 Statistical properties of regression on retention parameters. 182

2-11 Estimates of microstratigraphic K_{sat} 188

2-12 Estimates of microstratigraphic van Genuchten α (bar^{-1}) 189

2-13 Estimates of microstratigraphic van Genuchten n 190

2-14 Estimates of microstratigraphic hydraulic properties using flux-weighted velocity . . 209

1. Ambient Hydrology KTI – Infiltration

Account Number: **20-5708-861**
Collaborators: **Amvrossios Bagtzoglou, Gordon Wittmeyer**
Directories: **$SubRegBreath and as noted**

Objective: Perform detailed analysis of the spatial and temporal distribution of infiltration at Yucca Mountain (YM). A good deal of previous work is documented in the Scientific Notebook for the Subregional Flow and Transport Processes Research Project (subregional project) and various publications under the subregional project and the umbrella of the Iterative Performance Assessment and Performance Assessment Research projects. The research projects were closed out due to reorganization of the NRC and consequently CNWRA; infiltration work is largely being subsumed under the Ambient Hydrology KTI, with some applications possible under the Thermal Effects on Flow KTI in order to examine heating effects on infiltration. Initial efforts in the new project are to be directed towards documenting the work already completed in journal articles. Future work will depend very much on funding and time availability, but several avenues that may be explored include: (i) the impact of matrix-fracture interactions; (ii) watershed-scale modelling, with vegetation and lateral flow accounted for; (iii) geochemical tracer verification; and (iv) "shallow" diversion of infiltration due to the PTn layer.

1/26/96 Initial entry. SAS

Work on infiltration under the subregional project and IPA is currently being documented in two journal articles. The first article deals with the impacts of hydraulic properties on 1D infiltration; the second looks at meteorology, documents the alluvium flow model, and estimates spatial and temporal distributions of infiltration. All simulations to date have been 1D; the first sets examined semi-infinite alluvium columns, with later sets looking at a shallow alluvium layer over a fracture continuum. It is quite clear that the fracture continuum will allow far more water to infiltrate than the alluvium columns; a relatively thin alluvium coating (less than 50 cm) will shut off fracture flow entirely, but sufficiently deep alluvium (greater than 5 m) will allow the flow to resume; hillslopes and ridgetops are the most important infiltration areas; micrometeorology is not a great factor, nor is the fracture description if there is enough fracture porosity; alluvium hydraulic properties have a significant influence, increasing with depth, but the depth of alluvium is the single most important parameter; detailed hourly description of meteorology is only important near precipitation events; and it is critical to use arithmetic averaging or upstream weighting for conductivities in the fracture

continuum.

In the process of creating traces of infiltration rates, it became apparent that several of the cases with very shallow alluvium covers (2 cm and 5 cm) spuriously created mass for one or more storms. Increasing the resolution in the top layer from roughly 1 cm per element to 1 mm per element fixed the problem for the simulations that were rerun this week (temperature and precipitation perturbations). Unfortunately, even though the new results show excellent self-consistency, there is significant deviation between the coarse and fine cases (roughly 50 percent less infiltration for 2-cm cases). A revised set were set off today for the hydraulic properties, but it takes roughly a day per simulation so it will be several weeks before all are completed.

1/30/96 Data Analysis. SAS

Created matlab files to analyze the lowest flux trace from a set of breath runs. The workhorse file, **stat_infil.m**, is in ***$HOME2/Matlab/BreathUtil.*** Copies of the driver routine, **eval_all_stat.m**, must be put in the result directory of interest. Filled out a table for temporal behavior of infiltration in the paper on the spatial/temporal distribution of infiltration, aside from the 10-cm case which must be rerun due to accidental erasure of the trace files. The table is included here as Table 1-1. Also tracked down many of the figures to be included and rearranged the directory structure below ***$HOME2/Subreg*** to have better segregation of figures. New directories containing figures now are listed as ***FigureXxxx***, where ***Xxxx*** is one of ***Paper*** or ***YMElev.***

2/17/96 Error in viscosity units. SAS

A persistent mistake was found in the specification of viscosity, dating from the earliest runs using *breath. breath* uses consistent units for all variables; however, the *Matlab* files used to create inputs for *breath* consistently uses viscosities three orders of magnitude too large. There is no net impact on the results when saturated conductivity is provided as data, as *breath* requires intrinsic permeability rather than saturated conductivity and intrinsic permeability is obtained by scaling hydraulic conductivity with the incorrect viscosity, which in turn is scaled back internally to *breath.* Accordingly, test problems based on saturated conductivity have been correctly calculated, since intrinsic permeability and viscosity are incorrect in compensating ways. Many other simulations are perfectly valid. Unfortunately, all sequences of infiltration experiments performed with alluvium and fractures have alluvium permeability specified (fracture saturated conductivity is specified), so that the reported permeabilities are actually off by three orders of magnitude. The *breath* code has

Table 1-1: Statistical behavior of net infiltration (AAI in mm/yr).

Depth (cm)	Multiple of AAP	°C Added to AAT	AAI	Wettest Year AAI	Wettest Year Events	Driest Year AAI	Driest Year Events	Events Max	Events Min
2	1.0	0	58.2	172.5	5	9.5	1	7 (1)	1 (1)
2	0.9	0	48.1	149.5	5	7.9	1	6 (2)	1 (1)
2	1.1	0	67.0	196.5	5	11.16	1	10 (1)	1 (1)
2	1.0	+3	50.6	158.2	5	8.79	1	6 (2)	1 (2)
2	1.0	−3	68.7	191.2	5	10.34	1	10 (1)	1 (1)
5	1.0	0	31.0	124.7	7	0.29	0	7 (1)	0 (1)
5	0.9	0	23.7	101.2	5	> 0.01	0	7 (1)	0 (2)
5	1.1	0	38.6	147.9	5	2.98	1	5 (2)	1 (3)
5	1.0	+3	25.3	108.3	5	0.59	0	5 (1)	0 (1)
5	1.0	−3	38.7	148.3	5	2.18	1	6 (1)	1 (3)
10	1.0	0	12.5	60.1	4	> 0.01	0	4 (1)	0 (3)
10	0.9	0	8.73	42.8	4	> 0.01	0	4 (1)	0 (5)
10	1.1	0	TBD	TBD	TBD	TBD	TBD	TBD	TBD
10	1.0	+3	9.68	49.9	4	> 0.01	0	4 (1)	0 (4)
10	1.0	−3	16.8	81.8	4	> 0.01	0	4 (1)	0 (3)
15	1.0	0	4.61	26.7	2	> 0.01	0	2 (2)	0 (7)
15	0.9	0	2.65	13.9	1	> 0.01	0	2 (1)	0 (8)
15	1.1	0	6.26	33.3	3	> 0.01	0	3 (1)	0 (6)
15	1.0	+3	3.18	17.3	2	> 0.01	0	2 (1)	0 (8)
15	1.0	−3	7.74	45.8	4	> 0.01	0	4 (1)	0 (7)

a temperature-dependent viscosity option, which I have not used; this option uses viscosities that are off by two orders of magnitude. I corrected this viscosity calculation in *breath* versions 1.1, 1.2, and 1.3 today.

The fix is to relabel all references to permeability to a value three orders of magnitude lower. The results are actually more comforting than the originally reported interpretations implied, since the actual range of permeabilities is in the range of silty sands through clean sands, rather than clean sands through gravels, and indeed are representative of the range of values reported for YM as was reported by various USGS papers. In fact, if my simulations were reported using saturated conductivities, the results would have been consistent and it is quite possible that the persistent error would not have been found. The simulations were incorrectly presented in Stothoff et al.

(1995), Stothoff and Bagtzoglou (1996), Bagtzoglou et al. (1995), Stothoff et al. (1996), and the poster used for both Stothoff and Bagtzoglou (1995) and the 1995 Kearney Conference. It may yet be possible to save the version of Stothoff and Bagtzoglou (1996) that will be widely distributed.

3/8/96 Update figures and results. SAS

In preparing a series of slides for a Geological Society of America conference on 3/12/96, I am taking the opportunity to tabulate the results generated from a sequence of runs using a tight grid, as explained in the entry of 1/26/95. All hydraulic-property cases and the pressure and temperature cases were rerun for the 2-cm and 5-cm alluvium depths. The base case scenario was rerun for the 10-cm, 15-cm, 500-cm, and 1000-cm alluvium depths, as well as the semi-infinite alluvium case.

The results of the simulations are summarized in Table 1-2. The base-case weather is denoted by an "m"; perturbations in AAP and in AAT are denoted by "r" and "t", respectively. AAP is perturbed by multiplying all precipitation values by the noted perturbation; AAT is perturbed by adding (t+) or subtracting (t−) the noted perturbation. The alluvium and fracture codes both coalesce the permeability, porosity, and van Genuchten parameters into a 4-digit code. The codes are selected to allow one integer per parameter, and are translated in Table 1-3. The odd translation for fracture intrinsic permeability and van Genuchten scaling pressure are because saturated hydraulic conductivity and van Genuchten α created better codes. Note that the -3 factor in the intrinsic permeability codes is the correction for the improperly specified viscosity in earlier runs, so all runs are consistently labelled.

4/16/96 Update results and interpret. SAS

Over the past month, I've been running simulations with fairly extreme climatic change in order to examine what would be expected at YM. So far, only 2-cm and 5-cm alluvium depths have been run, since the deeper cases take much longer. The climatic change is accomplished by multiplying all precipitation by a constant factor and/or adding a constant temperature. For both 2-cm and 5-cm cases, all combinations of rain and temperature have been completed with rain multiplied by 2/3, 1, or 3/2, and -5, 0, or $+5$ degrees C added to the temperature. A similar sequence is underway for rain multiplied by 1/2, 1, or 2, and -10, 0, or $+10$ degrees C added to the temperature. I should probably run a 15-cm and semi-infinite sequence as well for completeness, but these would take a *long* time. The results are summarized in **af_cli.result** in ***$HOME1/RunCliFrac*** *(correction (dated 12/7/96):* ***$BREATH1/RunCliFrac****).*

Table 1-2: Summary of tight-grid infiltration simulation results

Weather Code	Weather Perturbation	Alluvium Depth (cm)	Alluvium Code	Fracture Code	Moisture Content	Flux (cm/yr)
m	0	2	5223	2713	0.0331	5.82
m	0	2	5223	2712	0.0331	5.89
m	0	2	5223	2714	0.0328	3.29
m	0	2	5223	2703	0.0328	7.32
m	0	2	5223	2723	0.0331	5.75
m	0	2	5223	2613	0.0331	5.90
m	0	2	5223	2813	0.0331	5.77
m	0	2	5223	0713	0.0330	5.19
m	0	2	5223	4713	0.0331	5.86
m	0	2	5222	2713	0.0218	7.05
m	0	2	5225	2713	0.0548	4.43
m	0	2	5213	2713	0.0324	5.92
m	0	2	5253	2713	0.0352	5.87
m	0	2	5123	2713	0.1015	6.17
m	0	2	5323	2713	0.0151	6.51
m	0	2	4223	2713	0.0293	6.20
m	0	2	6223	2713	0.0397	5.43
m	0	5	5223	2713	0.0484	3.10
m	0	5	5223	2712	0.0486	3.18
m	0	5	5223	2714	0.0484	1.72
m	0	5	5223	2703	0.0483	3.32
m	0	5	5223	2723	0.0486	3.08
m	0	5	5223	2613	0.0485	3.15
m	0	5	5223	2813	0.0486	3.07
m	0	5	5223	0713	0.0485	2.69
m	0	5	5223	4713	0.0486	3.17
m	0	5	5222	2713	0.0331	4.30
m	0	5	5225	2713	0.0750	1.56
m	0	5	5213	2713	0.0505	3.22
m	0	5	5253	2713	0.0469	2.93
m	0	5	5123	2713	0.1219	3.69
m	0	5	5323	2713	0.0251	3.28
m	0	5	4223	2713	0.0380	3.37
m	0	5	6223	2713	0.0625	3.05
t−	3.0	2	5223	2713	0.0381	6.87
t+	3.0	2	5223	2713	0.0294	5.06
r*	0.9	2	5223	2713	0.0324	4.81
r*	1.1	2	5223	2713	0.0338	6.90
t−	3.0	5	5223	2713	0.0562	3.87
t+	3.0	5	5223	2713	0.0423	2.53
r*	0.9	5	5223	2713	0.0465	2.37
r*	1.1	5	5223	2713	0.0503	3.86

Table 1-3: Summary of alluvium ($abcd$) and fracture ($efgh$) parameter codes

Code	Parameter	Translation
a	Intrinsic permeability k (cm^2)	$k = 10^{-a-3}$
b	van Genuchten m	$m = b/10$
c	van Genuchten scaling pressure P_0 (gm/cm-s^2)	$P_0 = c \times 10^4$
d	Porosity ε	$\varepsilon = d/10$
e	Intrinsic permeability k (cm^2)	$k = 1.14694 \times 10^{-e-3}$
f	van Genuchten m	$m = f/10$
g	van Genuchten scaling pressure P_0 (gm/cm-s^2)	$P_0 = 980 \times 10^{-g}$
h	Porosity ε	$\varepsilon = 10^{-h}$

Doubling rain and subtracting 10 degrees C from the temperature yields the most infiltration of all cases considered. For the 2-cm case, a factor of 4.3 increase is generated; for the 5-cm case, a factor of 6.6 increase is generated. Overall, this suggests that roughly a factor of 5 to 6 increase should be expected for this climatic condition, taking into account the importance of shallow covers relative to deeper covers. This increase could be quantified better using the newly developed colluvium-balance model discussed in the Geomorphology chapter.

4/17/96 Thoughts on creating an infiltration PDF. SAS

The original motivation for examining shallow infiltration was to provide a PDF for the deep percolation fluxes past the repository. Ross and I planned to have my shallow infiltration fluxes feed into his deep percolation models. At the time, my idea was to construct a response surface for shallow infiltration as a function of whatever parameters were found to be important. It is now years later, but my work is reaching a point where construction of such a PDF is in sight.

An infiltration PDF is not a particularly well-defined concept. Ideally, one would construct many realizations of the entire mountain, from the surface to the water table, and pass in the appropriate boundary fluxes. The TSPA approach breaks the mountain into representative columns, each with its own infiltration flux. I believe that the PDF of interest is actually the PDF describing fluxes in each column, and presumably the fluxes in the columns are correlated. Accordingly, the shallow infiltration work can only be step one in the process, albeit a critical link between climate and deep percolation.

If the infiltration work is split into shallow and deep components, I believe that the best

that the shallow infiltration work can do is to pass off plausible realizations of shallow fluxes to the deep percolation model, which in turn uses realizations of the stratigraphy and hydraulic properties to calculate fluxes through the repository. If indeed the fluxes at the repository in the deep model are insensitive to the degree of spatial variability in the shallow distributions, as I suspect, the smoothest distributions yielding minimal deviation at the repository should be used. A grid of spatially averaged infiltrations would be appropriate, perhaps on a 10-pixel spacing.

Ross' deep percolation work (Bagtzoglou et al., 1995) suggests that the repository is rather insensitive to focused recharge. Another approach that might be taken is to calculate the average infiltration over the area "upstream" of the repository. Unfortunately, the upstream area would be different for each realization, so that some representative area would need to be designated. The entire DEM feels excessive, while the repository footprint is too small. Perhaps the channel in Solitario Canyon to east of the footprint, extending a total of twice the north-south extent of the footprint?

The response surface idea can come into play at a second level in the average-infiltration approach. The first level is the construction of infiltration at a pixel as a function of parameter values. The second level is the construction of the average upstream infiltration as a function of parameter values. The response surface would assume that a single value of each hydraulic property is sampled and applied to the entire domain. Alternatively, it is possible to randomly assign properties to each pixel from an appropriate distribution and generate many realizations, calculating the average infiltration for each realization. Both of the approaches should be performed, using corresponding property PDFs, in order to see if important differences appear. I suspect that the two approaches will give essentially identical PDFs for shallow infiltration (some sort of law of large numbers), even if correlation between parameters is present.

In my model, the spatio-temporal distribution of shallow infiltration can be captured with 8 parameters: (i) four alluvium hydraulic properties (K_{sat}, porosity, and two van Genuchten parameters); (ii) two alluvium-depth properties; and (iii) average temperature and precipitation. The alluvium hydraulic properties could easily be functions of space. The average temperature and precipitation may be available from the geologic and other records (e.g., the Devil's Hole data, packrat middens). The alluvium-depth properties, however, are big unknowns; I feel these should be constants for a realization. The YM field trip planned for the near future will aid in constraining the alluvium-depth properties.

Given that the alluvium-depth properties and the climatic properties are constants for a realization, there is no reason to suspect that the two average-infiltration approaches would yield a

different PDF unless there is some systematic bias for hydraulic properties as a function of colluvium depth. Consider the environment of deposition. Shallow covers tend to be cobbly, with outcrops of rock. There may be some trend towards low spatial-average porosity, high permeability, and coarser grains in the shallower cover. Are shallow covers coarser? Something to check on the field trip, but how? Perhaps portable grain-size distributions, timing infiltration rates. Upon second thought, such ideas are silly – it would be very difficult to find discernable trends in the 2-cm through 15-cm regimes. It doesn't matter once the depths are greater than 0.5 m, since there is no infiltration to speak of anyway for such cases.

Since the two average-infiltration approaches should yield consistent PDFs, it makes sense to construct the response surface. I suspect that a reasonably detailed 8-dimensional surface could be calculated in hours; setting up the software could take a day or two, since the software should take advantage of new information from additional simulations as they might become available. Enforcing consistency between various simulations with various degrees of reliability may be a headache, as I have migrated to tighter and tighter numerical standards over time.

One issue that should be addressed is the issue of climatic change. I've talked to Dave Turner and Mike Miklas about retrieving climatic records. The idea would be to generate a series of plausible climatic-change realizations based on available data and feed it through the response surface to generate plausible traces of average infiltration. The resultant trace could be compared to TSPA traces. The deep percolation model really needs to be flogged to get the response of the repository horizon to infiltration rates for this to be most useful, but a nice paper could come out of the work.

4/23/96 Watershed modelling. SAS

Dr. David Woolhiser will be consulting to CNWRA on the subject of watershed modelling. A number of discussions have taken place between Woolhiser, Gordon, Ross, and myself, with the intent of scoping out the work to be performed. After these discussions, we have decided to break out the work into several packages of roughly $10 k apiece. The first package will be simulation of a representative wash feeding into Solitario Canyon from the west, which would be a surrogate for wash-scale modelling of easterly of Yucca Crest. The first package will test the methodology and feasibility of future work. Further packages would include the full Solitario Canyon watershed, and perhaps some detailed side-slope simulations with lateral subsurface flow.

To date, we have sent Woolhiser relatively limited information on the site. He has requested

additional information including

- a large contour map of the Solitario Canyon watershed;
- a contour map of slopes in the Solitario Canyon watershed;
- available information on infiltration;
- available information on saturated conductivity;
- channel cross-sections; and
- photographs of the channel cross-sections (for roughness estimates).

A field trip to YM is being planned for the near future, at which time channel cross-sections and photographs can be obtained. In addition, I will obtain measurements of alluvium depths to compare with my geomorphology model, and perhaps some limited infiltration sampling using a falling-head permeameter can be performed as well. According to Woolhiser, a representative channel section or two midway between incoming washes would probably be sufficient for his needs, with 3 or 4 sections in representative washes. Photographs of each section should be taken, roughly 50 feet downstream.

Woolhiser has software available that should be able to generate the weather conditions at the resolution required for his model.

5/18/96 Summary of field trip observations. SAS

This past week, Ross Bagtzoglou, Gordon Wittmeyer, and I went to Solitario Canyon to obtain field measurements and observations. Ross and Gordon concentrated on surveying wash cross-sections for the mid- to lower-canyon reaches, while I concentrated on walking the mid- to lower-canyon from rim to rim taking spot measurements of colluvium depths and trying to make observations useful for comparison with computational models. My field observations are documented in a field book, CNWRA Controlled Copy number 175.

The first field day, May 13, we spent basically getting together procedures and familiarizing ourselves with the site and equipment. Ross and Gordon wrestled with the surveying equipment and data logger all day, finally becoming comfortable with the equipment after successfully surveying a motel room that evening. During the day, they located well USW H-7 (on the other side of the road

from Plug Hill) as a benchmark and made one cross-section at a stream-gage station adjacent to Plug Hill. Additional cross-sections were stymied by a recalcitrant data logger, apparently confused by a mixup in coordinates input for the first two locations.

I spent part of the first field day making measurements of alluvium to the west and northwest of the USW H-7 pad, walking up a sideslope to the crest and returning down a small wash. Wherever I took alluvium depth measurements, I marked a nearby bush with surveyor's tape with the idea of having the points surveyed in subsequently. As it turned out, we did not get a chance to survey the points due to delays caused by unfamiliarity with the equipment.

In order to estimate shallow alluvium/colluvium depths, I brought a tile probe with the idea of poking a hole into the alluvium until further advances were rejected. The tile probe is a metal rod with a diameter of 1/2 in, with a metal tip 4 cm long and a padded handle. The base of the adapter attached to the handle is 124 cm from the tip. I brought a 10-lb hammer attachment to replace the handle, in order to help drive the tile probe. I scored the probe, creating very distinctive grooves at 10, 20, 30, 40, and 50 cm distances from the tip, for quick depth and length estimates.

Proceeding up the slope from the USW H-7 pad to the west crest, point measurements ranged up to 44 cm. At one representative mid-slope location, depths were 27, 36, and 42 cm within 2 m; at another, depths were 17, 21, and 37 cm. At the crest, depths were typically 2 to 4 cm in places, at others 6 to 8 cm. Just below the crest, pockets of 12 to 18 cm colluvium were found, increasing with distance below crest to at least 37 cm. Walking down the rill, the channel was found to consist of bare rock in places, particularly at narrow and/or steep reaches. As the channel flattened, the scoured zones disappeared. Judging from the walls of the channel in scoured zones, alluvium depths could be as much as 2 m in places, but it is difficult to tell for sure. Certainly ridges between subwashes are up to 2 m.

It quickly became obvious that the idea of the tile probe was not going to work in alluvium over a certain depth or in regions with numerous chunks of rock, since rejection due to rubble was so likely compared to rejection due to bedrock. Accordingly, I concentrated use of the probe in shallow zones generally less than 40 cm in depth. These zones are of the most interest for infiltration estimates anyway.

The second part of the first day, I walked north along the bottom of Solitario Canyon further than well USW H-6. The stream channel morphology is rather confused in the entire stretch I walked north from Plug Hill. It appears that there are typically two channels, one for the eastern side of Solitario Canyon and one for the western side, but the channels are not strongly distinct and tend to braid. The bottom of the channel is not uniform, with patches of similar materials ranging from

very fine through gravel. There is brush in most of the channel, with somewhat less brush in the most active portions of the channel. There is a great deal of variability at a scale less than the 30 m x 30 m resolution provided by the DEMs we've been using, so that the cross-sections are essential. Unfortunately, in order to fully capture the stream channels, cross-sections would be required at a much higher density (every 20 to 50 m, I estimate) than Gordon and Ross set out to perform. Gordon and Ross were going by Woolhiser's estimates of one cross-section per side wash.

The second field day, I walked or crossed each of the washes in the watershed draining to the north of the USW H-7 pad. The watershed consists of 6 or 7 washes to the north and west of the pad. Proceeding to the north, I walked the Boomerang Point crestline, crossed to near the Jet Ridge crestline, and dropped back into the USW H-6 watershed. This day, I used Global Position System (GPS) pack to provide approximate latitude and longitude at selected locations. The GPS equipment is supposed to place one within 100 m of the correct location; if a second station is used, differential methods are supposed to yield sub-meter accuracy. Our original intent was to use a reference station and a rover station; however, we found that the supplied batteries were only good for 4-1/2 to 5 hours and we did not have four batteries to cover the full day. Upon return, I hear that motorcycle batteries might do the trick for a reference station.

The third field day, I was in Las Vegas and received a NTS badge and GET training.

The fourth (and my last) field day, I walked up the east part of Solitario Canyon to Yucca Crest, arriving not far from USW-UZ6. Again I used the GPS equipment without a reference station. I started at a trench apparently dug to expose the Solitario Canyon fault, and passed some terracing exposing the upper half of the PTn outcrop. Once at the Crest, I proceeded down the wash north of Highway Ridge to the first of two sets of trenches scraping away the alluvium cover from bedrock. The trenches extend from ridgetop to ridgetop. Due to time constraints, I only examined the southerly trench closely. This trench shows very little alluvial cover at the channel bottom, increasing to 1 or 1.5 m within 10 m of the bottom, and gradually thins to less than 10 cm at the top. Returning to the crest on the southern side of the roadway, I was able to observe the wash to the south as well. I returned to Solitario Canyon slightly north of USW H-3. Upon my return, judging from aerial photographs I was able to observe terrain typical of the western and central portions of the repository footprint; further to the east, the wash channels become wider and have little in the way of scouring in the channel bottoms.

During the four field days, Gordon and Ross completed on the order of 15 cross-sections, extending up Solitario Canyon most of the way from Plug Hill to USW H-6. The original plans to survey the entire canyon channel were discarded due to the messy nature of the channel above this

point and due to time constraints. The day after I left, Gordon and Ross visited the ESF.

Based on the three days of walking around and poking colluvium, it is clear that there are some problems with the colluvium model hooked together with the infiltration response surface, although the basic approach is sound. In general, even on ridgetops there are very few places that have less than 3 or 4 cm colluvium cover, and these places are usually exfoliation shards overlying bedrock. TC caprock boulders are generally massive and unfractured. Along crestlines, TC caprock exposures cover 50 to 90 percent of the surface (visually estimated). Moving downhill easterly from the crests, TC caprock boulders on the order of meters in length appear, get smaller and sparser, then disappear. In the cracks between TC caprock outcrops at the crestlines, it is typical for fine sand through loess to be present with depths at least 3 cm and less than 6 cm. Depths increase with distance from the crestline, averaging 10 cm or so between the larger boulders and increasing to 15 to 20 cm as the boulders decrease in size. There are occasional pockets with deeper colluvium, typically less than twice the average depths for the area. I saw few washes cutting directly into the caprock, aside from the western portions of crestlines, although it was not uncommon for caprock boulders to be sliding along other TC units into washes to the east.

Most of the exposures east of crestlines are TC units. Generally these are not highly fractured near the caprock but increase with depth. Any TC units below the caprock do not appear distinctive to my admittedly untrained eye. Chunks of the lower TC tend to be much smaller than the TC caprock boulders, generally being less than 50 cm. In the steepest portions of washes cutting TC units, bare country rock may be exposed, particularly in wash channels and up to 10 m above the channels in places. The washes on the west of Solitario Canyon tend to be steeper and shorter than the washes on YM proper. The YM washes tend to develop long regular reaches with uniform sideslopes, very nice for modelling. Based on a trench north of Highway Ridge, maximum alluvium depth on sideslopes should not be much more than 1 to 2 m, near the channel bottom. It appears that the long regular slopes are steepened at the base, due to removal of colluvium due to stream action during rainfall. It may be possible to estimate the depth of alluvium by projecting sideslopes out to midchannel in the upper portions of the washes.

All along the steep portions to the west of Yucca Crest, pockets may be as much as 40 cm, but generally are in the 5 to 15 cm range. A considerable amount of bare outcrop is present, as much as 50 percent or more of the surface area. Even partway down the flatter slopes, depths may not be more than 50 to 100 cm.

There are distinctive stripes of dark, highly varnished scree alternating with light, clean scree on many of the wash slopes. Stripes may be as little as 1 to 2 m on center and may be tens

of meters on center. Invariably the dark scree is raised relative to the clean scree, suggesting that runoff is focused on the clean scree and washes it. It may be safe to assume that the darker the scree, the higher it is relative to the adjacent light scree.

Two difficulties arise when comparing the infiltration conceptual model work with field observations. The first difficulty is in treating the regions near the crestlines. Although colluvium depths, where present, are generally greater than I've been assuming, the areal average might not be too bad. However, the flow modelling assumes that there is uniform depths of colluvium everywhere, while the actual situation is patchier and deeper. An obvious way of treating the actual situation is to decrease the porosity to account for the proportion of surficial area that is impermeable boulder. It may be that reducing porosity is essentially equivalent to reducing depth, since the volume available for flow is reduced by either approach. If so, accounting for boulder size and area may not be tremendously important in the colluvium model.

The second difficulty is in treatment of wash channels. The colluvium model breaks down when factors other than gravity become important, such as overland water flow. It should not be difficult to include a factor increasing colluvium fluxes due to streamflow, which will get rid of the (arbitrary) 20 m depths in upper channels. Unfortunately, all of the action is on a scale that is subgrid compared to the DEM measurements. The channels are only 1 to 2 m wide where the rock is bare, yet the grid is 30 m on a side. It may be necessary to overlay a refined grid on wash bottoms to properly capture infiltration, at least in upper portions of the washes. As the channel bottoms are relatively narrow, there may not be a great deal of infiltration relative to ridgetops.

5/28/96 Summary of second field trip observations. SAS

As an adjunct to a Technical Exchange on the NRC audit of the DOE TSPA-95 performance assessment document, which was held in Las Vegas, a group of 8 NRC/CNWRA/consultant personnel took a tour of the ESF at YM(myself, C. Glenn, B. Behlke, M. Bell, A. Campbell, R. Manteufel, J. Walton, G. Stirewalt). The tour took place May 24, 1996. The tour was led by Alan ? of the DOE mapping team and hydrologic input was provided by Alan Flint of the USGS.

One of the more important observations that Alan Flint made regards lateral diversion in and near the PTn bedded tuffs. Previous TSPA analyses have assumed that lateral diversion may be strongly impacted by a very low permeability unfractured layer just below the PTn. However, the ESF borehole exposes a section of PTn that appears to be rather frequently, on the order of every 10 to 20 m by my observation, punctuated by small-offset faults. The offsets tend to be

less than a meter, and may easily have been missed in boreholes. The following day, I took a walk up from Solitario Canyon to Yucca Crest and noticed some small (10 to 20 cm) offsets at one PTn exposure. Alan Flint's observation is that lateral diversion is probably not going to be very significant, because the frequent offsets in the low-permeability unit should minimize the most significant source of lateral flow.

Along the way in the ESF tour, various chlorine-36 sampling locations were pointed out by A. Flint and A. Campbell from the Fabryka-Martin et al. (1996a) draft report. We also saw the heavily fractured zone, 1 km in length and still being encountered by the TBM. The fractures seemed to alternate between zones of fracture spacings less than 10 cm to zones where the spacing is more on the order of 30 to 40 cm.

As it rained (fairly heavily in spots) on May 24, I was inspired to take another walking tour of YM on May 25. Based on wetting front observations, which penetrated roughly 3.5 to 6.5 cm in various representative areas, and on water in exposed lithophysae, I estimate 1 to 2 cm of rain took place. I noticed that on Yucca Crest, enhanced wetting took place in the gaps between outcrops (10 cm and larger in spots), while under rubble scree on sideslopes less wetting took place (dry soil was not uncommon). While walking about, a storm cell drifted overhead and roughly a half hour of rain occurred. A total of no more than 5 minutes of reasonably heavy rain occurred, with most of the interval light to nearly non-existent. Exposed rubble faces were definitely wet; however, vertical sides tended to be dry with wetting fronts occurring at the top of perhaps 1 to 3 cm. Fifteen minutes after rain ceased, little or no trace of the event could be detected.

I also examined four of the trenches that are exposed in what I think is Split Wash or the next wash north (the wash with the Ghost Dance pavement and the wash immediately north of this wash). Each of these are sufficiently downstream that the wash bottom is at least 10 m wide. In this region, what I believe Alan Flint refers to as channel terraces are exposed. It appears that currently active wash channels are cutting into the terraces. Depth to bedrock at the deepest point in the trenches ranged from 2.5 to 4 m, as best as I could estimate. However, once the slope of the ground increased from the relatively flat terrace to side slope, cover decreased to the more typical 10 to 50 cm. It should be possible to identify these deeper zones simply by the slope or break in slope.

I also had the opportunity to talk with Alan Flint about his site-scale modelling work. He demonstrated time-traces of moisture content in various neutron-probe boreholes. In one channel terrace probe, lateral subsurface flow was clearly evident. He is currently using a 3-event (upgrading to 5-event) Markov-chain model to generate daily precipitation and daily mean temperature read-

ings. Each rainfall event is redistributed to essentially perch on the colluvium/bedrock interface at the end of the day, where it infiltrates according to matrix and fracture properties. Each Scott and Bonk (1984) layer has matrix properties assigned, either from direct measurement or from analog. Fractures are grouped into 3 size classes, and further subdivided into filled/unfilled areal fractions. Pixel size is 90 m on a side; no lateral diversion is considered. Evapotranspiration is a part of the model.

Pondering the site visit, it seems that the DEM is somewhat unwieldy for colluvium-flow calculations, as it completely misses meter-scale features such as wash channels. Ideas of quasi-1D flow-tube analyses occurred to me as being particularly appropriate for YM. Each flow tube would carry along local information on topography, width, depth, shape, vegetation, etc., in the form of integer categories or classes. Accordingly, the information could be encoded very compactly in the form of bit substrings within a few integers. Vegetation is another tricky topic inspired by discussions with Alan Flint, which it would be very nice to have a better handle on.

8/27/96 Pondering questions relevant to performance. SAS

In brief, work to date has focused on

- 1D simulations
- bare soil (no vegetation)
- no matrix-fracture interaction
- instantaneous lateral redistribution
- long-term average impacts due to
  - hydraulic properties
  - meteorologic input
- spatial distribution of surface cover
- spatial distribution of AAI
- to a minor extent, response to climatic change

Most of the work is documented in a journal article currently in preparation. The text and figures for the article will be included in this notebook upon submission to the journal and internally documented.

After the completion of work to date, it is my opinion that numerical modelling can give reasonable estimates of spatial distributions for relative AAI, the relative response of AAI to climatic change, but not absolute magnitudes for AAI. Since almost all precipitation ends up returning to the atmosphere, small errors in evaporation estimates may yield large errors in AAI estimates. Thus, the large area of interest with associated high heterogeneity levels and complex physical behavior preclude more than bounding estimates for AAI.

A number of future investigation directions can be considered.

- The validity and conservativism of the 1D approach could be examined using 3D simulations with discrete fractures on the grid-block scale for the DEM (roughly 30 m x 30 m). A 2D or 3D code would need to be assembled, presumably with the additional processes of vegetation and snow considered. Studies on the grid-block scale would be aimed at ascertaining the impact of heterogeneity and fracture spacings.
- Hillslope- and watershed-scale studies can be examined to see if lateral redistribution would significantly alter the predicted spatial distributions for AAI. Again a 2D or 3D code would need to be assembled, similar or identical to the code for the grid-block-scale simulations.
- Detailed process-level simulations, on the scale of a single fracture, could be undertaken to see how the matrix might affect infiltration magnitudes and timings. Code development is required.
- Additional 1D simulations could be undertaken to see how vegetation and snow might affect infiltration magnitudes and timings. Code development is required.
- The simulations performed to date can be squeezed to obtain the most information possible. Perhaps the most important additional information regards the timing and magnitude of infiltration pulses. The weekly trace of fluxes for each simulation can be examined relative to the rainfall input to determine the pulse description as a function of precipitation description. Perhaps comparison to the bucket approach would be in order. Analysis and *Matlab* code development required.
- Given infiltration-pulse information, the spatial distribution and timings of fluxes through the PTn can be estimated. The important question is what time-scale pulses through the PTn

have and how uniform the distribution of fluxes at the bottom of the PTn would end up being, so that the representativeness of quasi-steady-state approaches can perhaps be assessed. A logical first step might be 1D simulations using the output from one or more of the 10-yr shallow simulations. Again, some sort of 3D simulator may be in order. Predictions of travel times through the PTn could be made prior to tests in the ESF.

A key point in nearly all of these future directions is the common thread of required code development. Even in 1D, additional refinements to *breath* are necessary, while 3D codes are not available at CNWRA that have the proper capabilities.

8/28/96 Data bibliography. SAS

As discussed above, my studies examining the spatial distribution of AAI may be extended to below the PTn layer. If this is the case, it is extremely useful to collect all data pertaining to ambient unsaturated-zone hydrology at YM. I started collecting this type of information last month, as I needed to verify some of the information regarding alluvium depths measured in boreholes and trenches collected by Hannah Castellaw almost a year previously in order to double-check predictions of depths from DEM slopes. It took some time to find her sources, and in the interim I located additional information nestled in the CNWRA library. The current entry summarizes some of the information available.

Flint and Flint (1995) provide a summary of 99 neutron-probe boreholes, including locations, elevations, classifications, dates, alluvium depths, and lithology, as well as some analysis of the data. The entire moisture-content data set for all boreholes has been ordered from the DOE and should be arriving within the week, on tape. Attempts to email the data set were stymied due to the CNWRA inability to receive email greater than 1 Mb in size (the data set consists of two files of 12+ and 14.5+ Mb, respectively). The DOE system manager was not available to set up an anonymous ftp site.

The Flint and Flint (1995) neutron-probe locations are provided in Nevada State Plane (NSP) coordinates, not the CNWRA standard of Universal Transverse Mercator (UTM). Information on the locations and elevations of most of the YM boreholes are also specified in a data file obtained from the DOE in January, 1994, with specifications for 243 boreholes. Alluvium depths are not specified, although various other sources of information are available including Fernandez et al. (1994), Schenker et al. (1995), and numerous drilling log reports and summaries. Some of the most recent boreholes are not in the DOE tape and locations are available from other sources

and are only specified in NSP coordinates. I have collected the available information in directory ***$HOME2/Matlab/3Ddata***, with **neutron_hole.dat** containing the most complete information.

Flint and Flint (1990) provide data from 73 samples in 9 boreholes, all in nonwelded and bedded tuffs (i.e., PTn, Calico Hills). Each sample is precisely located within the respective borehole. The emphasis is on studying data-determination methods in relatively permeable and porous YM cores, presumably because these are faster to analyse. Porosity, grain density, bulk density, intrinsic permeability (measured 4 ways), relative permeability versus saturation (measured 2 ways), and potential versus water content (measured 3 ways) are tabulated. Some analysis comparing the measurement techniques for the intrinsic permeability values is performed. No attempt to estimate van Genuchten parameters is made, and it seems to me that the data is not of sufficiently high quality to make the attempt.

Rautman et al. (1995) provide data obtained from a sampling grid along 1.4 km of the PTn outcrop in Solitario Canyon, with a total of about 330 core samples obtained from 26 vertical transects. Bulk properties (porosity, bulk density, and particle density) are presented for all samples; sorptivity and saturated hydraulic conductivity are presented for almost all samples (except where handling damaged the sample). Locations of vertical (upslope) transects are specified as a northward offset to a transect reported by Flint et al. (1996b), with core samples located relative to the base of the sampled sequence. Distinct vertical trends in the properties are shown in plots, and high r^2 values ($r^2 > 0.824$) were obtained between the 4 bulk properties.

Flint et al. (1996b) provide data obtained from 5 vertical and 3 horizontal sampling transects, with a total of 656 core samples. Bulk properties (porosity, bulk density, and particle density) are presented for all samples; either measured or estimated saturated hydraulic conductivity is presented for most samples; and sorptivity is presented for some samples for two horizontal transects. In addition, moisture retention information is obtained for 41 of the samples, with estimated van Genuchten and Brooks-Corey parameters. Relative-permeability information was not determined. Regression equations are presented for properties as a function of porosity. Arguments were made that porosity values can be used to estimate van Genuchten parameters; perhaps additional information can be gleaned from the sorptivity information. The report appears to be the best current source for property data suitable for modelling.

The five vertical transects presented by Flint et al. (1996b) are further analyzed by McKenna and Rautman (1995) to examine correlation information. The correlation structure appears to be nonstationary horizontally. Appropriate downhole sampling strategies are suggested.

Schenker et al. (1995) collect and reference a large number of data sets and impose PDF

descriptions on them. Most of the data are from cores extracted from boreholes; transect sampling information from Rautman et al. (1995) and Flint et al. (1996b) does not appear. Porosity and bulk density have 1234 and 2173 measurements, respectively. There are 257 saturated hydraulic conductivity values from 8 boreholes. The matrix van Genuchten parameters are reportedly determined from the original pressure/saturation data sets by the authors, yielding 211 property estimates; however, the set of estimates is not directly available. Fracture properties are estimated using fracture spacing and orientation data from four boreholes (G-1, G-4, a #1, and GU-3), saturated bulk conductivity data from the saturated zone in 7 boreholes (G-4, H-1, H-3, H-4, b #1, p #1, and J-13) and bulk gas permeabilities from barometric fluctuations observed in 2 boreholes (UZ-1 and a #4). Lots of extrapolation is required due to the sparseness of the fracture data.

10/5/96 ACNW, change in PI. SAS

I attended the ACNW meeting in Las Vegas on September 26 and 27, 1996. My impressions are discussed in the trip report. However, there are a few important issues in particular that should be examined.

- Five independent estimates of infiltration (surface modeling by A. Flint, isotopic tracers, fracture coatings, thermal profiles, and core-sample moisture contents and pressures) all point to fluxes on the order of 1 to 10 mm/yr.
- Fault zones are considered highly permeable (1000 Darcy) horizontally, but less so vertically.
- In general, gas bulk permeabilities are on the order of 2 to 10 Darcy.
- Inverse modeling pulls the TSw matrix permeabilities up 1 or 2 orders of magnitude above core information.
- First-cut drift-scale 2D heterogenous-matrix simulations are underway with dripping requiring a transient pulse of 280 mm/yr.
- G. Bodvarsson claims that the ECM and the dual-permeability models must be identical at steady state. *Note: I think this is not correct and may explain the shift in TSw permeabilities he is obtaining.*

Last week, I became PI for the Unsaturated and Saturated Flow under Isothermal Conditions (USFIC) KTI, as I have the most hours allocated and Gordon has relatively few hours. Upcoming duties include a presentation on the USFIC KTI work at the Annual Program Review on November

13, 1996, and on December 5, 1996. The first (45 min + 15 min) presentation is to focus on technical and programmatic aspects, with subtopics including

- Status of subissue(s) resolution
- Integration with other KTIs
- Analysis of infiltration/percolation
- Results of sensitivity analyses
- Work priorities for 1997-98

The second (60 min) presentation is to focus on technical, programmatic, and managerial aspects, with subtopics including

- Infiltration/percolation rates
- Preferred conceptual model for fracture-matrix flow
- Future climate scenario and formation of perched water
- Relationship to total system performance
- Strategy for review of viability analysis

Issues involving infiltration and percolation should be straightforward to discuss. The two technical issues that will be difficult to discuss will be the preferred conceptual model for fracture-matrix flow and the future climate scenario related to the formation of perched water. I take these topics as spurs to perform some quick calculations and have discussions with Ross and others. In particular, testing Bodvarsson's opinion on the steady-state equivalence of the ECM and dual-permeability approaches is in order, as is coming up with a contour plot of areal AAI as a function of precipitation and temperature.

10/16/96 Start of alluvium/bedrock simulations. SAS

The approach that Alan Flint is taking to estimating shallow infiltration, as he has described it to me, essentially fills the alluvium pore space with as much water as will fit and runs off the excess (i.e., infinite alluvium conductivity), then using evapotranspiration to mine water back to the

atmosphere. A perched-water system is assumed to exist above the bedrock due to the infiltration events. Water moves into the bedrock assuming gravity drainage within the bedrock. Three classes of fracture sizes, fractions of filled and unfilled fractures, and matrix permeability are combined to yield an equivalent conductivity for the 7 classes. In contrast, I have completely neglected the matrix, filled fractures, and transpiration, and have used highly resolved simulations to capture the dynamics of flow in detail.

I have observed that in simulations with bedrock exposed (i.e., alluvium with permeability less than 10^{-8} cm^2), essentially no infiltration occurs. I have not considered the case of alluvium overlying bedrock, however. I hypothesize that little or no infiltration will occur until several meters of alluvium cover the bedrock. When the alluvium/matrix interface is below the active zone, flow should be essentially steady through the bedrock at the bedrock K_{sat} or the semi-infinite infiltration rate for the alluvium, whichever is smaller. When the active zone interacts with the matrix/bedrock interface, I suspect that the low-permeability bedrock will prevent significant infiltration. As verification of this hypothesis, I am setting up several simulations to probe the behavior of alluvium overlying unfractured bedrock.

The Tiva Canyon tuff microstratigraphy is of primary interest. According to Flint et al. (1996b), the shardy base has a mean K_{sat} of 1.6×10^{-6} m/s ($k = 1.6\times10^{-9}$ cm^2= 5.0×10^4 mm/yr), while the remaining Tiva Canyon layers have K_{sat} ranging from 3.1×10^{-9} to 3.0×10^{-12} m/s (k ranges from 3.1×10^{-12} to 3.0×10^{-15} cm^2, or 98 to 0.95 mm/yr). None of these should exhibit bare-soil infiltration if the low-permeability matrix-only results can be extrapolated.

To test the hypothesis, the base-case colluvium over three material cases will be examined: (i) shardy base, (ii) caprock, and (iii) upper lithophysal. These cases are representative of the range of k and are of interest in their own right. Samples BT26Hs, PW19s, and TPC52s will be used to determine van Genuchten properties, using the 2-parameter estimates. A summary of properties is shown in Table 1-4, with the colluvium and base-case fracture properties shown for reference. Initially, a 10-cm and a 25-cm depth-of-cover case will be run for each, as representative cases. Further examination may suggest additional cases.

10/19/96 First results for alluvium/bedrock simulations. SAS

Four of the six runs have completed 3 cycles of boundary conditions: both shardy-base cases, the 10-cm caprock case, and the 25-cm upper-lithophysal case. Each of the cases erroneously used colluvium permeabilities 1000 times larger than desired, due to incompletely correcting the

Table 1-4: Summary of colluvium and matrix properties used in simulations.

Material	K_{sat} m/s	ε	θ_r	van Genuchten α MPa^{-1}	van Genuchten m	van Genuchten P_0 ($\times 10^6$) gm cm^{-1}s^{-2}
Colluvium	9.8×10^{-6}	0.300	0.000	50.0[1]	0.200	0.2[2]
Caprock	3.1×10^{-9}	0.105	0.002	5.00	0.301	2.0
Upper lithophysal	8.9×10^{-12}	0.108	0.001	2.90	0.310	3.4
Shardy base	1.6×10^{-6}	0.235	0.035	3.01	0.237	3.3
Fracture	0.011	0.001	0.000	10^5	0.700	9.8×10^{-5}

[1] Correct value is 500 (2/26/97) SAS

[2] Correct value is 0.02 (2/26/97) SAS

viscosity value in the new input-file generation routine **ingen_am.m** in ***$BREATH2/Subreg/-MakekmpoKmao***. The input and output cases are renamed correctly to reflect this error, and **ingen_am.m** was corrected. The matrix properties are correct.

None of the cases are particularly near cyclic steady state, but some conclusions can already be drawn from the first results. The shardy base is permeable enough that significant infiltration can occur, perhaps 10 mm/yr or more. Interestingly, there are indications that deeper cover provides more infiltration for the shardy base, opposite to the alluvium/fracture case. The caprock case shows some indications of infiltration as well, perhaps on the order of 1 mm/yr. The upper lithophysal case is drying out from the initial condition of 0.25 mm/yr.

Based on this rather limited set of runs, a few conclusions are presenting themselves to me:

- The capillary barrier effect is turned around for the case of matrix underlying alluvium, so that water is preferentially drawn into the matrix.
- The conclusions regarding alluvium cases that allow and disallow infiltration may not be far off for a shallow cover over bedrock.
- There may be some additional infiltration due to cover protection.
- Materials as permeable as the caprock are probably dominated by fracture flow for shallow covers and matrix flow for deeper covers.
- As the permeability increases from the caprock, matrix flow dominates.

- As the permeability decreases from the caprock, fracture flow dominates.

The only microstratigraphic layers more permeable than the caprock, according to Flint et al. (1996b), are located in the sequence including the Tiva Canyon shardy base through the nonwelded units of the Yucca Mountain and Pah Canyon Tuffs to above the Topopah Spring upper lithophysal zone. These microstratigraphic layers are essentially the PTn layer addressed in my previous analyses, perhaps a little larger, which only is about 5 percent of the total subregional outcrop area. Accordingly, I expect that the alluvium/fracture results considered before would not be significantly modified for most of the subregional area.

A much more definitive modeling approach can be conceived with some modification to *breath*. The idea is to have multiple interacting continua throughout the bedrock, all with a common pressure in the alluvium. The multiple-continuum approach will allow partitioning between the fractures and matrix to be examined, particularly since separate continua can be defined for various fracture-aperature size classes. The approach is also essential for considering deep-percolation processes.

12/7/96 Updated results for alluvium/bedrock simulations.

SAS

A new file was created in ***$BREATH1/RunTightAM*** entitled **am_all.result** to document the results of alluvium/matrix simulations. The file follows a generic standard with many entries not used. The columns of the result file are, in order:

- Depth of soil (cm),
- Alluvium code (see Table 1-3),
- Bedrock code (Table 1-4 for properties),
- Perturbation code

  b0 Base case (precipitation and temperature may vary),

  e0 Longwave radiation is scaled,

  s0 Shortwave radiation is scaled,

  v0 Vapor density is scaled,

  w0 Windspeed is scaled,

  ge Solar aspect is rotated east (perturbation in degrees),

gw Solar aspect is rotated west (perturbation in degrees),

gn Solar aspect is rotated north (perturbation in degrees),

gs Solar aspect is rotated south (perturbation in degrees),

- Perturbation,
- Precipitation multiplier,
- Temperature shift,
- Average soil moisture content at the interface, and
- Average net infiltration (cm/yr).

Most of the values in the file should be viewed as order of magnitude results rather than fully converged, as more cycles are required for full convergence in almost all cases. The runs are primarily useful for screening where fracture flow would dominate. From the runs, it appears that significant matrix infiltration can occur for the Tiva Canyon caprock and shardy units, while fracture flow should dominate in Tiva Canyon upper lithophysal and Topopah Springs lower nonlithophysal units.

The shardy unit is considered part of the PTn, has large infiltration, and is the most permeable unit of any of the microstratigraphic layers considered. The 10-cm case has AAI approximately 24 percent of AAP, while the 25-cm case has AAI approximately 16 percent of AAP. The remainder of the PTn should have smaller AAI. Assuming that the PTn as a whole yields AAI roughly equivalent to 10 to 20 percent of AAP is probably justified based on these simulations. Note that in the FY96 Annual Progress Report (Bagtzoglou et al., 1997), my assumption was that 10 percent of AAP enters the PTn, and I found that the overall sensitivity to the PTn unit is quite low.

The Tiva Canyon caprock matrix shows behavior unlike any other unit considered, as AAI *increases* with soil depth for the two soil depths considered. Experience from early semi-infinite experiments suggests that essentially no infiltration should occur for exposed materials with this permeability. A cover of soil appears to provide a permeable zone to allow water to penetrate the subsurface while protecting caprock from evaporative processes, and the difference in bubbling pressure between soil and caprock preferentially sucks water into the bedrock. The caprock is laterally extensive over the repository, primarily in regions where my colluvium/fracture models predict high AAI, so revisiting this material with *breath* modified to consider both bedrock and fractures simultaneously would be appropriate. Note that one would expect that the caprock should never have much more than 50 cm of cover.

Today I tried to finalize the table of atmospheric influences on infiltration for a colluvium/fracture system. The table is in ***$BREATH1/RunCliFrac*** and is called **af_egsvw.result**, abstracting the results of simulations run over the period from July through November. The simulations do not consider changes in precipitation or temperature. The columns of the result file are, in order:

- Depth of soil (cm),
- Alluvium code (see Table 1-3),
- Fracture code (see Table 1-3),
- Perturbation code

  b0 Base case (precipitation and temperature do not vary),

  e0 Longwave radiation is scaled,

  s0 Shortwave radiation is scaled,

  v0 Vapor density is scaled,

  w0 Windspeed is scaled,

  ge Solar aspect is rotated east (perturbation in degrees),

  gw Solar aspect is rotated west (perturbation in degrees),

  gn Solar aspect is rotated north (perturbation in degrees),

  gs Solar aspect is rotated south (perturbation in degrees),
- Perturbation,
- Average soil moisture content at the interface, and
- Average net infiltration (cm/yr).

The values in the file have reliably reached cyclic steady state.

An important observation was made during the finalization process. The final simulations in the colluvium/fracture set of simulations overlapped the first soil/bedrock simulations. I had previously noticed that there are cases where the combination of soil and underlying material require such small time steps during a large infiltration event that a simulated hour may not complete within the 10000-time-step limit. For the last simulation, I imposed a 50000-time-step limit for each hour; during large infiltration events even this limit might be reached before the

hour was up, but more than half of the events exceeding 10000 time steps completed before 50000 time steps were finished. For the case with the larger limit on the number of time steps, larger net infiltration was obtained than would have been expected (5.5 mm/yr rather than roughly 1 mm/yr). The implication is that my estimates of AAI are too low in some (but not all) cases. I suspect that the error is generally additive, on the order of several mm/yr, rather than being a multiplicative error. Unfortunately, it is not possible to untangle which simulations yield underpredictions without rerunning the simulations. I believe that sensitivity predictions may be relatively unaffected, but there is some question regarding the appropriate decay in infiltration with soil depth.

12/8/96 Estimating regression relationships for AAI. SAS

As part of estimating regression relationships between hydraulic properties, climatic variables, and AAI, I fit the data to predicted values using a least-squares fit. Say, for example, that the relationship is

$$\log_{10}\left(\frac{AAI}{AAP}k^{1/2}\right) = \alpha_0 + \alpha_1\left[\left(\frac{m}{m_0}\right)^2 - 1\right] + \alpha_2\left[\left(\frac{P_0}{P}\right)^{1/2} - 1\right] + \alpha_3\left[\left(\frac{\varepsilon}{\varepsilon_0}\right) - 1\right], \tag{1-1}$$

where k is intrinsic permeability, m is van Genuchten $m = 1 - 1/n$, P is bubbling pressure (the reciprocal of van Genuchten α in the units used here), ε is porosity, a subscript 0 represents a reference value for the parameter, and the α values are hydraulic-parameter sensitivity constants.

For any particular simulation, the only unknowns in the relationship are the α values. Thus, for a simulation, one can write the equation as

$$C_0 = \alpha_0 + \alpha_1 C_1 + \alpha_2 C_2 + \alpha_3 C_3, \tag{1-2}$$

where the C values result from evaluating the hydraulic-property functions. Combining all simulations results in the matrix relationships

$$\left[\mathbf{C}_1\ \mathbf{C}_2\ \mathbf{C}_3\right]\{\alpha\} = \{\mathbf{C}_0\}, \tag{1-3}$$

where bold-face represents a vector. When provided with linear equations having a matrix that is not square, *Matlab* solves the equations using least squares (exactly the appropriate behavior). Any reported regressions are coded using *Matlab* to take advantage of this feature.

1/7/97 Documenting plots for ANS-1997 submission. SAS

Budhi was invited to give an invited talk at the American Nuclear Society (ANS) convention in June, 1997. A summary of the talk is required for the conference, consisting of 450 to 900 words. The summary presents the methodology for creating infiltration maps and sensitivity maps, in an extremely schematic fashion. Included in the summary are two plots, one of my latest base infiltration map and a newly created sensitivity plot for sensitivity of infiltration to soil depth.

The plots were generated with a master *Matlab* driver called **do_sens_eval.m**, which in turn calls a number of other routines. The current versions of required files and concommitant input were stored in a subdirectory of ***$HOME2/Matlab/YMInfil*** entitled ***ANS96***. The directory was stored in a tar file entitled **ANS96_plotgen_tar**, which was in turn compressed using the gzip command (appending ".gz" to the file name).

Sensitivity S_k of areal-average AAI to generic parameter α_k can be calculated using normalized sensitivity coefficients (Sykes et al., 1985)

$$S_k = \frac{\alpha_k}{AAI}\frac{\mathrm{d}AAI}{\mathrm{d}\alpha_k} \tag{1-4}$$

$$S_k = \alpha_k \frac{\mathrm{d}\ln AAI}{\mathrm{d}\alpha_k} \tag{1-5}$$

The sensitivity coefficients are calculated by using first-order derivatives between a high and low perturbation, normalized by a reference value. In general, sensitivity coefficients will change as the set of base input values change. For the example problem, the base-case soil depth was uniformly multiplied by 0.9 and 1.1 to provide perturbations. Values of S_k less than or equal to 0 were arbitrarily set to 10^{-32} for plotting purposes (the most-negative value was on the order of -10^{-16}). Note that sensitivities are largest on sideslopes and are zero wherever depth does not change infiltration (e.g., deep soil, PTn outcrops under current modeling shortcuts).

1/8/97 Documenting 1996 annual report work. SAS

An archive file was created in both ***$HOME2/Matlab/YMInfil*** and in ***$HOME2/Matlab/-ColluvWaste*** documenting the input files and limited output files used to generate figure 10-4 and tables 10-1 and 10-2 in chapter 10 of the NRC High-Level Radioactive Waste Program Annual Progress Report, Fiscal Year 1996. Both archive files are called **AnnRep96_tar**; both are compressed. The file in ***$HOME2/Matlab/YMInfil*** includes all of the files from ***$HOME2/Matlab/ColluvWaste***, for completeness, and is submitted to QA as formal documentation of the

results. A couple of files were added or fixed up for readability and reproducibility of results. Description of the process is in a ReadMe file in the archive.

1/13/97 Documenting alluvium regression.

Alluvium depths are not well captured by the equilibrium mass-wasting scheme in areas of deep alluvium, partly due to the irregular topography of the washes. In order to have a reasonable representation for deep alluvium, in August, 1995, Ross Bagtzoglou developed a regression for alluvium depth b as a function of slope s:

$$b = 47 \exp(-0.32s). \tag{1-6}$$

The regression was based on borehole information for b and the nearest-neighbor values from the DEM for s. No borehole classification was performed, and ad-hoc data censoring was used for the regression. Due to time constraints, the work was performed very quickly.

I revisited the regression expression last summer, and decided that it is probably better to use an expression of the form

$$\ln(b) = a + b \ln(s). \tag{1-7}$$

I pulled together as much available information on alluvium depths as I could find and sorted it into a file called **neutron_hole.dat** in ***$HOME2/Matlab/3Ddata***. Neutron-borehole data is reported by Flint and Flint (1995); other data sources are noted in **neutron_hole.dat**. I pulled neutron-borehole data from channels and terraces into separate files (**chan.dat**, and **st.dat**, respectively); other boreholes with reported alluvium depths were pulled into file **well.dat**. A total of 110 boreholes are included in these three classes; an additional 64 boreholes are not considered.

Boreholes with shallow covers (i.e., ridgetops, sideslopes) are not considered further, as I feel that alluvium depths for these boreholes are not reported with sufficient accuracy and are in a range of depth that should be handled by the mass-wasting approach anyway.

For the regression, each of the boreholes was assigned the slope of the nearest-neighbor pixel in the DEM. An additional censoring process eliminated all boreholes with unreported soil depths or having soil depths less than 1 m, leaving a total of 37 boreholes, conveniently grouped as 9 channel boreholes and 28 deep-alluvium boreholes. The data points and regression lines are shown in Figure 1-1, manually generated by regressing all data using **regress_set.m** and further processing with the **show_regress.m** routine. I feel that it is questionable whether the overall

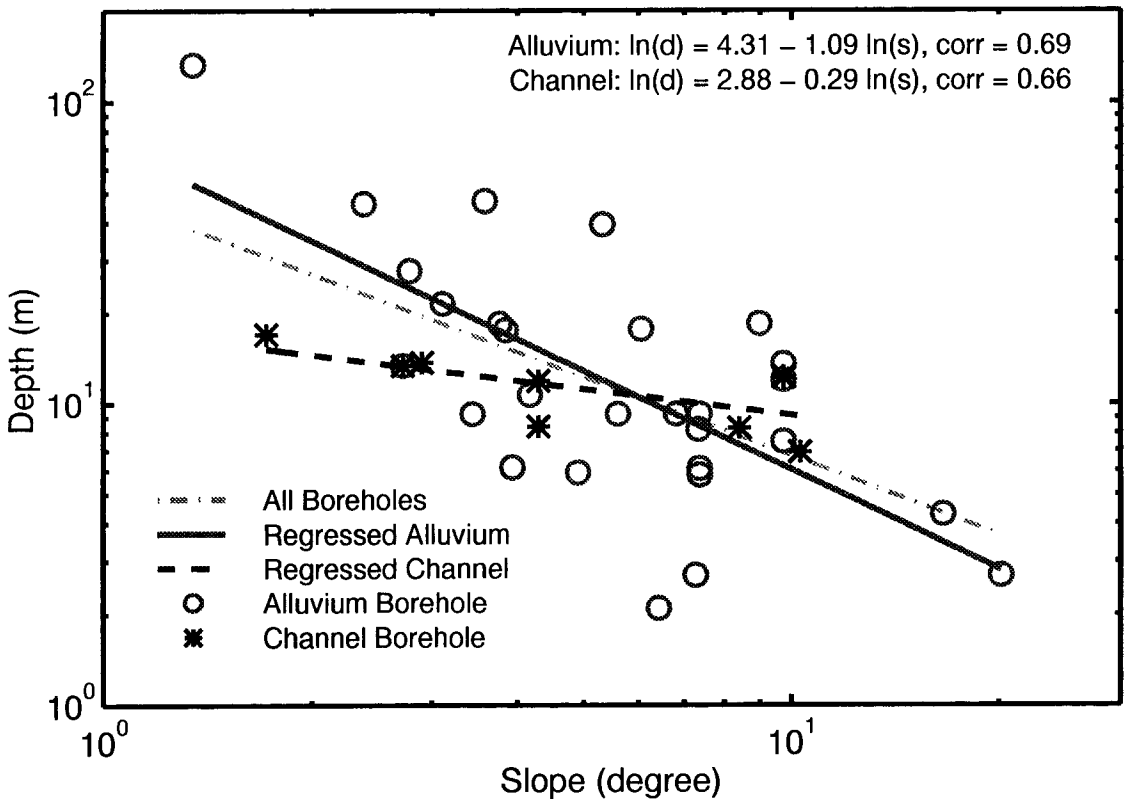

Figure 1-1: 1/13/97. Regression of borehole alluvium depths with nearest-neighbor DEM slopes.

regression should use the channel data, as the pixels are larger than the channel width. Even if the channel data is included, the regression line is not tremendously changed. As a note, the correlation coefficient with the original formulation is 0.59 and 0.58 for the channel and terrace, respectively; using the new formulation the correlation coefficient is 0.66 and 0.69, respectively.

1/15/97 Documenting infiltration abstractions. SAS

In ***$HOME2/Matlab/YMInfil/SubregSpaceDist***, abstractions for *AAI* as a function of material and meteorologic properties are examined using **find_best_regress.m**. Abstractions for *AAI* as a function of material properties were originally developed in the summer of 1996. The abstractions were developed "by eye" and are more formally documented here.

The deep-alluvium abstraction originally developed is in the form

$$\log_{10}\left(\frac{AAI}{AAP}k^{1/2}\right) = \alpha_0 + \alpha_1\left[\left(\frac{m}{m_0}\right)^2 - 1\right] + \alpha_2\left[\left(\frac{P_0}{P}\right)^{1/2} - 1\right] + \alpha_3\left[\left(\frac{\varepsilon}{\varepsilon_0}\right) - 1\right], \tag{1-8}$$

where

- k is intrinsic permeability,
- m is van Genuchten $m = 1 - 1/n$,
- P is bubbling pressure (the reciprocal of van Genuchten α in the units used here), and
- ε is porosity.

A subscript 0 represents a reference value for the parameter ($m_0 = 0.2$, $P_0 = 2000$ Pa, and $\varepsilon_0 = 0.3$), and the α values are hydraulic-parameter sensitivity constants. Equation 1-8 was originally reported by Bagtzoglou et al. (1997).

Using **find_best_regress.m** and **f_deep_hyd_fit.m**, a best-fit exponent was determined using the 28 material-property-variation simulations in **alluv.result** that have non-negative infiltration. Also, the impact of assuming a $\log_{10}$ relationship instead of a scaling relationship can be determined. These are performed by flipping switches at the top of **find_best_regress.m**.

Using the more formal abstraction process, a better regression is

$$\log_{10}\left[\frac{AAI}{AAP}\left(\frac{k}{k_0}\right)^{1/2}\right] = \alpha_0 + \alpha_1\left[\left(\frac{m}{m_0}\right)^{\beta_1} - 1\right] + \alpha_2\left[\left(\frac{P}{P_0}\right)^{\beta_2} - 1\right] + \alpha_3\left[\left(\frac{\varepsilon}{\varepsilon_0}\right)^{\beta_3} - 1\right], \tag{1-9}$$

where k_0 is 10^{-8} cm^2 and the β values are fitting exponents. A plot of the least-squares fit for the exponents is shown in Figure 1-2, where the fit for each curve only uses simulations with the parameter varying. Note that there is more noise in the value for P than in the other parameters.

The best-fit coefficients are shown in Table 1-5. The least-squares fit is also shown for the counterpart of the formal abstraction equation using logarithms,

$$\log_{10}\left[\frac{AAI}{AAP}\left(\frac{k}{k_0}\right)^{1/2}\right] = \alpha_0 + \alpha_1\log_{10}\left(\frac{m}{m_0}\right) + \alpha_2\log_{10}\left(\frac{P}{P_0}\right) + \alpha_3\log_{10}\left(\frac{\varepsilon}{\varepsilon_0}\right). \tag{1-10}$$

The best scaling fit is better than the logarithm fit for each parameter. If the logarithm of k is examined, however, the associated α coefficient is -0.495 and associated logarithm fit is 0.258, strongly supporting pulling k into the left-hand side as is done in Equation 1-9.

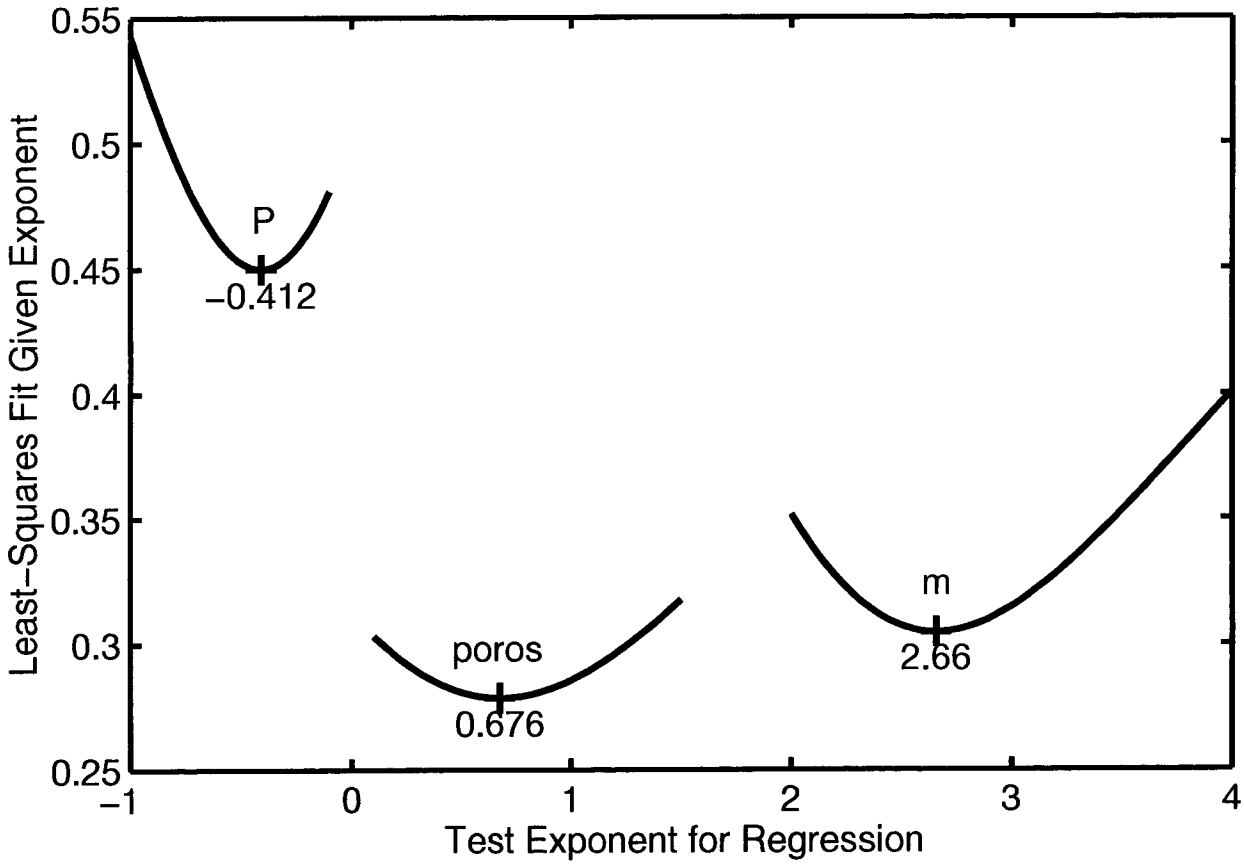

Figure 1-2: 1/15/97. Least-squares fit of simulation prediction to abstraction prediction for various exponents in Equation 1-9.

Table 1-5: Best-fit abstractions to material properties in deep alluvium.

Parameter	α	β	Fit	Log Fit
Scaling Constant	-1.38165	—	0.587745	1.09475
van Genuchten m	0.42505	2.6576	0.304383	0.821475
P	2.05672	-0.41248	0.449886	0.50599
ε	-1.39944	0.67568	0.278631	0.633175

Table 1-6: Regression values for deep-alluvium meteorologic abstraction.

Parameter	Exponent	Scale Fit	Curvature	Log Fit
AAL	-0.03723	0.308036	0.0284408	0.289575
AAP	-0.2889	0.419721	0.486325	0.440836
AAT	-15.96	0.648594	0.000370696	0.700391
AAV	2.075	0.323644	0.0174236	0.357603
AAW	0.2412	0.304608	0.0112994	0.28684

1/20/97 Documenting infiltration abstractions. SAS

In ***$HOME2/Matlab/YMInfil/SubregSpaceDist***, abstractions for *AAI* as a function of material and meteorologic properties are examined using **find_best_regress.m**. Abstractions for *AAI* as a function of material properties were originally developed in the summer of 1996. The abstractions were developed "by eye" and are more formally documented here.

A routine called **f_deep_met_fit.m** was developed to check out the appropriateness of abstractions in the form of a scaling or a logarithmic representation, identical to the approach followed for material properties. Some trial-and-error runs were followed to pick reasonable base values for exponents, varying one parameter at a time. The value of the sought exponent was observed to shift about, depending on the values of the remaining exponents. Accordingly, the *Matlab* routine **fmins** was used to perform a global minimization for all meteorologic-variable exponents simultaneously. A modified version of **f_deep_met_fit.m** entitled **f_deep_met_reg.m** was created to follow the format required by **fmins**.

Two sets of regression results are presented in Table 1-6, for simultaneously determined exponents and for logarithmic regression, labelled Scale Fit and Log Fit, respectively. Each reported fit only uses simulations where the variable of interest is perturbed (including the base value of the variable). The column entitled Curvature represents the second derivative of the scale fit with respect to the variable, and is a measure of sensitivity; the larger the value of curvature, the better the exponent is determined. The logarithmic fit does not admit this measure. The best fit is to *AAP*; the worst fit is to *AAT*. The exponent for *AAL*, *AAV*, and *AAW* is roughly within a value of ± 1; the exponent for *AAP* is better determined and the exponent for *AAT* is much more poorly determined.

Based on comparing the fits reported in Table 1-6, it can be concluded that a logarithmic representation should be used for *AAL* and *AAW* and a scaled representation should be used for

Table 1-7: Regression coefficients for deep-alluvium meteorologic abstraction. *Correction dated 1/23/97: Two curvature numbers were incorrectly transcribed. Correct numbers are italicized in the table.* SAS

Parameter	Exponent	Coefficient	Fit	Curvature
AAL	—	-1.52051	0.312029	—
AAP	-0.2416	-5.56806	0.420087	0.4858
AAT	-16.67	0.945489	0.649914	0.700391 *0.000366185*
AAV	2.138	0.281891	0.326738	0.357603 *0.0171413*
AAW	—	-0.321916	0.307231	—

the remaining variables. The best-fit coefficients for this representation are shown in Table 1-7. The parameters without a reported value for exponent are represented using a logarithmic representation.

1/22/97 Documentation of USGS data acquisition. SAS

I set up ***$HOME2/AmbientKTI/3Ddata*** as an archive for site-specific data acquired from or reported by DOE or subcontractors, such as core-sample data. Today A. Ramos typed in the moisture-retention data from Appendix II of Flint et al. (1996b). He double-checked his typing and I confirmed each number. I noticed that the original report is missing a number for sample TPC27s and for sample TPC15s. The original wordperfect file is called **usgs_ofr95-280_app2.wp** and an ASCII version is called **usgs_ofr95-280_app2.asc**. File **Sources** in the same directory documents this procedure.

Sources also documents previously obtained data residing in the same directory. The complete neutron-probe data discussed by Flint and Flint (1995) was obtained from the DOE office in September, 1996. Table 4 from Rautman et al. (1995) was obtained from C. Rautman on November 6, 1996, using email. Tables I-1 through I-8 from Flint et al. (1996b) were obtained directly from L. Flint on November 4, 1996, also by email.

1/24/97 Deep-alluvium meteorology regressions. SAS

I have noticed an increasing sensitivity of AAI to meteorologic properties as AAI decreases. Work to date has used the deep-alluvium regression equation the form

$$\log_{10}(H) = \alpha_0 + \sum_i \alpha_i U_i, \tag{1-11}$$

where $H = (AAI/AAP)U_k$, U_i represents a normalized value for parameter i, and the α values are constants. Two forms of U_i are considered, (i) the scaling fit (e.g., $U_{AAV} = [(AAV/AAV_0)^\beta - 1]$), and (ii) the logarithmic fit (e.g., $U_{AAL} = \log_{10}(AAL/AAL_0)$). Note that both forms are zero for the base case of the parameter. Results for the two forms are discussed in the entry for 1/20/97, in which it was determined that AAL and AAW are probably better fit using the logarithmic form and AAP, AAT, and AAV are probably better fit using the scaling form.

In order to account for this sensitivity, I postulate that the deep-alluvium regression equation for meteorologic properties is in the form

$$\log_{10}(H) = \alpha_0 + \sum_i \alpha_i U_i + [a_0 + a_1 \log_{10}(H)] \sum_j \alpha_j U_j \tag{1-12}$$

$$= \frac{\alpha_0 + \sum_i \alpha_i U_i + a_0 \sum_j \alpha_j U_j}{(1 - a_1) \sum_j \alpha_j U_j}, \tag{1-13}$$

where index i represents a parameter that is insensitive to H and index j represents a parameter that is sensitive to H. Note that a_0 is arbitrarily set to 1 if there are no parameters considered insensitive to H. Again using *Matlab* routine fmins, I created a file to evaluate the least-squares fit of the simulation data to the regression equation with **f_deep_met_eval.m**. Although thousands of iterations are required to reach convergence, the new formulation significantly improves the data fit. For example, overall least-square-fits from 1/20/97 for simultaneous fits of AAP, AAT, and AAV are about 1.5 times larger than the new formulation provides. The form in Equation 1-13 is more general than a similar equation that uses $[a_0 + a_1 U_(k)]$ as the scale, although the latter form should work as well.

Hint for the future: the solution procedure appears to really benefit from periodic restarts. Perhaps the solution steps get too small and the restart enlarges them.

2/14/97 Daily-averaged meteorology. SAS

Insofar as A. Flint typically uses daily meteorologic values when simulating infiltration, and I have been using hourly values in the vicinity of rainfall events and monthly values otherwise, and as daily

simulations run faster than hourly simulations, I'm starting a few test cases to check on whether it actually makes a significant difference. I had looked at this years ago and found that averaging makes a relatively small difference, most important near precipitation events, and precipitation is the most important variable to capture. The simulations used 2-cm grids rather than the 1-mm grids I currently am using, so perhaps the conclusion may be altered.

Met files are generated in ***$HOME2/AuxRain/Climate***. A meteorology file with daily inputs averaged from the Desert Rock data, **dr_0d0d_24as.met**, was generated using **make_ave_metseq('dr_0d0d_24as.met', 24)**. The met file was created by averaging all fair-day met values in a window of 30 days around each day, then overwriting the days with precipitation with the original, unaveraged, values for those days. It is possible to change the size of the window for averaging and the window for not averaging by changing hard-coded numbers in the call to **move_metave.m**.

The met file was copied to ***$SubRegBreath/RunTightAM*** and a sequence of simulations was started with 50 cm of alluvium over porous bedrock. These simulations took on the order of 3 days with hourly values.

2/27/97 Daily-averaged meteorology results and calcite. SAS

Directory ***$SubRegBreath/RunTightAM/ResultDir*** holds the results of ten simulations of daily meteorology compared to hourly meteorology. The simulations are designated by **_ds** following both **reg07** and **reg08**. These designators represent bedrock cases 1 and 2, respectively, derived from regressed relationships by Flint et al. (1996b). The comparable cases with hourly meteorology are missing the **_ds** designator.

The *Matlab* routine **make_DH_Plot** was created to plot the results as shown in Figure 1-3. The plots show convergence over repeated input cycles to a constant value of decadal-average flux with depth; complete convergence occurs when the decadal-average flux is constant over all depths. Perturbations from the base meteorology are labeled $2/3P$, $3/2P$, $T+5$, and $T-5$, for multipliers in precipitation (P) and shifts of temperature (T) uniformly applied to all values.

Two items are of particular interest in Figure 1-3. First, although the two bedrocks have permeabilities different by an order of magnitude, AAI remains essentially unchanged. More importantly, there is significant difference between the hourly and daily meteorologic inputs, with the hourly values yielding significantly higher infiltration. With the current procedure for handling evaporation, I conclude that the simulator cannot be trusted to yield reliable results with daily

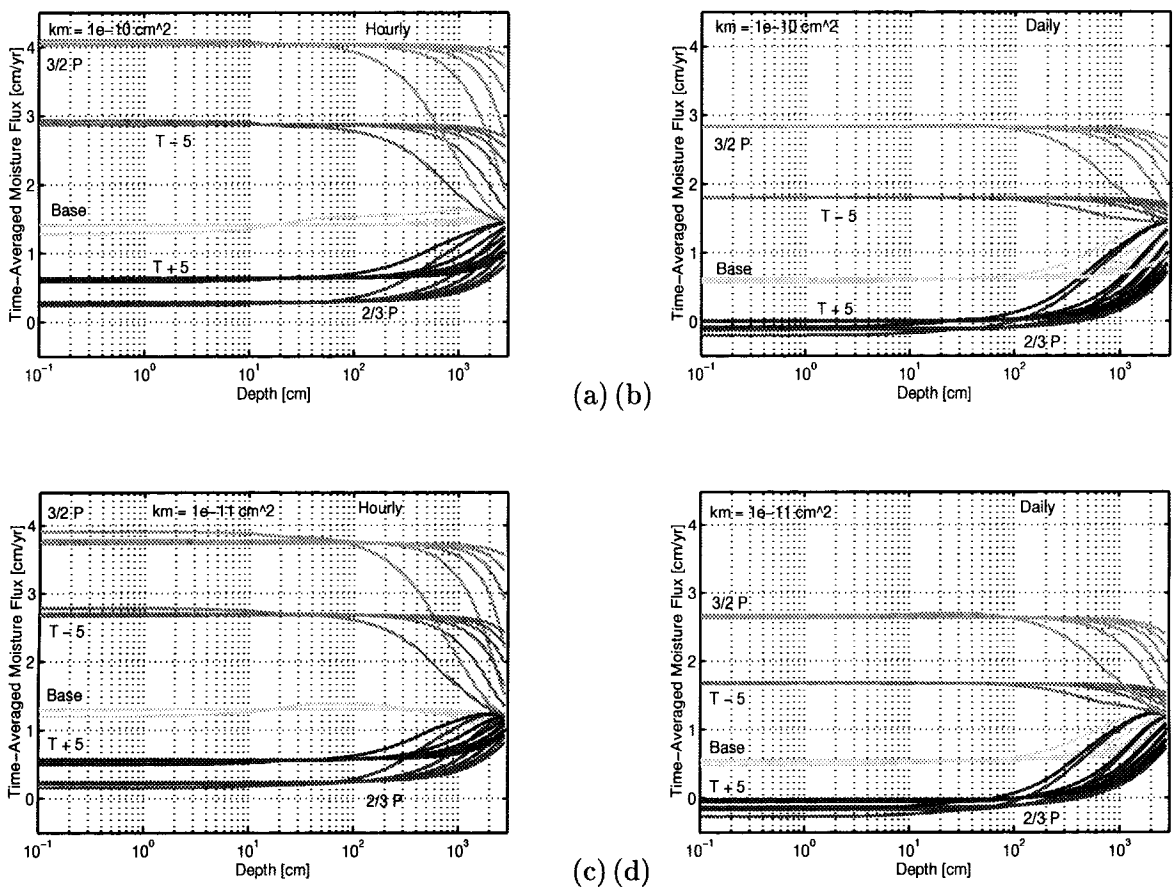

Figure 1-3: 2/27/97. Time history of decadal-average moisture flux after each of 6 decades, as a function of AAP and AAT, for (a) hourly meteorologic input and bedrock 1, (b) daily meteorologic input and bedrock 1, (c) hourly meteorologic input and bedrock 2, and (d) daily meteorologic input and bedrock 2.

inputs.

I have thus far examined the behavior of deep soil, soil overlying open fractures, and soil overlying bedrock. The one related case that remains to be investigated is the behavior of soil overlying fractures filled with calcite. It is reported by Flint et al. (1996a) that measured values for saturated hydraulic conductivity on fracture-fill materials averages 43.2 mm/day (5×10^{-7} m/s or approximately 5×10^{-10} cm^2). No van Genuchten properties are reported. The fracture-filling permeability is almost as large as the most permeable bedrock. After consulting with Gordon Wittmeyer, it is probably not unreasonable to have fracture fillings with $\varepsilon = 0.1$, van Genuchten

$\alpha = 100$ MPa^{-1}, and van Genuchten $n = 2$ (van Genuchten $m = 0.5$).

In ***$SubRegBreath/RunTightAM***, I am setting off a set of simulations assuming that the matrix is impermeable, fracture pore space is representative of the fracture classes in TCw as reported by Flint et al. (1996a), and the fracture-filling properties are as above. The three classes have reported fracture pore volume of 2.6×10^{-5}, 2.6×10^{-4}, and 2.6×10^{-3}, for 2.5 μm, 25 μm, and 250 μm fractures, respectively. Since porosity must also account for fracture pore space, filling porosity will be 2.6×10^{-4} (rounded to 10^{-4}). Precasting behavior suggests that infiltration will increase with increasing soil depth (to the order of 1 m), due to the capillary attraction that calcite has relative to soil, but infiltration should be relatively small due to the rather small net porosity. Files with **cal3**, **cal4**, and **cal5** for fracture properties represent fracture pore volumes of 10^{-3}, 10^{-4}, and 10^{-5}, respectively.

In conversations with L. Flint (USGS) today, she clarified the weighting schemes that were used by Flint et al. (1996a) assign the values of 0.09, 0.055, 0.005, 0.025, 0.8, and 0.025 as the weights for open 2.5 μm, open 25 μm, open 250 μm, filled 2.5 μm, filled 25 μm, and filled 250 μm fractures, respectively. She also will send me data packets with the full set measured values, Without having the data in front of her, Lorrie independently used the thinking that Gordon used to suggest how the filling properties would be different from matrix properties.

3/1/97 Preliminary calcite simulations. SAS

Three simulations have completed, each with 10 cm of soil over fillings with total porosity of 10^{-4}, 10^{-5}, and 10^{-6}, respectively. Interestingly, the three porosity cases do not appear to yield total infiltrations that are significantly different. The fractures respond very quickly, due to the small pore volume and high permeability, so it is adequate to use 2 decades for simulations. Partial results for deeper soils show decreases in infiltration with depth, similar to open fractures. A sequence of simulations for **cal3** and **cal4** were fired with the standard set of climate variations (AAP and AAT). A similar set of simulations, varying filling properties, will be run subsequently.

An error was found in the UZFLOW module converting meters to feet. The error came directly from the *Matlab* routine that calculates AAP, AAT, and AAT on each pixel of a DEM. Accordingly, all previous reported predictions for AAI are slightly incorrect, and should be slightly increased. Over the range of YM elevations (1100 to 1500 m), corrected values of AAP are 8 to 13 mm/yr larger, AAT are 0.65 to 0.9 °C cooler, and AAT are 1.2×10^{-7} to 1.4×10^{-7} drier.

4/10/97 Trip report for Yucca Mountain fieldwork. SAS

The remainder of this entry is adapted from the trip report for a two-day trip to Yucca Mountain to perform characterization field work. Field documentation for the trip is in CNWRA notebooks 175 (soils and vegetation) and 217 (Solitario Canyon measurements).

Persons Present

The trip to Yucca Mountain (YM), on March 26 28, 1997 was undertaken by S. Stothoff and J. Winterle (CNWRA), D. Groeneveld and J. Thompson (Natural Resources, Inc.), and D. Or (Utah State University).

Background and Purpose of Trip

CNWRA is working with D. Groeneveld, D. Or, and J. Thompson to aid in characterizing the impact of vegetation upon shallow infiltration. Transpiration is a process included in DOE models but not considered in CNWRA modeling efforts to date. The intent of the CNWRA work is to incorporate vegetation into infiltration-modeling efforts in a plausible and defensible manner, with appropriate modeling of soil-moisture uptake by plants of particular interest. The trip was inspired by the need for field-checking hypothesized relationships between vegetation and bedrock type, soil cover, slope, and solar loading. In a parallel effort, watershed-scale modeling is being performed by D. Woolhiser. Soil permeability in the wash channels is one of the critical parameters in the watershed-scale model. J. Winterle accompanied the group to obtain soil permeabilities in Solitario Canyon channels, which will be used in the watershed-scale model.

Summary of Activities

The field work was split into three activities: (i) a spot-check vegetation survey verifying the more-detailed TRW vegetation work and examining factors governing the distribution of individual species (D. Groeneveld and J. Thompson); (ii) a spot-check of soil-permeability measurements to verify more-detailed United States Geological Survey (USGS) work, as well as examination of plant rooting distributions (D. Or and S. Stothoff); and (iii) channel permeability measurements in Solitario Canyon (J. Winterle). The vegetation survey was conducted over four days while

the remaining work was performed over two days. Prior to the main trip, D. Groeneveld flew a photographic airborne survey of plant distributions, augmenting a collection of coarser-scale photographs taken previously by EG&G.

Overall Impressions

The trip was extremely useful in orienting Or to the YM site and to identifying and refining hypotheses regarding the spatial distribution of plants and plant uptake patterns. Soil measurements taken during field activities will provide direct input into modeling activities. The trip was also useful in planning future activities with Groeneveld and Or.

Interpretations Based on Field Observations

Prior to the field excursion, aerial photographs were examined and it was noticed that linear vegetation features could be identified, particularly along Yucca Crest. As a working hypothesis, it was felt that these linear features represent fissures in the bedrock that the plants were able to take advantage of for water uptake. To verify this hypothesis, several pits were dug adjacent to flourishing plants. Two pits were dug along an apparent linear feature in the Tiva Canyon caprock. Bedrock was reached at a depth of approximately 30 to 40 cm under the plants and in both pits a fissure of approximately 5 to 15 cm was identified, aligned with the vegetation feature, that was densely populated with roots. In one of the pits, a carbonate layer was identified within the fissure at a depth of roughly 5 cm below soil/bedrock contact; in the other, no distinct carbonate layer was identified to a depth of about 20 to 30 cm but there did appear to be increasing carbonate concentrations in the soil with depth.

Plant roots were exposed at three additional sites with shallower soil. At one site, in caprock, both plants exposed had roots predominantly within fissures or extending to fissures. At the second site, in caprock, the plant selected was in the center of a pocket of soil several meters across, with bedrock cropping out on three sides and a soil depth of at least 30 to 40 cm directly under the plant. Although a fissure existed, the plant did not appear to take special advantage of the fissure but appeared to take advantage of runoff from the surrounding bedrock. Nearby plants in fissures between bedrock outcrops appeared more verdant. At the third site, on a side slope in the upper lithophysal unit of the Tiva Canyon formation, the plants were rooted in rubble with 30 cm of cover. For these locations, typical of ridgetops and side slopes, the use of unrestricted rooting systems

reported in the literature is precluded due to the strong influence of bedrock.

In all locations examined, the soil cover was sandy loam to loam with bedrock fragments, and was rather permeable. The fine portion of the soil appears to be æolian in nature wherever it was examined. Although permeabilities and soil depths were only determined at a few locations, soil samples were collected at scattered locations (including each vegetation transect). Roughly two dozen soil samples were obtained. The similarity of the samples suggests that it would be reasonable to assume that soils are reasonably similar over the entire mountainside (except perhaps in areas with sorting due to overland flow such as washes and wash channels), consistent with Flint et al. (1996a).

Four ponded-head permeameter measurements were made at three sites with relatively shallow slopes along Yucca Crest and Highway Ridge. Measured saturated conductivity values ranged from 1.2×10^{-3} to 4.9×10^{-3} cm/s. The smallest reading occurred at a site where a large rock was subsequently found to lie directly under the disk; the next-largest reading was 2.9×10^{-3} cm/s. For comparison, Flint et al. (1996a) reported soil conductivities in the YM area of 5.6×10^{-4} to 3.8×10^{-3} cm/s based on soil-texture analysis. Three tension-head measurements (two readings with different suctions at one site, one reading at another site) were also obtained, indicating consistent values. The measured values are remarkably similar.

Rock particles found in the soil ranged from small pebbles through cobble-sized blocks. In the pits and in trenches with bedrock exposed, the bedrock was considerably more irregular than the soil surface implying that vegetation may be preferentially located in locally deeper pockets of soil where water can be stored for longer periods after precipitation.

The welded Tiva Canyon units do not exhibit gullying along the side slopes of the washes over the proposed repository footprint, suggesting that erosional processes are not dominated by overland flow. The high permeability of the shallow soils and the dense carbonates existing in fractures exposed by trenches in the TCw units below the caprock further suggest that lateral flow is likely to be primarily along the soil/bedrock interface rather than as overland flow. The distribution of vegetation suggests that lateral flow may be significant; vegetation is relatively sparse at the top of slopes and relatively dense at points where slopes flatten. Note that the existence of subsurface lateral flow is also suggested by neutron-probe measurements.

Based on topography, soil depth, and bedrock materials, the ground surface over the repository footprint can be divided into four categories:

Tiva Canyon caprock on ridgetops. Slopes are generally moderate (less than 10 degrees) with

shallow soils (0 to 40 cm with pockets greater than 60 cm). The bedrock is generally massive with fissures spaced sufficiently far apart in places to provide significant organization to vegetation. The fissures are typically 5 to 15 cm in aperture, and appear to form by æolian soils filling between boulders. Bedrock is irregular in topography, with at least 40 cm variation possible within the space of 2 m. The bedrock is sufficiently permeable that moisture may interact significantly with it over periods of days to weeks. Soil fills the fissures to a depth of at least 5 to 30 cm, with carbonate fillings possible. Roots are common, almost ubiquitous, within fractures. Net infiltration may be quite significant due to shallow soils. Several vegetation transects were taken in this environment, 4 soil-permeability and 2 bedrock-permeability measurements were made, and 5 bedrock-exposure pits were dug.

Tiva Canyon welded units (i.e., lithophysal units) below the caprock. Slopes are generally moderate to steep (10 to 45 degrees). Scree exists where slopes are greater than roughly 40 degrees. Bedrock is irregular in topography, although perhaps less so than for the caprock. There is some evidence of stairstepping in the bedrock surface that is not echoed in the soil profile, which may provide localized pockets for vegetation. Fractures are typically narrow in aperture (less than 1 cm) but closely spaced. The fractures appear to be filled with carbonates as a rule, and generally not penetrated by roots except for perhaps a few localized zones with wider apertures. Vegetation is predominantly Great Basin on the north-facing slopes and Mojavian on the south-facing slopes, with vegetation densities about twice as large on the north-facing slopes. Vegetation increases in density downslope. Net infiltration may be significant due to shallow soils. Lateral redistribution along the soil/bedrock interface may also be significant. Several vegetation transects were taken in this environment, a pair of soil-permeability measurements were taken, and several trenches and pavements were examined in detail.

Alluvium-filled washes. Slopes are shallow and soils tend to be greater than 1 m in depth. Net infiltration may not be significant, due to the large storage capacity of the soils and the presence of vegetation. This environment was not examined in detail, aside from one or two vegetation transects.

The west face of Yucca Crest. Slopes are quite steep, as much as 50 degrees. Numerous strata are exposed, ranging from densely welded to nonwelded. Soil pockets exist of as much as 50 cm even in the steepest slopes. Vegetation is dominated by crack-dwelling species. Overland flow should be significant, as evidenced by gully formation. Of the four environments this environment is by far the most complex to model however, relatively little of the repository footprint is overlain by this category. The environment was not examined in detail, aside from daily hikes up and down to Yucca Crest.

Hydraulic Conductivity Measurements in Solitario Canyon

J. Winterle obtained 13 hydraulic conductivity measurements for the stream beds in Solitario Canyon and its side canyons. These measurements were obtained using a Guelph Permeameter which is used by augering a hole 20 to 40 cm deep into the sediments and measuring infiltration of water out of the bottom of this hole while a constant water level is maintained in the hole. There were problems with this technique involving difficulty in augering holes due to the presence of large cobbles, and a tendency for the holes to collapse due to the lack of cohesiveness of the sediments. Nevertheless, 13 measurements were obtained with hydraulic conductivities on the order of 10^{-3} to 10^{-1} cm/s. These values are consistent with published values for silty sands and gravels. It should be noted that 10^{-2} cm/s is the upper limit of the range of hydraulic conductivities for which the Guelph permeameter is designed, thus the values outside of this range may not be as accurate as the lower values; however, they do represent a good order-of-magnitude estimate. Samples of sediments were obtained from the auger holes and their hydraulic conductivities are currently being measured in the laboratory. Locations of each of the conductivity measurements was recorded using a GPS unit. The GPS measurements are accurate to the nearest 100 m. Table 1-8 summarizes the data collected.

Problems Encountered

The real-time differential GPS did not function properly, almost certainly due to operator error. Reported measurements are therefore only accurate to within 100 m.

4/27/97 Conversion of neutron-probe data to matlab format.

The complete set of neutron-probe readings from the 98 neutron-probe boreholes plus UZ-7 (described by Flint and Flint (1995)), obtained September, 1996, from the DOE office, were converted to *Matlab* format. An awk script (**reduce_neut.awk**) converted the ASCII file to a reduced format, and a *Matlab* script converted it to a binary format for fast reads. Two additional *Matlab* scripts were created to examine the plots as a time history, **plot_neut.m** and **plot_neut_set.m**. Borehole UZ-7 is designated as neutron-probe borehole number 99. The scripts are stored in ***$HOME2/AmbientKTI/3Ddata.***

The awk conversion uses the csh sequence "`zcat neutron_* | nawk -f reduce_neut.awk`

Table 1-8: Hydraulic conductivity measurements in Solitario Canyon on March 27 and 28, 1997.

Sample #	UTM (m) N	UTM (m) E	Hydraulic Conductivity (cm/s)	Notes
1	546637	4077467	0.04	silty coarse gravels; many large cobbles
2	546517	4077632	0.02	coarse gravel with fine silty sand
3	546794	4077389	0.07	sandy coarse gravel
4	546826	4077651	0.05	well-sorted, pea-sized gravel
5	546772	4077250	0.002	silty, sandy gravel; large cobbles
6	546667	4077103	0.007	silty, sandy gravel; a few large cobbles
7	546612	4076972	0.002	silty coarse gravel
8	546593	4076710	0.012	sandy gravel; a few large cobbles
9	546597	4076410	0.02	sandy gravel
10	547186	4079275	0.1	coarse sand and gravel
11	547135	4078848	0.04	well-sorted pea-gravel with coarse sand
12	547121	4078681	0.01	well-sorted pea-gravel with coarse sand
13	547021	4078283	0.002	silty overbank sediments stream channel well-sorted pea-gravel

> `neut.date_num_dep_mc`".

There appears to have been some adjustment of elevations in late 1985, judging from offsets in all boreholes with records that early.

5/9/97 Documentation of upper-bound infiltration estimates. SAS

If the temperature and thermal conductivity profiles of a rock mass are known, one can calculate the energy flux due to conduction. If the actual energy flux through the rock mass differs from the conductive flux, it must be due to advection (i.e., energy transported through liquid or vapor fluxes). When a vertical column has smaller conductive fluxes than actual fluxes, it may be due to cool infiltrating water warming while moving to depth or upward vapor transport with an associated large latent-heat transport. In order to estimate infiltration fluxes when moisture movement is predominantly vertical, one can use an analytic solution or a numerical simulator accounting for both conductive and advective fluxes, and adjust the infiltration flux until the measured temperature profile is obtained. Lachenbruch and Sass (1977) presented a relationship that indicates that the reduction in apparent heat flux is roughly proportional to the volume of infiltrating water, the

thermal gradient, and the distance considered. Typically it is assumed that vapor flux is negligible, although this assumption is not necessary if the vapor flux can be accounted for. Implicit in the approach is the assumption that the liquid and rock remain in thermal equilibrium.

One of the advantages of the method is the lack of necessity for knowing details of how the liquid moves within the rock. On the other hand, it is necessary to have an independent estimate for the thermal flux, which can be difficult to obtain. It is also necessary to know thermal conductivities, but these are typically quite well constrained.

Estimates of thermal and liquid fluxes throughout the NTS are presented by Sass et al. (1980) and Sass and Lachenbruch (1982), with the results summarized by Sass et al. (1988). Sass et al. (1988) analyzed a set of boreholes in the YM area, with resulting estimates of conductive and total heat fluxes from the saturated zone (SZ) into the unsaturated zone (UZ) of 40 ± 9 and 49 ± 8 mW/m^2, respectively, with an average heat flux in the UZ of about 41 mW/m^2. Sass et al. (1988) contour conductive heat fluxes in the YM area (Figure 15 by Sass et al., 1988), which indicates that conductive fluxes are 70 to 74 mW/m^2 southeast through southwest of YM; roughly 60 mW/m^2 in the southwest part of Midway Valley; roughly 50 mW/m^2 in and near Fortymile Wash, Dune Wash, Yucca Wash, and Solitario Canyon (SC); and roughly 30 to 40 mW/m^2 over the repository footprint and north past Drillhole Wash. Sass et al. (1988) suggest that there may be an apparent reduction of heat flow from the SZ to the UZ of 5 to 10 mW/m^2, and calculate that this apparent reduction of heat flow could be achieved by 2 to 5 mm/yr net infiltration and about 8 mW/m^2 reduction would be achieved if 0.1 mm/yr of water were vaporized. Lateral flow in the shallow SZ is also considered a possible source of local anomalies. Sass et al. (1988) also note (without further comment) that apparent heat flux is negatively correlated with elevation; one might infer that lateral diversion to lower topographic areas may be occurring, although the study by Rousseau et al. (1996), discussed below, would suggest the opposite due to the insulating properties of alluvium.

An implication of the analysis by Sass et al. (1988) is that, at least locally over the repository block and Drillhole Wash, deficits in the apparent heat flux that occur in the UZ may be as much as 20 mW/m^2[assuming that 10 mW/m^2 is roughly equivalent to 5 mm/yr infiltration, as calculated by Sass et al. (1988)], so that locally about 10 mm/yr infiltration might be estimated. When estimating infiltration, it may be better to estimate the vertical heat flux from boreholes that are unlikely to have significant infiltration. Infiltration fluxes in deep alluvium and not close to channels are likely to be quite small, so that the boreholes in Midway Valley and south of YM in deep alluvium may be more representative of regional vertical heat flux. If so, vertical heat flux could be as much as 60 to 75 mW/m^2 and local deficits at YM could be as much as 45 mW/m^2,

implying that locally more than 20 mm/yr infiltration could be inferred from the thermal data. Assuming that the UZ heat flux is 60 mW/m^2, heat-flux deficits on the order of 15 to 30 mW/m^2in the area of the repository block and Drillhole Wash could be justified, implying that local infiltration rates may be 7 through 15 mm/yr in this area.

One significant advantage of the heat-flux method is that it can yield upper-bound estimates for infiltration rates. Assuming that the regional heat flux is 85 mW/m^2, neglecting all other sources of reduction in apparent heat flux such as lateral flow in the SZ and vapor fluxes, using a value of 35 mW/m^2 as the average apparent heat flux over the repository block, and using the rule-of-thumb that 10 mW/m^2 reduction in apparent flux is equivalent to 5 mm/yr infiltration, one finds that the maximum average infiltration over the repository block is about 25 mm/yr.

The chloride mass balance technique, as applied by Fabryka-Martin et al. (1996b), assumes that average Cl^- concentration multiplied by total flux is conserved, or

$$C_o P = CI, \tag{1-14}$$

where

- P is average precipitation rate,
- C_o is the Cl^- concentration corresponding to the average Cl^- deposition rate,
- C is the Cl^- concentration in a well-mixed reservoir at depth, and
- I is the net infiltration.

Knowing the average precipitation rate, Cl^- concentration corresponding to the average Cl^- deposition rate, and Cl^- concentration in a well-mixed reservoir at depth, the percolation flux at depth can be determined. Yang et al. (1996) report Cl^- concentrations in perched water of 4.1 to 15.5 mg/L, with 15 of the 17 reported values no greater than 8.3 mg/L and a Cl^- concentration of 7 mg/L at NRG-7a (the nearest borehole to UZ-4 and UZ-5 with a reported perched-water sample). Using the same precipitation rate (170 mm/yr) and Cl^- concentration (0.62 mg/L) as Fabryka-Martin et al. (1996b), and assuming that the perched water is well mixed with the matrix waters, calculated net infiltration is 25.7, 12.7, and 6.8 mm/yr for concentrations of 4.1, 8.3, and 15.5 mg/L, respectively.

An infiltration value of about 26 mm/yr would represent an upper bound based upon the perched-water chloride data; if the matrix waters do not mix completely with the perched water, infiltration values may be lower. The estimated infiltration values are more consistent with the shallow infiltration estimates than the estimates from the PTn, however, suggesting that a considerable portion of the infiltrating water may bypass the PTn matrix. The upper-bound value

obtained by chloride mass balance on perched water, 26 mm/yr, is remarkably consistent with the upper-bound value obtained by geothermal heat-flux calculations.

5/19/97 Revisiting alluvium regression.

Since the discussion of 1/13/97, additional information on alluvium depths, borehole location, and borehole geomorphic classification (e.g., channel, sideslope) has been gleaned from the literature and the data file obtained with the site atlas. I incorporated the new information to obtain regression coefficients.

As it turns out, I was not able to reproduce the original slopes calculated by Hannah Castellaw in August, 1995. Apparently she used the slope at the nearest neighbor of the DEM, with all calculations performed in ArcInfo. I tried to use: (i) the slope at the nearest neighbor, (ii) the interpolated slope from the slope at the four nearest neighbors, and (iii) the interpolated slope from the elevations at the four nearest neighbors. None of these matched the previous slopes, although some were close. Unfortunately, the regressions exhibit poorer fits than before, particularly for the channels (although the channels have many more points now). It may be that Hannah used a different DEM coordinate grid; she has not worked at CNWRA for a year or two, so it will be difficult or impossible to retrace the exact calculations. There does seem to be quite a bit of scatter.

I revised the set of files used to estimate regression coefficients in ***$HOME2/Matlab/-3Ddata***. New data files were created in the format that the load_well file expects, and the other load routines call load_well. The original data and *Matlab* files all have ".1" appended. The routine that calculates the slope at the borehole locations is called calc_pt_slope; internally there are switches to calculate the slope according to the three options mentioned above.

5/25/97 Results of 1D simulations.

Over the last several months, a series of *breath* version 1.2 simulations were run examining the impact of alluvium-filled fissures and calcite-filled fractures. These simulations used the same strategy as was used for the open fractures, in that the bedrock was assumed impermeable and the porosity of the filling was lowered to account for the fracture porosity. The alluvium simulations use kmpo5223_aKmao5222 as the base case, while the calcite simulations use kmpo5223_cKmao7554 as the base case. The alluvium simulations used soil depths of 10, 25, and 50 cm; the calcite simulations

Table 1-9: Summary of alluvium (*abcd*) and fracture (*efgh*) parameter codes

Code	Parameter	Translation
Soil cover (kmpo*abcd*_aKmao*efgh*)		
a	Intrinsic permeability k (cm^2)	$k = 10^{-a-3}$
b	van Genuchten m	$m = b/10$
c	van Genuchten scaling pressure P_0 (gm/cm-s^2)	$P_0 = c \times 10^4$
d	Porosity ε	$\varepsilon = d/10$
Soil-filled fissure (kmpo*abcd*_aKmao*efgh*)		
e	Intrinsic permeability k (cm^2)	$k = 10^{-a-3}$
f	van Genuchten m	$m = f/10$
g	van Genuchten scaling pressure P_0 (gm/cm-s^2)	$P_0 = c \times 10^4$
h	Porosity ε	$\varepsilon = 10^{-h}$
Calcite-filled fracture (kmpo*abcd*_cKmao*efgh*)		
e	Saturated hydraulic conductivity K_{sat} (cm^2)	$K_{sat} = 10^{-e}$
f	van Genuchten m	$m = f/10$
g	van Genuchten scaling pressure P_0 (gm/cm-s^2)	$P_0 = 10^g$
h	Porosity ε	$\varepsilon = 10^{-h}$

used soil depths of 10, 25, 50, 100, and 150 cm. The alluvium simulations used fracture-alluvium porosity values of 10^{-2}, 10^{-3}, and 10^{-4}. The calcite simulations had a nearly full suite of calcite perturbations for soil depths of 10, 25, 50, 100, and 150 cm (2 perturbations calcite permeability, and calcite van Genuchten m; 1 perturbation for calcite P_0 and porosity) and a full suite of 2 perturbations for all soil properties with a soil depth of 10, 25, or 50 cm. The codes for the output files are discussed in Table 1-9. Note that the code for alluvium-filled should have been kmpo*abcd*_akmpo*efgh* and the code for calcite-filled should have been kmpo*abcd*_cKmpo*efgh* for clarity.

The average flux over the second decade, averaged over the depths of 1 to 10 m, were extracted using extract_qstate.m (coded in *Matlab*) for all simulations. Similarly, the decadal average moisture content in the node above the soil/fracture interface was extracted for each case. All values were stored in **af_allcli.result** in ***$BREATH2/Subreg***. The net-infiltration results are summarized in Table 1-10.

Several conclusions can drawn from the simulation results. The alluvium results suggest that as the fracture aperture decreases, net infiltration increases. The effect decreases as the soil depth increases, and is not tremendously large in any case. The calcite results suggest that the

Table 1-10: Net infiltration (mm/yr) for various cases with soil- and calcite-filled fractures

Code	10-cm	25-cm	50-cm
kmpo5223_aKmao5222	17.2	7.13	4.44
kmpo5223_aKmao5223	21.4	8.30	4.92
kmpo5223_aKmao5224	22.4	8.53	4.99
kmpo5223_cKmao7554	17.4	8.55	4.85
kmpo4223_cKmao7554	14.7	2.70	0.42
kmpo6223_cKmao7554	21.6	13.8	10.7
kmpo5123_cKmao7554	18.2	12.9	8.66
kmpo5323_cKmao7554	21.5	12.0	8.24
kmpo5213_cKmao7554	26.3	17.6	12.7
kmpo5253_cKmao7554	10.3	1.25	0.13
kmpo5222_cKmao7554	23.0	15.8	11.6
kmpo5225_cKmao7554	9.48	1.80	0.29
kmpo5223_cKmao6554	33.1	14.8	8.08
kmpo5223_cKmao8554	3.31	1.81	1.43
kmpo5223_cKmao7454	15.2	7.50	4.78
kmpo5223_cKmao7654	19.2	9.21	4.70
kmpo5223_cKmao7564	42.6	23.6	14.2
kmpo5223_cKmao7555	17.5	8.57	4.87

alluvium properties are not important relative to calcite properties when soil is 10 cm, but dominate when soil is 50 cm. Variation in calcite properties yields largest change in net infiltration when soils are shallow and are muted somewhat when soils are deep. The calcite property having strongest impact on net infiltration appears to be P_0, followed by K_{sat}.

The capillary properties of alluvium and calcite may be the most important parameters for calculating bare-soil infiltration. It appears that the ratio of alluvium P_0 to calcite P_0 is a controlling factor on infiltration. As the ratio gets smaller (calcite has finer pores relative to alluvium) net infiltration increases. One can attribute this to the propensity of calcite to imbibe moisture and not release it back to the soil to satisfy evaporation.

The variation of moisture content with net infiltration for the bottom node of the soil follows the general patterns ascertained before. There is a clear trend for drier soil with increasing net infiltration when the fracture-filling properties are changed, however, whether the filling is calcite or soil (note that only soil porosity was varied).

6/11/97 Documentation of soil sample analysis. SAS

During the annual CNWRA QA audit, in which the USFIC KTI was audited, an issue of data collection was raised. During the YM field trip examining shallow infiltration processes in caprock, documented in the entry dated 4/10/97, 23 soil samples were collected and analyzed for electrical conductivity and percent hydrometer estimates of grain size and texture, by Utah State University Analytical Laboratories (Utah State University, Logan, UT 84322-4830, 801/797-2217). The reported analysis is dated 17 April, 1997; I have filed a copy of the results in my file cabinet. These samples were collected at various locations around YM at the suggestion of David Groeneveld and Dani Or (consultants hired for their expertise in characterizing shallow flow processes).

Typically our QA program requires that such analyses be planned prior to data collection and that verification of the analysis procedure be performed in order to be fully complient with QA requirements. I was made aware of their recommendation while we were in the field and did not realize that an external agency (albeit an agency at the same university that Dani Or is an employee of) was to perform the analyses. Note that the soil samples are only intended for qualitative verification of our observations that all of the fine materials at the site are remarkably similar and are not intended for numerical estimates or to provide data for regulatory positions. We will have to note that data was not collected under CNWRA QA procedures if and when we use the information.

6/30/97 Root growth simulations for caprock paper. SAS

I am writing a paper documenting our investigations of hydrologic issues regarding the interaction of vegetation with fissures in TCw caprock environments with Dani Or and David Groeneveld (consultants). The paper consists of three major components: (i) a description of field observations, (ii) simulation of the impact of vegetation on hydrologic behavior in the presence of fissures, and (iii) simulation of root growth in the presence of fissures. David has been writing the description of the fieldwork. Dani has been performing 2D simulations of a vertical cross-section with 5 fissures overlain by soil using HYDRUS-2D, which is an enhancement of SWMS-2D (Šimůnek et al., 1992), in order to examine the hydrologic behavior component. I have been attempting to use Version 2.0 of a 3D code developed at UC-Davis by Jan Hopmans, Volker Clausnitzer, and Francesca Somma that explicitly models individual roots and distributes uptake to the surrounding nodes.

The root-growth code does not have a name; I will refer to it as Root-Growth Simulation Model (RootSim) from now on. RootSim is a research-level code, so it has a number of shortcomings

that would not be expected in a production code and that make it difficult to use for our purposes. Some shortcomings include:

- Every element must be the same size and rectangular shape.
- Properties are defined by node rather than element.
- Boundary conditions are restricted to a mixture of:
  - one (time-varying) flux value (as many nodes as desired),
  - one (time-varying) head value (as many nodes as desired).
- Gravity drainage is not allowed.
- The code relies on a non-portable random-number generator.

The code was run through a FORTRAN static analyzer code, for_study (called fstudy on bashful), provided by Cobalt Blue. SPARC version 2.0.1 was used for the test. A number of errors and warnings were identified, either through compilation messages, fstudy, or tracking down errors in simulation behavior, including:

- 24 overlength lines
- a branch into a block
- variable *init* used before being initialized
- calling subroutine ChInit when chemistry is disabled (thereby changing *dtMaxC*)
- 9 unused common blocks in routines
- 13 changes in common blocks between routines (different variable names)
- 21 instances where precision was lost (real to integer or double precision to single precision)
- rand is system-dependent (and does not work for SGI)

The common-block and lost-precision messages were ignored; the remaining messages were fixed. The rand problem was accommodated by writing a short C routine to use the rand48 routine provided as part of the SGI library. In addition, a modification was made so that the **outfem** output files also include *cAvg*, so that the output file can be reused as a restart file without

modification. Modifications and suggested modifications are further documented in file **Errors** in ***$HOME2/AmbientKTI/Root***.

Several tests have been run trying to get appropriate simulations for the paper. The physical problem entails a shallow soil atop a soil-filled fissure next to a matrix block, with a plant starting either directly over the fissure or starting at some distance, with the idea being to compare some measure (e.g., total plant mass) at the end of the simulation. Dani set up the original input files based on the documentation, and some properties were not totally appropriate for YM. Some of the plant properties have never even been measured.

Through a process of trial and error, I've modified the problem from the original set up by Dani. Problem setup and changes include:

- A relatively small domain is being modeled (an 11x12x36 grid, 25 mm on an element side). This represents a tradeoff between computational speed and grid refinement.
- Soil depth is about 10 cm and the fissure is about 15 cm wide (only half is modeled). The "about" is due to the node-defined material properties.
- Bedrock material properties are TCw cuc, with retention parameters for sample PW19s, composite-sample caprock K_{sat} (Flint et al., 1996b).
- Soil retention parameters are for a loamy soil (Dani refers to a Carsel and Parrish, 1988) and K_{sat} is texture-estimated for YM soil (Schmidt, 1989).
- Soil strength has caused difficulties in simulations. Soil strength is defined in the code to be $(1-\theta)^3 S_{smax}$, where θ is effective saturation and S_{smax} is soil strength at residual saturation (with apparently arbitrary units). The **root.in** input file defines a soil strength at which growth ceases for each type of material. Dani changed the bedrock retention properties to artificially maintain very dry (very strong) conditions. I put realistic retention properties, and the roots acted as though the bedrock was clay. Changing the bedrock strength to an extremely large value (10^{32}) caused numerical problems (NaN for root-tip location), which I interpret as due to overenthusiastic adjustment to strength gradients, so I cut it back to 10^8 and gradually increased to 10^{11}. Results are not totally satisfactory due to the transition zone between nodes where properties change in an uncontrolled manner. I also had problems by making maximum soil strength too large (14) compared to the plant-growth cutoff at residual saturation (6), which I fixed by making the maximum soil strength 6 as well.
- Appropriate boundary and initial conditions are difficult to provide with the version of the code we have available. One can provide either a constant-head or constant-flux bottom

condition and both tend to misrepresent the available water. Either a no-flow or specified-head (representing equilibrium with the atmosphere) top condition may work. I have been running into problems with balancing available water with rock availability. The latest solution is to provide wetting events every 15 or 30 days and have no-flow boundaries at the bottom. I initially used initial conditions at 50 cm suction head.

- The current conditions have been changed to 300 cm suction head in soil (field capacity of 0.3 bar) and 3000 cm (3 bar) suction head in the rock, redistributed with 15 days of evaporation (15 bar) at the top and no flow at the bottom. Rain (7.5 mm) is applied at 15, 30, 45, and 75 days, and evaporation continues throughout at 5 bar.
- When very wet conditions occur, the plant over bedrock develops more biomass than the plant over the fissure, even though the fissure plant has much greater penetration. The bedrock plant is apparently using the bedrock as an additional source of moisture and developing along the bedrock interface. I am not totally convinced that this is not an artifact of the slushy material-property zone, but the caprock *is* quite permeable.

7/8/97 Modification of Scott and Bonk electronic version. SAS

An electronic ARC/INFO coverage of Scott and Bonk (1984) geology is one of the data sets included on the DOE tape discussed in the 3/23/97 entry. There are 118 polygons that do not have a lithologic attribute and one alluvium polygon that is mislabeled as ym. Jim Prikryl extracted the coverage in UTM format last week and I have started entering the missing coverages by visual inspection. All work is in ***$HOME2/Matlab/YMGeology***. The updated coverage information is listed as **scotbonu.wat**; the original coverage is stored in subdirectory ***Orig***.

7/11/97 Regression for TPA shallow infiltration. SAS

It was brought to my attention that the UZFLOW module of the TPA3 code, which predicts infiltration on a pixel-by-pixel basis over YM, was predicting far more mean annual infiltration (MAI) than mean annual precipitation (MAP) under full glacial conditions. The regression formula features bicubics in both MAP and mean annual temperature (MAT), and apparently these cause problems outside the range of interpolation. The formulation is for soil over an open-fracture continuum.

I revisited the form of the regression equation and have come up with a more robust (and

simpler) formulation that appears to work well even through 4× current MAP and -15 °C cooler than current MAT. The formulation fails for soil depths greater than 25 cm, but these depths should have negligible infiltration for the system considered and can be set to zero. For very shallow soils (< 10 cm) and extremely cool and wet conditions (beyond the range simulated), the formulation predicts MAI in excess of MAP. These cases should have MAI set to equal MAP.

The regression equation is intended to account for several facets of MAI behavior in this system: (i) MAI generally changes logarithmically with changing inputs; (ii) MAI is more sensitive to changing inputs when soil depths are larger; and (iii) MAI is more sensitive to changing inputs when MAI is small. The simplest form of an equation satisfying these conditions is

$$H = B^{b_1}[\sum_{i=1}^{N} a_i f_i(u_i)](1 + b_2 H), \tag{1-15}$$

where

- H is $\log_{10}(MAI/MAP)$
- a_i is a regressed constant
- b_i is a regressed constant
- u_i is a normalized regression variable (e.g., MAP, MAT)
- $f_i(u_i)$ is a regression relationship for variable u_i
- B is $(b\varepsilon)/(b_0\varepsilon_0)$
- b is soil depth
- b_0 is base-case soil depth
- ε is porosity
- ε_0 is base-case porosity

In ***$HOME2/Matlab/YMInfil/SubregSpaceDist*** I created two new *Matlab* routines, **run_sreg.m** and **f_regshal2.m**, that perform the regression using the formulation.

7/14/97 More regression for TPA shallow infiltration. SAS

In ***$HOME2/Matlab/YMInfil/SubregSpaceDist*** I created a new *Matlab* routine, **eval_TPA_fun.m**, that evaluates the function in Equation 1-15 (with best-fit constants) for every pixel in the standard YM DEM with soil depths given in **basecaseDepth.mat**. The areal-average MAI resulting from the formula, both as MAI and as normalized, is shown in Figure 1-4(a) and (b), respectively.

Following up on the incentive to examine the results in detail, I collected the simulations performed to date in **am_all.result** in ***$BREATH1/RunTightAM***. I modified the format of

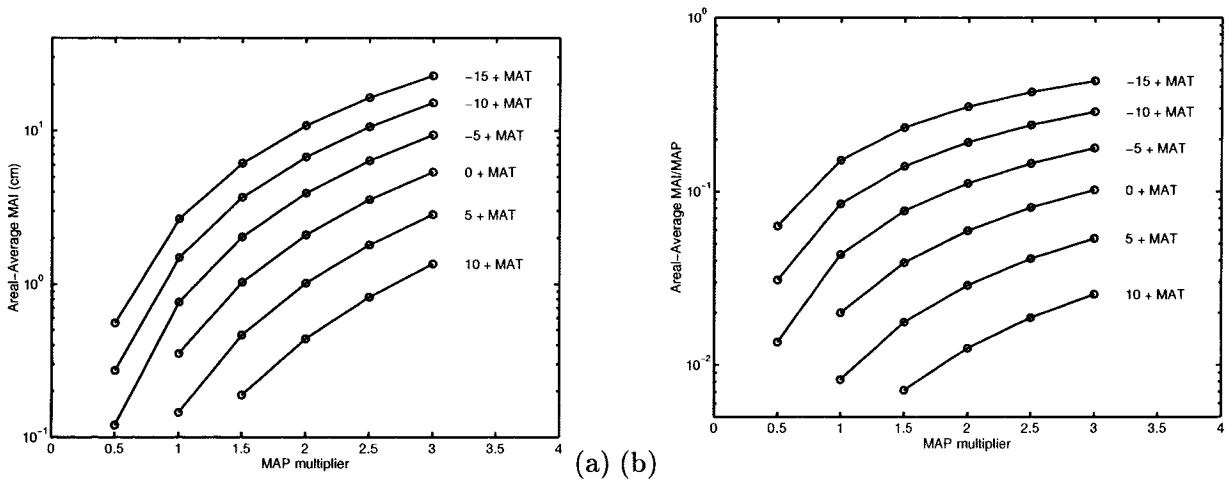

Figure 1-4: 7/14/97. Areal-average MAI for YM area, using regression formula based on soil/open-fracture system, (a) in dimensional form, and (b) in nondimensional form.

the file to include the date that the simulation was completed. I cursorily examined the soil-over-calcite simulations to check on the sensitivity to depth and climate. By plotting the simulations with the fracture code of **cal3** against the areal-average simulations, it appears that even though the calcite simulations do not span the same range as the soil-over-fracture simulations, the change in infiltration with climate should have similar trends. Overall infiltration may be greater with the calcite due to the lesser sensitivity to soil depth (e.g., 10 cm soil depth has 29 mm/yr while 50 cm soil depth has 7 mm/yr MAI). Fracture properties have a much greater impact on MAI for the calcite simulations than for the open-fracture simulations; permeability and bubbling pressure are the two big players, along with soil porosity.

A cursory check of simulations with base-case alluvium filling fissures with various soil depths and fissure porosities suggests that the falloff of MAI with soil depth has a characteristic slope, as the **cal3** simulations have about 1.5 times as much MAI for a given soil depth. Interestingly, MAI increases slightly as fissure porosity decreases.

10/10/97 Modification to scientific notebook. SAS

Today I created a new chapter in this notebook, entitled "Ambient Hydrology KTI – Hydraulic Properties," and moved entries from this chapter to the new chapter. The entries include:

- 8/29/96,
- 9/21/96,
- 9/24/96,
- 3/23/97,
- All entries from 8/31 through 10/8/97.

The intention is to segregate entries into related groups, in order to improve clarity. No alterations were made to any entry (except for the move itself).

4/12/98 Documentation of future-climate analog trip. SAS

The following is a nearly verbatim copy of a trip report discussing a visit to potential future-climate analog sites in southern Nevada. The trip took place April 5 through 8, 1998, and was reported by S. Stothoff.

Background and purpose of trip

The majority of work characterizing infiltration at YM has assumed that present-day conditions exist and relatively little work has been performed that addresses infiltration under future climatic conditions. The infiltration model used in the NRC's TPA3 exercises conservatively neglects transpiration. Under current climatic conditions, the atmospheric evaporation demand is so much larger than precipitation that neglecting transpiration provides infiltration estimates that are only moderately conservative. However, under the cooler and moister conditions that are anticipated to occur in future glacial cycles, neglecting transpiration is expected to have a much more significant impact on infiltration predictions.

An infiltration model incorporates transpiration by specifying total soil-water uptake and the distribution of that uptake with depth. In order to calibrate an infiltration model, it is necessary to identify the vegetation expected for the particular climate and geomorphic environment. Given the expected vegetation, it may be possible to estimate appropriate plant rooting depths and uptake patterns from the literature.

Analogs to YM under future climatic conditions, if found, will be used to calibrate the vegetative patterns used as input to the infiltration model. As information on the hydrologic

behavior of the sideslopes at YM is least well characterized of all environments at YM, the washes are the primary analog environment that is sought. Analogs to the caprock environment are also sought, with secondary importance. Analog sites were identified within sight of YM in earlier fieldwork (i.e., the Prow, Shoshone Mountain), but the analogs are not sufficient to characterize the range of climatic and geomorphic environments encountered at YM under a glacial cycle. Additional potential analog locations were identified from topographic maps, geologic maps, and aerial surveys. These locations include Rainier Mesa, on the Nevada Test Site (NTS); Timber Mountain and the North Pahroc Range (both in Lincoln County); the Grapevine Range (near Beatty, NV); and the Montezuma Range (near Goldfield). The current trip assessed the viability of these potential sites for future field work, with particular regard to matching bedrock, soil, vegetation, slope, annual precipitation, and mean air temperature to expected future conditions at YM. It is expected that not all of these characteristics will be matched perfectly.

Summary of activities

The fieldwork was intended to quickly identify potential sites for subsequent follow-up studies in greater depth. It is difficult to characterize soil and bedrock characteristics from aerial surveys, so the primary emphasis for this trip was to identify appropriate soil and bedrock characteristics. A primary criterion was that elevations were generally in the range of 6,000 to 8,000 ft, providing precipitation and temperatures similar to anticipated future climates at YM. After elevation, the next criterion used in screening was to identify formations with densely welded tuffs, which are fairly rare. Appropriate slopes and soil depths were secondary criteria for matching.

Several good analog locations were identified, in the Grapevine Mountains, Timber Mountain, and Rainier Mesa. The North Pahroc Range was found less useful for analog work, while the Montezuma Range was not investigated due to time constraints.

The geomorphic characteristics of portions of lower Phinney Canyon, in the Grapevine Mountains, are strongly analogous to YM washes, featuring densely welded and quite fractured tuffs, north- and south-facing slopes, and thin soils with plentiful rock shards. The Phinney Canyon site may have slightly lower fracture densities and slightly thicker soils than YM. Ground access requires 4WD vehicles and nearly 1-1/2 hr driving from pavement; however, within the canyon access is equivalent to that obtained in YM washes. Air access is unlimited.

Timber Mountain, north of Hiko in Lincoln County, offers outcrops of moderately welded tuff, nonexistent to shallow soils, and general characteristics strongly reminiscent of the caprock at

YM. The soils appear to be developing in situ, with perhaps less æolian component than apparent at YM. Ground access requires 4WD vehicles and 10 mi driving from pavement. The last 1/2 mi was hiked, due to mud and uncertain conditions; it should be possible to move closer later in the year. Moderate hiking (1/2 mi) may be required to visit prime sites. Air access is unlimited.

Rainier Mesa, approximately 1 hr drive north of Gate 100 in the NTS, is capped by moderately welded tuffs strongly reminiscent of Yucca Crest. Below the mesa top, sequences of densely welded to nonwelded tuffs form long slopes reminiscent of the west flank of YM. Soil thicknesses also appear to be similar to YM, although the soils appear to have much greater organic contents. Further, infiltration estimates are available, based on measurements of dripping into the N tunnel. Ground access is on pavement, perhaps with some dirt roads. Unlike the other sites, air access may be limited or unavailable due to NTS restrictions, and camping is not an option, requiring 1-1/2 hr drive to the nearest motel.

The North Pahroc Range, between Hiko and Caliente in Lincoln County, offers north- and south-facing sideslopes at angles similar to YM washes and soils generally similar to YM soils. However, the bedrock is not as densely welded as the Tiva Canyon welded units, thereby is less fractured. Also, the easily accessible slopes are generally at a lower elevation than the other sites, yielding an analog to a warmer and drier future climate than the other sites. Areas with what appears to be densely welded tuff are visible from the road, but access would require extensive hiking on steep terrain. Ground access requires 4WD vehicles, but is better than either Timber Mountain or Phinney Canyon. Air access is unlimited.

Impressions/conclusions

Overall impressions

The trip was useful in identifying analog sites. The trip successfully identified several good analogs for future work, although it is desirable to have additional reconnaissance from the air (particularly at Timber Mountain and Rainier Mesa). Fieldwork will not be possible for some time, however, as snow exists at higher elevations (up to 1 m thicknesses were observed) and soils are frozen.

Juniper and piñon pine are efficient at extracting soil moisture due to the large rooting systems for these plants. Packrat midden studies (Brown et al., 1997) indicate that juniper was present at elevations below 500 m in the Great Basin during the last glacial period (significantly lower than the base of YM). During the visit to Nevada, juniper was found at elevations less

than 6,000 ft in some locations but piñon/juniper associations were absent at significantly higher elevations in other locations along the periphery of the NTS and Nellis AFB. If the 6,000-ft elevation represents a representative future-climate analog, both cases with and lacking vegetation should be examined to ascertain whether YM would be expected to have these species present in future conditions.

The presence in April of significant amounts of snow and frozen soil, with snowdrifts of up to 1 m in depth, suggests that it may be important to consider snow when modeling infiltration under future climates. None of the YM infiltration modeling to date has considered snow, as snow is not important at YM under current climatic conditions. Under current conditions, most infiltration occurs during the winter; if the ground is frozen, however, infiltration would be expected to peak when the snow melts. It may be that larger infiltration pulses would occur under such conditions, if the total winter precipitation infiltrated over a few weeks.

Summary of field observations

Timber Mountain

Timber Mountain is located approximately 35 mi northwest of Caliente and 40 mi north of Alamo, in Lincoln County, Nevada. Timber Mountain is located far enough east to significantly attenuate the effects of the Sierra Nevada rain shadow. Ground access to the Timber Mountain site is via a 4WD dirt road proceeding 10 mi northwest from the White River Narrows. Air access is not restricted.

The Shingle Pass Tuff (Tsp) unit, identified as densely welded by du Bray et al. (1987), is of primary interest for analog studies. The Tsp unit, described as pinkish-gray to pale-red-purple by du Bray et al. (1987), is a crystal-rich tuff similar in welding and fracturing to the caprock at YM. The peak of Timber Mountain is 8,600 ft in elevation. Areas with Tsp outcrops range from 6,000 to 8,100 ft in elevation, with the most accessible areas (within 1/2 mi of the roadway) roughly 6,600 to 7,000 ft in elevation. Areas outside this range in elevation would require hiking several miles, although the hiking does not appear to be strenuous. A northeast-southwest trending ridge, at approximately latitude 37° 57'30" N and longitude 115° 5' W, appears to be a good analog site for the YM crest.

Soils in the Tsp outcrop areas are thin to nonexistent. Much of the soil appears to be forming in situ, and first impressions suggest that a smaller æolian component is present than at

YM. Frost heave is evident in spots. Traces of overland sheet flow were also observed. Plentiful piñon and juniper are present.

North Pahroc Range (Boundary Wash)

The Pahroc area is also in Lincoln County. The North and South Pahroc Ranges are separated by US Route 93 approximately 25 mi west of Caliente. The primary ground access to higher elevations in the Pahroc ranges is through Boulder Wash Road, a 4WD road cutting through the North Pahroc Range from Dry Lake Valley to White River Narrows roughly 25 mi southwest of Timber Mountain. Accessible areas are all less than 7,000 ft in elevation, with the roadway less than 6,000 ft in elevation. Air access is unlimited.

Sideslopes north and east of the roadway feature moderately welded crystal-rich tuffs, and slopes that are generally shallower than the washes at YM. Two types of bedrock were observed within 1/4 mi of the road, a pale lavender tuff and a reddish-brown tuff, with the reddish-brown tuff appearing more welded and more suitable for future work. Fractures appear to be more widely spaced than the Tiva Canyon welded (TCw) unit at YM. Soils appear to be fairly comparable to those at YM. Appearing and disappearing streams where soil pinches out were observed, providing evidence of downslope lateral subsurface flow. Juniper were present, but much more sparsely than at Timber Mountain. Ground access to the base of the slopes is easy, but significant uphill hiking is required to reach higher elevations.

A bowl at higher elevations was noted south of Boundary Wash Road, with bedrock apparently more welded than the sideslopes northeast of the road. Snow was present, particularly on north-facing slopes at the bowl elevation. A hike to the bowl was abandoned partway due to time constraints, but portions of the hike were quite steep and strenuous and would be difficult to attempt with significant equipment. Other ridges south of the road might serve as an analog, but again would require significant effort to reach.

The Boundary Wash area is an adequate analog site, although other analog sites were identified with better characteristics. Unattractive features of the site include significant hiking, moderate welding, and low elevation. It may be worthwhile to consider limited study of the area as a supplemental analog for partial glaciation. Any studies would be likely be most practical if aerial analysis were the primary study mode, with limited ground confirmation.

Grapevine Mountains (Phinney Canyon)

Phinney Canyon, an east-draining canyon in the Grapevine Mountains, is located between Scotty's Castle (in Inyo County, California) and Beatty, Nevada. Phinney Canyon is in Nye County, several miles east of the junction between Inyo County, Esmeralda County (Nevada), and Nye County. The Grapevine Mountains are likely to feel significant effects of the Sierra Nevada rain shadow. Ground access to the Grapevine Mountain site is via a series of 4WD dirt road proceeding west from Rhyolite, north past Bullfrog Mountain to Sarcobatus Flat, and west to Phinney Canyon. Travel time from Beatty to Phinney Canyon is between 1-1/4 to 2 hr. Air access is not restricted.

Portions of the lower Phinney Canyon appear to be rather analogous to the washes at YM, especially two stretches of south-facing slope and at least one stretch of north-facing slope between the elevations of 6,000 and 6,600 ft. In these areas, the tuff is densely welded, with shards exhibiting the characteristic clinkstone clatter. Fracture patterns are quite reminiscent of densely welded TCw sideslopes, as best as can be ascertained from outcrop observations. Soils were also quite reminiscent of the YM washes, with similar sizes and percentages of rock shards, although the soils may be somewhat thicker.

A small snowmelt stream on the southfacing side of the canyon was located along a small fault, forming a waterfall. Under the waterfall, a cave was hollowed out to perhaps 2-m depth. Dripping from ceiling fractures was observed at numerous locations within the cave, apparently arising from stream infiltration several meters above.

The vegetation was somewhat anomalous in the lower portions of Phinney Canyon. Typically, juniper is observed at lower elevations than piñon, but in Phinney Canyon juniper was much sparser at the lower elevations than was piñon. Juniper was primarily observed on sideslopes, with thin soils. Piñonwas quite dense in the wash bottom, reaching several meters in height.

The roadway was impassable due to snow at roughly 6,200 ft elevation. Drifts were as deep as 1 m at higher elevations, although deep depressions in the snow cover were formed at the base of most plants.

The Phinney Canyon site appears to be an excellent analog to YM washes, certainly the best of any site examined. Fractures may be slightly further apart than at YM, and soils may be somewhat thicker, but overall the site is highly recommended.

Rainier Mesa

Rainier Mesa, in the north-central portion of the NTS, rises to an elevation of roughly 7,000 ft. Rainier Mesa is topped with a moderately welded tuff caprock quite reminiscent of Yucca Crest with more boulders. Estimates of fluxes into the N-tunnel drifts provide information on net infiltration at Rainier Mesa, which can be used to calibrate infiltration models. Access to Rainier Mesa is by paved road, although camping at the site is unlikely to be allowed so that roughly 3 hr of driving will be required each day. Also, air access is strictly controlled and it may not be possible to obtain the aerial photographs required to quantify vegetation densities.

A carpet of snow up to 1/2 m thick covered the top of Rainier Mesa, closing the road and limiting observational opportunity. It appears that soils are similar to Yucca Crest, albeit with much greater organic content. Piñon, juniper, and mountain oak were found on the mesa caprock.

Long slopes extend from the mesa caprock to the valleys below, featuring hundreds of meters of densely welded through nonwelded tuffs. These slopes are reminiscent of the portions of the western flank of YM that lie above the Paintbrush Tuff nonwelded (PTn) outcrop. Densely welded tuffs, visible in road cuts, appear to be almost identical to the densely welded portions of the TCw tuff. These slopes may serve as an analog to the Solitario Canyon side of YM, although the lack of gully formation limits the analogy to Topopah Spring welded (TSw) exposures at YM. The slopes may also serve as an analog to the washes, but may suffer from the lack of a wash bottom collecting water. Perhaps the contrast between Rainier Mesa slopes and Phinney Canyon slopes may provide insight into lateral flow processes in the washes.

Conditions are currently very moist on the NTS. Yucca Lake is currently full to beyond the playa dimensions, and the alluvium at various locations on the Test Site is essentially saturated.

Problems encountered

None.

Pending actions

None.

Recommendations

Use the Phinney Canyon site for an analog to the YM washes, concentrating resources into evaluating the relatively poorly characterized sideslope environments. The Phinney Canyon studies should receive the highest priority for fieldwork. Analysis of aerial photography should be the primary study tool for the remaining sites, with limited ground confirmation of aerial observations. As much use should be made of aerial observations as is possible, as data acquisition is relatively fast, informative, and inexpensive.

Attachments

Annotated photographs of the potential analog sites examined during the trip were attached to the trip report. These are not included here.

References

Bagtzoglou, A. C., N. M. Coleman, E. C. Pearcy, S. A. Stothoff, and G. W. Wittmeyer. 1997. Unsaturated and Saturated Flow Under Isothermal Conditions. In B. Sagar (Ed.), *NRC High-Level Radioactive Waste Program FY96 Annual Progress Report*, Volume NUREG/CR-6513, No. 1, Washington, DC, pp. 10–1–10–28. Nuclear Regulatory Commission.

Bagtzoglou, A. C., S. A. Stothoff, and M. A. Muller. 1995. *Progress Towards Estimating Infiltration and Deep Percolation at the Yucca Mountain Site.* , Center for Nuclear Waste Regulatory Analyses, San Antonio, TX.

Brown, T., S. Conrad, S. Wirth, J. Cochran, and J. Emery. 1997. *Plausible Future Climate States at the Area 5 Radioactive Waste Management Site, Nevada Test Site.* SNL-?, Sandia National Laboratories, Albuquerque, NM.

du Bray, E. A., D. O. Hurtubise, and C. A. Bannister. 1987. *Geologic Map of the Weepah Spring Wilderness Study Area, Lincoln and Nye Counties, Nevada 1:50,000.* Miscellaneous Field Studies Map MF-1922, United States Geological Survey, Denver, CO.

Fabryka-Martin, J. T., P. R. Dixon, S. Levy, B. Liu, H. J. Turin, and A. V. Wolfsberg. 1996a. *Systematic Sampling for Chlorine-36 in the Exploratory Studies Facility.* LA-CST-TIP-96-001, Los Alamos National Laboratory, Los Alamos, NM.

Fabryka-Martin, J. T., H. J. Turin, A. V. Wolfsberg, D. Brenner, P. R. Dixon, and J. A. Musgrave. 1996b. *Summary Report of Chlorine-36 Studies.* LA-CST-TIP-96-003, Los Alamos National Laboratory, Los Alamos, NM.

Fernandez, J. A., J. B. Case, C. A. Givens, and B. C. Carney. 1994. *A Strategy to Seal Exploratory Boreholes in Unsaturated Tuff.* SAND93-1184, Sandia National Laboratories, Albuquerque, NM.

Flint, A. L., J. A. Hevesi, and L. E. Flint. 1996a. *Conceptual and Numerical Model of Infiltration for the Yucca Mountain Area, Nevada.* Milestone 3GUI623M, Department of Energy, Las Vegas, NV.

Flint, L. E. and A. L. Flint. 1990. *Preliminary Permeability and Water-Retention Data for Nonwelded and Bedded Tuff Samples, Yucca Mountain Area, Nye County, Nevada.* Open-File Report 90-569, United States Geological Survey, Denver, CO.

Flint, L. E. and A. L. Flint. 1995. *Shallow Infiltration Processes at Yucca Mountain, Nevada–Neutron Logging Data 1984-93.* Water-Resources Investigations Report 95-4035, United States Geological Survey, Denver, CO.

Flint, L. E., A. L. Flint, C. A. Rautman, and J. D. Istok. 1996b. *Physical and Hydrologic Properties of Rock Outcrop Samples at Yucca Mountain, Nevada.* Open-File Report 95-280, United States Geological Survey, Denver, CO.

Lachenbruch, A. H. and J. H. Sass. 1977. Heat Flow in the United States and the Thermal Regime of the Crust. In H. G. Heacock (Ed.), *The Earth's Crust*, Volume Geophysical Monograph 20, pp. 626–675. Washington, DC: American Geophysical Union.

McKenna, S. A. and C. A. Rautman. 1995. *Summary Evaluation of Yucca Mountain Surface Transects with Implications for Downhole Sampling.* SAND94-2038, Sandia National Laboratories, Albuquerque, NM.

Rautman, C. A., L. E. Flint, A. L. Flint, and J. D. Istok. 1995. *Physical and Hydrologic Properties of Rock Outcrop Samples From a Nonwelded to Welded Tuff Transition, Yucca Mountain, Nevada.* Water-Resources Investigations Report 95-4061, United States Geological Survey, Denver, CO.

Rousseau, J. P., E. M. Kwicklis, and D. C. Gillies (Eds.). 1996. *Hydrogeology of the Unsaturated Zone, North Ramp Area of the Exploratory Studies Facility, Yucca Mountain, Nevada*, Water-Resources Investigations Report 96-????, Denver, CO. United States Geological Survey. Draft dated 8/29/96.

Sass, J. H. and A. H. Lachenbruch. 1982. *Preliminary Interpretations of Thermal Data from the Nevada Test Site.* Open-File Report 82-973, United States Geological Survey, Reston, VA.

Sass, J. H., A. H. Lachenbruch, W. W. Dudley, Jr., S. S. Priest, and R. J. Munroe. 1988. *Temperature, thermal conductivity, and heat flow near Yucca Mountain, Nevada: Some tectonic and hydrologic implications.* Open-File Report 87-649, United States Geological Survey, Denver, CO.

Sass, J. H., A. H. Lachenbruch, and C. W. Mase. 1980. *Analysis of Thermal Data From Drill Holes UE25a-3 and UE25a-1, Calico Hills and Yucca Mountain, Nevada Test Site.* Open-File Report 80-826, United States Geological Survey, Menlo Park, CA.

Schenker, A. R., D. C. Guerin, T. H. Robey, C. A. Rautman, and R. W. Barnard. 1995. *Stochastic Hydrogeologic Units and Hydrogeologic Properties Development for Total-System Performance Assessments.* SAND94-0244, Sandia National Laboratories, Albuquerque, NM.

Schmidt, M. R. 1989. Classification of Upland Soils by Geomorphic and Physical Properties Affecting Infiltration at Yucca Mountain, Nevada. Master's thesis, Colorado State University, Fort Collins, CO.

Scott, R. B. and J. Bonk. 1984. *Preliminary Geologic Map (1:12,000 scale) of Yucca Mountain, Nye County, Nevada, with Geologic Cross Sections.* Open-File Report 84-494, United States

Geological Survey, Denver, CO.

Šimůnek, J., T. Vogel, and M. T. van Genuchten. 1992. *The SWMS_2D code for simulating water flow and solute transport in two-dimensional variably saturated media V. 1.1.* Research Report No. 126, U. S. Salinity Laboratory, ARS USDA, Riverside, CA.

Stothoff, S. A. and A. C. Bagtzoglou. 1995. Estimation of Recharge at Yucca Mountain, Nevada. In *Supplement to Eos, Transactions*, Volume 76, Washington, DC, pp. F242. American Geophysical Union.

Stothoff, S. A. and A. C. Bagtzoglou. 1996. Subregional Hydrogeologic Flow and Transport Processes. In B. Sagar (Ed.), *NRC High-Level Radioactive Waste Research at CNWRA, July–December 1995*, Volume CNWRA 95-02S, San Antonio, TX, pp. 9–1–9–20. Center for Nuclear Waste Regulatory Analyses.

Stothoff, S. A., A. C. Bagtzoglou, and H. Castellaw. 1996. Estimation of Spatial Distribution of Recharge Factors at Yucca Mountain, NV. In *Proceedings of the International Conference on Application of Geographic Information Systems in Hydrology and Water Resources Management*, Vienna, Austria. International Association of Hydrological Sciences.

Stothoff, S. A., H. M. Castellaw, and A. C. Bagtzoglou. 1995. Estimation of Spatial Distribution of Recharge Factors at Yucca Mountain. In B. Sagar (Ed.), *NRC High-Level Radioactive Waste Research at CNWRA, January–June 1995*, Volume CNWRA 95-01S, San Antonio, TX, pp. 9–5–9–12. Center for Nuclear Waste Regulatory Analyses.

Sykes, J. F., J. L. Wilson, and R. W. Andrews. 1985. Sensitivity Analysis for Steady State Groundwater Flow Using Adjoint Operators. *Water Resources Research 21*(3), 359–371.

Yang, I. C., G. W. Rattray, and P. Yu. 1996. *Interpretations of Chemical and Isotopic Data From Boreholes in the Unsaturated Zone at Yucca Mountain, Nevada.* Water-Resources Investigations Report 96-4058, United States Geological Survey, Denver, CO.

2. Ambient Hydrology KTI – Hydraulic Properties

Account Number: **20-5708-861**
Collaborators: **Jim Winterle, Gordon Wittmeyer**
Directories: **$HOME2/AmbientKTI/3Ddata and as noted**

Objective: Perform detailed analysis of the spatial distribution of hydraulic properties at YM and their effects on flow. Topics include investigation of USGS-measured properties and analyses, as well as predictions of their impact on flow.

Some of the work was documented in the notebook chapter entitled "Ambient Hydrology KTI – Infiltration." This chapter was created on October 10, 1997, immediately following the October 8, 1997, printout of the scientific notebook. Relevant prior entries in the other chapter were moved to this chapter upon creation of the chapter, in order to improve clarity of presentation in both chapters.

8/29/96 Revisiting PTn modelling ideas.

SAS

Further discussions with English and Sitakanta suggest that examining the behavior of the PTn layer may be of the most direct use to PA. For example, the appropriateness of the various models for flow in the subsurface can be examined (i.e., ECM versus dual-permeability versus weeps) by examining the time behavior of pulses reaching the top of the PTn layer. If extremely long time scales at the bottom of the PTn are observed, the ECM model may be in order. If extremely short time scales are observed, the weeps model is in order. Intermediate cases presumably would require the dual-permeability model).

A second question that can be examined is the issue of the spatial distribution of fluxes leaving the PTn layer. There are direct implications for the distribution of fluxes at the drift scale, since the TSw units are relatively homogeneous from the PTn to the repository. My conceptual model of drift-scale processes under ambient conditions has high relative humidity at all flow packages and relatively few packages contact a dripping fracture (i.e., dripping fractures are widely spaced). In this case, the drips are a strong focussing mechanism, shielding most surrounding packages. Studying the behavior of the PTn layer may shed some light on the relative spacing of dripping fractures.

9/21/96 Setting up 1D PTn modelling. SAS

Two detailed sources of information are available for unsaturated-zone tuff properties, Rautman et al. (1995) and Flint et al. (1996). The Rautman et al. (1995) data set is finely resolved in both the lateral and vertical directions, but only covers part of the PTn layer and does not provide van Genuchten properties for the samples. The Flint et al. (1996) data set consists of 8 transects, covering the full range of layers in less detail. The Flint et al. (1996) data set does provide several measurements of van Genuchten properties, however.

The Flint et al. (1996) data set will be used to test the behavior of wetting pulses, since it provides a much longer vertical transect (the Solitario Canyon transect, in particular) and some van Genuchten information. Two approaches are immediately obvious: (i) use average layer thicknesses and properties, based on Tables 2, 5, and I-1; and (ii) use Table I-1 for fullest spatial resolution but supplement properties as necessary. The idea would be to assume fracture flow with the wetting pulses translated undamped from surface conditions as a top boundary condition, with the top boundary at the top of the shardy base of the Tiva Canyon Tuff, and use gravity drainage bottom conditions in fractures to correspond to the Topopah Spring Tuff vitric caprock and lower layers. There are between 20 and 25 measured K_{sat} values within the roughly 35 m section of the transect of interest, with perhaps 35 additional core samples that do not have K_{sat} values. It is not clear whether the reported transect distance is vertical distance, horizontal distance, or along-ground distance, but assuming that the slope is roughly 30 degrees in this region, the vertical section of nonwelded tuff is about 20 m, about twice the thickness considered by Rautman et al. (1995).

As a first cut, the detailed stratigraphy implied by Table I-1 of Flint et al. (1996) will be assembled into detailed layering. For points where K_{sat} and van Genuchten properties are missing, the regressions provided by Tables 3 and 6 will be used. Between each data reading, K_{sat} and van Genuchten α will be loglinearly interpolated and van Genuchten n will be linearly interpolated. Initial conditions will be provided by using the steady-state vertical ODE approach discussed in the PA Research and Ambient Hydrology projects.

The regression equation for K_{sat} as a function of porosity for the welded and nonwelded portions of the Solitario Canyon transect in Table 3 of Flint et al. (1996), based on 36 samples and with an r^2 value of 0.90, is:

$$K_{sat} = -13.9 + 33.1\varepsilon - 30.8\varepsilon^2, \tag{2-1}$$

where K_{sat} is in m/s. Based on Figure 11, it appears that the regressed equation is actually for $\log_{10}(K_{sat})$, which makes much more sense.

From Table 6 of Flint et al. (1996), based on 10 samples and with r^2 values of 0.01 and 0.44 for van Genuchten α and n, respectively, the regression relationships are:

$$\alpha = 0.49 + 0.31\varepsilon, \tag{2-2}$$

$$n = 0.95 + 1.94\varepsilon, \tag{2-3}$$

where α is in units of MPa^{-1}.

Parenthetical note:

My suspicion is that the van Genuchten regression relationships could be significantly improved by solving for all samples simultaneously, since there is considerable latitude in changing the α and n parameters without greatly affecting the fit between data and formula. The simultaneous-solution procedure minimizes the least-squares sum of squares,

$$Y = \sum_{i=1}^{N} [\theta_i - \hat{\theta}(P_i)]^2, \tag{2-4}$$

where θ_i is a measured saturation value and $\hat{\theta}$ is the corresponding predicted saturation value for measured pressure P_i. The prediction formula is

$$\hat{\theta} = \hat{\theta}(\alpha, n, \theta_{res}, P), \tag{2-5}$$

$$\alpha = C_0 + C_1\varepsilon, \tag{2-6}$$

$$n = C_2 + C_3\varepsilon, \tag{2-7}$$

$$\theta_{res} = C_4 + C_5\varepsilon. \tag{2-8}$$

The minimization takes place when the gradients of Y are zero, or

$$F = \frac{dY}{dC_j} = -2\sum_{i=1}^{N} [\theta_i - \hat{\theta}(P_i)] \frac{d\hat{\theta}_i}{dC_j} = 0. \tag{2-9}$$

Newton's method is convenient for this minimization, which simply states that for each iteration k,

$$J(\mathbf{x}_k) s_k = -F(\mathbf{x}_k), \tag{2-10}$$

$$\mathbf{x}_{k+1} = \mathbf{x}_k + s_k, \tag{2-11}$$

where $J(\mathbf{x}_k)$ is the Jacobian and $\mathbf{x}$ is the vector of unknowns C_j. It shouldn't be too difficult to check this out on the data presented by Flint et al. (1996).

9/24/96 First results from 1D PTn modelling. SAS

After a good deal of putting together *Matlab* code and some *breath* debugging, the first set of PTn simulations were run using the base-case infiltration traces for 2-cm and 5-cm colluvium over a fracture continuum. The 2-cm case has weekly outputs of flux, while the 5-cm case has daily flux outputs; both cases have fluxes that are higher than almost any pixel value would show, so the simulations are probably more extreme than will be observed in future work.

All work is done in ***/home2/sierra/stothoff/Matlab/PTnCheck***. The input files for *breath* are created using **fix_FFRI_dat.m**, which in turn uses **extract_qw.m**, **pre_ydot_setup.m**, and **ydot_setup.m**. The built-in *Matlab* ODE solver ode23s is used to create initial conditions for the temporal average of the input flux, using **ydot_setup.m**. Output is examined using **show_stuff.m** and **new_show_seq('t', 'nf\1;col\co;plot\pl;nseq\1;last\10')**.

Several cases were tried, varying (i) the assumption for the continuum underlying the PTn layer and (ii) the input flux case. The 2-cm input-flux case was run using 2 m of fracture continuum, 2 m of TS58 material, and 20 m of TS58 material. The last material case was also run using the 5-cm input-flux case. All cases use 5-cm nodal spacing.

Several observations were made:

- The fracture continuum below the PTn causes time steps on the order of 3 seconds, while simulations using the matrix below complete in minutes of CPU time.
- The steady-state moisture profile is very different for fractures underlying the matrix and for tuff underlying; the fractures cause the PTn to be essentially saturated in locations, while the tuff allows much drier profiles *even with the same flux.*
- The flux distribution is very peaky. Over the period of a day, fluxes can jump by 4 orders of magnitude, then decay exponentially.
- The flux pulse propagates essentially instantaneously (less than a day) through the PTn layer, but the pulse magnitude decreases exponentially with depth.
- The moisture content responds by a few percent in the same timeframe.
- The gravity drainage condition 2 m below the bottom dampens the peakiness significantly relative to the 20-m depth.

- There are roughly 2 pulses a year, although the pulses are clumped. As the colluvium depth increases further, the number of pulses will decrease.

There are several implications to the work:

- Capturing flux pulses with moisture-content readings may be a hopeless endeavor.
- Steady-state assumptions may be appropriate for calculating moisture contents.
- Using the gravity-drainage assumption with moisture contents must be examined carefully, since structural features and heterogeneity can modify moisture contents without modifying fluxes.
- It may not be that bad to use the ECM assumptions below the PTn, as there is indeed strong damping in the input signal.

The current *breath* approach must be augmented to provide more realistic simulations. In particular, it is still not possible to check the ECM assumptions since there is no possibility for more than one continuum below the PTn. Also, the saturation profile in the PTn is strongly impacted by the lower-layer assumptions. An approach that may bear fruit is to allow several continua to dangle off the bottom of the PTn, each independent except that the same pressure exists in each one at the bottom of the PTn. One continuum might be the matrix, with the rest being fracture sets. Occasional lower cross-links between the fracture continua might okay.

The augmented approach would allow the investigation of which fracture set(s) kick in, if any. In addition, the saturation in each set may be able to be translated into an equivalent wetted length, which can than be used to intersect with the drifts.

It may be considerably more difficult to construct a steady-state solver for this case, since there are multiple threads of flux joining at a middle node. Shooting may be necessary.

3/23/97 Data from DOE. SAS

A CD-ROM disk was received from L. Flint about two weeks ago that contains the entire set of matrix-property core-sample measurements from 31 boreholes, including 23 neutron-probe boreholes and 8 deeper boreholes. A total of nearly 5000 samples have properties reported. The CD-ROM disk is entitled "Matrix Properties" and is dated 3/2/97. The CD-ROM disk has one

file, entitled **database.wk4**, which is a file in Lotus 1-2-3 version 4.0 format. The CNWRA does not have software current enough to be capable of reading this format; however, the Net Force contractors to the CNWRA were able to convert the file to Lotus 1-2-3 version 3.0 format, which is capable of being read. E. Pearcy was able to pull this into Excel and output it in tab-delimited ASCII form. I stored both the Lotus 1-2-3 version 3.0 file, entitled **database.wk4**, and the tab-delimited ASCII form, entitled **usgs_borehole_db.asc**, in ***$HOME2/AmbientKTI/3Ddata***. The original CD-ROM will be delivered to B. Mabrito and stored in the QA vault.

A second set of data was obtained from the NRC, which consists of a 8-mm tape that copies a CD-ROM with numerous ARC-VIEW coverages stored as 99 themes. The themes range from base-map information (e.g., Nellis Air Force Range boundaries, roads) through contour maps, borehole locations, ecological study plots, a digitized version of the Scott and Bonk stratigraphy, and various other information. The files take up roughly 31 Mb. The original CD-ROM resides at the NRC offices. The CD-ROM was accompanied by a user's guide dated May 1, 1996, with 18 pages plus 3 appendices. I am maintaining the tape in my office until the information can be transferred to disk in an accessible location.

8/31/97 Investigation of USGS UZ properties. SAS

Files for the following investigations can be found in ***$HOME2/AmbientKTI/3Ddata***.

On 8/28, Amit Armstrong requested that I provide estimates of the layer properties for the TPA sensitivity exercises. The idea is to use the microstratigraphy property information (including porosity, particle density, and K_{sat}) provided by Flint (1996), in conjunction with the layer microstratigraphy thicknesses extracted from the recently obtained DOE Earthvision model, to estimate the equivalent thicknesses of the TPA subareas. Amit provided layer thicknesses and a mapping of the sublayers into the TPA layers.

In Table 7 of the Flint (1996) report, K_{sat} for the individual sublayers is reported as a mean and a standard deviation. The K_{sat} mean statistics are reported for three cases: (i) geometric mean of raw K_{sat} values, (ii) power-law mean of raw K_{sat} values, and (iii) geometric mean of K_{sat} values derived from regression equations applied to all measured porosities. In each case, the standard deviation is reported on the raw values. The combination of log-10 mean and base-10 standard deviation renders these statistics unsuitable for coming up with a distribution.

This spring, Lorrie Flint sent me the database used in the Flint (1996) report. The database includes UZ core properties from 31 boreholes. I have not had a chance to examine the database in

detail, but this represents a good opportunity to digest it. I created two *Matlab* routines (extract_k.m and show_pdk.m) to extract information from the database and to show results. A total of 589 K_{sat} measurements were made, of which 188 were less than 5×10^{-12} m/s (0.16 mm/yr). At first blush, the raw K_{sat} statistics would be best to use for estimating layer properties; however, as the numerous low-K_{sat} measurements are not considered in the statistics for the raw values, second thought suggests that it may be appropriate to use the far more numerous porosity samples to estimate properties.

There have been a number of UZ formation classification schemes at YM. In Table 1 by Flint (1996), correspondences between the classification scheme of Buesch et al. (1996), Scott and Bonk (1984), and Montazer and Wilson (1984) are shown. For the most part, correspondences are clearly denoted, although based on comparing Figure 12 by Flint (1996) and a direct plot, it appears that there may be discrepancies in the assignment of units:

- Although apparently assigned to the TC hydrogeologic unit in Table 1, all of the Tptrn unit with porosity less than a cutoff value (perhaps 9 percent?) seemed to have been assigned to the TR hydrogeologic unit in Figure 12.
- There are two high-porosity, low-K_{sat} outliers not shown in Figure 12 (from the BT2 and BT4 units, respectively).

Flint (1996) provides regression relationships between porosity and the remaining hydraulic properties, as porosity is far easier to measure than most other properties. Three categories are identified: (i) microfractured, (ii) altered, and vitric/crystallized.

The microfractured category has samples from vitrophyres assigned to it (i.e., Tptrv1 and Tptrv3 from the Topopah Spring Tuff). The microfractured category reportedly includes the TC and PV3 hydrogeologic units. In addition, one sample each from the crystallized and welded Tptrn, Tptpul, and Tptpln units is assigned to the microfractured category due to visible microfractures.

The altered category includes all lithostratigraphic units below the vitric/zeolitic boundary (BT1, CHZ, BT, PP4, PP3, PP2, PP1, BF3, and BF2) plus the CMW (an altered portion at the base of the Tiva Canyon formation). As Flint (1996) notes, there are crystallized and vitric units within the "altered" category, but the assignment was done for simplicity in developing predictive equations.

The vitric/crystallized category includes everything left over after the other categories are considered.

Although one can wish that the hydrogeologic layers would be relatively homogeneous within each layer, unfortunately the properties are not necessarily homogeneous. As can be seen in the section of borehole SD7 displayed in Figure 10 by Flint (1996), zeolites occur in samples from the CHV, CHZ, BT, PP4, PP2, and PP1 hydrogeologic layers, while zeolites are missing from samples in the BT1, CHV, PP3, PP2, and BF3 hydrogeologic layers. Flint (1996) suggest that the presence of alteration can be estimated by a significant change in porosity after drying at elevated temperatures. Two porosity measurements were obtained for each sample: (i) dried at a temperature of 60 °C and a relative humidity of 65 percent, and (ii) dried at 105 °C and an ambient relative humidity ($<$ 20 percent). Flint (1996) suggests that if the two porosity measurements differ by 0.05, the sample is altered. Areas in SD7 with the 5-percent differential porosity but not having zeolites (in the form of clinoptilolite) are reported to have vapor-phase minerals tridymite and cristobalite, although elevated cristobalite without tridymite does not exhibit the differential porosity.

Other areas with the 5-percent differential are pointed out as occurring at the base of the Tiva Canyon Tuff, and are attributed to alteration to clay (such as smectite). It is pointed out that the extent of alteration appears to be related to the topographic location of the borehole. Boreholes in narrow upwash channels may receive more frequent runoff, hence infiltration maintains higher water contents. Flint (1996) implies that alteration to clay is due to wet conditions. Despite the presence of the differential, these altered high-porosity samples tend to also have high K_{sat}.

A method for discriminating between alteration to zeolites and alteration to clays is offered by Flint (1996) using measurements of particle density obtained in two ways: (i) calculated from bulk density and porosity, and (ii) directly measuring the volume of the solid particles using helium pycnometry. Approximately 180 samples from UZ16 (judging from Figure 11 by Flint (1996)) were analyzed using the two techniques. For zeolitic samples, the calculated particle density almost invariably was greater than the measured density, by an average of about 0.07 g/cm^3 (my estimate), and the measured particle density was always less than 2.5 g/cm^3. For nonwelded vitric samples, the calculated particle density was less than the measured density when the calculated density was less than 2.35 g/cm^3 and gradually switches above that value; however, the zeolitic samples tend to have a larger differential. The nonwelded vitric samples tend to have somewhat larger particle densities than the zeolitic.

The welded crystallized samples had calculated particle densities uniformly greater than 2.45 g/cm^3, while the densely welded vitric samples had calculated particle densities uniformly less than 2.45 g/cm^3. Three classes could be distinguished from these samples: (i) welded/crystallized, (ii) nonwelded vitric, and (iii) nonwelded zeolitic or densely welded vitric. Despite the usefulness of the technique, helium-pycnometric measurements did not appear to be made on the majority of

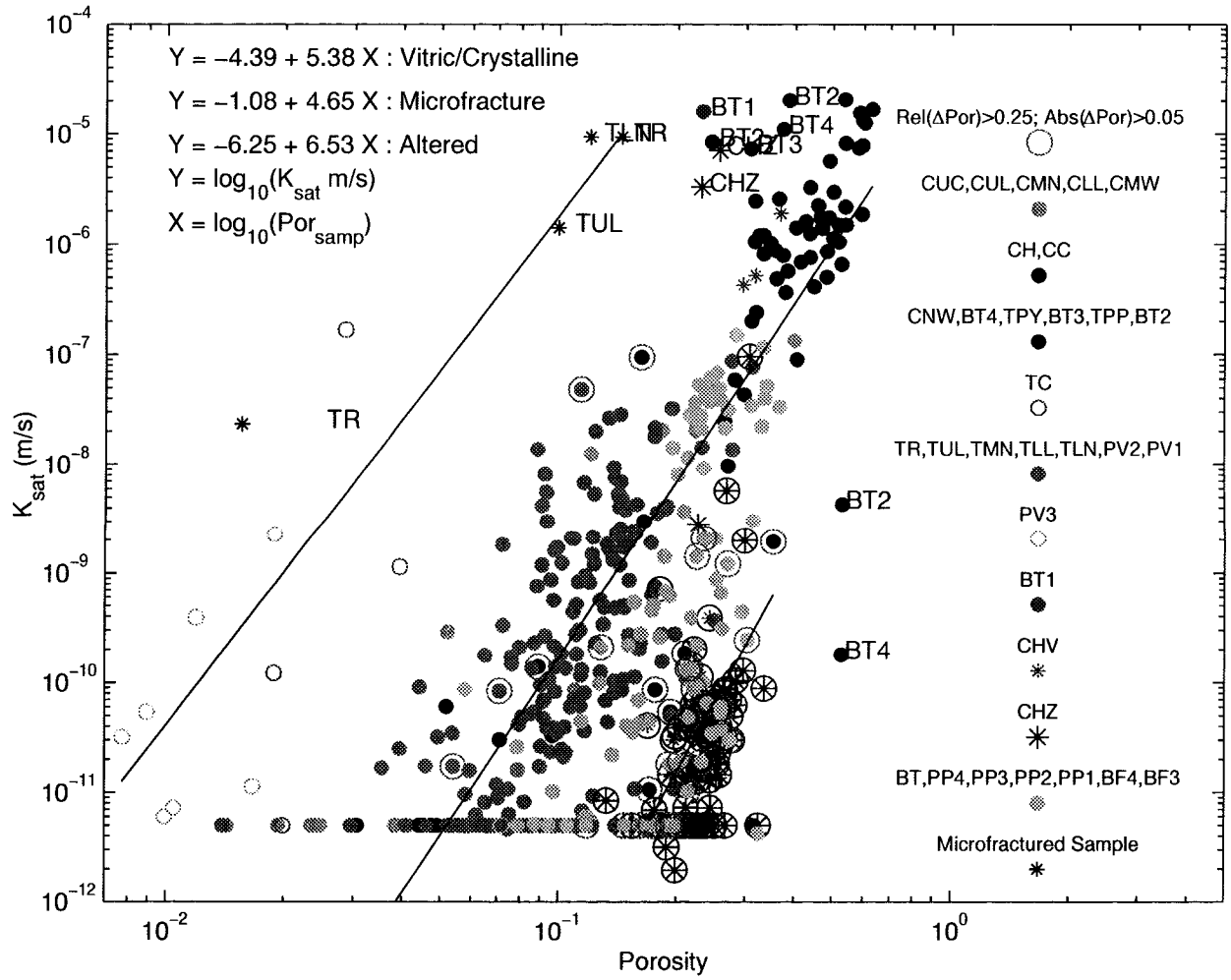

Figure 2-1: 8/31/97. The complete set of measured K_{sat} values in the USGS database.

YM samples.

The complete set of measured K_{sat} values in the database reported on by Flint (1996) are shown in Figure 2-1. The database reports three microstratigraphic classifications for each sample, corresponding to the Buesch et al. (1996) nomenclature: (i) formation (e.g., Tpc, Tpt); (ii) zone, where applicable (e.g., pul, rn); and (ii) subzone, where applicable (e.g., pv2, rv2). Where the formation has no subzones, the database repeats the zone identification for the subzone. The generating routine is *Matlab* show_pdk.m.arch091097.

In Figure 2-1, the microstratigraphic zones are grouped into the nomenclature of Montazer

and Wilson (1984) according to Table 1 of Flint (1996).

The samples considered microfractured are the TC and PV3 units (denoted with small circles), and obviously microfractured samples (denoted with black asterisks). For consistency with Figure 12 of Flint (1996), the TC unit consists of only the Tptrv1 subzone in Figure 2-1, even though the Tptrn subzone appears to be classified as TC in Table 1 of Flint (1996).

The remaining samples are color-coded, broadly by formation. Outlying samples are labeled according to unit. Classification into the BT1a and BT1 hydrogeologic units is not clear from Table 1 by Flint (1996); the one Tpbt1 sample was placed into the BT1 hydrogeologic unit. As alteration is a key component of the property-classification scheme proposed by Flint (1996), any sample meeting the 5-percent porosity-change criterion is circled.

Based on Figure 2-1, it can be argued that five general categories exist for the samples:

- Microfractured, low (< 0.05) porosity
- Microfractured, high (> 0.05) porosity
- Zeolitic
- Vitric/crystallized
- Inexplicably high (> 0.5) porosity, low-permeability

Flint (1996) lumps the first two categories, and never presents data in the last category. It is not clear where the high-porosity microfractured category turns into the vitric/crystallized category; some of the high-permeability bedded-tuff samples may fall into the microfractured category due to handling difficulties. It is also not clear where the zeolitic and the vitric/crystallized categories turn into each other; many of the "altered" samples in Figure 12 by Flint (1996) appear to fall squarely into the vitric/crystallized category.

9/9/97 Further investigation of USGS UZ properties. SAS

It is my feeling that a successful use of matrix properties to predict matrix K_{sat} should have one formula for all cases (except, perhaps, for the microfractured cases). Accordingly, I played with various forms of a predictive relationship and have come up with a set of formulae that better match the non-microfractured data than the estimates in the database provided by L. Flint. I

used a least-squares measure to make quantitative evaluations of the fit of the prediction to the measured data:

$$\log_{10}(M) = \left[\sum_{i=1}^{N}(Y_i - Y_{mi})^2\right]^{1/2}, \tag{2-12}$$

where M is the performance measure, Y_i is the ith predicted value of $\log_{10}(K_{sat})$, and Y_{mi} is the ith measured value of $\log_{10}(K_{sat})$.

There are a number of properties measured for each core sample, including:

- Bulk density (at 65 and 105 °C)
- Porosity (at 65 and 105 °C)
- Particle density (at 65 and 105 °C)
- Volumetric water content (at 65 and 105 °C)
- Saturation (at 65 and 105 °C)
- Tuff unit, zone, and subzone

In addition, some of the core samples have subsamples for which porosity and K_{sat} are measured.

I systematically tested all sets of 1-, 2-, 3-, and 4-parameter regression equations. The linear and loglinear predictions for each of the parameters were tested, as well as calculated absolute and relative change in particle density, bulk density, and porosity. In order to systematically test regression equations, I created a *Matlab* routine (test_usgs_regr.m) that ran through all possible combinations using all vitric/crystalline and altered samples with measured K_{sat} above the measurement limit (5×10^{-12} m/s) and porosity greater than 0.05. The samples denoted microfractured were not used, although I think that some of the samples retained could be classified microfractured.

For reference, performance measure M is 15.7 when using the estimated K_{sat} values in the database and is 19.1 when using a linear regression on subsample porosity (23.9 for $\log_{10}$ regression). The estimated K_{sat} values are thus off by a mean value of more than an order of magnitude (i.e., a factor of 16 for the USGS regression). The USGS regression also has 6 coefficients: two for the altered, three for the unaltered, and an exponent in the unaltered equation.

The best single regression fit (13.1) occurs, rather surprisingly, for $\log_{10}$ saturation at 65 °C. Saturation provides the single best predictor; all 4 values of M, for the 65 and 105 °C pairs (i.e.,

linear and $\log_{10}$), are better than the USGS estimate, which is based on classifying samples into bins and using two regression equations). Even better, only 2 coefficients are used.

A significant improvement occurs with one more variable, porosity. In this case, the best match occurs with saturation at 65 °C and the subsample porosity, with M dropping to 8.22. Considering three variables, the best match occurs with $\log_{10}$ of the subsample porosity, porosity at 65 °C, and volumetric water content at 105 °C, yielding an M value of 7.62. The case with four variables yields the same set as the 3-variable case, with the saturation at 65 °C added, and M drops to 7.46. Clearly the parsimonious selection would use two variables, a saturation and a porosity, with a total of 3 coefficients. Note that there is not a tremendous difference between predictions using different types of porosity measurement or water content measurement. Also note that the difference between the USGS estimate and the 2-parameter estimate in log space is $1.196 - 0.914 = 0.28$, which is a significant but not outstanding improvement.

The estimated K_{sat} using the best-fit 1-, 2-, and 3-parameter equations, as well as the USGS-estimated K_{sat}, are plotted as a function of the measured K_{sat} in Figure 2-2. The closer a point lies to the diagonal line, the better the fit. The *Matlab* routine generating the plots is archived as test_usgs_regr.m.arch091097 in ***$HOME2/AmbientKTI/3Ddata***.

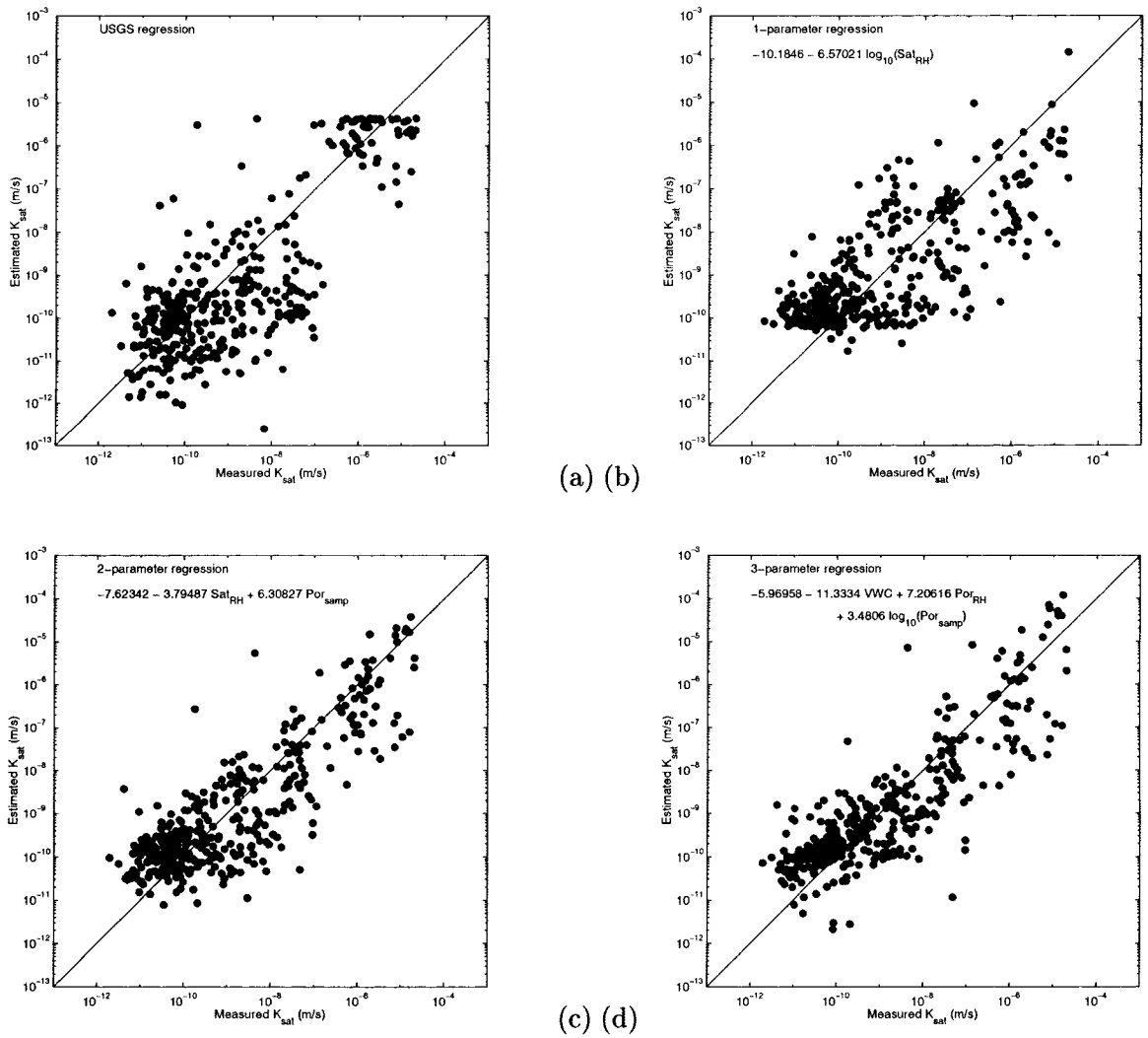

Figure 2-2: 9/9/97. Comparison of best-estimate K_{sat} and measured K_{sat} using (a) the USGS database, (b) the best 1-parameter regression, (c) the best 2-parameter regression, and (d) the best 3-parameter regression.

The best-fit regression equations are:

$$\log_{10}(K) = -10.1846 - 6.57021 \log 10(\theta_{65}), \tag{2-13}$$

$$= -7.62342 - 3.79487\theta_{65} + 6.30827\varepsilon_{sample}, \tag{2-14}$$

$$= -5.96958 - 11.3334VWC_{105} + 7.20616\varepsilon_{65} + 3.4806 \log_{10}(\varepsilon_{sample}), \tag{2-15}$$

where a subscript of 65 denotes the measurement at 65 °C, a subscript of 105 denotes the measurement at 105 °C, a subscript of *sample* denotes the subsample measurement, θ is saturation, ε is porosity, and VWC is volumetric water content.

In the following plots, important components of the regression equations are shown graphically for each borehole. Components include: (i) porosity at 65 °C (shown both as a bar height and a color); (ii) saturation at 65 °C; (iii) particle-density difference (absolute density by bar height, relative density by color); (iv) measured K_{sat} where available (blue dots); (v) estimated K_{sat} (USGS are green dots, best 2-parameter regression are red dots); (vi) formation identification. The *Matlab* routine generating the plots is archived as show_usgs_db.m.arch091797 in ***$HOME2/-AmbientKTI/3Ddata***. The *Matlab* routine converting the ASCII database into a *Matlab* binary (".mat") file is archived as make_flint_db_to_mat.m.arch091797, and the resulting file is archived as usgs_bhdb.mat.arch091797.

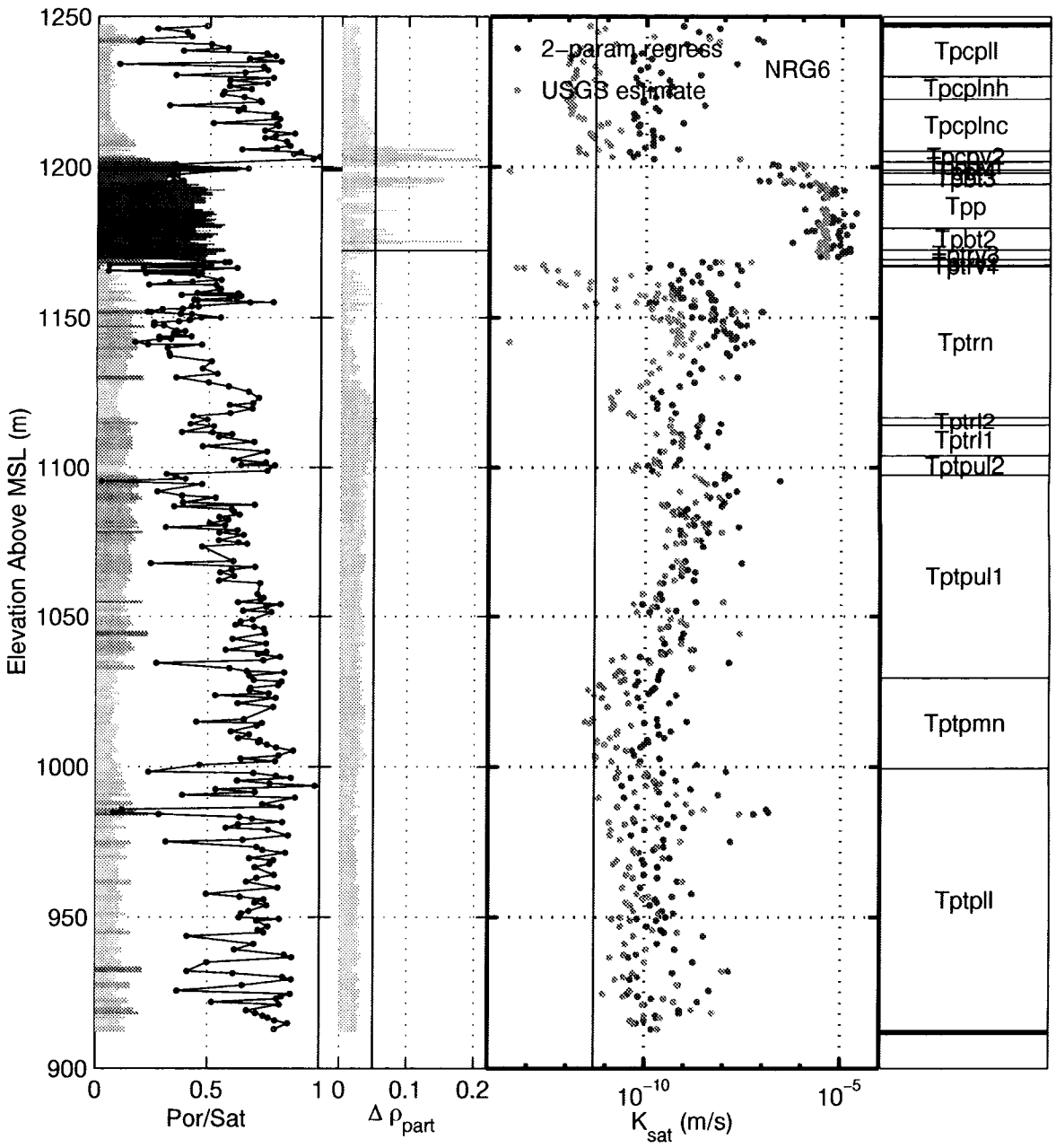

Figure 2-3: 9/9/97. **BHprofile_NRG6_c.eps**. Porosity, saturation, change in particle density, and measured and estimated values for K_{sat} in borehole NRG6.

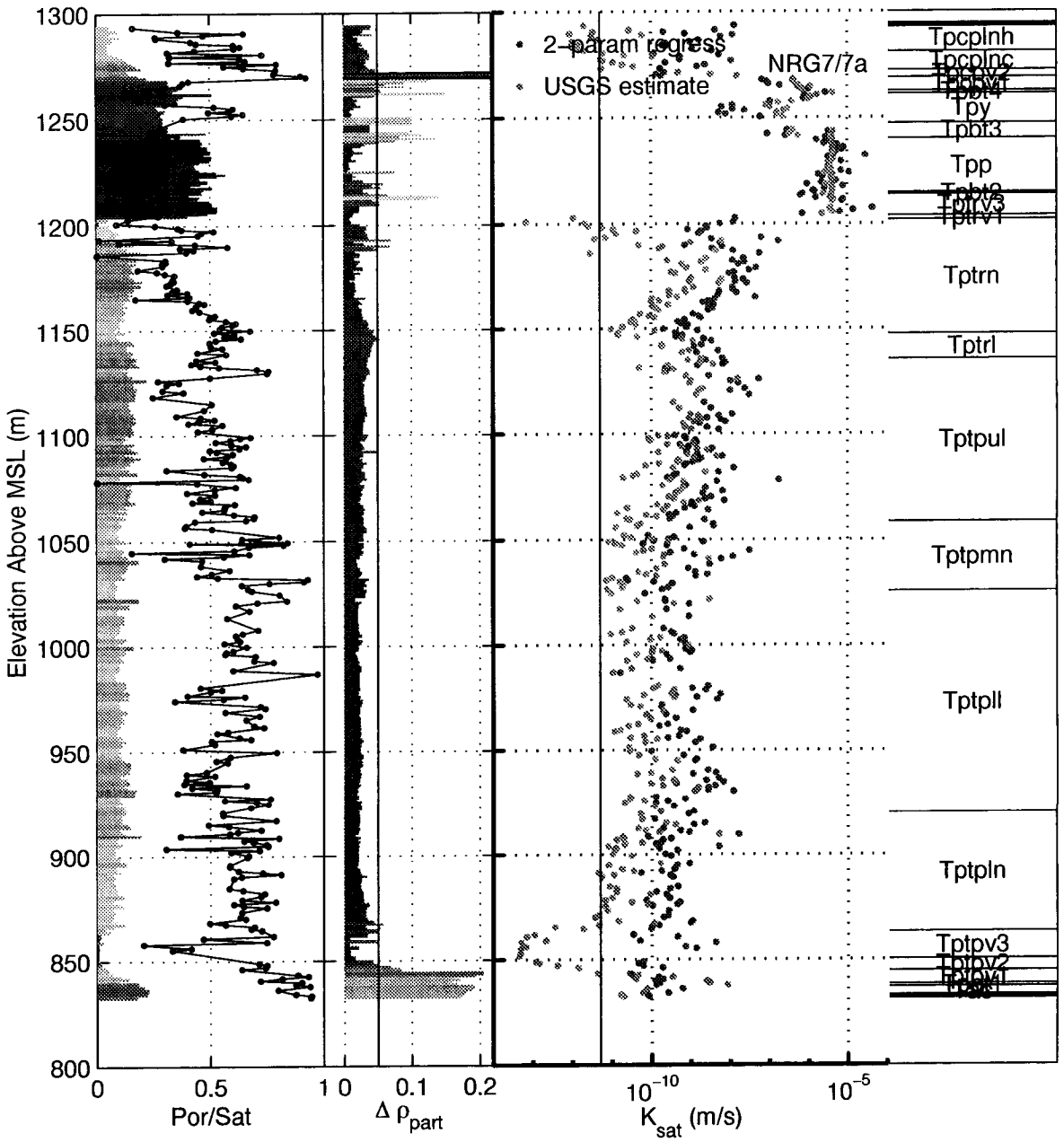

Figure 2-4: 9/9/97. **BHprofile_NRG77a_c.eps.** Porosity, saturation, change in particle density, and measured and estimated values for K_{sat} in borehole NRG7/7a.

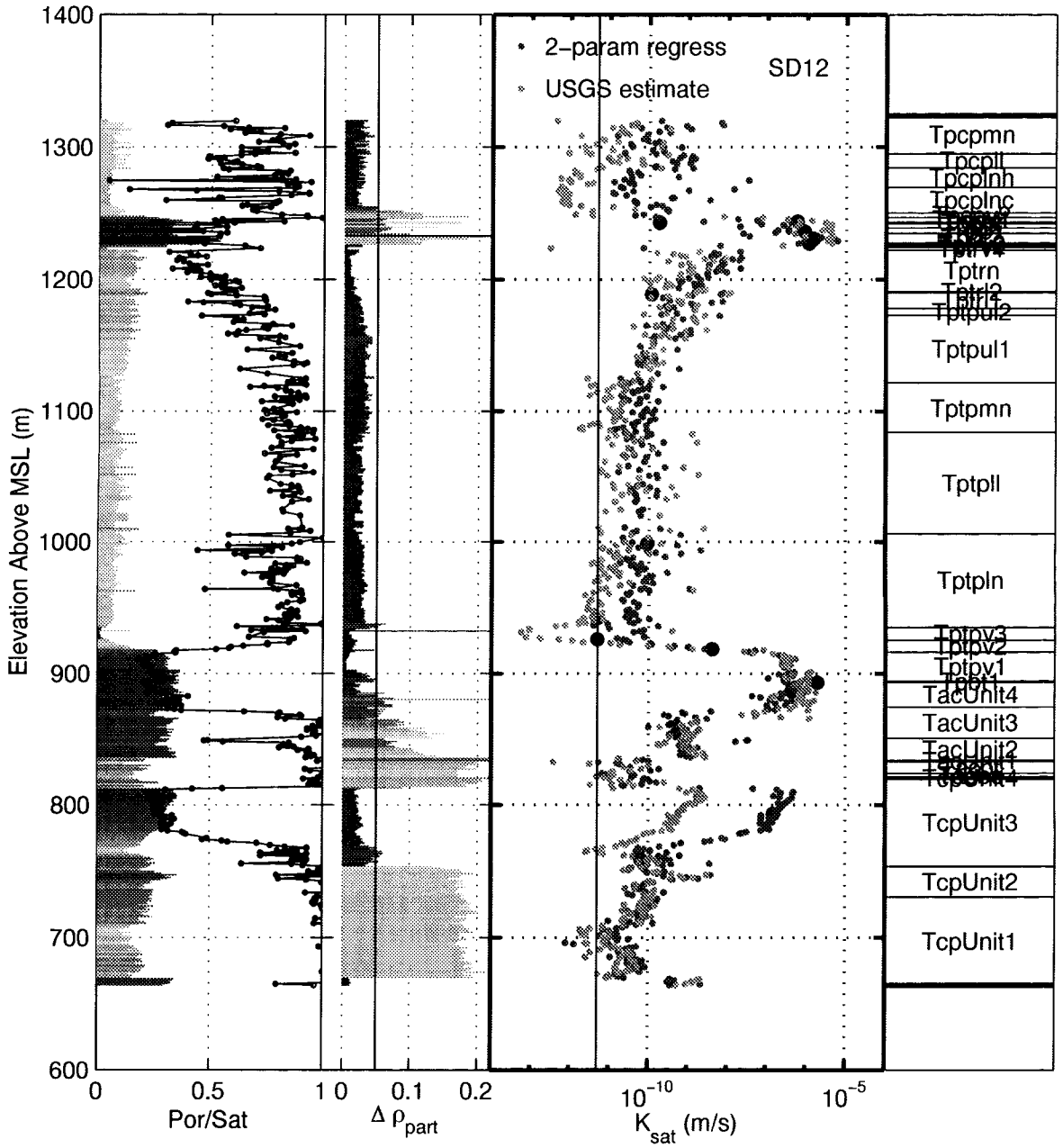

Figure 2-5: 9/9/97. **BHprofile_SD12_c.eps**. Porosity, saturation, change in particle density, and measured and estimated values for K_{sat} in borehole SD-12.

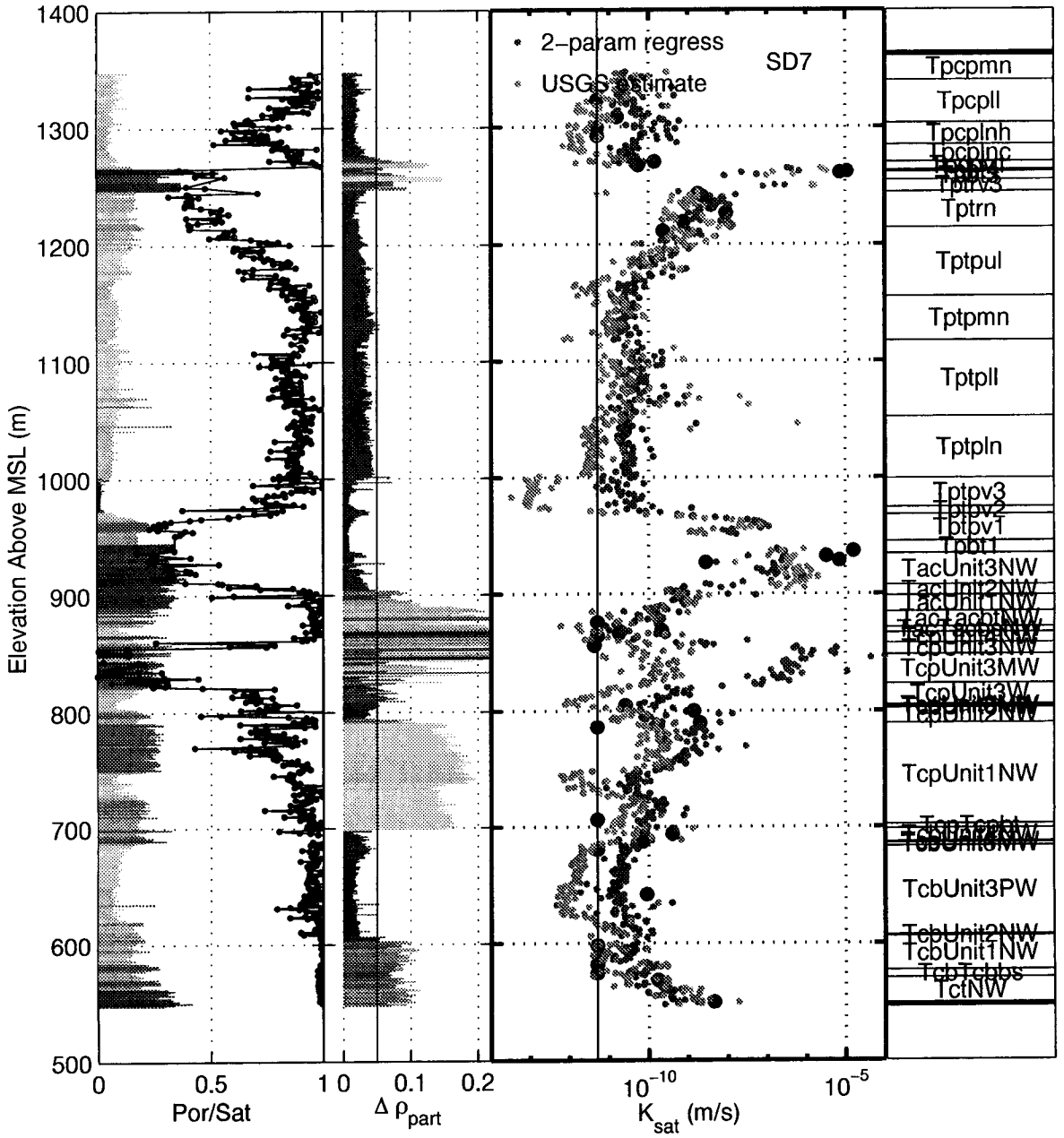

Figure 2-6: 9/9/97. **BHprofile_SD7_c.eps**. Porosity, saturation, change in particle density, and measured and estimated values for K_{sat} in borehole SD-7.

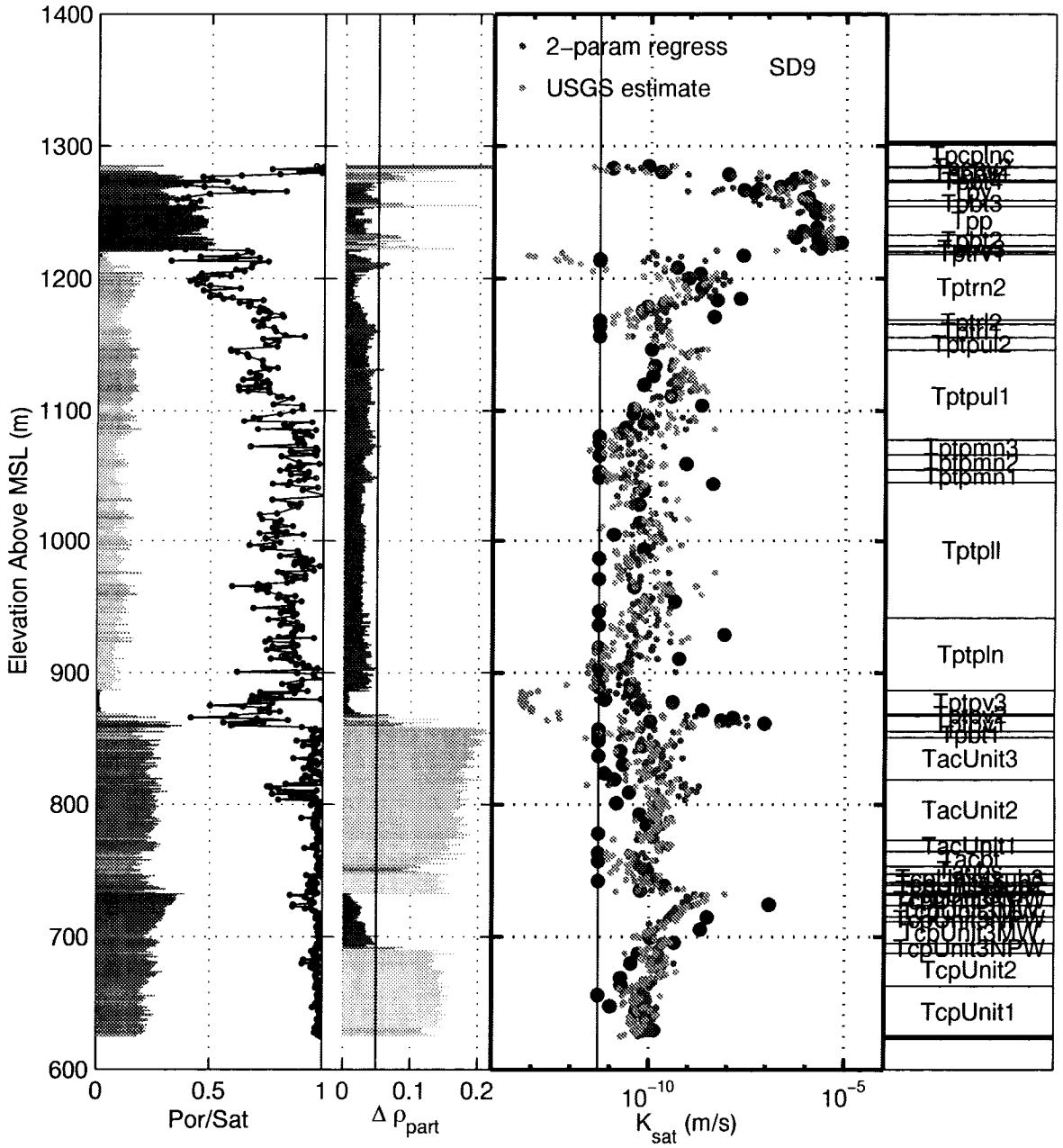

Figure 2-7: 9/9/97. **BHprofile_SD9_c.eps**. Porosity, saturation, change in particle density, and measured and estimated values for K_{sat} in borehole SD-9.

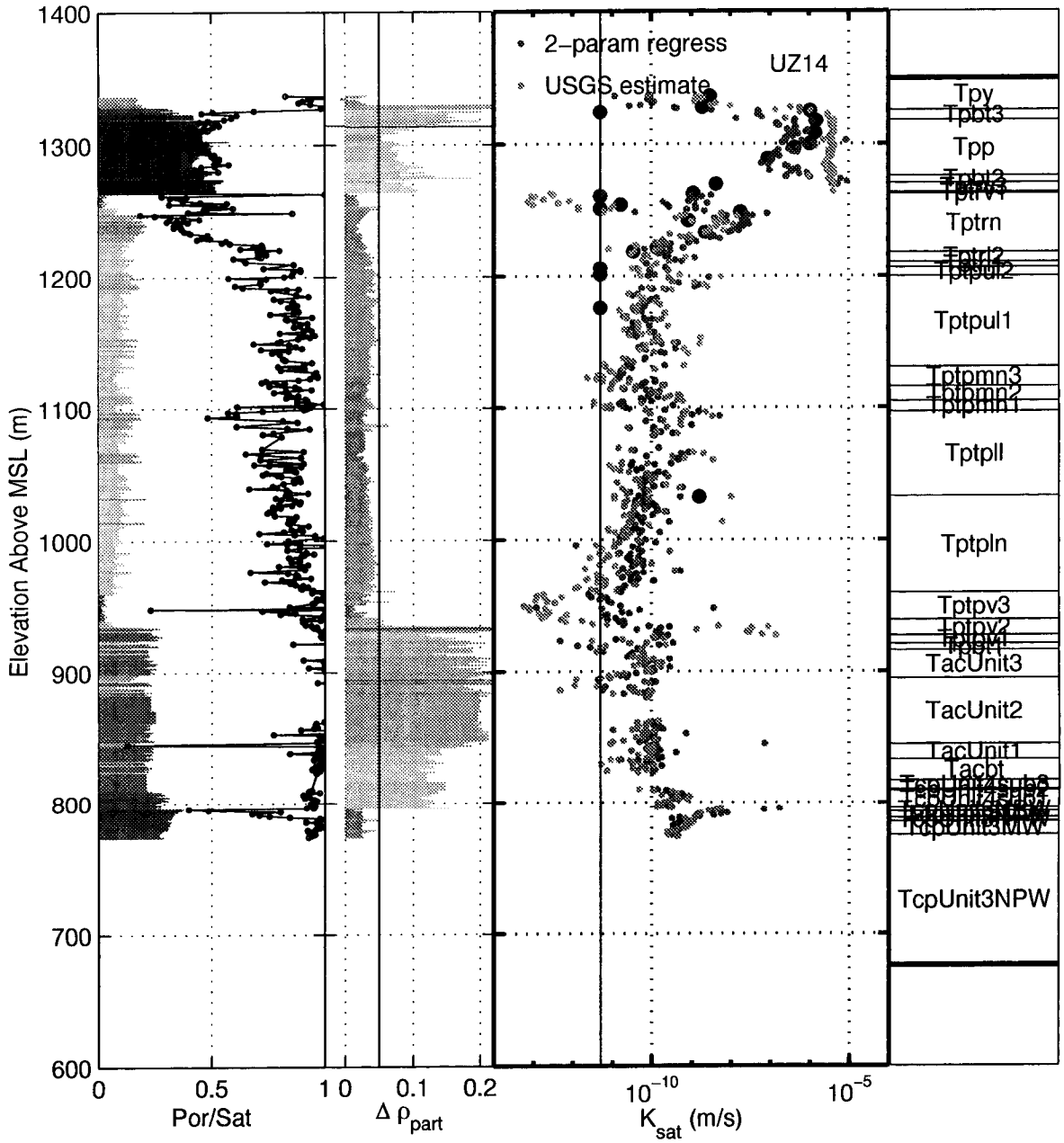

Figure 2-8: 9/9/97. **BHprofile_UZ14_c.eps.** Porosity, saturation, change in particle density, and measured and estimated values for K_{sat} in borehole UZ-14.

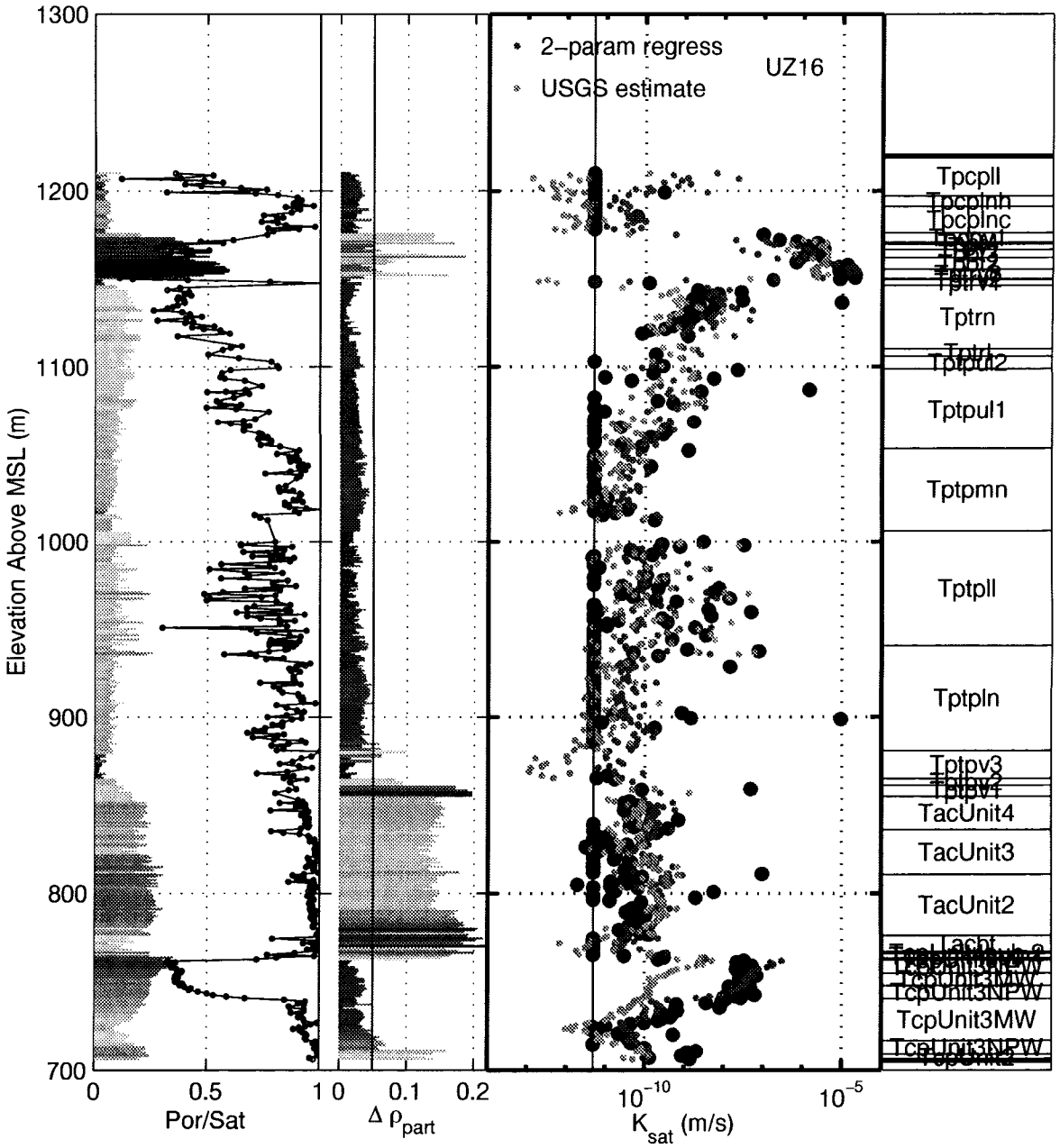

Figure 2-9: 9/9/97. **BHprofile_UZ16_c.eps**. Porosity, saturation, change in particle density, and measured and estimated values for K_{sat} in borehole UZ-16.

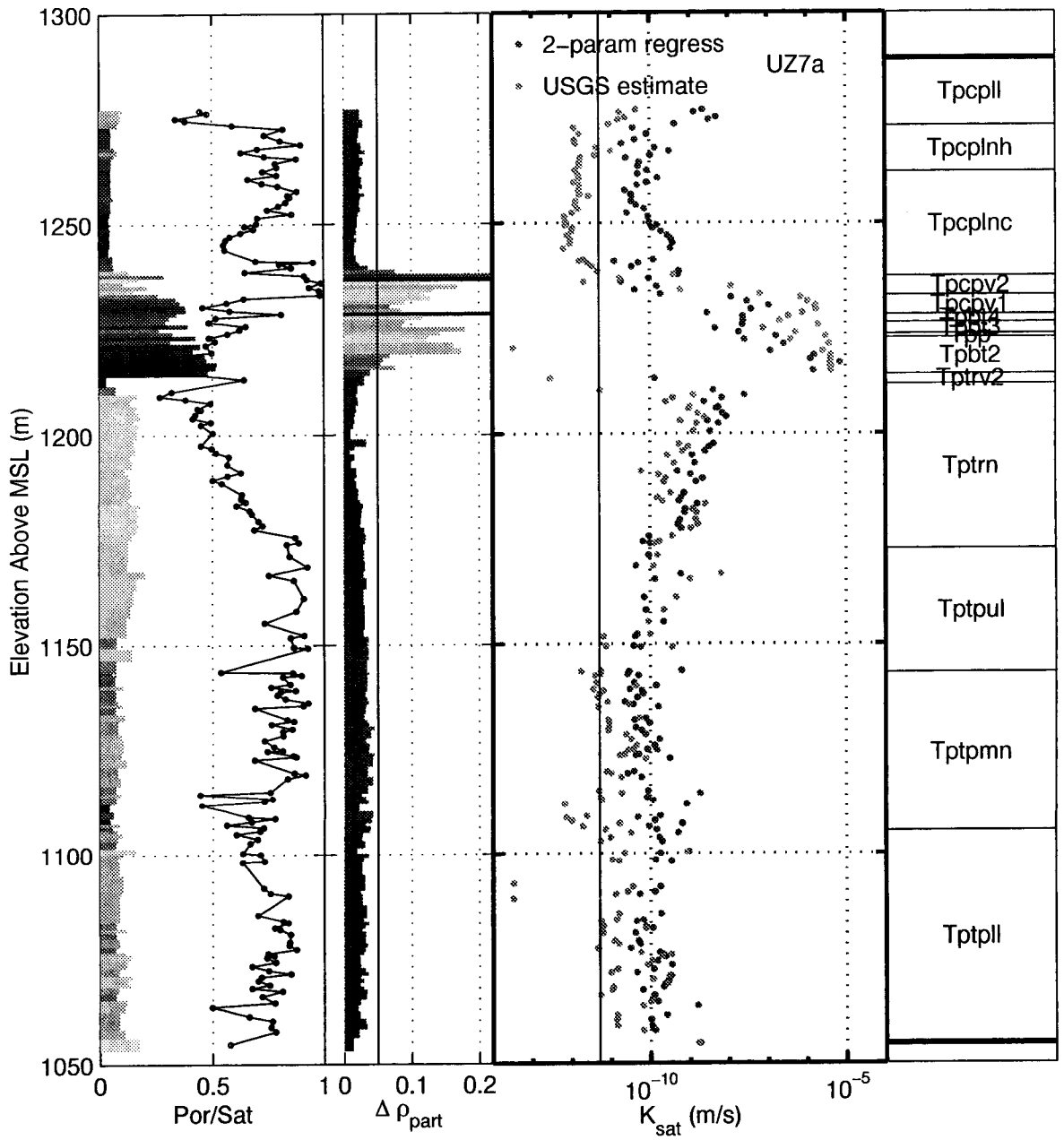

Figure 2-10: 9/9/97. **BHprofile_UZ7a_c.eps**. Porosity, saturation, change in particle density, and measured and estimated values for K_{sat} in borehole UZ-7a.

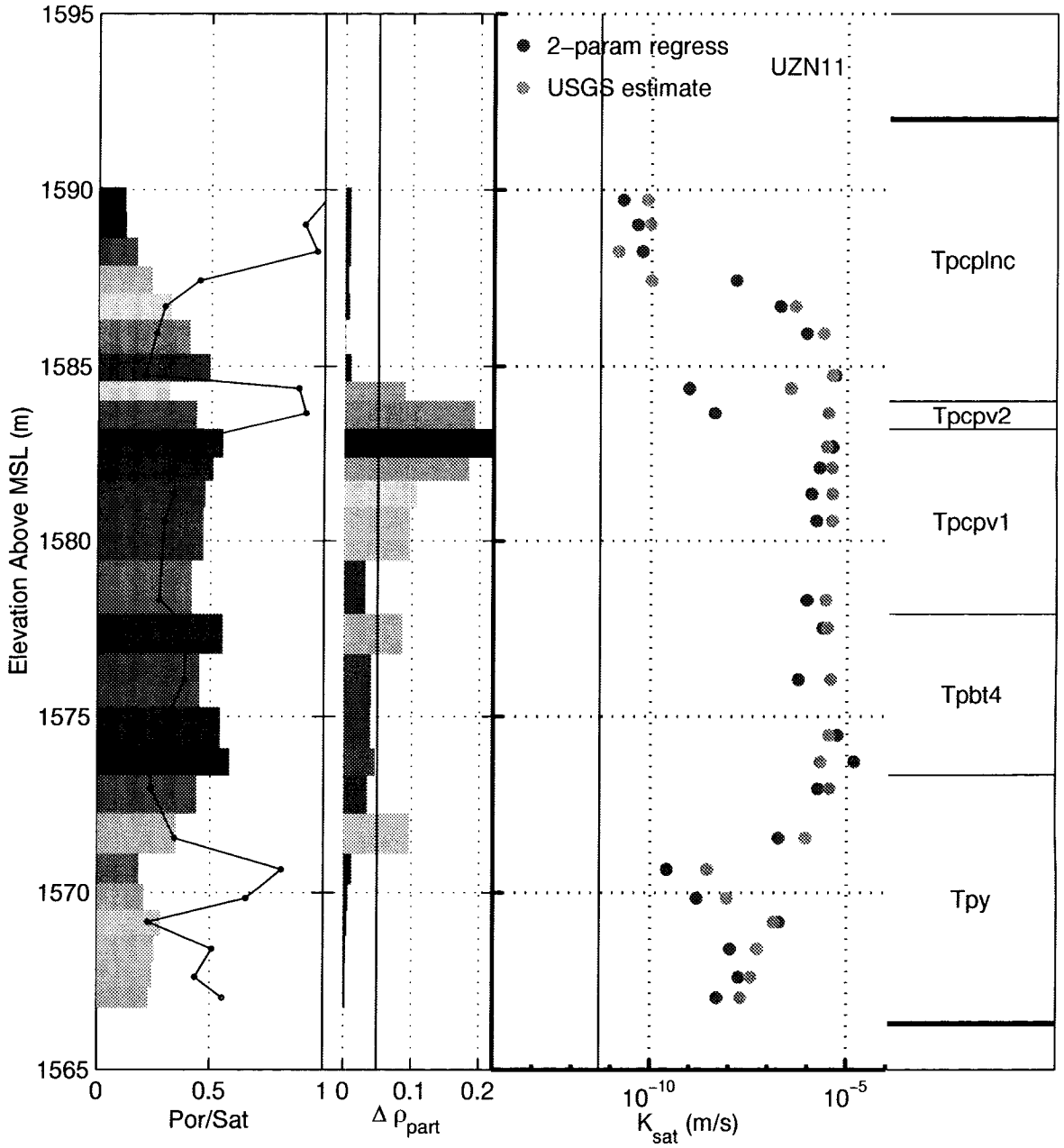

Figure 2-11: 9/9/97. **BHprofile_UZN11_c.eps**. Porosity, saturation, change in particle density, and measured and estimated values for K_{sat} in borehole N11.

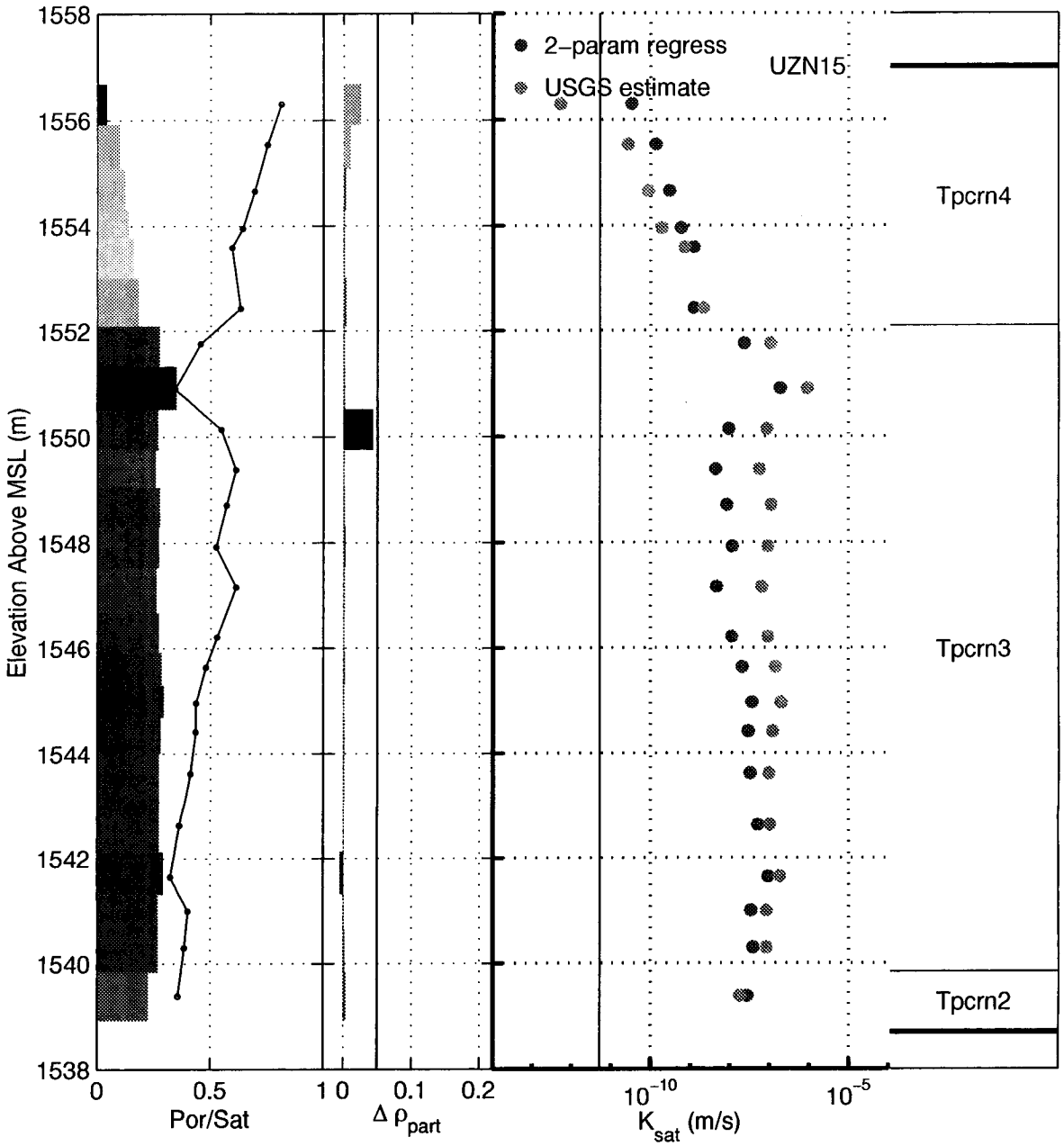

Figure 2-12: 9/9/97. **BHprofile_UZN15_c.eps**. Porosity, saturation, change in particle density, and measured and estimated values for K_{sat} in borehole N15.

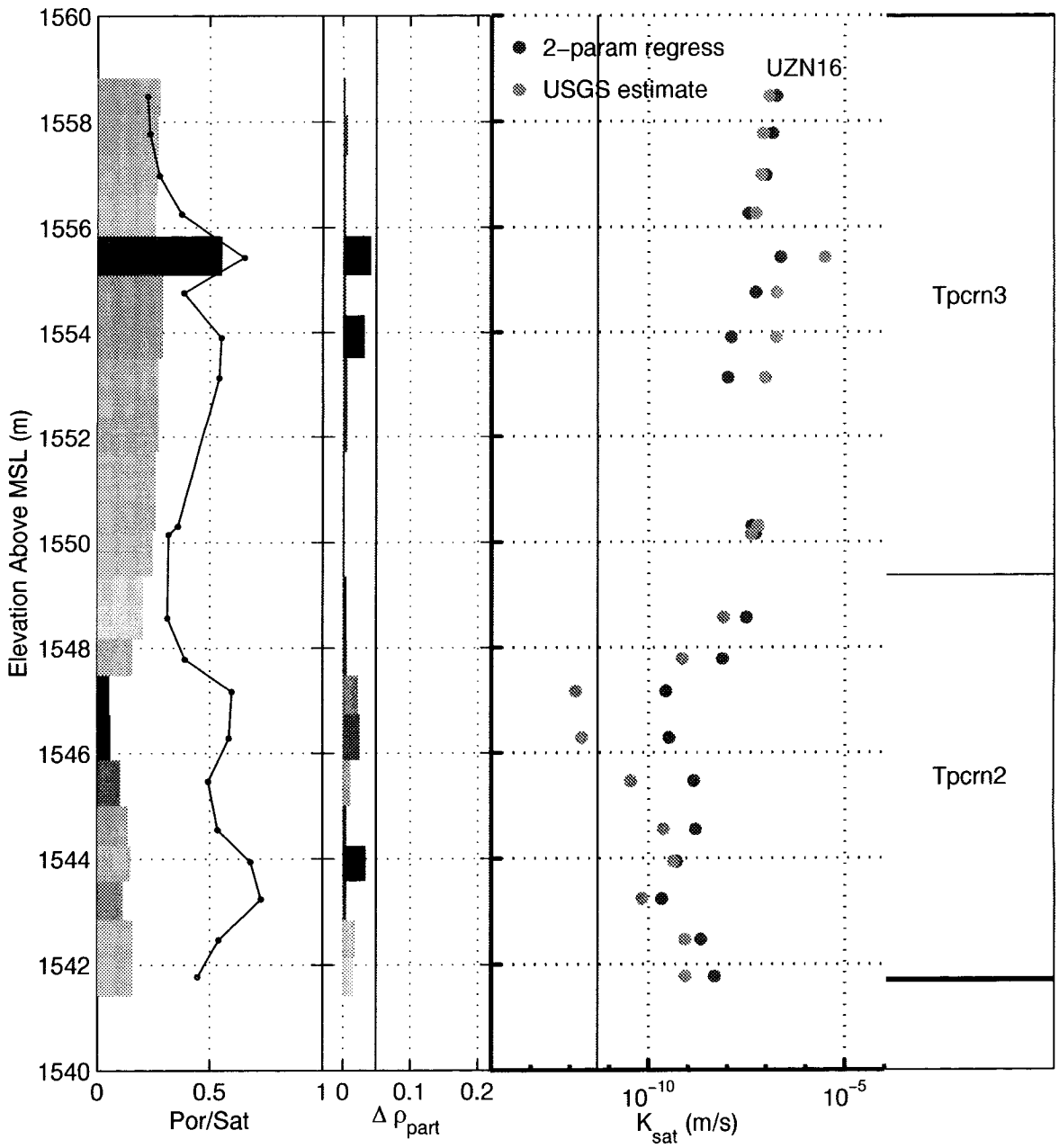

Figure 2-13: 9/9/97. **BHprofile_UZN16_c.eps**. Porosity, saturation, change in particle density, and measured and estimated values for K_{sat} in borehole N16.

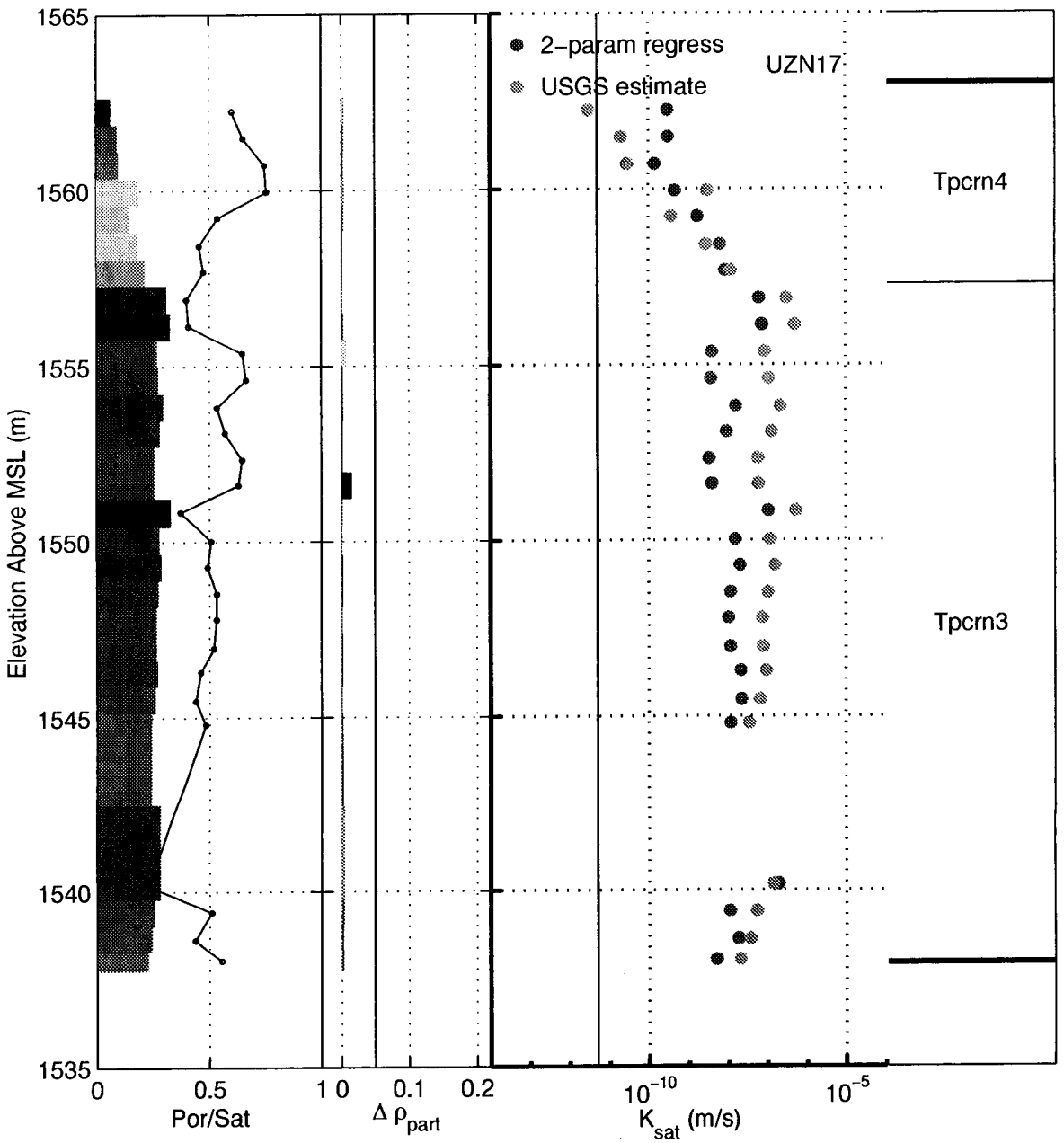

Figure 2-14: 9/9/97. **BHprofile_UZN17_c.eps**. Porosity, saturation, change in particle density, and measured and estimated values for K_{sat} in borehole N17.

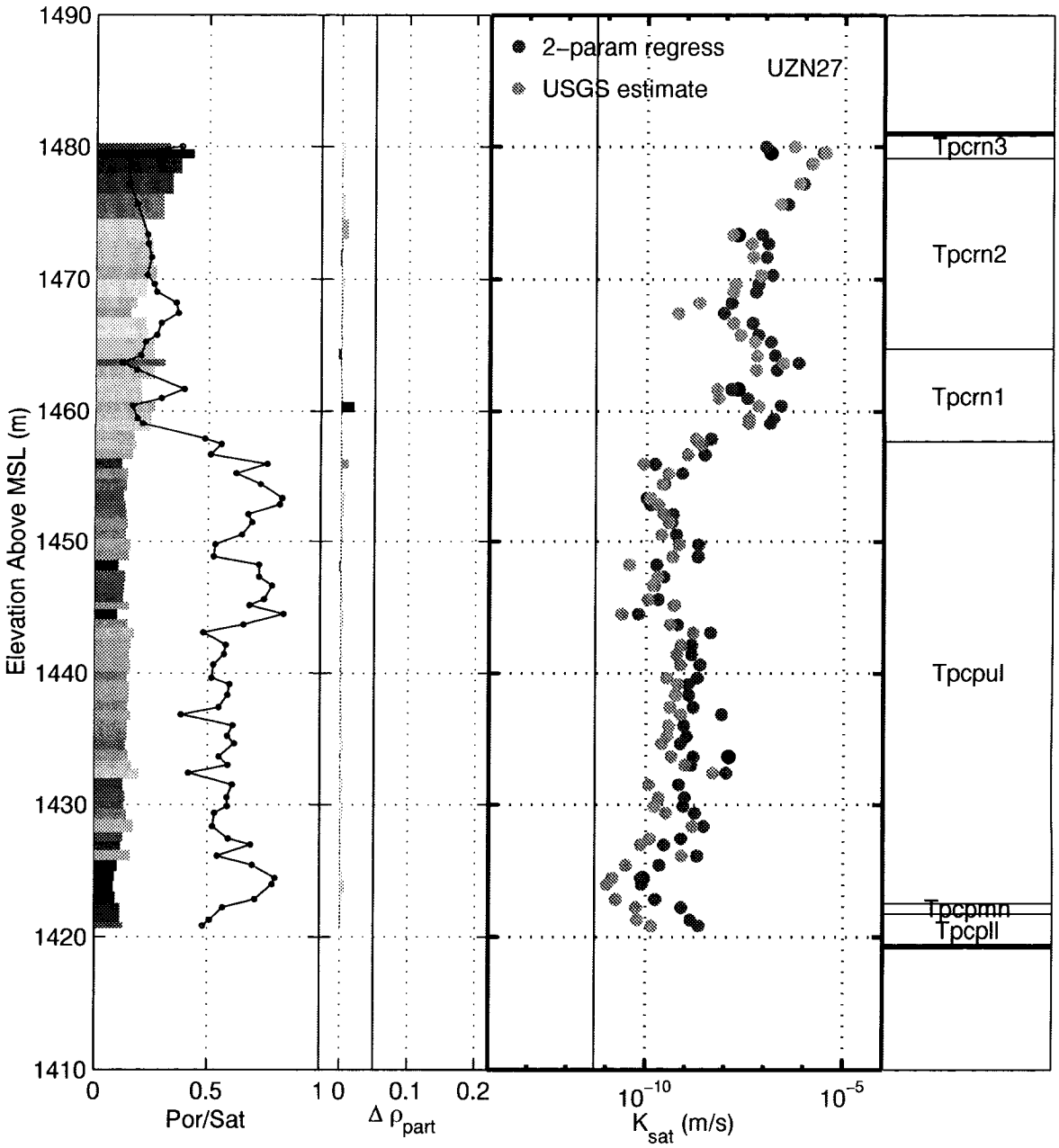

Figure 2-15: 9/9/97. **BHprofile_UZN27_c.eps**. Porosity, saturation, change in particle density, and measured and estimated values for K_{sat} in borehole N27.

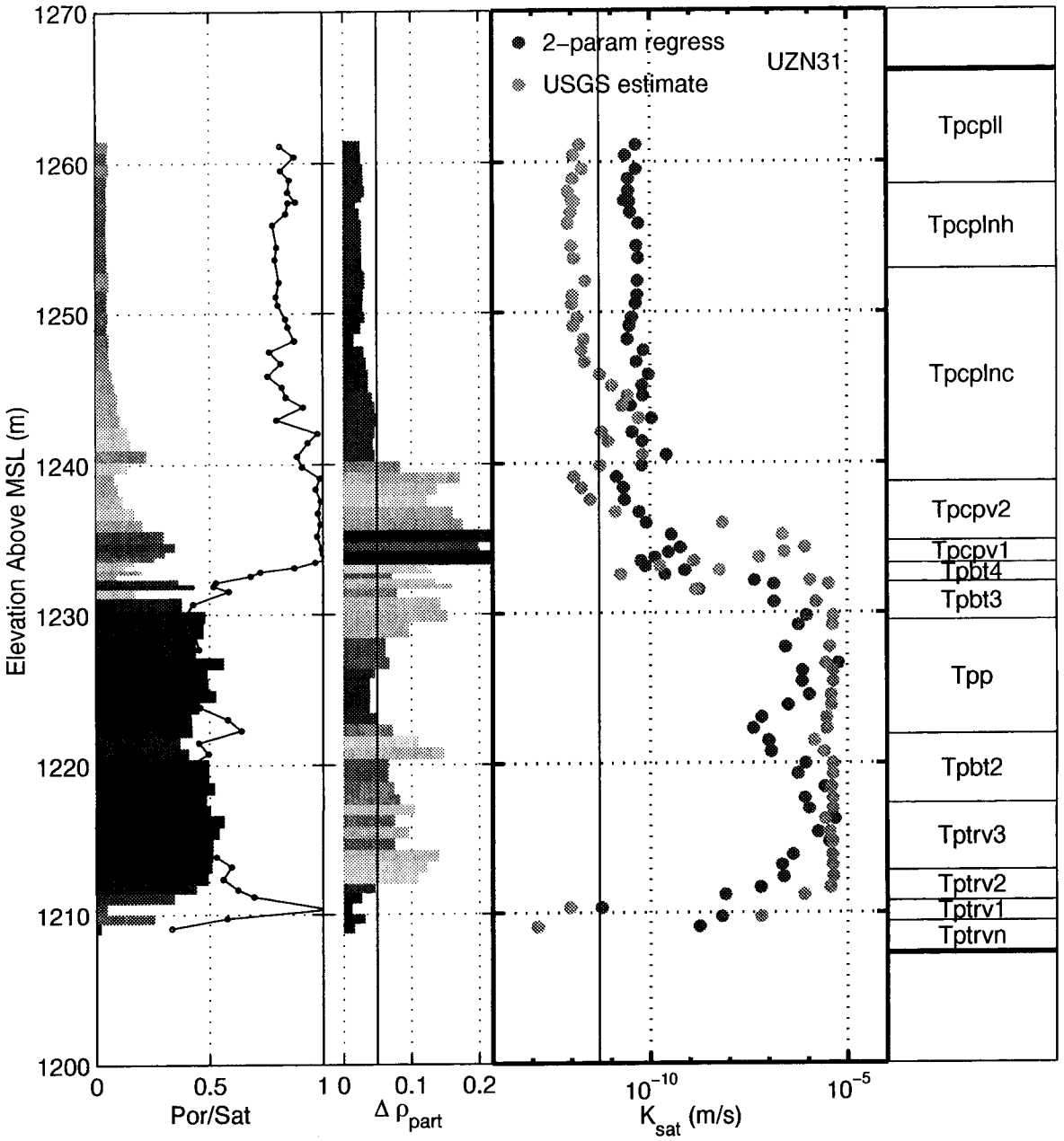

Figure 2-16: 9/9/97. **BHprofile_UZN31_c.eps**. Porosity, saturation, change in particle density, and measured and estimated values for K_{sat} in borehole N31.

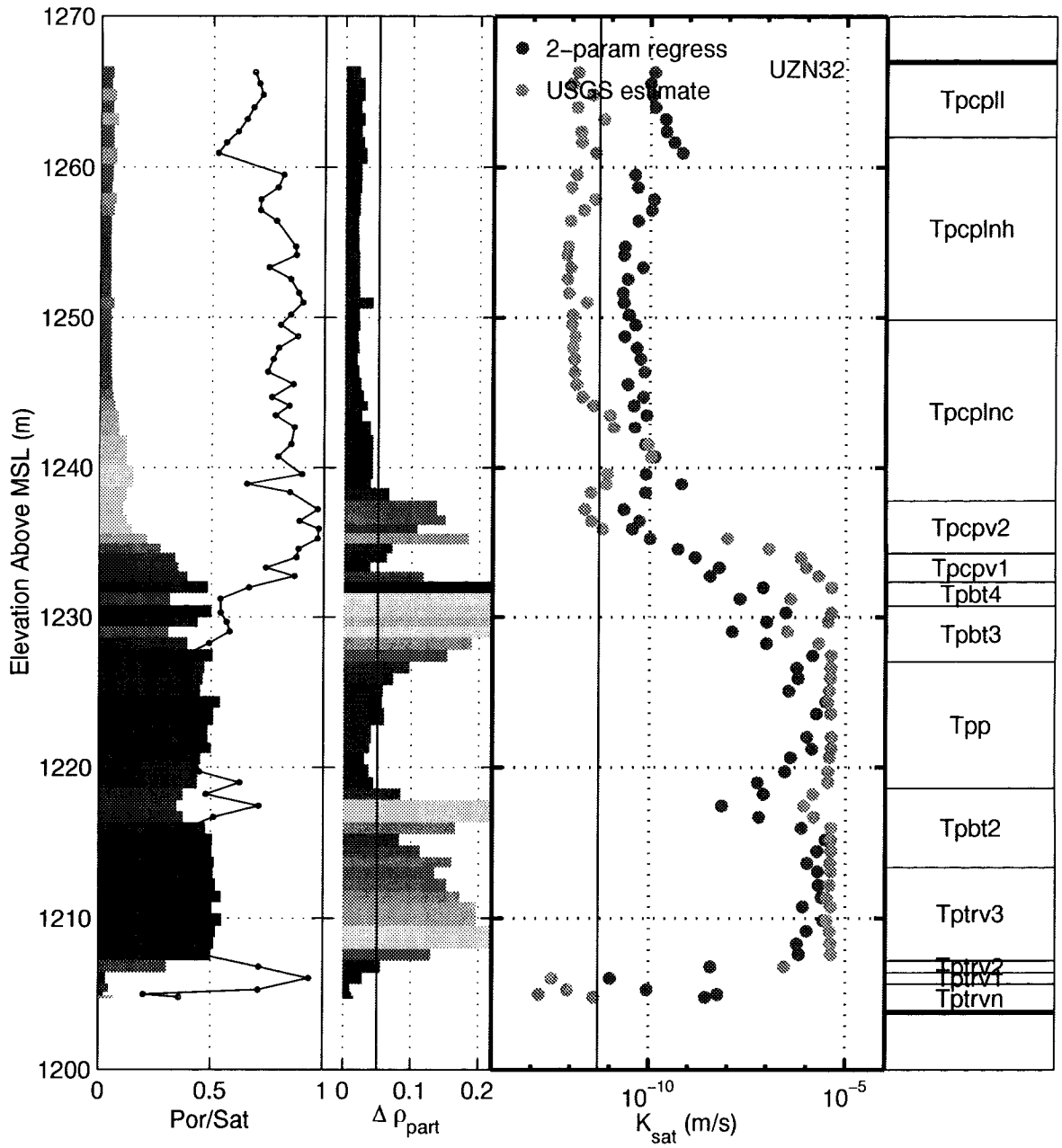

Figure 2-17: 9/9/97. **BHprofile_UZN32_c.eps**. Porosity, saturation, change in particle density, and measured and estimated values for K_{sat} in borehole N32.

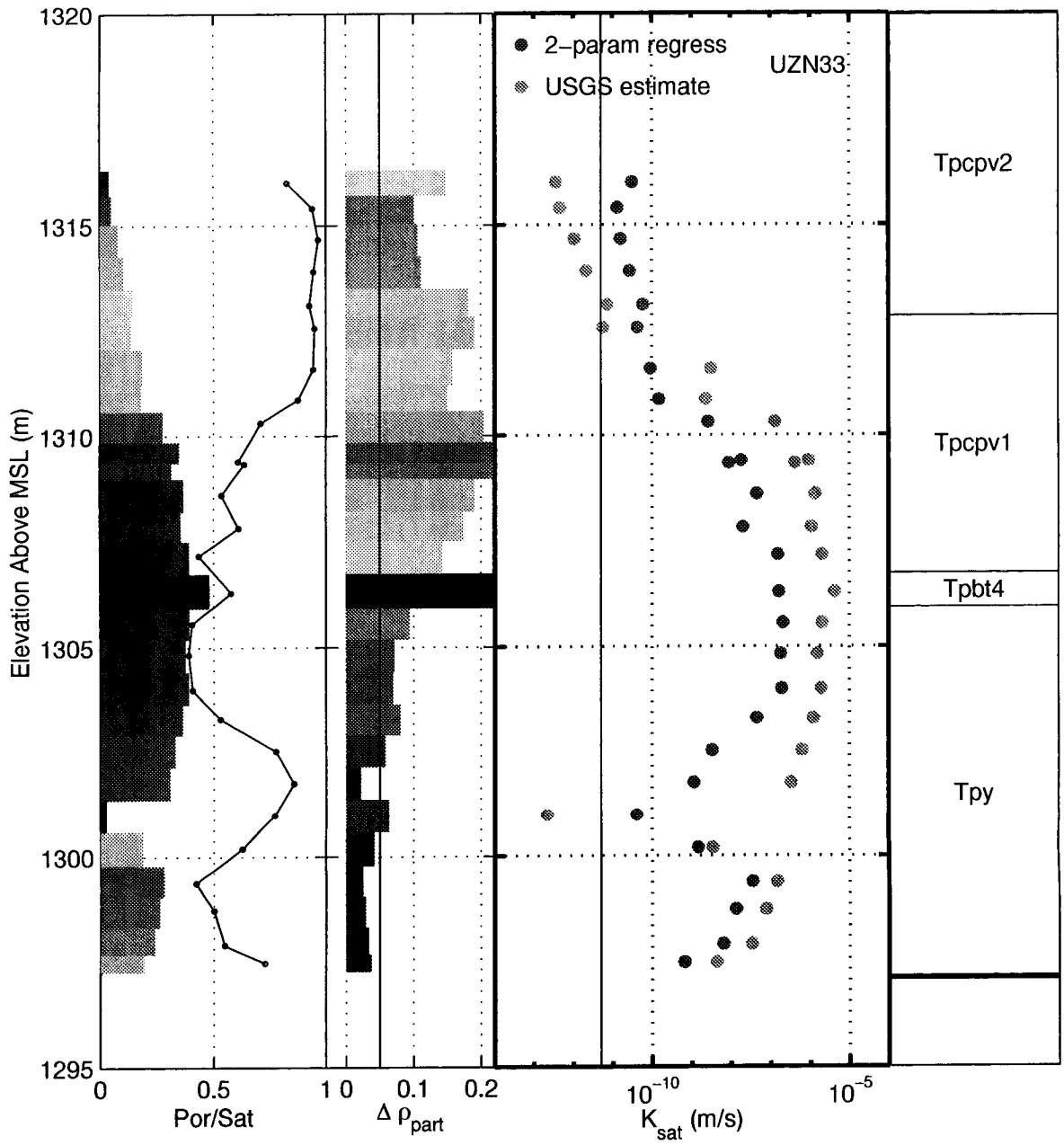

Figure 2-18: 9/9/97. **BHprofile_UZN33_c.eps**. Porosity, saturation, change in particle density, and measured and estimated values for K_{sat} in borehole N33.

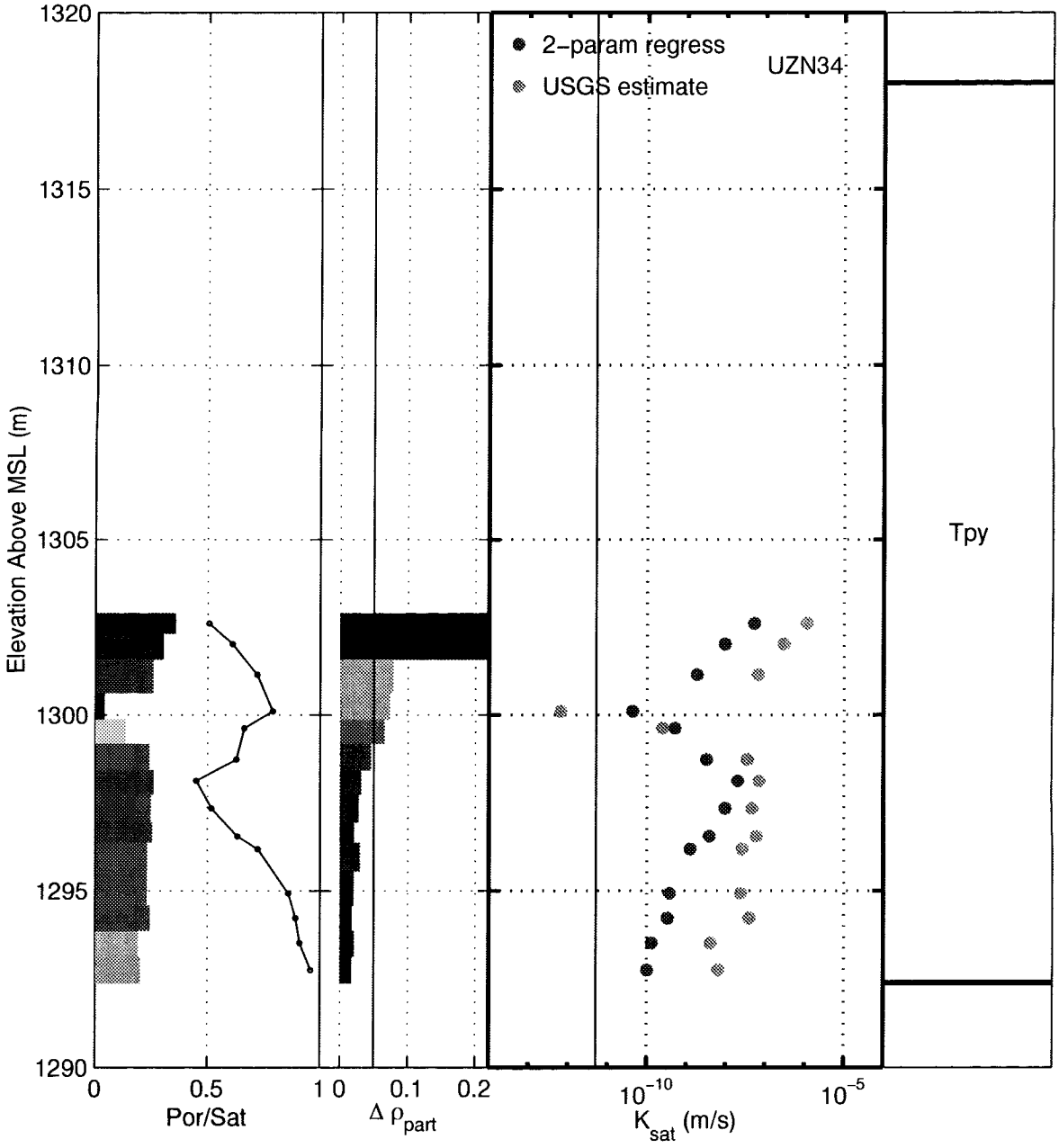

Figure 2-19: 9/9/97. **BHprofile_UZN34_c.eps**. Porosity, saturation, change in particle density, and measured and estimated values for K_{sat} in borehole N34.

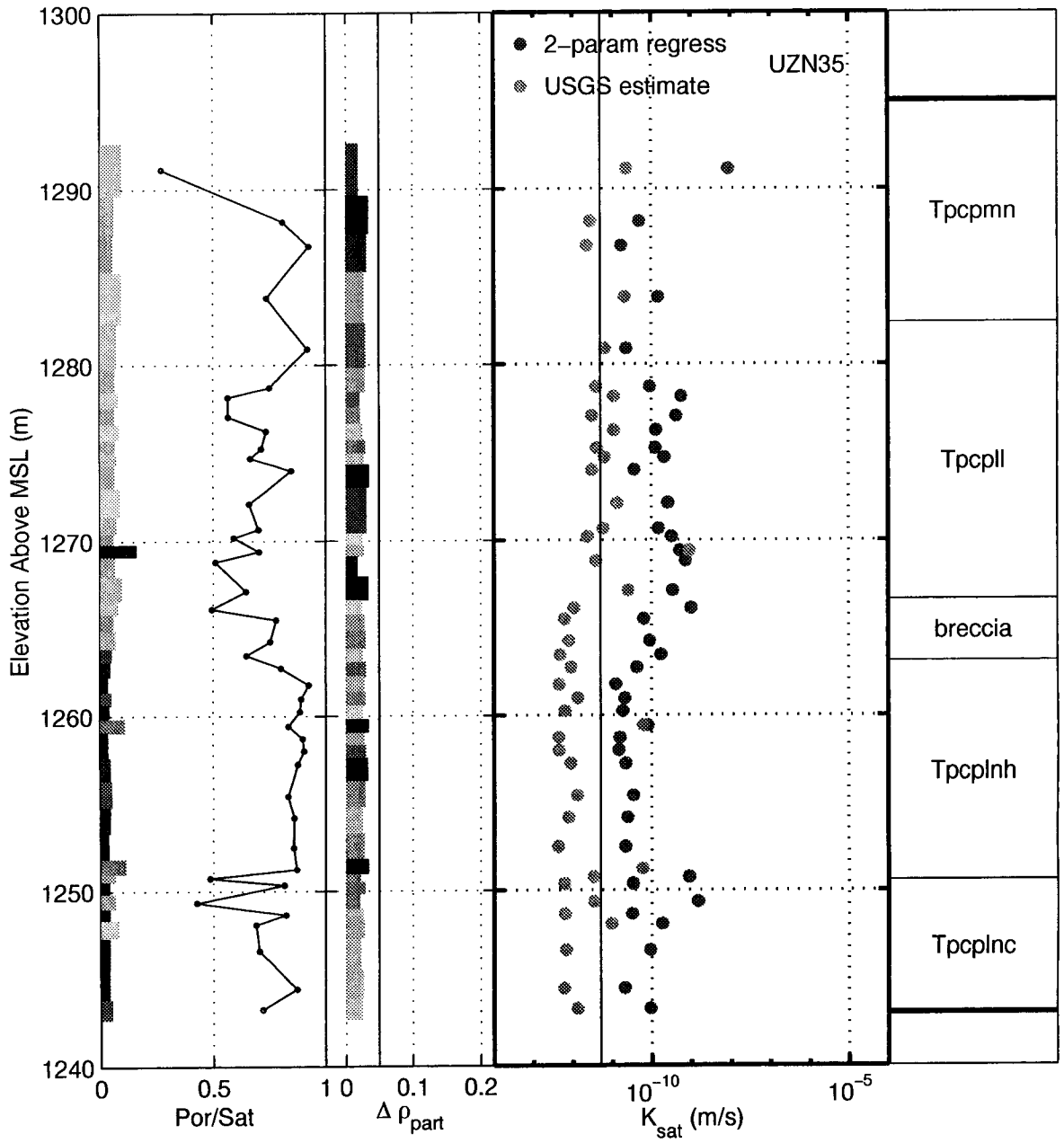

Figure 2-20: 9/9/97. **BHprofile_UZN35_c.eps**. Porosity, saturation, change in particle density, and measured and estimated values for K_{sat} in borehole N35.

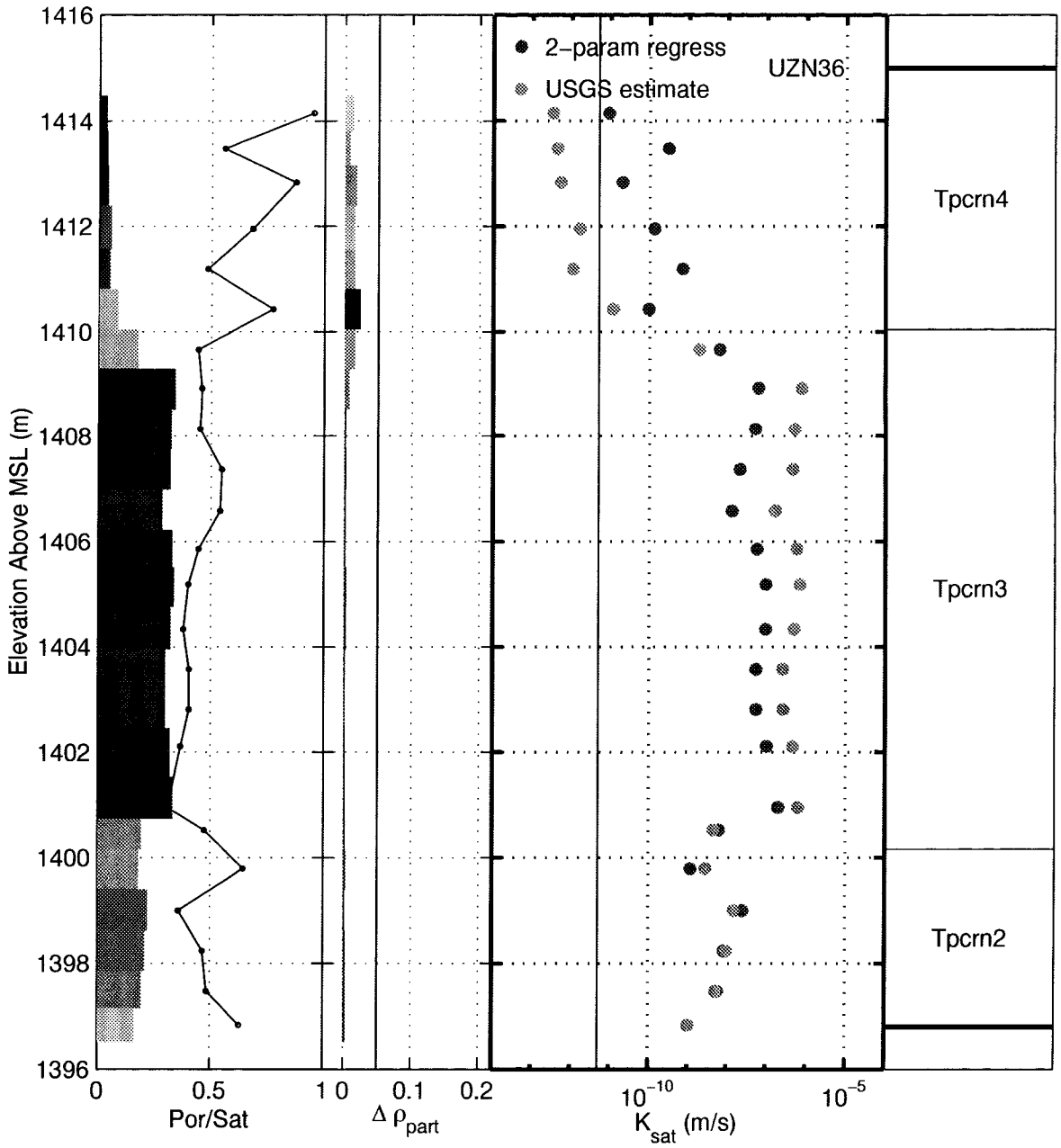

Figure 2-21: 9/9/97. **BHprofile_UZN36_c.eps.** Porosity, saturation, change in particle density, and measured and estimated values for K_{sat} in borehole N36.

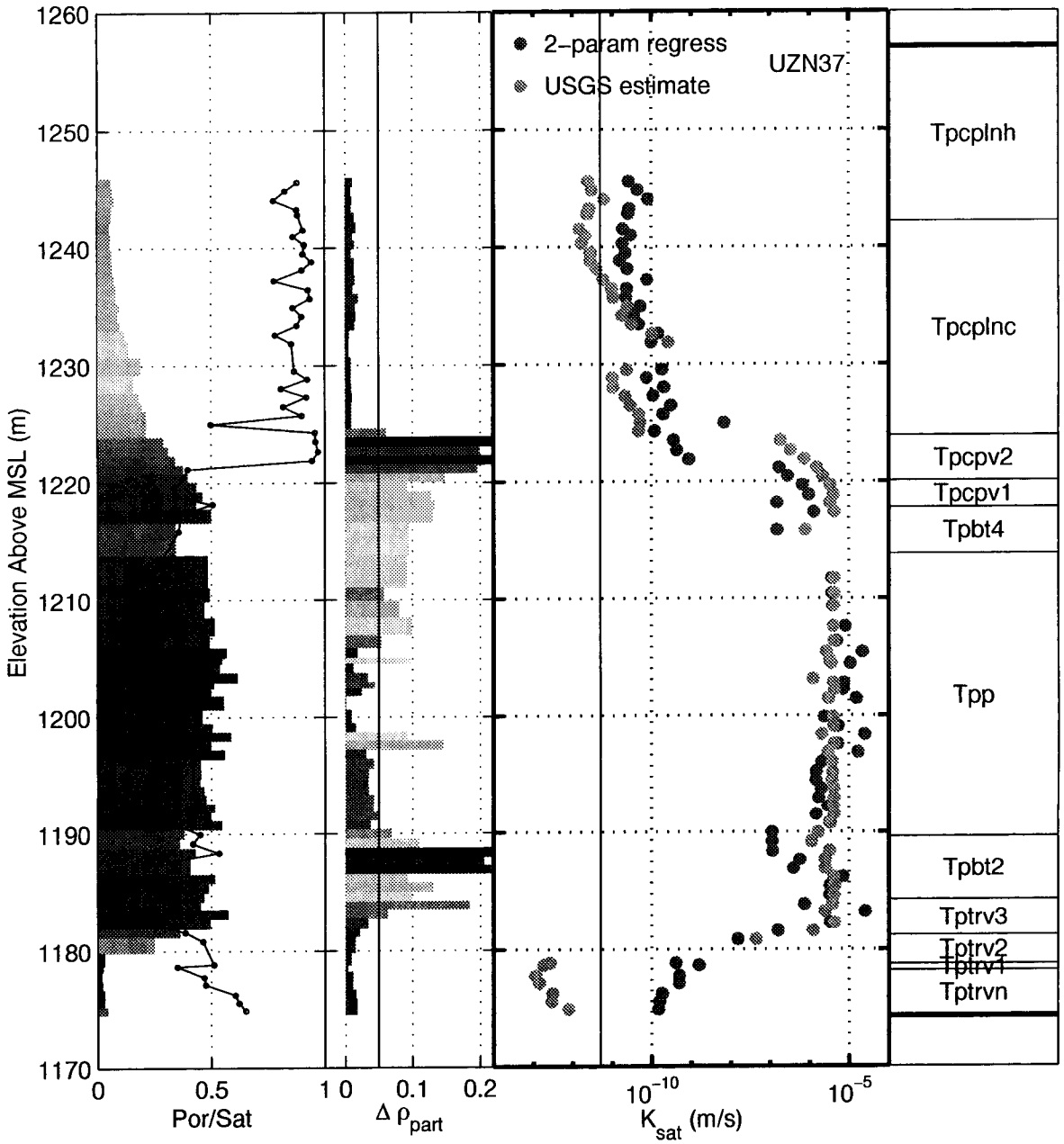

Figure 2-22: 9/9/97. **BHprofile_UZN37_c.eps**. Porosity, saturation, change in particle density, and measured and estimated values for K_{sat} in borehole N37.

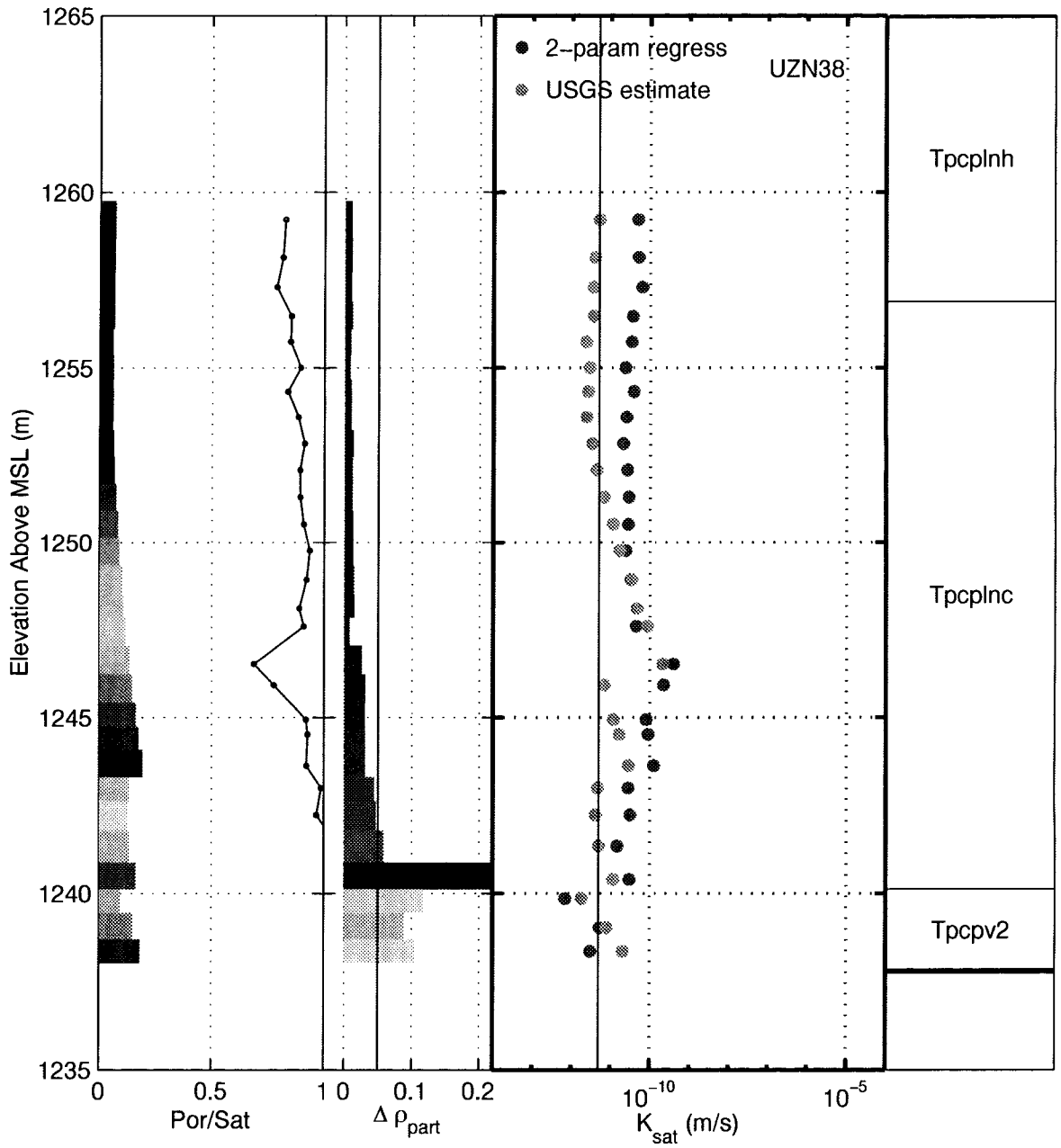

Figure 2-23: 9/9/97. **BHprofile_UZN38_c.eps**. Porosity, saturation, change in particle density, and measured and estimated values for K_{sat} in borehole N38.

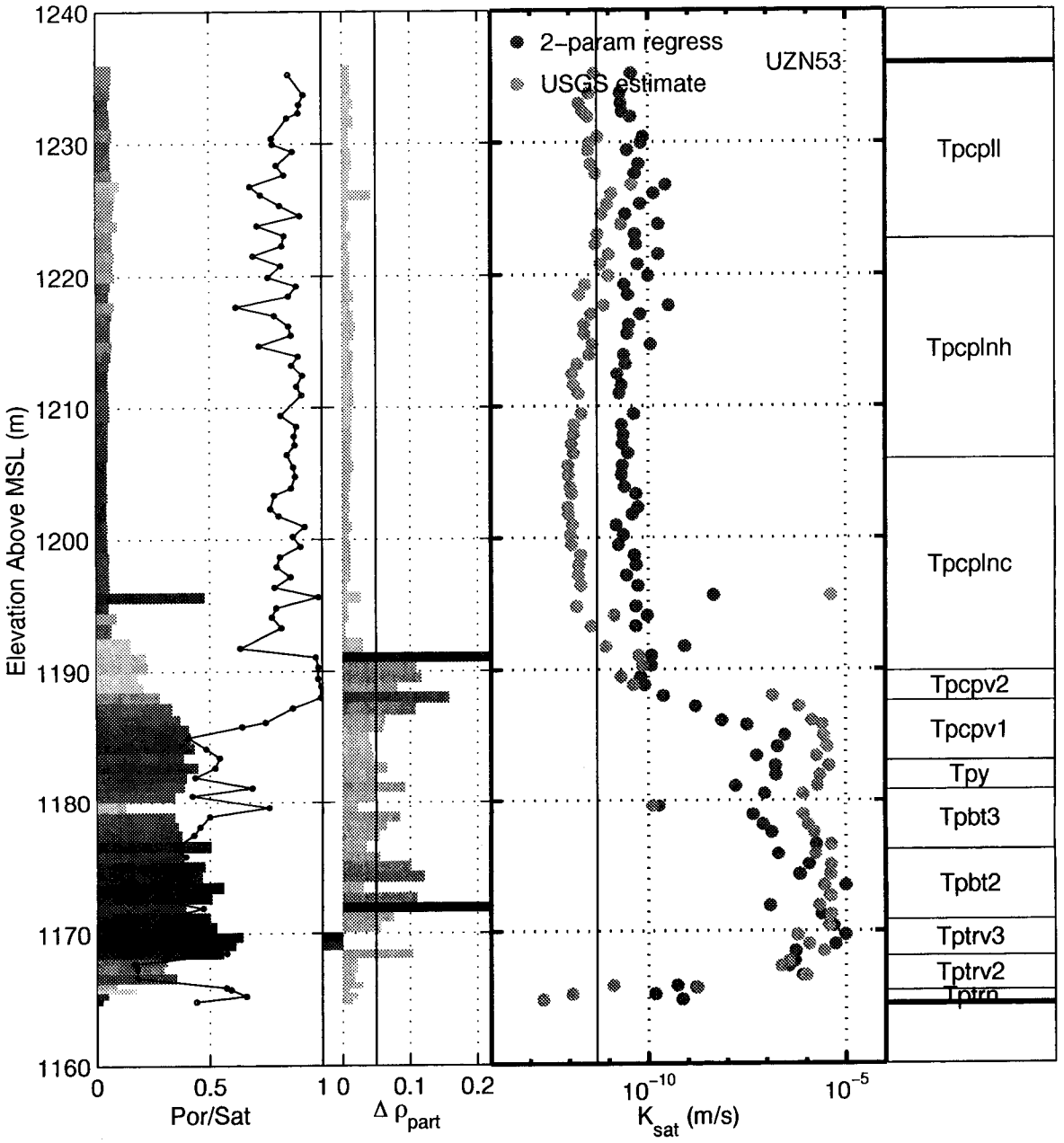

Figure 2-24: 9/9/97. **BHprofile_UZN53_c.eps**. Porosity, saturation, change in particle density, and measured and estimated values for K_{sat} in borehole N53.

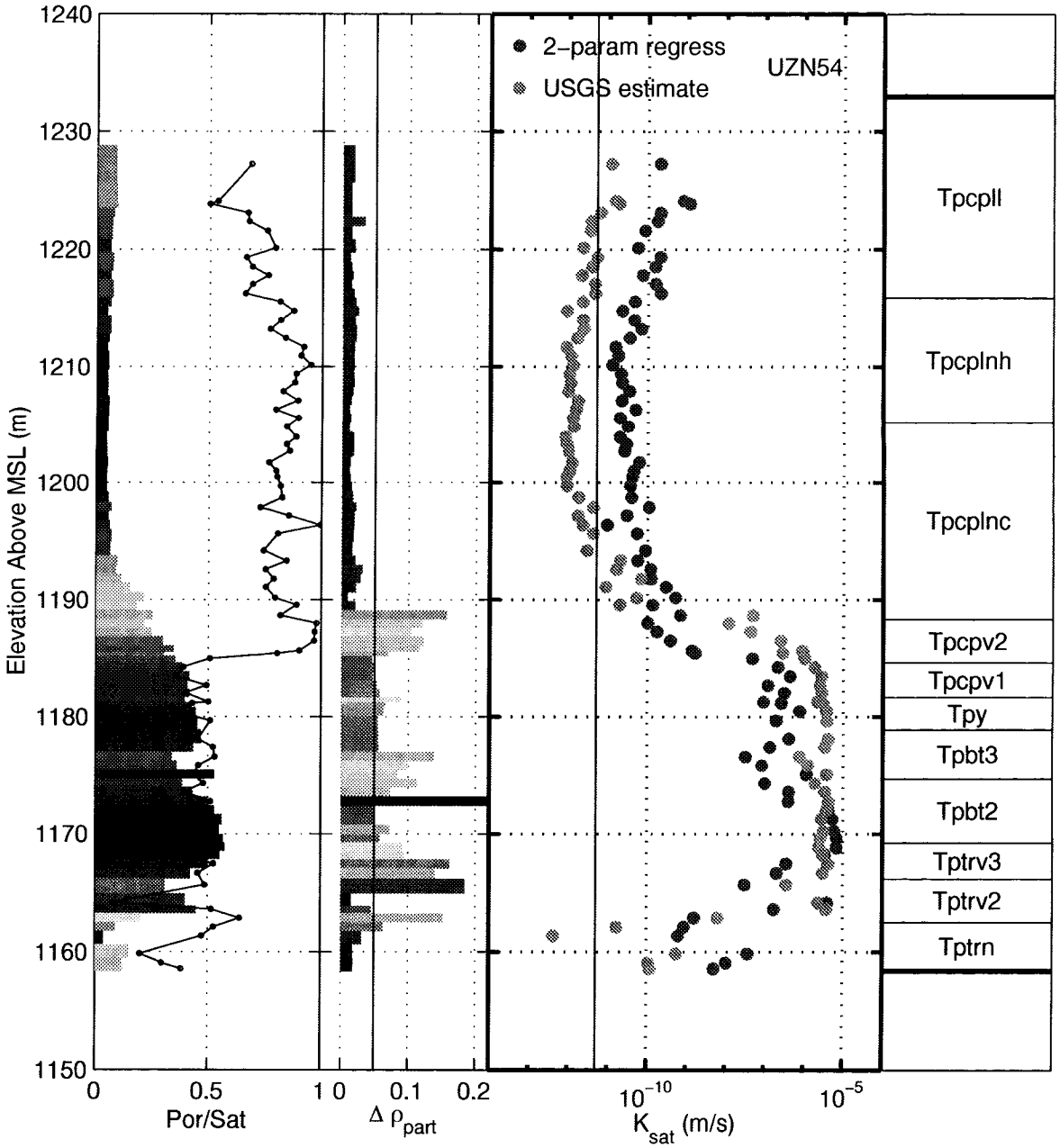

Figure 2-25: 9/9/97. **BHprofile_UZN54_c.eps**. Porosity, saturation, change in particle density, and measured and estimated values for K_{sat} in borehole N54.

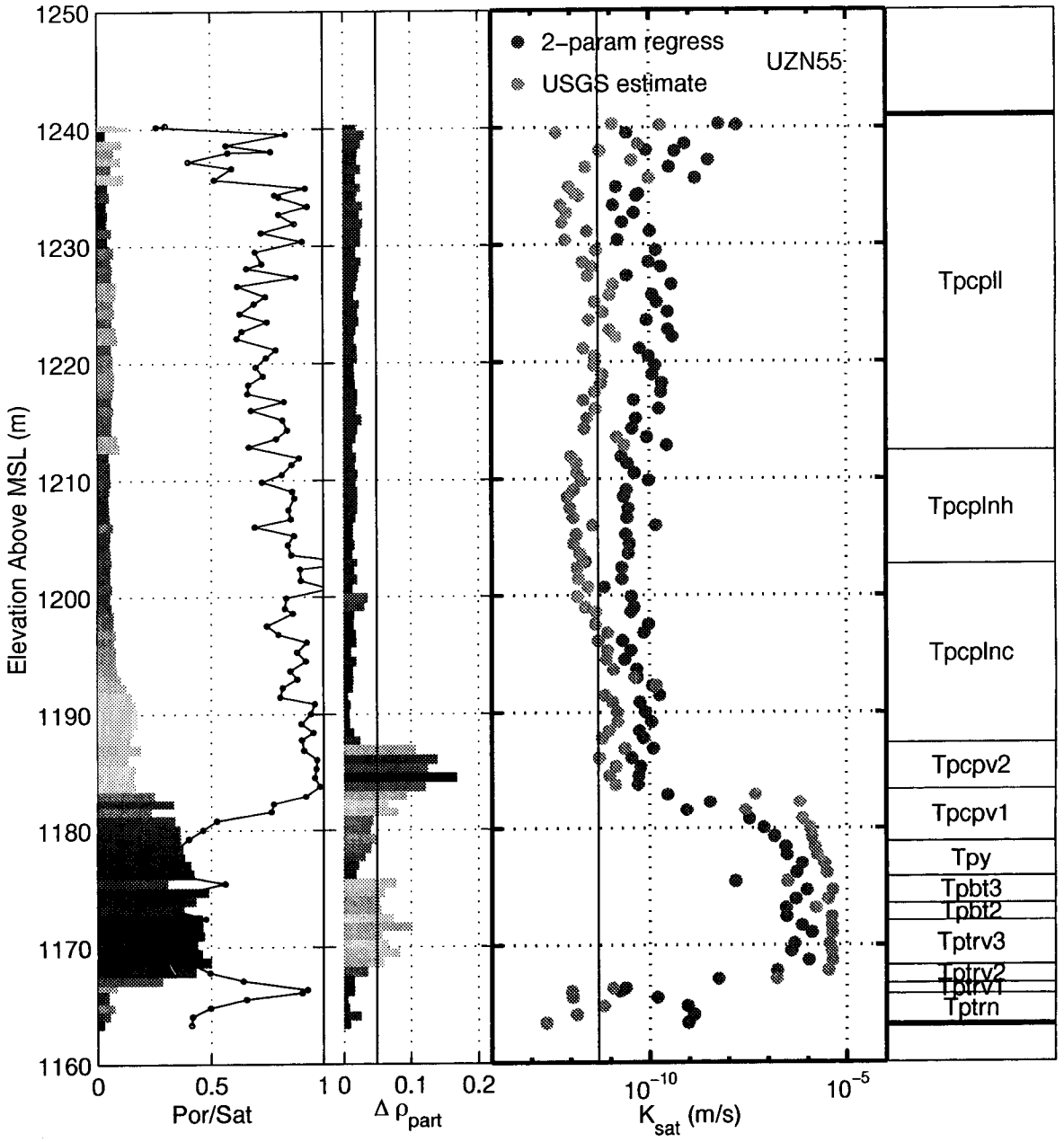

Figure 2-26: 9/9/97. **BHprofile_UZN55_c.eps**. Porosity, saturation, change in particle density, and measured and estimated values for K_{sat} in borehole N55.

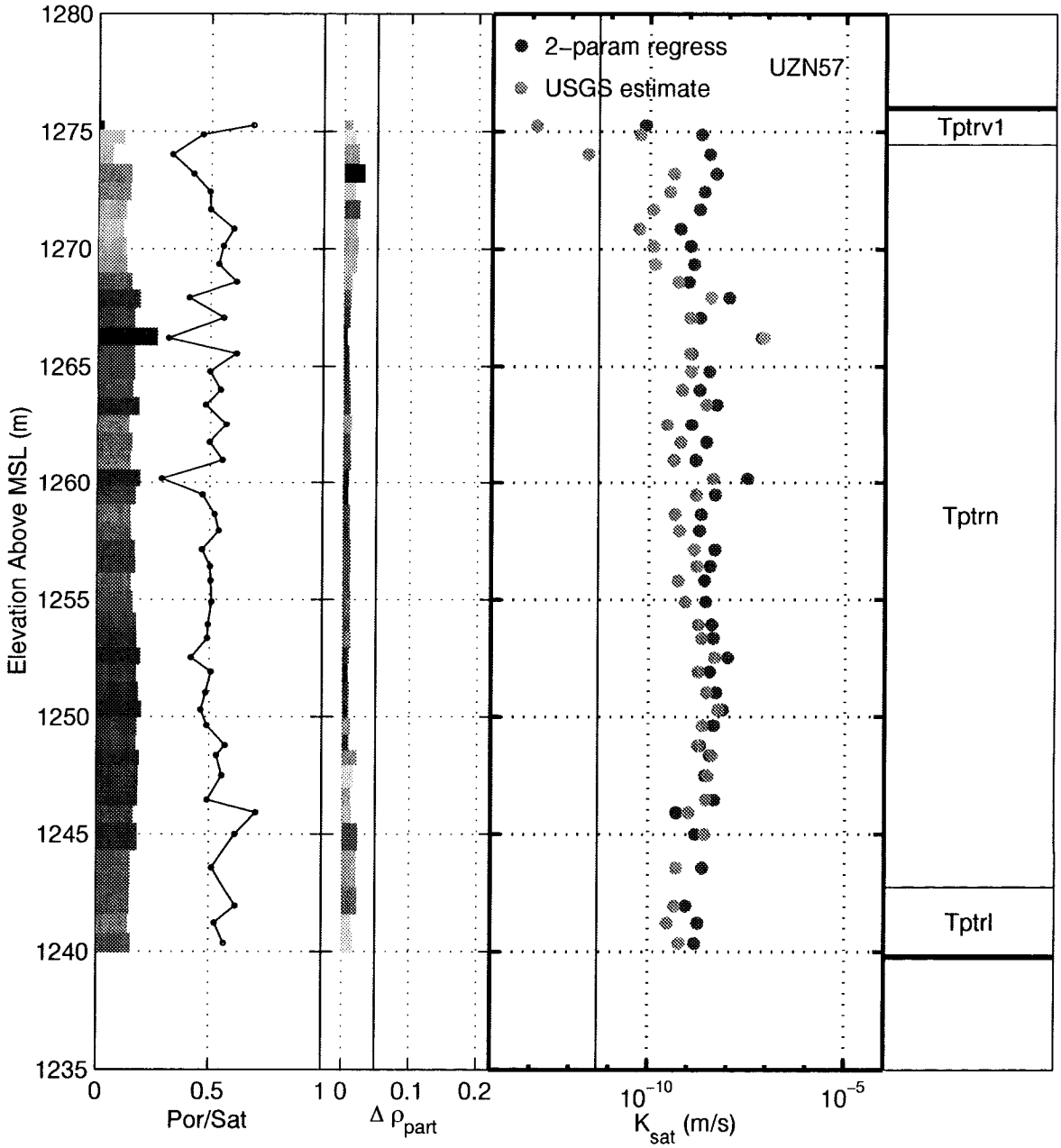

Figure 2-27: 9/9/97. **BHprofile_UZN57_c.eps**. Porosity, saturation, change in particle density, and measured and estimated values for K_{sat} in borehole N57.

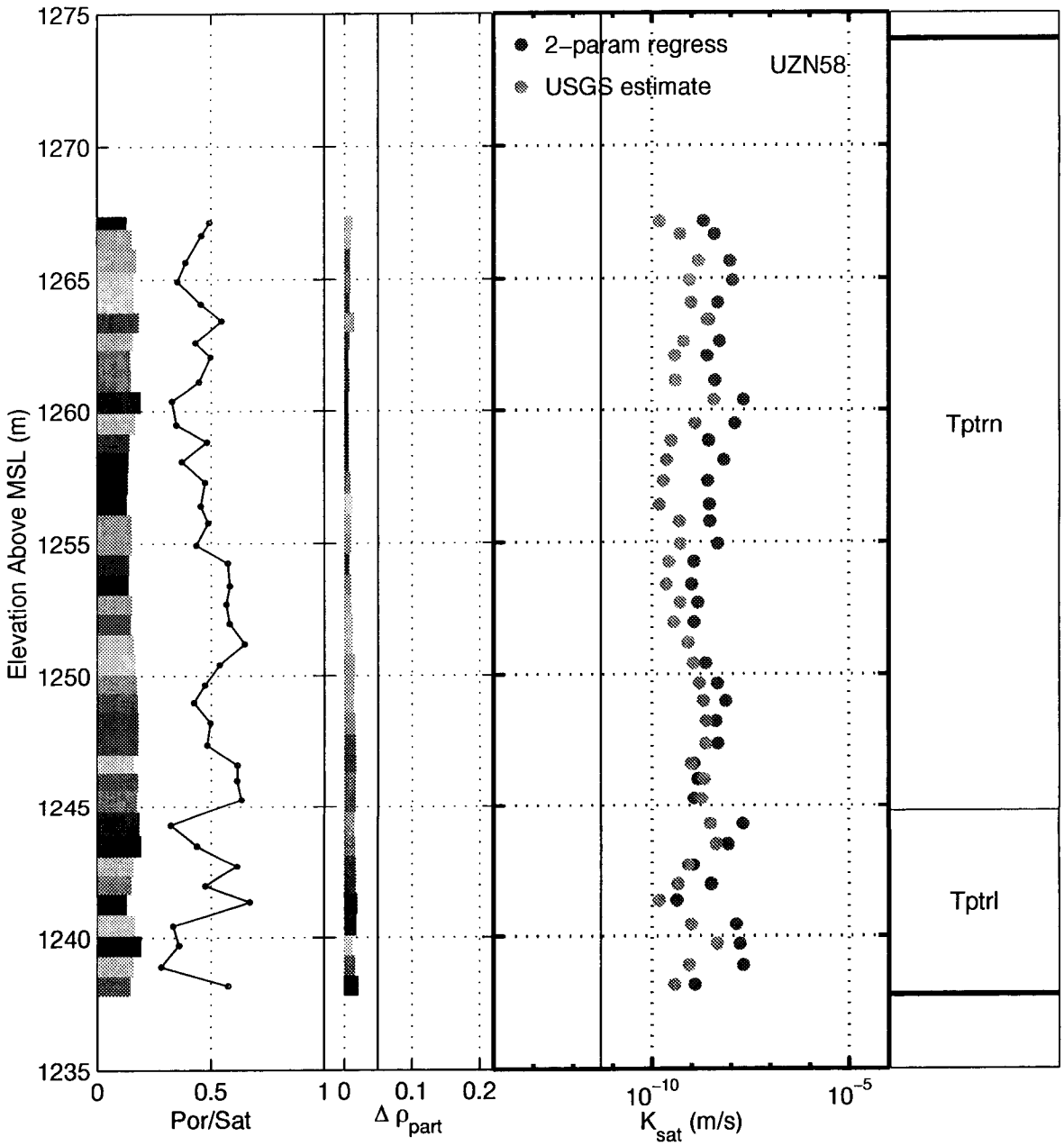

Figure 2-28: 9/9/97. **BHprofile_UZN58_c.eps**. Porosity, saturation, change in particle density, and measured and estimated values for K_{sat} in borehole N58.

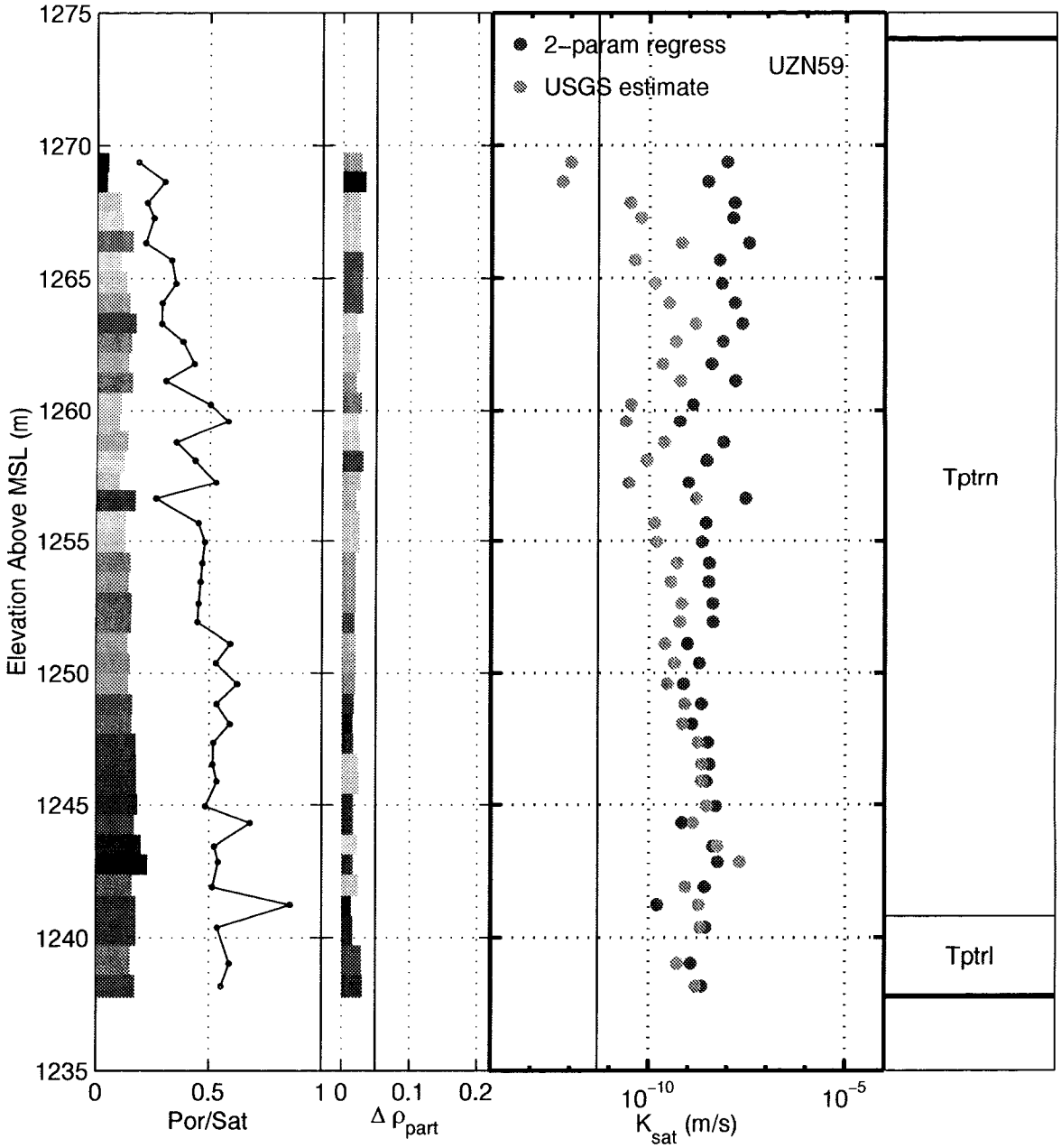

Figure 2-29: 9/9/97. **BHprofile_UZN59_c.eps.** Porosity, saturation, change in particle density, and measured and estimated values for K_{sat} in borehole N59.

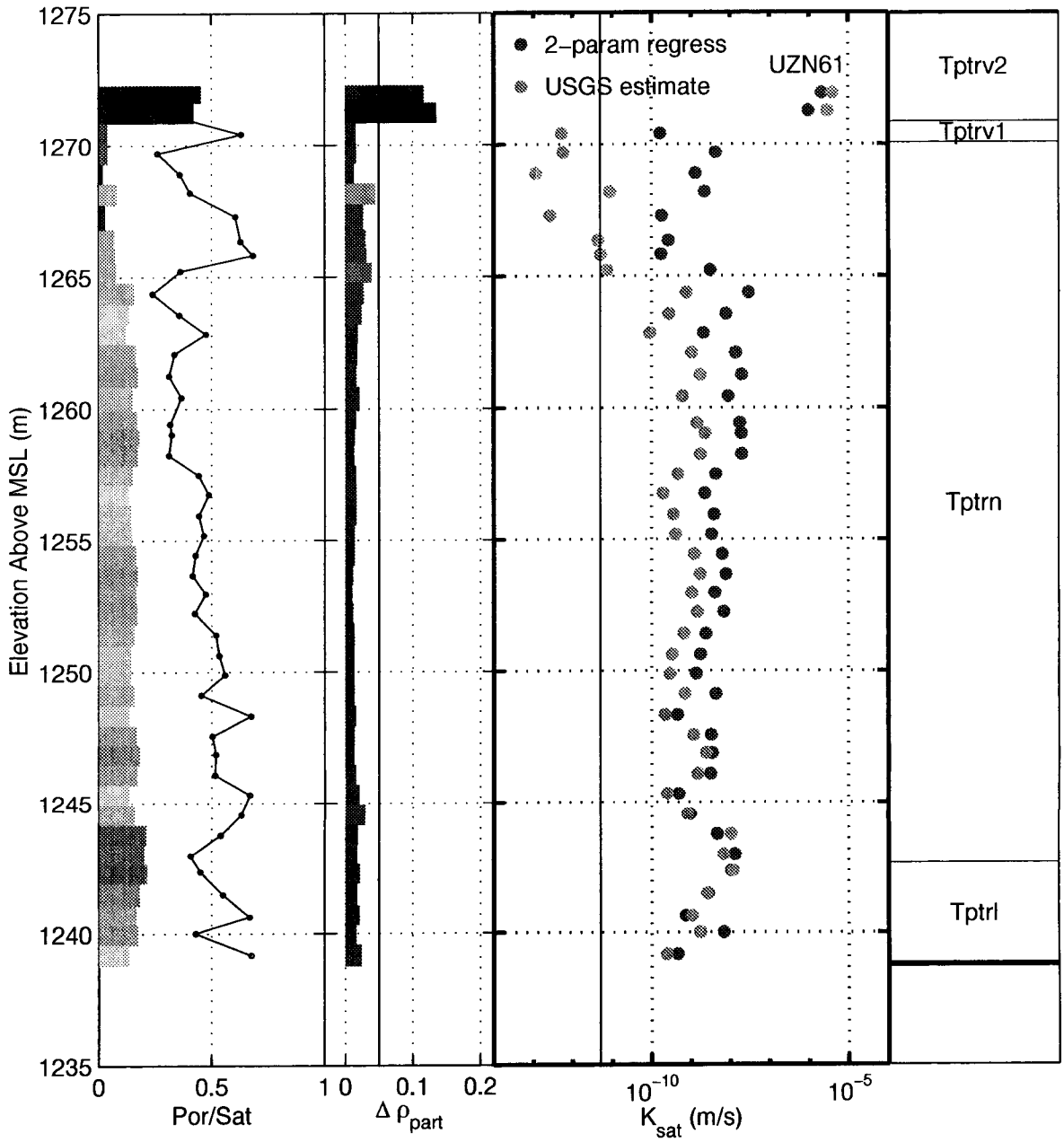

Figure 2-30: 9/9/97. **BHprofile_UZN61_c.eps**. Porosity, saturation, change in particle density, and measured and estimated values for K_{sat} in borehole N61.

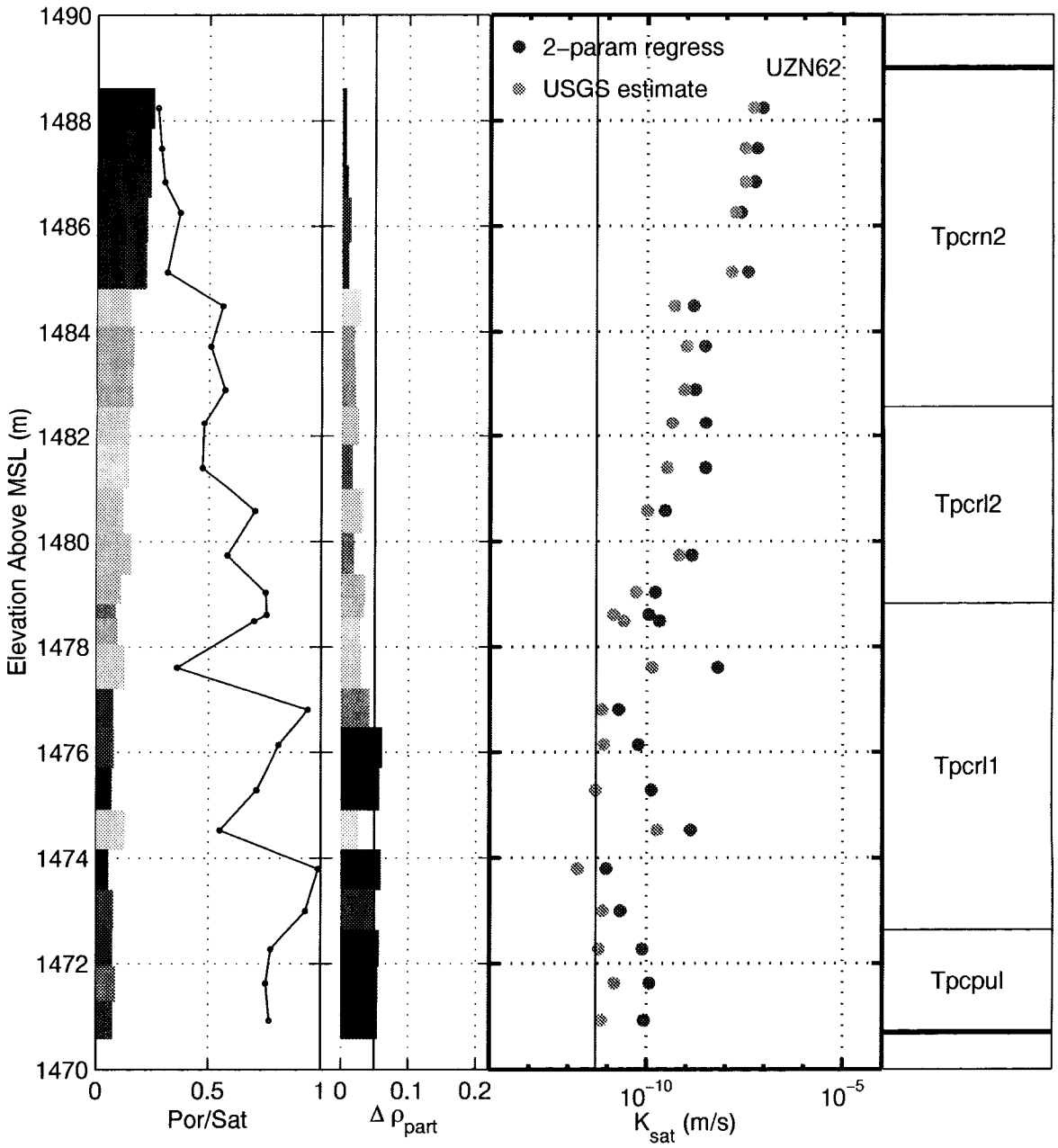

Figure 2-31: 9/9/97. **BHprofile_UZN62_c.eps**. Porosity, saturation, change in particle density, and measured and estimated values for K_{sat} in borehole N62.

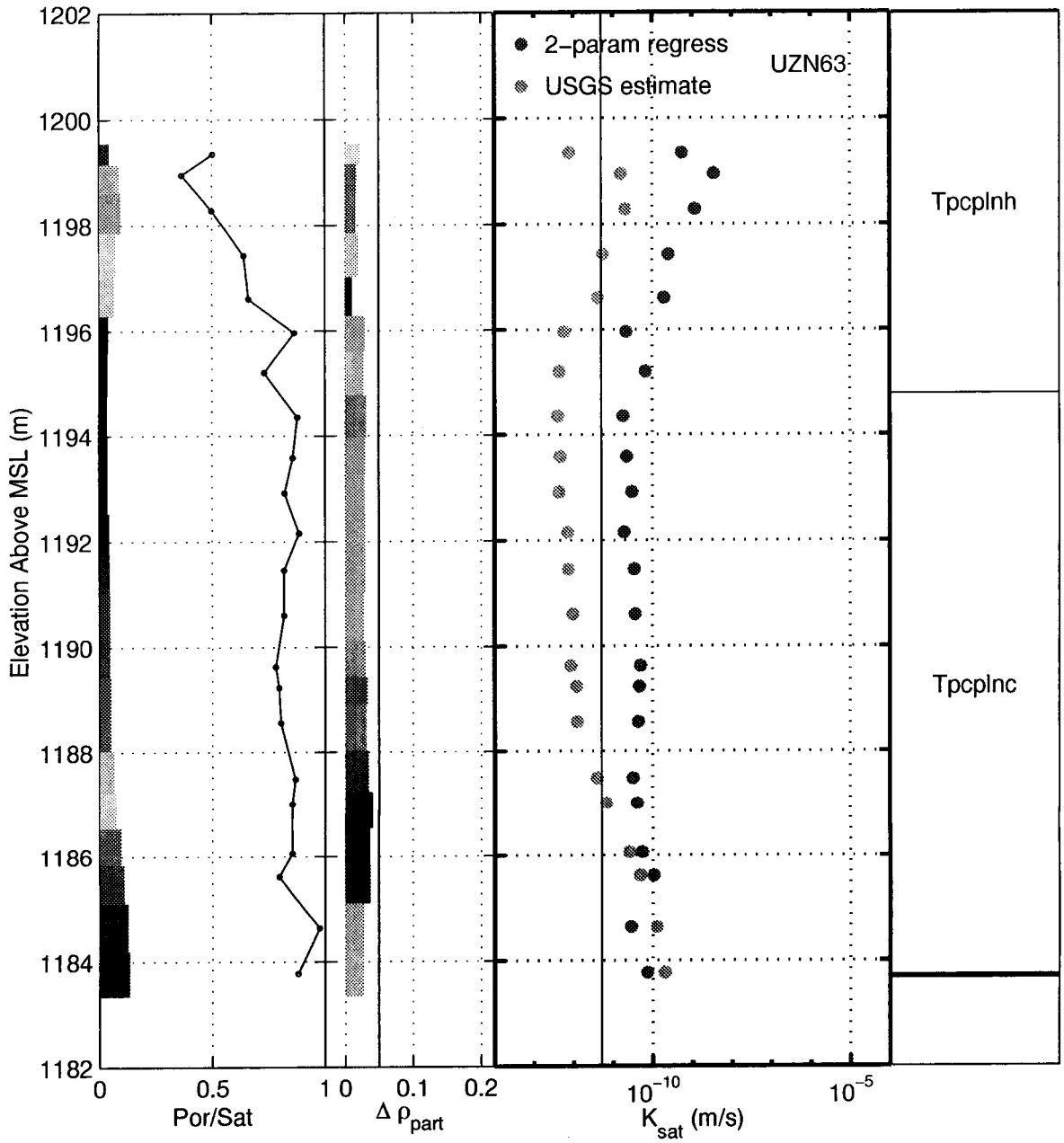

Figure 2-32: 9/9/97. **BHprofile_UZN63_c.eps**. Porosity, saturation, change in particle density, and measured and estimated values for K_{sat} in borehole N63.

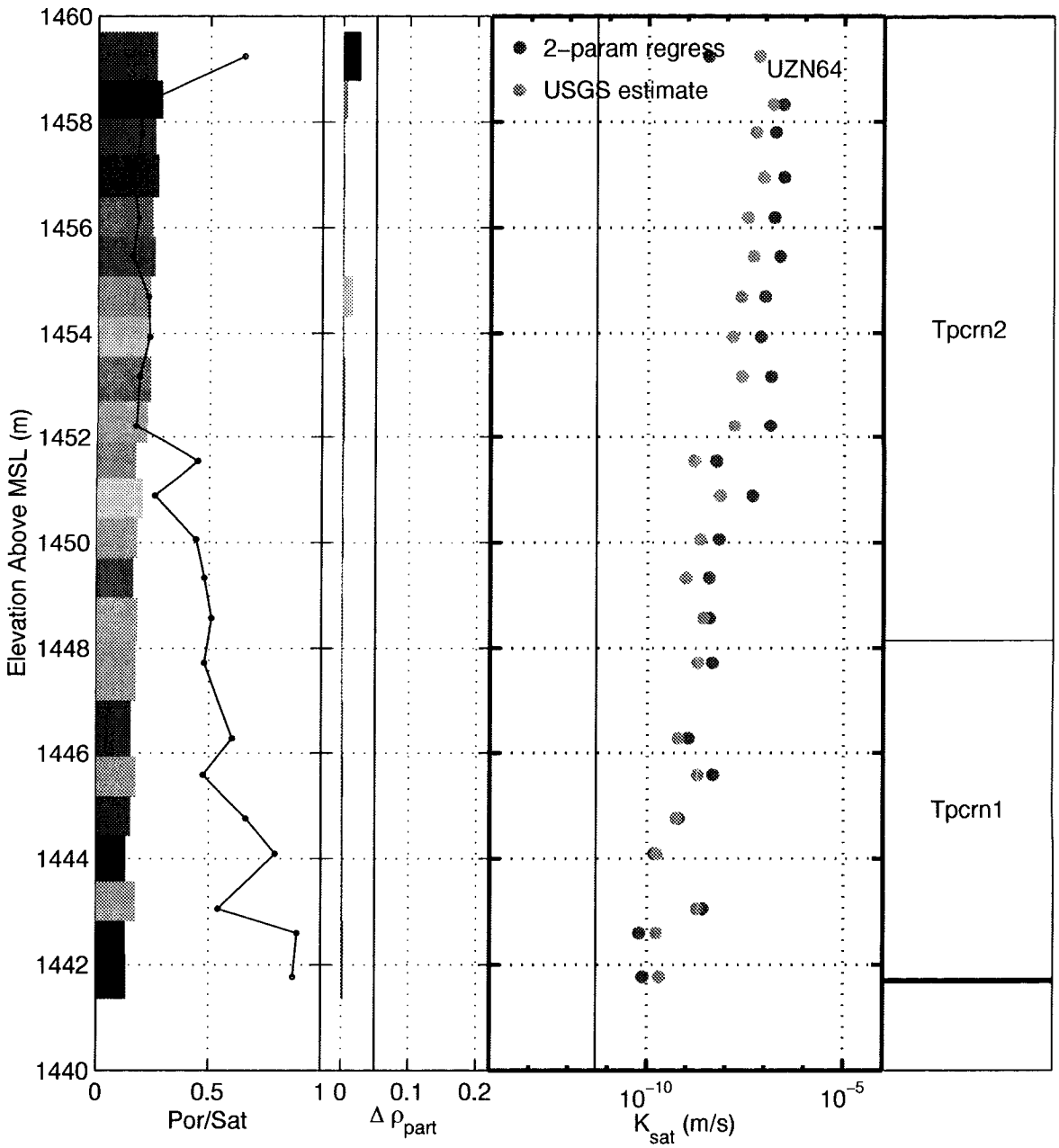

Figure 2-33: 9/9/97. **BHprofile_UZN64_c.eps**. Porosity, saturation, change in particle density, and measured and estimated values for K_{sat} in borehole N64.

9/17/97 Further investigation of USGS UZ properties. SAS

In ***$HOME2/AmbientKTI/3Ddata***, I created a *Matlab* routine, show_usgs_db_ksat.m, that plots the K_{sat} values for each formation using all boreholes having K_{sat} values for the formation, either measured or estimated using my regression. A small location map, idealized formation map, and statistical information are part of each plot. The creating routine is saved with a .arch091697 appended.

The plots are shown in the following pages. The statistical descriptions are summarized in the tables following the plots.

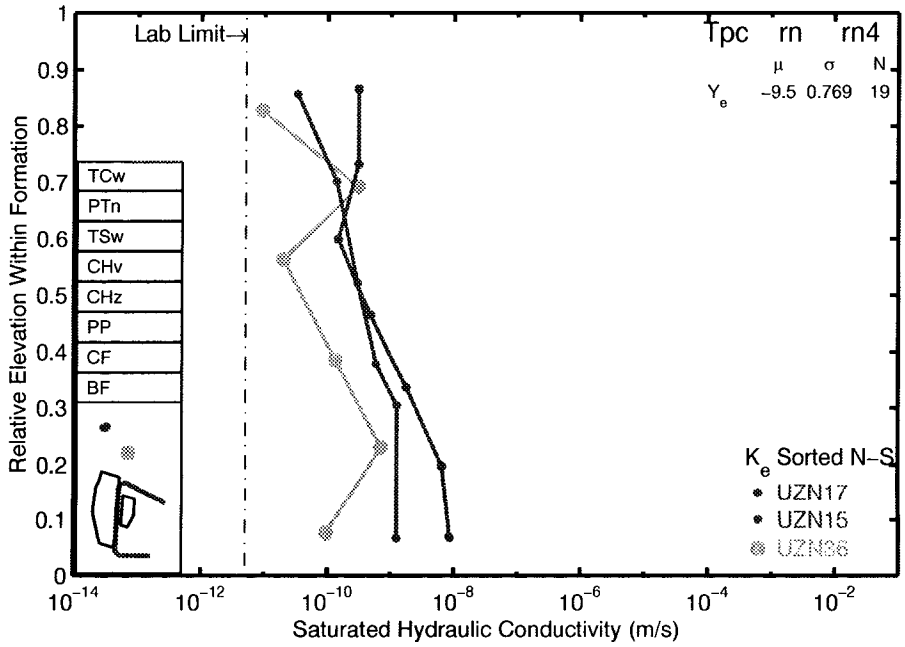

(a)

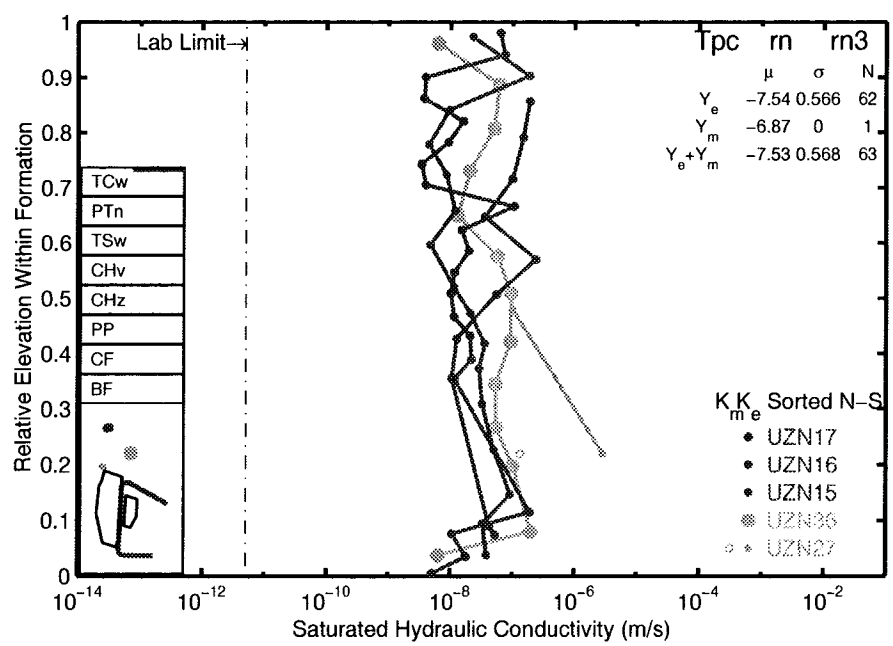

(b)

Figure 2-34: 9/17/97. All CNWRA-estimated and USGS-measured K_{sat} values in formation: (a) Tpcrn4 (**FormK_Tpcrn4_c.eps**), and (b) Tpcrn3 (**FormK_Tpcrn3_c.eps**).

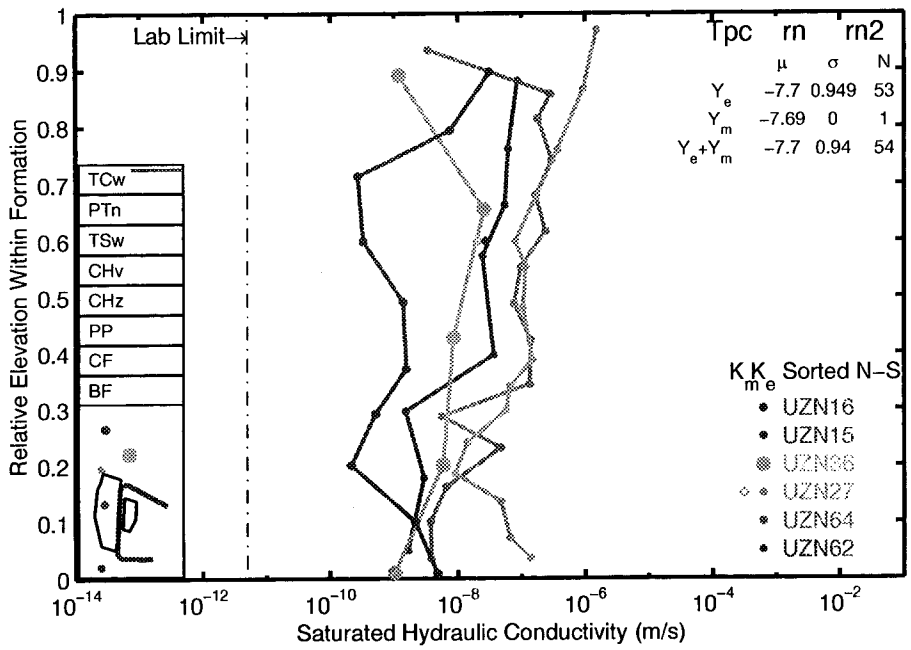

(a)

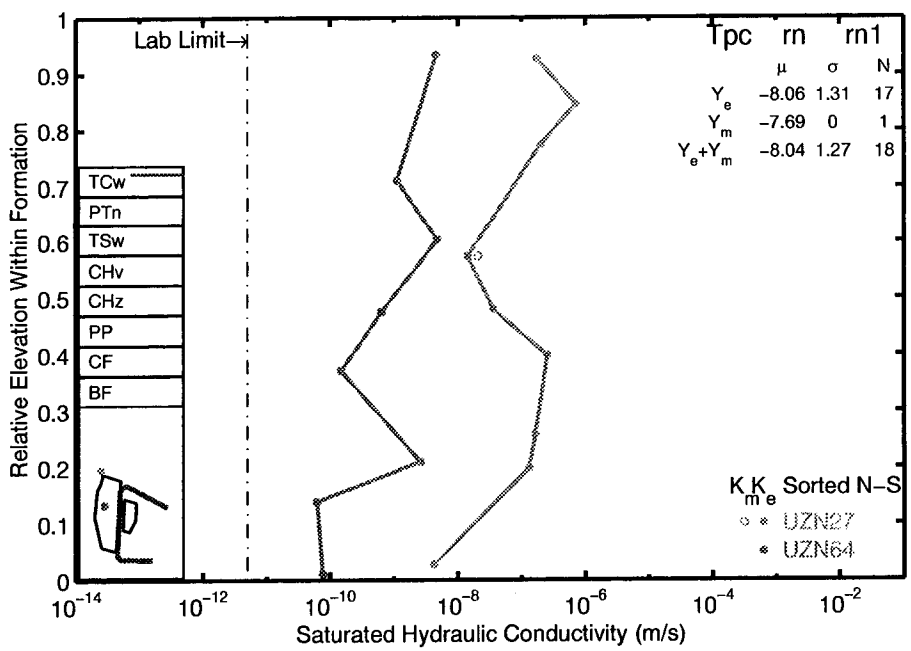

(b)

Figure 2-35: 9/17/97. All CNWRA-estimated and USGS-measured K_{sat} values in formation: (a) Tpcrn2 (**FormK_Tpcrn2_c.eps**), and (b) Tpcrn1 (**FormK_Tpcrn1_c.eps**).

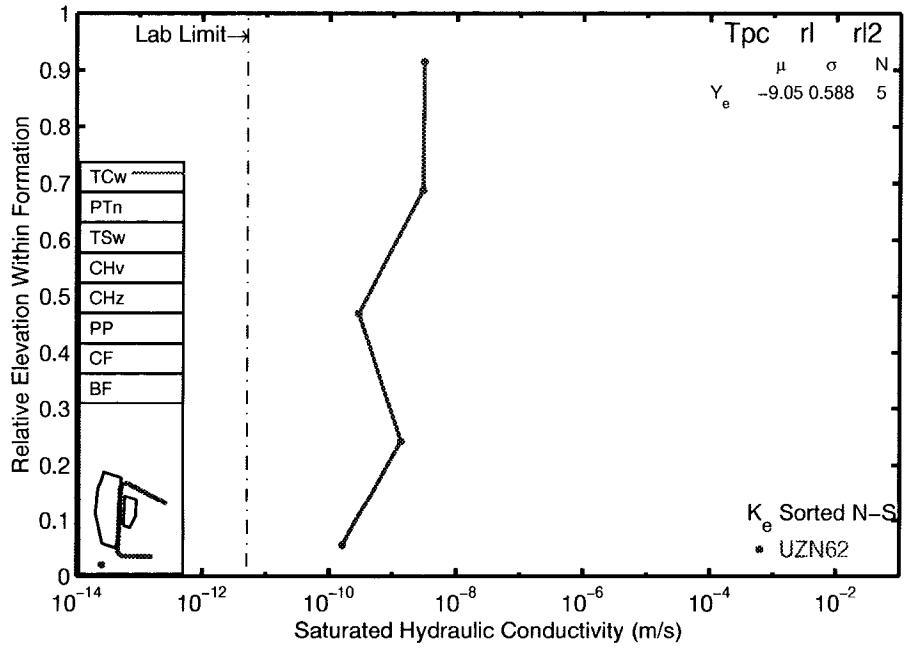

(a)

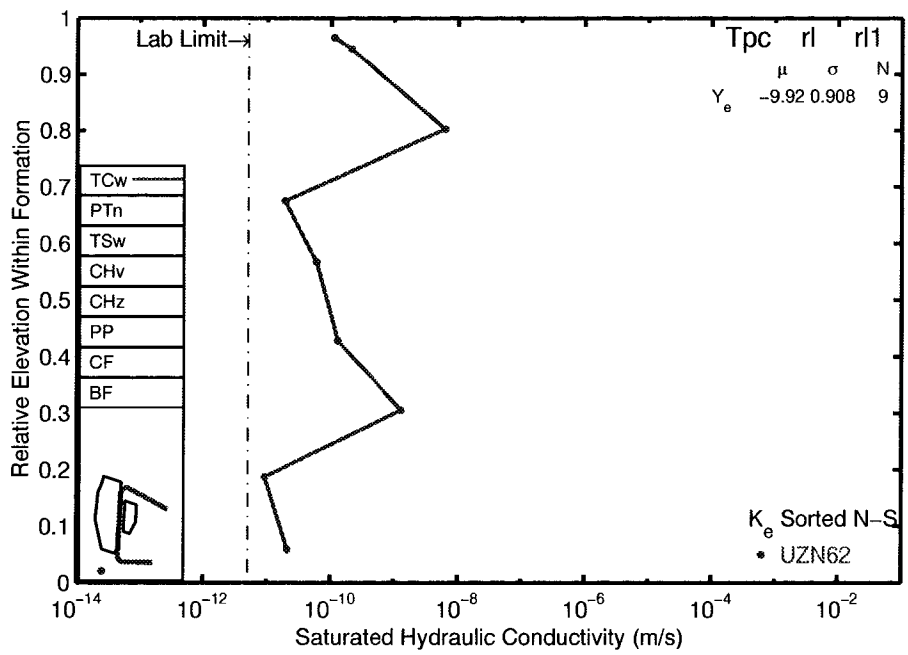

(b)

Figure 2-36: 9/17/97. All CNWRA-estimated and USGS-measured K_{sat} values in formation: (a) Tpcrl2 (**FormK_Tpcrl2_c.eps**), and (b) Tpcrl1 (**FormK_Tpcrl1_c.eps**).

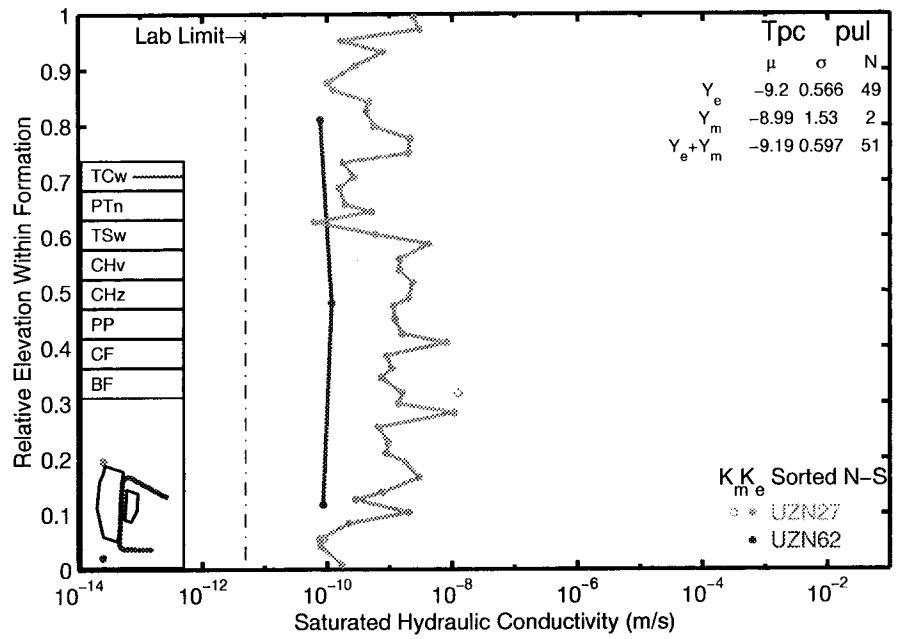

(a)

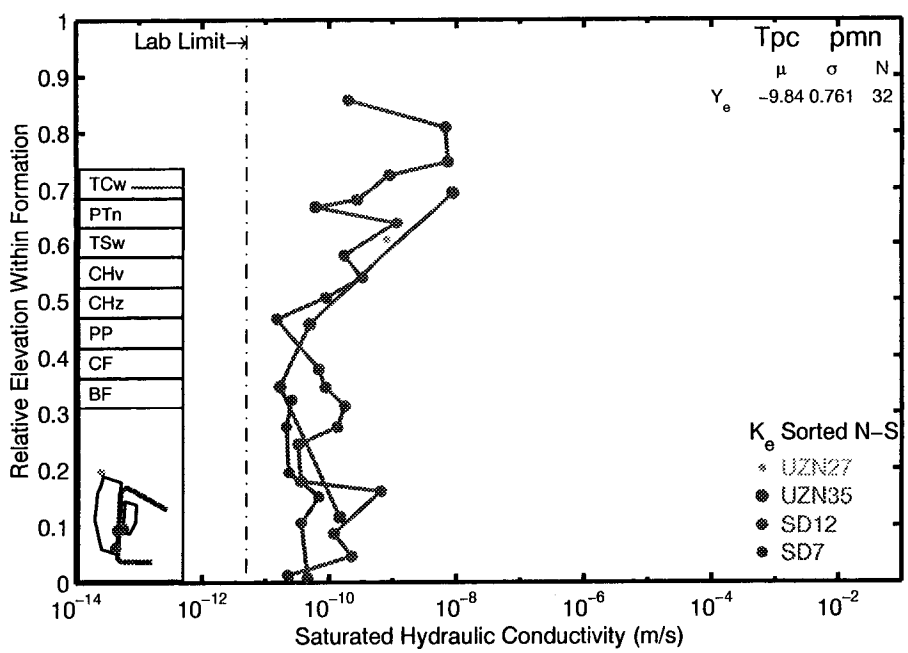

(b)

Figure 2-37: 9/17/97. All CNWRA-estimated and USGS-measured K_{sat} values in formation: (a) Tpcpul (**FormK_Tpcpul_c.eps**), and (b) Tpcpmn (**FormK_Tpcpmn_c.eps**).

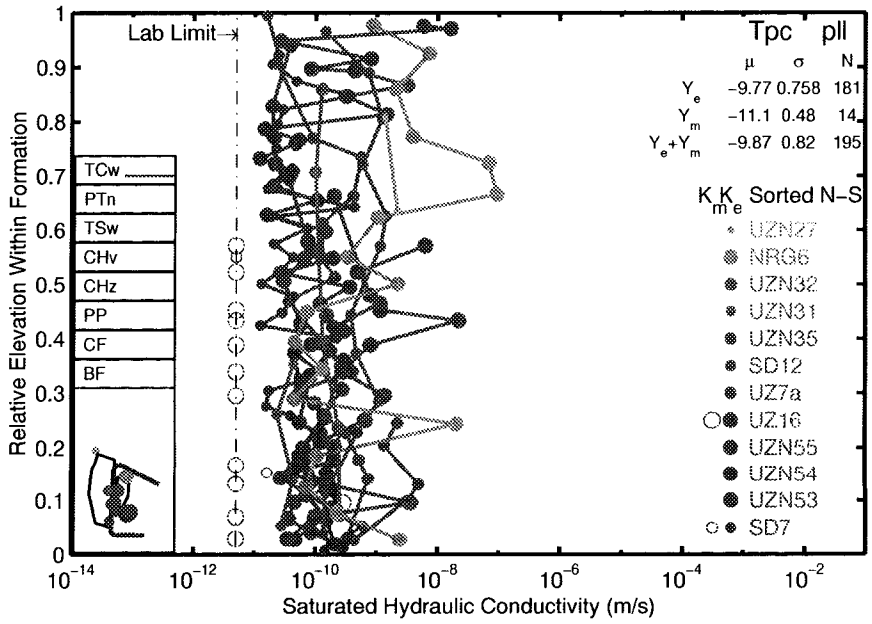

(a)

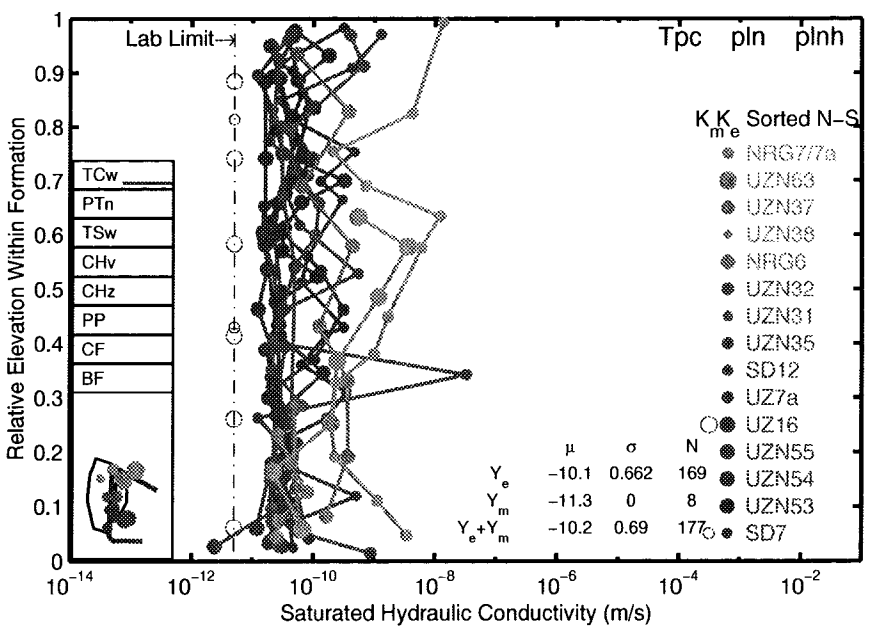

(b)

Figure 2-38: 9/17/97. All CNWRA-estimated and USGS-measured K_{sat} values in formation: (a) Tpcpll (**FormK_Tpcpll_c.eps**), and (b) Tpcplnh (**FormK_Tpcplnh_c.eps**).

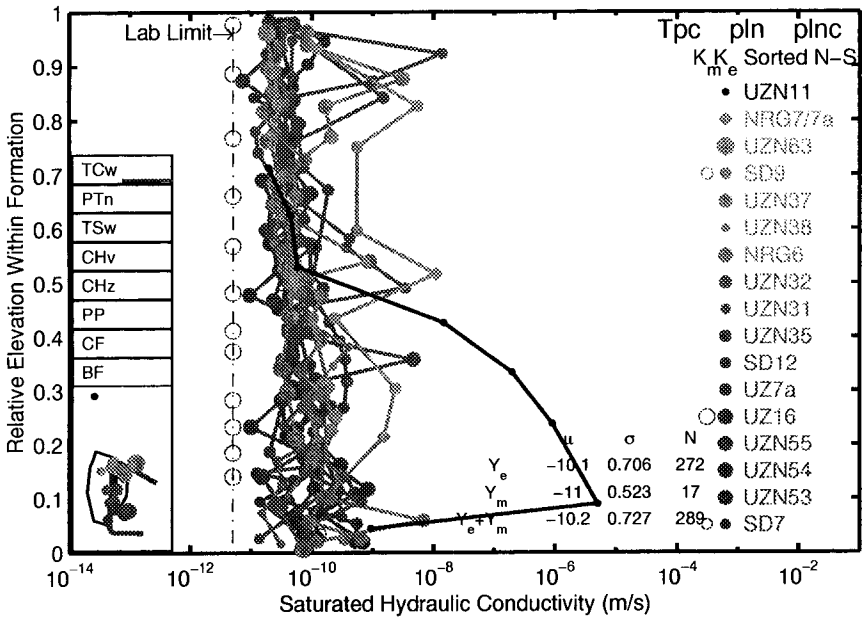

(a)

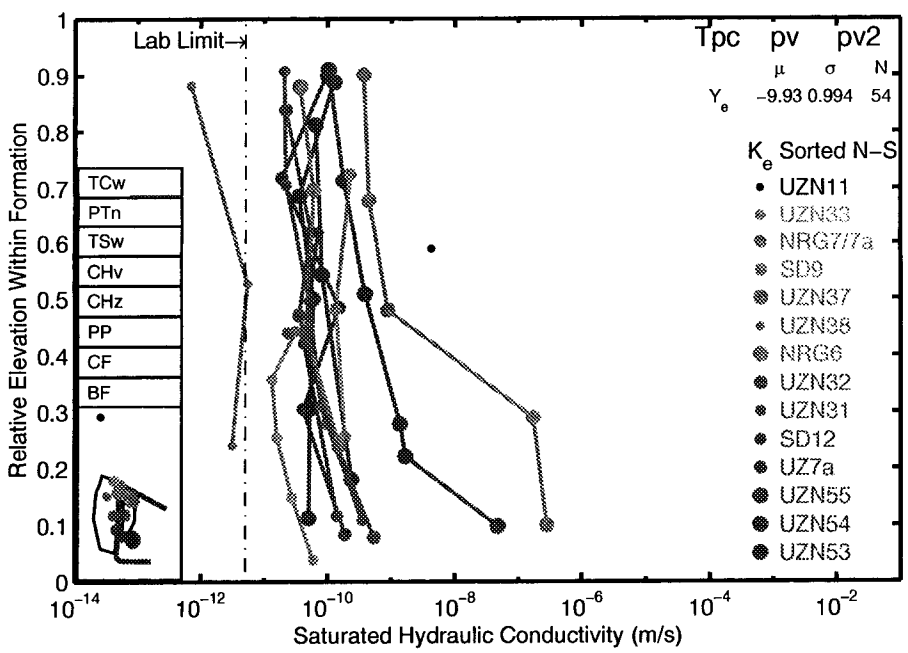

(b)

Figure 2-39: 9/17/97. All CNWRA-estimated and USGS-measured K_{sat} values in formation: (a) Tpcplnc (**FormK_Tpcplnc_c.eps**), and (b) Tpcpv2 (**FormK_Tpcpv2_c.eps**).

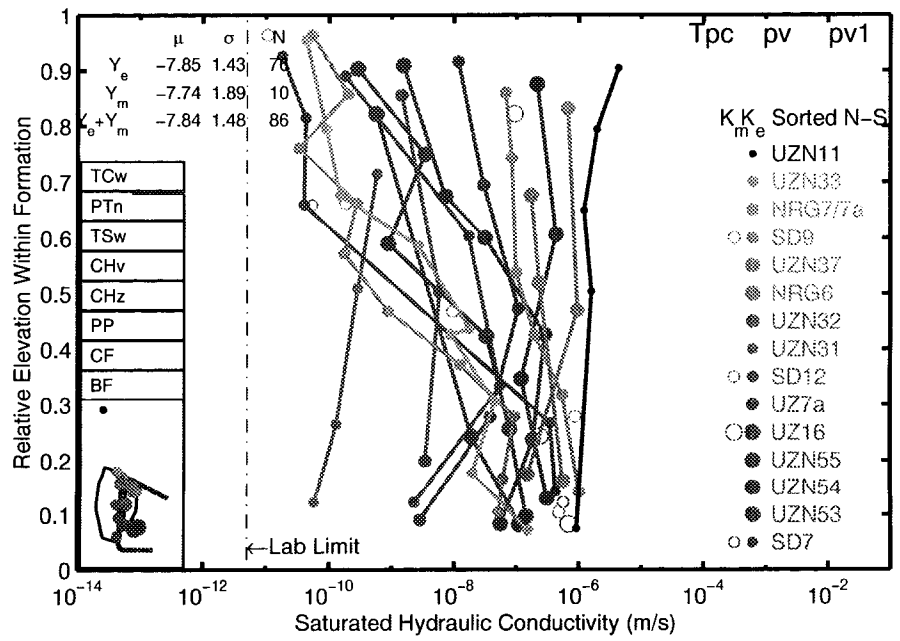

(a)

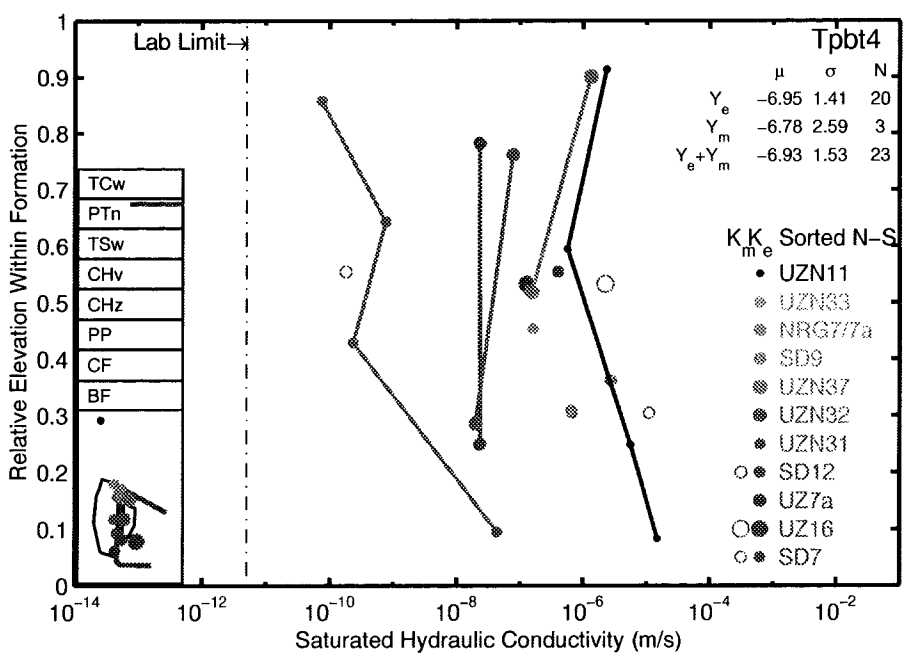

(b)

Figure 2-40: 9/17/97. All CNWRA-estimated and USGS-measured K_{sat} values in formation: (a) Tpcpv1 (**FormK_Tpcpv1_c.eps**), and (b) Tpbt4 (**FormK_Tpbt4_c.eps**).

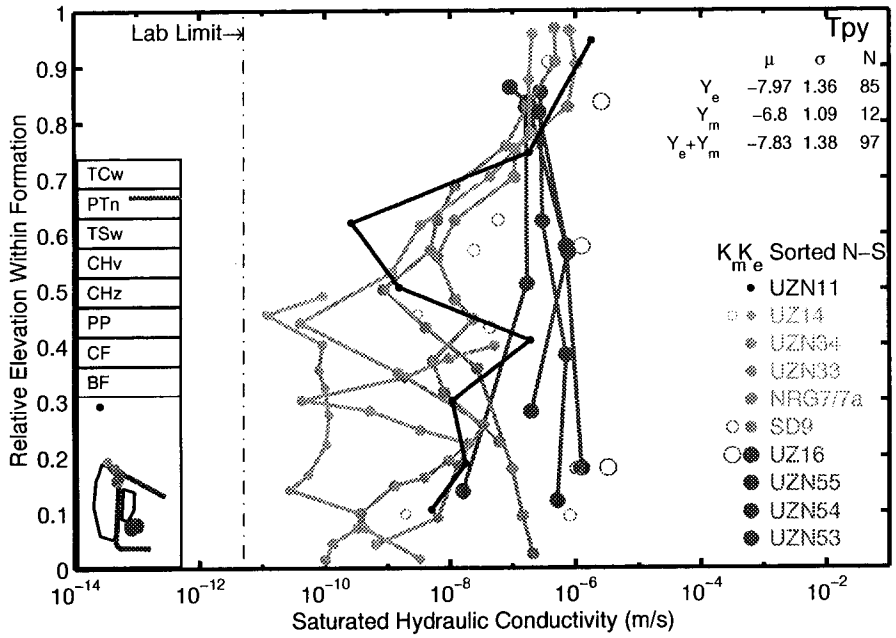

(a)

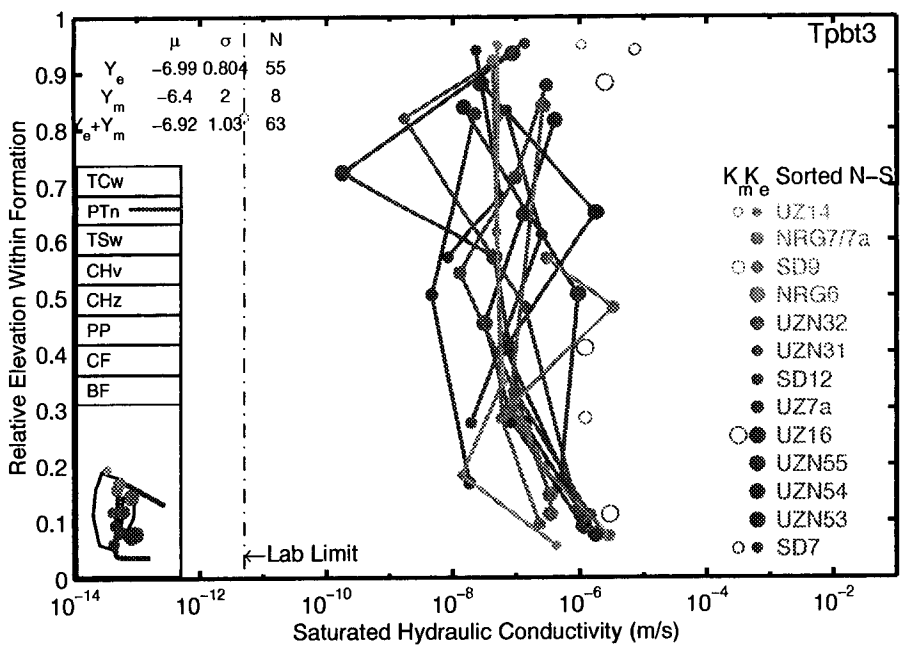

(b)

Figure 2-41: 9/17/97. All CNWRA-estimated and USGS-measured K_{sat} values in formation: (a) Tpy (**FormK_Tpy_c.eps**), and (b) Tpbt3 (**FormK_Tpbt3_c.eps**).

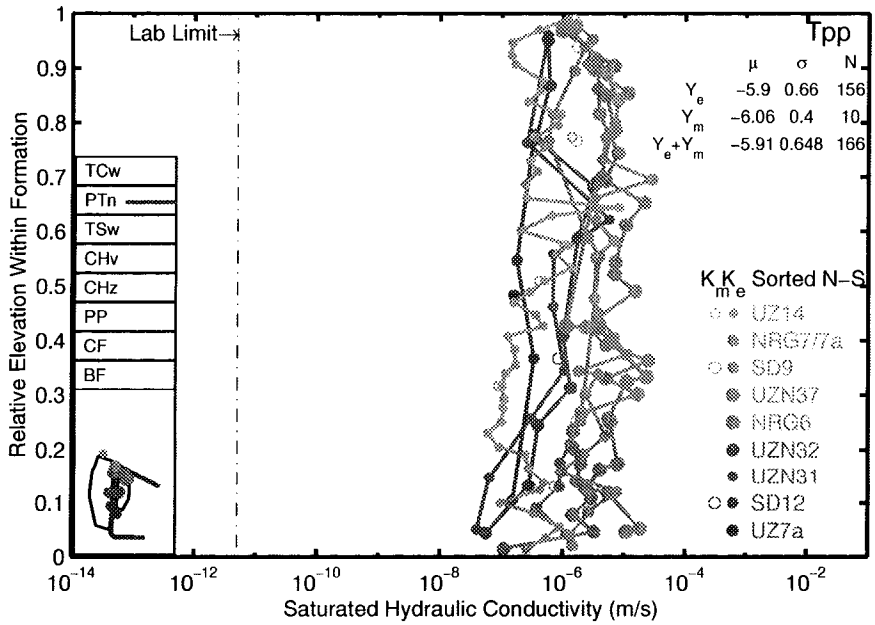

(a)

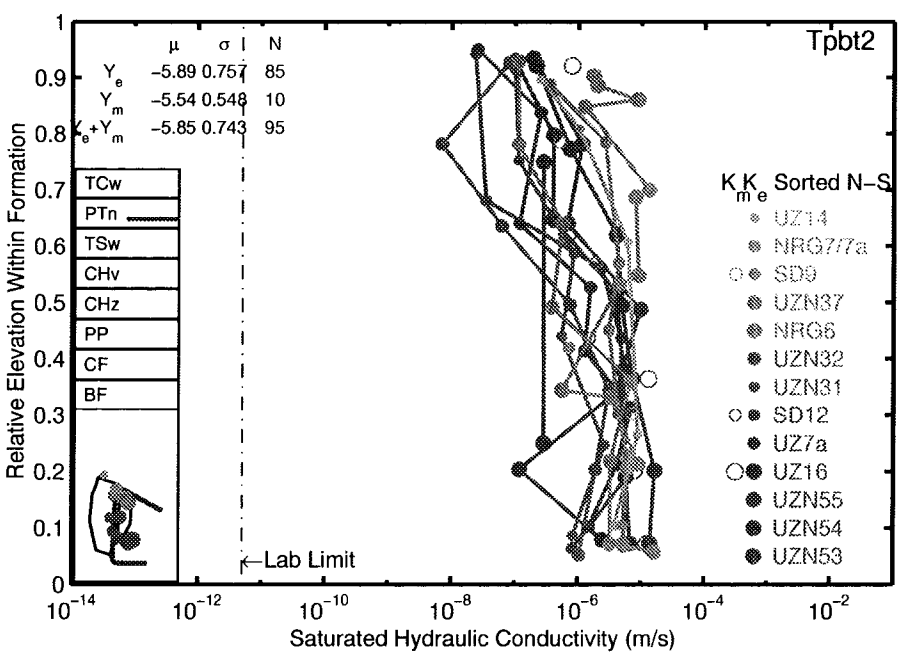

(b)

Figure 2-42: 9/17/97. All CNWRA-estimated and USGS-measured K_{sat} values in formation: (a) Tpp (**FormK_Tpp_c.eps**), and (b) Tpbt2 (**FormK_Tpbt2_c.eps**).

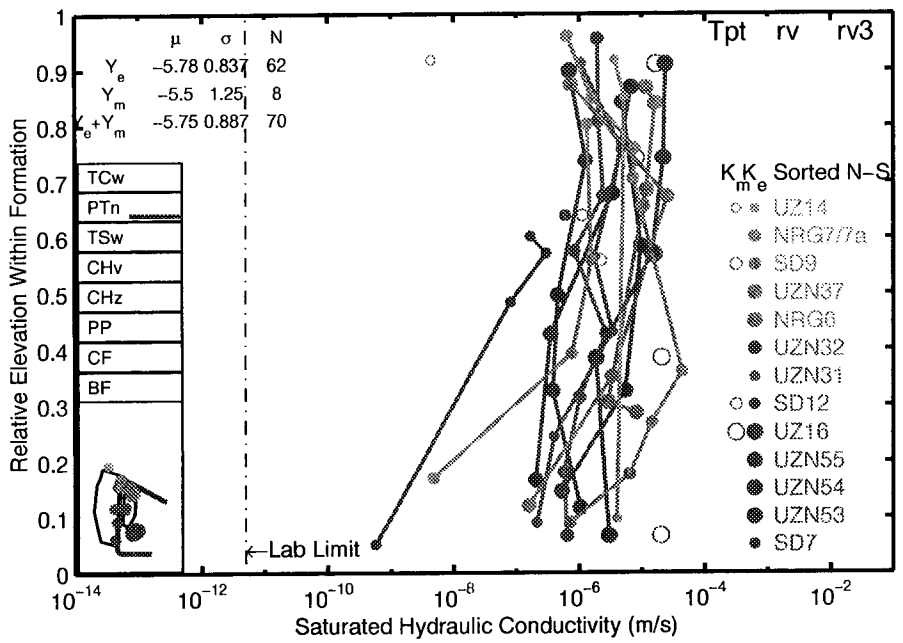

(a)

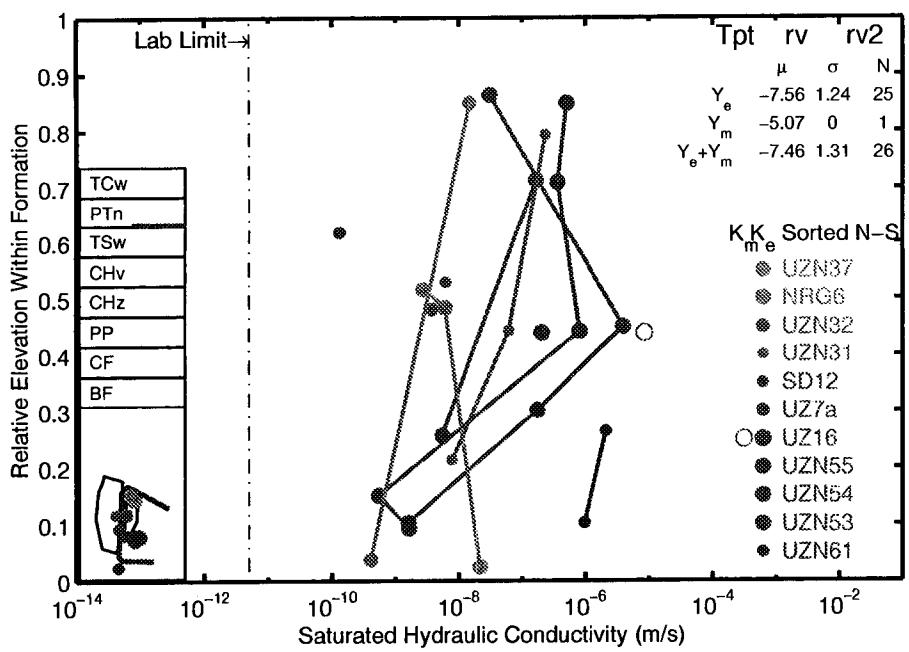

(b)

Figure 2-43: 9/17/97. All CNWRA-estimated and USGS-measured K_{sat} values in formation: (a) Tptrv3 (**FormK_Tptrv3_c.eps**), and (b) Tptrv2 (**FormK_Tptrv2_c.eps**).

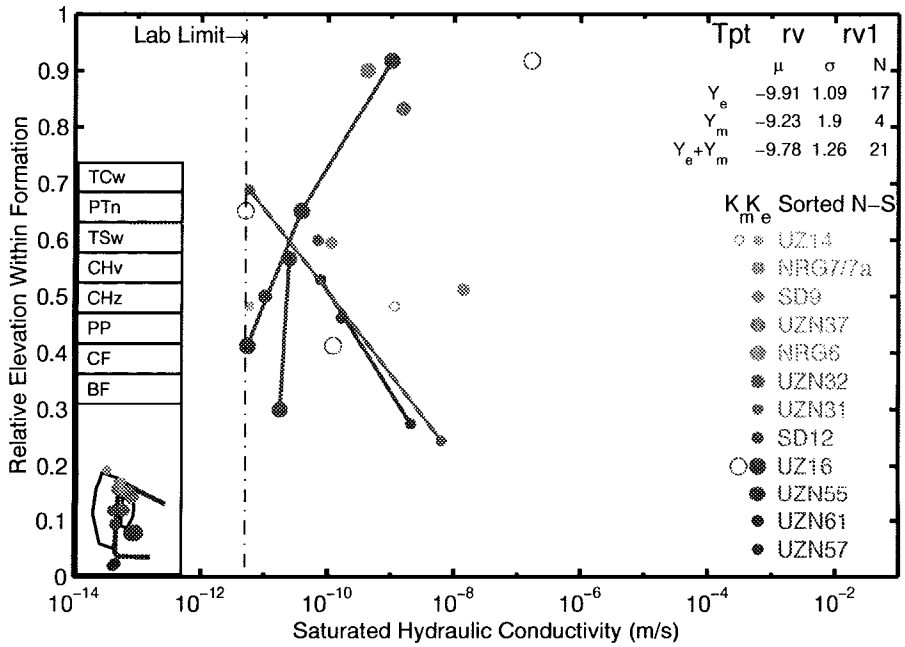

(a)

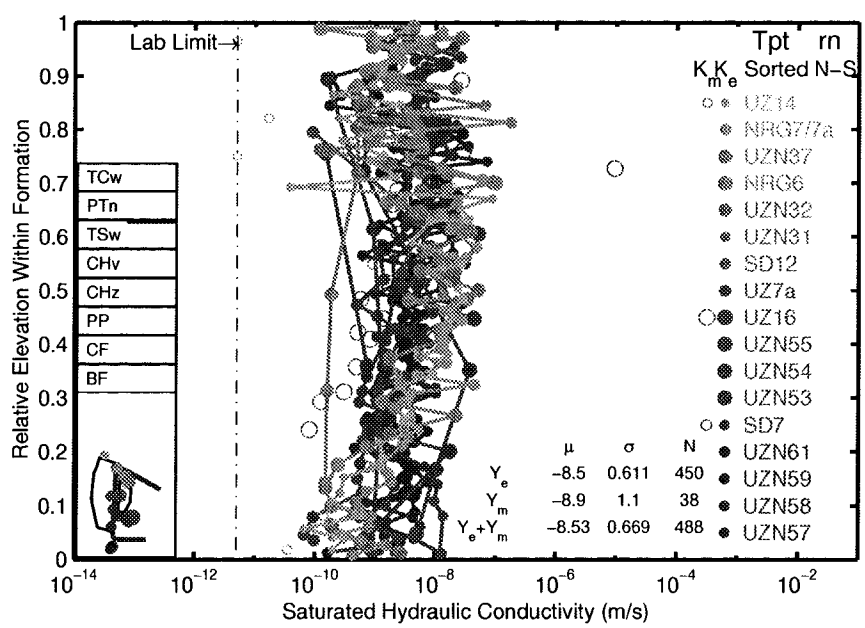

(b)

Figure 2-44: 9/17/97. All CNWRA-estimated and USGS-measured K_{sat} values in formation: (a) Tptrv1 (**FormK_Tptrv1_c.eps**), and (b) Tptrn (**FormK_Tptrn_c.eps**).

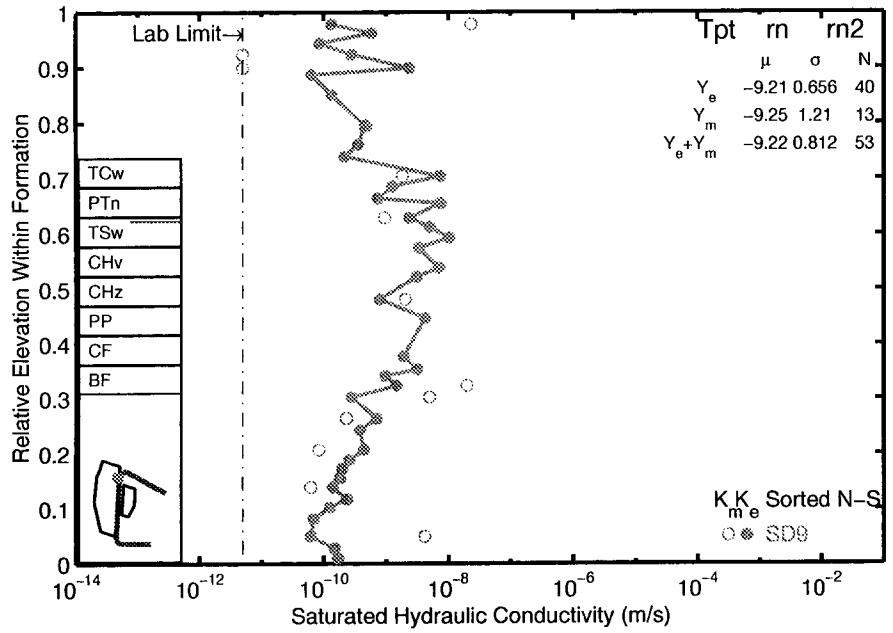

(a)

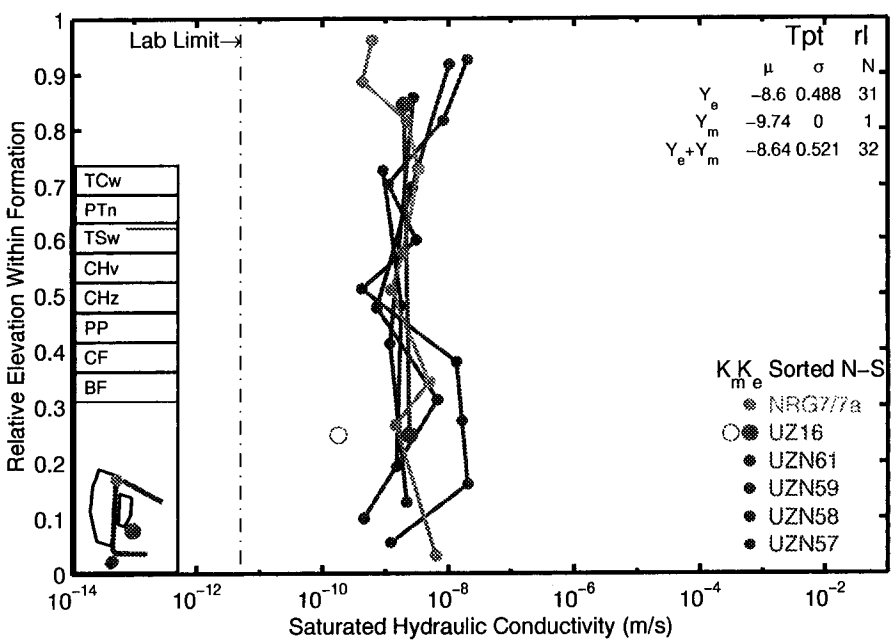

(b)

Figure 2-45: 9/17/97. All CNWRA-estimated and USGS-measured K_{sat} values in formation: (a) Tptrn2 (**FormK_Tptrn2_c.eps**), and (b) Tptrl (**FormK_Tptrl_c.eps**).

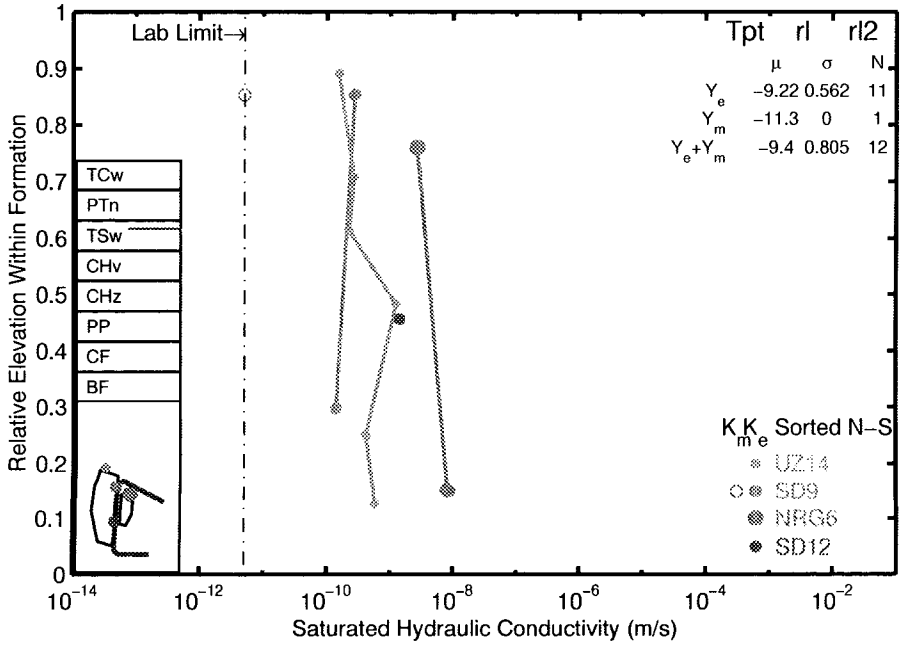

(a)

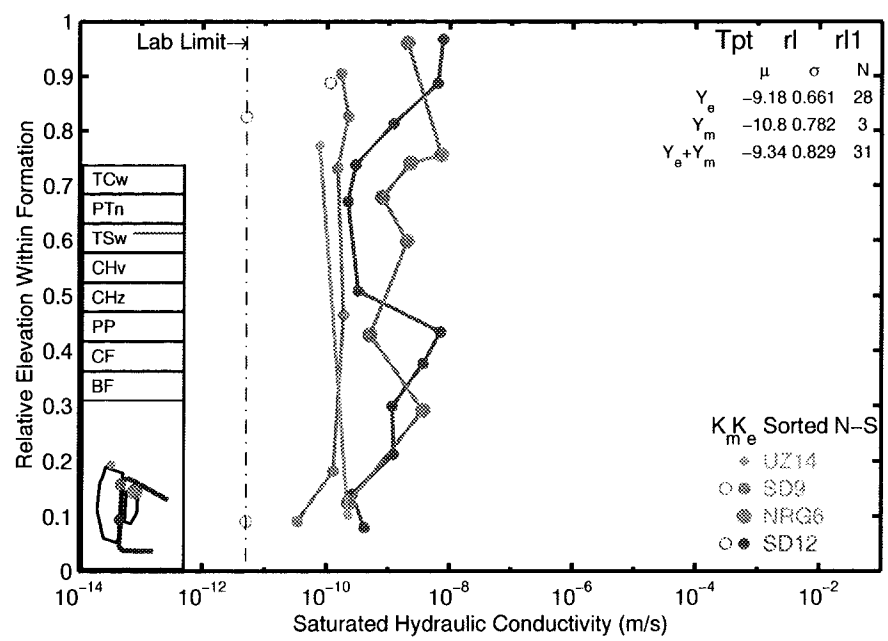

(b)

Figure 2-46: 9/17/97. All CNWRA-estimated and USGS-measured K_{sat} values in formation: (a) Tptrl2 (**FormK_Tptrl2_c.eps**), and (b) Tptrl1 (**FormK_Tptrl1_c.eps**).

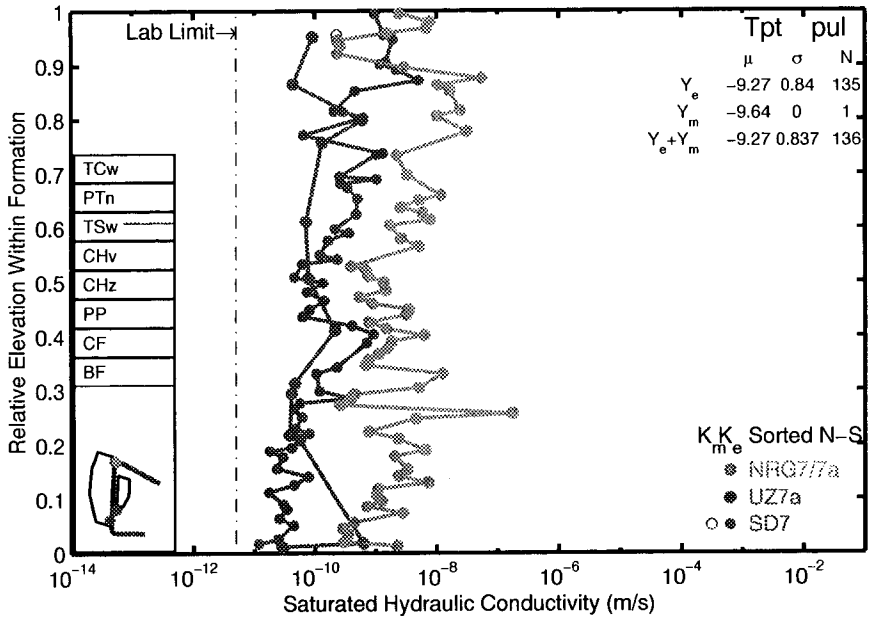

(a)

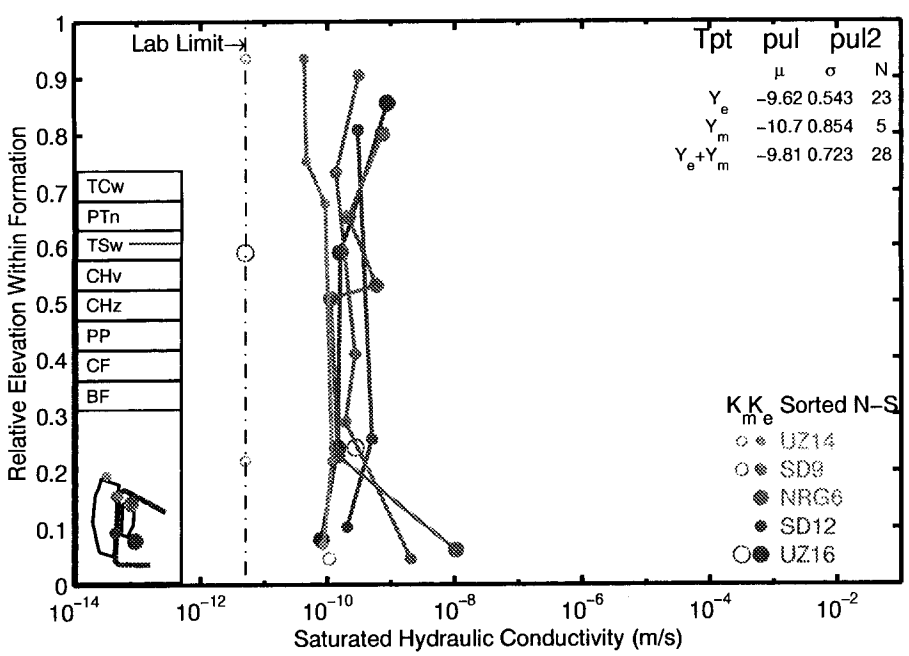

(b)

Figure 2-47: 9/17/97. All CNWRA-estimated and USGS-measured K_{sat} values in formation: (a) Tptpul (**FormK_Tptpul_c.eps**), and (b) Tptpul2 (**FormK_Tptpul2_c.eps**).

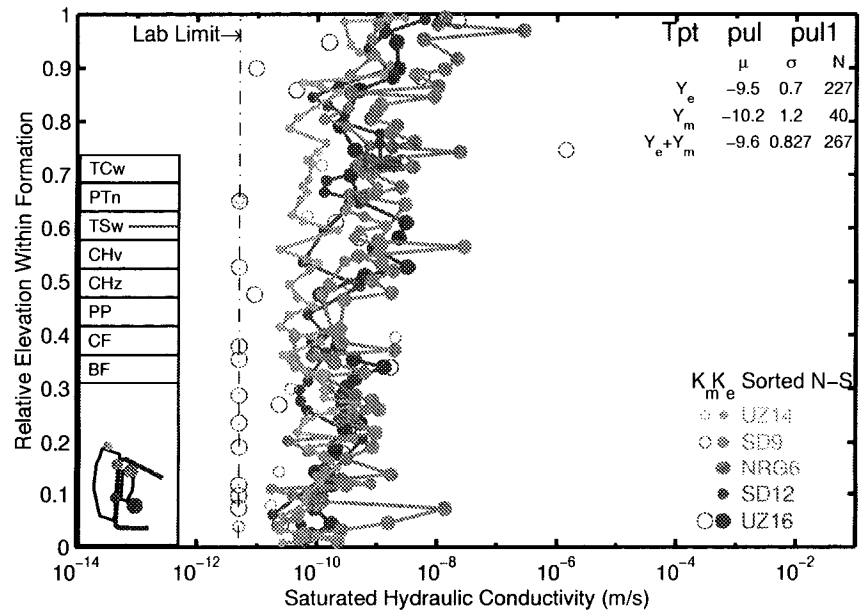

(a)

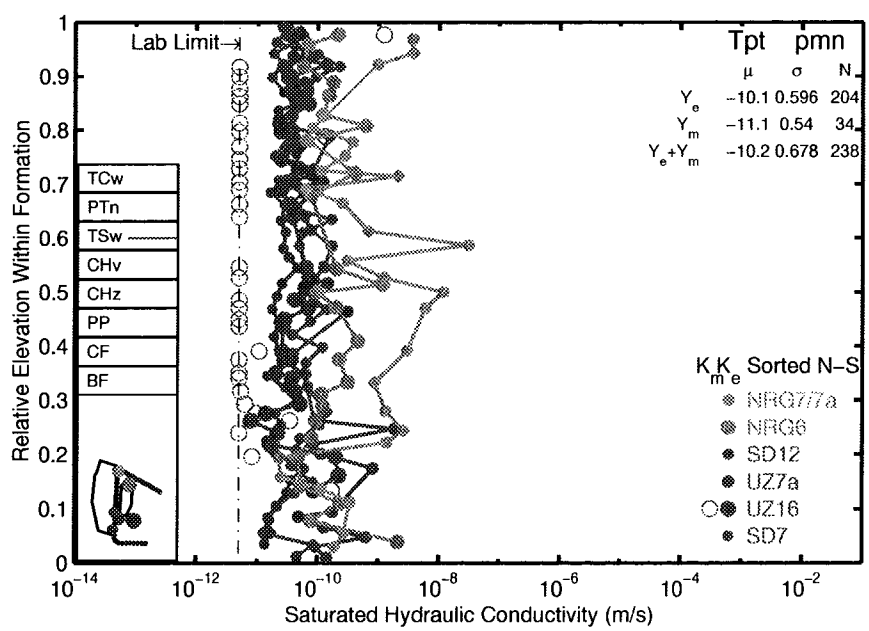

(b)

Figure 2-48: 9/17/97. All CNWRA-estimated and USGS-measured K_{sat} values in formation: (a) Tptpul1 (**FormK_Tptpul1_c.eps**), and (b) Tptpmn (**FormK_Tptpmn_c.eps**).

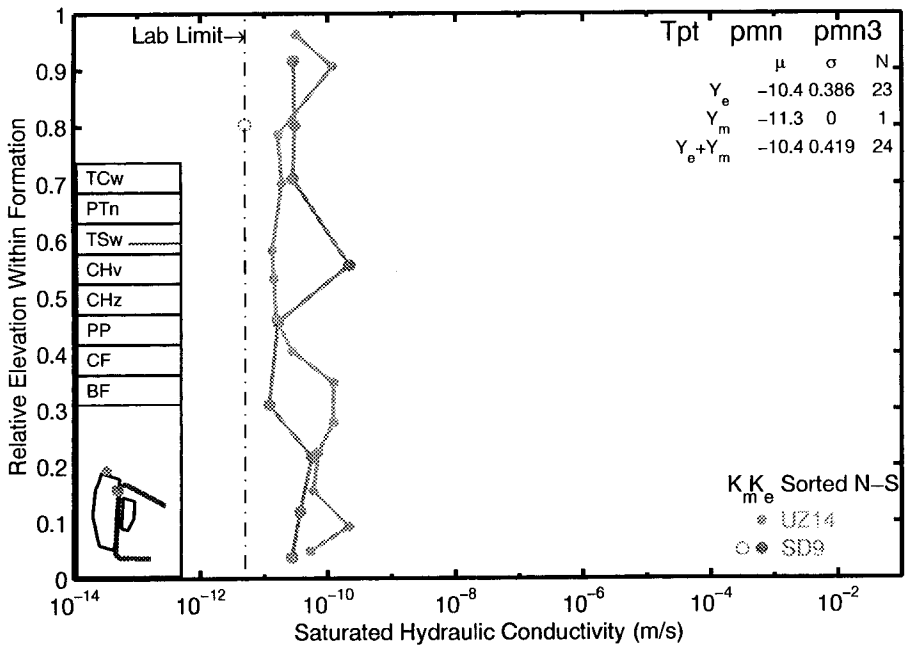

(a)

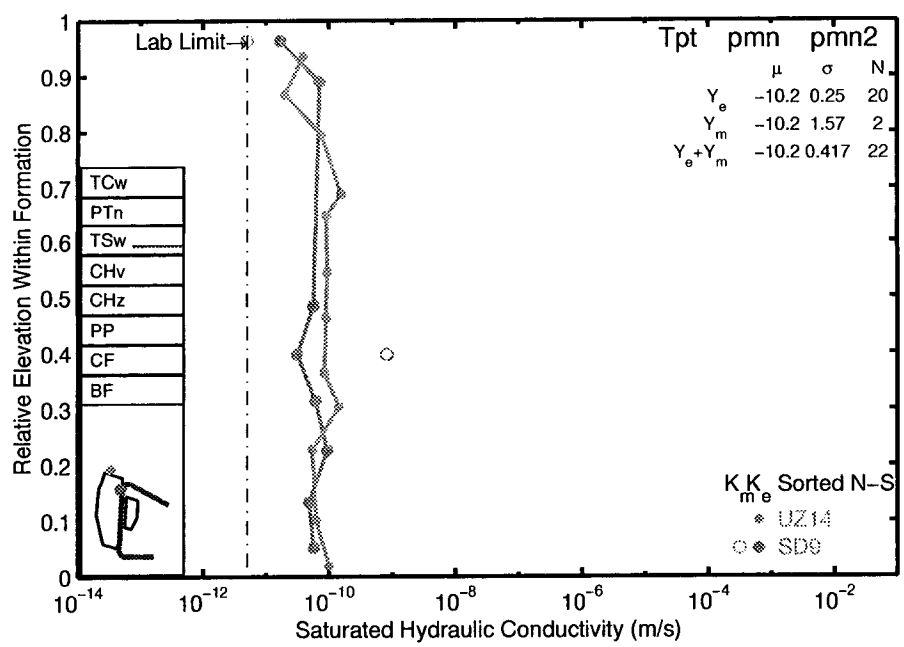

(b)

Figure 2-49: 9/17/97. All CNWRA-estimated and USGS-measured K_{sat} values in formation: (a) Tptpmn3 (**FormK_Tptpmn3_c.eps**), and (b) Tptpmn2 (**FormK_Tptpmn2_c.eps**).

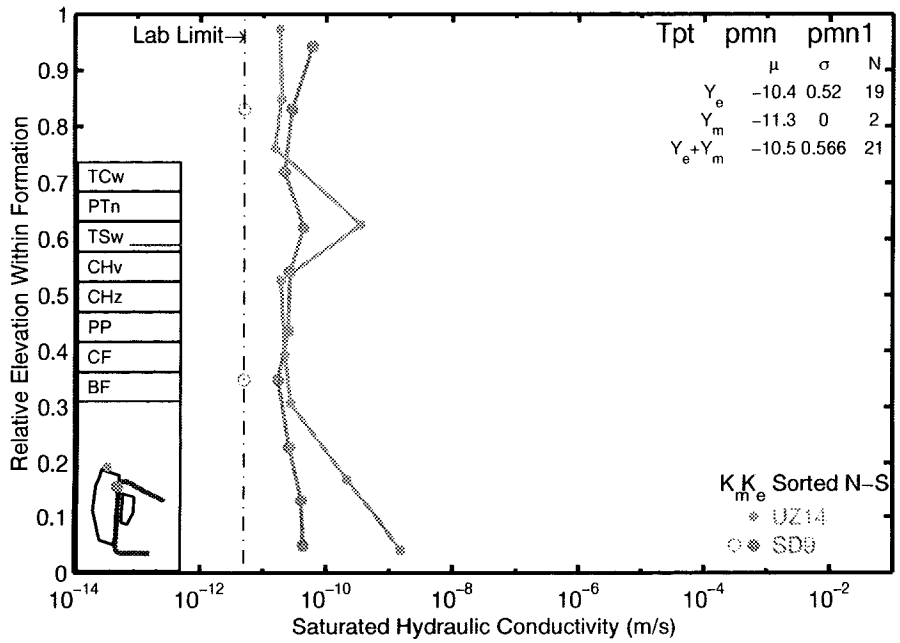

(a)

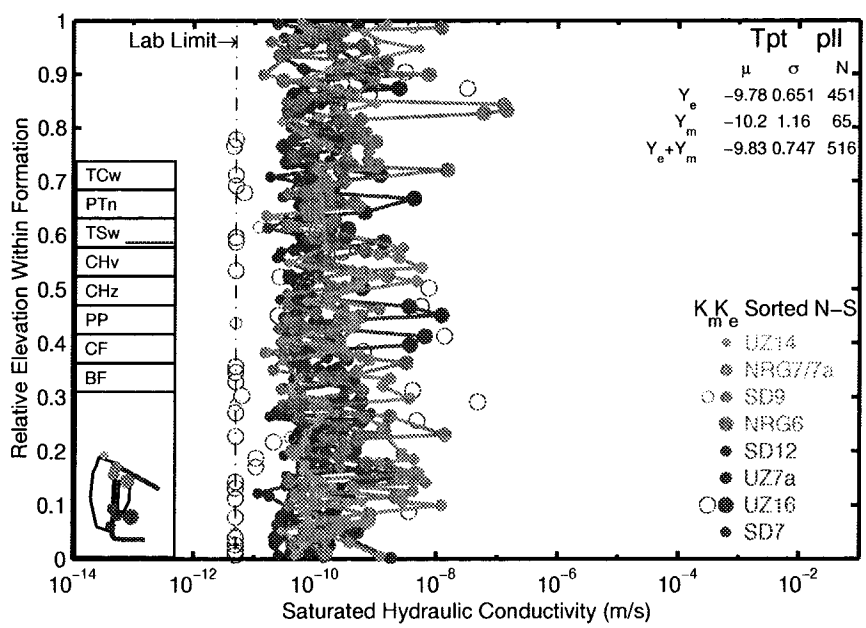

(b)

Figure 2-50: 9/17/97. All CNWRA-estimated and USGS-measured K_{sat} values in formation: (a) Tptpmn1 (**FormK_Tptpmn1_c.eps**), and (b) Tptpll (**FormK_Tptpll_c.eps**).

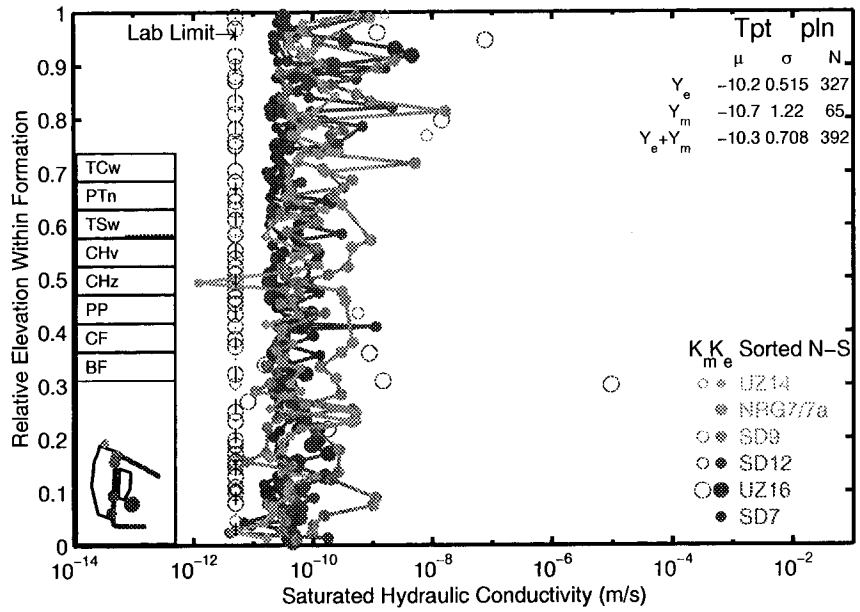

(a)

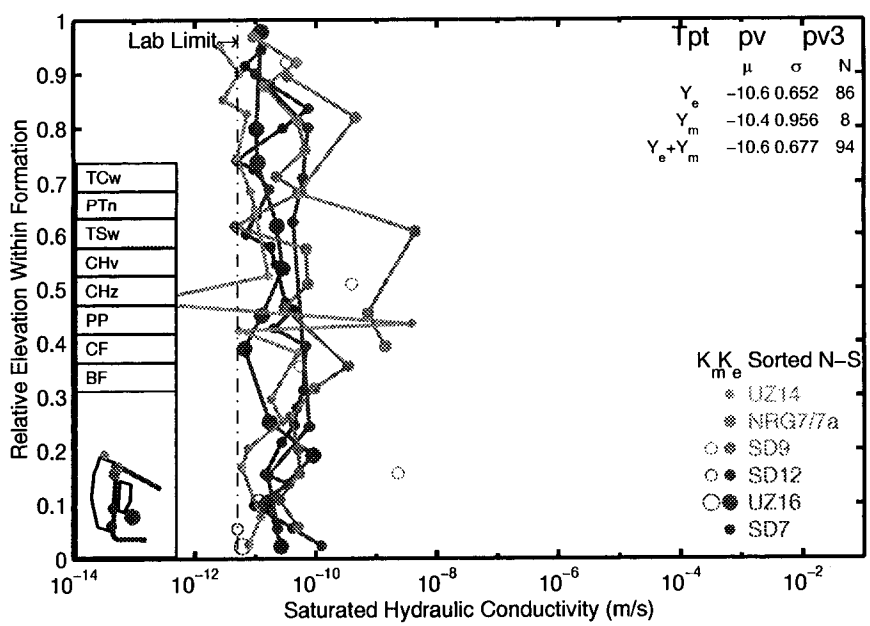

(b)

Figure 2-51: 9/17/97. All CNWRA-estimated and USGS-measured K_{sat} values in formation: (a) Tptpln (**FormK_Tptpln_c.eps**), and (b) Tptpv3 (**FormK_Tptpv3_c.eps**).

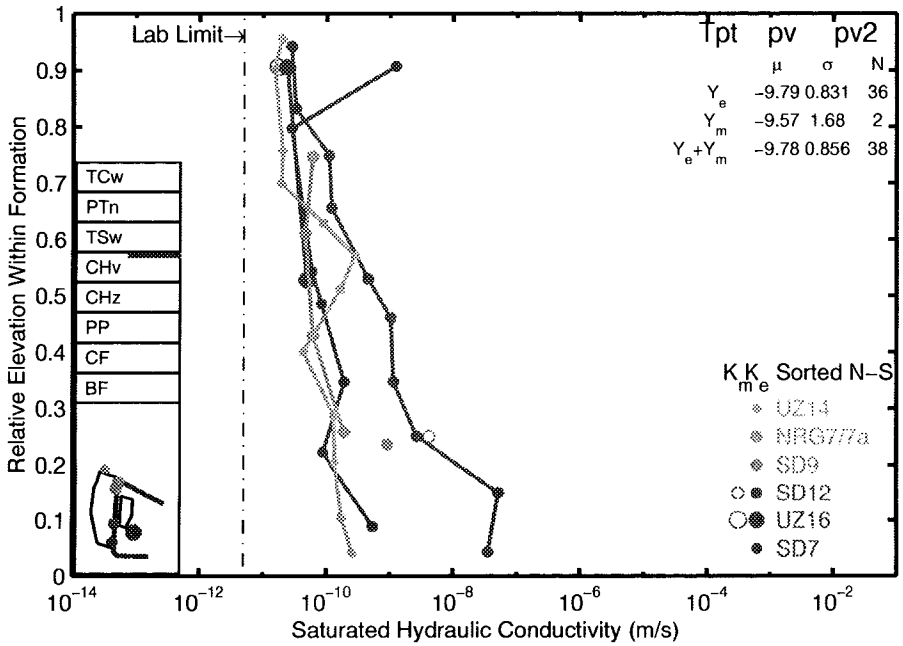

(a)

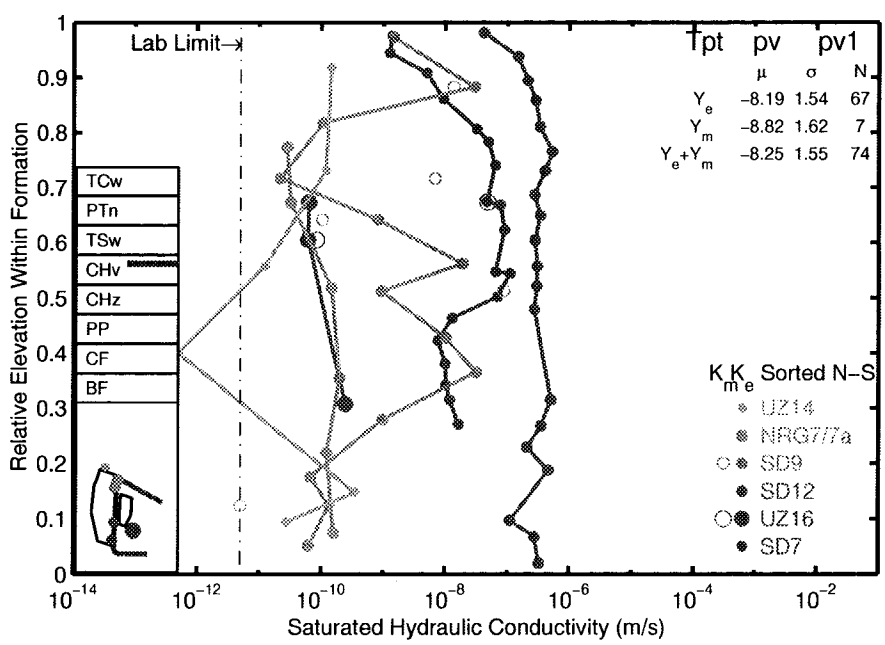

(b)

Figure 2-52: 9/17/97. All CNWRA-estimated and USGS-measured K_{sat} values in formation: (a) Tptpv2 (**FormK_Tptpv2_c.eps**), and (b) Tptpv1 (**FormK_Tptpv1_c.eps**).

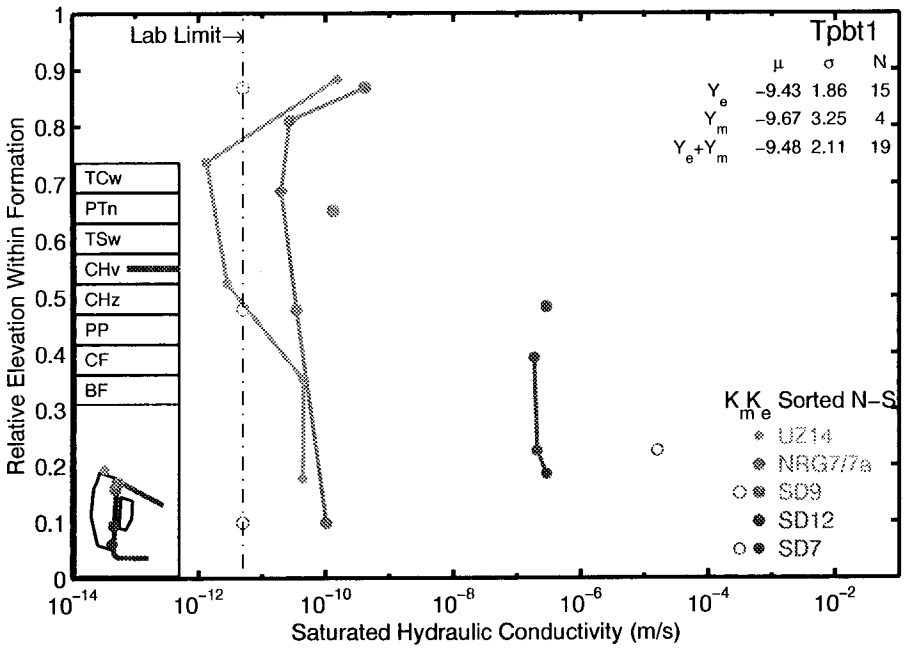

(a)

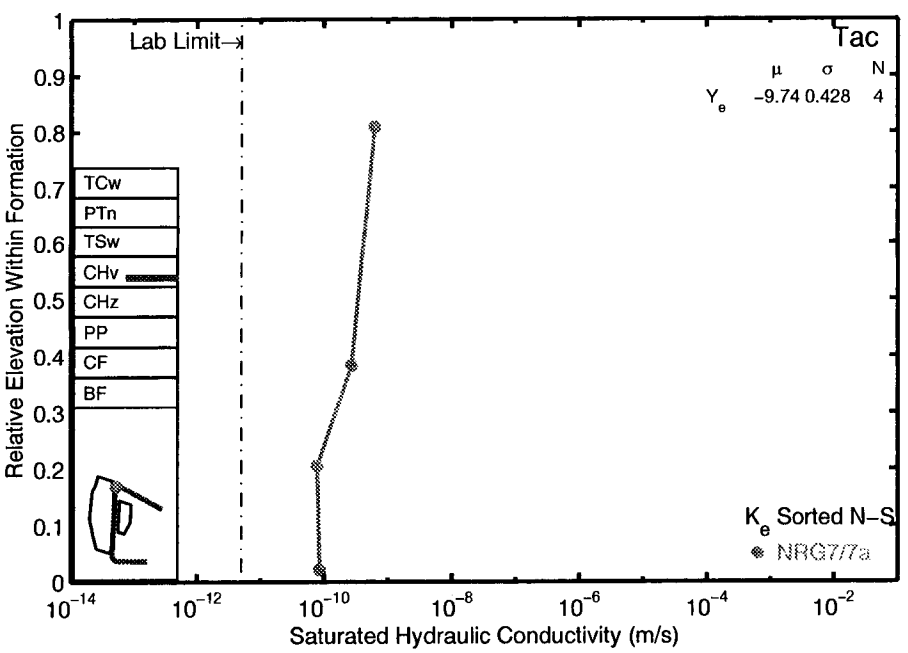

(b)

Figure 2-53: 9/17/97. All CNWRA-estimated and USGS-measured K_{sat} values in formation: (a) Tpbt1 (**FormK_Tpbt1_c.eps**), and (b) Tac (**FormK_Tac_c.eps**).

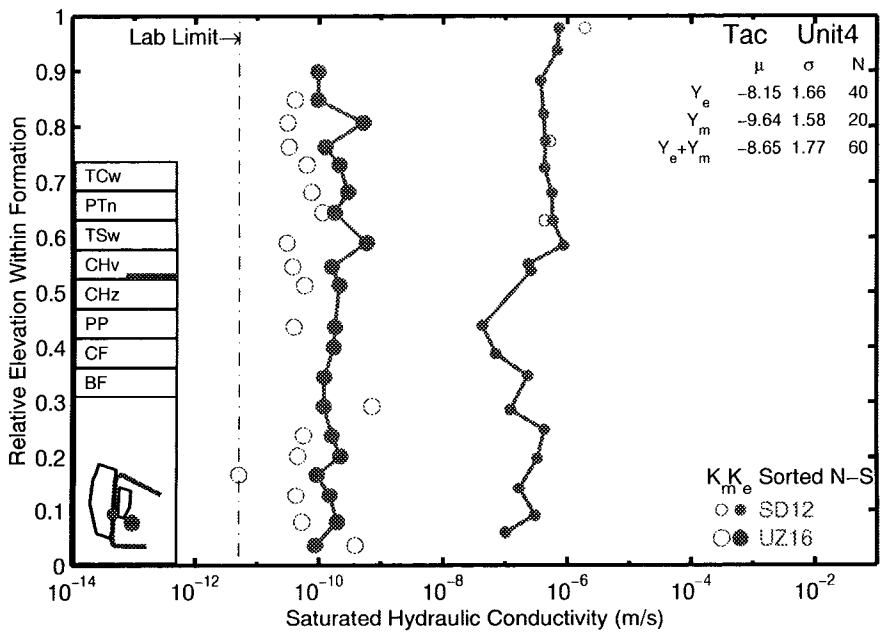

(a)

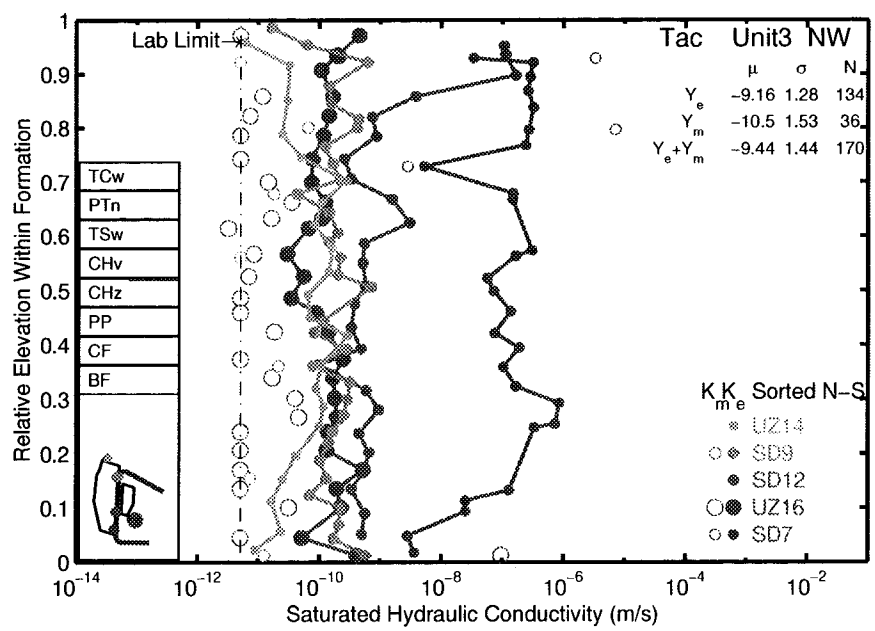

(b)

Figure 2-54: 9/17/97. All CNWRA-estimated and USGS-measured K_{sat} values in formation: (a) TacUnit4 (**FormK_TacUnit4_c.eps**), and (b) TacUnit3NW (**FormK_TacUnit3NW_c.eps**).

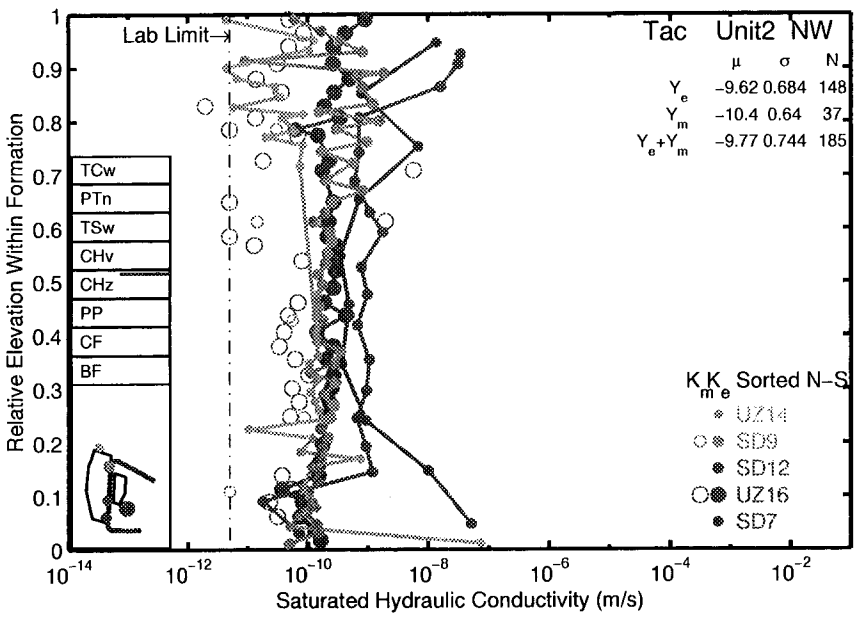

(a)

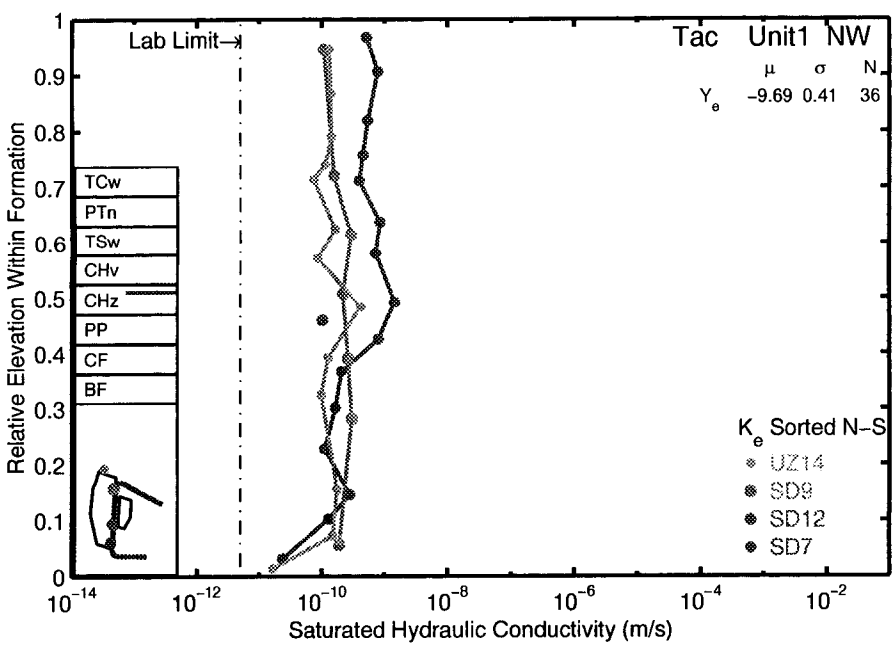

(b)

Figure 2-55: 9/17/97. All CNWRA-estimated and USGS-measured K_{sat} values in formation: (a) TacUnit2NW (**FormK_TacUnit2NW_c.eps**), and (b) TacUnit1NW (**FormK_TacUnit1NW-_c.eps**).

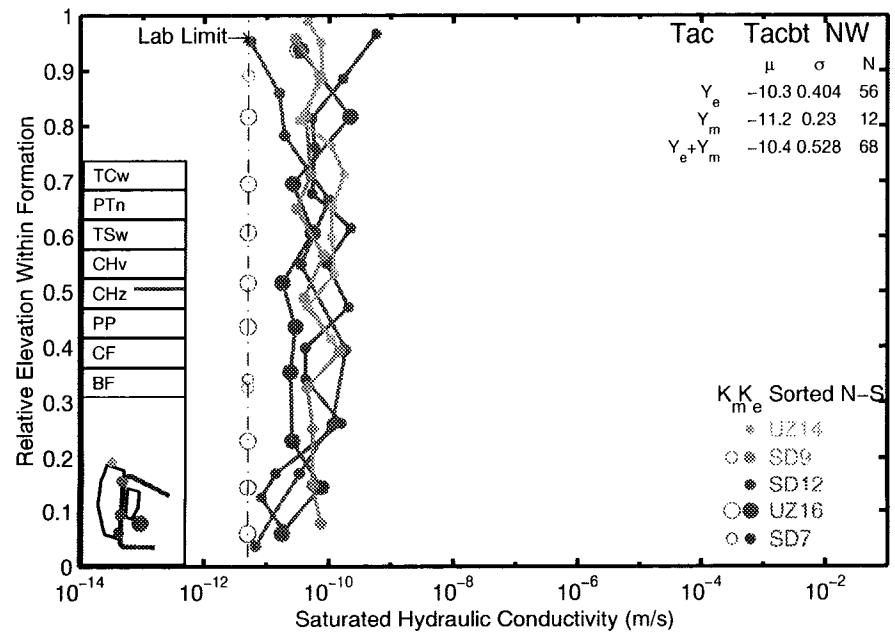

(a)

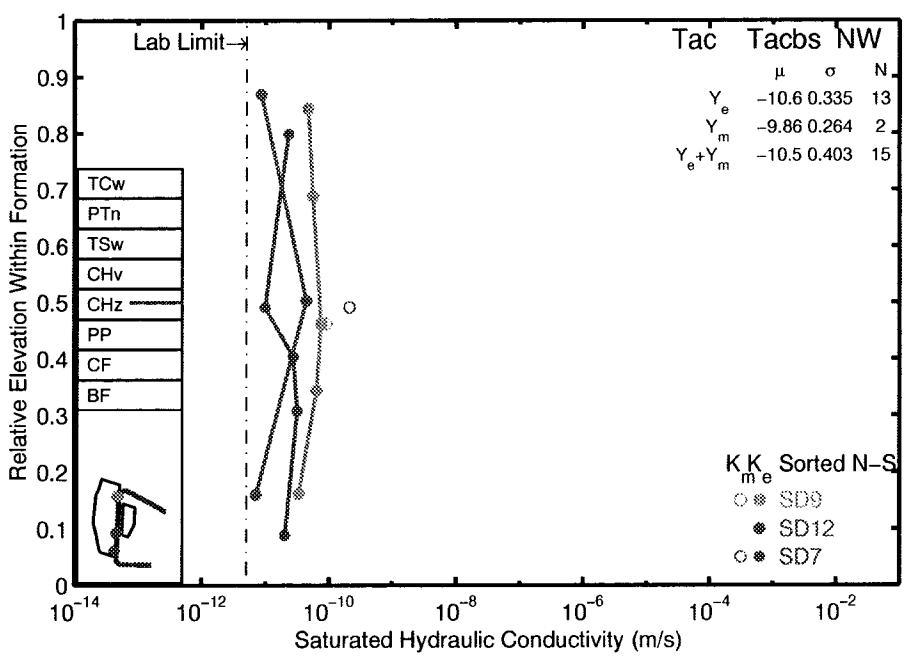

(b)

Figure 2-56: 9/17/97. All CNWRA-estimated and USGS-measured K_{sat} values in formation: (a) TacbtNW (**FormK_TacbtNW_c.eps**), and (b) TacbsNW (**FormK_TacbsNW_c.eps**).

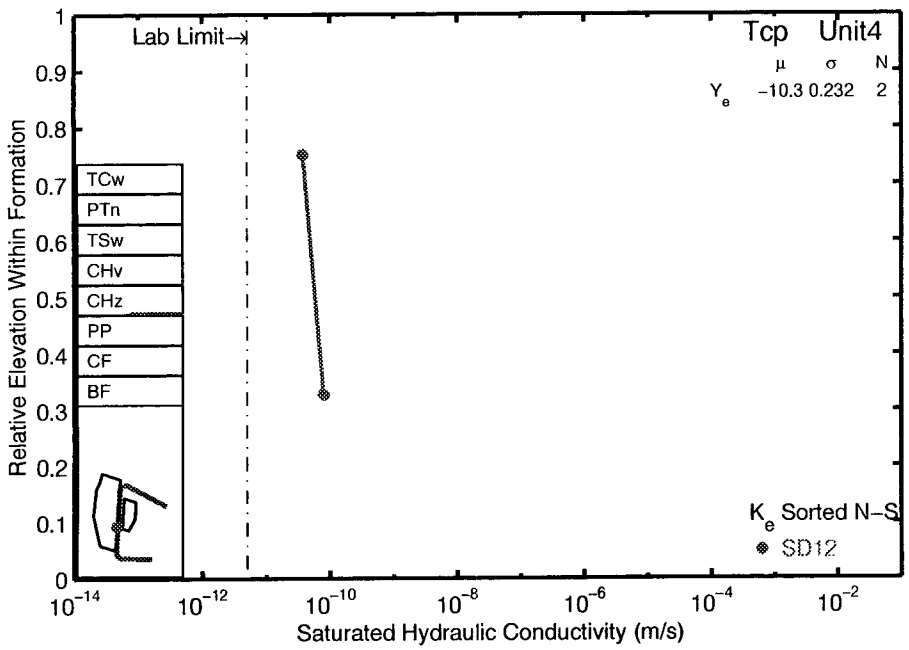

(a)

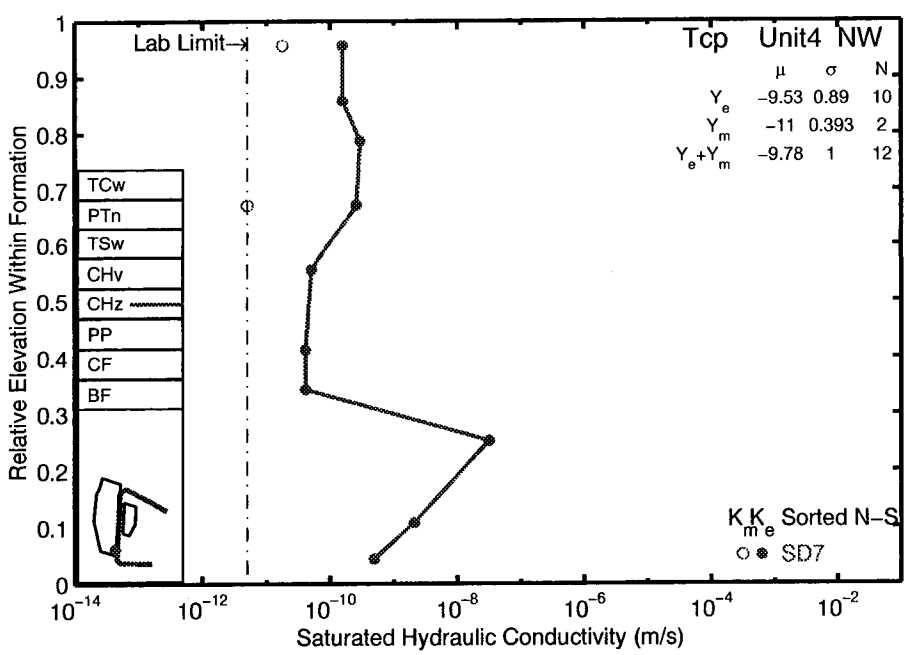

(b)

Figure 2-57: 9/17/97. All CNWRA-estimated and USGS-measured K_{sat} values in formation: (a) TcpUnit4 (**FormK_TcpUnit4_c.eps**), and (b) TcpUnit4NW (**FormK_TcpUnit4NW_c.eps**).

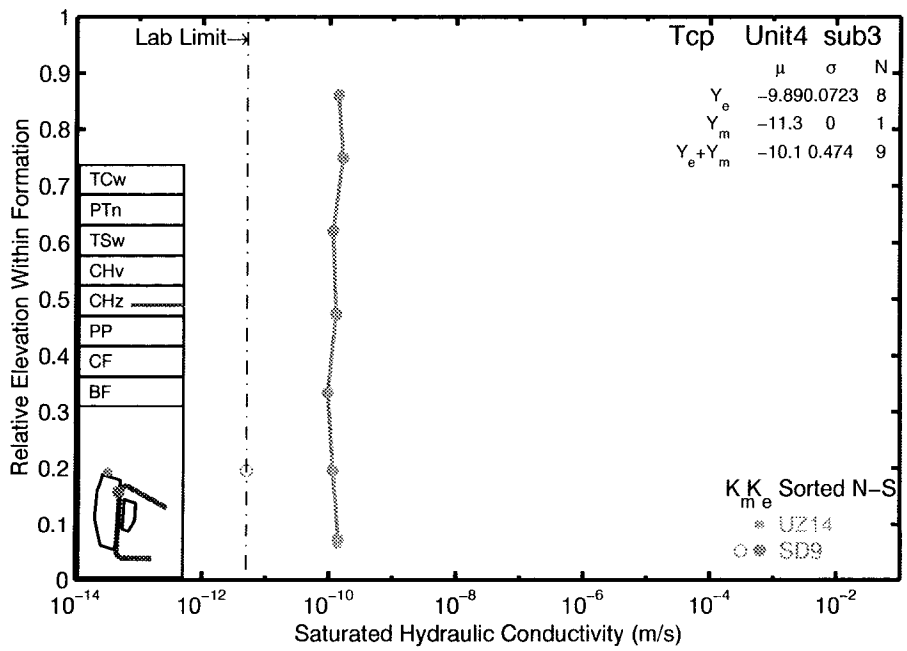

(a)

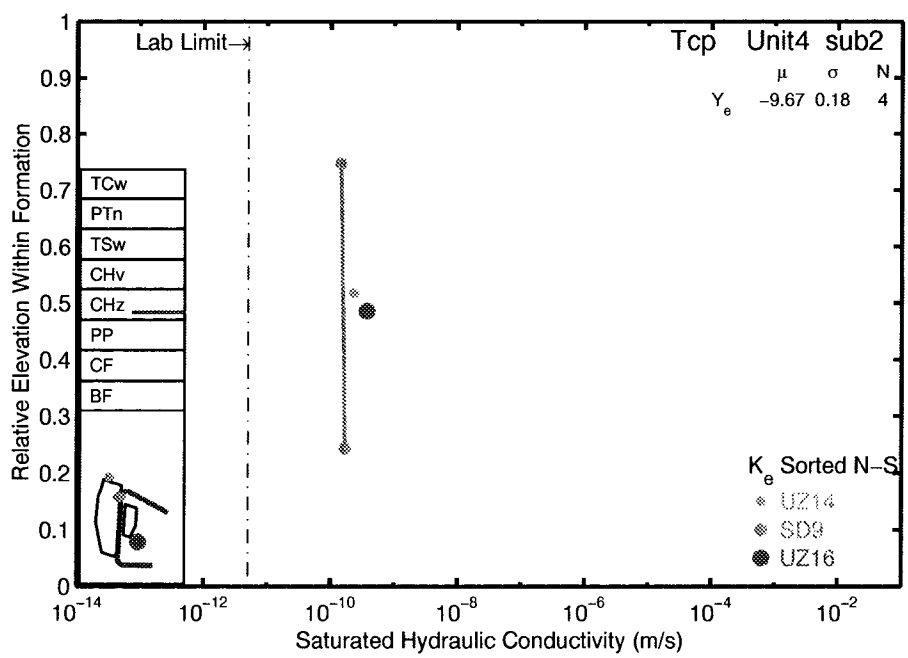

(b)

Figure 2-58: 9/17/97. All CNWRA-estimated and USGS-measured K_{sat} values in formation: (a) TcpUnit4sub3 (**FormK_TcpUnit4sub3_c.eps**), and (b) TcpUnit4sub2 (**FormK-_TcpUnit4sub2_c.eps**).

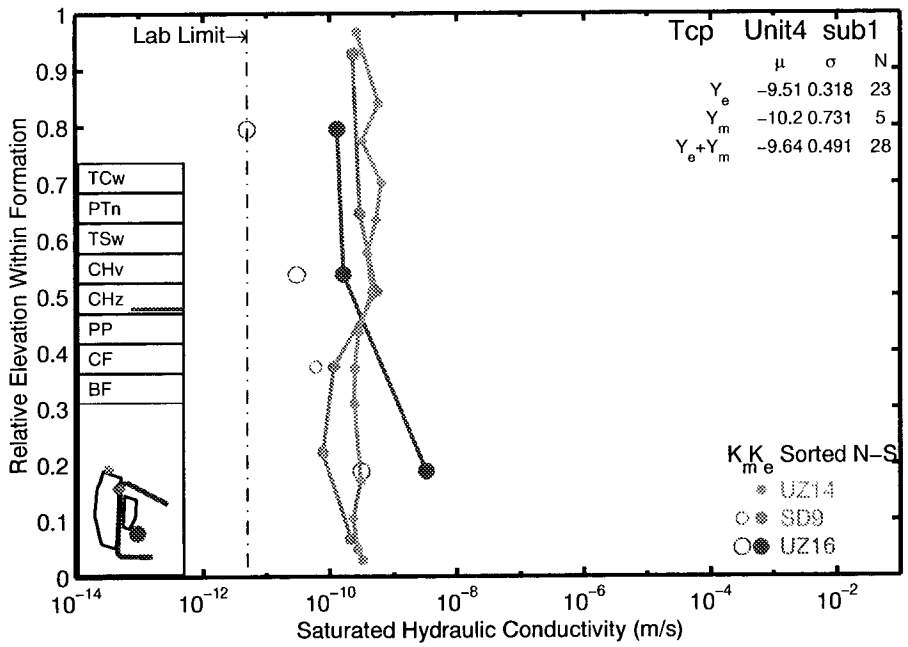

(a)

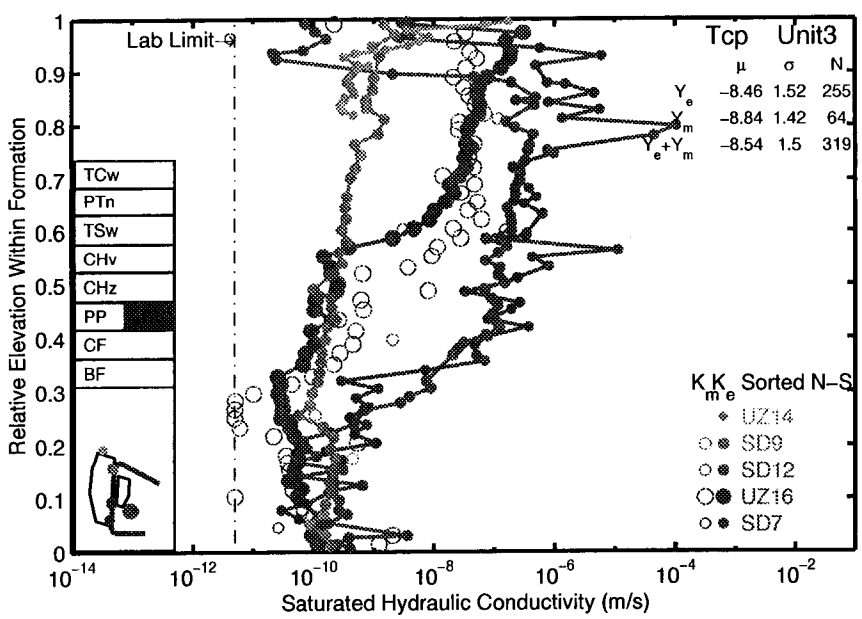

(b)

Figure 2-59: 9/17/97. All CNWRA-estimated and USGS-measured K_{sat} values in formation: (a) TcpUnit4sub1 (**FormK_TcpUnit4sub1_c.eps**), and (b) TcpUnit3 (**FormK_TcpUnit3_c.eps**).

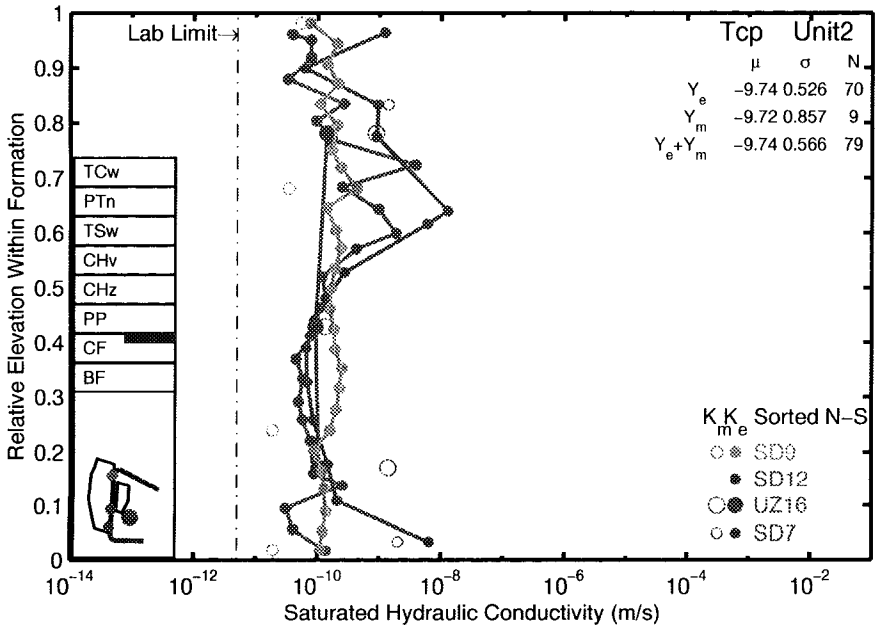

(a)

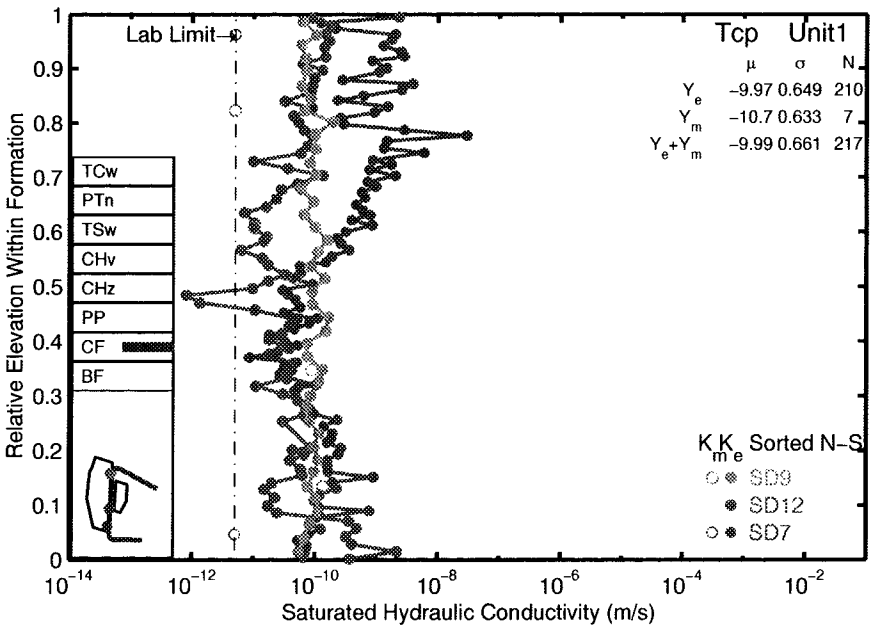

(b)

Figure 2-60: 9/17/97. All CNWRA-estimated and USGS-measured K_{sat} values in formation: (a) TcpUnit2 (**FormK_TcpUnit2_c.eps**), and (b) TcpUnit1 (**FormK_TcpUnit1_c.eps**).

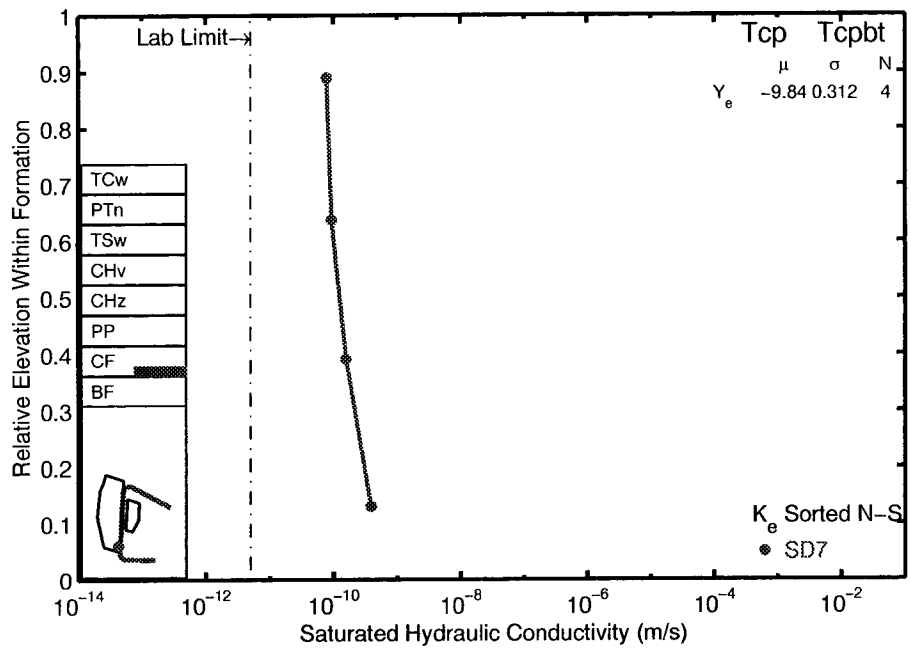

(a)

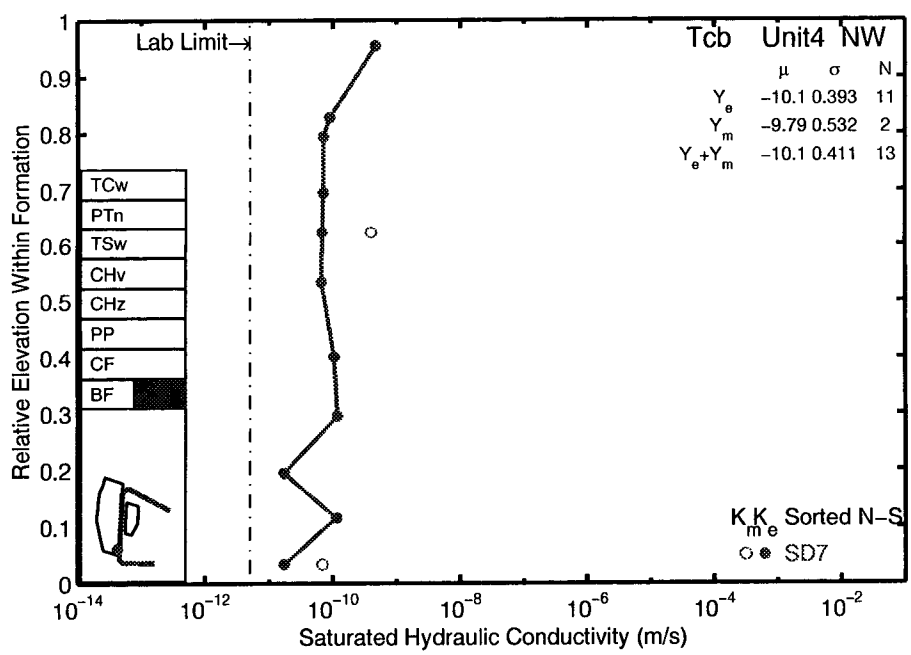

(b)

Figure 2-61: 9/17/97. All CNWRA-estimated and USGS-measured K_{sat} values in formation: (a) Tcpbt (**FormK_Tcpbt_c.eps**), and (b) TcbUnit4NW (**FormK_TcbUnit4NW_c.eps**).

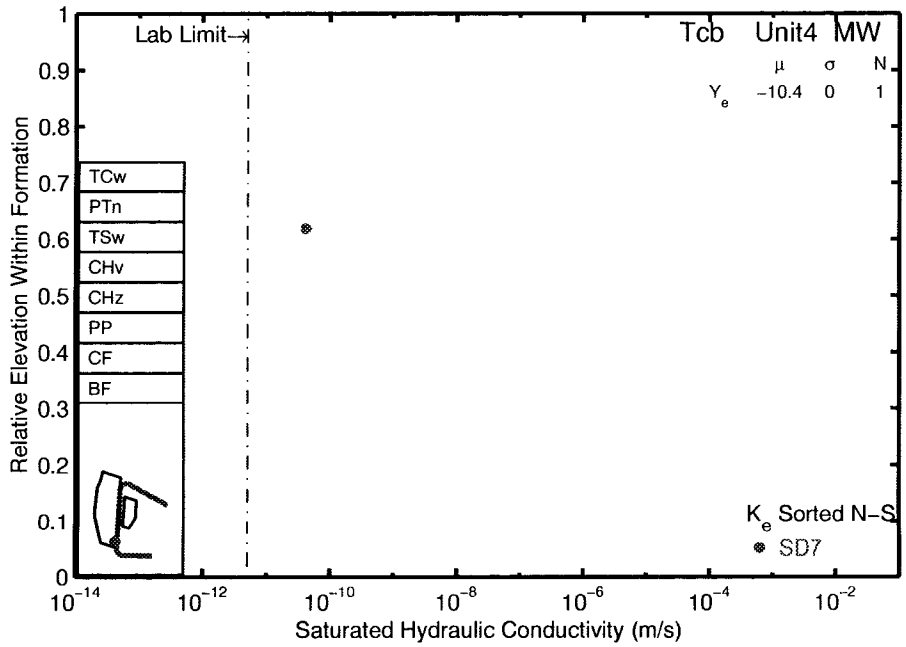

(a)

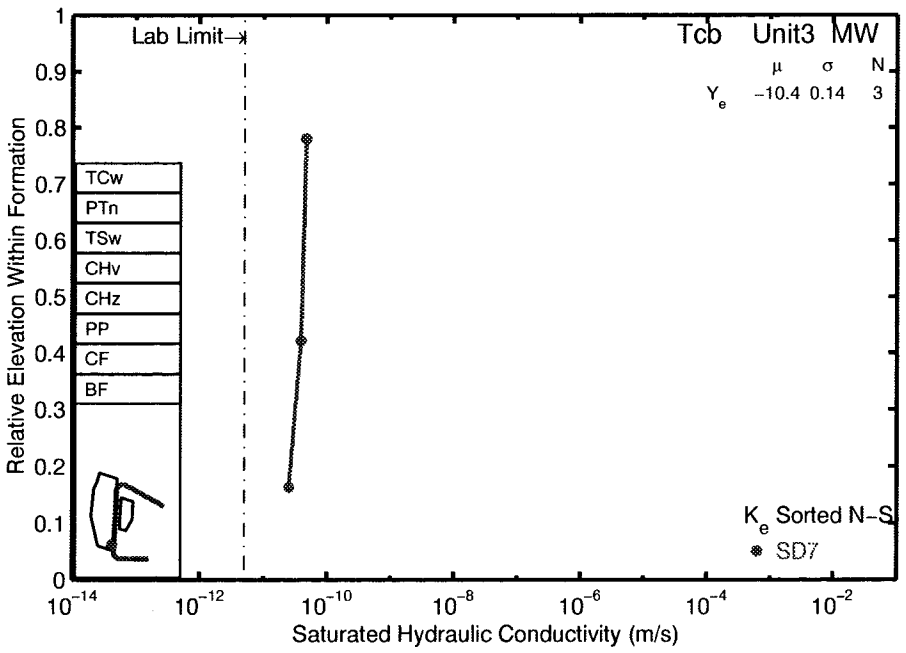

(b)

Figure 2-62: 9/17/97. All CNWRA-estimated and USGS-measured K_{sat} values in formation: (a) TcbUnit4MW (**FormK_TcbUnit4MW_c.eps**), and (b) TcbUnit3MW (**FormK-_TcbUnit3MW_c.eps**).

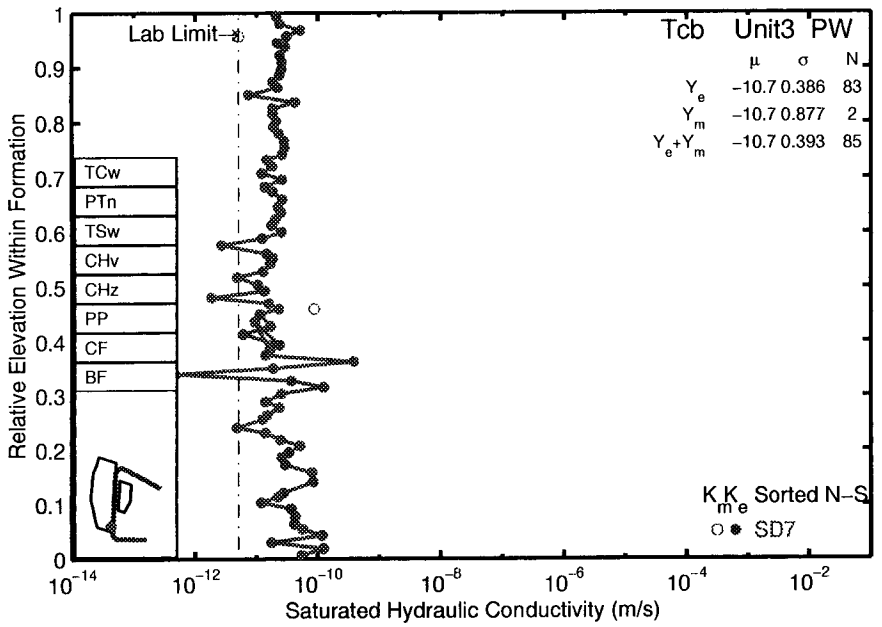

(a)

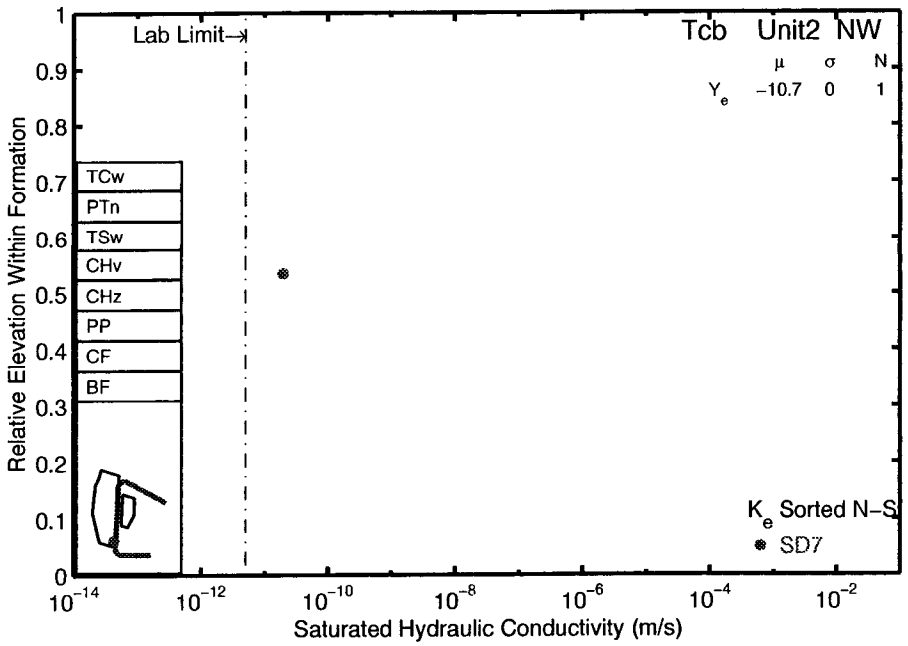

(b)

Figure 2-63: 9/17/97. All CNWRA-estimated and USGS-measured K_{sat} values in formation: (a) TcbUnit3PW (**FormK_TcbUnit3PW_c.eps**), and (b) TcbUnit2NW (**FormK_TcbUnit2NW-_c.eps**).

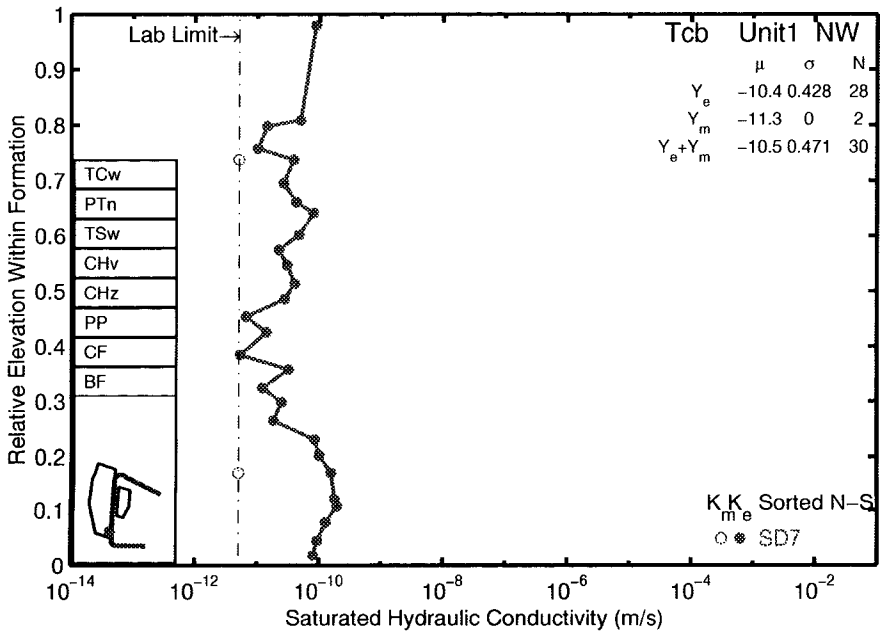

(a)

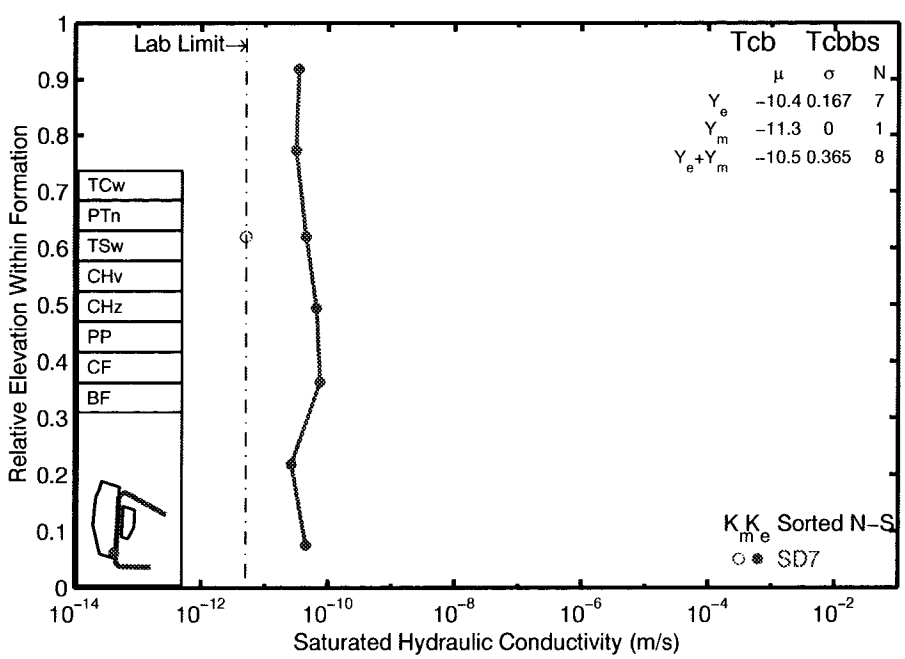

(b)

Figure 2-64: 9/17/97. All CNWRA-estimated and USGS-measured K_{sat} values in formation: (a) TcbUnit1NW (**FormK_TcbUnit1NW_c.eps**), and (b) Tcbbs (**FormK_Tcbbs_c.eps**).

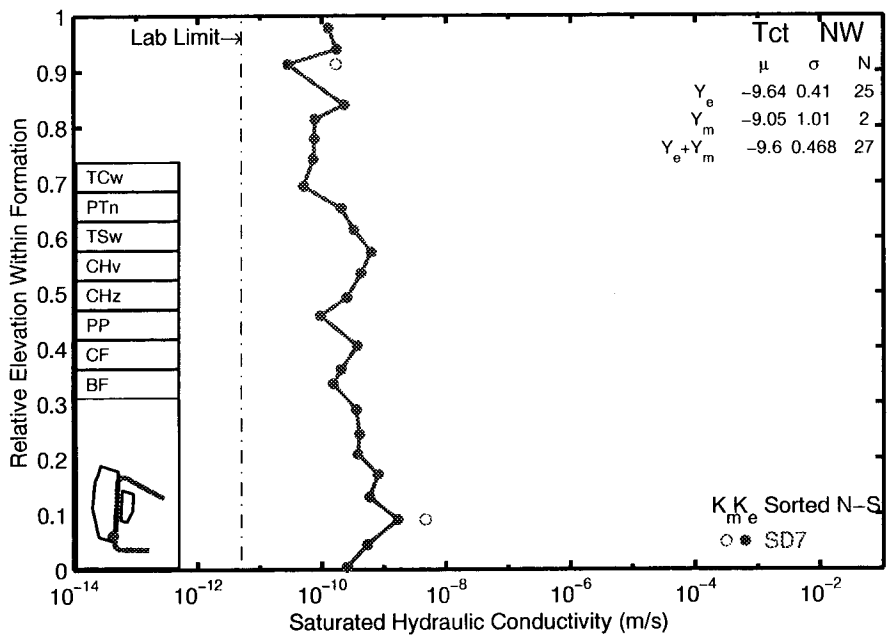

Figure 2-65: 9/17/97. All CNWRA-estimated and USGS-measured K_{sat} values in formation TctNW (**FormK_TctNW_c.eps**).

Table 2-1: Statistical description of $Y = \log_{10}[K_{sat}\ (m/s)]$ in TCw.

Formation			SAS Estimated			Measured			All		
Form	Zone1	Zone2	μ	σ	N	μ	σ	N	μ	σ	N
Tpc	rn	rn4	-9.497	0.769	19				-9.497	0.769	19
Tpc	rn	rn3	-7.541	0.566	62	-6.875	0	1	-7.53	0.568	63
Tpc	rn	rn2	-7.704	0.949	53	-7.693	0	1	-7.703	0.94	54
Tpc	rn	rn1	-8.064	1.31	17	-7.69	0	1	-8.043	1.27	18
Tpc	rl	rl2	-9.05	0.588	5				-9.05	0.588	5
Tpc	rl	rl1	-9.917	0.908	9				-9.917	0.908	9
Tpc	pul		-9.201	0.566	49	-8.985	1.53	2	-9.193	0.597	51
Tpc	pmn		-9.841	0.761	32				-9.841	0.761	32
Tpc	pll		-9.774	0.758	181	-11.14	0.48	14	-9.872	0.82	195
Tpc	pln	plnh	-10.15	0.662	169	-11.3	0	8	-10.2	0.69	177
Tpc	pln	plnc	-10.1	0.706	272	-10.99	0.523	17	-10.15	0.727	289
Tpc	pv	pv2	-9.93	0.994	54				-9.93	0.994	54

Table 2-2: Statistical description of $Y = \log_{10}[K_{sat}\ (m/s)]$ in PTn.

Formation			SAS Estimated			Measured			All		
Form	Zone1	Zone2	μ	σ	N	μ	σ	N	μ	σ	N
Tpc	pv	pv1	-7.851	1.43	76	-7.741	1.89	10	-7.839	1.48	86
Tpbt4			-6.947	1.41	20	-6.784	2.59	3	-6.925	1.53	23
Tpy			-7.97	1.36	85	-6.803	1.09	12	-7.826	1.38	97
Tpbt3			-6.99	0.804	55	-6.405	2	8	-6.915	1.03	63
Tpp			-5.903	0.66	156	-6.058	0.4	10	-5.913	0.648	166
Tpbt2			-5.885	0.757	85	-5.539	0.548	10	-5.849	0.743	95
Tpt	rv	rv3	-5.784	0.837	62	-5.503	1.25	8	-5.752	0.887	70
Tpt	rv	rv2	-7.556	1.24	25	-5.074	0	1	-7.46	1.31	26

Table 2-3: Statistical description of $Y = \log_{10}[K_{sat}\ (m/s)]$ in TSw.

Formation			SAS Estimated			Measured			All		
Form	Zone1	Zone2	μ	σ	N	μ	σ	N	μ	σ	N
Tpt	rv	rv1	-9.907	1.09	17	-9.233	1.9	4	-9.778	1.26	21
Tpt	rn		-8.5	0.611	450	-8.903	1.1	38	-8.532	0.669	488
Tpt	rn	rn2	-9.215	0.656	40	-9.255	1.21	13	-9.225	0.812	53
Tpt	rl		-8.603	0.488	31	-9.741	0	1	-8.639	0.521	32
Tpt	rl	rl2	-9.222	0.562	11	-11.3	0	1	-9.396	0.805	12
Tpt	rl	rl1	-9.178	0.661	28	-10.85	0.782	3	-9.339	0.829	31
Tpt	pul		-9.265	0.84	135	-9.638	0	1	-9.268	0.837	136
Tpt	pul	pul2	-9.617	0.543	23	-10.69	0.854	5	-9.808	0.723	28
Tpt	pul	pul1	-9.503	0.7	227	-10.17	1.2	40	-9.603	0.827	267
Tpt	pmn		-10.11	0.596	204	-11.07	0.54	34	-10.25	0.678	238
Tpt	pmn	pmn3	-10.41	0.386	23	-11.3	0	1	-10.44	0.419	24
Tpt	pmn	pmn2	-10.2	0.25	20	-10.19	1.57	2	-10.2	0.417	22
Tpt	pmn	pmn1	-10.38	0.52	19	-11.3	0	2	-10.47	0.566	21
Tpt	pll		-9.776	0.651	451	-10.21	1.16	65	-9.831	0.747	516
Tpt	pln		-10.22	0.515	327	-10.74	1.22	65	-10.31	0.708	392
Tpt	pv	pv3	-10.59	0.652	86	-10.43	0.956	8	-10.57	0.677	94

Table 2-4: Statistical description of $Y = \log_{10}[K_{sat}\ (m/s)]$ below TSw (CHnv, CHnz, PP, UCF, UBF).

Formation			SAS Estimated			Measured			All		
Form	Zone1	Zone2	μ	σ	N	μ	σ	N	μ	σ	N
Tpt	pv	pv2	-9.793	0.831	36	-9.574	1.68	2	-9.781	0.856	38
Tpt	pv	pv1	-8.193	1.54	67	-8.825	1.62	7	-8.253	1.55	74
Tpbt1			-9.426	1.86	15	-9.675	3.25	4	-9.479	2.11	19
Tac			-9.738	0.428	4				-9.738	0.428	4
Tac	Unit4		-8.153	1.66	40	-9.636	1.58	20	-8.648	1.77	60
Tac	Unit3	NW	-9.159	1.28	134	-10.47	1.53	36	-9.438	1.44	170
Tac	Unit2	NW	-9.615	0.684	148	-10.4	0.64	37	-9.772	0.744	185
Tac	Unit1	NW	-9.693	0.41	36				-9.693	0.41	36
Tac	Tacbt	NW	-10.27	0.404	56	-11.23	0.23	12	-10.44	0.528	68
Tac	Tacbs	NW	-10.56	0.335	13	-9.865	0.264	2	-10.47	0.403	15
Tcp	Unit4		-10.26	0.232	2				-10.26	0.232	2
Tcp	Unit4	NW	-9.528	0.89	10	-11.02	0.393	2	-9.777	1	12
Tcp	Unit4	sub3	-9.894	0.0723	8	-11.3	0	1	-10.05	0.474	9
Tcp	Unit4	sub2	-9.667	0.18	4				-9.667	0.18	4
Tcp	Unit4	sub1	-9.513	0.318	23	-10.23	0.731	5	-9.642	0.491	28
Tcp	Unit3		-8.465	1.52	255	-8.841	1.42	64	-8.54	1.5	319
Tcp	Unit2		-9.742	0.526	70	-9.723	0.857	9	-9.739	0.566	79
Tcp	Unit1		-9.965	0.649	210	-10.73	0.633	7	-9.99	0.661	217
Tcp	Tcpbt		-9.836	0.312	4				-9.836	0.312	4
Tcb	Unit4	NW	-10.13	0.393	11	-9.785	0.532	2	-10.08	0.411	13
Tcb	Unit4	MW	-10.38	0	1				-10.38	0	1
Tcb	Unit3	MW	-10.44	0.14	3				-10.44	0.14	3
Tcb	Unit3	PW	-10.68	0.386	83	-10.68	0.877	2	-10.68	0.393	85
Tcb	Unit2	NW	-10.7	0	1				-10.7	0	1
Tcb	Unit1	NW	-10.41	0.428	28	-11.3	0	2	-10.47	0.471	30
Tcb	Tcbbs		-10.37	0.167	7	-11.3	0	1	-10.48	0.365	8
Tct		NW	-9.641	0.41	25	-9.053	1.01	2	-9.598	0.468	27

Based on the set of figures, there appears to be little in the way of systematic spatial variability in the material properties, either vertically or horizontally. The systematic variability that is present is almost exclusively associated with the bedded units (e.g., PTn, CH). Examples of possible systematic spatial variability within a subzone include: (i) Tpy (north/south), (ii) Tpcpv1 (east/west), (iii) units transitional from nonzeolitic to zeolitic.

Bedded units also tend to have the largest unsystematic variability. This can be seen in the tables, in which most bedded units have standard deviations greater than 1 and most low-permeability units have standard deviations less than 1. Some of the lower variability in the low-permeability units is due to including those K_{sat} values at the laboratory limit for measured K_{sat} when calculating the statistical measures.

There is little point in breaking several of the zones into subzones, at least based on K_{sat}. Candidates for consolidation include:

- Tpcrn3 through Tpcrn1 (μ ranges from -7.53 through -8.04)
- Perhaps Tpcrl2 through Tpcpul (μ ranges from -9.05 through -9.92)
- Tpcmn through Tpcpv2 (μ ranges from -9.84 through -10.2)
- Tpp through Tptrv3 (μ ranges from -5.75 through -5.91)
- Tptrn through Tptrl1 (μ ranges from -8.53 through -9.40)
- Tptpul through Tptpul1 (μ ranges from -9.27 through -9.81)
- Tptpmn through Tptpv3 (μ ranges from -9.83 through -10.47)
- Tac Unit3 through Tac Unit1 (μ ranges from -9.44 through -9.77)
- Tacbt through Tacbs (μ ranges from -10.44 through -10.47)
- All Tcp Unit4 subzones (μ ranges from -9.64 through -10.26)
- Tcp Unit2 through Tcpbt (μ ranges from -9.74 through -9.99)
- All Tcb (μ ranges from -10.08 through -10.7)

9/23/97 Investigation of USGS retention properties. SAS

The USGS has only presented data for retention properties on core samples obtained from outcrops (Flint et al., 1996), to the best of my knowledge. As documented in the 1/22/97 entry, these data were entered electronically by A. Ramos from Appendix II in the report by Flint et al. (1996). I created two *Matlab* files, show_reten.m and ss_logpcap_eval.m, in ***$HOME2/AmbientKTI/-3Ddata***, to investigate the retention properties.

The procedure Flint et al. (1996) followed was to use RETC for the data of each core sample individually, obtaining van Genuchten α and m, then regressing these into a global relationship. Thoughts on the Flint et al. (1996) procedure are discussed in the 9/21/96 entry, but in short my opinion is that it would be more fruitful to try to perform simultaneous regressions.

The idea behind today's investigation is to create a regression for all measured points simultaneously, using the intrinsic *Matlab* function fmins to minimize

$$u = \sum_{i=1}^{N} [\log_{10}(P_{mi}) - \log_{10}(P_{ei})]^2, \tag{2-16}$$

$$P_e = P_0(\theta^{-1/m} - 1)^{1-m}, \tag{2-17}$$

$$\log_{10}(P_{0i}) = a_0 + a_1 V_{1i} + a_2 V_{2i}, \tag{2-18}$$

$$m_i = b_0 + b_1 V_{3i} + b_2 V_{4i}. \tag{2-19}$$

where

- u is the objective function,
- P_m is measured capillary pressure,
- P_e is estimated capillary pressure,
- m is van Genuchten $m = 1 - 1/n$,
- P_0 is bubbling pressure (the reciprocal of van Genuchten α in the units used here),
- V_{ji} are the variables being regressed against, and
- a_j, b_j are the regression constants.

Flint et al. (1996) report pairs of volumetric water content (VWC) and capillary pressure (P_c) in their Appendix II. Data from two subsamples (TS47s, CH60s) were discarded, as properties (e.g., porosity) for the parent core samples were either not determined or were not reported in the electronic data set. Several VWC/P_c pairs had only one of the pair reported, or had a zero value for VWC; these pairs were also discarded.

The measured porosity of some core samples was not consistent with the VWC reported at

a P_c of 0.01 bar [note that Flint et al. (1996) assume full saturation at 0.01 bar]. Accordingly, for the purposes of regression, effective saturation was calculated by multiplying all VWC values for a sample by $0.999/VWC_0$, where VWC_0 is VWC at 0.01 bar; also, the porosity for each subsample was assumed to be VWC_0. Because of this inconsistency, the core-sample value for the difference between porosity at 65 and 105 °C was used as a candidate regression parameter, but not either porosity value individually.

All combinations of 1-parameter and 2-parameter fits for both P_0 and m were exhaustively checked for the best value of u. The 8 candidate regression variables, v, included VWC_0, bulk density at both 65 and 105 °C, particle density at both 65 and 105 °C, and change in porosity, bulk density, and particle density between 65 and 105 °C. The optimal fit provided by the best set and the worst set of parameters was not greatly different, differing by only about one-third, and all optimal fits were on the order of 10 (mean error for a measured/estimated P_0 pair is about one order of magnitude). The insensitivity to regression parameter is probably due to: (i) a high degree of correlation between the various parameters for each sample, and (ii) considerable noise in the data. A spot check for several combinations of parameters suggests that worse fits would be obtained for P_0 rather than $\log_{10}(P_0)$ and for $\log_{10}(m)$ rather than m.

9/24/97 Thoughts on assignment of layer properties. SAS

The actual flow path of a water particle in a heterogeneous medium is likely to be quite tortuous. Under certain restrictive conditions, a heterogeneous porous medium can be replaced with an equivalent homogeneous porous medium. When saturated flow is 1D, and the flow is perpendicular to the heterogeneity (like a bundle of tubes), the flow is in parallel and the equivalent K_{sat} is the area-weighted arithmetic average of K_{sat} for the individual tubes. When saturated flow is 1D, and the flow is parallel to the heterogeneity (layers), the flow is in series and the equivalent K_{sat} is the length-weighted harmonic average of the individual tube K_{sat}s. If the heterogeneity relationship is more complicated, or the flow is not saturated, the picture muddies considerably and a unique K_{sat} cannot be determined in general.

When dealing with unsaturated media, the actual task is to determine equivalent values of K_{sat}, ε, α, m, and dispersivity so that a box containing the equivalent porous medium behaves like a box containing the heterogeneous medium, over the range of fluxes of interest. For YM, there is a tremendous upscaling that must be accomplished, from the core scale (5 cm on a side) to the formation scale (1 to 100 m thick by km^2).

A method that is useful for upscaling, and I believe is used in the petroleum industry, involves repeatedly averaging stochastically generated blocks of material, with each averaging occurring at a larger scale. At each scale, one creates the equivalent medium for 2, 4, or 8 blocks (depending on dimensionality). Averaging is typically performed for steady state conditions.

In the most rigorous approach, one would create a series of simulations with the original medium. For YM conditions, each simulation would presumably have 8 or more blocks, pressure conditions imposed at top and bottom, and no-flow conditions on the vertical sides (allowing lateral flow within the domain but not between averaging blocks). The equivalent properties would then be found by matching the flux and travel time results for each of the boundary conditions. It seems to me that the best that one could hope for would be to end up with pressure matches for the top and bottom of the formation and arbitrary variation in between.

It seems that one might do well trying to obtain an equivalent porous medium composed of several distinct media with different volumetric fractions; the distinct media might be preselected, with the job becoming obtaining the volumetric fractions. A first approach to picking media might be to: (i) determine the porosity distribution (for example) of a layer, (ii) pick out say 8 quantiles for porosity, and (iii) assign mean values for the other properties in each quantile.

In the case of YM, my feeling is that heterogeneity has much smaller correlation lengths in the vertical than in the horizontal, particularly for bedded tuffs. Welded tuffs should be almost isotropic at a small scale.

I think that an approach with merit would be to create many short columns, perhaps a correlation length in vertical dimension, pick a set of values of the medium properties for each end, and assume that the properties vary linearly/loglinearly between ends. The sets of properties should be appropriately correlated. The equivalent-medium properties can be obtained from building up a retention curve and a relative-permeability curve for the equivalent medium by averaging the contributions from each of the columns.

Actually, using the theory that lateral redistribution of pressure is efficient enough that pressure everywhere at the same relative height within a layer is approximately equal and gravity drainage is the primary condition of interest, a better approach would be to simply generate the arithmetic-mean response curves for each layer by imposing a gravity-drainage assumption for a series of capillary pressures and abstracting the mean responses. Arithmetic means should be taken of $k(P_c)$ and $\theta(P_c)$. It should be relatively efficient to calculate K_{sat}, α, and m for the effective medium using this approach.

9/29/97 More thoughts on assignment of layer properties. SAS

A major component of generating layer properties by averaging core-sample properties is generating the set of random core-sample properties that are to be averaged. In order to generate properties, the statistical distribution of the properties must be known. However, these properties can only be estimated from the sampled values. According to Benjamin and Cornell (1970), in their section 4.1.2, the mean of a distribution estimated from samples is itself a random variable, normally distributed in the limit of many samples. Benjamin and Cornell (1970), in their section 4.3.2, further note that regression equations have uncertain coefficients as well.

The sample mean, $\bar{X}$, and sample variance, S^2, of n observations, X_i, from a random distibution are

$$\bar{X} = \frac{1}{n}\sum_{i=1}^{N} X_i, \tag{2-20}$$

$$S^2 = \frac{1}{n-1}\sum_{i=1}^{N}(X_i - \bar{X}). \tag{2-21}$$

The expected value and variance of $\bar{X}$ are

$$\mathrm{E}[\bar{X}] = m_X, \tag{2-22}$$

$$\mathrm{Var}[\bar{X}] = \frac{\sigma_X^2}{n}, \tag{2-23}$$

where m_X and σ_X are the true mean and standard deviation of the underlying physical process. Note that the variance of $\bar{X}$ would include correlation terms if the observations were not mutually independent. The expected value and variance of S^2 are

$$\mathrm{E}[S^2] = \sigma_X^2, \tag{2-24}$$

$$\mathrm{Var}[S^2] = \frac{2\sigma_X^4}{n-1}, \tag{2-25}$$

where it is assumed that X is normally distributed when deriving the expression for $\mathrm{Var}[S^2]$.

The regression equations have the form

$$y_j = a + \sum_{i=1}^{N} b_i x_{ij} + \epsilon_j, \tag{2-26}$$

where y_j is the jth observation of the predicted variable y, the x_{ij} values represent observations of N predictor variables, and ϵ_j represents a normally distributed zero-mean noise. To estimate the

a and b_i constants, one chooses $\hat{a}$ and $\hat{b}_i$ such that the sum of squares, or

$$\sum_{j=1}^{M}\left[y_j - \left(\hat{a} + \sum_{i=1}^{N}\hat{b}_i x_{ij}\right)\right]^2, \tag{2-27}$$

is minimized by taking the derivative with respect to the coefficients, yielding

$$\sum_{j=1}^{M} 2\left[y_j - \left(\hat{a} + \sum_{i=1}^{N}\hat{b}_i x_{ij}\right)\right](-1) = 0, \tag{2-28}$$

$$\sum_{j=1}^{M} 2\left[y_j - \left(\hat{a} + \sum_{i=1}^{N}\hat{b}_i x_{ij}\right)\right](-x_{kj}) = 0, \tag{2-29}$$

where $k = 1, 2, \ldots, N$. The equations reduce to

$$M\left(\bar{y} - \hat{a} - \sum_{i=1}^{N}\hat{b}_i\bar{x}_i\right) = 0, \tag{2-30}$$

$$\sum_{j=1}^{M} y_j x_{kj} - \hat{a}\bar{x}_k - \sum_{i=1}^{N}\hat{b}_i x_{ij} x_{kj} = 0, \tag{2-31}$$

$$\bar{y} = \frac{1}{n}\sum_{j=1}^{M} y_i, \tag{2-32}$$

$$\bar{x}_k = \frac{1}{n}\sum_{j=1}^{M} x_{kj}, \tag{2-33}$$

and finally to

$$\hat{a} = \bar{y} - \sum_{i=1}^{N}\hat{b}_i\bar{x}_i, \tag{2-34}$$

$$\sum_{j=1}^{M} y_j x_{kj} - M\hat{a}\bar{x}_k - \sum_{i=1}^{N}\hat{b}_i x_{ij} x_{kj} = 0, \tag{2-35}$$

$$\bar{y} = \frac{1}{M}\sum_{j=1}^{M} y_j, \tag{2-36}$$

$$\bar{x}_k = \frac{1}{M}\sum_{j=1}^{M} x_{kj}. \tag{2-37}$$

Benjamin and Cornell (1970) note that the obvious estimator for σ^2, the assumed-constant variance of Y given x, is the average of the squared residuals. This turns out to be

$$s^2 = \hat{\sigma^2} = \frac{1}{M-N-1}\sum_{j=1}^{M}\left[y_j - \left(\hat{a} + \sum_{i=1}^{N}\hat{b}_i x_{ij}\right)\right]^2. \tag{2-38}$$

Further, when the sample size is sufficiently large, $N = 1$, the values of y_i are uncorrelated, and the values of y_i have the same variance,

$$B = \sum_{j=1}^{M} c_j y_j, \tag{2-39}$$

$$c_j = \frac{x_j - \bar{x}}{\sum_{j=1}^{M}(x_j - \bar{x})^2}, \tag{2-40}$$

$$\mathrm{E}[B] = \mathrm{E}[\sum_{j=1}^{M} c_j y_j] = \sum_{j=1}^{M} c_j \mathrm{E}[y_j] = a\sum_{j=1}^{M} c_j + b\sum_{j=1}^{M} c_j x_j = b, \tag{2-41}$$

$$\mathrm{Var}[B] = \mathrm{Var}[\sum_{j=1}^{M} c_j y_j] = \sum_{j=1}^{M} c_j^2 \mathrm{Var}[y_j] = \mathrm{Var}[y_j]\frac{\sum_{j=1}^{M} x_j^2 - M\bar{x}}{(\sum_{j=1}^{M} x_j^2 - M\bar{x})^2} = \frac{s^2}{M s_X^2}, \tag{2-42}$$

$$\mathrm{Var}[A] = \mathrm{Var}[\bar{y} - b\bar{x}] = \frac{\mathrm{Var}[y_j]}{M} + \bar{x}^2 \mathrm{Var}[B] = \frac{s^2}{M}\left(1 + \frac{\bar{x}^2}{s_X^2}\right). \tag{2-43}$$

Expanding upon the procedure outlined in section 4.3.2 by Benjamin and Cornell (1970), the corresponding estimators for two-variable regression equations are

$$B_1 = \frac{C_{10}C_{22} - C_{20}C_{12}}{C_{11}C_{22} - C_{12}C_{21}}, \tag{2-44}$$

$$B_2 = \frac{C_{20}C_{11} - C_{10}C_{21}}{C_{11}C_{22} - C_{12}C_{21}}, \tag{2-45}$$

$$C_{10} = \sum_{j=1}^{M}(x_{1j} - \bar{x}_1)y_j, \tag{2-46}$$

$$C_{20} = \sum_{j=1}^{M}(x_{2j} - \bar{x}_2)y_j, \tag{2-47}$$

$$C_{11} = \sum_{j=1}^{M}(x_{1j}^2 - \bar{x}_1^2) = M s_1^2, \tag{2-48}$$

$$C_{22} = \sum_{j=1}^{M}(x_{2j}^2 - \bar{x}_2^2) = M s_2^2, \tag{2-49}$$

$$C_{12} = C_{21} = \sum_{j=1}^{M}(x_{1j}x_{2j} - \bar{x}_1\bar{x}_2) = M s_{12} = M\rho s_1 s_2, \tag{2-50}$$

$$C_{11}C_{22} - C_{12}C_{21} = M^2 s_1^2 s_2^2 (1 - \rho^2), \tag{2-51}$$

where ρ is the correlation coefficient. The equations can be arranged to yield

$$B_1 = \sum_{j=1}^{M} \beta_{1j} y_j, \tag{2-52}$$

$$B_2 = \sum_{j=1}^{M} \beta_{2j} y_j, \tag{2-53}$$

$$\beta_{1j} = \frac{C_{22}(x_{1j} - \bar{x}_1) - C_{12}(x_{2j} - \bar{x}_2)}{M^2 s_1^2 s_2^2 (1-\rho^2)}, \tag{2-54}$$

$$\beta_{2j} = \frac{C_{11}(x_{2j} - \bar{x}_2) - C_{21}(x_{1j} - \bar{x}_1)}{M^2 s_1^2 s_2^2 (1-\rho^2)}. \tag{2-55}$$

Noting that

$$\sum_{j=1}^{M} \beta_{1j} = 0, \tag{2-56}$$

$$\sum_{j=1}^{M} \beta_{1j} x_{1j} = 1, \tag{2-57}$$

$$\sum_{j=1}^{M} \beta_{1j} x_{2j} = 0, \tag{2-58}$$

the corresponding variances are

$$\begin{aligned} \mathrm{Var}[B_1] &= \mathrm{Var}[y_j] \sum_{j=1}^{M} \left(\frac{C_{22}(x_{1j} - \bar{x}_1) - C_{12}(x_{2j} - \bar{x}_2)}{C_{11}C_{22} - C_{12}C_{21}} \right)^2 \\ &= s^2 \frac{C_{22}}{C_{11}C_{22} - C_{12}C_{21}} = \frac{s^2}{M} \left[\frac{1}{s_1^2(1-\rho^2)} \right], \end{aligned} \tag{2-59}$$

$$\begin{aligned} \mathrm{Var}[B_2] &= \mathrm{Var}[y_j] \sum_{j=1}^{M} \left(\frac{C_{11}(x_{2j} - \bar{x}_2) - C_{21}(x_{1j} - \bar{x}_1)}{C_{11}C_{22} - C_{12}C_{21}} \right)^2 \\ &= s^2 \frac{C_{11}}{C_{11}C_{22} - C_{12}C_{21}} = \frac{s^2}{M} \left[\frac{1}{s_2^2(1-\rho^2)} \right], \end{aligned} \tag{2-60}$$

$$\begin{aligned} \mathrm{Var}[A] &= \mathrm{Var}[\bar{y} - b_1\bar{x}_1 - b_2\bar{x}_2] = \frac{\mathrm{Var}[y_j]}{M} + \bar{x}_1^2 \mathrm{Var}[B_1] + \bar{x}_2^2 \mathrm{Var}[B_2] \\ &= \frac{s^2}{M} \left[1 + \frac{\bar{x}_1^2}{s_1^2(1-\rho^2)} + \frac{\bar{x}_2^2}{s_2^2(1-\rho^2)} \right]. \end{aligned} \tag{2-61}$$

Note that when x_1 and x_2 are not correlated ($\rho = 0$), the expressions for the variances simplify.

These ideas can be generalized to be handled using matrix algebra, as listed by, for example, Lapin (1983). The set of observations,

$$\hat{y}_j = A + \sum_{i=1}^{N} B_i x_{ji} + \epsilon, \tag{2-62}$$

can be written in matrix form as

$$\mathbf{y} = \mathbf{X}\mathbf{b} + \epsilon, \tag{2-63}$$

where $\mathbf{y}$ is the column of observations, $\mathbf{X}$ is the matrix of individual-variable observations (each row is a data point and each column is a variable, with the first column all ones), $\mathbf{b}$ is the vector of unknown coefficients. Rewriting, the coefficients are found by solving

$$\mathbf{b} = (\mathbf{X}'\mathbf{X})^{-1}\mathbf{X}'\mathbf{y}. \tag{2-64}$$

The sum of squared residuals is

$$S^2_{Y\cdot 12\ldots} = \frac{1}{M-N-1}(\mathbf{y}'\mathbf{y} - \mathbf{b}'\mathbf{X}'\mathbf{y}), \tag{2-65}$$

and the sample variance-covariance pairs are provided by

$$S^2_{Y\cdot 12\ldots}(\mathbf{X}'\mathbf{X})^{-1} = \frac{1}{M-N-1}(\mathbf{y}'\mathbf{y} - \mathbf{b}'\mathbf{X}'\mathbf{y})(\mathbf{X}'\mathbf{X})^{-1}, \tag{2-66}$$

where the standard error for b_k is the square root of the kth diagonal element.

The above discussion relates to estimating K_{sat} in core samples using other measured properties (i.e., saturation, porosity). In previous entries, it was found that the best regression equation for predicting K_{sat} from measured properties is

$$\log_{10}(K_{sat}) = a + b_1\theta_{65} + b_2\varepsilon_{sample} + \epsilon. \tag{2-67}$$

The best-fit regression equations found before are:

$$\log_{10}(K_{sat}) = -10.1846 - 6.57021 \log 10(\theta_{65}), \tag{2-68}$$

$$= -7.62342 - 3.79487\theta_{65} + 6.30827\varepsilon_{sample}, \tag{2-69}$$

$$= -5.96958 - 11.3334\, VWC_{105} + 7.20616\varepsilon_{65} + 3.4806 \log_{10}(\varepsilon_{sample}), \tag{2-70}$$

where a subscript of 65 denotes the measurement at 65 °C, a subscript of 105 denotes the measurement at 105 °C, a subscript of *sample* denotes the subsample measurement, θ is saturation, ε is porosity, and VWC is volumetric water content. For these equations, the sample coefficient of multiple determination, $R^2 = 1 - [\sum(Y - \hat{Y})]/[\sum(Y - \bar{Y})]$, total sum of squared error, S^2, and standard error of b_k (using Equation 2-66) are as shown in Table 2-5. The standard errors correspond to the coefficents listed as above. Notice that as the explained error increases, the uncertainty in the coefficients also increases.

Table 2-5: Statistical properties of regression on K_{sat}.

Source	R^2	S^2	Standard Error in Equation Coefficient			
			a	b_1	b_2	b_3
USGS database	0.512	–	–	–	–	–
1-Parameter	0.574	1.25	6.20×10^{-3}	8.31×10^{-2}	–	–
2-Parameter	0.715	0.84	4.03×10^{-2}	3.90×10^{-2}	1.81×10^{-1}	–
3-Parameter	0.735	0.78	3.17×10^{-1}	3.06×10^{-1}	7.97×10^{-1}	2.19×10^{-1}

There are uncertainties in the regression-equation coefficients as well as the underlying properties. In order to estimate layer-wide K_{sat} values given a statistical description of all relationships, first the underlying populations of θ and ε must be generated using the statistical descriptions of the two variables. Since the two variables are correlated, an appropriate procedure is to first generate the distribution for one, using sample statistics, then generate the distribution for the other using conditional mean and variance (Benjamin and Cornell, 1970, section 3.6.3). Assuming mutual normality,

$$\mu_{Y|X} = \mu_Y + \rho\frac{\sigma_Y}{\sigma_X}(x - \mu_x), \tag{2-71}$$

$$\sigma^2_{Y|X} = (1 - \rho^2)\sigma^2_Y. \tag{2-72}$$

Once the underlying population samples are determined, these are plugged into the regression equation for $\log_{10}(K_{sat})$ and random noise (ϵ) applied based on the standard deviation about the regression plane. The integrated value for K_{sat} can then be determined from the population.

Since each of the coefficients in the equations are themselves uncertain, the coefficients must also be sampled. The resulting distribution of average K_{sat} more fully reflects the underlying uncertainties than a single averaged value using the mean coefficients determined from regression analysis.

A difficulty arises when considering retention properties. The USGS procedure, in which retention properties are determined for each core sample individually and the regression coefficients are then determined, lends itself to the same kind of analysis discussed above for K_{sat}, although the variability in the individual saturation measurements is muted. The procedure I followed (using all core samples simultaneously to determine retention parameters) does not lend itself to the determination of regression-parameter uncertainties, even though the overall fit to the data is at least as good as obtained with the USGS procedure.

10/2/97 Layer properties. SAS

I created *Matlab* routine do_ksat_layerest.m to estimate K_{sat} for each layer. The idea is to generate many realizations of θ_{65} and ε_{sample}, use the regression equation for $\log_{10}(K_{sat})$ with ϵ added, and take the mean of the collection of realizations. I found that the underlying distributions for θ_{65} and ε_{sample} were sometimes quite skewed if they were near one end of their range (e.g., ε near 0 or θ near 1). The Type-I largest- and smallest-value distributions (Benjamin and Cornell, 1970, Section 3.3.3) conveniently describe shapes similar to the apparent skewed distributions. In cases where computed skew is less than half of the skew for the Type-I distribution, I assume that the distribution is normal; otherwise, the appropriate Type-I distribution is used.

There are difficulties in estimating bounded properties such as ε or θ using unbounded distributions. I made no attempt to resolve this problem, except for using the skewed distributions, primarily because some reported measured values fell outside the physically valid range and the regression is based on the full reported range of measured values. I do not believe that there should be a strong impact on estimated values for K_{sat}.

As it turns out, the linearity of the regression equation allows correlation between ε and θ to be ignored when calculating geometric mean. I verified this by comparing cases having normal distributions for both ε and θ. Identical geometric and means were obtained (to within the noise from 10^4 samples) considering correlation and neglecting correlation. However, correlation does appear to have an impact on arithmetic mean, as much as 2 orders of magnitude.

The comparison between data, USGS estimates, and my estimates are shown in Table 2-6. During repeated trials with the same number of realizations, the geometric mean of my estimated K_{sat} varies in the 3rd decimal place, while the arithmetic mean varies within a factor of about 1/3. In most cases, the geometric mean calculated using the many-realization approach was within a factor of 3 of the USGS estimate for the same layer. The USGS estimates are significantly different from my estimate (at least an order of magnitude) for 11 of the 30 layers; when there is a significant discrepancy my estimates usually honor the measured values somewhat better. Explanations for cases with estimates at least an order of magnitude difference include: (i) no measured K_{sat} values (CCR); (ii) measured K_{sat} is between the 2 estimates and K_{sat} subsamples are not representative (CW); (iii) measured K_{sat} values are between the 2 estimates (BT3, TR, TM1); and (iv) USGS estimates are significantly further from measured values (CMW, CNW, TC, PV3, PP3, BF3).

It is interesting to note that an arithmetic-mean layerwide K_{sat}, appropriate when gravity drainage is occurring and pressure is equalized horizontally within the layer, suggests that current

MAI estimates (<30 mm/yr or $<10^{-9}$ m/s) can be accommodated as deep percolation in the TSw without recourse to fracture flow. At and below the potential repository, only the TM1, BT, and BF3 units would perhaps require fracture flow to accommodate MAI rates.

10/7/97 Display of estimated fits. SAS

The *Matlab* routine do_ksat_layerest.m used to estimate layer properties was augmented to plot the ε, θ, and K_{sat} values for the core samples and generated realizations. The figures are displayed on the following pages. There were 10^6 realizations used to generate mean values; only 1 in 20 realizations are plotted. In each figure, the mean (arithmetic for ε and θ, geometric for K_{sat}) of each sample set is denoted with a large circle and crosshair; the crosshair has the same color as the corresponding data source.

Table 2-6: Layerwise estimates of K_{sat} (m/s). 10^{-10} m/s is equal to 3.16 mm/yr.

	Measured		USGS Estimate		SAS Estimate		
Unit	Number Obs.	Geom. Mean	Number Obs.	Geom. Mean	Number Obs.	Geom. Mean	Arith. Mean
CCR	0	–	9	1.55×10^{-12}	10^5	1.05×10^{-10}	2.27×10^{-9}
CUC	3	3.81×10^{-8}	101	3.86×10^{-8}	10^5	3.01×10^{-8}	2.09×10^{-5}
CUL	1	1.25×10^{-8}	98	5.72×10^{-10}	10^5	1.25×10^{-9}	3.06×10^{-6}
CW	38	7.27×10^{-12}	599	3.77×10^{-12}	10^5	8.88×10^{-11}	6.43×10^{-9}
CMW	4	4.98×10^{-10}	90	8.84×10^{-12}	10^5	9.48×10^{-11}	6.30×10^{-9}
CNW	8	3.06×10^{-8}	101	2.55×10^{-7}	10^5	8.84×10^{-9}	9.52×10^{-6}
BT4	3	1.64×10^{-7}	32	6.77×10^{-7}	10^5	1.22×10^{-7}	5.85×10^{-5}
TPY	2	3.31×10^{-8}	43	1.68×10^{-8}	10^5	2.39×10^{-9}	5.18×10^{-7}
BT3	18	2.81×10^{-7}	85	7.85×10^{-7}	10^5	6.80×10^{-8}	2.75×10^{-6}
TPP	10	8.75×10^{-7}	156	3.65×10^{-6}	10^5	1.26×10^{-6}	2.58×10^{-5}
BT2	19	3.17×10^{-6}	170	1.86×10^{-6}	10^5	8.54×10^{-7}	3.45×10^{-5}
TC	10	8.82×10^{-11}	71	6.15×10^{-13}	10^5	5.42×10^{-10}	2.55×10^{-8}
TR	45	1.67×10^{-9}	438	3.98×10^{-10}	10^5	3.20×10^{-9}	6.85×10^{-8}
TUL	51	5.44×10^{-11}	455	2.26×10^{-10}	10^5	4.50×10^{-10}	1.36×10^{-7}
TMN	39	8.98×10^{-12}	266	1.50×10^{-11}	10^5	6.91×10^{-11}	2.74×10^{-9}
TLL	65	6.22×10^{-11}	451	7.20×10^{-11}	10^5	1.69×10^{-10}	8.71×10^{-9}
TM2	48	2.59×10^{-11}	225	1.79×10^{-11}	10^5	6.82×10^{-11}	1.68×10^{-9}
TM1	17	6.88×10^{-12}	102	4.85×10^{-12}	10^5	4.63×10^{-11}	5.59×10^{-10}
PV3	8	3.73×10^{-11}	86	1.53×10^{-13}	10^5	2.61×10^{-11}	1.09×10^{-8}
PV2	4	7.32×10^{-10}	39	7.39×10^{-11}	10^5	1.56×10^{-10}	5.76×10^{-8}
BT1	9	5.87×10^{-10}	79	2.60×10^{-9}	10^5	4.40×10^{-9}	2.55×10^{-5}
CHV	6	5.51×10^{-7}	69	2.13×10^{-7}	10^5	4.29×10^{-8}	1.68×10^{-6}
CHZ	87	2.88×10^{-11}	293	1.08×10^{-10}	10^5	1.79×10^{-10}	3.40×10^{-9}
BT	14	9.14×10^{-12}	69	1.40×10^{-11}	10^5	4.70×10^{-11}	4.58×10^{-10}
PP4	8	2.72×10^{-11}	47	9.61×10^{-11}	10^5	2.37×10^{-10}	3.88×10^{-9}
PP3	30	2.00×10^{-8}	166	2.93×10^{-10}	10^5	1.79×10^{-8}	1.51×10^{-5}
PP2	25	2.84×10^{-10}	140	5.60×10^{-11}	10^5	1.89×10^{-10}	2.44×10^{-9}
PP1	27	4.88×10^{-11}	245	3.15×10^{-11}	10^5	1.01×10^{-10}	4.36×10^{-9}
BF3	2	2.09×10^{-11}	86	2.10×10^{-12}	10^5	2.12×10^{-11}	1.93×10^{-10}
BF2	5	3.96×10^{-11}	65	5.03×10^{-11}	10^5	8.53×10^{-11}	1.29×10^{-9}

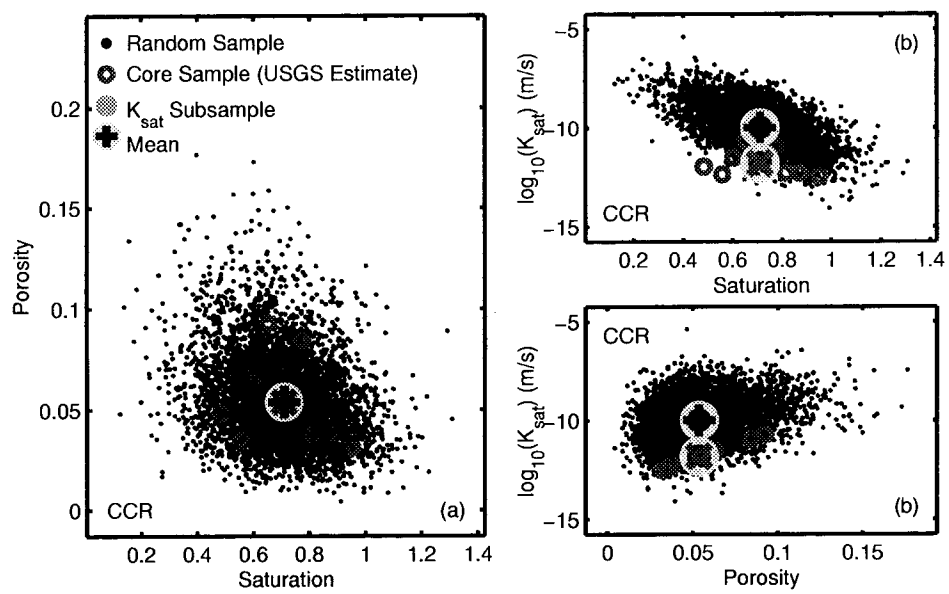

Figure 2-66: 10/7/97. **Disp_DBstat_CCR_c.eps**. Measured and generated formation values for (a) saturation and porosity, (b) saturation and estimated saturated hydraulic conductivity, and (c) porosity and estimated saturated hydraulic conductivity.

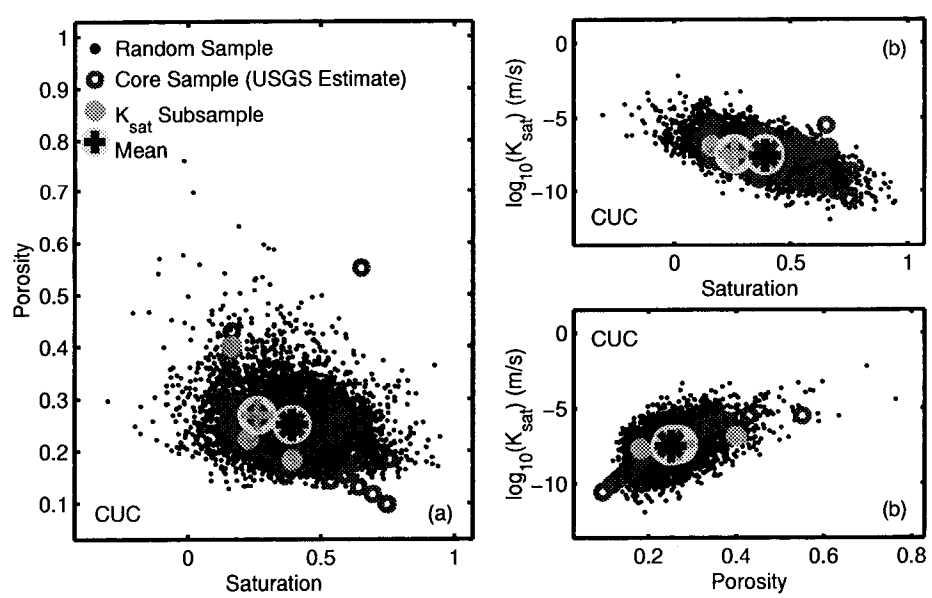

Figure 2-67: 10/7/97. **Disp_DBstat_CUC_c.eps**. Measured and generated formation values for (a) saturation and porosity, (b) saturation and estimated saturated hydraulic conductivity, and (c) porosity and estimated saturated hydraulic conductivity.

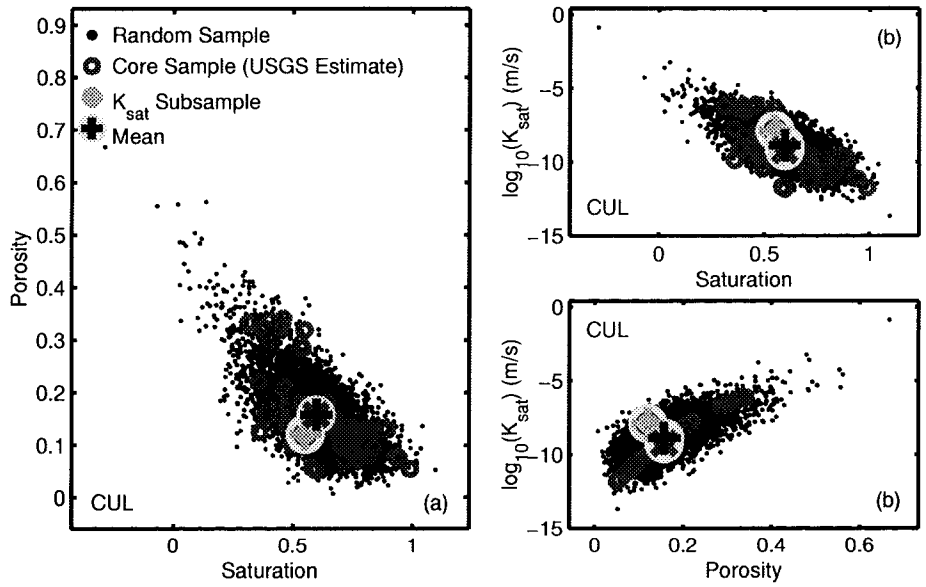

Figure 2-68: 10/7/97. **Disp_DBstat_CUL_c.eps.** Measured and generated formation values for (a) saturation and porosity, (b) saturation and estimated saturated hydraulic conductivity, and (c) porosity and estimated saturated hydraulic conductivity.

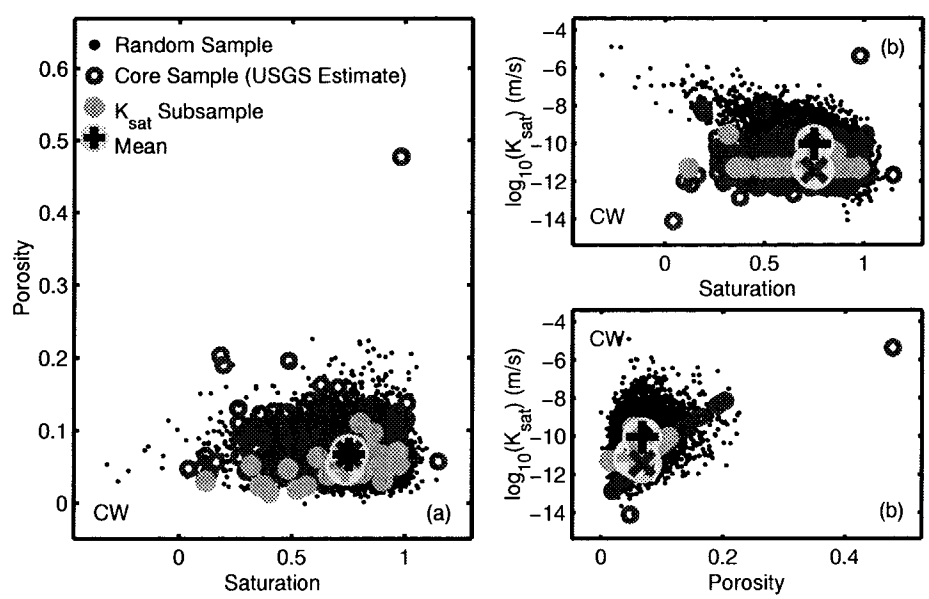

Figure 2-69: 10/7/97. **Disp_DBstat_CW_c.eps.** Measured and generated formation values for (a) saturation and porosity, (b) saturation and estimated saturated hydraulic conductivity, and (c) porosity and estimated saturated hydraulic conductivity.

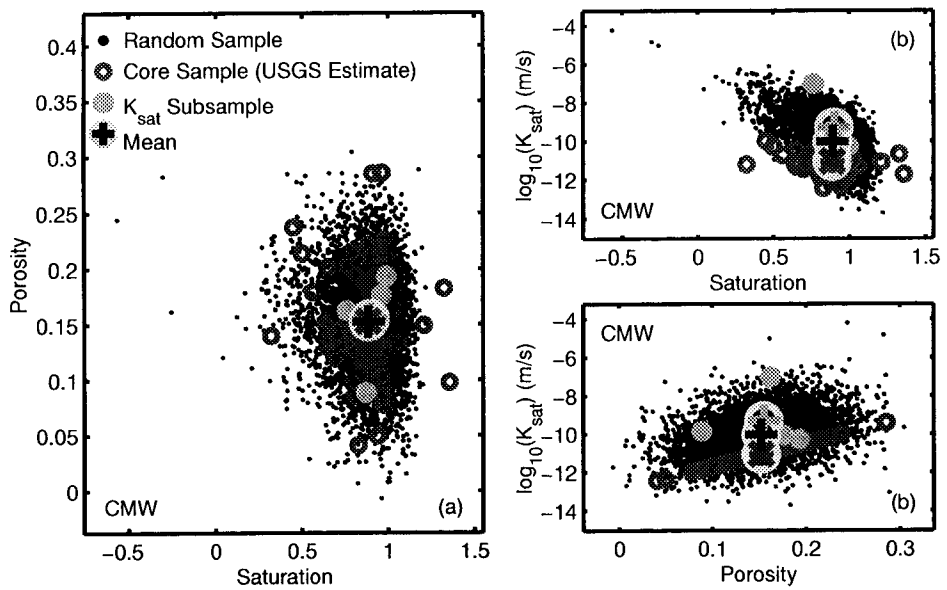

Figure 2-70: 10/7/97. **Disp_DBstat_CMW_c.eps.** Measured and generated formation values for (a) saturation and porosity, (b) saturation and estimated saturated hydraulic conductivity, and (c) porosity and estimated saturated hydraulic conductivity.

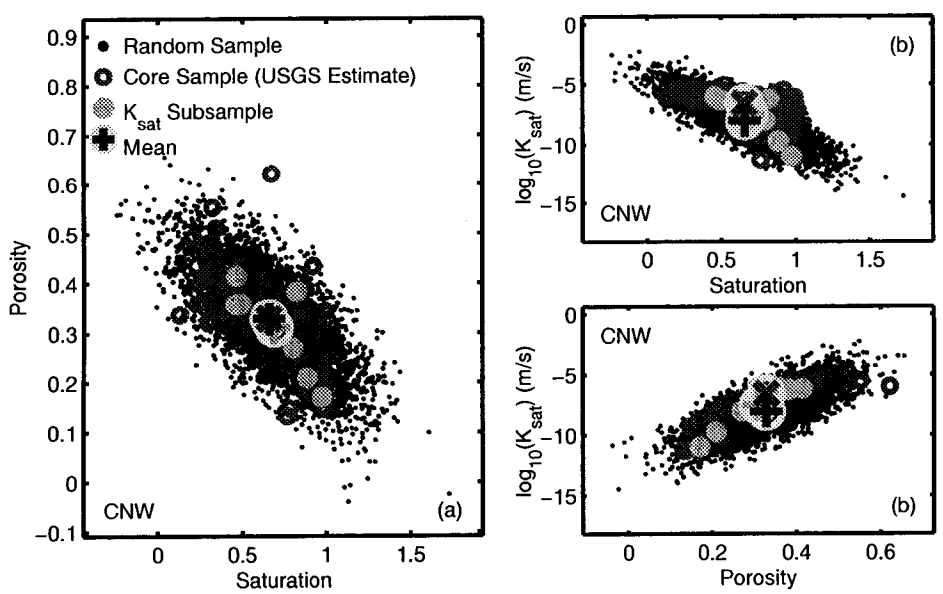

Figure 2-71: 10/7/97. **Disp_DBstat_CNW_c.eps.** Measured and generated formation values for (a) saturation and porosity, (b) saturation and estimated saturated hydraulic conductivity, and (c) porosity and estimated saturated hydraulic conductivity.

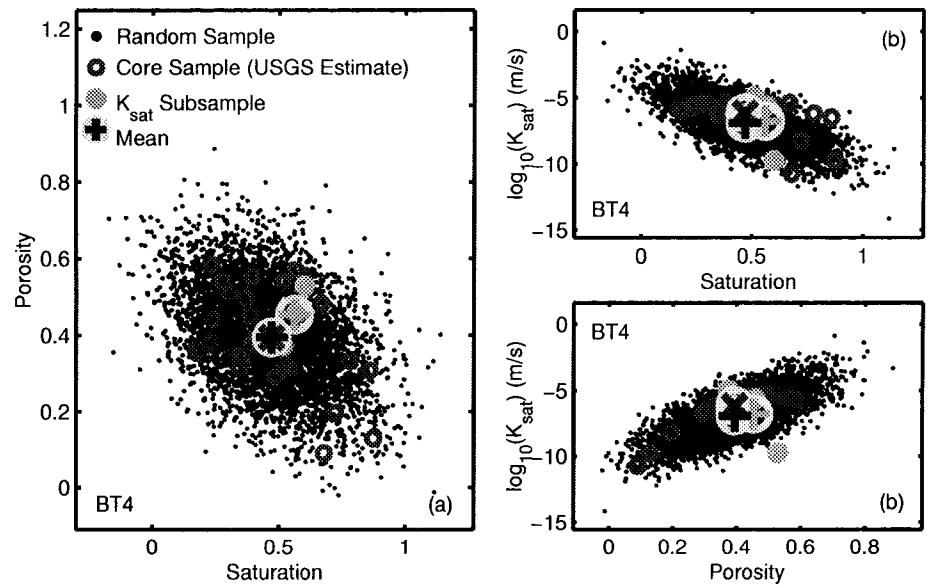

Figure 2-72: 10/7/97. **Disp_DBstat_BT4_c.eps**. Measured and generated formation values for (a) saturation and porosity, (b) saturation and estimated saturated hydraulic conductivity, and (c) porosity and estimated saturated hydraulic conductivity.

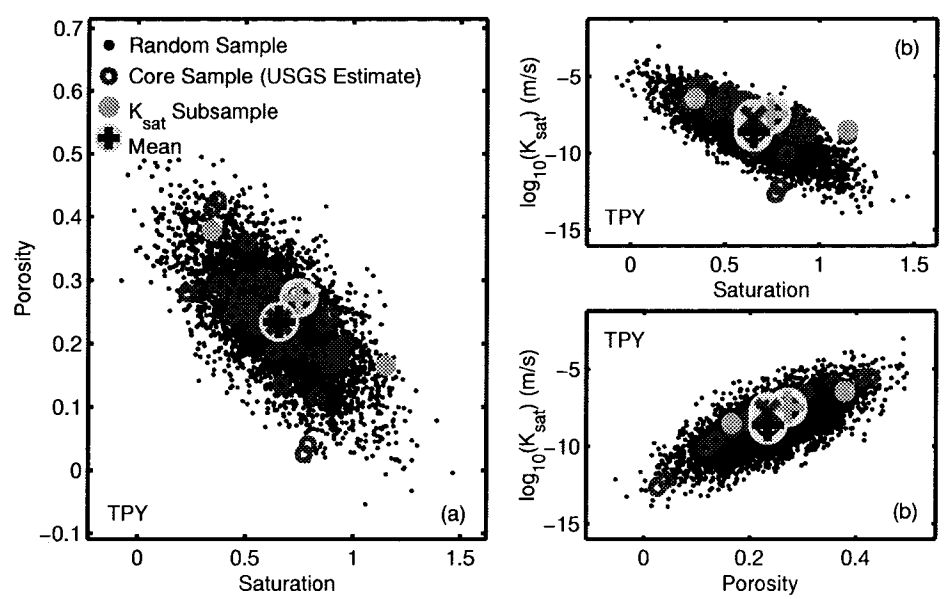

Figure 2-73: 10/7/97. **Disp_DBstat_TPY_c.eps**. Measured and generated formation values for (a) saturation and porosity, (b) saturation and estimated saturated hydraulic conductivity, and (c) porosity and estimated saturated hydraulic conductivity.

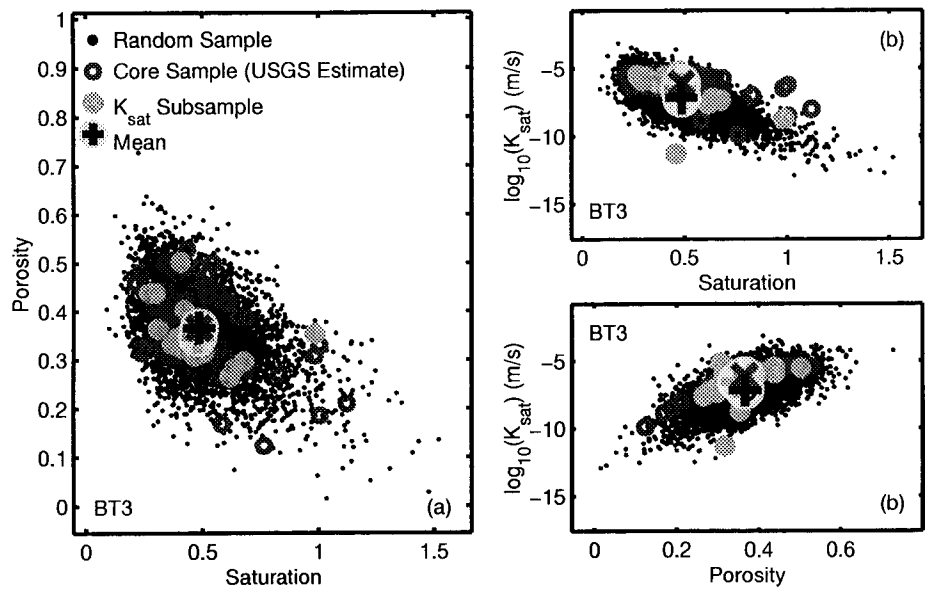

Figure 2-74: 10/7/97. **Disp_DBstat_BT3_c.eps.** Measured and generated formation values for (a) saturation and porosity, (b) saturation and estimated saturated hydraulic conductivity, and (c) porosity and estimated saturated hydraulic conductivity.

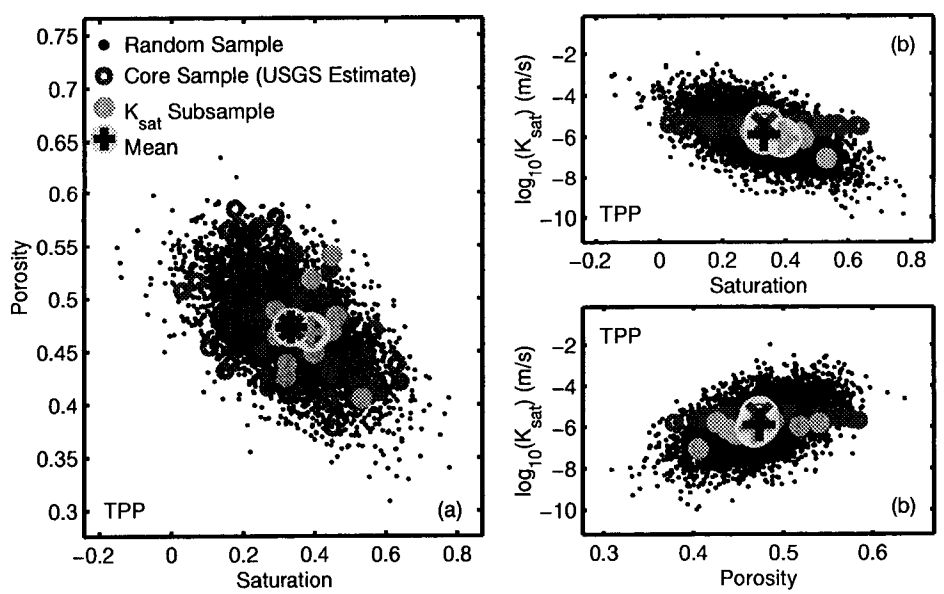

Figure 2-75: 10/7/97. **Disp_DBstat_TPP_c.eps.** Measured and generated formation values for (a) saturation and porosity, (b) saturation and estimated saturated hydraulic conductivity, and (c) porosity and estimated saturated hydraulic conductivity.

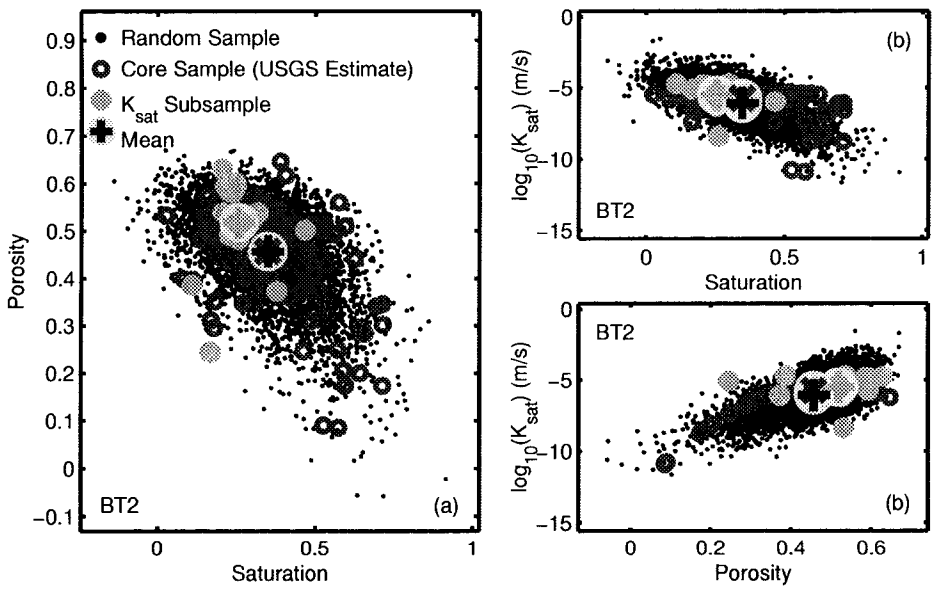

Figure 2-76: 10/7/97. **Disp_DBstat_BT2_c.eps**. Measured and generated formation values for (a) saturation and porosity, (b) saturation and estimated saturated hydraulic conductivity, and (c) porosity and estimated saturated hydraulic conductivity.

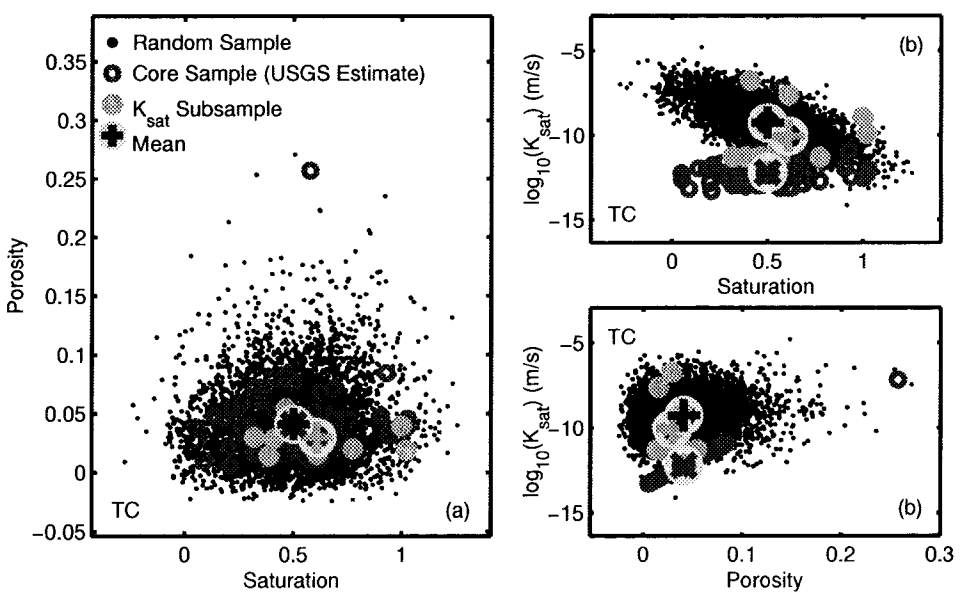

Figure 2-77: 10/7/97. **Disp_DBstat_TC_c.eps**. Measured and generated formation values for (a) saturation and porosity, (b) saturation and estimated saturated hydraulic conductivity, and (c) porosity and estimated saturated hydraulic conductivity.

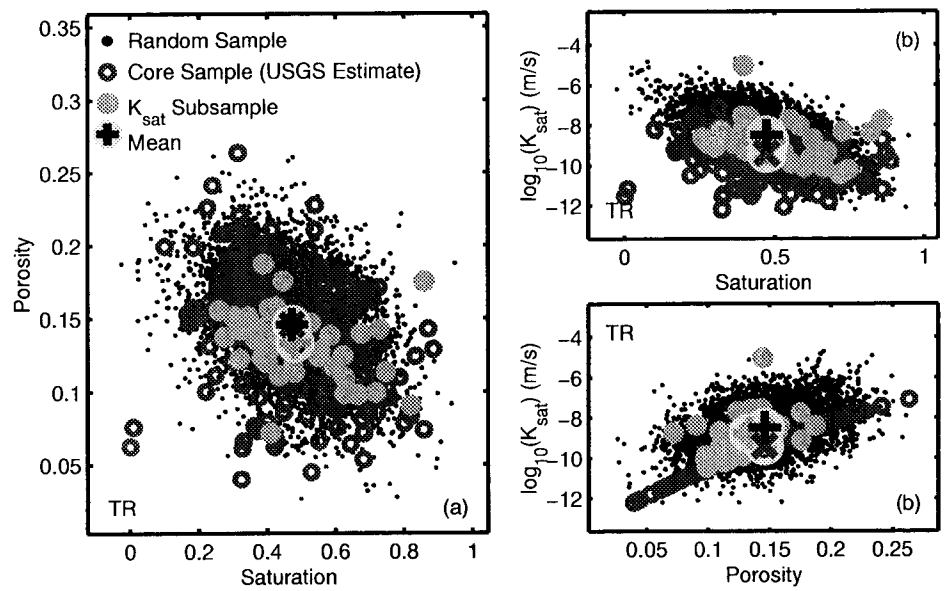

Figure 2-78: 10/7/97. **Disp_DBstat_TR_c.eps.** Measured and generated formation values for (a) saturation and porosity, (b) saturation and estimated saturated hydraulic conductivity, and (c) porosity and estimated saturated hydraulic conductivity.

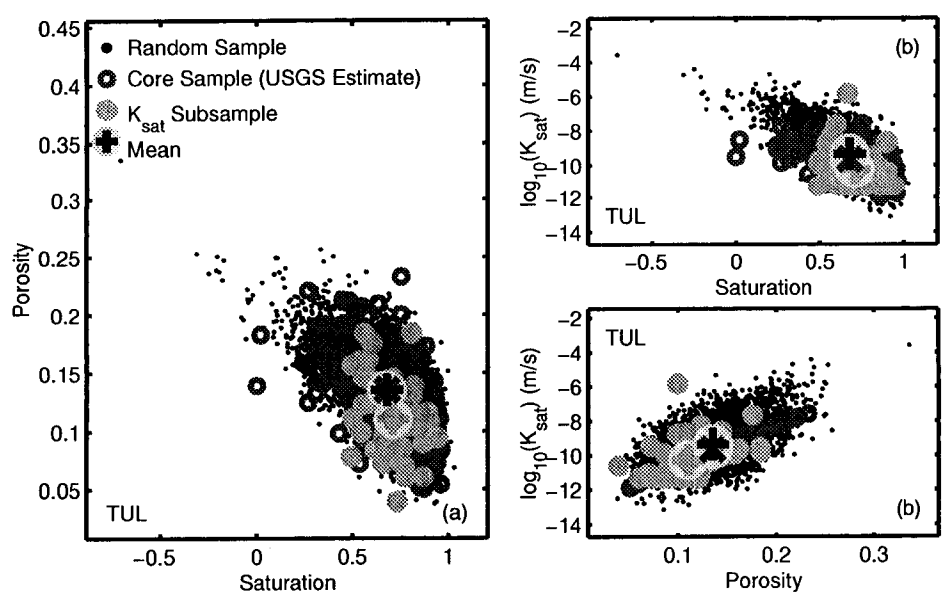

Figure 2-79: 10/7/97. **Disp_DBstat_TUL_c.eps.** Measured and generated formation values for (a) saturation and porosity, (b) saturation and estimated saturated hydraulic conductivity, and (c) porosity and estimated saturated hydraulic conductivity.

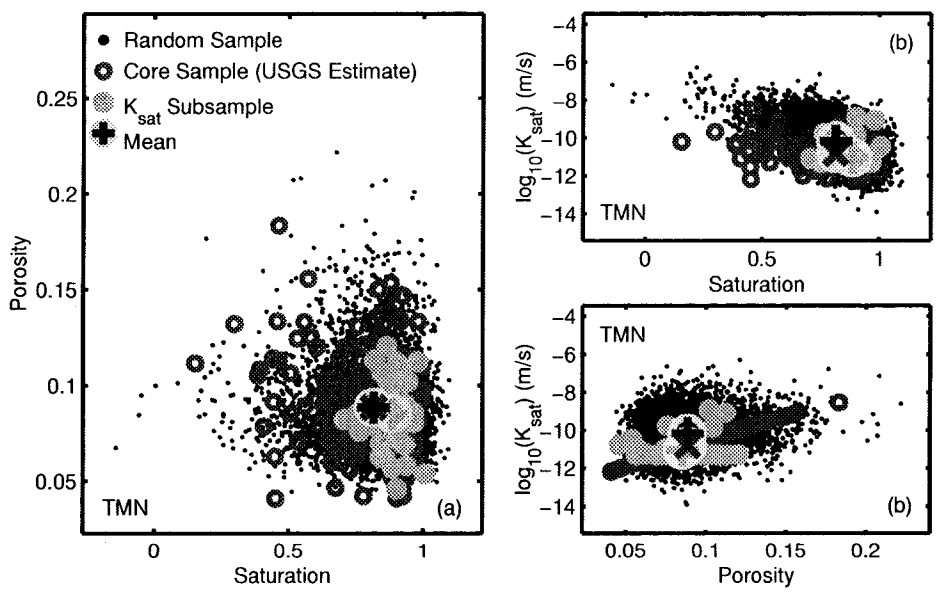

Figure 2-80: 10/7/97. **Disp_DBstat_TMN_c.eps.** Measured and generated formation values for (a) saturation and porosity, (b) saturation and estimated saturated hydraulic conductivity, and (c) porosity and estimated saturated hydraulic conductivity.

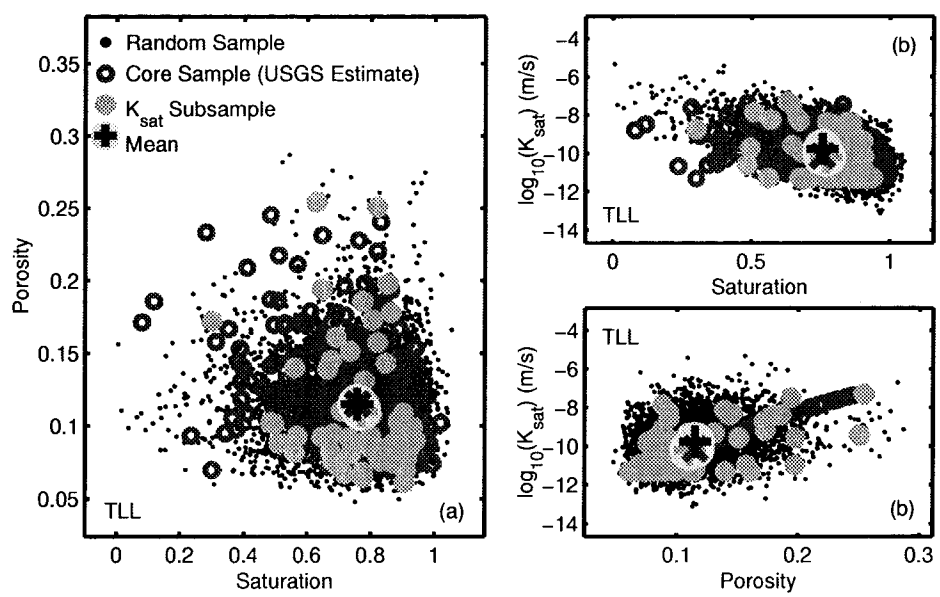

Figure 2-81: 10/7/97. **Disp_DBstat_TLL_c.eps.** Measured and generated formation values for (a) saturation and porosity, (b) saturation and estimated saturated hydraulic conductivity, and (c) porosity and estimated saturated hydraulic conductivity.

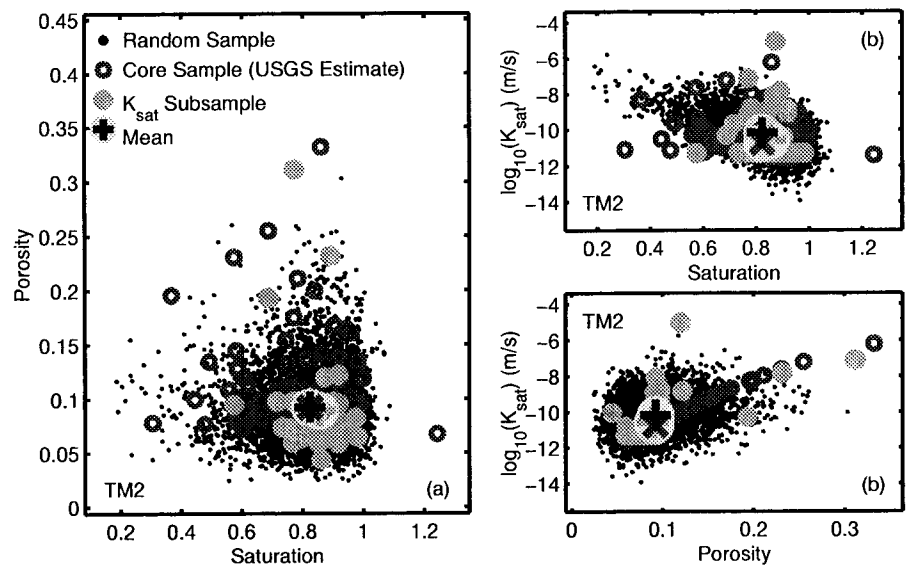

Figure 2-82: 10/7/97. **Disp_DBstat_TM2_c.eps.** Measured and generated formation values for (a) saturation and porosity, (b) saturation and estimated saturated hydraulic conductivity, and (c) porosity and estimated saturated hydraulic conductivity.

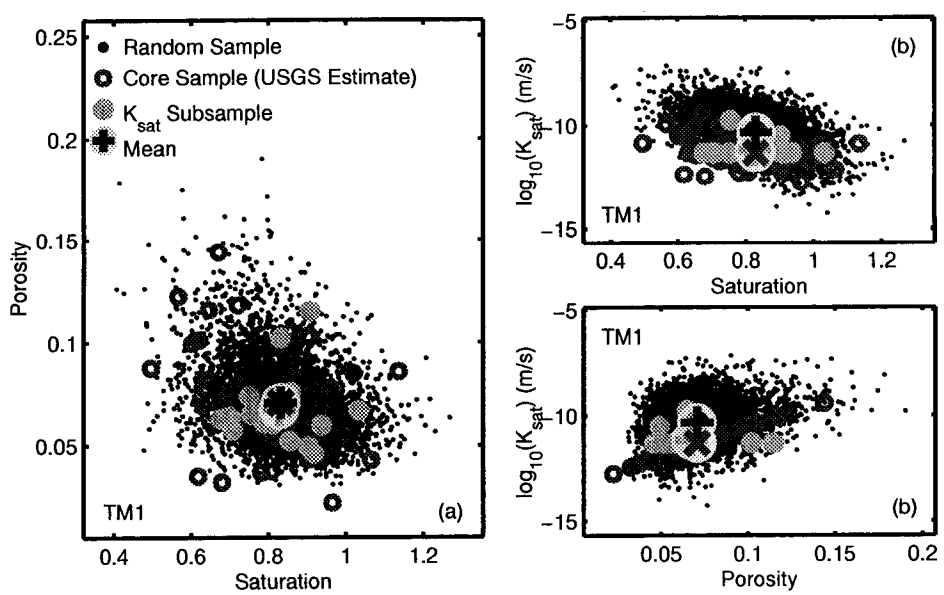

Figure 2-83: 10/7/97. **Disp_DBstat_TM1_c.eps.** Measured and generated formation values for (a) saturation and porosity, (b) saturation and estimated saturated hydraulic conductivity, and (c) porosity and estimated saturated hydraulic conductivity.

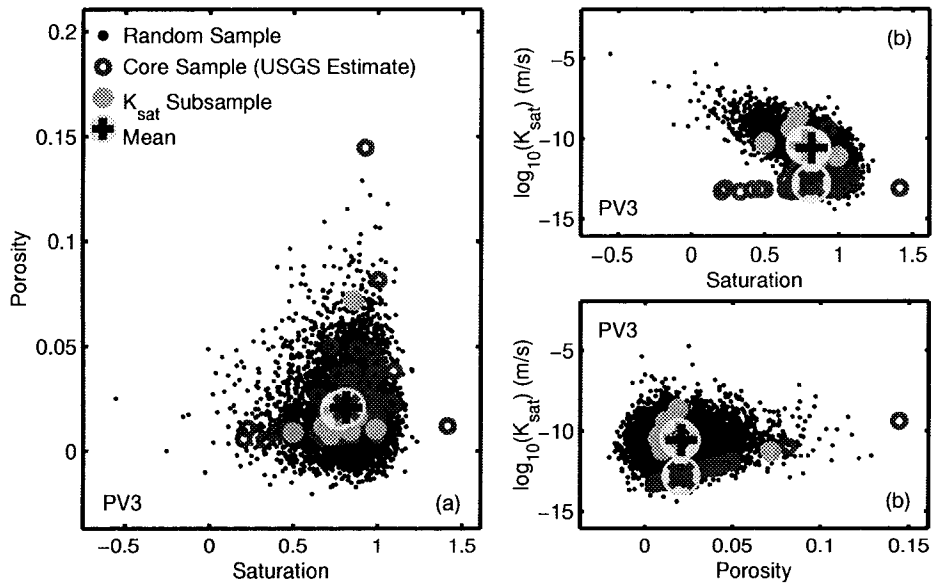

Figure 2-84: 10/7/97. **Disp_DBstat_PV3_c.eps.** Measured and generated formation values for (a) saturation and porosity, (b) saturation and estimated saturated hydraulic conductivity, and (c) porosity and estimated saturated hydraulic conductivity.

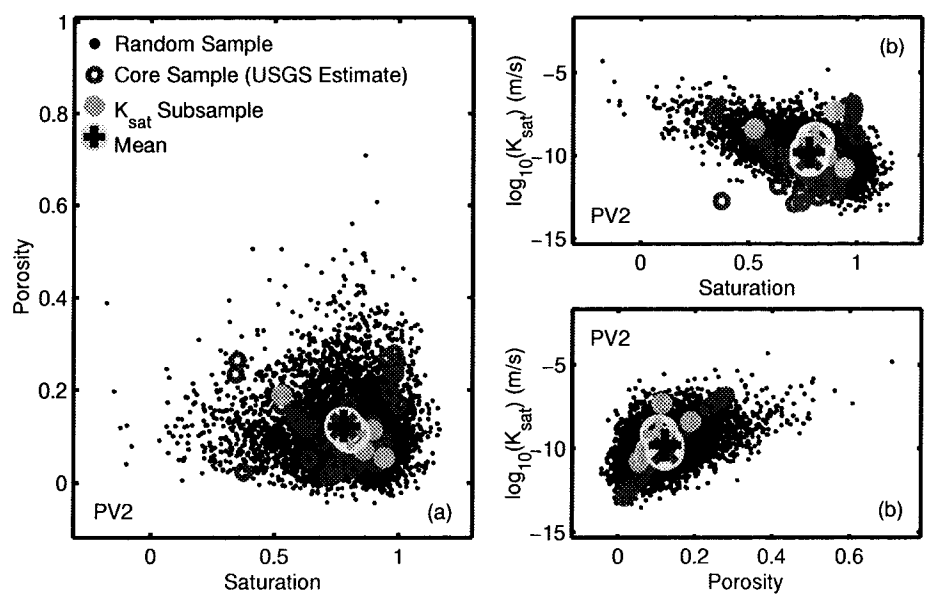

Figure 2-85: 10/7/97. **Disp_DBstat_PV2_c.eps.** Measured and generated formation values for (a) saturation and porosity, (b) saturation and estimated saturated hydraulic conductivity, and (c) porosity and estimated saturated hydraulic conductivity.

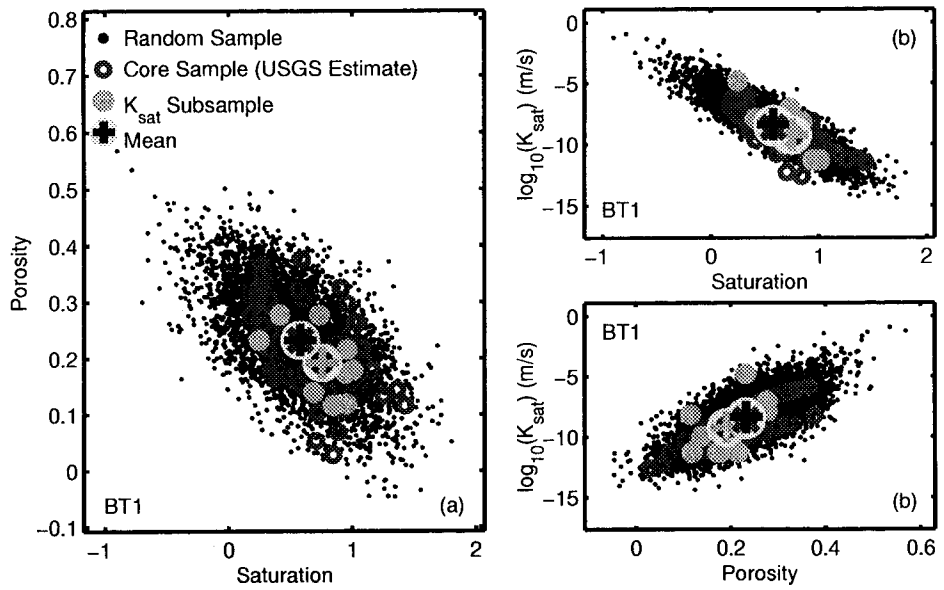

Figure 2-86: 10/7/97. **Disp_DBstat_BT1_c.eps**. Measured and generated formation values for (a) saturation and porosity, (b) saturation and estimated saturated hydraulic conductivity, and (c) porosity and estimated saturated hydraulic conductivity.

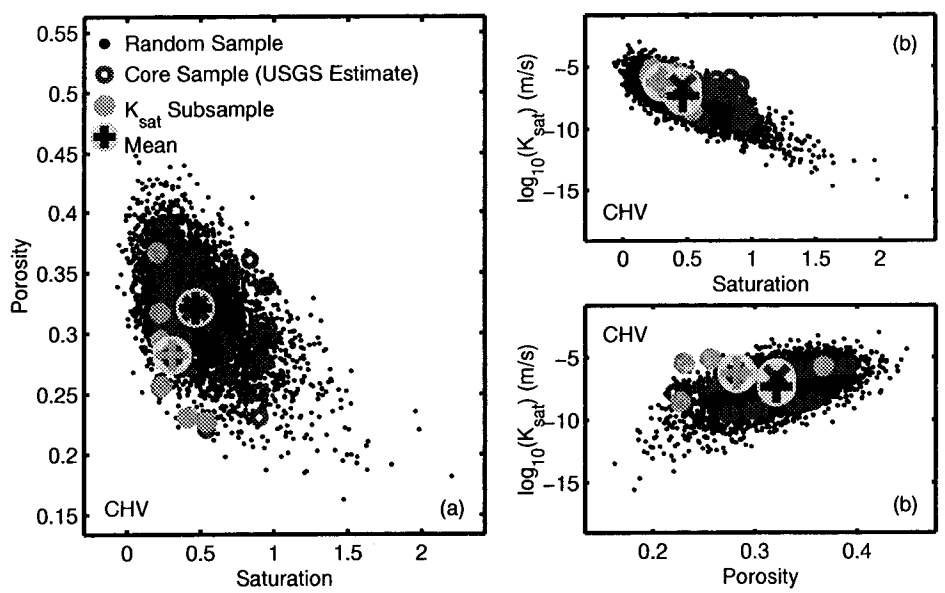

Figure 2-87: 10/7/97. **Disp_DBstat_CHV_c.eps**. Measured and generated formation values for (a) saturation and porosity, (b) saturation and estimated saturated hydraulic conductivity, and (c) porosity and estimated saturated hydraulic conductivity.

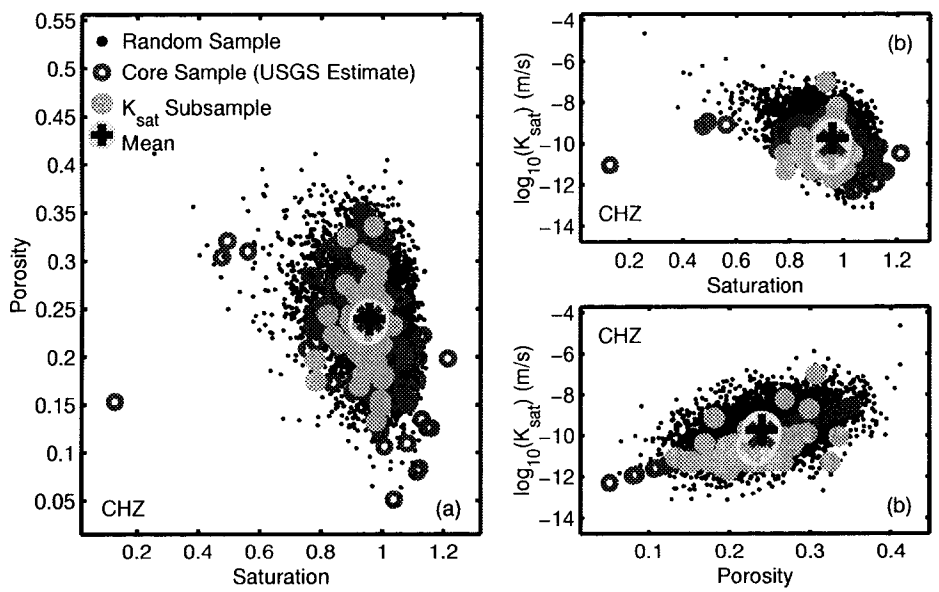

Figure 2-88: 10/7/97. **Disp_DBstat_CHZ_c.eps.** Measured and generated formation values for (a) saturation and porosity, (b) saturation and estimated saturated hydraulic conductivity, and (c) porosity and estimated saturated hydraulic conductivity.

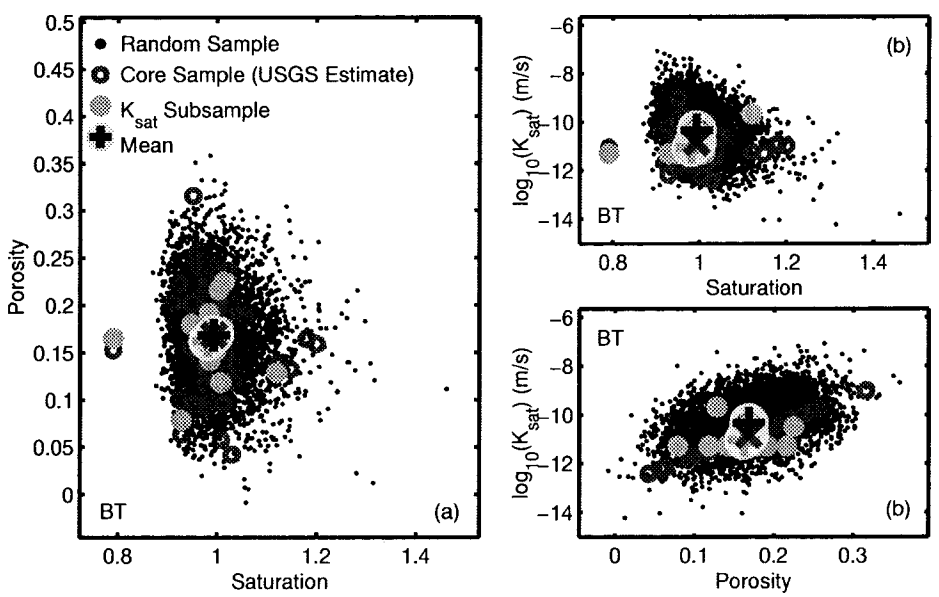

Figure 2-89: 10/7/97. **Disp_DBstat_BT_c.eps.** Measured and generated formation values for (a) saturation and porosity, (b) saturation and estimated saturated hydraulic conductivity, and (c) porosity and estimated saturated hydraulic conductivity.

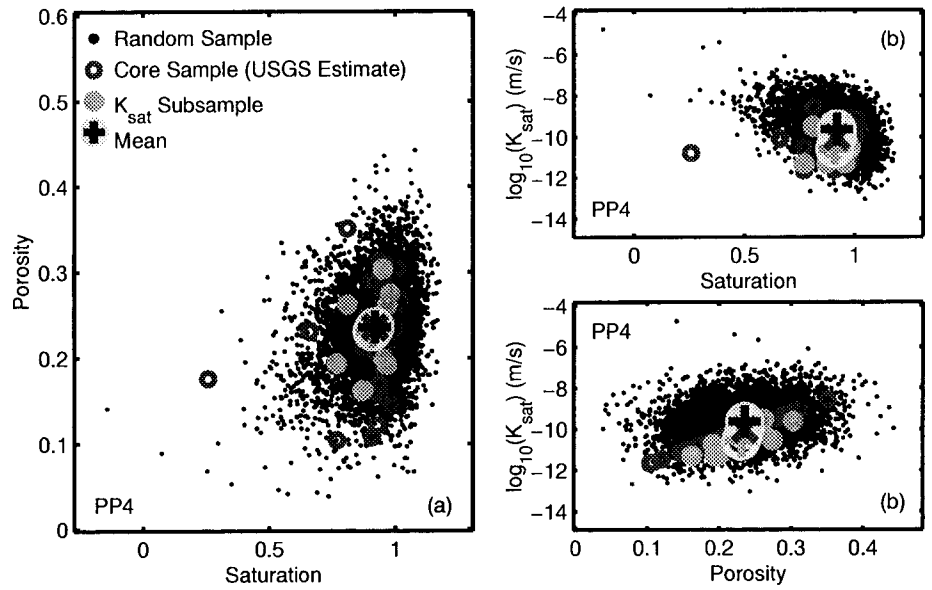

Figure 2-90: 10/7/97. **Disp_DBstat_PP4_c.eps**. Measured and generated formation values for (a) saturation and porosity, (b) saturation and estimated saturated hydraulic conductivity, and (c) porosity and estimated saturated hydraulic conductivity.

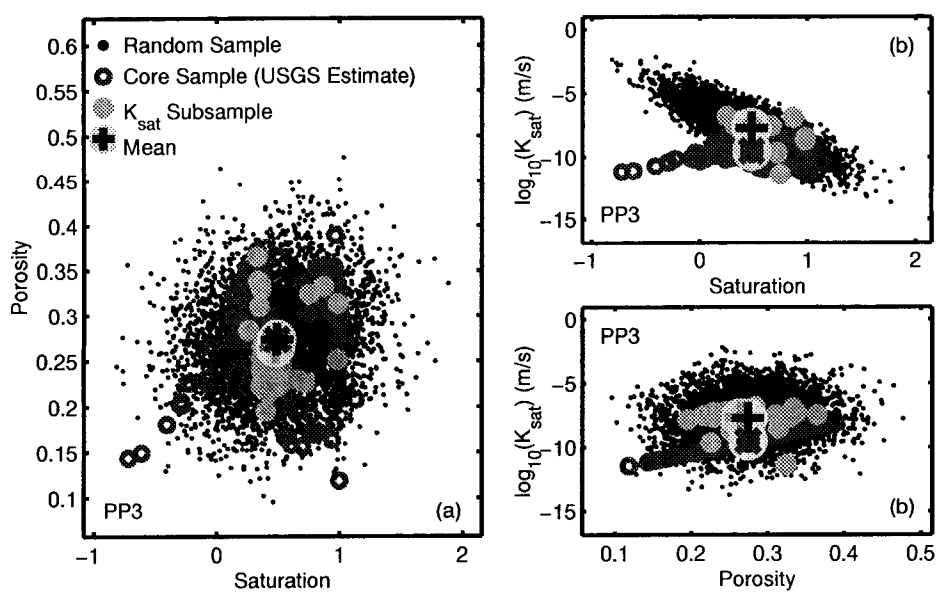

Figure 2-91: 10/7/97. **Disp_DBstat_PP3_c.eps**. Measured and generated formation values for (a) saturation and porosity, (b) saturation and estimated saturated hydraulic conductivity, and (c) porosity and estimated saturated hydraulic conductivity.

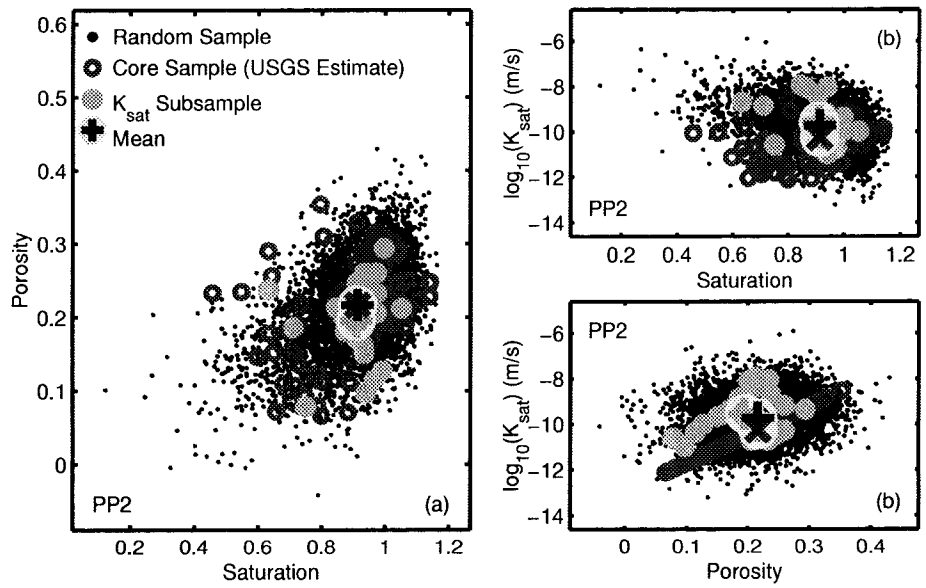

Figure 2-92: 10/7/97. **Disp_DBstat_PP2_c.eps.** Measured and generated formation values for (a) saturation and porosity, (b) saturation and estimated saturated hydraulic conductivity, and (c) porosity and estimated saturated hydraulic conductivity.

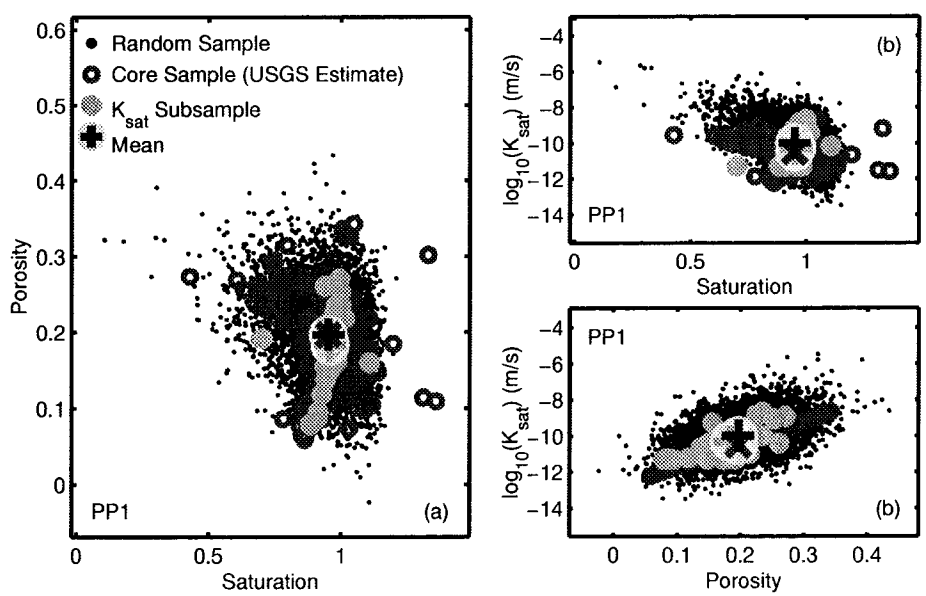

Figure 2-93: 10/7/97. **Disp_DBstat_PP1_c.eps.** Measured and generated formation values for (a) saturation and porosity, (b) saturation and estimated saturated hydraulic conductivity, and (c) porosity and estimated saturated hydraulic conductivity.

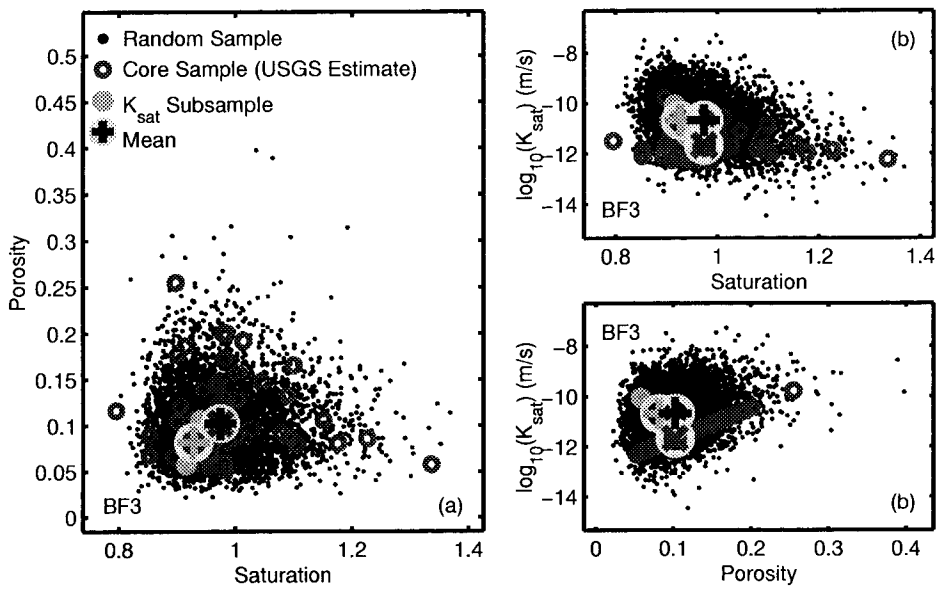

Figure 2-94: 10/7/97. **Disp_DBstat_BF3_c.eps**. Measured and generated formation values for (a) saturation and porosity, (b) saturation and estimated saturated hydraulic conductivity, and (c) porosity and estimated saturated hydraulic conductivity.

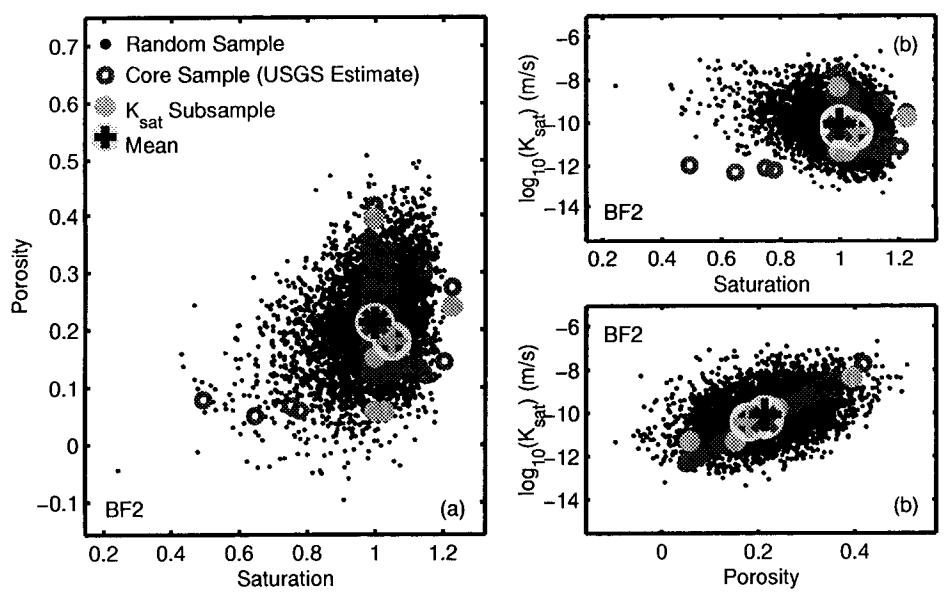

Figure 2-95: 10/7/97. **Disp_DBstat_BF2_c.eps**. Measured and generated formation values for (a) saturation and porosity, (b) saturation and estimated saturated hydraulic conductivity, and (c) porosity and estimated saturated hydraulic conductivity.

10/10/97 Further insights into statistics. SAS

I obtained further insight into the inferences that can be derived from retention data while on a trip to San Antonio. Some of the comments that Robert Mason made last week and yesterday sank in, and reading chapters by Mason et al. (1989) also provided insight. The actual object of the retention measurements is to be able to provide the capillary pressure/moisture content relationship for all core samples, even though this will be done in numerical simulations.

The regression equation was originally written

$$u = \sum_{i=1}^{N} [\log_{10}(P_{mi}) - \log_{10}(P_{ei})]^2, \tag{2-73}$$

$$P_e = P_0(\theta^{-1/m} - 1)^{1-m}, \tag{2-74}$$

$$\log_{10}(P_{0i}) = a_0 + a_1 V_{1i} + a_2 V_{2i}, \tag{2-75}$$

$$m_i = b_0 + b_1 V_{3i} + b_2 V_{4i}. \tag{2-76}$$

where

- u is the objective function,
- P_m is measured capillary pressure,
- P_e is estimated capillary pressure,
- m is van Genuchten $m = 1 - 1/n$,
- P_0 is bubbling pressure (the reciprocal of van Genuchten α in the units used here),
- V_{ji} are the variables being regressed against, and
- a_j, b_j are the regression constants.

In the original equation, it turns out that the components of $\log_{10}(P_{0i})$ are linearly incorporated, so that uncertainty in the a_i values would be directly estimated if the expression for m_i were also linearly incorporated. However, the nonlinear nature of the equation makes it difficult to directly estimate the uncertainty of the b_i coefficients.

In section 26.3 by Mason et al. (1989), the first difficulty is addressed by an approximation for the components of $\mathbf{X}$ in Equation 2-66 (repeated below)

$$S^2_{Y\cdot 12\ldots}(\mathbf{X}'\mathbf{X})^{-1} = \frac{1}{M-N-1}(\mathbf{y}'\mathbf{y} - \mathbf{b}'\mathbf{X}'\mathbf{y})(\mathbf{X}'\mathbf{X})^{-1}, \tag{2-77}$$

where the standard error for b_k is the square root of the kth diagonal element and the entries of $\mathbf{X}$ are the observed predictor variables X_{ij} in linear estimation. When the observations are explained by $f(X_{ij}, \beta_k)$, the approximation is to use $w_{ir} = \partial f(X_{ij}, \beta_k)/\partial \beta_r$ instead of X_{ij}.

The w_{ir} components are as follows:

$$\frac{\partial f(\theta,\beta_k)}{\partial \beta_r} = \frac{\partial \log_{10}(u)}{\partial \beta_r} = \frac{1}{\ln 10}\frac{1}{u}\frac{\mathrm{d}u}{\mathrm{d}m}\frac{\partial m}{\partial \beta_k} \tag{2-78}$$

$$\frac{\mathrm{d}u}{\mathrm{d}m} = \frac{\mathrm{d}[(\theta^{-1/m}-1)^{1-m}]}{\mathrm{d}m} \tag{2-79}$$

$$\tag{2-80}$$

It would probably be easier to evaluate this function numerically than analytically.

As pointed out by R. Mason, a second difficulty arises from the considerable noise in the measurements, so that estimates of the uncertainties in van Genuchten coefficients may be strongly affected by measurement noise. In fact, the noise is probably more due to resolution problems. At high VWC, VWC is easy and P is difficult to measure (P is reported in quanta of 1.4 bar, with many repetitions of low values). At low VWC, VWC is difficult and P is easy to measure, (VWC is reported in quanta of 0.001, with many repetitions of low values). The issue of measurement error is dealt with in chapter 28.1 by Mason et al. (1989). Additional information must be included to handle measurement error, typically ρ (the correlation between predictor and response errors) and $\lambda = \sigma_v^2/\sigma_u^2$ (the ratio of measurement-error variances for response and predictor variables). The maximum-likelihood estimators for intercept and slope are

$$b_0 = \bar{y} - b_1\bar{x}, \tag{2-81}$$

$$b_1 = s(\lambda,\theta) + [s(\lambda,\theta)^2 + t(\lambda,\theta)]^{1/2}, \tag{2-82}$$

$$s(\lambda,\theta) = \frac{s_{yy} - \lambda s_{xx}}{2(s_{xy} - \theta s_{xx})}, \tag{2-83}$$

$$t(\lambda,\theta) = \frac{\lambda s_{xy} - \theta s_{yy}}{s_{xy} - \theta s_{xx}}. \tag{2-84}$$

The original text does not raise t to a power; this should be checked.

The structural-model approach for estimating uncertainty in the presence of measurement errors yields the following expressions:

$$\hat{\mu}_x = \bar{x}, \tag{2-85}$$

$$\hat{\sigma}_x^2 = s_{xx} - \hat{\sigma}_u^2, \tag{2-86}$$

$$\hat{\sigma}_v^2 = \lambda\hat{\sigma}_u^2, \tag{2-87}$$

$$\hat{\sigma}_u^2 = \frac{s_{yy} - 2b_1 s_{xy} + b_1^2 s_{xx}}{(b_1-\theta)^2 + (\lambda - \theta^2)}. \tag{2-88}$$

Assuming that ρ is zero (measurement errors in x and y are uncorrelated), the equations

reduce to:

$$s(\lambda, \theta) = \frac{s_{yy} - \lambda s_{xx}}{2 s_{xy}}, \tag{2-89}$$

$$t(\lambda, \theta) = \lambda, \tag{2-90}$$

$$\hat{\sigma}_u^2 = \frac{s_{yy} - 2 b_1 s_{xy} + b_1^2 s_{xx}}{b_1^2 + \lambda}. \tag{2-91}$$

Although there is undoubtedly measurement error in the USGS data, quantifying the error is not straightforward and is primarily due to resolution rather than other factors. For the time being, it is probably not necessary to account for measurement error; this can be revisited at a later time if deemed appropriate.

10/12/97 Documentation of layer properties and retention estimation. SAS

A first attempt to estimate layerwide-average K_{sat} is reported in Table 2-7. These values were calculated by a *Matlab* routine I created called do_ksat_layerdev.m. The routine used was copied to an archive file with the designation .archive101297. In the table, the mean and standard deviation of both geometric and arithmetic averages are calculated, incorporating uncertainties in both the regression coefficients and the descriptions of θ and ε. A total of 10^4 parameter realizations were used for each realization of the regression coefficients; 10^4 realizations of the regression coefficients were used as well.

In the plots displayed in the entry for 10/7/97, correlation was incorporated whenever one of the two variables appeared to be normally distributed but was not incorporated when both were deemed to be skewed. In the estimation of layer statistics, correlation was always considered by using a form of the skewed equations with the mean of the skewed distribution subtracted out. Realizations of the variable with the most skew are generated first, using the CDF as before, then realizations of the other variable. Realizations of the second variable are found using a mean and standard deviation calculated using the expressions for $\mu_{Y|X}$ and $\sigma_{Y|X}$ discussed in the entry for 9/29/97, and calculating the CDF for the second variable with $\sigma_{Y|X}$ and the original skew. This procedure is only different from before when both variables are skewed (e.g., welded units).

As discussed in the entry for 9/23/97, a complete set of regressions were performed for the available retention data. The best fits were obtained when P_0 was fit using VWC and a particle density (either at 65 or 105 °C, although the 105 °C fits were slightly better), with relatively little impact from the m estimate. The best fits for m using two parameters were obtained when both

Table 2-7: Estimates of mean and standard deviation for average K_{sat} (m/s) over a layer, reported as $\log_{10}(K_{sat})$. Both geometric and arithmetic means are reported. 10^4 replicates of 10^4 realizations were used.

Unit	Geometric Average		Arithmetic Average	
	$\hat{\mu}$	$\hat{\sigma}$	$\hat{\mu}$	$\hat{\sigma}$
TMN	-10.16	0.5332	-8.606	0.5823
TLL	-9.773	0.5779	-7.895	0.6724
TM2	-10.16	0.4844	-8.830	0.5032
TM1	-10.33	0.4282	-9.251	0.4302
PV3	-10.58	0.6842	-8.643	0.7880
PV2	-9.804	0.8403	-7.529	0.9314
BT1	-8.350	1.4034	-4.619	1.4593
CHV	-7.362	0.9665	-5.730	0.9685
CHZ	-9.744	0.4669	-8.449	0.4848
BT	-10.33	0.3830	-9.335	0.3852
PP4	-9.622	0.5635	-8.440	0.5702
PP3	-7.736	1.4243	-4.815	1.4526
PP2	-9.716	0.5971	-8.609	0.5981
PP1	-9.989	0.5459	-8.449	0.5885
BF3	-10.67	0.3766	-9.685	0.3792
BF2	-10.07	0.6496	-8.892	0.6529

particle and bulk densities were used. The worst fits were obtained when porosity information was neglected when estimating both P_0 or m.

When either P_0 or m was estimated using 1 parameter while the other was estimated using 2 parameters, the best fits were obtained with the 2-parameter model using VWC and particle density (again with the 105°C estimate for particle density slightly better than the 65°C estimate) with either bulk density or VWC. In both cases, if the parameter in the 1-parameter fit was restricted to be one of the parameters in the 2-parameter fit, the best estimate was obtained using VWC for the repeated parameter.

If no more than 2 parameters are to be measured for the combination of P_0 and m, again the best two are particle density and VWC. The best fit was obtained with VWC and particle density at 105°C for P_0 and either of the two alone for m (VWC provides a slightly better fit).

If only one parameter is to be used for both, ε is best, followed by bulk density (65°C is slightly better). The best combinations over all categories are shown in Table 2-8. The best combinations with restrictions on the number of parameters, as well as the worst fits, are shown in Table 2-9.

The generally poor showing for ε (as opposed to VWC) might be because a subsample of the original core was used for retention measurements while the subsample porosity is significantly variable at the sub-core scale.

Table 2-8: Best estimated fits to retention data using USGS outcrop data.

Fit Type	P_0		m		$SS^{1/2}$
	X_1	X_2	X_1	X_2	
Best Fit	ρ_p^{105}	VWC_0	ρ_b^{65}	ρ_p^{105}	8.84
	ρ_p^{105}	VWC_0	ρ_b^{105}	ρ_p^{105}	8.86
	ρ_p^{105}	VWC_0	ρ_b^{65}	ρ_p^{65}	8.86
	ρ_p^{105}	VWC_0	ρ_b^{65}	ρ_b^{105}	8.87
	ρ_p^{105}	VWC_0	ρ_b^{65}	$\Delta\rho_b$	8.87
	ρ_p^{105}	VWC_0	ρ_p^{65}	ρ_b^{105}	8.87
	ρ_p^{105}	VWC_0	ρ_b^{65}	$\Delta\varepsilon$	8.88
	ρ_p^{105}	VWC_0	ρ_b^{105}	$\Delta\varepsilon$	8.88
	ρ_p^{105}	VWC_0	$\Delta\rho_b$	VWC_0	8.89
	ρ_p^{105}	VWC_0	ρ_p^{65}	VWC_0	8.90
	ρ_p^{105}	VWC_0	$\Delta\varepsilon$	VWC_0	8.90
	ρ_p^{105}	VWC_0	ρ_b^{65}	VWC_0	8.91
	ρ_p^{105}	VWC_0	ρ_b^{65}	–	8.91
	ρ_p^{105}	VWC_0	ρ_b^{105}	$\Delta\rho_p$	8.92
	ρ_p^{105}	VWC_0	ρ_b^{105}	VWC_0	8.92
	ρ_p^{105}	VWC_0	ρ_b^{105}	–	8.92
	ρ_p^{105}	VWC_0	$\Delta\rho_p$	VWC_0	8.94
	ρ_p^{105}	VWC_0	VWC_0	–	8.94
	ρ_p^{65}	VWC_0	ρ_b^{65}	ρ_p^{105}	8.95
	ρ_p^{65}	VWC_0	ρ_p^{105}	VWC_0	8.95
	ρ_p^{65}	VWC_0	ρ_b^{105}	ρ_p^{105}	8.95
	ρ_p^{105}	VWC_0	$\Delta\rho_b$	$\Delta\rho_p$	8.97
	ρ_p^{105}	VWC_0	ρ_p^{65}	$\Delta\rho_b$	8.98
	ρ_p^{105}	VWC_0	ρ_p^{65}	$\Delta\varepsilon$	8.99
	ρ_p^{105}	VWC_0	$\Delta\rho_b$	$\Delta\varepsilon$	8.99

Table 2-9: Restricted fits to retention data using USGS outcrop data.

Fit Type	P_0		m		$SS^{1/2}$
	X_1	X_2	X_1	X_2	
$N(P_0) = 1$	VWC_0	–	ρ_p^{105}	VWC_0	9.28
	ρ_b^{65}	–	ρ_p^{105}	VWC_0	9.39
	ρ_b^{105}	–	ρ_p^{105}	VWC_0	9.40
	VWC_0	–	ρ_p^{65}	VWC_0	9.51
	ρ_b^{105}	–	ρ_p^{65}	VWC_0	9.61
$N(m) = 1$	ρ_p^{105}	VWC_0	ρ_b^{65}	–	8.91
	ρ_p^{105}	VWC_0	ρ_b^{105}	–	8.92
	ρ_p^{105}	VWC_0	VWC_0	–	8.94
	ρ_p^{105}	VWC_0	$\Delta\rho_b$	–	9.00
	ρ_p^{105}	VWC_0	$\Delta\varepsilon$	–	9.00
$N(P_0 + m) <= 3$	ρ_p^{105}	VWC_0	ρ_b^{65}	ρ_p^{105}	8.84
	ρ_p^{105}	VWC_0	ρ_b^{105}	ρ_p^{105}	8.86
	ρ_p^{105}	VWC_0	$\Delta\rho_b$	VWC_0	8.89
$N(P_0 + m) <= 2$	ρ_p^{105}	VWC_0	VWC_0	–	8.94
	ρ_p^{105}	VWC_0	ρ_p^{105}	–	9.00
	ρ_p^{65}	VWC_0	ρ_p^{65}	VWC_0	9.08
$N(P_0) = 1, N(m) = 1$	VWC_0	–	ρ_p^{105}	–	10.3
	VWC_0	–	ρ_p^{65}	–	10.4
	VWC_0	–	$\Delta\varepsilon$	–	10.7
	VWC_0	–	$\Delta\rho_b$	–	10.7
	VWC_0	–	$\Delta\rho_p$	–	10.7
$N(P_0 + m) = 1$	VWC_0	–	VWC_0	–	10.7
	ρ_b^{65}	–	ρ_b^{65}	–	11.3
	ρ_b^{105}	–	ρ_b^{105}	–	11.3
	$\Delta\rho_b$	–	$\Delta\rho_b$	–	12.3
Worst Fit	ρ_p^{105}	$\Delta\rho_b$	$\Delta\varepsilon$	$\Delta\rho_p$	12.5
	ρ_p^{65}	$\Delta\rho_b$	$\Delta\rho_b$	$\Delta\rho_p$	12.5
	ρ_p^{105}	–	ρ_p^{105}	–	12.5
	ρ_p^{65}	–	ρ_p^{105}	–	12.5
	ρ_p^{105}	$\Delta\rho_p$	ρ_p^{105}	$\Delta\rho_b$	12.5

10/13/97 Retention estimation. SAS

The similarity between estimates of fit to the retention data can be explained by correlation between parameters. Correlation coefficients between VWC_0 and other parameters are as follows:

- $\rho_b^{65} = -0.915$,
- $\varepsilon^{65} = 0.883$,
- $\rho_p^{65} = -0.706$,
- $\rho_b^{105} = -0.917$,
- $\varepsilon^{105} = 0.904$,
- $\rho_p^{105} = -0.689$,
- $\Delta\rho_b = -0.462$,
- $\Delta\varepsilon = 0.551$, and
- $\Delta\rho_p = 0.522$.

One would expect that little additional explanatory power is achieved when a highly correlated parameter is added. The relative success of the cases with VWC and ρ_p^{105} for estimating P_0 may be due to the lack of correlation between the pair; note that the next best group of fits is provided by cases with the next worse correlation (i.e., VWC and ρ_p^{65}). It appears that the overall fit is best when VWC, ρ_b, and ρ_p are all used, while ρ_b and ρ_p are measured at different temperatures. On the other hand, the Δ parameters have relatively low correlation to VWC and little explanatory power. Apparently deviations in properties occurring due to drying have relatively little explanatory power.

The best overall fit only uses 3 measured variables (not 4); however, there is not a tremendous dropoff when only 2 variables are measured ($SS^{1/2}$ goes from 8.84 to 8.94). For simplicity of generating random realizations and due to the relatively good fit, the estimation of layerwise properties will use the best 2-variable model (5 coefficients):

$$P_0 = a_1 + b_{11}\,VWC_0 + b_{12}\rho_p^{105}, \tag{2-92}$$

$$m = a_2 + b_{21}\,VWC_0. \tag{2-93}$$

The best-fit coefficients for the 2-variable model are reported in Table 2-10. Following the procedure for estimating uncertainty in coefficients discussed in the 10/10/97 entry, the uncertainty for the best-fit coefficients are also reported in Table 2-10. For this set of coefficients, R^2 is 0.865.

Table 2-10: Statistical properties of regression on retention parameters.

Statistic	P_0 Coefficients			m Coefficients	
	a_1	b_{11} (VWC_0)	b_{12} (ρ_p^{105})	a_2	b_{21} (VWC_0)
$\hat{\mu}$	12.512	-4.51416	-3.80632	0.302373	0.115806
$\hat{\sigma}$	1.0494	0.41451	0.313008	0.0127992	0.0523755

One can estimate new coefficients using the $\partial f/\partial\beta$ matrix with the previous best-fit coefficients used to evaluate f. One would expect that there would be little difference in the two sets of coefficients. It is somewhat disconcerting that a different set of coefficients are in fact obtained. The estimated values for the P_0 coefficients are slightly different, but the estimated values for the m coefficients are quite different (roughly the same magnitude but with opposite sign). In particular, using the newly found coefficients to regress for m results in m values that are always negative! The $\hat{\sigma}$ values in Table 2-10 were evaluated with the new coefficients for self-consistency; values estimated using the old coefficients to multiply the matrix are roughly 4 times larger. Despite the obvious deviation from near-linearity implied by this finding, estimates for $\hat{\sigma}$ appear to be qualitatively reasonable and so will be used for further work.

In order to generate samples with more than 2 correlated parameters, the following form will be used:

$$\mathbf{u} = \mathbf{C}\epsilon, \tag{2-94}$$

where $\mathbf{u}$ is the vector of normalized variates $[u_i = (x_i - \mu)/\sigma]$, $\mathbf{C}$ is the correlation matrix, and ϵ is normally distributed $[N(0,1)]$ noise. This matrix form is the lag-0 simplification of a lag-0/lag-1 expression by Matalas (1967). The actual realization of x_i is directly calculated from u_i for normally distributed variables. For skewed variables, my idea is to use u_i to obtain the cumulative probability, $F(u_i)$, assuming that u_i is a normal variate, then get the value for u_i in the skewed distribution that has the same $F(u)$ using table lookup. A revised u_i can be obtained from table lookup on $F(u)$ for the skewed variable, and finally x_i is calculated from the revised u_i. The procedure may break down when the variables are greatly skewed.

I just noticed that Lapin (1983) discusses a method for estimating bounds on correlation coefficients using normally distributed Fisher's Z'. The formulas are

$$Z' = \frac{1}{2}\ln\left(\frac{1+r}{1-r}\right), \tag{2-95}$$

$$\mu_{Z'} = \frac{1}{2}\ln\left(\frac{1+\rho}{1-\rho}\right), \tag{2-96}$$

$$\sigma_{Z'} = \frac{1}{(n-3)^{1/2}}, \tag{2-97}$$

where n is the number of samples and r is the estimated ρ. A realization for ρ is found by rearranging:

$$\rho_i = \frac{b_i - 1}{b_i + 1}, \tag{2-98}$$

$$b_i = \exp[2(Z' + \sigma_{Z'}\epsilon_i)], \tag{2-99}$$

where ϵ_i denotes a sample from a $N(0,1)$ distribution. Each of the correlation coefficients within $\mathbf{C}$ can presumably be sampled independently using this procedure.

10/16/97 Retention-estimation progress.

SAS

A *Matlab* routine, do_laydev_all.m, was created in the ***$HOME2/AmbientKTI/3Ddata*** directory, to investigate the layer-average hydraulic properties for each microstratigraphic unit. The procedure was outlined before, and is summarized below.

- Estimate regression coefficients and their uncertainties for K_{sat} using est_ksat_params.m. The regressed fit is for θ^{65} and ε_{sample}.
- Estimate regression coefficients and their uncertainties for P_0 and m using est_reten_params.m The regressed fit for P_0 is for VWC_0 and ρ_p^{105}. The regressed fit for m is for VWC_0.
- Assume that the statistics for ε^{65} are equivalent to the statistics for ε_{sample}.
- Assume that the statistics for ε^{65} are equivalent to the statistics for VWC_0.
- Generate many realizations of the regression coefficients predicting $\log_{10}(K_{sat})$, $\log_{10}(P_0)$, and m. Use the same realizations for each layer so that layer combinations can be considered with comparable regressions.
- For each microstratigraphic layer of interest:

- Estimate mean, standard deviation, skew, and cross-correlations for θ^{65}, ε^{65}, and ρ_p^{105}.
- Estimate standard deviation of the mean, standard deviation, and cross-correlations.
- For each statistic realization in a layer:
  * Sample the mean, standard deviation, and cross-correlation for θ^{65}, ε^{65}, and ρ_p^{105}.
  * Generate many samples of the predictor properties.
  * Predict regressed variables from the samples. Noise is included for K_{sat} but not the retention properties (there is no direct way to calculate per-sample noise).
  * Calculate layer-wide, channel, and nonchannel hydraulic-property averages at various levels of capillary pressure.
  * Calculate hydraulic properties for the averages.

Using this procedure, some preliminary observations can be made. For the purposes of discussion, I will denote high-flux samples as channels and low-flux samples as barriers, although "barrier" would be more properly termed "noncontributor." I will denote cases with all samples included as "composite." To determine whether a sample is a channel or a barrier, the samples are first sorted by flux and the cumulative flux from lowest to highest is found. Barrier samples are those samples with cumulative flux less than a small fraction of the total flux (e.g., 0.01 of total flux), with the fraction of samples defined as a barrier denoted by f_b. Channel samples are the remaining samples, with the fraction of samples defined as a channel denoted by f_c. Aggregate parameters are defined as the parameters derived from performing a regression to fit the layer-mean properties [i.e., arithmetic mean of (i) all samples, (ii) channels, (iii) barriers].

- For any particular set of regression coefficients, the predicted variability of m is rather small within a formation, while the variability of K_{sat} and P_0 is quite significant.
- Welded units tend to have aggregate properties that are quite similar to the core sample properties, while nonwelded units tend to have aggregate properties that are somewhat different.
- f_c tends to decrease as conditions become drier.
- f_c tends to be larger for welded units.
- Under dry conditions, f_c can be miniscule for nonwelded units, implying that extreme channelling would occur.
- Both P_0 and m tend to be lower than composite in channels and higher than composite otherwise, while K_{sat} is opposite in behavior.

- Average velocity tends to be slower than that predicted using average channel flux, saturation, and porosity. In nonwelded tuffs, the discrepancy can be as much as 2 to 3 orders of magnitude; in welded tuffs, the discrepancy is generally well less than an order of magnitude. As fluxes increase, the discrepancy decreases.

- For nonwelded tuffs (based on several BT2 realizations)
  - Aggregate K_{sat} tends to be slightly larger than averaged K_{sat} (a factor of 2 or so) for all three categories.
  - Channel K_{sat} tends to be larger than composite K_{sat}, by up to an order of magnitude.
  - Barrier K_{sat} tends to be more than an order of magnitude less than composite K_{sat}.
  - There is not much difference between averaged channel, barrier, and composite P_0 and m.
  - Both aggregate P_0 and aggregate m tend to decrease relative to the comparable averaged property. The decreases are more extreme when extracting P_0 and m from retention than from conductivity.
  - m tends to decrease by 15 to 35 percent using retention fits.
  - P_0 tends to decrease by 1 to 4 orders of magnitude using retention fits.
  - Fraction of samples corresponding to channels can be less than 0.01 and greater than 0.3.

- For nonwelded tuffs (based on several TMN realizations)
  - Aggregate K_{sat} tends to be slightly larger than averaged K_{sat} (a factor of 3 or so) for all three categories.
  - Channel K_{sat} tends to be larger than composite K_{sat}, by about an order of magnitude.
  - Barrier K_{sat} tends to be more than an order of magnitude less than composite K_{sat}.
  - There is negligible difference between averaged channel, barrier, and composite P_0 and m.
  - Both aggregate P_0 and aggregate m tend to decrease relative to the comparable averaged property. The decreases are more extreme when extracting P_0 and m from retention than from conductivity, but the changes are only by a few percent.
  - Fraction of samples corresponding to channels can be less than 0.1 and greater than 0.4.

10/20/97 Hydraulic-property preliminary results. SAS

I set off a set of runs to get a feel for the behavior of the estimates. I tried to do a 12-hr simulation, which should have been possible with 150 realizations of regression coefficients, 6 microstratigraphic layers, and 10^4 realizations of hydraulic properties per realization of regression coefficients. Preliminary trials took 50 seconds for one set of hydraulic-property realizations. Surprisingly, the entire set took more than 2 days. I hope this is due to paging due to the size of memory used to save the results in one array.

Several observations can be made from the first set of results.

- There is very high correlation between layer-average properties (i.e., $\rho > 0.996$ for P_0, $\rho > 0.91$ for m) estimated using retention and conductivity values for units TMN, TLL, TM2, TM1, and PV3. In the less-welded PV2, $\rho = 0.96$ for P_0 and $\rho = 0.68$ for m.
- There is very low correlation between one layer-average property and any other (max[abs(ρ)] $<$ 0.092 for all layers other than PV2, and < 0.3 for PV2).
- There is high correlation (> 0.9) between layer-average K_{sat} and both channel and barrier K_{sat}; however, the means are different, with channel K_{sat} larger and barrier K_{sat} lower than layer-average.
- As channel flow becomes a smaller fraction of the total flow,
  - Both channel and barrier K_{sat} increase (but continue to bracket the mean); changes can be more than 2 orders of magnitude. Correlation with layerwide properties also decreases (as low as 0.7), more so for the barrier realizations.
  - P_0 is essentially unaffected.
  - Channel m tends to decrease with a concomitant decrease in correlation with layerwide properties. The deterioration in correlation is more marked with properties determined from conductivity; ρ ranges from 0.63 to 0.94. The change in mean is more marked with properties determined from retention; mean(Δm) ranges from -0.011 to -0.068.
- The velocity discrepancy can only be estimated at low fluxes (e.g., 0.01 mm/yr), as fluxes greater than K_{sat} cannot be satisfied with matrix-only gravity drainage. It is disturbing that complex numbers pop up, as K_{sat} should generally be large enough to accommodate. The complex numbers arise when porosity is negative, a problem for layers with porosity less than 0.1. Based on cases that may include complex velocities, I find that:

- Even at 0.01 mm/yr, layers TM1, PV3, and PV2 have complex velocities in at least one realization; PV3 has more than half of the velocities complex.
- The correlation between velocity using averaged values and aggregate values is not particularly large at best, deteriorating as welding decreases.

10/21/97 More hydraulic-property preliminary results. SAS

I fixed the problem with complex velocities in two steps. The first step was to provide an additional distribution option for generating raw-property samples. When every value of the generating population is positive, the skew is positive, and the skew of the base-10 logarithm is less than half that of the raw variables, the invoked distribution is lognormal rather than extreme-value. This step took care of most of the complex-variable problem; however, an occasional few velocities still were created with very small imaginary parts (apparently roundoff error, since the imaginary part is typically 10^{-16} times smaller than the real part). I simply took the real part of the velocities in such cases.

At the same time as fixing the complex-velocity problem, I changed the output so that only information for one layer at a time is in memory. This removed the problem with computational speed, suggesting that memory limitations were causing paging.

10/28/97 Hydraulic-property results. SAS

The results from 500 realizations of material properties are shown in the following figures, all generated using files **show_several_laydev.m** and **show_laydev.m** in the ***$HOME2/Ambient-KTI/3Ddata*** directory. The generating files are archived with **archive102897** appended. In the following figures, subfigures a through f are entitled **LayMat_Ks_XXX_c.eps**, **LayMat_Corr_-XXX_c.eps**, **LayMat_Pr_XXX_c.eps**, **LayMat_Pk_XXX_c.eps**, **LayMat_Mr_XXX_c.eps**, and **LayMat_Mk_XXX_c.eps**, respectively, where **XXX** refers to the microstratigraphic layer.

The results are also displayed in Table 2-11 (K_{sat} results), Table 2-12 (van Genuchten α results), and Table 2-13 (van Genuchten n results). My calculations were performed using P_0 and m, then converted to the corresponding α and n to be consistent with USGS results.

Table 2-11: Estimates of microstratigraphic K_{sat}. Geometric means and standard deviations are of $\log_{10}(K_{sat})$ are shown.

Unit	Core (USGS)		Core (CNWRA)		Geometric Mean of Equivalent Layer							
					Full		$Q_{Bfrac} = 0.001$		$Q_{Bfrac} = 0.01$		$Q_{Bfrac} = 0.1$	
	μ	σ	μ	σ	μ	σ	μ	σ	μ	σ	μ	σ
TMN	1.50×10^{-11}	0.57	6.91×10^{-11}	0.56	3.59×10^{-9}	0.65	5.66×10^{-9}	0.71	1.20×10^{-8}	0.76	8.09×10^{-8}	0.81
TLL	7.20×10^{-11}	0.76	1.67×10^{-10}	0.65	2.39×10^{-8}	0.95	5.84×10^{-8}	1.2	1.92×10^{-7}	1.3	1.32×10^{-6}	1.2
TM2	1.79×10^{-11}	0.77	6.79×10^{-11}	0.53	3.51×10^{-9}	0.63	5.52×10^{-9}	0.69	1.18×10^{-8}	0.77	8.12×10^{-8}	0.85
TM1	4.85×10^{-12}	0.52	4.66×10^{-11}	0.46	6.39×10^{-10}	0.50	8.03×10^{-10}	0.49	1.21×10^{-9}	0.49	3.60×10^{-9}	0.50
PV3	1.53×10^{-13}	0.54	2.59×10^{-11}	0.65	2.64×10^{-8}	1.0	1.43×10^{-7}	1.4	6.74×10^{-7}	1.4	2.32×10^{-6}	1.1
PV2	7.39×10^{-11}	1.9	1.55×10^{-10}	0.80	6.78×10^{-8}	1.2	2.44×10^{-7}	1.4	8.97×10^{-7}	1.5	4.44×10^{-6}	1.3
BT1	2.60×10^{-9}	1.8	4.38×10^{-9}	1.7	4.53×10^{-4}	1.6	8.02×10^{-3}	1.7	2.71×10^{-2}	1.6	4.38×10^{-2}	1.6
CHV	2.13×10^{-7}	0.99	4.30×10^{-8}	1.1	3.34×10^{-6}	1.0	6.08×10^{-6}	1.0	1.09×10^{-5}	1.0	3.84×10^{-5}	1.0
CHZ	1.08×10^{-10}	0.61	1.79×10^{-10}	0.53	4.07×10^{-9}	0.58	5.56×10^{-9}	0.59	9.38×10^{-9}	0.62	3.68×10^{-8}	0.67
BT	1.40×10^{-11}	0.63	4.69×10^{-11}	0.41	4.88×10^{-10}	0.49	5.95×10^{-10}	0.49	8.67×10^{-10}	0.49	2.39×10^{-9}	0.49
PP4	9.61×10^{-11}	0.69	2.37×10^{-10}	0.50	3.75×10^{-9}	0.67	4.98×10^{-9}	0.74	7.95×10^{-9}	0.75	3.01×10^{-8}	0.77
PP3	2.93×10^{-10}	0.67	1.81×10^{-8}	1.4	1.82×10^{-5}	1.5	6.40×10^{-5}	1.5	1.89×10^{-4}	1.6	1.12×10^{-3}	1.5
PP2	5.60×10^{-11}	0.76	1.91×10^{-10}	0.46	2.61×10^{-9}	0.69	3.21×10^{-9}	0.69	4.82×10^{-9}	0.69	1.55×10^{-8}	0.72
PP1	3.15×10^{-11}	0.69	1.02×10^{-10}	0.62	4.86×10^{-9}	0.67	7.83×10^{-9}	0.71	1.65×10^{-8}	0.76	1.02×10^{-7}	0.82
BF3	2.10×10^{-12}	0.48	2.12×10^{-11}	0.38	2.58×10^{-10}	0.58	3.16×10^{-10}	0.60	4.64×10^{-10}	0.64	1.32×10^{-9}	0.71
BF2	5.03×10^{-11}	1.0	8.43×10^{-11}	0.55	1.49×10^{-9}	0.77	1.99×10^{-9}	0.78	3.25×10^{-9}	0.80	1.17×10^{-8}	0.86

Table 2-12: Estimates of microstratigraphic van Genuchten α (bar^{-1}). USGS estimate is from Table 8 by Flint (1996) and is probably arithmetic. CNWRA estimates are geometric, with $\log_{10}(\alpha)$ standard deviations shown.

	Core (USGS)			Core (CNWRA)			$\psi - \theta$		$k - \theta$	
Unit	N	μ	σ	N	μ	σ	μ	σ	μ	σ
TMN	3	0.064	0.013	266	0.170	0.168	0.184	1.571	0.183	1.577
TLL	3	0.273	0.105	451	0.279	0.156	0.416	1.588	0.245	1.578
TM2	1	0.047	0.005	225	0.238	0.174	0.290	1.570	0.219	1.579
TM1	1	0.022	0.002	102	0.169	0.164	0.154	1.566	0.164	1.579
PV3	3	0.010	0.003	86	0.022	0.119	0.010	1.512	0.024	1.545
PV2	1	1.255	0.652	39	0.046	0.329	0.013	1.556	0.064	1.553
BT1	2	9.800	8.695	79	0.061	0.445	0.091	1.516	0.092	1.572
CHV	2	9.800	8.695	69	0.068	0.537	0.054	1.523	0.159	1.607
CHZ	4	0.394	0.125	293	0.101	0.269	0.064	1.513	0.092	1.560
BT	1	0.015	0.001	69	0.145	0.366	0.072	1.579	0.214	1.659
PP4	1	0.010	0.001	47	0.180	0.317	0.037	1.558	0.195	1.584
PP3	3	1.817	0.599	166	1.443	0.310	0.841	1.623	1.392	1.633
PP2	3	0.072	0.012	140	0.437	0.293	0.271	1.610	0.398	1.623
PP1	2	0.179	0.060	245	0.139	0.413	0.151	1.577	0.274	1.649
BF3	1	0.036	0.010	86	0.316	0.249	0.265	1.612	0.442	1.653
BF2	1	0.012	0.001	65	0.151	0.442	0.099	1.590	0.207	1.611

Observations that were made in the 10/20/97 entry are well supported with the additional realizations. Note that correlation is generally very low between material properties, with very high correlation between P_0 estimated from retention data versus conductivity data and somewhat less high correlation between m obtained from the same pair of data sets.

In general, I expect that it may not be necessary to be sophisticated when using the retention properties estimated using the regression approach outlined herein. The variation in retention properties between channel and barrier is relatively small and no strong correlation appears to exist between material properties.

The results outlined here, although based on USGS-estimated core-sample properties, are strikingly different in several ways. The USGS-presented estimates of average core-sample properties (Flint, 1996) have considerably smaller variation in P_0 and considerably larger variation in m.

Table 2-13: Estimates of microstratigraphic van Genuchten n. USGS estimate is from Table 8 by Flint (1996).

Unit	Core (USGS)			Core (CNWRA)			$\psi - \theta$		$k - \theta$	
	N	μ	σ	N	μ	σ	μ	σ	μ	σ
TMN	3	1.470	0.076	266	1.455	0.005	1.437	0.030	1.438	0.028
TLL	3	1.294	0.051	451	1.461	0.008	1.449	0.035	1.448	0.030
TM2	1	1.713	0.078	225	1.456	0.008	1.438	0.030	1.445	0.029
TM1	1	2.141	0.267	102	1.450	0.005	1.427	0.030	1.442	0.028
PV3	3	1.592	0.127	86	1.438	0.004	1.424	0.039	1.428	0.033
PV2	1	1.310	0.075	39	1.463	0.020	1.401	0.060	1.421	0.035
BT1	2	1.294	0.072	79	1.491	0.021	1.460	0.065	1.433	0.038
CHV	2	1.294	0.072	69	1.514	0.010	1.391	0.052	1.416	0.037
CHZ	4	1.290	0.037	293	1.493	0.013	1.426	0.056	1.474	0.041
BT	1	1.909	0.111	69	1.475	0.013	1.453	0.039	1.418	0.035
PP4	1	3.035	0.404	47	1.492	0.014	1.410	0.047	1.454	0.039
PP3	3	1.455	0.071	166	1.502	0.014	1.437	0.048	1.475	0.043
PP2	3	1.603	0.081	140	1.487	0.015	1.445	0.038	1.468	0.040
PP1	2	1.454	0.078	245	1.482	0.014	1.402	0.037	1.403	0.035
BF3	1	1.680	0.202	86	1.458	0.010	1.417	0.032	1.413	0.032
BF2	1	2.477	0.275	65	1.486	0.021	1.361	0.041	1.427	0.038

The USGS estimates for the 15 layers I considered are based on a total of 31 samples.

My estimated range in layer-average P_0 is typically 8 to 10 orders of magnitude, with a standard deviation equivalent to more than an order of magnitude. My estimated geometric-mean van Genuchten α for each layer ranges from 0.0097 to 1.39 bar^{-1}, with a standard deviation for $\log_{10}(\alpha)$ of between 1.51 and 1.66, while the USGS core sample data has a range from 0.01 to 9.8 bar^{-1} in the same layers (apparently arithmetic mean, since there are no more than 4 samples for any layer).

On the other hand, my estimated range in m is quite small, with relatively little variation between layers. The estimated layer-average m ranges from 0.264 to 0.321, with standard deviation ranging from 0.0134 to 0.0341. Equivalently, layer-average n ranges from 1.36 to 1.46, with standard deviation ranging from 0.0279 to 0.652. For the same layers, the USGS mean values for n range from 1.29 to 3.035, with standard errors ranging from 0.037 to 0.404.

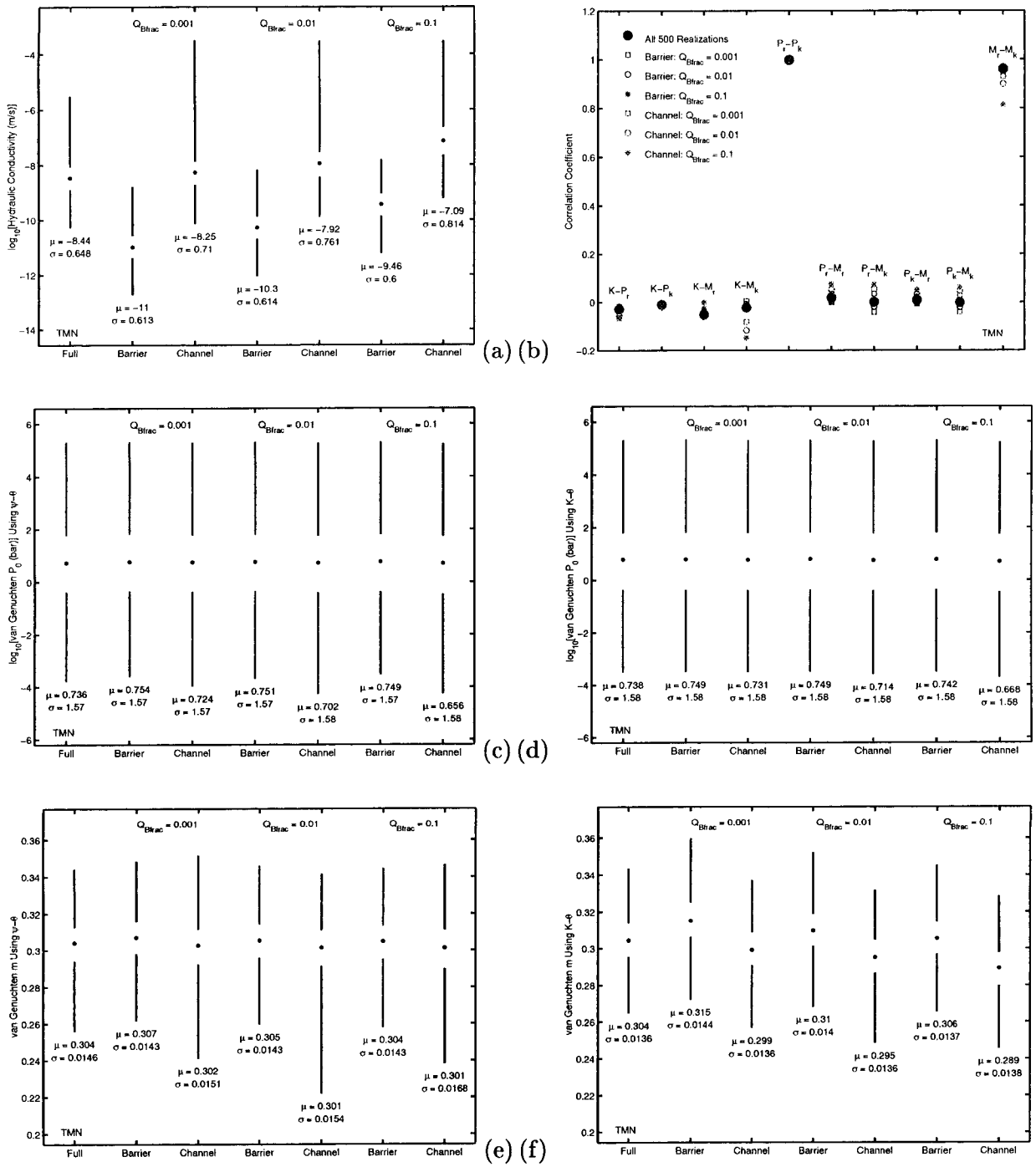

Figure 2-96: 10/28/97. Estimated properties for layer TMN. Correlation between material properties (b), and quartiles for: (a) equivalent K_{sat}, P_0 using retention and conductivity (c and d, respectively); and m using retention and conductivity (e and f, respectively).

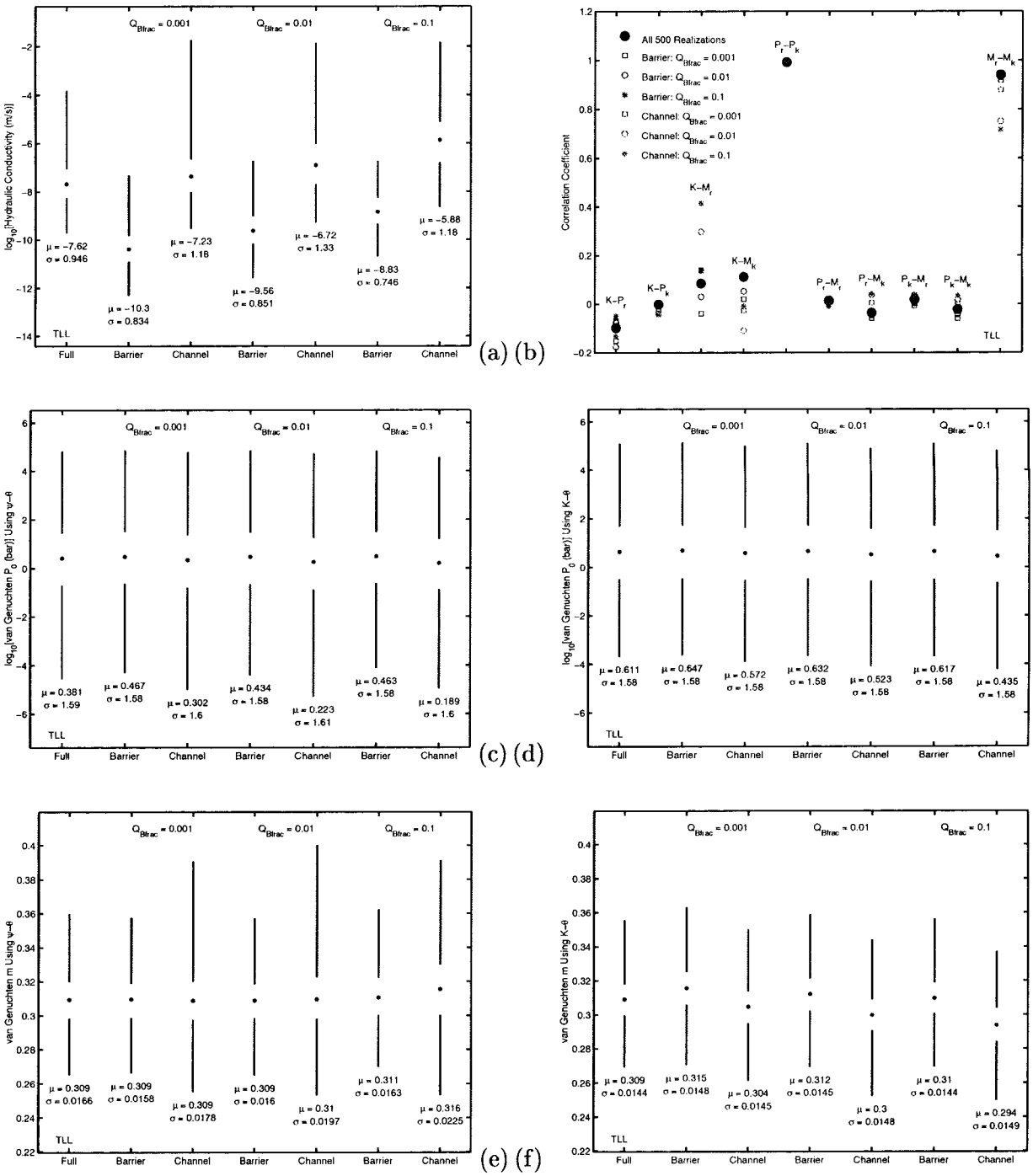

Figure 2-97: 10/28/97. Estimated properties for layer TLL. Correlation between material properties (b), and quartiles for: (a) equivalent K_{sat}, P_0 using retention and conductivity (c and d, respectively); and m using retention and conductivity (e and f, respectively).

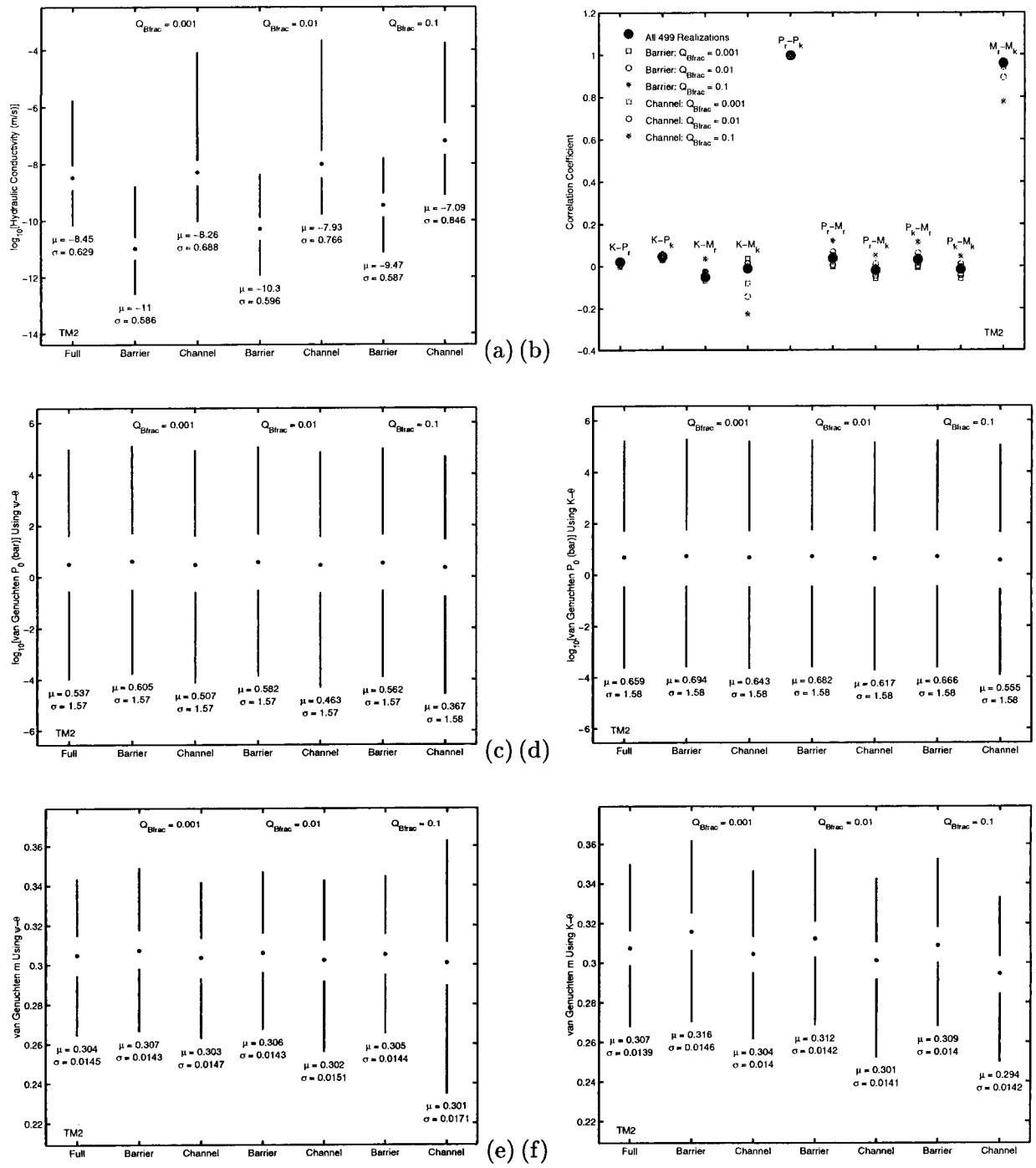

Figure 2-98: 10/28/97. Estimated properties for layer TM2. Correlation between material properties (b), and quartiles for: (a) equivalent K_{sat}, P_0 using retention and conductivity (c and d, respectively); and m using retention and conductivity (e and f, respectively).

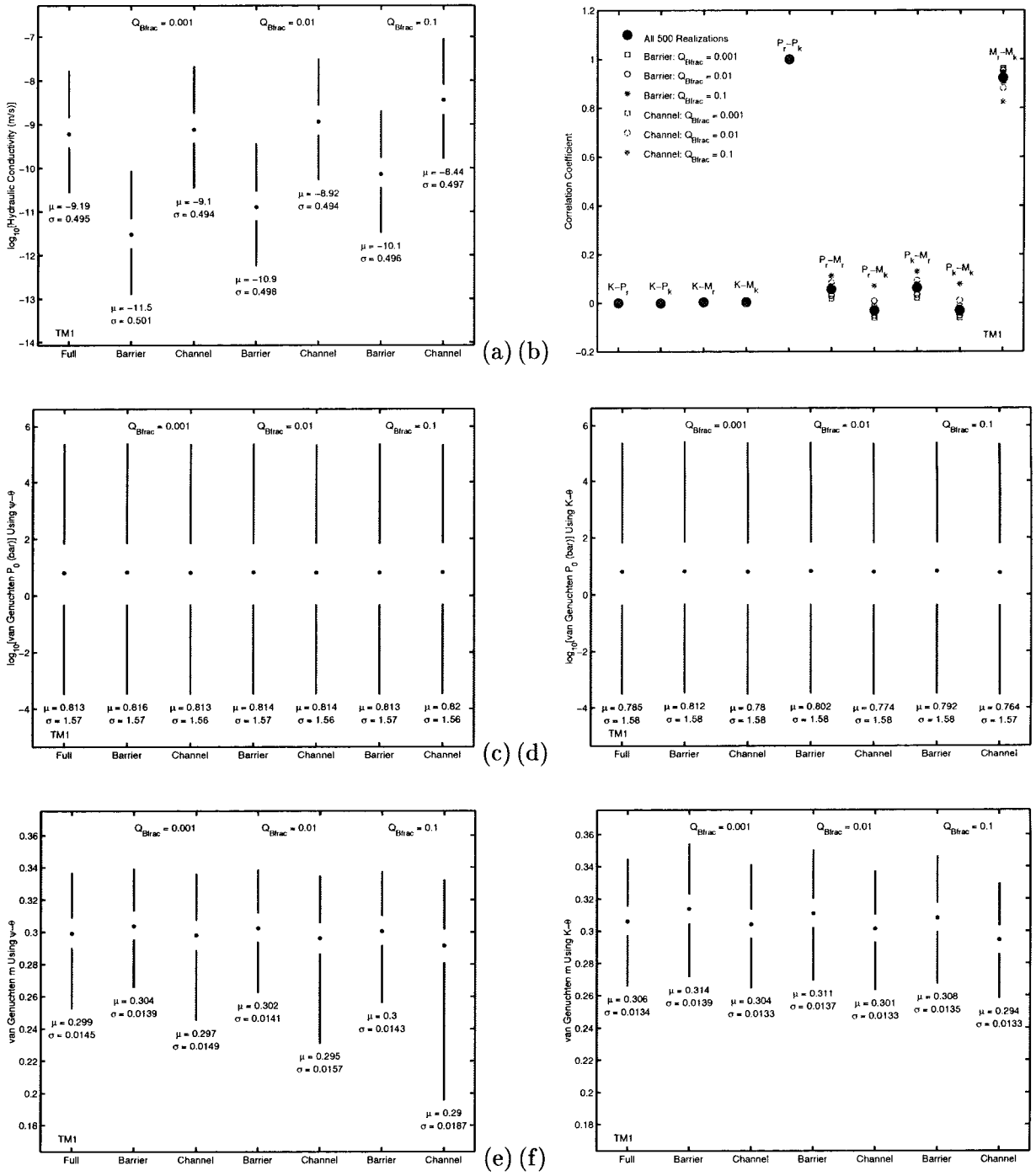

Figure 2-99: 10/28/97. Estimated properties for layer TM1. Correlation between material properties (b), and quartiles for: (a) equivalent K_{sat}, P_0 using retention and conductivity (c and d, respectively); and m using retention and conductivity (e and f, respectively).

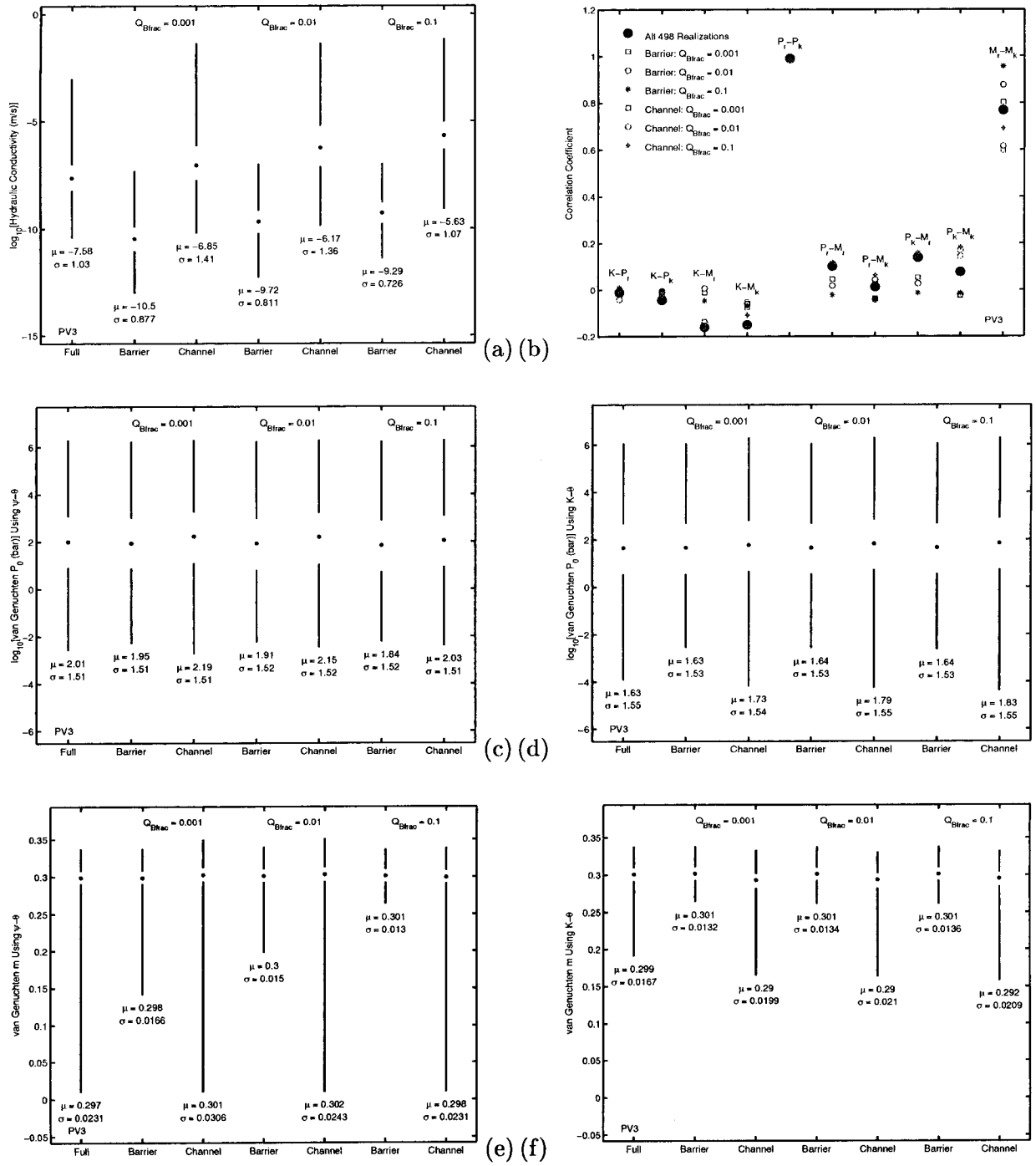

Figure 2-100: 10/28/97. Estimated properties for layer PV3. Correlation between material properties (b), and quartiles for: (a) equivalent K_{sat}, P_0 using retention and conductivity (c and d, respectively); and m using retention and conductivity (e and f, respectively).

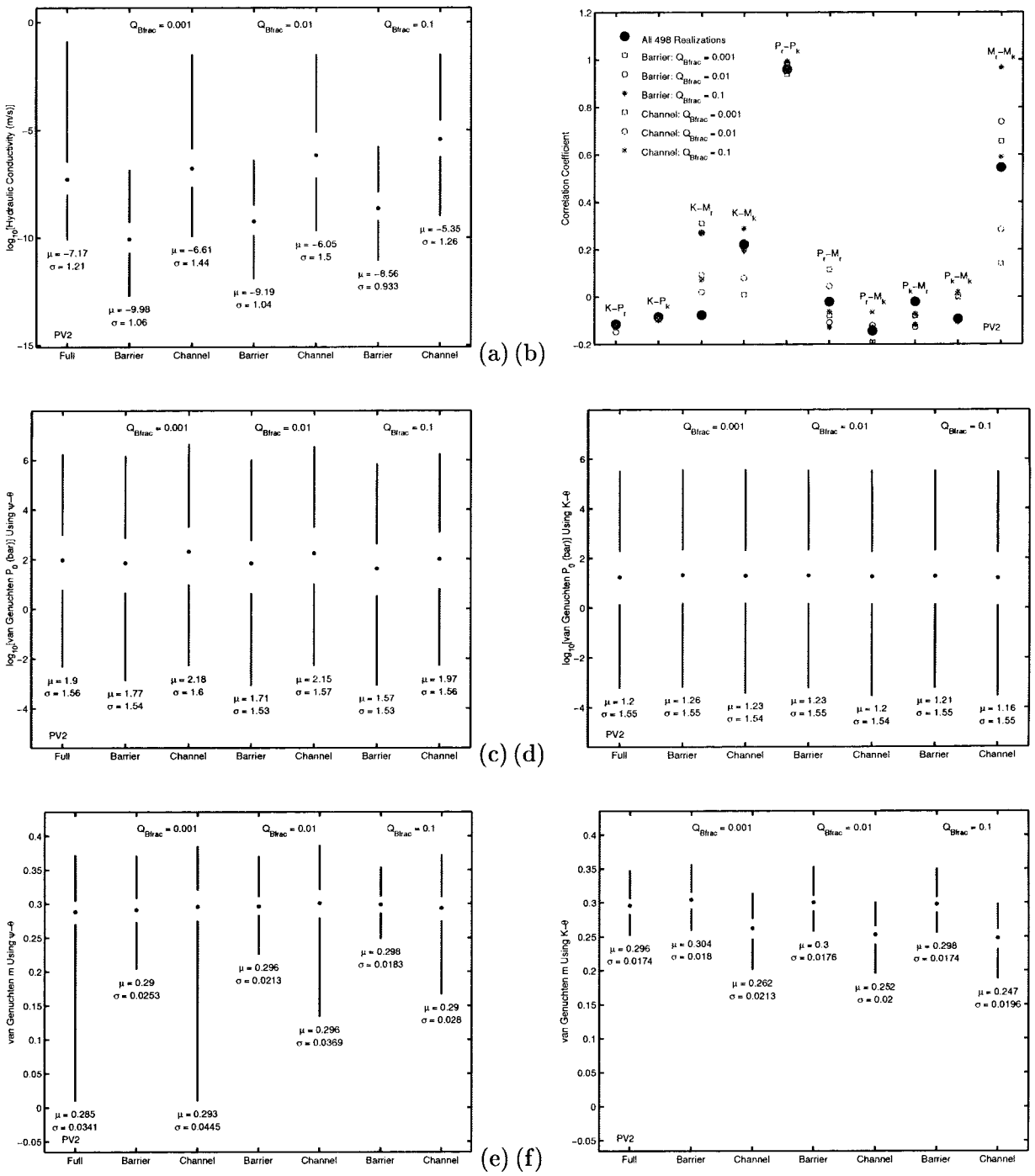

Figure 2-101: 10/28/97. Estimated properties for layer PV2. Correlation between material properties (b), and quartiles for: (a) equivalent K_{sat}, P_0 using retention and conductivity (c and d, respectively); and m using retention and conductivity (e and f, respectively).

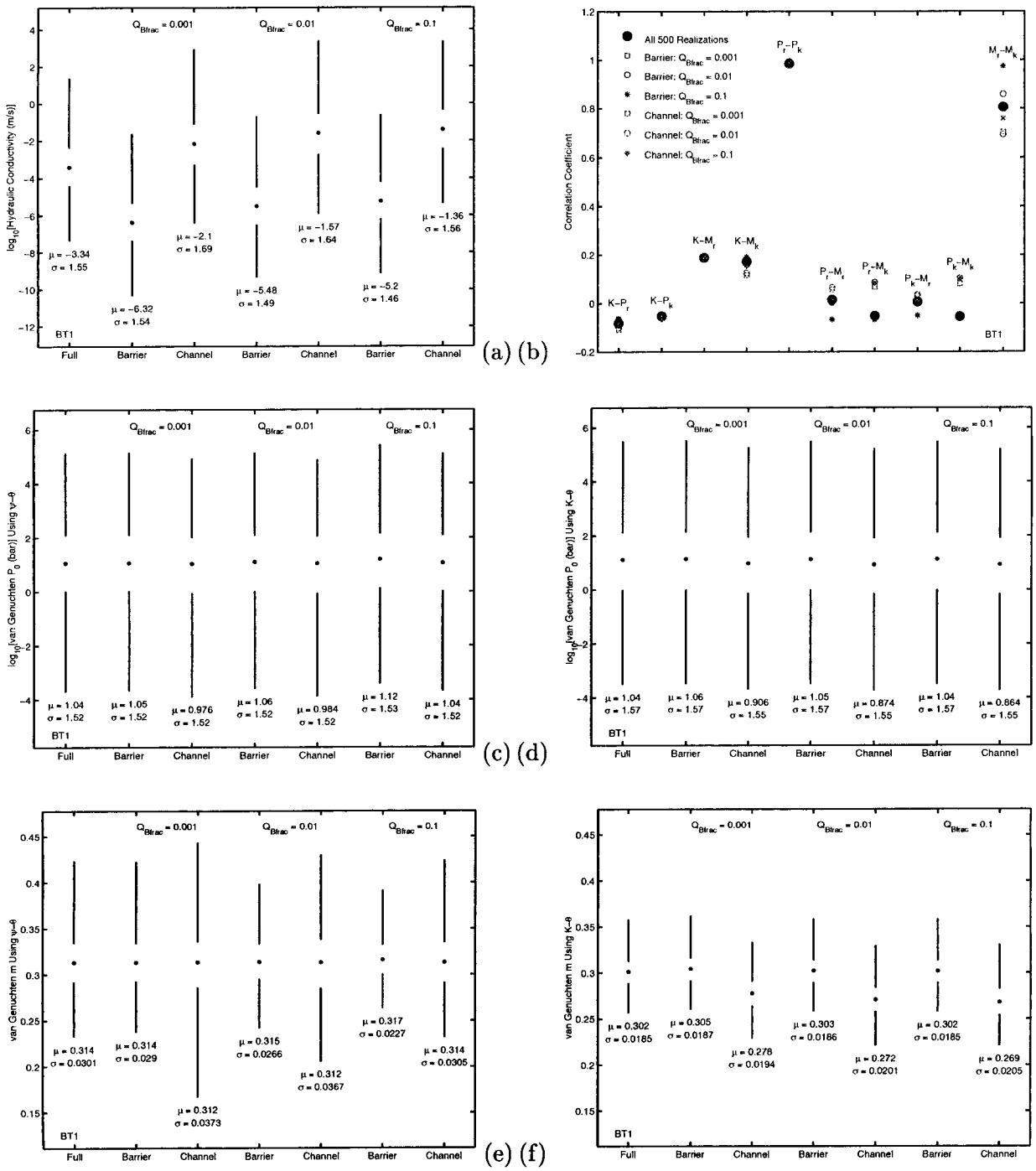

Figure 2-102: 10/28/97. Estimated properties for layer BT1. Correlation between material properties (b), and quartiles for: (a) equivalent K_{sat}, P_0 using retention and conductivity (c and d, respectively); and m using retention and conductivity (e and f, respectively).

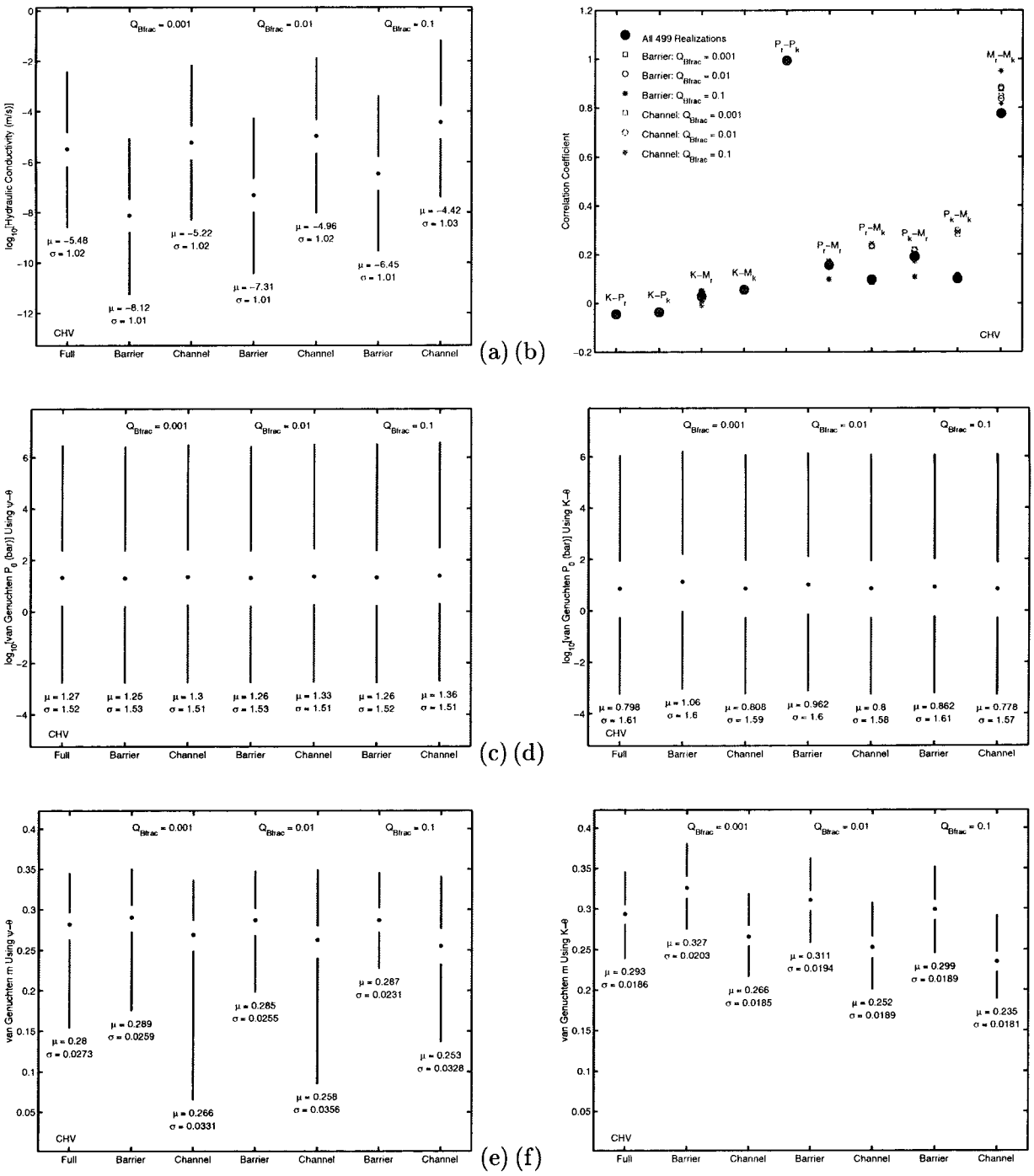

Figure 2-103: 10/28/97. Estimated properties for layer CHV. Correlation between material properties (b), and quartiles for: (a) equivalent K_{sat}, P_0 using retention and conductivity (c and d, respectively); and m using retention and conductivity (e and f, respectively).

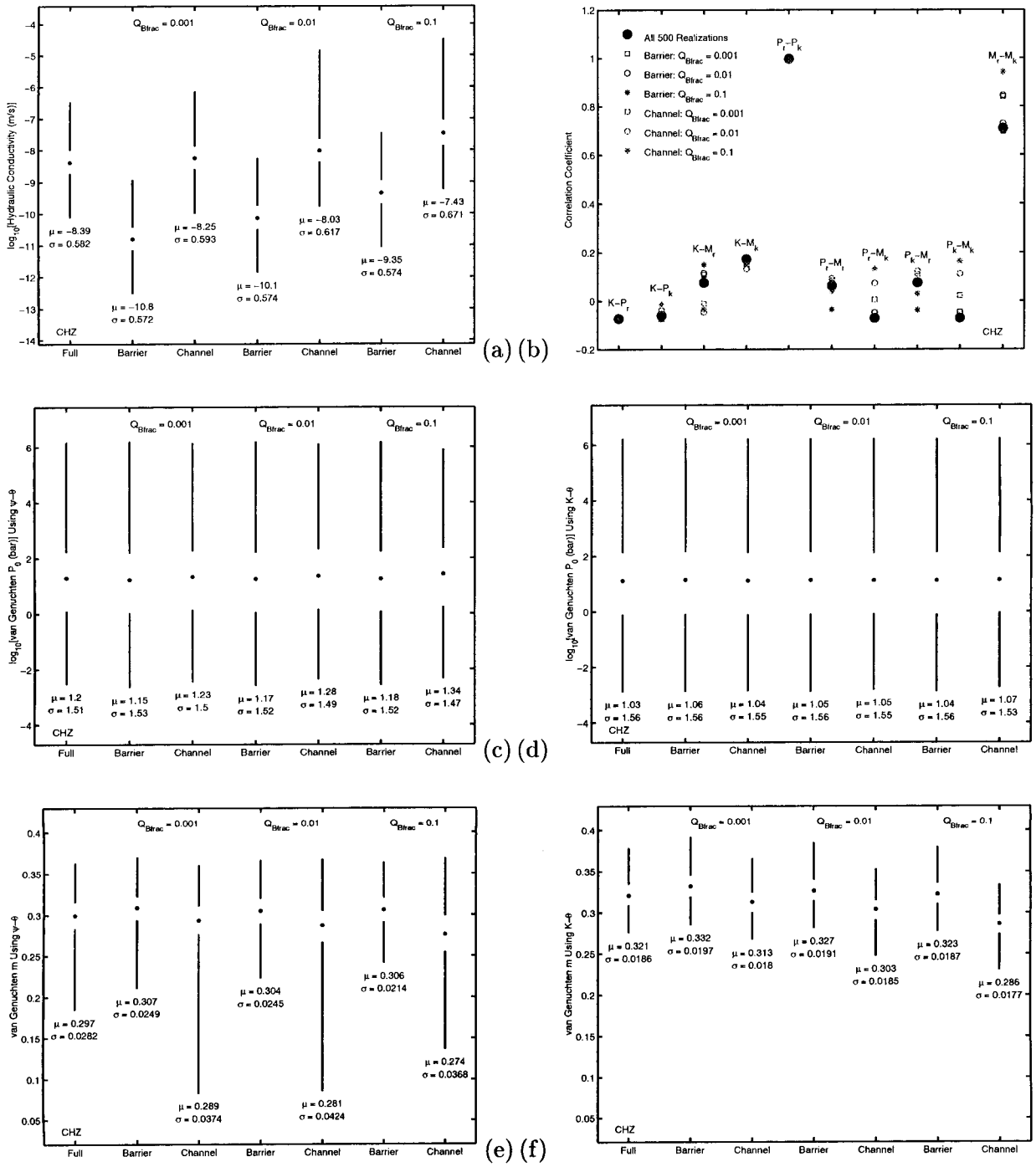

Figure 2-104: 10/28/97. Estimated properties for layer CHZ. Correlation between material properties (b), and quartiles for: (a) equivalent K_{sat}, P_0 using retention and conductivity (c and d, respectively); and m using retention and conductivity (e and f, respectively).